Universidade do Minho
Escola de Engenharia

Inês Gonçalves Costa

Prestressed Carbon Fibre laminates applied according to Near Surface Mounted technique to increase the flexural resistance of Reinforced Concrete beams

janeiro de 2014

Universidade do Minho
Escola de Engenharia

Inês Gonçalves Costa

Prestressed Carbon Fibre laminates applied according to Near Surface Mounted technique to increase the flexural resistance of Reinforced Concrete beams

Tese de Doutoramento
Engenharia Civil

Trabalho efectuado sob a orientação do
Professor Doutor Joaquim António Oliveira de Barros

janeiro de 2014

ACKNOWLEDGMENTS

The present work was developed at the University of Minho under the supervision of Professor Joaquim Barros. I would like to express my deepest gratitude to all institutions and individuals who made this research project possible, namely:

- The financial support provided by the Portuguese Foundation for the Science and Technology (FCT), grant number SFRH/BD/61756/2009;

- University of Minho, through the Institute for Sustainability and Innovation in Structural Engineering and the Department of Civil Engineering (DEC), for providing the facilities and resources to develop this project;

- Professor Joaquim Barros for his support, encouragement, enthusiasm, and especially for giving me intellectual freedom in my work and for making me grow as a researcher;

- To all my family, colleagues and friends that, directly or indirectly, contributed to the development of this work.

ABSTRACT

A new technique for the flexural strengthening of reinforced concrete (RC) beams is investigated in this work, which consists of bonding prestressed carbon fibre reinforced polymer (CFRP) laminates into slits open on the concrete cover (near surface mounted technique - NSM). According to the conducted literature review, prestressed FRP systems for the flexural strengthening of RC elements have already been applied successfully using the externally bonded reinforcing technique (EBR). In the context of prestressed EBR, significant improvements are reported in RC elements in service conditions, such as increase of the load carrying capacity, durability and structural integrity. The NSM technique is, however, more effective for the flexural strengthening of RC elements than EBR. Therefore, the research carried out aims to combine the intrinsic benefits of using NSM-CFRP with those derived from the application of prestressed EBR-CFRP. In this scope, the conducted research has covered a variety of topics, considered to be the most relevant to allow a thorough analysis of the effectiveness of this technique.

As the literature review suggests that the long-term effects of prestressing RC elements can be negatively influenced by the compliance of the used adhesive, an experimental program was carried out to determine the long term behaviour of the epoxy-based adhesive adopted in the strengthening operations. In the course of this work, three series of RC beams flexurally strengthened in flexure with NSM-CFRP laminates were produced, monitored and tested up to failure, and the obtained results are herein presented and discussed.

All prestressed RC beams were monitored during prestress release, as well as for approximately 40 days after prestress transfer, to assess the evolution of the strain loss along the CFRP laminate. The results showed that the greatest losses of prestress are located near the free-ends of the laminate, while in the central zone of the RC beams the prestress load was preserved over time. Finally, all the RC beams were tested up to failure, and showed that the prestressed NSM-CFRPs are not capable of increasing the ultimate load carrying capacity of the RC beams (in relation to non-prestressed NSM-CFRPs), but significant benefits in terms of service load carrying capacity were obtained. Despite the observed benefits, the application of prestress resulted in a significant loss of ductility of the RC beam.

After the concluding of all the experimental tests, all stages of the prestressing process were modelled numerically, and in all cases a high level of agreement with the experimental results was observed. Based on these results, as well as in the physical concepts behind the numerical formulations, an analytical approach is proposed to assess both the evolution of the CFRP strain profile over time, as well as the load-deflection relationship of the strengthened RC beams.

RESUMO

Uma nova técnica para o reforço à flexão de vigas de betão armado (BA), que consiste na aplicação de laminados de carbono (CFRP na nomenclatura inglesa) pré-esforçados colados em entalhes abertos no betão de recobrimento (NSM na nomenclatura inglesa), foi investigada neste trabalho. De acordo com a revisão da bibliográfica efetuada, os sistemas de FRP pré-esforçados já foram aplicados com sucesso usando a técnica de colagem externa (EBR na nomenclatura inglesa). No contexto do EBR pré-esforçado, melhorias significativas em elementos de BA sob condições de serviço são relatadas, tais como aumento da capacidade de carga, da durabilidade e da integridade estrutural. A técnica NSM é, no entanto, mais eficaz para o reforço à flexão de elementos de BA que a técnica EBR. Sendo assim, a investigação levada a cabo tem o intuito de combinar os benefícios intrínsecos da utilização de CFRP-NSM com os decorrentes da aplicação de CFRP-EBR pré-esforçado. Neste âmbito, a investigação realizada abrange uma variedade de tópicos, considerados os mais relevantes para permitir uma análise aprofundada da eficácia desta técnica.

Como a revisão da literatura sugere que os efeitos a longo prazo dos elementos de BA pré-esforçados com FRP podem ser influenciados negativamente pela deformabilidade ao longo do tempo do adesivo utilizado, foi realizado um programa experimental para determinar o comportamento diferido do adesivo epóxido usado nas operações de reforço. No decorrer deste trabalho, três séries de vigas de BA reforçadas com laminados de CFRP-NSM pré-esforçados foram produzidas, monitorizadas e testadas até à rotura, e os resultados obtidos são aqui apresentados e discutidos.

Todas as vigas de BA pré-esforçadas foram monitorizadas durante a libertação do pré-esforco, bem como durante cerca de 40 dias após transferência do pré-esforço, para avaliar a evolução da perda de extensão ao longo do laminado de CFRP. Os resultados mostraram que as maiores perdas de pré-esforço estão localizadas perto das extremidades livres do laminado, enquanto na zona central das vigas de BA a tensão de pré-esforço foi preservada ao longo do tempo. Finalmente, todas as vigas de BA foram testadas até à rotura, mostrando que os laminados CFRP-NSM pré-esforçados não são capazes de aumentar capacidade resistente última das vigas de BA (em relação aos laminados CFRP-NSM passivos), mas benefícios significativos foram obtidos em termos de resistência em condições de serviço. Apesar dos benefícios observados, a aplicação de pré-esforço resultou numa perda significativa de ductilidade da viga de BA.

Após a conclusão de todos os ensaios experimentais, todas as etapas do processo de pré-esforço foram modeladas numericamente e em todos os casos foi observado um elevado grau de concordância com os resultados experimentais. Com base nestes resultados, bem como nos conceitos físicos subjacentes às formulações numéricas, é proposta uma abordagem de cálculo analítica para avaliar tanto a evolução do perfil de extensões no CFRP ao longo do tempo, bem como a relação força-flecha das vigas de betão armado reforçadas segundo a técnica desenvolvida no presente trabalho.

TABLE OF CONTENTS

LIST OF FIGURES

LIST OF TABLES

Chapter 1

INTRODUCTION

1.1 MOTIVATION

Fibre Reinforced Polymer (FRP) materials are nowadays being proposed to strengthen Reinforced Concrete (RC) elements as a viable alternative to other traditional strengthening solutions, such as section enlargement or external plate bonding. FRPs are recognized to present several noteworthy characteristics such as low weight, high tensile strength, durability, and are resistant to corrosion. In the past decades, these materials have been object of extensive research in order to propose strengthening systems that can take full advantage of their high performance.

Presently, in the scope of flexural strengthening of RC beams, one the most efficient FRP-based strengthening techniques is the Near Surface Mounted (NSM), which consists on bonding the FRP material (a laminate or a rod) into a groove open on the concrete cover. This strengthening strategy is especially suitable when a significant increase of load carrying capacity is required with minimum duration of strengthening operations and minimal esthetical impact. In terms of efficacy, FRPs have already demonstrated their ability to significantly increase the load carrying capacity of RC elements.

In recent years, the possibility of using prestressed NSM-FRPs is being explored by several researchers, since supplementary benefits in relation to passive NSM-FRP can be obtained, such as closure of existing cracks, retardation of the appearance of new fissures, resulting in benefits in terms of structural integrity and concrete durability. Moreover, prestressing is known to

significantly improve the load carrying capacity at deflection levels corresponding to the serviceability limit states.

However, the research on RC elements strengthened with prestressed NSM-FRP is still in its developing stage and much more investigation needs to be carried out. One of the essential topics that has not yet received substantial attention is related to the assessment of the long term losses of prestress inherit to this technology.

1.2 OBJECTIVES

The aim of the research reported in this thesis is the evaluation of the effectiveness of prestressed NSM-CFRP laminates in the context of the flexural strengthening of RC beams. This research is especially dedicated to evaluate and quantify three of most relevant aspects associated to this strengthening system:

- the instantaneous prestress losses,
- the long term prestress losses,
- the effectiveness of the proposed technique in terms of load carrying capacity and deflection, particularly at the serviceability limit state.

Three series of RC beams strengthened in flexure with NSM-CFRP laminates were produced, monitored, and tested up to failure, and the obtained results are herein presented and discussed. The numerical modelling of all the beams composing the experimental program is also presented and analysed. Additionally, an analytical approach aiming to quantify the prestress losses associated with this technology is proposed. Moreover, the applicability of the cross section design approach defined in Eurocode 2 for the case of prestressed NSM-CFRP strengthened elements is also appraised.

It is expected that this research work will constitute a valuable contribution for the definition of design codes dealing with RC elements strengthened with prestressed FRPs.

1.3 STRUCTURE OF THE THESIS

Besides the chapters of Introduction and Conclusions, this thesis comprises six other chapters related to the main stages of this research work.

- Literature Review

In this chapter, the results of a profound analysis of several scientific research works dealing with structural strengthening with FRP materials are presented and analysed. The most relevant experimental research programs aiming to evaluate the long term performance of composite materials in general are also presented.

- Adhesive characterization

This chapter reports the characterization of the instantaneous and long term behaviour of the epoxy adhesive used in the prestress applications, as well as the assessment of the CFRP-adhesive-concrete bond performance. Additionally, this chapter includes a section dedicated to the modelling of the tensile creep of the epoxy adhesive.

- Prestress application

The results of prestress application to 10 reinforced concrete beams are reported in this chapter. The monitoring results prior to, and during prestress transfer are presented and discussed. The strain loss along the prestressed CFRP laminate is also reported, and the adopted process to remove the strain variations resulting from environmental effects is detailed.

- Failure tests on prestressed beams

In Chapter 5, 16 reinforced concrete beams were loaded up to failure in a four-point bending configuration. The benefits and weaknesses resulting from prestress application observed in the failure tests of these beams are presented and discussed.

- Numerical Models

All the stages associated with prestress application (instantaneous and long term effects) as well as the effectiveness of the strengthening system were modelled, and the obtained results are presented and discussed.

- Analytical Models

A comprehensive analytical approach, corresponding to the stages modelled in the previous chapter, is proposed, and its predictive performance is assessed.

Chapter 2

LITERATURE REVIEW

In this Chapter a careful analysis of relevant experimental and numerical works available in literature, dealing with FRP systems for structural strengthening, was performed. This literature review is divided in the following four main topics:

- Structural strengthening with fibre reinforced polymers materials, including the main advantages and limitations of this type of reinforcements and a summarized analysis of the existing strengthening techniques for application;
- Strengthening with prestressed fibre reinforced polymers, where some of the most significant investigations on this topic are presented and compared;
- Long term properties of fibre reinforced polymers systems, where the long term behaviour of the intervening composite materials is evaluated to assess which are expected to be most relevant for the loss of prestress during the structure's life and
- Creep of epoxy-based adhesives, which during this literature review was systematically suggested to be the most relevant effect on the long-term performance of prestressed FRP structures.

2.1 STRENGTHENING WITH FIBRE REINFORCED POLYMERS

Over the years, several strengthening techniques using fibre reinforced polymers (FRP) have been investigated and developed. In some countries, the use of these materials is already well accepted as is the case of Europe, North America and Japan where several structures have already been successfully built with composite bars (ACI 440R-96). However, the use of composite materials is

not limited to the simple substitution of steel by composite bars, but can also be used in repair, rehabilitation and retrofitting operations. By 1996, the ACI report (ACI 440R-96) already reported several examples of strengthening of concrete structures with FRP. Lately, several research works can be found in literature dealing with these composite materials bonded on reinforced concrete structures (Bakis *et al.* 2002), as well as on masonry (Shrive 2006), timber (Yeoh *et al.* 2011) and steel elements (Hollaway & Cadei 2002, Zhao & Zhang 2007).

Like any other material, Fibre Reinforced Polymers (FRPs) have advantages and disadvantages associated with their use. On the positive side, FRPs exhibit low weight, high tensile strength and modulus, durability, electromagnetic permeability and are corrosion free (ACI 440R-96). On the other hand, the performance of these materials can decrease significantly by the action of freeze/thaw cycles, as well as by the exposure to high and low temperatures, and may be vulnerable to vandalism acts (Barros *et al.* 2007).

There are nowadays several techniques that rely on the use of composite materials to restore and improve the load carrying capacity of reinforced concrete columns, beams and slabs. Columns are in general strengthened by confining the cross section with FRP sheets, capable of wrapping around the element, forming a continuous (full wrapping) or discrete (strips) an external jacket that restrains the element's dilation, as schematized in Figure 1 (Lopez-Anido and Naike 2000). This external strengthening is commonly known as EBR (Externally Bonded Reinforcement), and has shown to be capable of increasing both the load carrying capacity and the ductility of the RC columns (*fib* 2001).

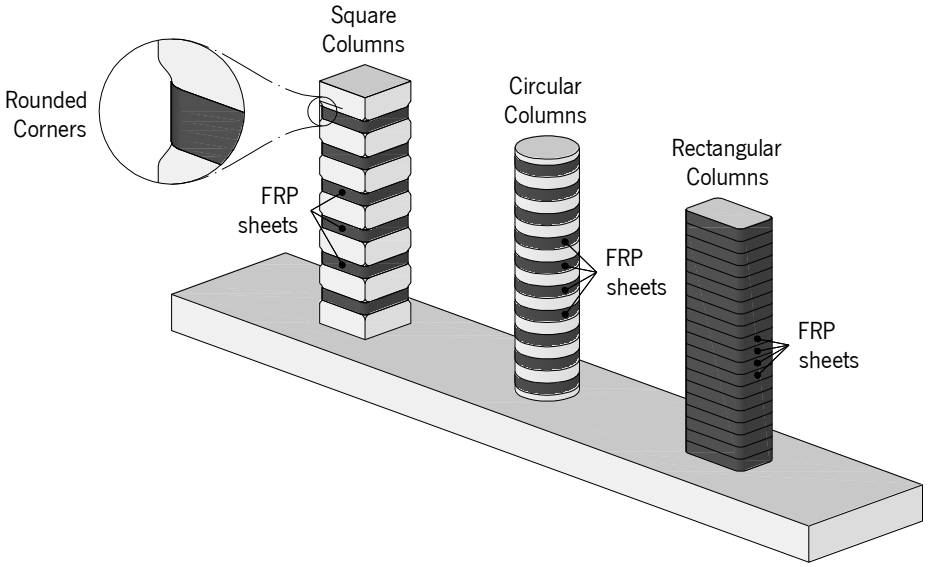

Figure 1 – Representation of column discrete and continuous confinement with FRP sheets.

The EBR technique can also be applied to beams and slabs to improve their flexural load carrying capacity, either in the form of FRP sheets or laminates (illustrated in Figures 2 and 3), and is an effective process to increase the cracking propagation resistance of the elements, and to increase stiffness after cracking initiation (Wight *et al.* 2001, El-Hacha *et al.* 2003 e Barros & Fortes 2005). The shear capacity of reinforced concrete beams can also be increased by wrapping their cross section continuously or with discrete strips, using U configuration (in the lateral faces and the soffit of the beam) in the continuous or strip configuration, or just by gluing the FRP systems in the lateral faces of the beam using the same continuous or strip arrangement.

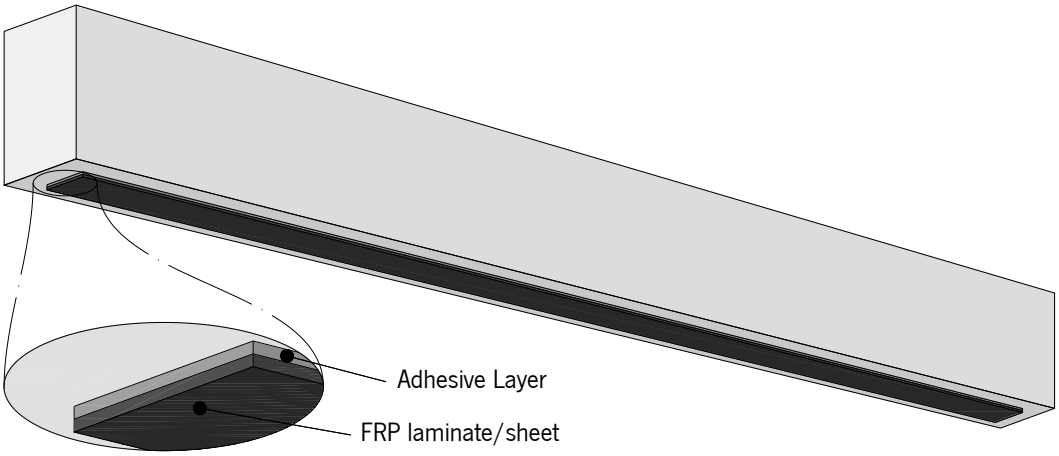

Figure 2 – Representation of the flexural strengthening of beams with EBR-FRP sheets/laminates.

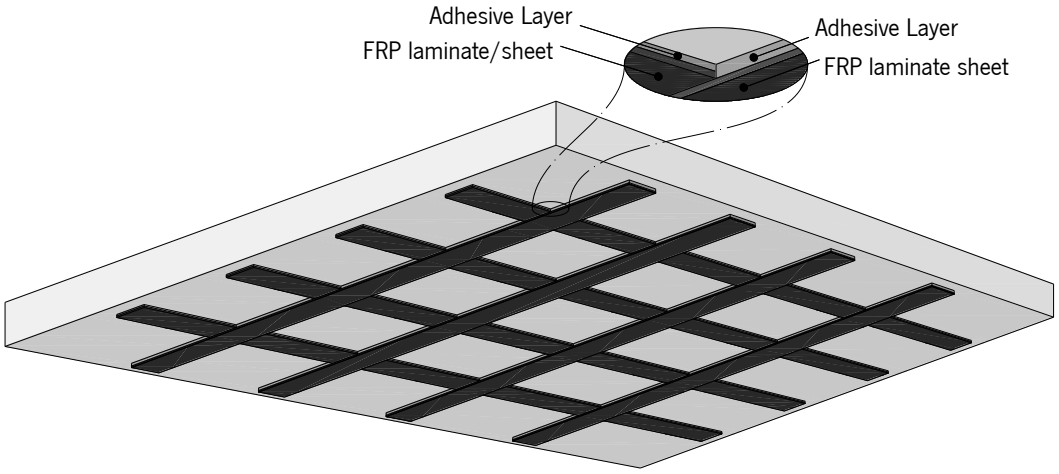

Figure 3 – Representation of the flexural strengthening of slabs with EBR-FRP sheets/laminates.

Unfortunately, the EBR technique is known to be disadvantageous in some circumstances, particularly when these composite reinforcements are directly exposed to UV incidence for long periods, causing the reinforcement to gradually lose its properties and when a high level of stress is installed in the FRP reinforcement, since they can debond prematurely without achieving the full capacity of the FRP. In order to circumvent these limitations, a similar technique was developed:

the Near Surface Mounted (NSM). This technique consists on bonding the FRP material (a laminate or a rod) in a groove made on the concrete cover, limiting the region exposed to UV radiation, and also increasing the area in contact with the concrete and, therefore, diminishing the chances of premature debonding (Figure 4).

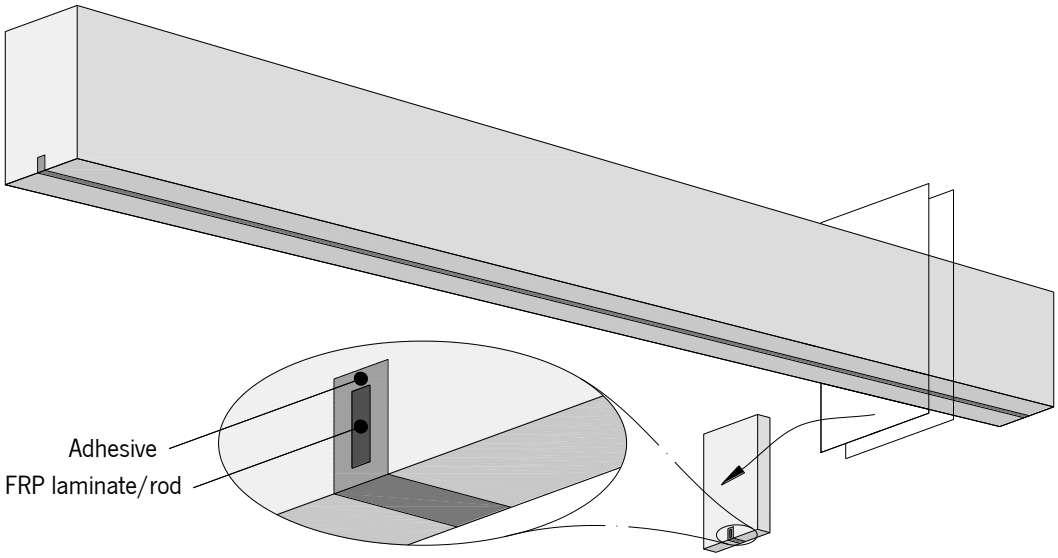

Figure 4 – Representation of the flexural strengthening of beams with NSM-FRP laminates/rods.

Tests on simply supported RC members strengthened with NSM laminates carried out at the University of Minho (Barros & Fortes 2005, Barros *et al.* 2007 Bonaldo *et al.* 2008, Dalfré & Barros 2013) have shown that NSM laminates debond or fail, in fact, at much higher strain than EBR strengthening systems. Using NSM, premature debonding is no longer the predominant failure mode. The delamination of the concrete cover is the most current failure mode (also designated by concrete cover rip-off failure mode – Barros *et al.* 2011) when using NSM technique.

Due to the characteristics of the application of NSM technique, it seems to be specially adjusted to increase the resistant negative bending moments of continuous RC elements (Dalfré & Barros 2013). Indeed, the opening process of the slits can be easily executed in the hogging regions (in the zones of the negative bending moments) by conventional equipment used to open the crack control joints in flooring applications.

In 2007, a comprehensive experimental program was carried out by Barros *et al.* from which it was concluded that the capacity to increase the load carrying capacity of reinforced concrete beams is limited by the existing steel reinforcement since the higher it is, the lower seems to be the potential of the FRP to improve the load carrying capacity of the member. Other researches were also carried

out in this topic in other laboratories, and the benefits of the NSM technique observed at University of Minho were also pointed out (Jung *et al.* 2005, Seracino *et al.* 2007, Bilotta *et al.* 2011 and Sena-Cruz *et al.* 2012).

Identical to the shear strengthening using the EBR technique, illustrated in Figure 5, the NSM reinforcement can also be used to improve the shear capacity of reinforced concrete beams. As none of these techniques is capable of upgrading the shear/punching resistance of concrete slabs, recently, another method of strengthening capable of meeting this goal, designated as Embedded Through-Section (ETS, represented in Figure 6), has been investigated with significant success (Chaallal *et al.* 2011, Mofidi *et al.* 2012 and Barros & Dalfré 2013).

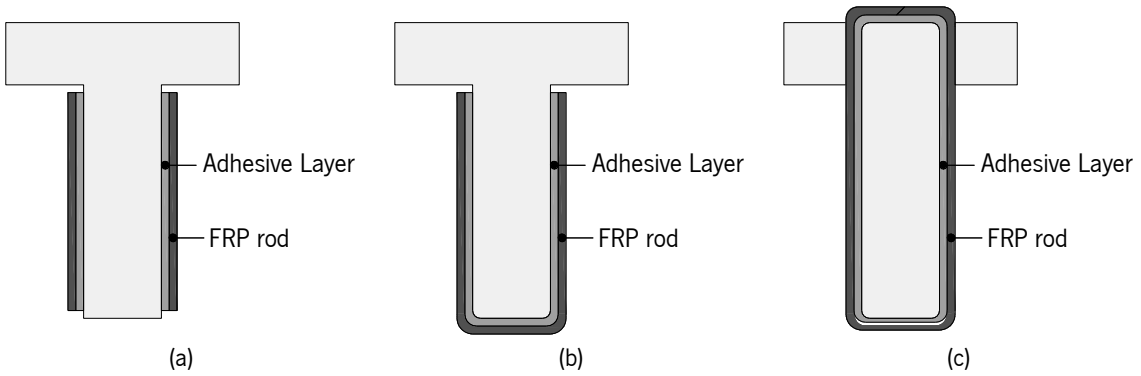

Figure 5 – Externally bonded shear strengthening (adapted from CNR-DT 2004 and *fib* 2001): (a) side bonding, (b) U-wrapped and (c) fully-wrapped.

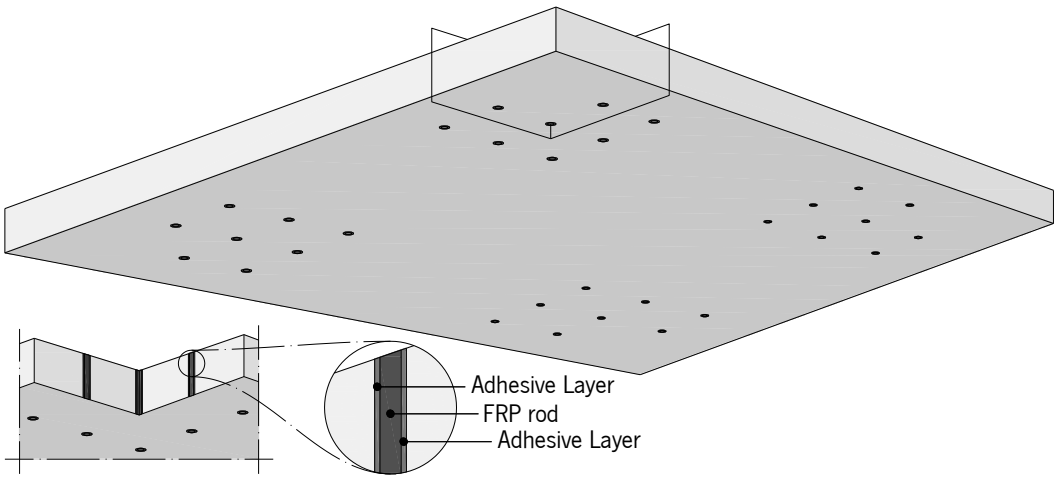

Figure 6 – Representation of the external aspect of a slab strengthened with ETS bars.

2.2 STRENGTHENING WITH PRESTRESSED FIBRE REINFORCED POLYMERS

Prestressed concrete is a building technology developed to take advantage of the superior capacity of the concrete under compression to create a material that is robust both under tension and

compression. The prestressed tendons commonly used for this purpose, are made of high strength steel, and activated before applying any external loads. The elements built with using this technology allow the utilization of longer spans, thinner slabs and require fewer joints (Amato 2009).

In cases where environmental effects are a limitation for the use of prestressed steel reinforcement, namely due to corrosion and excessive crack widths (Amato 2009), composite materials can also be referred as a viable alternative. Since in general, while strengthening a structure, some actions such as the self-weight and at least a part of the service load cannot be completely removed prior to FRP application, the increment resulting from the strengthening operation may be not as significant as expected. Prestressed FRPs are therefore a reasonable alternative to boost even further the advantages of FRP strengthening (Motavalli *et al.* 2011).

Concerning the prestressed composite reinforcement, bibliographic research shows that limited investigation has been conducted in this scope. Similarly to non-prestressed FRP reinforcement presented in Section 2.1, prestressed FRPs can be used to reinforce columns, beams and slabs in order to improve their flexural and shear behaviour (Motavalli *et al.* 2011). Despite the reduced amount of research published in this topic, by 2002, Bakis *et al.* already reported the existence of 11 bridges built with pretensioned FRP-reinforced concrete girders and 10 with posttensioned girders. Some of these bridges include (Fam 1995):

- the pedestrian Lünen'sche Gasse, built in Düsseldorf in 1980 using unbonded prestressed Glass FRP (GFRP) bars;
- the Ulenbergstrasse Bridge (1986), the first road bridge using prestressed GFRP tendons built in Düsseldorf;
- the Calgary Beddington Trail Bridge, in Canada, inaugurated in 1993, built with pretensioned CFRP tendons;
- a demonstration bridge built in the early 90’s by Sumitomo Construction Company, in Japan, using posttensioned internal and external Aramid FRP (AFRP).

In most of the analysed works the authors (Wight *et al.* 2001, Nordin & Täljsten 2006, Gaafar & El-Hacha 2008) recognize that the use of prestressed FRP elements presents benefits of high significance, namely: the closure or reduction of the width of existing cracks and the retardation of the appearance of new fissures, resulting in benefits in terms of structural integrity and concrete durability. Other benefits are also reported such as: restitution of internal prestress lost by a structural member (Wight *et al.* 2001) or the decrease of the stress level in the existing steel reinforcement (Nordin & Täljsten 2006).

For some years now, three different methods of prestress application are recognized (Wight *et al.* 2001 and Wang *et al.* 2012):

- Indirect prestress (Figure 7a), by introducing an inverse curvature/camber on the element, followed by the application of ordinary FRP strengthening. Prestress is therefore attained when the mechanism inducing the negative curvature is removed;
- Direct tension on the reinforcement material in a stressing bed (Figure 7b). The tensioned material is transported afterwards to its final position and bonded in place;
- Direct tension on the reinforcement material in-place, using the RC member as reaction frame (Figure 7c).

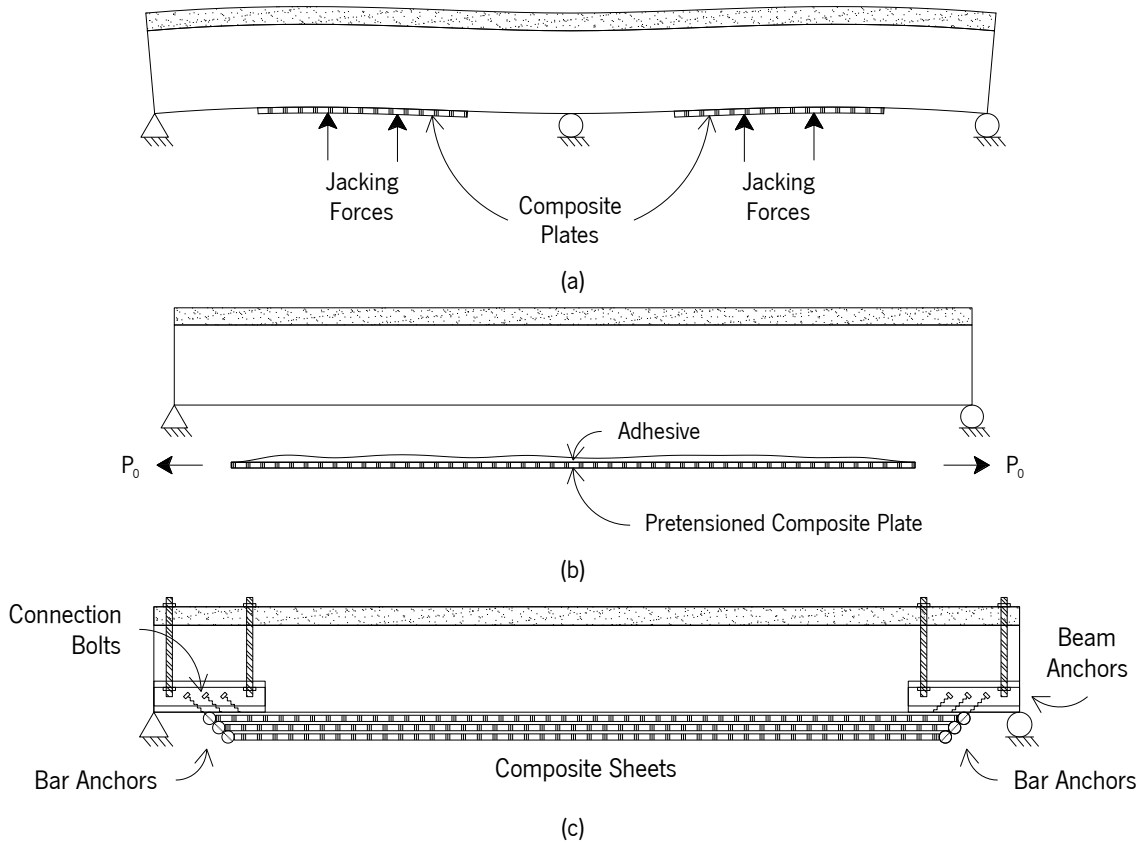

Figure 7 – EBR prestress strengthening systems reported on literature: (a) External prestressing of two-span continuous girder (Saadatmanesh & Ehsani 1991); (b) Schematic sketch of pretensioning arrangement (Deuring 1993 and Meier 1995); (c) FRP Prestressing System (Wight *et al.* 2001)

The first system, in which prestress is introduced indirectly by initially deforming the original structure, is not only impractical in most cases, but it also introduces a reduced amount of prestress in the element (Wang *et al.* 2012). Additionally, this technique can only be applied in the sagging regions of the reinforced concrete elements.

Experimental tests performed by Wight *et al.* (2001), using the third system above-mentioned, proved that EBR-based prestress techniques increase significantly the load carrying capacity of simply supported RC elements at Serviceability Limit States (SLS). Additionally, prestressed FRPs can recover part of the installed permanent deformation (Gaafar & El-Hacha 2008), which is of major importance to increase concrete durability and structural integrity since, as already mentioned, it can reduce the width or even close existing cracks.

Nevertheless, as previously revealed for the case of passive FRP strengthening, NSM-based prestress technique can probably be even more effective than EBR-based (Nordin & Täljsten 2006, Gaafar & El-Hacha 2008), since in general the serviceability limit conditions are only moderately improved by this last technique, and the end peeling of the FRP in the anchorage zone is still the dominant failure mode.

Currently, there is few work reported in literature on NSM-based prestress technique that can actually be applied on job site. Most of the tested specimens were strenghtened in the sagging region, but the strengthening tasks were performed as if it was a hogging region (Nordin & Täljsten 2006, Barros *et al.* 2013) *i.e.*, the elements are initially turned over, strengthened, and finally turned over again to its original position in order to be tested. The scheme in which the hydraulic jacks are being placed (in line with the FRP and beyond the boundaries of the element) is impracticable in real cases. Only Gaafar & El-Hacha, (2008) claim to have a system that allows this technique to be applied in job-site, and Barros (2009) is currently refining the design of a system for the application of prestress to Carbon FRP (CFRP) laminates.

Some supplementary noteworthy observations were encountered in the course of this literature review. For example, Nordin & Täljsten (2006), using 10×10 mm^2 prestressed CFRP rods applied according to the NSM technique to strengthen 200×300×4000 mm^3 reinforced concrete beams realized that the applied stress was efficiently transferred to the surrounding concrete even without the use of any special device to anchor the CFRP. It is also worth mentioning that, analysing their results, the loss of ductility in relation to the non-prestressed beams (BS1 and BS2 in Table 1 and BM1 and BM2 in Table 2) was remarkable.

While in the series strengthened with a CFRP of 160 GPa elastic modulus (Table 1) the final deflection of the non-prestressed beam was about 50~55 mm, after the application of 20% of prestress it was reduced in 40% *i.e.*, 33 mm. The same observation can me made based on the results using a CFRP laminate of 250 GPa elastic modulus (Table 2) where the deformation of the

0% prestress beams ranged between 37~41 mm and the reduction observed by the application of 19% of prestress was nearly 30%.

Table 1 - Summary of the experimental results from Nordin & Täljsten (2006) using a CFRP of 160 GPa elastic modulus.

Beam	$\%f_{FRP}$	f_c	f_{ct}	$l_{b,frp}$	δ_{cr}	P_{cr}	δ_y	P_y	δ_u	P_u
	[MPa]	[MPa]	[MPa]	[MPa]	[mm]	[kN]	[mm]	[kN]	[mm]	[kN]
Reference	-	61	3.5	-	1.2	10	33	70	61	75
BS1	-	64	3.6	3200	2.0	14	22	90	50	123
BS2	-	62	3.5	4000	1.9	13	23	87	55	117
BPS1	10	68	3.8	4000	2.4	20	25	97	46	121
BPS2	10	68	3.8	4000	2.0	21	23	95	44	121
BPS3	12	66	3.6	3200	2.3	23	26	105	38	120
BPS4	12	64	3.5	4000	2.3	23	26	108	39	123
BPS5	20	67	3.7	3200	2.2	26	28	119	33	122
BPS6	20	67	3.7	4000	-	-	28	117	107	148

$\%f_{FRP}$ is the applied prestress level, expressed as a percentage of the CFRP tensile strength; f_c and f_{ct} are the concrete compressive and tensile strength; $l_{b,frp}$ is the length of CFRP bonded to the concrete beam; δ and P represent the mid-span deflection and applied load and the subscripts cr, y and u denote the previous quantities measured at crack initiation, yielding and failure, respectively.

Table 2 - Summary of the experimental results from Nordin & Täljsten (2006) using a CFRP of 250 GPa elastic modulus.

Beam	$\%f_{FRP}$	f_c	f_{ct}	$l_{b,frp}$	δ_{cr}	P_{cr}	δ_y	P_y	δ_u	P_u
	[MPa]	[MPa]	[MPa]	[MPa]	[mm]	[kN]	[mm]	[kN]	[mm]	[kN]
Reference	-	61	3.5	-	1.2	10	33	70	61	75
BM1	0	64	3.6	3200	1.8	11	28	105	41	122
BM2	0	65	3.6	4000	1.8	11	27	106	37	122
BPM1	16	63	3.5	3200	2.5	25	28	121	32	128
BPM2	16	62	3.5	4000	2.8	25	28	122	33	132
BPM3	27	65	3.6	3200	3.7	32	28	129	30	131
BPM4	19	66	3.7	4000	2.3	23	28	121	29	123

$\%f_{FRP}$ is the applied prestress level, expressed as a percentage of the CFRP tensile strength; f_c and f_{ct} are the concrete compressive and tensile strength; $l_{b,frp}$ is the length of CFRP bonded to the concrete beam; δ and P represent the mid-span deflection and applied load and the subscripts cr, y and u denote the previous quantities measured at crack initiation, yielding and failure, respectively.

Gaafar & El-Hacha (2008) reported the tests performed on 200×400×5150 mm^3 reinforced concrete beams prestressed with 2 NSM strips of 2×16 mm^2, and verified a considerable increase of the load at cracking and yielding initiation. This increase was, however, followed by a significant reduction of the ductility, since the deflection at failure was dramatically decreased (60% of prestress

conducted to failure at a deflection level of approximately 50% of the deflection observed in the non-prestressed beam).

Table 3 - Summary of the experimental results from Gaafar & El-Hacha (2008).

Beam / Prestress Level	f_c [MPa]	δ_{cr} [mm]	P_{cr} [kN]	δ_y [mm]	P_y [kN]	δ_u [mm]	P_u [kN]
Reference	46	1.1	11	29.0	78	152	84
0%	46	1.6	16	27.6	92	118	135
20%	43	1.2	22	27.0	106	103	148
40%	40	1.1	30	26.3	112	77	149
60%	40	2.6	42	26.8	126	58	149

f_c is average concrete compressive strength; δ and P represent the mid-span deflection and applied load and the subscripts cr, y and u denote the previous quantities measured at crack initiation, yielding and failure, respectively.

Unlike the experimental programs previously presented in which the beams were monotonically loaded up to failure, Badawi & Soudki (2008) performed cyclic tests on beams strengthened with prestressed NSM-FRPs up to 40% and 60% of their ultimate capacity. According to the obtained results, the application of prestress increased the fatigue capacity of the original reinforced concrete beams. Failure was essentially dominated by the rupture of the tensile reinforcement, mainly due to the accumulation of slippage between CFRP and adhesive that caused an increase of the average stress installed on the steel bars.

Presently, several authors have been suggesting that, although the load carrying capacity and deformational behaviour of this type of prestressed elements could be easily quantified by conventional methods, such as section analysis or finite elements analysis, the understanding on the long term losses inherit to this technology is still limited (Quantrill & Hollaway 1997, Nordin & Täljsten 2006, Wang *et al.* 2012). In fact, several works are being presented aiming the quantification of the creep effects associated to FRP strengthening, mostly addressing the behaviour of EBR (Diab & Wu 2007, Wu & Diab 2007 and Meaud *et al.* 2011). However, none of them separates the contribution related to each of the materials to comprehend the relative significance of the materials involved.

2.3 LONG TERM PROPERTIES OF FIBRE REINFORCED POLYMERS SYSTEMS

Several authors have already mentioned in their works that the creep of the adhesive plays an important role on the long term behaviour composite system (Quantrill & Hollaway 1997, Nordin & Täljsten 2006, Wang *et al.* 2012). In reality, regarding the long term performance of the

composite system, few authors have dedicated their efforts to the assessment of the performance each intervening materials (Diab & Wu 2007, Wu & Diab 2007 and Meaud *et al.* 2011).

Apart from changes in applied external actions, the long term performance of a CFRP-adhesive-concrete system is only expected to be affected by the creep, shrinkage or relaxation of each of the components of the system. While the creep and shrinkage of concrete have already been comprehensively studied over the years, limited information is available regarding the creep/shrinkage/relaxation of composite materials.

2.3.1 FRP relaxation

Bibliographic research has shown that FRPs are known to present low prestress losses, as a result of their relatively low elastic modulus (Lopez-Anido & Naike 2000), and lower stress relaxation than steel strands (Dolan *et al.* 2001 and Sayed-Ahmed 2002). In fact, even though FRP materials are able of exhibiting an elastic modulus close to 200 GPa, most of the materials available reveal to have an average maximum stiffness of about 160 GPa. As Figure 8 shows, a high elastic modulus can be interpreted either as a disadvantage or an advantage since for higher elastic moduli the tensile stress mobilized is greater, but the pre-stress loss is also larger.

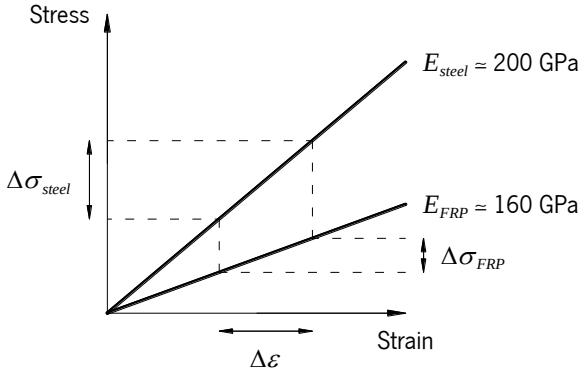

Figure 8 – Stress relaxation comparison between steel and FRP.

Nevertheless, Wang *et al.* (2012) carried out relaxation tests in CFRP sheets and concluded that the relaxation loss due to sustained deformation levels ranging between 40% and 56% of the material's tensile strength was determined to be 2.2% to 6.6%, as demonstrated in Figure 9. Moreover, this relaxation was mostly concentrated in the first 100 hours of sustained deformation, as depicted in Figure 9 and, after this period it becomes almost negligible. These authors have even suggested that the measured relaxation measured is primarily caused by the relaxation of the resin and straightening of fibres. The carbon fibres themselves are identified as having no relaxation whatsoever (Dolan *et al.* 2001).

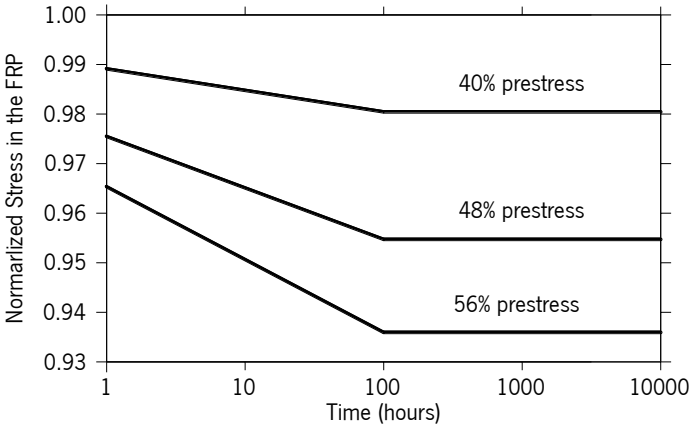

Figure 9 – Stress relaxation in CFRP sheets (adapted from Wang *et al.* 2012).

According to Dolan *et al.* (2001) the relaxation losses in FRP tendons can be caused by three main sources: the relaxation of resin which bonds the fibres together, the lack of parallelism between individual fibres and the relaxation of fibre itself. Due to these reasons, the relaxation is a characteristic attributable to the fibre type and is generally lower than 12% over the life of the structure. In the case of CFRP tendons, relaxation losses of approximately 5% are reported.

Based on these assumptions, it is suggested that FRP relaxation is not a relevant effect for the long-term performance of NSM-CFRP laminates. Since in FRP laminates the fibre content is particularly large when compared to FRP sheet coupons, the matrix bonding them together will take only a small portion of the applied load and therefore, the first source of relaxation may be ignored. Regarding the alignment of the fibres, since FRP laminates are produced by machines, in opposition to FRP sheets, which are manually applied, no significant eccentricities are expected along each fibre and as a result, the second source of relaxation may also be disregarded. Finally, as carbon fibres themselves are reported to have no relaxation, the total amount of relaxation expected is even more reduced.

2.3.2 Adhesive shrinkage

Of all the phenomena previously exposed, the adhesive shrinkage and creep are the two remaining effects to be evaluated in this strengthening system and they are usually not determined for the specific case of Civil Engineering applications. In the context of polymer science, where volumetric shrinkage is most commonly appraised, it is usually observed as a phenomenon related to the polymer chain movement and molecular rearrangement. In the liquid state the reorganization of the monomers is facilitated by the ability of these elements of flowing within the resin. However, after a certain stiffness level (gel time) has been achieved, this mobility is severely

reduced and therefore, the formation of the polymer chains causes the material to contract (Khoun & Hubert 2010). The volumetric shrinkage of epoxy-based adhesives is generally restricted to the shrinkage occurred during the curing process and is found to be within the range 2~7% (Li *et al.* 2004, Yu *et al.* 2005 and Khoun & Hubert 2010).

Concerning the epoxy-based adhesives used in structural applications they reveal such an insignificant shrinkage coefficient, that this parameter is often not even quantified in most materials' datasheets. However, when complete cure is achieved, the shrinkage coefficient variation becomes negligible, as suggested by Yu *et al.* (2005) and Khoun & Hubert (2010), and the long-term behaviour of the adhesive is no longer shrinkage dependent, but creep-dependent as it will be revealed hereafter.

2.3.3 Adhesive creep

Creep, which is usually defined as the increase of deformation of a material under sustained stress, is known to be a phenomenon of major importance when dealing with adhesives. The analysed specialized bibliography has, in general, revealed that the mechanical performance of adhesives changes in fact with time, mainly due to the applied stress and environmental exposure (mostly temperature and humidity) (Feng *et al.* 2005). Additionally, Dean (2007) has demonstrated that the creep deformation of epoxy adhesives is also sensible to small quantities of absorbed water and that, for creep times greater than one/two weeks, the progressive increase of absorbed water may influence the shape and parameters defining the creep curve.

Nonetheless, although little work was encountered dealing with this kind of phenomenon, the creep behaviour of plastics is already acknowledged by the scientific community and is, in general, usually fragmented in three major creep stages (ASTM 2990-01, Majda & Skrodzewicz 2009): primary creep, secondary creep and tertiary creep. As depicted in Figure 10, in the first phase the material adjusts its deformation level to the installed level of stress. This phase is followed by a stationary stage where creep gradually increases until a third phase is reached, where strain suddenly increases and fracture occurs. It is believed that this behaviour is valid under any applied stress, temperature and humidity. However, for low levels of applied stress, the time necessary to reach the tertiary creep state may be so long that it may never be achieved.

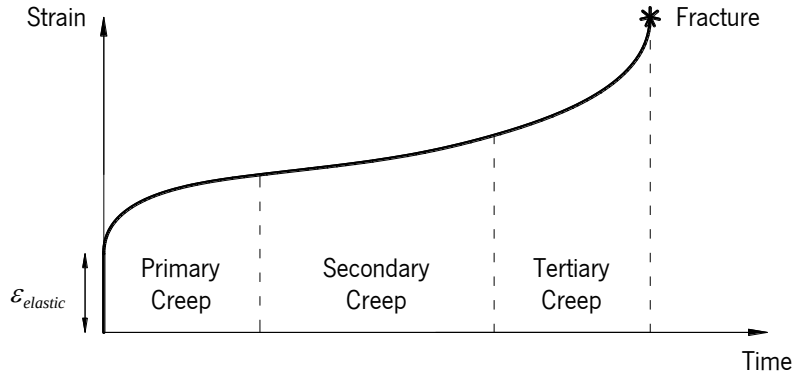

Figure 10 – The three stages of creep (at constant stress, temperature and humidity).

To fully understand the creep behaviour of adhesives, a careful bibliographic research was carried out focussed on the creep behaviour of epoxy-based materials. During this research it was found that the behaviour of plastic materials is frequently described by using classic rheological models that will be discussed in the next Section.

2.4 CREEP OF EPOXY-BASED ADHESIVES

The primary function of an adhesive in structural applications is to transmit stress equally over large areas without loss of integrity (Feng *et al.* 2005). Structural adhesives exhibit, however, notable viscoelastic behaviour, since their deformation, ε, under a constant stress, σ, varies significantly in time, as already mentioned. This behaviour is frequently modelled using rheological models and is usually illustrated by means of Hookean springs and Newtonian dashpots that replicate, respectively, the elastic and viscous components of the material's behaviour (Brinson & Brinson 2008). In Figures 11 to 13, the most common rheological models are presented:

- Maxwell Model – illustrated in Figure 11, this model is a 2-parameter model that results of associating, in series, a spring with E_M elasticity and a dashpot characterized by η_M dynamic viscosity;
- Kelvin Model – depicted in Figure 12, it is also a 2-parameter model that consists in combining, in parallel, a spring of elasticity E_K and a dashpot of η_K dynamic viscosity;
- Burgers Model – schematized in Figure 13, this 4-parameter model can be obtained by joining in series Maxwell and Kelvin's Model (E_M, η_M, E_K and η_K in Figure 13a) or, in alternative, by connecting two Maxwell models in parallel (E', η', E'' and η'' in Figure 13b).

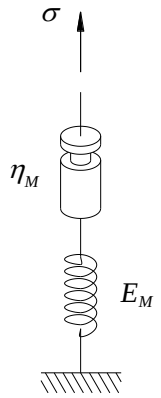

Figure 11 – Maxwell Model.

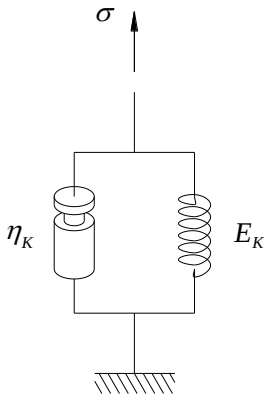

Figure 12 – Kelvin Model.

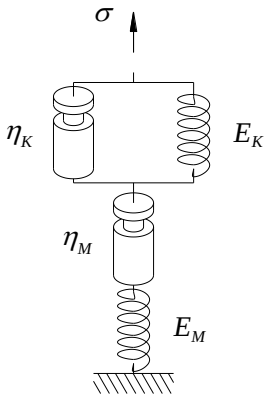

(a)

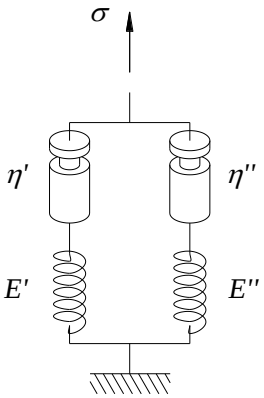

(b)

Figure 13 – Burgers model: (a) common configuration and (b) alternative configuration.

Although these models are the more recurrent in literature, there are several ways of combining springs and dashpots. In some cases, it is possible to create models like the generalized Maxwell Model or generalized Kelvin Model, depicted in Figures 14 and 15 (Brinson & Brinson 2008). In fact, Maekawa *et al.* (2011) have already modelled the long behaviour of concrete by using successions of rheological models to somehow isolate each of the effects disturbing the final deformational behaviour like temperature or environmental moisture.

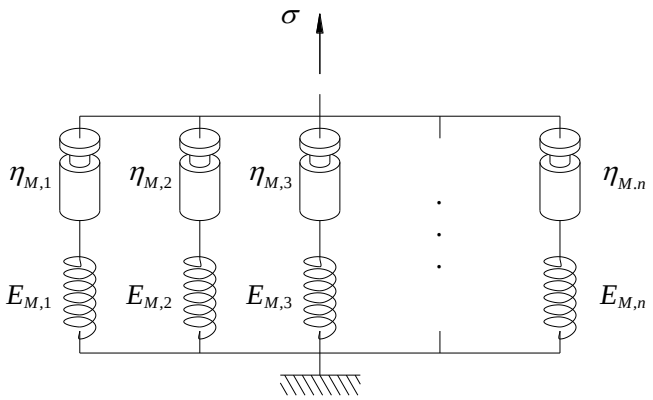

Figure 14 – Generalized Maxwell fluid.

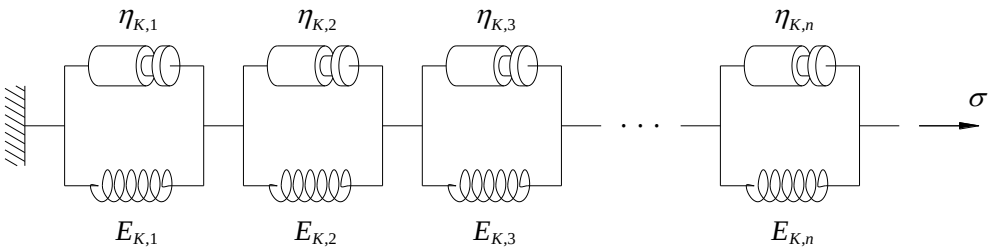

Figure 15 – Generalized Kelvin solid.

The components of these models, springs and dashpots, can exhibit virtually any behaviour, and depending on the choice of these curves, the final response of the system over time can be assessed. Since the consideration of linear elastic/viscous response (Figure 16) is usually able of producing exceptionally accurate results, the solution most frequently reported in literature is the one resulting from linear elastic springs and linear viscous dashpots.

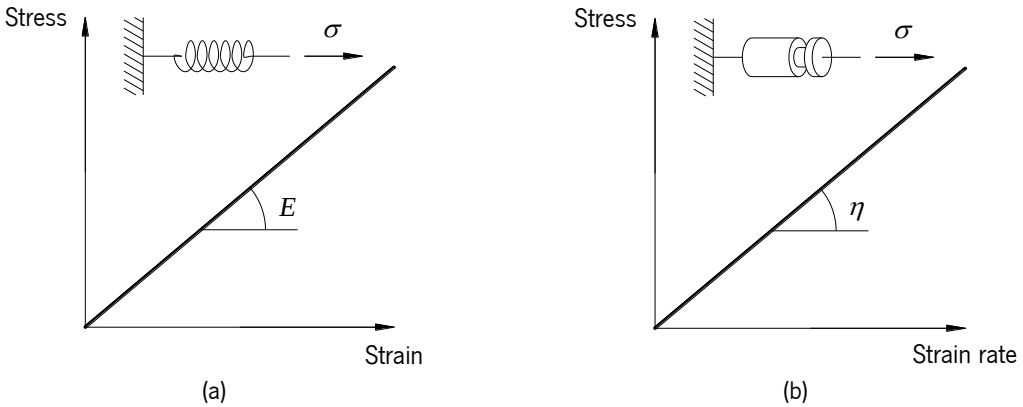

Figure 16 – Rheological elements with linear behaviour: (a) Hookean spring; (b) Newtonian dashpot.

It is relatively simple to obtain the solution of each of these models and, the deduction of each equation can be found in Annex A (from Costa & Barros 2011). Each of the classical models analysed presents different characteristics and the selection of the model to be used should be made by observing the material's behaviour.

When considering a constant applied stress, Maxwell's model describes strain as directly proportional to time (Eq. 1 and Figure 17). On the other hand, Kelvin's model (Eq. 2 and Figure 18) describes the behaviour of a material that is subjected to a constant stress as exhibiting a slow increase until a steady and constant deformation is achieved.

$$\varepsilon(t) = \frac{\sigma}{E_M} + \frac{\sigma}{\eta_M} t \tag{1}$$

$$\varepsilon(t) = \frac{\sigma}{E_K}\left(1 - e^{-\frac{E_K}{\eta_K}t}\right) \tag{2}$$

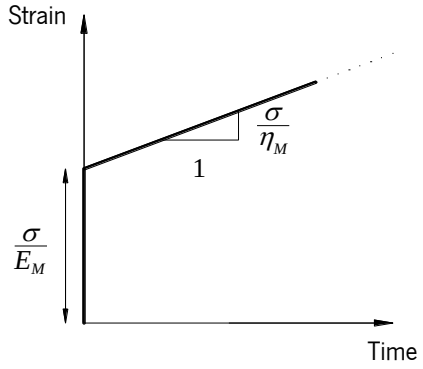

Figure 17 – Strain evolution in Maxwell Model.

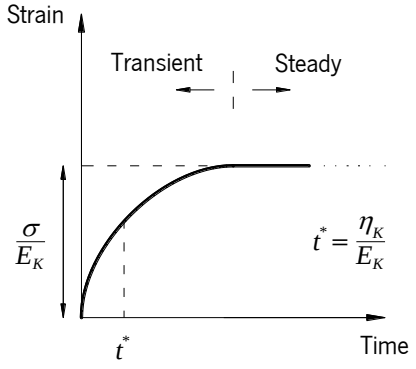

Figure 18 – Strain evolution in Kelvin Model.

Burgers model (Eq. 3 and Figure 19), which results literally from adding the previous two models, *i.e.*, using the superposition principle, has the potential to provide a more generalized solution.

$$\varepsilon(t) = \frac{\sigma}{E_M} + \frac{\sigma}{\eta_M}t + \frac{\sigma}{E_K}\left(1 - e^{-\frac{E_K}{\eta_K}t}\right) \tag{3}$$

These models have also the advantage of providing a qualitative assessment of each of the parameters involved. As detailed in Figures 17 to 19, each parameter is related to the slope of the curve (η_M), or a y-intercept value (E_K), or to a specific coordinate of the curve (E_M). Additionally, the parameter which is not clearly associated with any of the features of the curve, η_K, corresponds in fact to a specific time in the curve, the retardation time, t^*. This time instant, t^*, corresponds to the ratio between the dynamic viscosity coefficient, η_K, and the elastic modulus, E_K, as reported in Eq. 4. In the case of the Kelvin model, represents the precise instant when about 63% of the steady-state strain in achieved (Eq. 5).

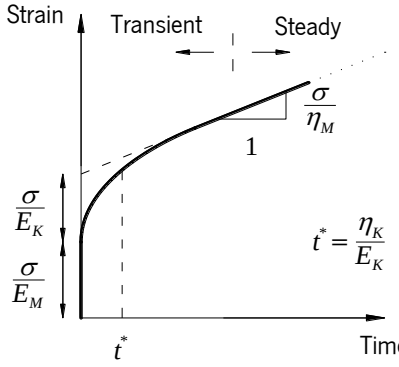

Figure 19 – Strain evolution in Burgers Model.

$$t^* = \frac{\eta_K}{E_K} \tag{4}$$

$$\varepsilon\left(t^*\right) = \frac{\sigma}{E_K}\left(1-\frac{1}{e}\right) \approx 0.63\frac{\sigma}{E_K} \tag{5}$$

2.4.1 Experimental investigation on the creep behaviour of adhesives

The components of the rheological models are at this point quantities of unknown magnitude. However, it is possible to estimate that at least the Maxwell modulus, E_M, of any adhesive would be roughly similar to the elastic modulus obtained by common tensile tests, usually provided by the technical data sheet of a material. Table 4 includes the viscosity coefficient values of gases, liquids and non-Newtonion fluids. Based on these values, the structural adhesives, which are in fact no more than rigid plastics, are expected to exhibit viscous components higher than 0.3 GPa.h since these values apparently tend to increase as the materials become stiffer.

Table 4 - Examples of viscosity coefficients of gases, liquids and non-Newtonion fluids (Sperling 1992).

Material	Viscosity coefficient
Air (100 kPa)	1×10^{-5} Pa·s
Water (25°C)	1×10^{-3} Pa·s
Olive oil (25°C)	0.1 Pa·s
Golden Syrup	100 Pa·s
Plastics	10^{12} Pa·s = 1000 GPa·s = 0.3 GPa·h
Glass	10^{21} Pa·s = 31710 GPa·yr

Three of the most noteworthy models encountered are presented in this Section. Although the proposed equations present roughly the same exponential form, the quantification of the parameters is made differently by the authors due to the distinct shape of experimental curves obtained. Furthermore, some of these solutions are not presented as deriving from classic rheological models, even though the solutions obtained show these equations to be rather similar to the classical formulations.

2.4.1.1 Feng *et al.* (2005)

Feng *et al.* (2005) suggested that it is possible to estimate the tensile creep strain, $\varepsilon_{creep}\left(t,T\right)$, by the exponential function shown in Eq. 6, which was re-written to improve the resemblance with the classical rheological models previously presented.

$$\varepsilon(t,T) = \frac{\sigma_0}{E_0} + \sigma_0 \left(\frac{1}{E_e} - \frac{1}{E_0} \right) \left(1 - e^{-\left(t/t^*\right)^{1-n}} \right) \quad (6)$$

where σ_0 is the applied stress level, E_0 the initial Young modulus, E_e is the equilibrium modulus given in Eq. 7, t^* is the relaxation time and n a coupling parameter related to moisture absorption.

$$E_e = 2G_r(1+\nu) \quad (7)$$

where G_r is the rubbery plateau shear modulus and ν the Poisson's ratio (ν = 0.5 since the material is in the rubbery state).

The unique feature in the model presented is related to the n parameter, whose influence is depicted in Figure 20. The value of n is in its essence related to the activation energy of the molecular motion. If a specimen is saturated, the presence of moisture assists molecular mobility and therefore decreases the amount of activation energy required, resulting in lower values of n. On the contrary, if the specimen is dry, the activation energy is higher, the value of n will thus be larger and the process is found to develop much slower, as demonstrated in Figure 20.

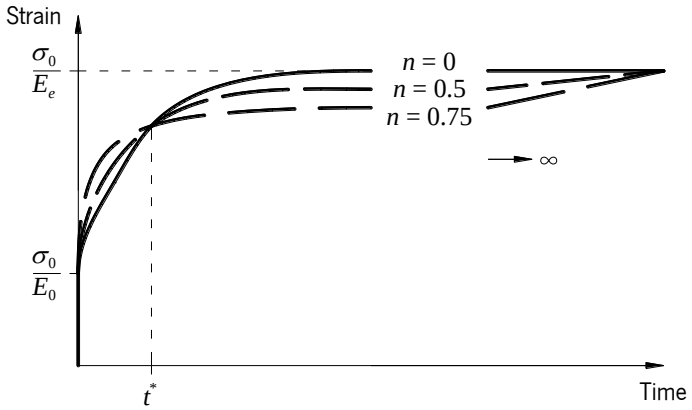

Figure 20 – Influence of moisture absorption (n) in creep response (Feng *et al.* 2005).

Feng *et al.* (2007) obtained in their tests values of n ranging from 0.51 to 0.73 for a model and a commercial epoxy adhesive system (used in the automotive industry) for levels of relative humidity up to 95% (Table 5).

In no other model the influence of moisture absorption was so clearly considered. Feng *et al.* (2007) concluded in their work that this physics-based coupling model was efficient to describe the long term creep behaviour of structural adhesives. Apart from the parameter n, Feng's model is quite similar to the Burgers model, although without the contribution of the Maxwell dashpot.

Table 5 - Parameters for the coupling model to fit the master curves (Feng *et al.* 2007).

System	E_0 [GPa]	E_e [GPa]	t^* [days]	n
Model epoxy adhesive system – Dry conditions	2.5	0.057	16204 (≈ 44 years)	0.73
Model epoxy adhesive system – Wet conditions	2.0	0.043	54	0.51
Commercial adhesive – Dry conditions	2.5	0.045	162	0.60

Note: the results in the original paper are defined in terms of D_0 and D_e, which represent the creep compliance, i.e., the inverse of the elastic components, E_0 and E_e.

2.4.1.2 Majda & Skrodzewicz 2009

Majda & Skrodzewicz (2009) proposed a model purely based on Burgers Model. The equation proposed by these authors reveals the two distinct creep components:

- Transient component: given by the exponential term resulting from the material's adjustment to the applied stress;
- Steady component: is the constant slope branch in Figure 21.

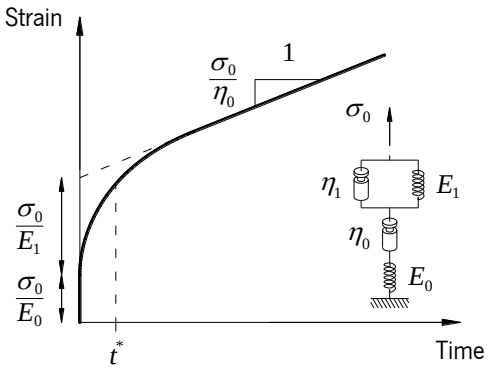

Figure 21 – Creep response according to Majda & Skrodzewicz (2009).

In mathematical terms, the creep response of Burgers model is by given the sum of the transient and steady creep components, as shown in Eq 8.

$$\varepsilon(t,T)=\frac{\sigma_0}{E_0}+\frac{\sigma_0}{\eta_0}t+\frac{\sigma_0}{E_1}\left(1-e^{-t/t^*}\right) \tag{8}$$

According to these authors, the retardation time is given by (Eq. 9)

$$t^*=\frac{\eta_1}{E_1} \tag{9}$$

Majda & Skrodzewicz (2009) also suggested that the coefficients of dynamic viscosity, η_0 and η_1, are primarily dependent on the applied stress (see Eq. 10 and11). Additionally, the elastic modulus of the relaxation response, herein designated as E_1, was also defined as a function of the applied stress (Eq. 12). Although these considerations are not compatible with the initial assumptions of the Burgers model response, the authors still obtained good results.

$$\eta_0(\sigma_0) = e^{a_1 - a_2\sigma_0} \tag{10}$$

$$\eta_1(\sigma_0) = e^{a_3 - a_4\sigma_0} \tag{11}$$

$$E_1(\sigma_0) = a_5{\sigma_0}^2 - a_6\sigma_0 + a_7 \tag{12}$$

To validate this model, an epoxy adhesive was tested under tensile creep (Majda & Skrodzewicz, 2009). The rheological properties (E_0, E_1, η_0 and η_1) were quantified by means of nonlinear regression analysis of the experimental creep tests at four different levels of applied stress, at a constant temperature of 22ºC (Table 6). Later, the different a_i coefficients can be obtained applying ordinary trend lines (logarithmic/quadratic regressions) as well as by non-linear regression (Table 7).

Table 6 – Parameters of the Burger's model determined on creep test of an epoxy adhesive at 22°C (Majda & Skrodzewicz 2009).

σ_0	E_0	η_0	E_1	η_1	t^*
[MPa]	[GPa]	[GPa·h]	[GPa]	[GPa·h]	[min]
15	2.232	22.4	1.173	0.48	24
20	2.232	4.12	0.788	0.23	18
25	2.232	1.49	0.896	0.07	5
30	2.232	0.36	1.380	0.06	3

Obs.: The tensile strength of the adhesive is 46.6 MPa.

Table 7 – Values of a_i for simple and non-linear regressions (Majda & Skrodzewicz 2009).

Coefficient	Unit	Trend line	Nonlinear Regression
a_1	ln(Pa·s)	35.8	37.38
a_2	Pa^{-1} ln(Pa·s)	27×10^{-8}	31.97×10^{-8}
a_3	ln(Pa·s)	30.3	30.72
a_4	Pa^{-1} ln(Pa·s)	14×10^{-8}	16.62×10^{-8}
a_5	Pa^{-1}	9×10^{-6}	12.27×10^{-6}
a_6	-	394	516.9
a_7	Pa	50.2×10^{8}	60.70×10^{8}

Note that like in Feng *et al.* (2007), the component that represents Kelvin's spring (E_e in Feng formulation and E_1 in this one), was also reported to be smaller than the instantaneous elasticity, indicating that maybe this qualitative observation may be perceived in other materials when modelled using these approaches.

2.4.1.3 Choi *et al.* (2007)

The experimental work carried out by Choi *et al.* (2007) is specially worth mentioning since, although it is not specifically designed to assess the long term properties of the epoxy adhesive, it presents the results of creep tests performed in double-shear specimens during 6 months. The paper reports the results of three creep specimens with different adhesive layer thickness and applied stress. The authors suggest that the total strain due creep also follows a simple exponential law (Eq. 13). Note that the shape of the curves proposed by Choi and Feng (when n is null) is particularly similar.

$$\varepsilon(t,T) = \frac{\sigma_0}{E_0} + \sigma_0 \frac{\phi_u(t_\infty)}{E_0}\left[1 - e^{-t/t^*}\right] \tag{13}$$

This equation, as previously observed, is rather similar to Kelvin's model (Figure 22) and, consequently, to the adhesive creep curve proposed by Feng *et al.* (2005). However, in the particular case of Choi's model, the parameter $\phi_u(t_\infty)$ is included to allow an accurate adjustment of the total response of the adhesive to different environmental conditions. This means that in $\phi_u(t_\infty)$, temperature, relative humidity and other external effects are considered together (see Table 8).

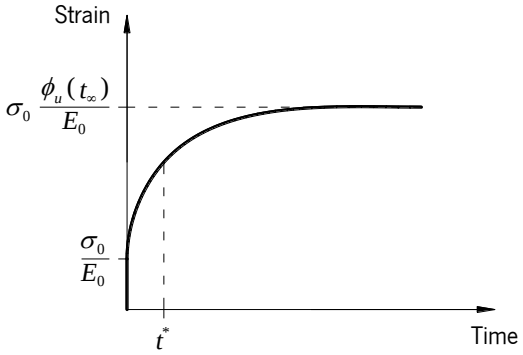

Figure 22 – Exponential creep strain response according to Choi *et al.* (2007).

Table 8 – Test results in laboratory environment – 20°C and 50% relative humidity (Choi *et al.* 2007).

Specimen	Epoxy thickness [mm]	σ_0 [MPa]	Monitored FRP	$\phi_u(t_\infty)$	t^* [days]
1	0.242	0.09	Face 1	1.17	43.3
			Face 2	1.02	2.1
2	0.176	0.17	Face 1	2.89	1.1
			Face 2	2.94	1.7
3	1.500	0.17	Face 1	2.59	0.2
			Face 2	2.39	0.1

Double-shear specimen ultimate resistance: 0.56 MPa.

2.4.2 Standards on Creep Behaviour

Both the American Society for Testing and Materials (ASTM) and the International Organization for Standardization (ISO) have already defined the procedure to assess the creep properties of plastic materials. Although these standards deal with the same phenomenon and are similar in content, they are not entirely equivalent.

2.4.2.1 ISO 899-1

ISO 899-1 is the official international standard for determining the creep behaviour of rigid and semi-rigid plastics under specified pre-treatment, temperature and humidity. According to this test method, load shall be applied smoothly to a standard specimen, as defined in ISO 527-2, within 1 to 5 seconds and maintained for at least 1000 hours (approximately 42 days). Strains, temperature and humidity should be measured according to the schedule presented in Figure 23.

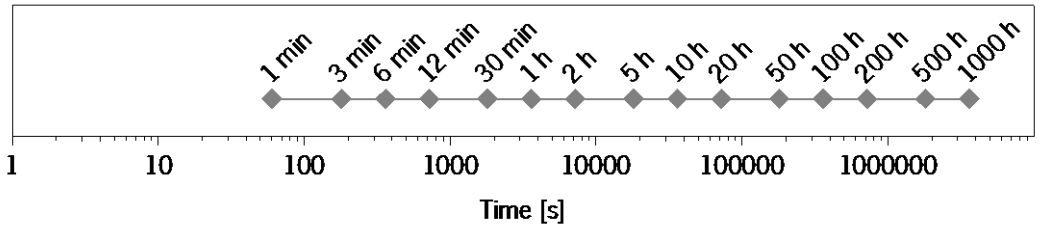

Figure 23 – Data acquisition schedule (ISO 899-1).

ISO 527-2 recommends bone-shape specimens to be moulded using the geometry depicted in Figure 24 (see also Table 9). These specimens shall be prepared according to the material's specifications or other appropriate standard. Test specimens shall be conditioned observing the applicable specification or other reasonable situation (as is the case of tests contemplating the evaluation of diverse environmental conditions).

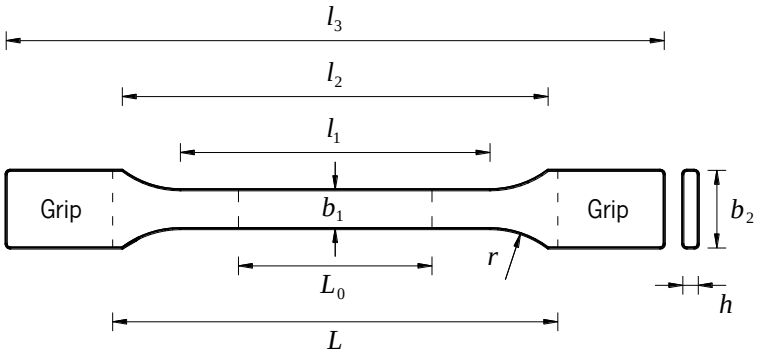

Figure 24 – Directly-moulded specimens (Type 1A, ISO 527-2).

Table 9 – Dimensions, in millimetres, of ISO 527-2 directly-moulded specimens (Type 1A).

Variable	Description	Dimension [mm]	Tolerance [mm]
b_1	Width of the narrow portion	10	± 0.2
b_2	Width at the ends	20	± 0.2
h	Preferred thickness	4	± 0.2
L	Initial free distance between grips	115	± 1
L_0	Gauge length	50	± 0.5
l_1	Length of the narrow parallel-sided portion	80	± 2
l_2	Distance between broad parallel-sided portions	104 to 113	-
l_3	Overall length	≥ 150	-
r	Radius	20 to 25	-

Creep tests are, in fact, an example of tests requiring varied environmental conditions to be applied. For different temperature and/or humidity level, one creep curve shall be obtained. To construct the desired creep curves, creep strains and/or creep moduli (defined in Eq. 14) are plotted against the logarithm of time, for every initial level of applied stress, σ, (see Figure 25). Isochronous curves, which consist in Cartesian plots of stress versus strain at specific time instants, similar to those depicted on Figure 25c, can also be presented. The initial stress to be applied is not rigorously defined in this standard and an appropriate choice of stress value is left to the user.

$$E_{creep}(t) = \frac{\sigma_0}{\varepsilon_{creep}(t)} \tag{14}$$

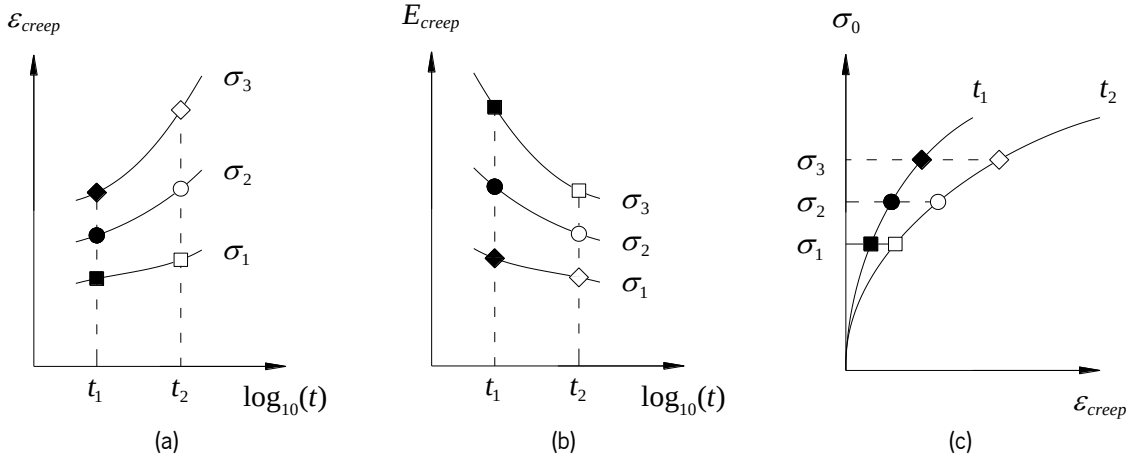

Figure 25 – Example of creep curves (ISO 899-1).
(a) Creep strain curves, (b) Creep modulus curves and (c) Isochronous stress-strain curves.

2.4.2.2 ASTM D 2990-01

ASTM D 2990-01 is the American Standard that deals with four of the major topics regarding creep of plastics: tensile creep, compressive creep, flexural creep and creep rupture. This standard, likewise ISO 699-1, also addresses creep of plastic materials under specified environmental conditions. Loading shall also be applied in the specimen rapid and smoothly in 1 to 5 seconds, and the strains shall be recorded at the time instants shown in Figure 26.

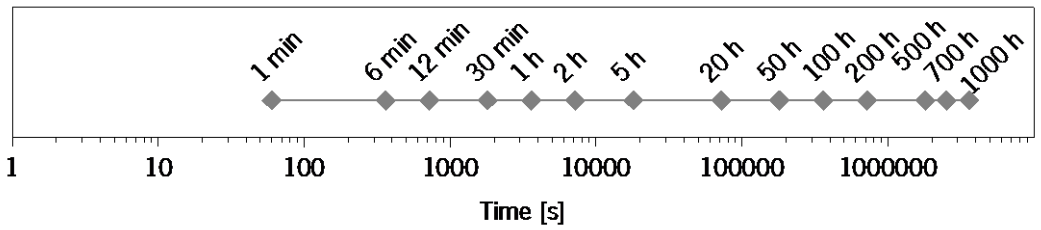

Figure 26 – Strain measurement schedule (ASTM D 2990-01).

To evaluate creep, the use of the normalized specimens produced according to ASTM D 638 is suggested. Thus standard, ASTM D 638, defines the procedure to determine the tensile properties of plastics. The geometry of these specimens is described in Figure 27 and by Table 10.

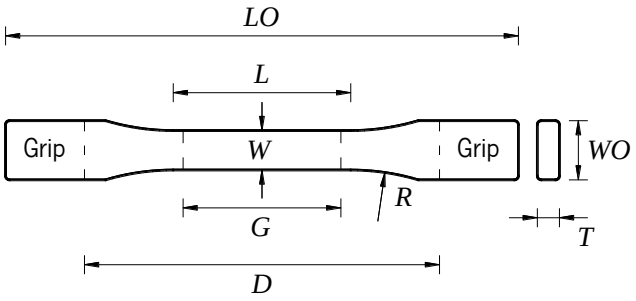

Figure 27 – Directly-moulded specimens (Type 1A, ISO 527-2).

Table 10 – Dimensions, in millimetres, of ASTM D 638 preferred specimens (Type I).

Variable	Description	Dimension	Tolerance
		[mm]	[mm]
D	Distance between grips	115	± 5
G	Gauge length	50	± 0.25
L	Length of narrow section	50	± 0.5
LO	Overall length	≥ 165	-
R	Radius of fillet	76	± 1
T	Thickness	≤ 7	-
W	Width of narrow section	19	+ 6.4
WO	Width at the extremities	80	± 2

Similarly to ISO 527-2, all surfaces of the specimen shall be free of visible flaws, scratches, or imperfections. The test specimens shall be conditioned at 23 ± 2°C and 50 ± 5% relative humidity for not less than 40 h prior to test, unless other justified conditioning method is applicable.

Comparatively to ISO 699-1, this standard gives additional information concerning the levels of stress to be applied, number of specimens, temperature, among others.

- Initial level of stress – Number and Magnitude

If the material exhibits typical viscoelastic behaviour, three levels of initial stress should be selected. If, on the other hand, the material under study is significantly affected by the applied stress, at least five levels of stress must be used. Regarding the magnitude of the load to be applied, for applied stress levels under 7 MPa, the selected levels of stress should be rounded off to multiples of 0.7 MPa. In the other hand, if the applied stress exceeds 7 MPa, the levels of stress should be rounded to multiples of 3.5 MPa. Furthermore, a given stress level is only considered relevant if the specimen does not fail in less than 1000 hours. These recommendations shall be applied to every selected temperature.

- Number of specimens

If the selected levels of stress are less than four, three specimens per stress level should be tested. In the all other cases, this number can be reduced to two. These tests should be equally repeated for each selected temperature.

- Temperature

To characterize the creep behaviour of a plastic material, two or more test temperatures should be used, as long as they cover the range of temperatures to which the material in question will be subjected during its working life. In the case of plastic materials whose dimensions are expected to vary due to the environment alone, ASTM suggests unloaded control specimens to be monitored simultaneously.

A minimum of three control specimens for every test temperature/environment is suggested. This instruction, although it is not intended to address all plastic materials, still alerts users to potential data contamination due to external causes (see Figure 28). If these control specimens are used and their results are applied to the creep test data itself, the reported data should be accompanied by an adequate label: "corrected", if environmental effects were deducted from the creep test data, or "uncorrected", if these effects were ignored.

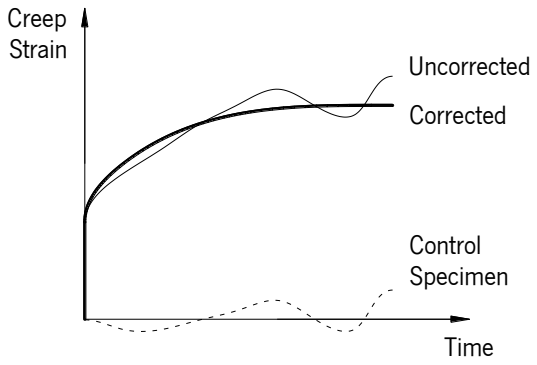

Figure 28 – Illustration of data contamination.

2.5 REFERENCES

ACI 440R-96 (1996). "State-of-the-Art Report on Fiber Reinforced Plastic (FRP) Reinforcement for Concrete Structures." *American Concrete Institute* (ACI), 68 pp.

Amato, L. R. (2009). "CFRP Tendons for the Pepair of Post-Tensioned, Unbonded Concrete Buildings." *MSc thesis*, Queen's University, Ontario, Canada.

ASTM D 638 (2003). "Standard Test Methods for Tensile Properties of Plastics." *American Society for Testing and Materials* (ASTM), Pennsylvania, US.

ASTM 2990 (2001). "Standard Test Methods for Tensile, Compressive, and Flexural Creep and Creep-Rupture of Plastics." *American Society for Testing and Materials* (ASTM), Pennsylvania, US, 20 pp.

Badawi, M. and Soudki, K. A. (2008). "Fatigue of RC beams strengthened with prestressed NSM CFRP rods." *Proceedings of the Fourth International Conference on FRP Composites in Civil Engineering* (CICE2008), Zurich, Switzerland, 22-24 July 2008, 6 pp.

Bakis, C. E.; Bank, L. C.; Brown, V. L.; Cosenza, E.; Davalos, J. F.; Lesko, J. J.; Machida, A.; Rizkalla, S. H. and Triantafillou, T. C. (2002). "Fiber-Reinforced Polymer Composites for Construction - State-of-the-Art Review." *Journal of Composites for Construction*, ASCE, 6(2), 73-87.

Barros, J. A. O. and Fortes, A. S. (2005). "Flexural strengthening of concrete beams with CFRP laminates bonded into slits." *Cement & Concrete Composites*, Elsevier, 27(4), 471-480.

Barros, J. A. O.; Dias, S. J. E. and Lima, J. L. T. (2007). "Efficacy of CFRP-based techniques for the flexural and shear strengthening of concrete beams." *Cement & Concrete Composites*, Elsevier, 29(3), 203-217.

Barros, J.A.O. (2009). "NSM Post-tensioned CFRP laminates for the flexural strengthening of RC beams", *Proceedings of the 9th International Symposium on Fiber Reinforced Polymer Reinforcement for Concrete Structures* (FRPRCS-9), Sydney, Australia, 13-15 July, 4pp.

Barros, J. A. O.; Costa, I. G. and Ventura-Gouveia, A. (2011). "CFRP Flexural and Shear Strengthening Technique for RC Beams: Experimental and Numerical Research." *Advances in Structural Engineering*, Multi-Science, 14(3), 551-571.

Barros, J. A. O. and Dalfré, G. M. (2013). "Assessment of the Effectiveness of the Embedded Through-Section Technique for the Shear Strengthening of Reinforced Concrete Beams." *Strain*, Wiley Publishing, 49(1), 75-93.

Bilotta, A.; Ceroni, F.; Di Ludovico, M.; Nigro, E.; Pecce, M. and Manfredi, G. (2011). "Bond Efficiency of EBR and NSM FRP Systems for Strengthening Concrete Members." *Journal of Composites for Construction*, ASCE, 15(5), 757-772.

Bonaldo, E.; Barros, J. A. O. and Lourenço, P. B. (2008). "Efficient Strengthening Technique to Increase the Flexural Resistance of Existing RC Slabs." *Journal of Composites for Construction*, ASCE, 12(2), 149-159.

Brinson, H. F.; Brinson, L. C. (2008). "Polymer Engineering Science and Viscoelasticity: An Introduction." *Springer Science+Business Media, LLC*, Springer, New York, US.

Chaallal, O.; Mofidi, A.; Benmokrane, B. and Neale, K. (2011). "Embedded Through-Section FRP Rod Method for Shear Strengthening of RC Beams: Performance and Comparison with Existing Techniques." *Journal of Composites for Construction*, ASCE, 15(3), 374-383.

Choi, K.-K.; Meshgin, P.; Taha, M. M. R. (2007). "Shear creep of epoxy as the concrete-FRP interfaces." *Composites Part B: Engineering*, Elsevier, 38(5-6), 772-780.

Costa, I. G. and Barros, J. A. O. (2011). "Creep of Adhesives - Review." *Report 11-DEC/E-03*, University of Minho, Guimarães, Portugal, 39 pp.

CNR-DT (2004). "Guide for the Design and Construction of Externally Bonded FRP Systems for Strengthening Existing Structures", *National Research Council*, Advisory Committee on Technical Recommendations for Construction, Rome, Italy, 154pp.

Dalfré, G. M. and Barros, J. A. O. (2013). "NSM technique to increase the load carrying capacity of continuous RC slabs." *Engineering Structures*, Elsevier, 56(-), 137-153.

Dean, G. (2007). "Modelling non-linear creep behaviour of an epoxy adhesive." *International Journal of Adhesion & Adhesives*, Elsevier, 27(8), 636-646.

Deuring, M. (1993). "Versta¨rken von Stahlbeton mit gespannten Faserverbundwerkstoffen." *Bericht Nr.224*, EMPA, Dubendorf, Switzerland (in German)

Diab, H. and Wu, Z. (2007). "A linear viscoelastic model for interfacial long-term behavior of FRP–concrete interface." *Composites Part B: Engineering*, Elsevier, 39(4), 722-730.

Dolan, C. W.; Hamilton, H. R., Bakis, C. E. and Nanni, A. (2001). "Design recommendations for concrete structures prestressed with FRP tendons." *FHWA-DTFH61-96-C-00019*, Federal Highway Administration, Washington, DC.

El-Hacha, R.; Wight, R. G. and Green, M. F. (2003). "Innovative System for Prestressing Fiber-Reinforced Polymer Sheets." *ACI Structural Journal*, American Concrete Institute, 100(3), 305-313.

Fam, A. Z. (1995). "Carbon Fibre Reinforced Plastic Prestressing and Shear Reinforcements for Concrete Highway Bridges." *MSc thesis*, University of Manitoba, Manitoba, Canada.

Feng, C. W.; Keong, C. W.; Hsueh, Y. P.; Wang, Y. Y.; Sue, H. J. (2005). "Modeling of long-term creep behavior of structural epoxy adhesives." *International Journal of Adhesion & Adhesives*, Elsevier, 25(5), 427-436.

fib (2001). "Externally bonded FRP reinforcement for RC structures." *The International Federation for Structural Concrete* (*fib*), Bulletin No. 14, Task Group 9.3 FRP reinforcement for concrete structures, Lausanne, Switzerland, 146 pp.

Gaafar, M. A. and El-Hacha, R. (2008). "Strengthening reinforced concrete beams with prestressed FRP near surface mounted technique." *Proceedings of the Fourth International Conference on FRP Composites in Civil Engineering* (CICE2008), Zurich, Switzerland, 22-24 July 2008, 6 pp.

Hollaway, L. C. and Cadei, J. (2002). "Progress in the technique of upgrading metallic structures with advanced polymer composites." *Progress in Structural Engineering and Materials*, John Wiley & Sons, 4(2), 131-148.

ISO 527-2 (1993). "Plastics - Determination of tensile properties - Part 2: Test conditions for moulding and extrusion plastics." *International Organization for Standardization* (ISO), Geneva, SZ, 8 pp.

ISO 899-1 (2003). "Plastics - Determination of creep behaviour - Part 1: Tensile creep." *International Organization for Standardization* (ISO), Geneva, SZ.

Jung, W.-T.; Park; Y.-H.; Park, J.-S.; Kang, J.-Y. and You, Y.-J. (2005). "Experimental investigation on flexural behavior of RC beams strengthened by NSM CFRP reinforcements." *Proceedings of the 7th International Symposium on Fiber Reinforced Polymer Reinforcement for Reinforced Concrete Structures* (FRPRCS-7), 12 pp.

Khoun, L. and Hubert, P. (2010). "Cure Shrinkage Characterization of an Epoxy Resin System by Two in Situ Measurement Methods." *Polymer Composites*, John Wiley & Sons, 31(9), 1603-1610.

Li, C.; Potter, K.; Wisnom, M. R. and Stringer, G. (2004). "In-situ measurement of chemical shrinkage of MY750 epoxy resin by a novel gravimetric method." *Composites Science and Technology*, 64(1), 55-64.

Lopez-Anido, R. A. and Naik, T. R. (2000). "Emerging Materials for Civil Engineering Infrastructure - State of the Art." *American Society of Civil Engineers*, Reston, Virginia, US.

Maekawa, K; Chijiwa, N. and Ishida, T. (2011). "Long-term deformational simulation of PC bridges based on the thermo-hygro model of micro-pores in cementitious composites." *Cement and Concrete Research*, Elsevier, 41(12), 1310-1319.

Majda, P.; Skrodzewicz, J. (2009). "A modified creep model of epoxy adhesive at ambient temperature." *International Journal of Adhesion & Adhesives*, Elsevier, 29(4), 396-404.

Mofidi, A.; Chaallal, O.; Benmokrane, B. and Neale, K. (2012). "Experimental Tests and Design Model for RC Beams Strengthened in Shear Using the Embedded Through-Section FRP Method." *Journal of Composites for Construction*, ASCE, 16(5), 540-550.

Motavalli, M.; Czaderski ,C. Pfyl-Lang, K. (2011). "Prestressed CFRP for Strengthening of Reinforced Concrete Structures: Recent Developments at Empa, Switzerland." *Journal of Composites for Construction*, ASCE, 15(2), 194-205.

Meaud, C.; Jurkiewiez, B. and Ferrier, E. (2011). "Investigation of creep effects in strengthened RC structures through double lap shear testing." *Composites Part B: Engineering*, Elsevier, 42(3), 359-366.

Meier, U. (1995). "Strengthening of structures using carbon fibre/epoxy composites." *Construction and Building Materials*, Elsevier, 9(6), 341-351.

Nordin, H. and Täljsten, B. (2006). "Concrete Beams Strengthened with Prestressed Near Surface Mounted CFRP." *Journal of Composites for Construction*, ASCE, 10(1), 60-68.

Quantrill, R. J. and Hollaway, L. C. (1998). "The flexural rehabilitation of reinforced concrete beams by the use of prestressed advanced composite plates." *Composites Science and Technology*, Elsevier, 58(8), 1259-1275.

Saadatmanesh, H. and Ehsani, M. R. (1991). "RC beams strengthened with GFRP plates. I: Experimental study." *Journal of Structural Engineering*, ASCE, 117(11), 3417-3433.

Sayed-Ahmed, E. Y. (2002). "Single and Multi-Strand Steel Anchorage Systems for CFRP Tendons/Stays." *4th Structural Speciality Conference of the Canadian Society for Civil Engineering*, Montréal, Québec, 5-8 June, 10pp.

Sena-Cruz, J. M.; Barros, J. A. O.; Coelho, M. R. F. and Silva, L. F. F. T. (2012). "Efficiency of different techniques in flexural strengthening of RC beams under monotonic and fatigue loading." *Construction and Building Materials*, Elsevier, 29(-), 175-182.

Seracino, R.; Raizal-Saifulnaz, M. R. and Oehlers, D. J. (2007). "Generic Debonding Resistance of EB and NSM Plate-to-Concrete Joints." *Journal of Composites for Construction*, ASCE, 11(1), 62-70.

Shrive, N. G. (2006). "The use of fibre reinforced polymers to improve seismic resistance of masonry." *Construction and Building Materials*, Elsevier, 20(4), 269-277.

Sperling, L.H. (1992). "Introduction to physical polymer science." *2nd Edition*, John Wiley. New York, US.

Wang, W.-W.; Dai, J.-G.; Harries, K. A. and Bao, Q.-H. (2012). "Prestress Losses and Flexural Behavior of Reinforced Concrete Beams Strengthened with Posttensioned CFRP Sheets." *Journal of Composites for Construction*, ASCE, 16(2), 207-216.

Wight, R. G.; Green, M. F. and Erki, M-A. (2001). "Prestressed FRP Sheets for Poststrengthening Reinforced Concrete Beams." *Journal of Composites for Construction*, ASCE, 5(4), 214-220.

Wu, Z. and Diab, H. (2007). "A linear viscoelastic model for interfacial long-term behavior of FRP-concrete interface." *Journal of Composites for Construction*, ASCE, 11(5), 477-486.

Yeoh, D.; Fragiacomo, M.; De Franceschi, Mary. and Boon, K. H. (2011). "State of the Art on Timber-Concrete Composite Structures: Literature Review." *Journal of Structural Engineering*, ASCE, 137(10), 1085-1095.

Yu, H.; Mhaisalkar, S. and Wong, E. (2005). "Cure shrinkage measurement of nonconductive adhesives by means of a thermomechanical analyzer." *Journal of Electronic Materials*, Springer, 38(4), 1177-1182.

Zhao, X.-L. and Zhang, L. (2007). "State-of-the-art review on FRP strengthened steel structures." *Engineering Structures*, Elsevier, 29(8), 1808-1823.

Chapter 3

ADHESIVE CHARACTERIZATION

Structural epoxy adhesives are one of the most important components of the NSM-CFRP strengthening system since they are responsible for adequately transferring stresses between CFRP and concrete. Any supplier of CFRP can provide or suggest the most appropriate adhesive to guarantee that the full resistance of the strengthening system can be fully mobilized. However, when investigating CFRP systems, either EBR or NSM, the determination of the adhesive's properties is usually limited to the citation of the technical datasheet of the material (El-Refaie *et al.*, 2003, Ashour *et al.*, 2004, *Barros et al.*, 2007) and when material characterization is performed in laboratory conditions, it is usually limited to the assessment of the tensile strength and elastic modulus of the adhesive and occasionally, the Poisson coefficient (Lorenzis *et al.*, 2002, Sena-Cruz and Barros, 2007, Seracino *et al.*, 2007). To capture the prestress effectiveness of NSM-CFRP laminates for the flexural strengthening of RC elements, the time dependent properties of the adhesives, mainly creep, should be assessed. Therefore, the present Chapter cover not only the instantaneous but also the long term behaviour of the relevant properties of the adopted adhesives, with a special focus was given to the tensile creep.

In the beginning of this work, it was planned to use a fast curing adhesive in combination with the NSM technique (Costa & Barros, 2013). However, preliminary tests, not reported in this document, suggested that the bond between CFRP and the fast curing adhesive selected was insufficient to replicate the effectiveness of the connection when using a normal curing adhesive recommended by the supplier. Nevertheless, it was decided to investigate the behaviour of the normal curing adhesive in order to shorten the period of time necessary to obtain the full capacity of the

connection, not only to speed up the strengthening application in laboratory conditions but also to be able to accelerate the application in job site.

3.1 TENSILE PROPERTIES

As a starting point to assess the effective curing time of the structural adhesive, the tensile strength and elastic modulus of the material were determined. For this purpose, dumbbell-shaped specimens of adhesive were prepared observing most of ISO 527-2 recommendations (see Figure 29 and Table 11) using an appropriate silicone mould. The moulding process was performed in all cases at room temperature and relative humidity of approximately 20ºC and 20%, respectively, and the mould was afterwards transported to cure in a climatic chamber where it was kept under a constant temperature of 20ºC and relative humidity of 60%.

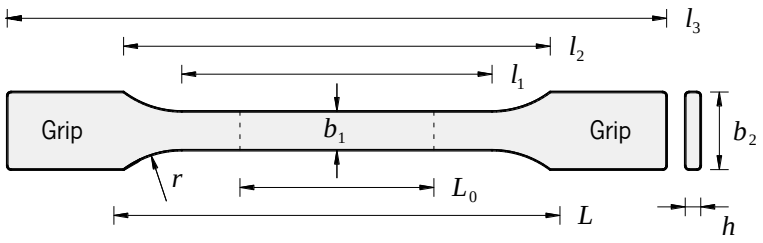

Figure 29 – Directly-moulded specimens recommended geometry (Type 1A, ISO 527-2).

Table 11 – Dimensions, in millimetres, of ISO 527-2 specimens.

Dimension	Description	Dimension [mm]	Tolerance [mm]	Used [mm]
b_1	Width of the narrow portion	10	± 0.2	10
b_2	Width at the ends	20	± 0.2	20
h	Preferred thickness	4	± 0.2	4
L	Initial distance between grips	$l_2{}_0^{+5}$	-	120
L_0	Gauge length	50	± 0.5	50
l_1	Length of the narrow portion	60	± 0.5	70
l_2	Distance in-between wider portions	106 to 120	-	120
l_3	Overall length	≥ 150	-	186
r	Radius	≥ 60	-	65

To prepare a batch of material the two parts of the adhesive (Figure 30a) are weighted respecting the 1:4 ratio recommended by the supplier, mixed and poured in the silicon mould, ignoring the occasional formation of voids since in real strengthening applications little can be done to prevent their appearance. After filling the mould, a rigid plastic film is placed on top of the material and the

specimens are levelled to the proper thickness using a roller pin (Figure 30d). After this, a glass sheet is placed on top of the specimens to prevent accidental damages before achieving full cure.

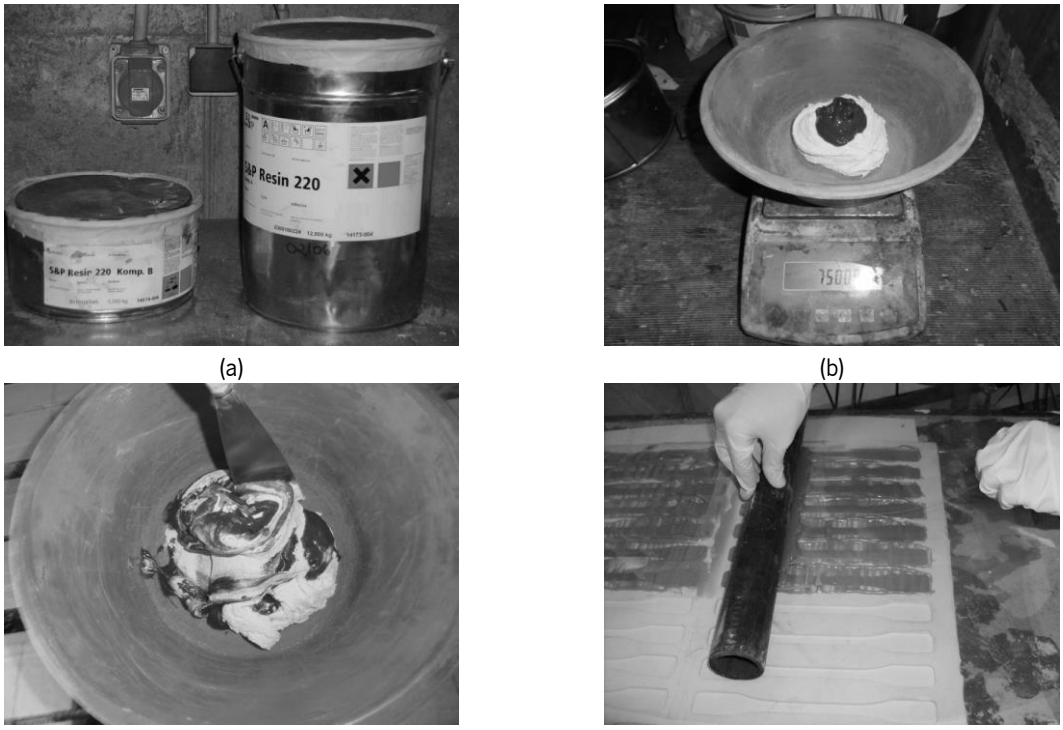

Figure 30 – Moulding the adhesive specimens: (a) Cans of adhesive, (b) Weighting the components of the adhesive, (c) Mixing the parts and (d) Surface levelling.

In this experimental program, six batches of 5 specimens each were prepared to assess the tensile strength and the elastic modulus of the adhesive at several ages. It was attempted to perform this test at early ages, as for example at 6 and 8 hours but, the material was still too deformable to allow being placed in the testing machine. As the tests before 24 hours were impossible to perform, the first batch of specimens was tested at 24 hours of age. The remaining batches were tested at 2, 3, 4 and 7 days of curing.

All the specimens were loaded in tension in a Universal Testing Machine equipped with a load cell of 50 kN capacity. Strains were recorded up to failure by using a clip-gauge with maximum opening of 12 mm applied in the 50 mm central portion of the specimen (see Figure 31). The specimens were loaded at a constant displacement ratio of 1 mm/min up to failure, taking the internal displacement transducer of the testing machine for control purposes, as recommended by ISO 527-2. Prior to testing, the width and thickness of each specimen were measured in the extremities of the control length as well as in the centre of the specimens to later allow the calculation of the applied axial stress. It is worth mentioning that no slippage was observed in between the testing jaws and the adhesive specimens.

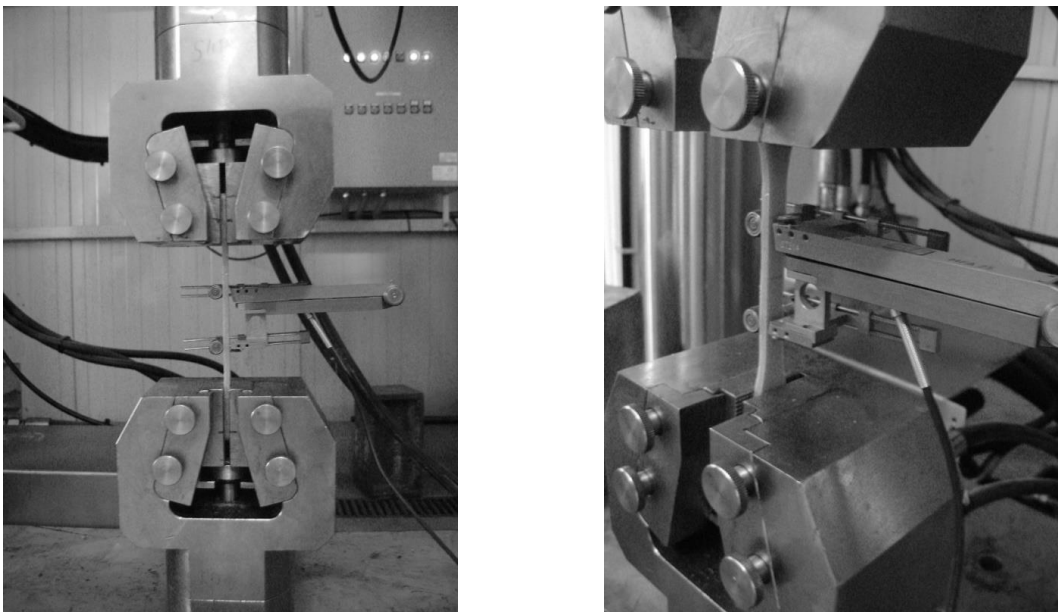

(a) (b)

Figure 31 – Tensile test set-up of the adhesives: (a) frontal view and (b) lateral view.

The location of failure and aspect of the failure plane in all the tests performed is presented in Figure 32. All specimens, despite the curing time, ruptured after achieving their maximum tensile strength. In Figures 32a, the specimens are positioned so that the left side corresponds to the part of specimen installed in the bottom grip while the right side is the part on the top grip.

In terms of failure plane location, it was observed that specimens typically failed outside the control length of 50 mm, since 17 of the 25 specimens ruptured outside the expected zone. However, this fact has no apparent relation with the positioning of the specimens in the machine (10 specimens failed close to the bottom grip and the remaining 7 close to the top grip) and is probably just related to the heterogeneity of the epoxy mixture.

Regarding the aspect of the failure planes, several voids were observed ranging between very small diameters (almost imperceptible to the naked eye) up to about 3 mm. According to this observation, at least in the cases of specimens with extremely large voids, as was the case of specimens SP-01, SP-14 and SP-24, the location of the failure plane could not possibly have been in the control length.

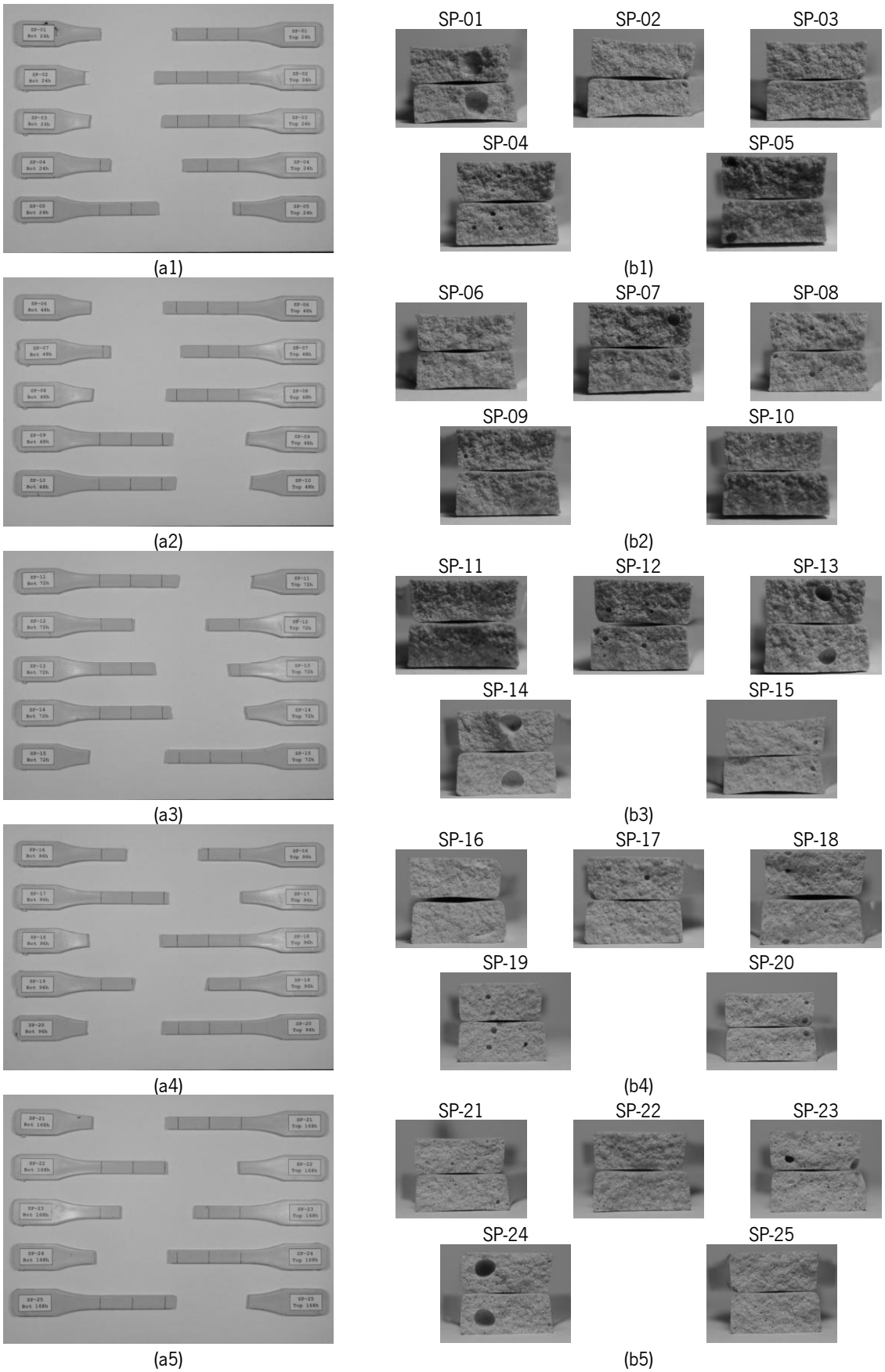

Figure 32 – Failure modes of the adhesive specimens. (a) Position of the failure plane, (b) Aspect of the failure plane, (1) 1 day, (2) 2 days, (3) 3 days, (4) 4 days and (5) 7 days.

In Table 12, the properties assessed in the course of this experimental program are presented. For each specimen, the elastic modulus, E_a, was determined according to ISO 527-1 as the linear regression of the stress-strain curve between 0.5‰ and 2.5‰. The correlation coefficient of the linear regressions, r^2, is also presented to demonstrate the linearity of the elastic modulus in this strain interval. The maximum tensile strength, f_a, strain at rupture, ε_a, and time to rupture t_a are also reported in Table 12. Based on the obtained results it was detected that the sample SP-01, which exhibited the largest void in the failure surface showed a tensile strength significantly lower than the other specimens in the series. Additionally, it is worth mentioning that, regardless the curing time, the adhesive presented an almost linear behaviour in the aforementioned strain interval, as proved by nearly unitary r^2 values.

Table 12 – Properties of the epoxy adhesives.

Specimen	Curing time [days]	E_a [GPa]	r^2	f_a [MPa]	ε_a [‰]	t_a [s]
SP-01	0.99	3.42	0.98841	14.7	4.586	75.2
SP-02	1.00	5.36	0.99554	19.2	5.102	83.5
SP-03	1.00	6.18	0.99429	18.8	3.559	75.6
SP-04	1.00	6.02	0.99194	18.6	3.978	79.2
SP-05	1.00	5.84	0.99625	19.2	3.833	76.1
SP-06	1.98	7.53	0.99605	20.9	3.200	71.0
SP-07	1.98	7.41	0.99162	20.8	3.066	72.5
SP-08	1.98	7.47	0.99006	21.4	3.224	73.0
SP-09	1.99	7.67	0.99485	21.9	3.362	73.4
SP-10	1.99	7.86	0.99826	20.5	2.757	69.1
SP-11	2.95	7.37	0.99579	21.2	3.142	77.6
SP-12	2.95	7.32	0.99773	21.3	3.320	73.9
SP-13	2.95	7.39	0.99613	21.3	3.259	71.0
SP-14	2.96	7.19	0.99337	19.0	2.686	74.7
SP-15	2.96	6.99	0.99781	18.4	2.455	70.6
SP-16	3.93	7.68	0.99701	20.2	2.750	68.1
SP-17	3.93	7.42	0.99585	20.5	3.050	70.2
SP-18	3.94	7.52	0.99619	21.5	3.339	90.4
SP-19	3.94	7.84	0.99362	22.6	3.669	75.9
SP-20	3.94	7.68	0.99629	20.7	2.964	71.5
SP-21	6.90	7.42	0.99516	19.5	2.622	66.7
SP-22	6.92	7.00	0.99417	20.5	3.200	70.4
SP-23	6.92	7.47	0.99475	21.1	3.154	68.8
SP-24	6.92	7.40	0.99587	21.3	3.153	74.4
SP-25	6.92	7.83	0.99550	20.8	2.868	67.6

In Figure 33, the evolution of the curing process can be clearly observed. Apart from the specimens tested at 1 day of age that exhibited, in general, a lower axial stiffness and strength, most specimens after the 2 days of age have apparently reached their maximum capacity.

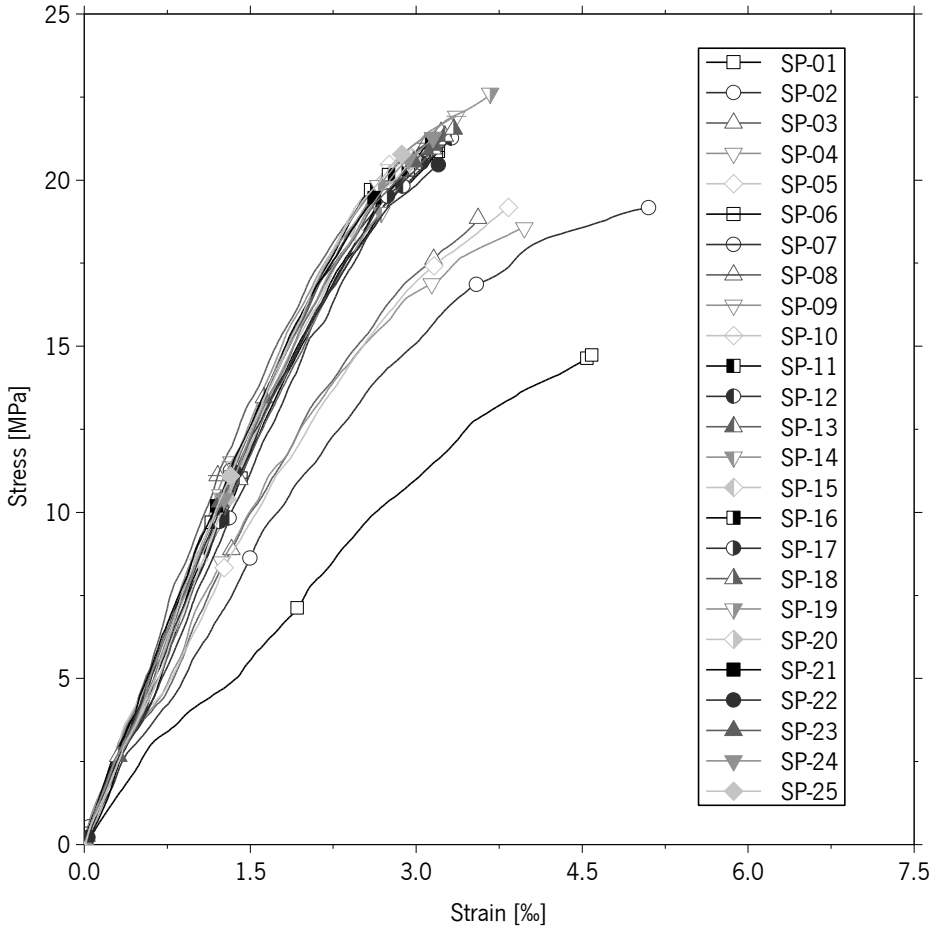

Figure 33 – Adhesive stress-strain curves.

Table 13 presents the average properties of the adhesive by age. According to the presented results, 1 day of curing time is definitely insufficient to attain the complete cure of the material in terms of stiffness, although the strength is almost fully developed. Regarding the results of the remaining batches, it is admissible that at 2 days of age complete cure is achieved. Note how the average properties at 2 days (E_a = 7.59 GPa and f_a = 21.1 MPa) are actually higher than average properties obtained for the recommended curing time (7 days, E_a = 7.42 GPa and f_a = 20.6 MPa).

Table 13 – Average properties of the epoxy adhesive.

Batch	Average Age [days]	E_a [GPa]	f_a [MPa]	ε_a [‰]
SP – 1 day	1.00	5.36 (1.13) {21%}	18.1 (1.9) {10%}	4.212 (0.624) {15%}
SP – 2 days	1.99	7.59 (0.18) {2%}	21.1 (0.6) {3%}	3.122 (0.23) {7%}
SP – 3 days	2.95	7.25 (0.17) {2%}	20.2 (1.4) {7%}	2.972 (0.381) {13%}
SP – 4 days	3.94	7.63 (0.16) {2%}	21.1 (1.0) {5%}	3.154 (0.357) {11%}
SP – 7 days	6.92	7.42 (0.29) {4%}	20.6 (0.7) {3%}	2.999 (0.249) {8%}
Average (without SP – 1 day)	-	7.47 (0.24) {3%}	20.8 (1.0) {5%}	3.062 (0.297) {10%}

Average (Standard deviation) {Coefficient of variation}

Based on these findings, it was attempted to fit an exponential curve to the totality of results obtained, as shown in Figure 34. As previously concluded from the analysis of Table 13, the adhesive achieves full resistance at shortly after 1 day of curing as visually observed in Figure 34.

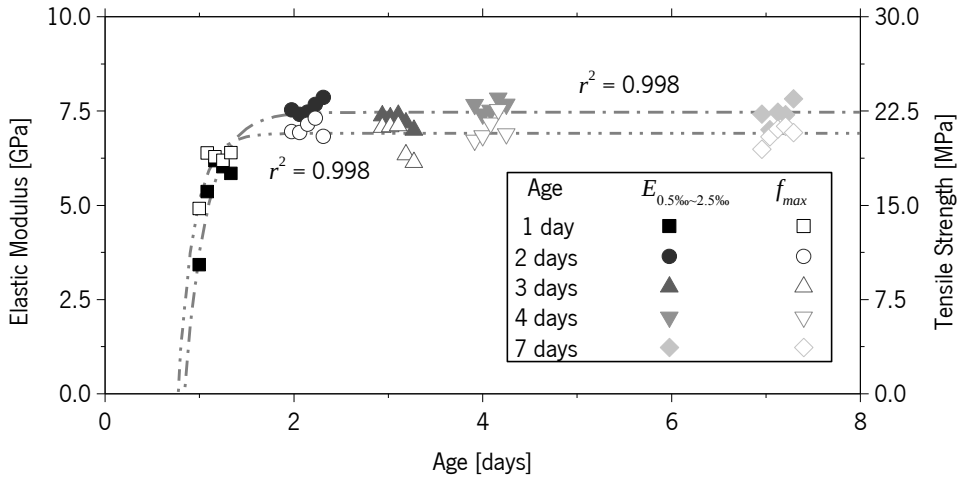

Figure 34 – Elastic modulus and tensile strength evolution with time.

Eq. 15 was selected to simulate the growth of the tensile strength and elastic modulus, since the parameters featured in this equation provide a good understanding of the behaviour that is being depicted:

- the constant A symbolizes the maximum value of the parameter y;
- the constant B determines the rate at which the parameter increases from zero to A;
- the constant C estimates the time, t, necessary to the parameter to be positive.

$$y(t) = A\left(1 - e^{-B(t-C)}\right) \quad (15)$$

Curve fitting was relatively effective as proven by the r^2 presented in Figure 34 the plot and in Table 14. According to the obtained results, stiffness and strength is expected to start developing at about 0.8 days (19 hours), and in a few hours, achieve full resistance.

Table 14 – Exponential regression of the experimental results.

Parameter	A	B	C	r^2
E_a	7.466	4.304	5.913	0.998
f_a	20.726	0.837	0.769	0.998

Based on these results, it was decided to continue the characterization of the NSM-CFRP system using two reference curing times: the curing time recommended by the manufacturer, 7 days, and an early curing time of 3 days. Although tensile testing proved that the adhesive is fully cured at 2 days of age, it was decided to adopt, for safety, a longer curing time. As a practical reference, as curing does not require any type of supervision, it is possible to take advantage of the weekends to allow the adhesive to mature. This reduction is also useful to later be able to speed up the prestress strengthening process.

3.2 PULLOUT BENDING TESTS

Pullout bending tests are commonly used to assess the bond performance of NSM-CFRP systems to be applied in flexural strengthening (Sena-Cruz and Barros, 2004, Costa and Barros, 2011). In the experimental program presented in this Section, in order to assess all the properties of the strengthening system, beam bending specimens were prepared to be tested at the reduced curing time (3 days) and recommended curing time (7 days). Each specimen was composed of two concrete blocks, with 500 mm of length and a cross section of 150 × 200 mm^2 connected in the top by a steel hinge and in the bottom by the 1.4 ×20 mm^2 CFRP laminate, as depicted in Figure 35. In one of the blocks, the CFRP was bonded to most of the concrete block to force failure to happen in the opposing block where the bond length, L_b, is much smaller. The bond lengths were estimated to maximize the applied load, in an attempt to cause CFRP failure. According to previous tests carried out in the University of Minho, using a single-shear pushing test configuration, a bond length of 90 mm was not sufficient to cause CFRP failure although about 1500 MPa of tensile stress was successfully applied in the CFRP (Costa and Barros, 2012). Therefore, the bonded lengths chosen to apply in this experimental program started in L_b = 100 mm and progressed up to

the double of this value. The pullout specimens were prepared in groups of three and four batches of adhesive were prepared, as detailed in Table 15. Although, ideally, at least three specimens per age/bond length should be used to account for material variability, it was decided to downsize the sampling size to two specimens per age/bond length and thus, two series of specimens (s1 and s2) were tested.

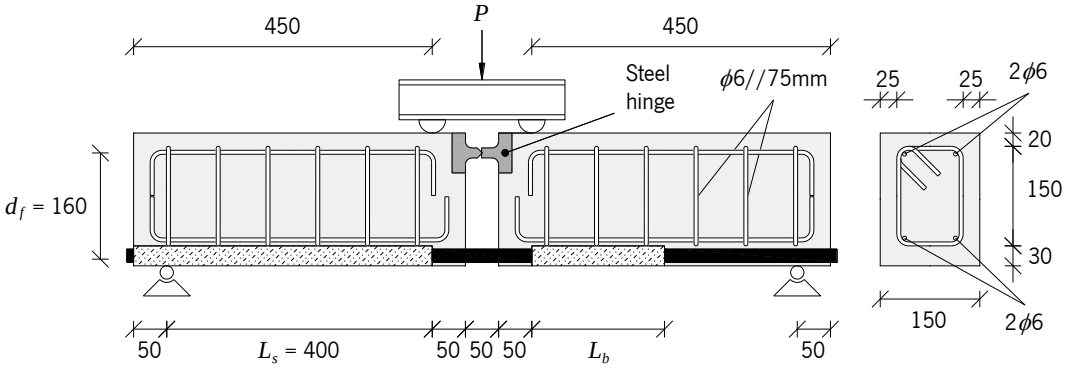

Figure 35 – Pullout test arrangement and dimensions (in millimetres).

Table 15 – Details of the pullout specimens.

Reference	Age [days]	Bond Length, L_b [kN]	Batch of adhesive
PB_3d_100mm_s1	3	100	1
PB_3d_150mm_s1	3	150	1
PB_3d_200mm_s1	3	200	1
PB_7d_100mm_s1	7	100	2
PB_7d_150mm_s1	7	150	2
PB_7d_200mm_s1	7	200	2
PB_3d_100mm_s2	3	100	3
PB_3d_150mm_s2	3	150	3
PB_3d_200mm_s2	3	200	3
PB_7d_100mm_s2	7	100	4
PB_7d_150mm_s2	7	150	4
PB_7d_200mm_s2	7	200	4

To better simulate the reality of a NSM-CFRP strengthened element each concrete block included a steel reinforcement, represented in Figure 36a (Barros *et al.*, 2011) and all concrete blocks were casted at the same time, as depicted in Figure 36b. Samples of concrete were collected during the casting and were tested at approximately the same time as the pullout specimens for the characterization of the compressive behaviour. After concrete cure, a 6 ×30 mm^2 notch was opened on the bottom surface of the blocks. The depth and width of the grooves were measured in the full bond block at every 100 mm (5 measurements) while in the block with smallest bonded length this

spacing between measurements was reduced to 50 mm (3 to 5 measurements depending on L_b). The average values of the executed measurements made are reported in Table 16, showing that the target dimensions of the grooves were in general respected.

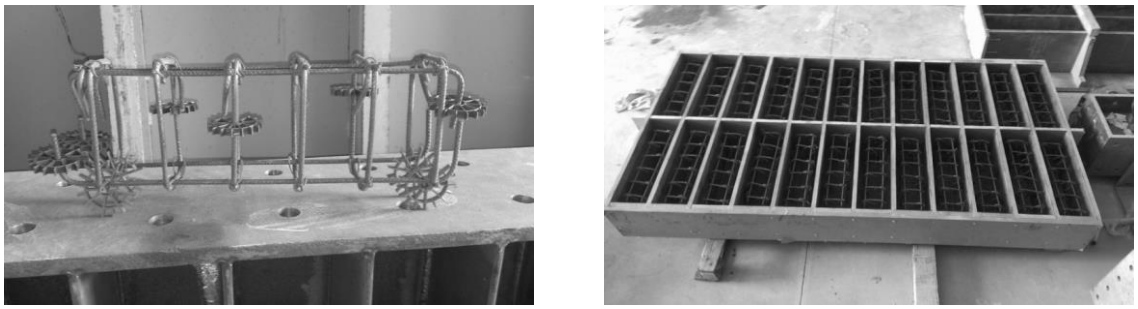

(a) (b)

Figure 36 – Casting preparation of the beam bending tests specimens: (a) finished aspect of the steel reinforcement and (b) mould preparation.

Table 16 – Groove dimensions of the beam bending test specimens.

Specimen	Full Bond		L_b	
	w_g [mm]	d_g [mm]	w_g [mm]	d_g [mm]
PB_3d_100mm_s1	6.839 (0.150) {2%}	30.093 (0.189) {1%}	6.863 (0.071) {1%}	29.205 (0.303) {1%}
PB_3d_150mm_s1	6.622 (0.337) {5%}	28.275 (0.745) {3%}	7.003 (0.173) {2%}	29.643 (0.213) {1%}
PB_3d_200mm_s1	6.674 (0.178) {3%}	30.378 (0.388) {1%}	6.462 (0.050) {1%}	29.859 (0.463) {2%}
PB_7d_100mm_s1	6.203 (0.377) {6%}	28.811 (1.970) {7%}	6.770 (0.108) {2%}	30.750 (0.276) {1%}
PB_7d_150mm_s1	6.292 (0.147) {2%}	30.542 (0.419) {1%}	6.646 (0.107) {2%}	29.745 (0.279) {1%}
PB_7d_200mm_s1	6.456 (0.181) {3%}	28.579 (1.610) {6%}	6.740 (0.058) {1%}	29.622 (1.737) {6%}
PB_3d_100mm_s2	6.398 (0.103) {2%}	29.522 (0.575) {2%}	6.513 (0.019) {0%}	29.132 (0.471) {2%}
PB_3d_150mm_s2	6.552 (0.144) {2%}	30.679 (0.626) {2%}	6.268 (0.498) {8%}	29.754 (0.327) {1%}
PB_3d_200mm_s2	6.765 (0.103) {2%}	30.412 (0.115) {0%}	6.720 (0.086) {1%}	30.025 (0.462) {2%}
PB_7d_100mm_s2	6.514 (0.103) {2%}	30.255 (0.633) {2%}	6.713 (0.028) {0%}	27.840 (0.064) {0%}
PB_7d_150mm_s2	6.553 (0.154) {2%}	28.944 (1.044) {4%}	6.999 (0.074) {1%}	29.378 (0.427) {1%}
PB_7d_200mm_s2	6.462 (0.310) {5%}	28.734 (1.079) {4%}	6.701 (0.205) {3%}	28.036 (0.703) {3%}

Average (Standard Deviation) {Coefficient of Variation}

After the preparation of the concrete blocks, the specimens were positioned in a work table for ensuring the alignment of the grooves of each pair of blocks. The blocks were then covered with masking tape, the boundaries of the bond length were marked and the grooves were later cleaned with compressed air to remove any existing dust (Figures 37a and 37b). The grooves were filled with the epoxy (Figure 37c) and then the CFRP laminate was inserted in the centre of the groove (Figure 37d). Finally, the strengthened surface was levelled and the excess of adhesive in the loaded and free ends was removed (Figures 37e and 37f). Due to the space required to perform these strengthening procedures, it was not possible to perform them in controlled environment,

such as was done in the previous tests. However, as these tests were carried out in August, the average temperature was in general 20ºC or higher.

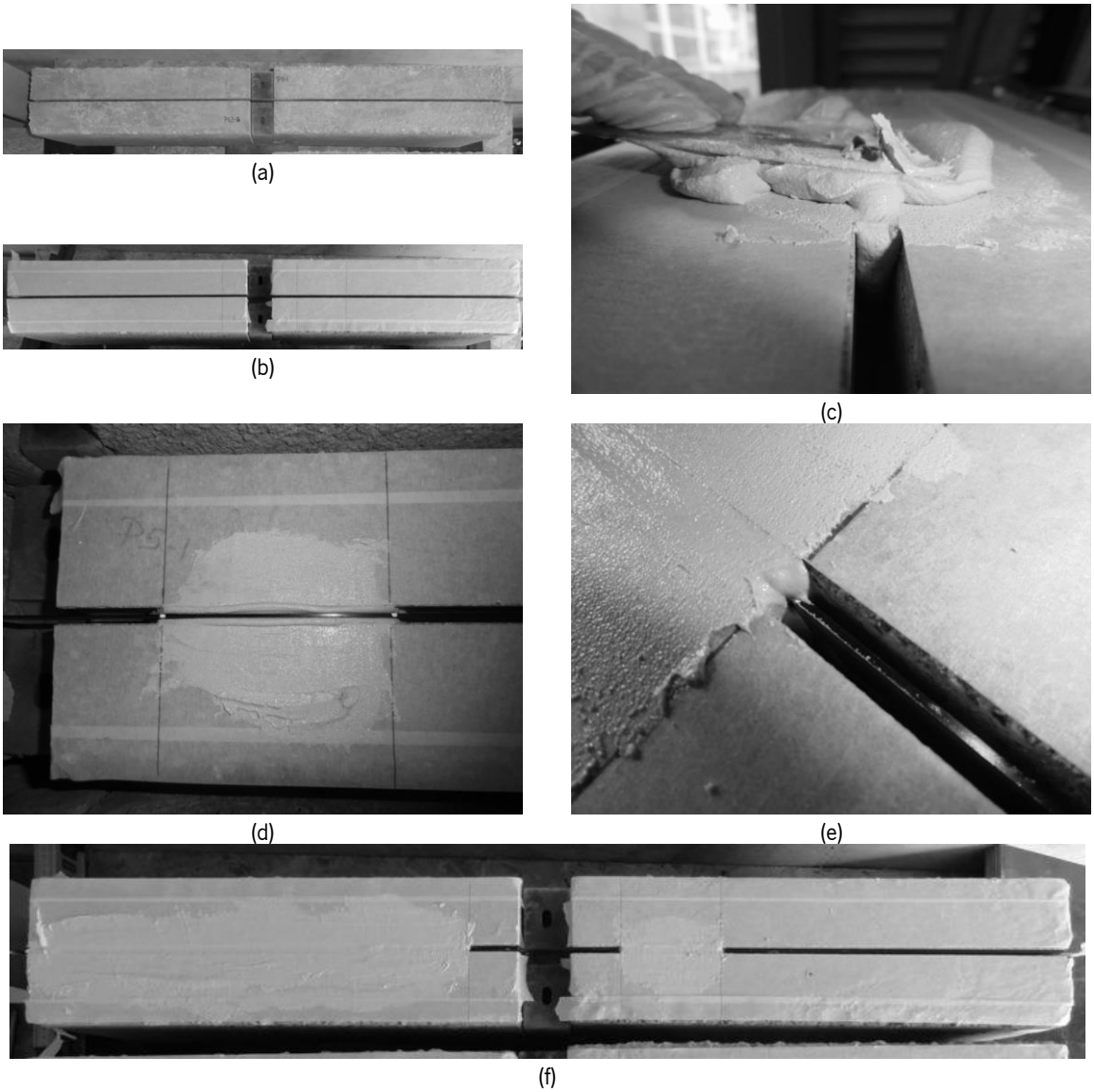

Figure 37 – Pullout bending test preparation: (a) alignment of the blocks, (b) protection of the blocks, (c) filling of the groove, (d) insertion and positioning of the CFRP laminate, (e) excess removal and (f) final aspect of the strengthened specimens.

The concrete used in these specimens was ordered from a concrete supplier and was requested to be a C25/30. However, as it can be observed in Table 17, the average compressive strength, f_c, was unexpectedly low (about 22.4 MPa) since the target average compressive strength of C25/30 is typically 33 MPa. Table 17 also reports the elastic modulus, E_c, obtained by testing the cylinders in accordance with the Portuguese Specification, E395.

One day before testing, the specimens were turned over, and the steel hinges were glued on the concrete blocks to complete specimen preparation. Each specimen was tested in the configuration depicted in Figure 38a. During the tests, the loaded-end slip of CFRP reinforcement was monitored by placing an LVDT in the edge of the concrete block and a backstop on the longitudinal CFRP (Figure 38b). Additionally, an LVDT was installed to measure the free-end slip, 100 mm after the end of the bonded length (Figure 38c). A strain gauge was installed in the centre of the CFRP laminate, aligned with the steel hinge to evaluate the applied strain during loading.

Table 17 – Concrete characterization.

Sample	f_c [MPa]	E_c [GPa]
1	23.9	-
2	26.1	24.2
3	16.4	22.5
4	23.3	18.0
Average	22.4	21.6
Standard Deviation	4.2	3.2
Coefficient of Variation	19%	15%

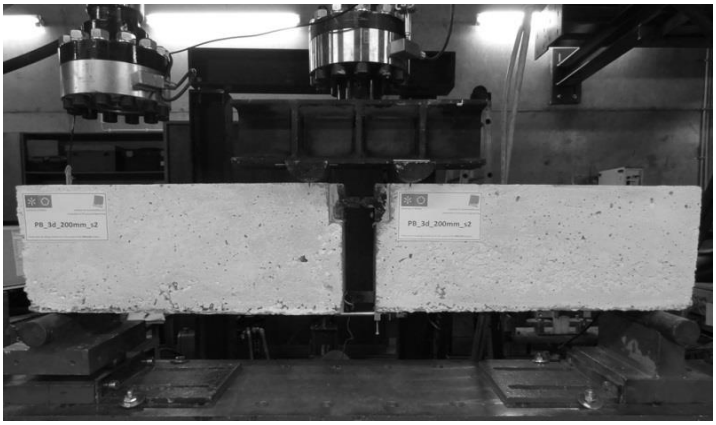

(a)

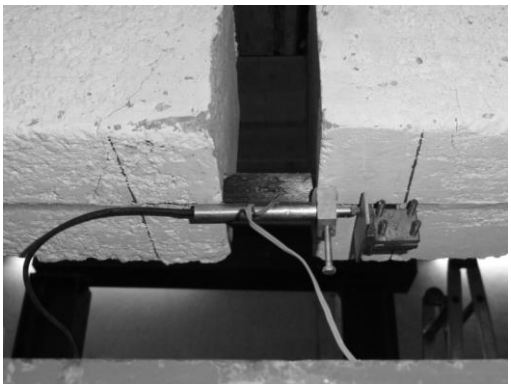

(b)

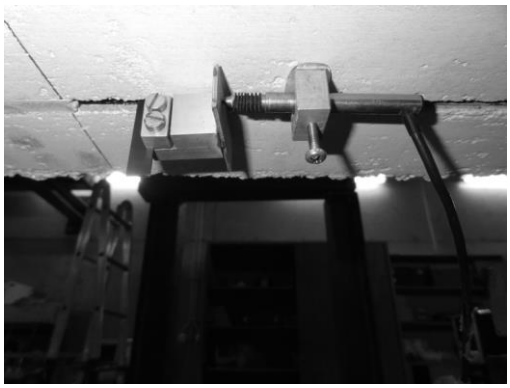

(c)

Figure 38 – Pullout bending test configuration: (a) general aspect including the hydraulic jack and controlling LVDT, (b) loaded-end slip monitoring configuration and (c) free-end slip monitoring configuration.

The specimens were loaded vertically at a constant rate of 0.005 mm/s, controlled by an LVDT attached to the hydraulic jack, visible in Figure 38a, and all specimens failed by debonding of the CFRP-adhesive group due to the low strength of the concrete. The failure of all specimens exhibited the same progression in all cases (see Figure 39). The first crack, identified in the pictures as 1, was a bending (vertical) crack located close to the free-end of the bond length. The appearance of this crack was predictable since this is a zone of resisting bending moment transition *i.e.*, where the ratio between resisting moment and applied moment is lower than in the CFRP strengthened zone. Subsequently, crack 2 has appeared, caused by the active transference of load from CFRP to the surrounding concrete. Finally, when failure occurred, crack 3 has suddenly formed, ripping the NSM-CFRP strengthening completely, avoiding further transference of load. When examining the zone of the CFRP strengthening during and after the tests, the detected cracks detected were localized in the concrete, confirming that up to the applied load levels, the efficiency of the bonding system was excellent.

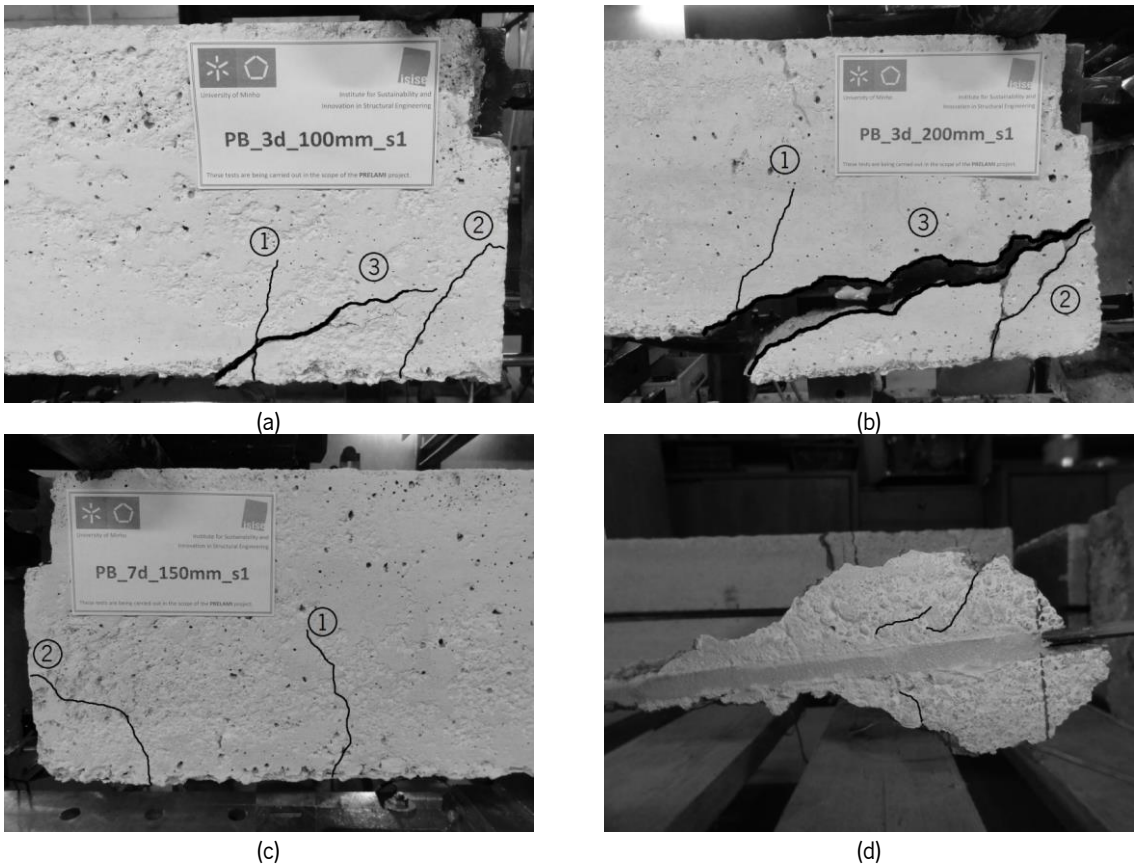

Figure 39 – Pullout bending failure progression: (a) L_b = 100 mm, (b) L_b = 150 mm, (c) L_b = 200 mm and (d) Detail of the NSM-CFRP pullout.

Failure was brittle and explosive and, as explained previously, the failure plane progressed along the cover of the concrete (Figure 40). In the case of the specimens bonded with 100 mm, rupture was not sufficient to destroy completely the concrete cover since, as exemplified in Figure 39a, cracks 2 and 3 did not intersect each other, most likely due to the lower energy generated at failure. In all other cases cracks 2 and 3 formed a continuous failure surface and the FRP strengthening and surrounding concrete cover were entirely separated from the concrete blocks.

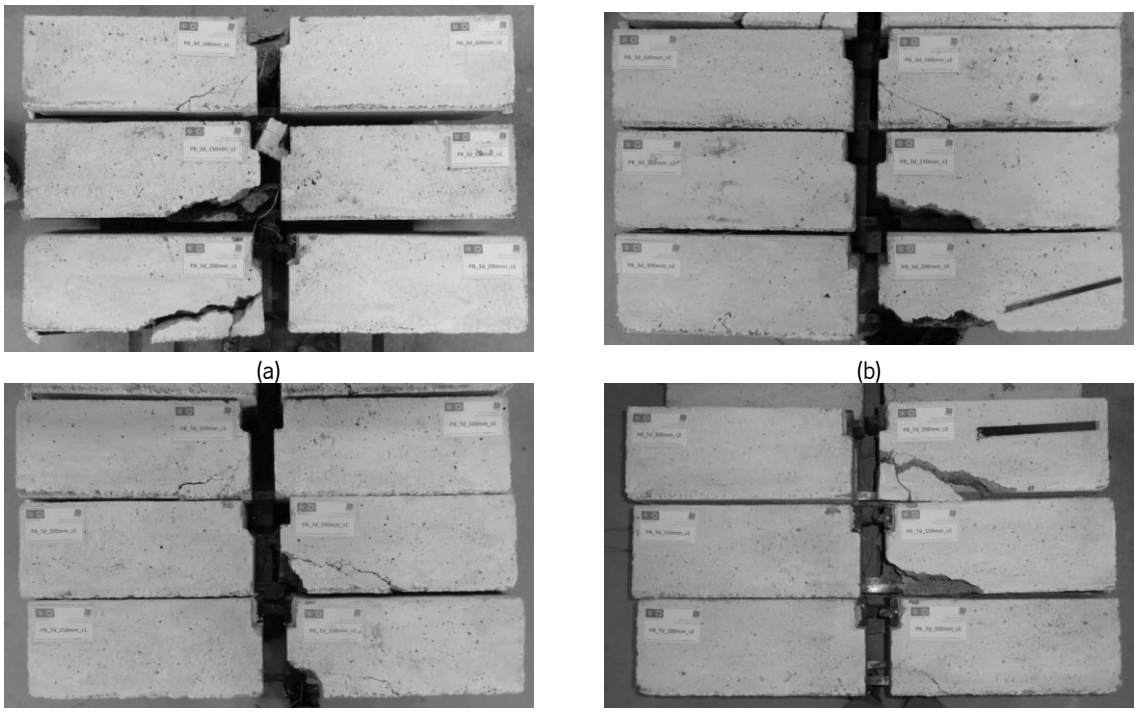

(a) (b) (c) (d)

Figure 40 – Pullout bending test failure: (a) 3 days – Series 1, (b) 3 days – Series 2, (c) 7 days – Series 1 and (d) 7 days – Series 2.

In terms of ultimate applied vertical load, P, no significant variation was observed between similar specimens at different ages, as shown in Table 18 although the average ultimate load of the specimens tested at 7 days was slightly higher than the load obtained in the specimens tested at 3 days. Based on the load and geometric properties of the specimens, several other parameters were calculated for each specimen:

- P_f, the maximum axial load applied in the CFRP, obtained from Eq. 16;
- σ_f, the maximum axial stress applied in the CFRP, according to Eq. 17;
- Σ_g, the average perimeter of the groove (based on the measurements given in Table 16 and calculated using Eq. 18);
- τ_{avg}, the average bond stress (Eq. 19).

$$P_f = \frac{P/2 \cdot L_s}{d_f} \tag{16}$$

where L_s is the horizontal distance from the support to the loaded-section (400 mm) and d_f is the depth of the CFRP at mid-span (160 mm), see Figure 35.

$$\sigma_f = \frac{P_f}{A_f} \tag{17}$$

where A_f is the cross sectional area of the CFRP (28 mm^2).

$$\Sigma_g = \frac{1}{n} \cdot \sum_{i=1}^{n} \left(w_{g,i} + 2d_{g,i} \right) \tag{18}$$

where $w_{g,i}$ and $d_{g,i}$ are, respectively, the width and depth of the groove in a given position of the smaller bond length, and n is the number of measured groove's cross section.

$$\tau_{avg} = \frac{P_f}{\Sigma_g \cdot L_b} \tag{19}$$

Table 18 – Pullout bending tests results.

Specimen	P [kN]	P_f [kN]	σ_f [MPa]	Σ_g [mm]	τ_{avg} [MPa]
PB_3d_100mm_s1	25.28	31.60	1129	65.273	4.841
PB_3d_150mm_s1	33.11	41.39	1478	66.288	4.162
PB_3d_200mm_s1	37.80	47.25	1688	66.180	3.570
PB_3d_100mm_s2	26.11	32.64	1166	68.270	4.781
PB_3d_150mm_s2	35.64	44.55	1591	66.136	4.491
PB_3d_200mm_s2	39.23	49.04	1751	65.984	3.716
PB_7d_100mm_s1	27.78	34.73	1240	64.777	5.361
PB_7d_150mm_s1	37.02	46.28	1653	65.775	4.690
PB_7d_200mm_s1	40.72	50.90	1818	66.770	3.812
PB_7d_100mm_s2	24.44	30.55	1091	62.393	4.896
PB_7d_150mm_s2	33.70	42.13	1504	65.754	4.271
PB_7d_200mm_s2	40.84	51.05	1823	62.773	4.066

Since the failure, and therefore the ultimate capacity of the NSM-CFRP system was clearly limited by the concrete strength, a variation of the ultimate load of about 19%, as reported in Table 17, is perfectly admissible. So, taking as basis the results presented in Table 18, the average of these values for each age was computed and is presented in Table 19. Observing the coefficient of variation in correspondence to each of the curing times, the specimens appear to have demonstrated particularly low variation. Due to this low variation, the results were again recollected and the

average results of all specimens by bond length was calculated (Table 20). Again, the variance of the results was not statistically significant since in all cases, the coefficients of variation were found to be very low, and significantly lower than those obtained in the compressive strength tests (19%) and elastic modulus (15%).

Table 19 – Pullout bending tests average results by age.

Specimen	P []kN	P_f [kN]	σ_f [MPa]	Σ_g [mm]	τ_{avg} [MPa]
PB_3d_100mm	25.70 (0.59) {2%}	32.12 (0.73) {2%}	1147 (26) {2%}	66.772 (2.119) {3%}	4.811 (0.043) {1%}
PB_3d_150mm	34.38 (1.79) {5%}	42.97 (2.24) {5%}	1535 (80) {5%}	66.212 (0.107) {0%}	4.327 (0.232) {5%}
PB_3d_200mm	38.52 (1.01) {3%}	48.14 (1.26) {3%}	1719 (45) {3%}	66.082 (0.139) {0%}	3.643 (0.103) {3%}
PB_7d_100mm	26.11 (2.36) {9%}	32.64 (2.95) {9%}	1166 (105) {9%}	63.585 (1.685) {3%}	5.129 (0.328) {6%}
PB_7d_150mm	35.36 (2.35) {7%}	44.20 (2.93) {7%}	1579 (105) {7%}	65.764 (0.015) {0%}	4.481 (0.296) {7%}
PB_7d_200mm	40.78 (0.08) {0%}	50.98 (0.11) {0%}	1821 (4) {0%}	64.772 (2.826) {4%}	3.939 (0.180) {5%}

Average (Standard Deviation) {Coefficient of Variation}

Table 20 – Pullout bending tests average results by bond length.

Specimen	P []kN	P_f [kN]	σ_f [MPa]	Σ_g [mm]	τ_{avg} [MPa]
PB_100mm	25.90 (1.43) {6%}	32.38 (1.78) {6%}	1157 (64) {5%}	65.178 (2.414) {4%}	4.970 (0.265) {5%}
PB_150mm	34.87 (1.80) {5%}	43.59 (2.25) {5%}	1557 (80) {5%}	65.988 (0.266) {0%}	4.404 (0.235) {5%}
PB_200mm	39.65 (1.43) {4%}	49.56 (1.79) {4%}	1770 (64) {4%}	65.427 (1.800) {3%}	3.791 (0.209) {6%}

Average (Standard Deviation) {Coefficient of Variation}

As regards to the monitoring system, the curves obtained during the tests were plotted in the following figures. Figure 41 depicts the vertical load versus the vertical displacement measured during the tests and shows that load developed at approximately the same rate in all specimens, especially in the specimens with L_b = 200 mm. On the other hand, in terms of vertical load versus loaded-end slip, depicted in Figure 42, the measurements were less coherent. It is believed that the reason of this inconsistency of results may be related to a deficient positioning of the stopper in relation to which the loaded-end slip was measured. While the stopper used to measure the free-end

slip can be positioned in any location since the CFRP laminate does not experience any elastic deformation after the bond length being finished, the loaded-end slip reading can be significantly affected by an inaccurate position. In fact, in some cases, some leftover adhesive was encountered in the zone where the loaded-end stopper was intended to be placed and, therefore, the location of this piece had to be sometimes readjusted in a few millimetres from the exact location of the beginning of the bond length. The readings provided by this device were, as a result, completely illogical. Note that the specimens with 7 days of age, were in the case of L_b = 150 mm (Figure 42b), the ones exhibiting higher deformational behaviour while in the case of L_b = 200 mm (Figure 42c), they were the stiffer ones. Due to these abnormal readings, it was decided not to take into account the loaded-end slip as a decisive parameter on the present study.

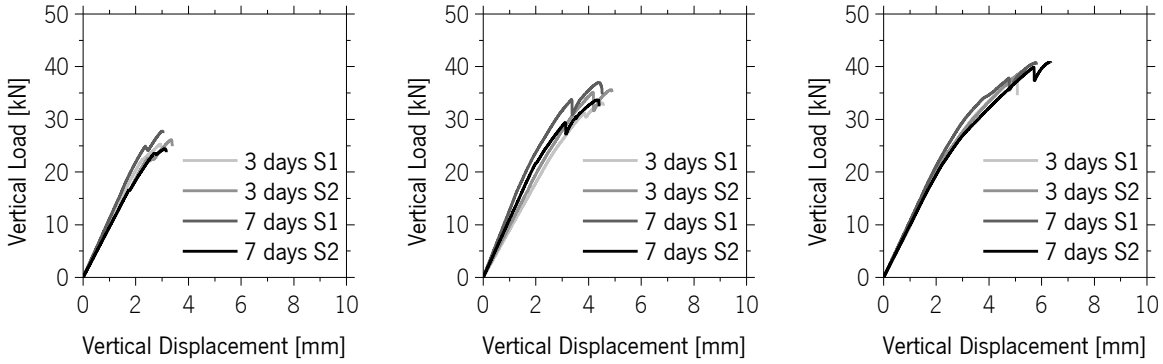

Figure 41 – Vertical Load versus Vertical Displacement: (a) L_b = 100 mm, (b) L_b = 150 mm and (c) L_b = 200 mm.

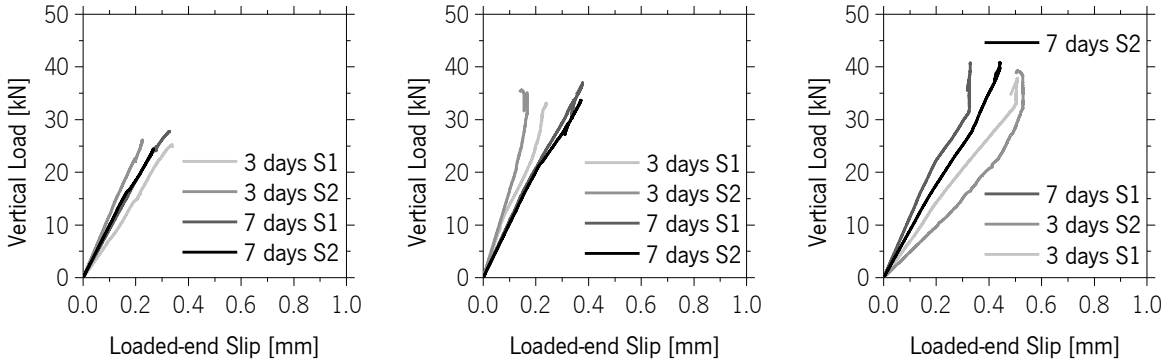

Figure 42 – Vertical Load versus Loaded-end Slip: (a) L_b = 100 mm, (b) L_b = 150 mm and (c) L_b = 200 mm.

Besides the loaded-end slip of the connection, the free-end slip was also registered during the tests as depicted in Figure 43. Observing these plots, the specimen PB_3d_200mm_s1 immediately stands out since its behaviour is clearly different to all the other specimens, even those with smaller bond length, since it exhibited an abnormal initial adjustment before reaching the initial stiffness observed in other specimens, and no reasonable explanation was found to this fact.

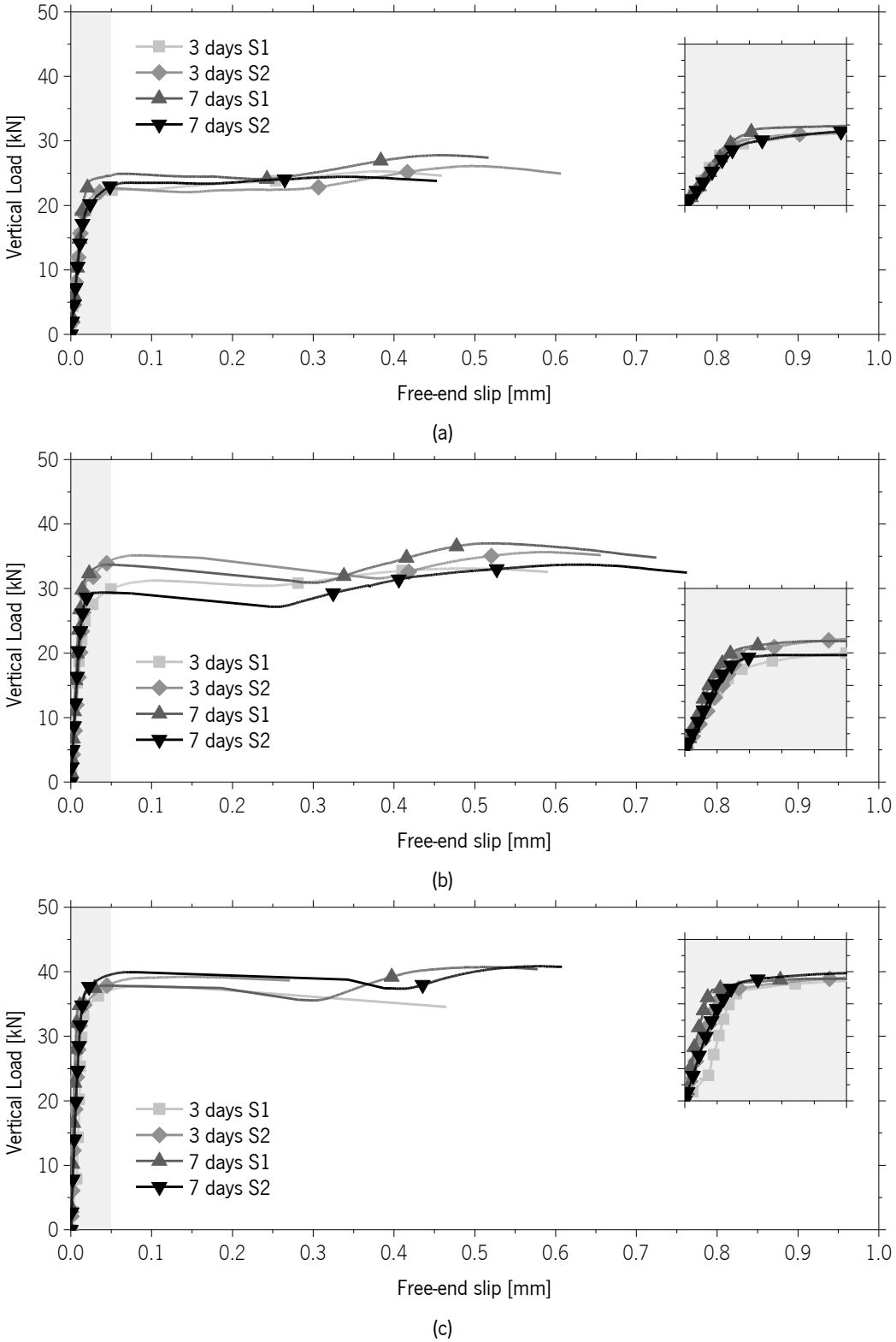

Figure 43 – Vertical Load versus free-end slip: (a) L_b = 100 mm, (b) L_b = 150 mm and (c) L_b = 200 mm.

The specimens with L_b = 150 mm also contrasted with the other two series given the larger scattering, visible in Figure 43b. This was especially due to specimens PB_3d_150mm_s1 and

PB_7d_150mm_s2, which presented substantially lower resistance when compared to the other specimens of that group. Apart from that, the evolution of the vertical load versus the free-end slip was nearly the same in all specimens regardless the curing time of the epoxy adhesive and the bond length used.

Observing now the stress versus strain measured in the strain gauge installed in the CFRP laminate the results were, as expected, linear up to failure (Figure 44). The elastic modulus of the CFRP was computed between 0.5‰ and 2.5‰, as it is in the case of material characterization and according to the obtained results, ranged between 179 and 236 GPa (Table 21), which is an abnormally wide range of values. According to the supplier, the elastic modulus recommended for design is 150 GPa and the average modulus obtained in quality control tests (obtained directly from the supplier) was about 185 GPa.

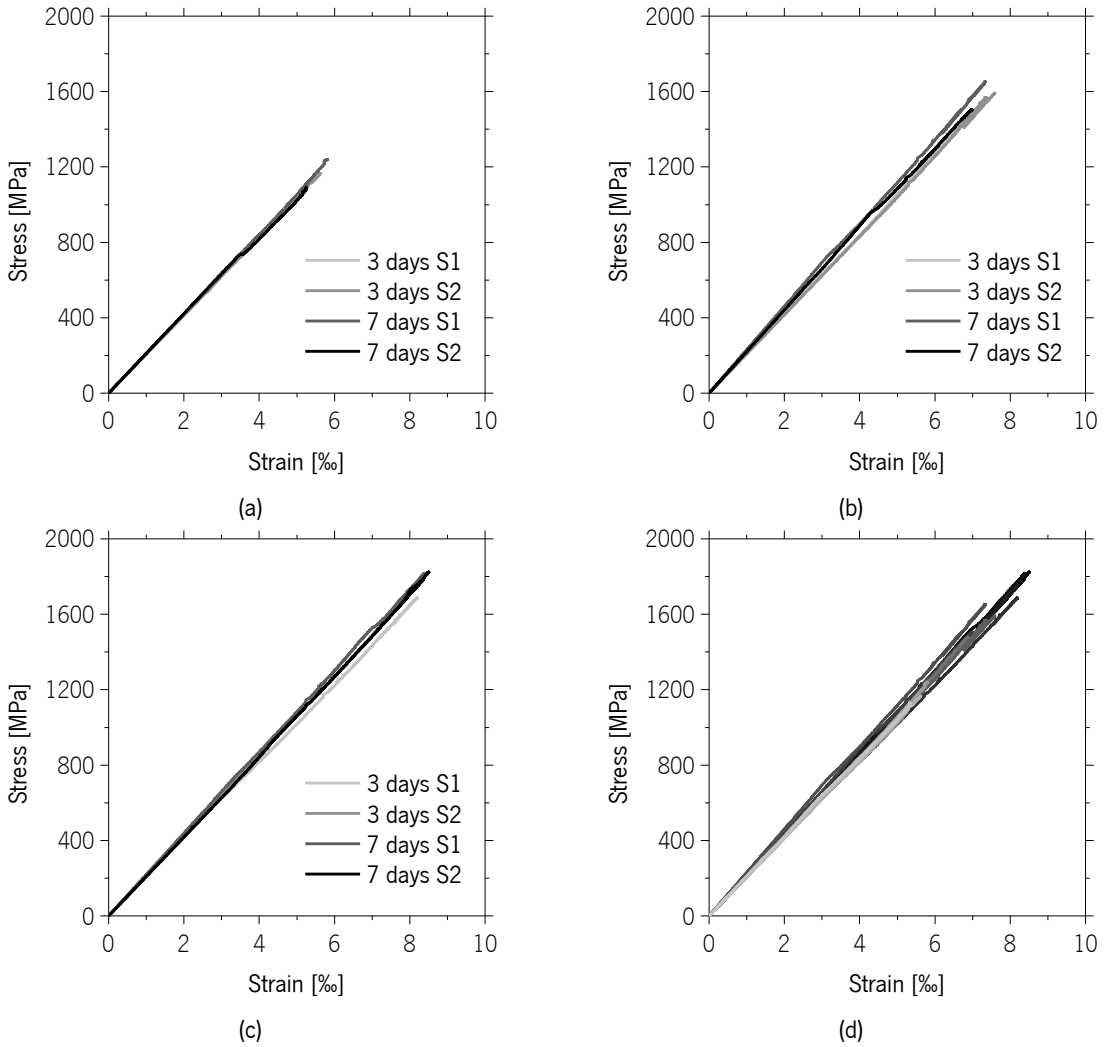

Figure 44 – Stress versus strain: (a) L_b = 100 mm, (b) L_b = 150 mm, (c) L_b = 200 mm and (d) All bond lengths.

Table 21 – Elastic modulus of the CFRP obtained from the pullout tests.

Specimen	E_f [GPa]	r^2	E_f [GPa]	E_f [GPa]	E_f [GPa]
PB_3d_100mm_s1	211	0.9998			
PB_3d_150mm_s1	212	0.9999	210 (2) {1%}		
PB_3d_200mm_s1	208	0.9999		210 (3) {1%}	
PB_3d_100mm_s2	206	1.0000			
PB_3d_150mm_s2	208	1.0000	209 (4) {2%}		
PB_3d_200mm_s2	214	0.9999			213 (7) {3%}
PB_7d_100mm_s1	210	1.0000			
PB_7d_150mm_s1	230	1.0000	220 (10) {5%}		
PB_7d_200mm_s1	219	1.0000		217 (8) {4%}	
PB_7d_100mm_s2	211	1.0000			
PB_7d_150mm_s2	220	1.0000	213 (6) {3%}		
PB_7d_200mm_s2	209	1.0000			

Average (Standard Deviation) {Coefficient of Variation}

Since the scattering of elastic modulus obtained was frankly abnormal, several reasons were pointed out in order to find an explanation for this occurrence. One first reason could be related to an imprecision in the dimensions of the specimens. According to this hypothesis of dimensional imprecision, it was concluded that d_f should be 184 mm (+ 24 mm in most of the specimens) to obtain an average elastic modulus of 185 GPa while if the distance to the support was wrong, L_s should be 347 mm (- 53 mm) to force the elastic modulus to become 185 GPa. If these dimensions were at some point simultaneously overlooked, one possible solution of this combination of parameters would be d_f =171 mm (+ 11 mm) and L_s = 372 mm (-28 mm). However, analysing the relative dimensions of the specimens on the photos taken during the test, although differences of a few millimetres were found in relation to the design dimensions, this hypothesis was found to be unrealistic. The remaining two hypotheses are related to the acquisition system: either the load cell was inappropriately calibrated, or the strain gauges were deficiently acquired. However, given the high linearity of the load-strain behaviour, it is not possible to indicate which signal could be more incorrect, if the hypothesis applies.

In conclusion, reducing the curing time of the adhesive from the recommended 7 days to 3 days was not found to decrease the bond effectiveness of the NSM-CFRP system in terms of load carrying capacity and therefore, in the experimental program presented in the subsequent Section, the tests will only be carried out for specimens with 3 days of age.

3.3 TENSILE CREEP BEHAVIOUR

After performing the tests presented in the previous Sections, where the integrity of the adhesive and bond effectiveness was confirmed despite the reduction of the curing time, it is important to study the behaviour of this adhesive over time since the creep behaviour of this material is expected to be determinant in the long-term performance of the prestress system. For this purpose, tensile creep tests were performed in standard specimens (previously presented in Figure 29) produced from the same epoxy adhesive. The containers of unmixed material were transported to a climatic chamber 24 hours prior to the moulding process in order to maintain the material at 20ºC and 60% of relative humidity at all times. The mixture of the adhesive's components was performed according to the specifications given by the manufacturer as previously described in Section 3.1. The evolution of the strain in the material was recorded for the required period of time, which corresponds to t = 1000 hours, and for three different levels of sustained load, like recommended by the standards that regulate this topic (ISO 899-1 and ASTM D 2990-01). The results of these tests allowed the construction of the creep curves, as well as the determination of the mechanical parameters that describe the tensile creep its behaviour of the tested adhesive.

The main objective of a tensile creep test is to measure the deformation of a given sample of material over time, under a constant load. The measurement of the deformations can be easily performed using any monitoring system, however, regarding the application of the load, there are several methods proposed in literature:

- Hydraulic systems: commonly used in a variety of creep tests, these systems usually produce very good results but require additional vigilance to avoid pressure losses (Feng *et al.*, 2005);
- Spring systems: the structure required for these systems is probably the smallest of all and load is applied by screwing a reasonably strong spring to the frame. This system may require the installation of additional monitoring to guarantee adequate load (Gamage *et al.*, 2009);
- Mechanical systems: these are the most primitive load application systems. Relying purely on the lever principle theyallow the application of moderately high loads using a reduced dead weight (Meshgin *et al.*, 2009).

The mechanical system was chosen to execute these tests was the mechanical, since it appears to be the one with less uncertainties associated to the loading, namely because the load has no possibility of variation over time. This is obviously one of the most important issues of these tests, since normative documentation requires the monitoring to last, at least, approximately 42 days. The creep table designed for this purpose (Figure 45) was also installed in the climatic chamber previously mentioned in order to guarantee constant environmental conditions during the tests.

As stated previously, specimens identical to the ones used for tensile tests were produced. These specimens were positioned in the apparatus clamps and properly anchored. Although the level of compression introduced in the end clamps was not assessed with precision using a dynamometric wrench, it revealed to be just enough to prevent the slippage of the extremities since no signs of slippage were observed in the end of the tests.

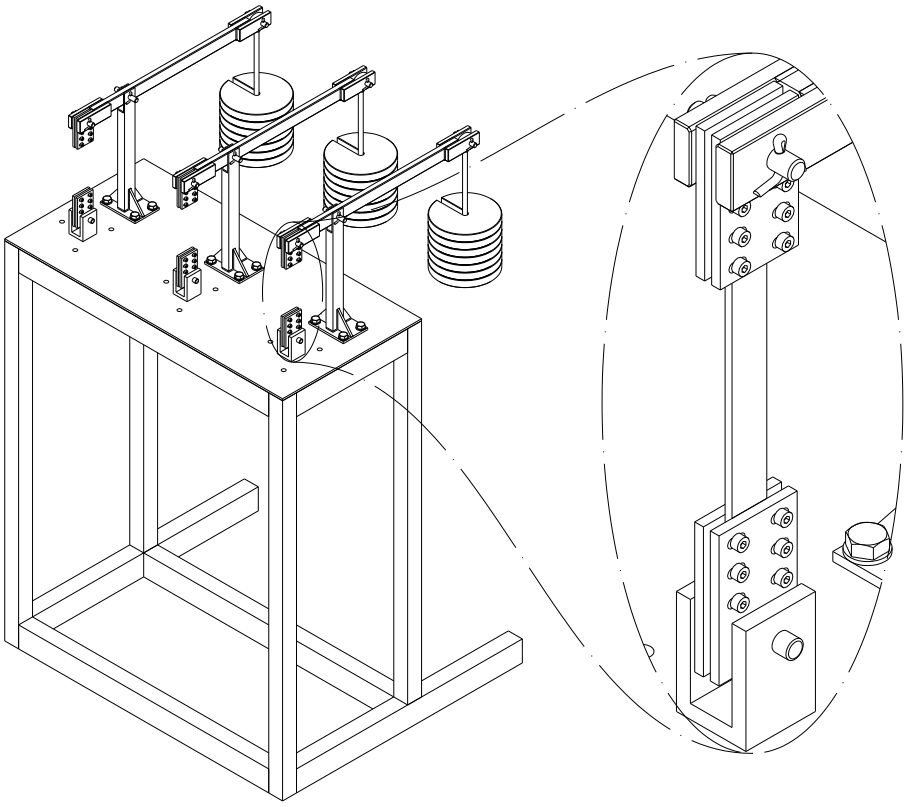

Figure 45 – Mechanical creep table.

Before placing the specimens in the creep table, they were carefully inspected to ensure that they were vertically aligned and accurately centred (see Figure 46). Each specimen was instrumented with two strain-gauges type BFLA-2-3-3L from TML, with a 2 mm measuring length installed precisely at the geometric centre of each face. A control specimen was also prepared and instrumented, to measure possible environmental effects on the material, on the electrical wires, as well as any other unexpected fluctuations in the results.

Note that the strain gauges used are not recommended to apply in epoxy materials but in CFRP elements. The applicability of a strain gauge is defined so that the thermal expansion of the strain gauge itself is compatible with the thermal expansion of the substrate material and therefore, as in this case temperature will be maintained during the testing period it was decided to use these strain gauges instead of acquiring the most appropriate ones.

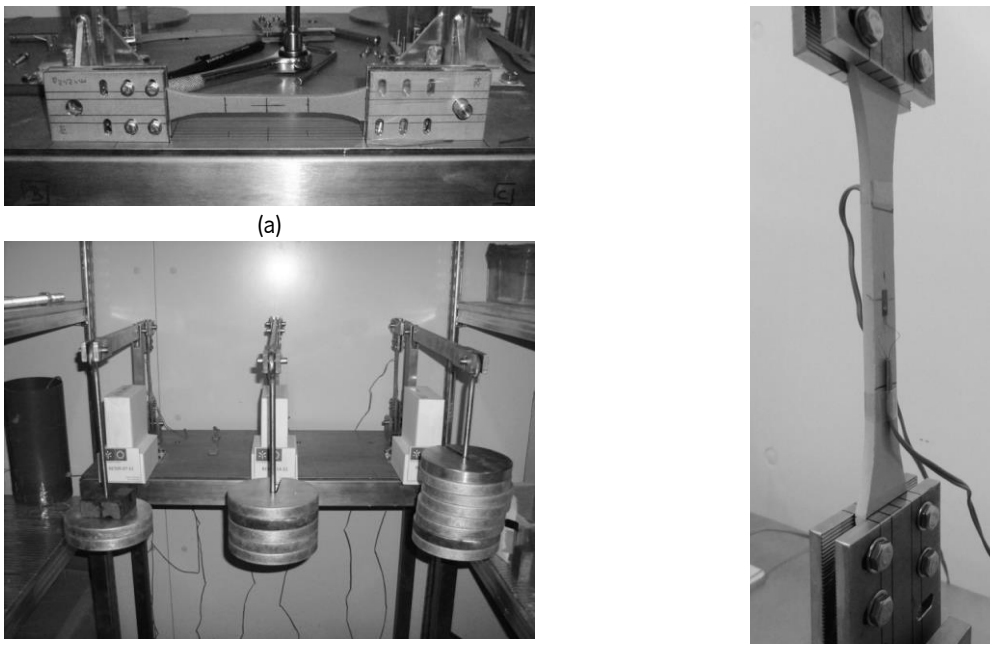

(a) (c) (b)

Figure 46 – Creep tests preparation: (a) Confirming centring and verticality of the specimens; (b) Placement of the specimens in the apparatus and (c) Specimens under sustained load.

Based on the intention of releasing the prestress force at 3 days of age of the adhesive, the creep tests were determined to start at 72 hours of age of the material. The following steps were followed prior to the beginning of the creep tests:

- Measure the cross section of the specimens and marking the specimens;
- Instrument the specimens with strain gauges in opposite faces;
- Place and align the specimens in the creep apparatus;
- Validate the connection of the strain gauges to the acquisition equipment.

Since ISO 699-1 does define a specific number of specimens to be tested, the recommendations of ASTM D 2990-01 were observed at this point. Therefore, as ASTM D 2990-01 determines the use of three specimens per applied load level, it was decided to execute three series of tensile creep tests, using three load levels per series. Each of the series executed was produced from a batch of adhesive mixed exactly 3 days prior to load application, using the same container of material. In each series, 14 specimens were prepared, 5 for material testing at time of loading (72 h of age, herein labelled as t = 0 h), 5 for material testing at the end of the creep test (1072 h of age, herein labelled as t = 1000 h) and 4 for creep testing (3 for tensile creep test and 1 for control purposes).

The instantaneous elastic modulus, E_a, calculated between 0.5‰ and 2.5‰, and tensile strength, f_a, were obtained for each series and are given in Table 22. In most cases, the variation of these

properties was not significant. However, for some unknown reason, Series III exhibited an extraneously low tensile strength, which persisted in time although the corresponding elastic modulus was fairly similar to the ones obtained in previous series.

Table 22 – Instantaneous properties of the creep specimens at time of loading and after 1000 h.

Series	Age of the Adhesive Container	t = 0 h		t = 1000 h		ΔE_a	Δf_a
		E_a	f_a	E_a	f_a		
		[GPa]	[MPa]	[GPa]	[MPa]	[%]	[%]
I	≈ 9 days	7.70 (0.16) {2%}	20.2 (2.2) {11%}	7.61 (0.29) {4%}	20.9 (1.3) {6%}	-1.1	3.3
II	≈ 69 days	6.79 (0.41) {6%}	20.3 (1.7) {8%}	6.36 (0.29) {5%}	17.7 (1.6) {9%}	-6.4	-13.2
III	≈ 124 days	6.72 (0.74) {11%}	15.0 (2.5) {16%}	7.36 (0.84) {11%}	15.7 (5.4) {35%}	9.6	4.5

'Age of the Adhesive Container" refers to the time between the arrival of the adhesive container to the laboratory and the mixture of material.

Average (Standard deviation) {Coefficient of variation}

$$\Delta E_a = \left(E_{a,t=1000h} - E_{a,t=0h}\right) / E_{a,t=0h}$$

$$\Delta f_a = \left(f_{a,t=1000h} - f_{a,t=0h}\right) / f_{a,t=0h}$$

In the tensile creep tests, the load was applied in the specimens in approximately 3 to 5 seconds using standard weights (steel plates). Additionally, and because the test table was not fully balanced, all the loads had to be adjusted taking into account the default load introduced by each lever. It was decided to apply three different levels of load with a maximum of approximately 60% of the tensile strength obtained in the preliminary tests (20.2 MPa, as reported in Table 13 for a curing period of 3 days), to avoid unexpected failures during the tests, resulting in the weight levels, W, presented in Table 23. Note that, percentages of strength presented in Table 23, $\%f_{max,0h}$ and $\%f_{\max,1000h}$, refer to the ratio between the applied stress (approximately 4 MPa, 8 MPa and 12 MPa) and the tensile strength obtained in that same batch of specimens, and not the reference strength (20.2 MPa). Therefore, in the case of Series III, since the tensile strength was abnormally low, the resulting stress levels are apparently overvalued. The applied stress, σ, was calculated according to the law of the lever, as reported in Eq. 20.

$$\sigma = \frac{W \cdot g \cdot \varphi}{A} \tag{20}$$

where W is the mass at the loaded end of the lever, g is the gravitational acceleration, φ is the ratio between the loaded span and the resisting span and A is the cross sectional area of the tested material.

Table 23 – Geometric properties of the specimens.

Series	Sample	W [kg]	A [mm²]	σ [MPa]	$\%f_{max,0h}$ [%]	$\%f_{1000h}$ [%]
I	A	6	43.486	4.32	21	21
	B	11	43.278	7.81	39	37
	C	17	43.067	11.94	59	57
II	A	6	41.272	4.55	22	26
	B	11	42.494	7.95	39	45
	C	17	45.296	11.35	56	64
III	A	6	42.003	4.47	30	28
	B	11	41.763	8.09	54	51
	C	17	43.487	11.82	79	75

The creep apparatus used magnifies the applied dead weight in 3 times meaning that φ = 3.

$\%f_{max,0h} = \sigma / f_{a,0h}$ and $\%f_{0h} = \sigma / f_{a,1000h}$.

The specimens were monitored during the required period of time and the strain-time curves constructed. At the beginning of the test it was noted that the instantaneous strains recorded were slightly lower than the ones expected. The average difference between experimental and theoretical strain was in most cases around 20% (see Table 24). However, given the velocity of load application, it is expectable to obtain a higher stiffness than in routine characterization tests, that are conducted at much a lower speed. The strains and variations reported in Table 24 were quantified as follows:

- $\varepsilon_{theo,0h}$ corresponds to the theoretical strain at the loading instant and is given by the ratio between the applied stress (in Table 23) and the correspondent elastic modulus at t = 0 h (in Table 22);
- $\varepsilon_{exp,0h}$ is the experimental strain, measured in the data acquisition system, at the beginning of the test, immediately after load application;
- $\Delta\varepsilon_{theo-exp}$, is the difference between theoretical and experimental strain, expressed in percentage, as defined in Eq. 21;
- $\overline{\Delta\varepsilon}_{theo-exp}$ is the average of $\Delta\varepsilon_{theo-exp}$ by considering the experimental strain values recorded in opposing strain gauges.

$$\Delta\varepsilon_{theo-exp} = \frac{\varepsilon_{theo,0h} - \varepsilon_{exp,0h}}{\varepsilon_{theo,0h}} \quad (21)$$

Table 24 – Instantaneous strain values obtained in the creep tests.

Series	Specimen	$\varepsilon_{theo,0h}$ [‰]	$\varepsilon_{exp,0h}$ [‰]	$\Delta\varepsilon_{theo-exp}$ [%]	$\overline{\Delta\varepsilon}_{theo-exp}$ %
I	A	0.562	0.456	19	21
			0.435	23	
	B	1.015	0.815	20	22
			0.763	25	
	C	1.551	0.947	39	17
			1.617	-4	
II	A	0.671	0.565	16	24
			0.456	32	
	B	1.171	1.053	10	24
			0.722	38	
	C	1.671	1.296	22	22
			1.311	22	
III	A	0.666	0.457	31	30
			0.474	29	
	B	1.204	0.858	29	25
			0.937	22	
	C	1.759	1.179	33	23
			1.546	12	

In terms of variation of strain in the unloaded specimens, a long-term amplitude of about 0.3‰ was measured (Figure 47). However, as in the second series of creep specimens, Series II, the strain gauge was located in the unloaded specimen was damaged during the 1000 hours period, and since the strain variation measured was relatively small when compared to the strain levels experienced by the samples, it was decided to use the data obtained directly from the creep specimens without attempting to remove any environmental effects.

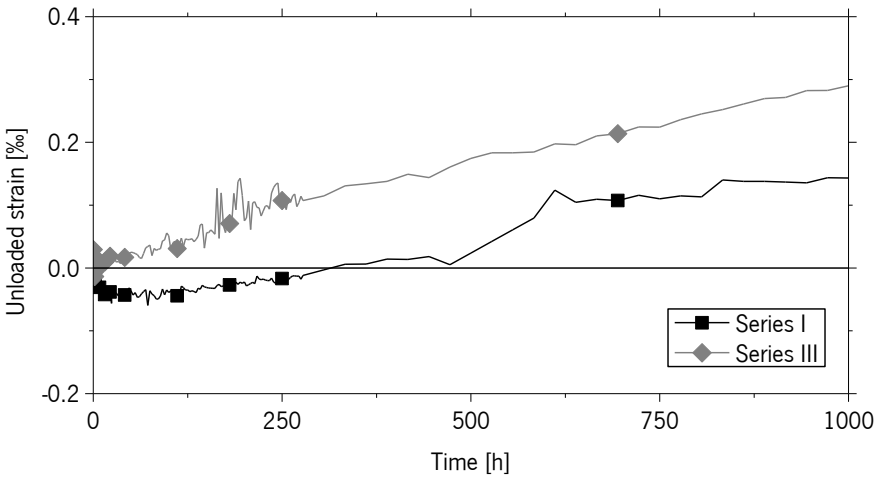

Figure 47 – Strain variation in the unloaded specimen.

The strains recorded in opposite faces have followed the same trend over time, as observable in Figures 48 to 50, in which the strain measured in opposite faces is plotted. Note that the specimen loaded with 12 MPa in Series I exhibited the largest scattering amongst all the results. This difference of strain between opposite faces is most likely due to the small length of the strain gauge combined with the heterogeneity of the adhesive mixture. Note that the mixture of the two components of the adhesive is performed manually and, while in the tensile tests, the reference length is 50 mm, in this case the smaller reference length (2 mm) may expose potential imperfections within the material. Strains were relatively similar over time in the remaining specimens. In Series III, the strains in the specimen loaded with 12 MPa actually intersected at about 250 hours.

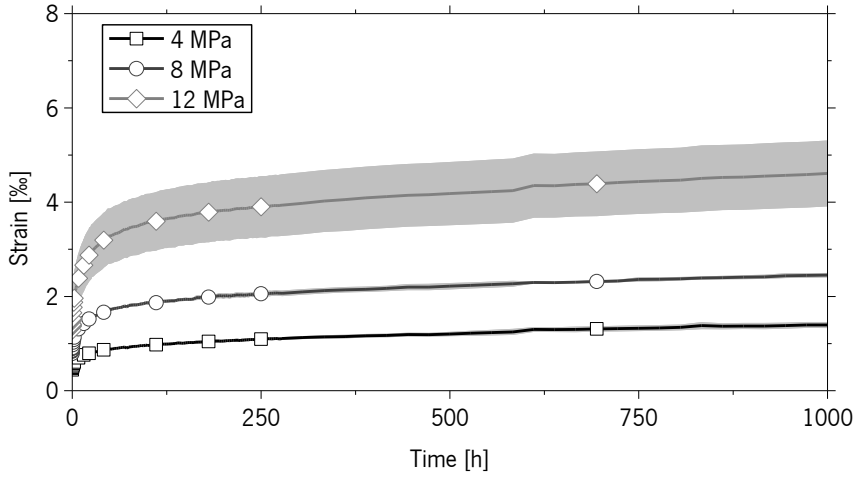

Figure 48 – Evolution of strains in Series I.

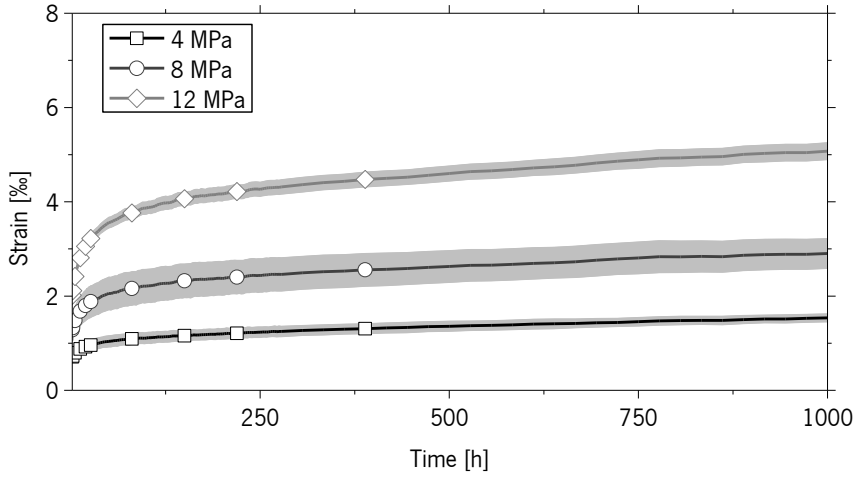

Figure 49 – Evolution of strains in Series II.

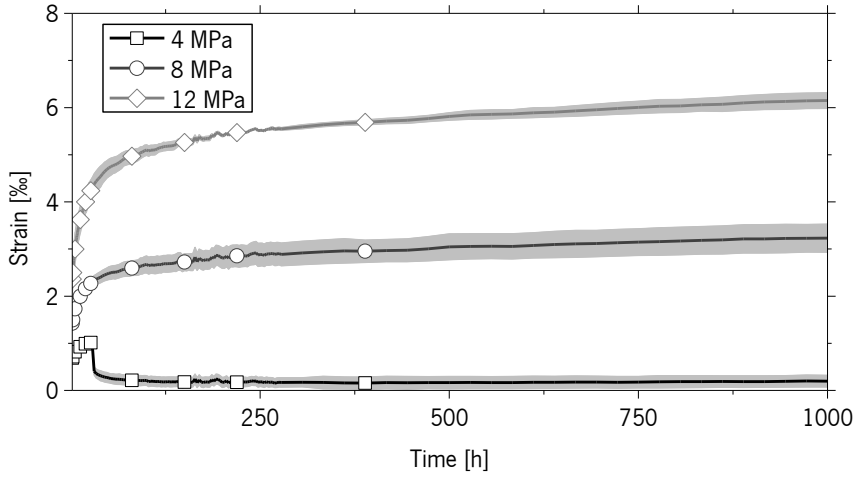

Figure 50 – Evolution of strains in Series III.

It is also worth noting that the specimen loaded with 4 MPa in Series III ruptured prematurely close to the fixing ends due to unknown reasons. The record of strains was maintained during the target period defined for the creep tests, being possible to capture the strain recuperation due to the unloading event, followed by a gradual stabilization process of the strain variation down to a certain residual strain. In fact, it is interesting to observe that after 250 h, the specimens exhibited a practically constant strain level with a fluctuation of about 0.015‰ while the reference specimen, without any load applied, presented a sequential strain increase of about 0.2‰. This observation was another of the reasons why no attempt to subtract environmental effects was made.

It was previously concluded in literature review (Chapter 2) that the creep behaviour of epoxy adhesives should somehow resemble one of three classical rheological models. Observing the shape of the creep curves obtained experimentally, it is evident that the best fit will be obtained using Burgers model (Figure 51).

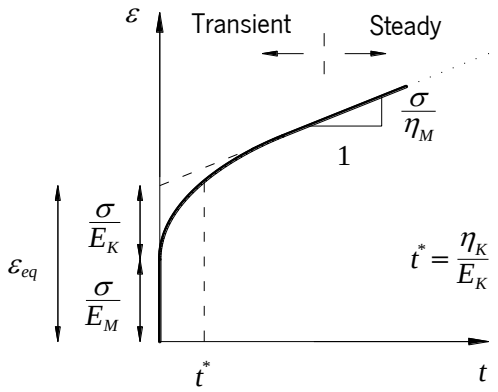

Figure 51 – Burgers model.

Given the difference of strains between opposite faces, the average strain values were considered to obtain the parameters that define this creep curve, mathematically described in Eq. 22. Each of the parameters of this expression can be easily obtained, since the majority of them are directly related to the distinctive characteristics of the curve.

$$\varepsilon(t) = \frac{\sigma}{E_M} + \frac{\sigma}{\eta_M} t + \frac{\sigma}{E_K}\left(1 - e^{-\frac{E_K}{\eta_K} t}\right) \tag{22}$$

where $\varepsilon(t)$ is the strain evaluated at a certain time instant t, σ is the applied stress, E_M and η_M are Maxwell's elastic modulus and coefficient of dynamic velocity, E_K and η_K are Kelvin's elastic modulus and coefficient of dynamic velocity.

Instead of attempting to determine all the parameters numerically by curve fitting, each one was determined individually according to the following procedure:

- The initial strain is inversely proportional to Maxwell's elastic modulus, E_M. In this case, E_M is given by Eq. 23.

$$E_M = \frac{\sigma}{\varepsilon_M} \tag{23}$$

where σ is the applied stress and ε_M is the strain at t = 0.

- Maxwell's coefficient of dynamic viscosity is inversely proportional to the slope of the steady-state branch, as given in Eq. 24.

$$\eta_M = \frac{\sigma}{\varepsilon'_M} \tag{24}$$

where ε'_M is the slope of the selected range of time values. In this work, the reference range selected to characterize this steady-state response was correspondent to the last third of the 1000 h period, *i.e.*, from t = 666.667 h to t = 1000 h.

- Kelvin's elastic modulus, E_K, is proportional to the ε-intercept value of the steady-state branch, as defined in Eq. 25.

$$E_K = \frac{\sigma}{\varepsilon_{eq} - \varepsilon_M} \tag{25}$$

where ε_{eq} is the ε-intercept value in correspondence to the previously selected range of time (666.667 h $\leq t \leq$ 1000 h).

- Kelvin's coefficient of dynamic viscosity, η_K, is commonly related to the retardation time t^*. The retardation time is known to be the time instant at which 63% of the Kelvin's steady-state strain is attained. This can be calculated by isolating Kelvin's terms in the equation, by subtracting the terms initially determined (Eq. 26). After reading in the plot the time necessary to achieve $0.63\,\varepsilon_K$, the coefficient of dynamic viscosity can be determined using Eq. 27.

$$\varepsilon_K(t) = \varepsilon(t) - \frac{\sigma}{E_M} + \frac{\sigma}{\eta_M} t \tag{26}$$

where $\varepsilon_K(t)$ is the strain due to the Kelvin's material model.

$$\eta_K = E_K \cdot t^* \tag{27}$$

Tables 25 and 26 present the most relevant obtained according to the process previously indicated. The obtained values are slightly higher than the ones previously found in literature review (Chapter 2). This fact is however reasonable since most of the studies analysed describe pure epoxy mixtures that typically display a much more rubbery behaviour. Conversely, the adhesive under study is in fact a structural adhesive and so, it is expectable to obtain not only a stiffer response, but also higher viscous components.

To assess the accuracy between the experimental and the analytical results, the Mean Absolute Percentage Error (MAPE) was calculated (Eq. 28) and is also reported in Table 26.

$$MAPE = \frac{100\%}{N} \sum_{i=1}^{N} \left| \frac{\varepsilon_{exp,i} - \varepsilon_{ana,i}}{\varepsilon_{exp,i}} \right| \tag{28}$$

where $\varepsilon_{exp,i}$ and $\varepsilon_{ana,i}$ are the experimental and analytical result of each sampling point i, respectively, and N is the number of sampling points.

The MAPE values reported in Table 26 suggest that the equation selected to characterize the creep behaviour of the adhesive exhibits remarkable potential. Observing Figures 52 to 54, this first approximation appears to produce a fairly good outcome. However, while after reaching the steady-state the behaviour of the adhesive is flawlessly predicted by Eq. 22, the first 250 hours were forecasted with much lower precision.

Table 25 – Notable points of the experimental creep curve.

Series	Specimen	σ [MPa]	ε_M [‰]	ε'_M [‰/h]	ε_{eq} [‰]	t^* [h]
	A	4.32	0.445	4.0987e-04	1.011	26
I	B	7.81	0.789	4.9927e-04	1.969	25
	C	11.94	1.282	8.8907e-04	3.750	22
	A	4.55	0.511	3.7700e-04	1.168	20
II	B	7.95	0.888	6.1171e-04	2.321	20
	C	11.35	1.304	1.0351e-03	4.080	20
	A	4.47	0.466	-	-	-
III	B	8.09	0.898	3.9384e-04	2.850	19
	C	11.82	1.363	6.6730e-04	5.499	19

Table 26 – Burgers equation parameters.

Series	Specimen	σ [MPa]	E_M [GPa]	η_M [GPa·h]	E_K [GPa]	η_K [GPa·h]	MAPE [%]
	A	4.32	9.71	10545	7.64	202	8
I	B	7.81	9.90	15640	6.62	164	9
	C	11.94	9.31	13425	4.84	105	10
	A	4.55	8.91	12079	6.93	137	10
II	B	7.95	8.96	13001	5.55	109	10
	C	11.35	8.71	10964	4.09	81	12
	A	4.47	9.61	-	-	-	-
III	B	8.09	9.02	20547	4.14	77	13
	C	11.82	8.67	17714	2.86	54	14

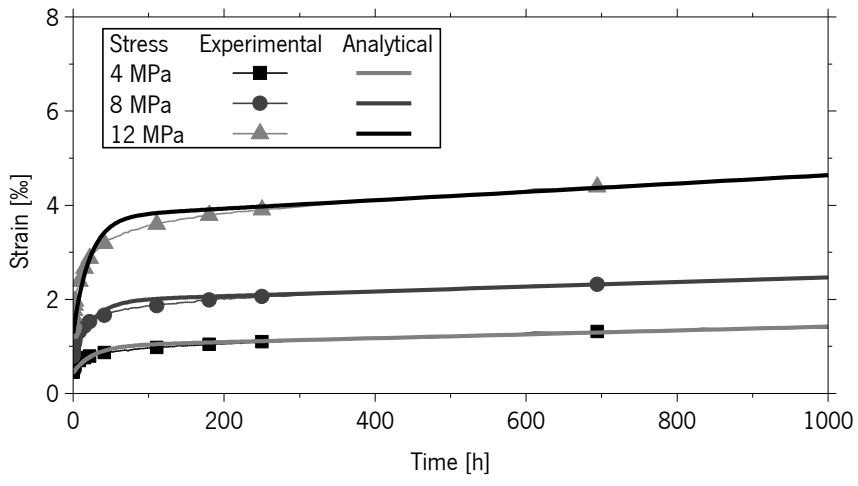

Figure 52 – Curve fitting of Series I experimental results by using Burgers model.

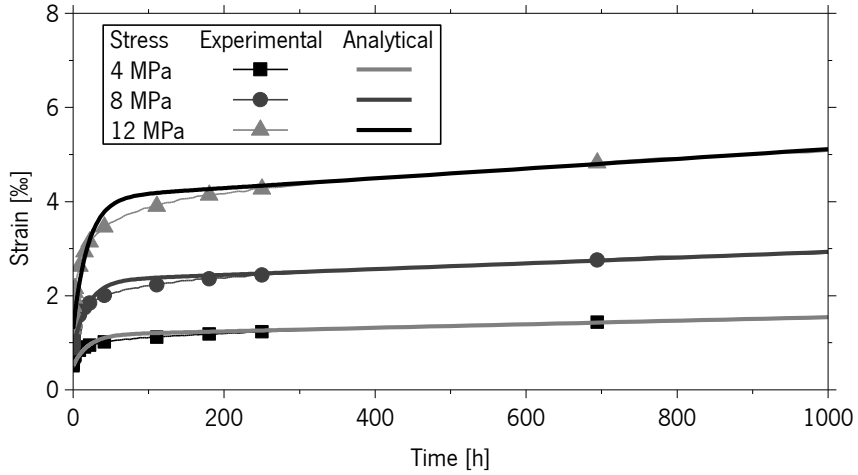

Figure 53 – Curve fitting of Series II experimental results by using Burgers model.

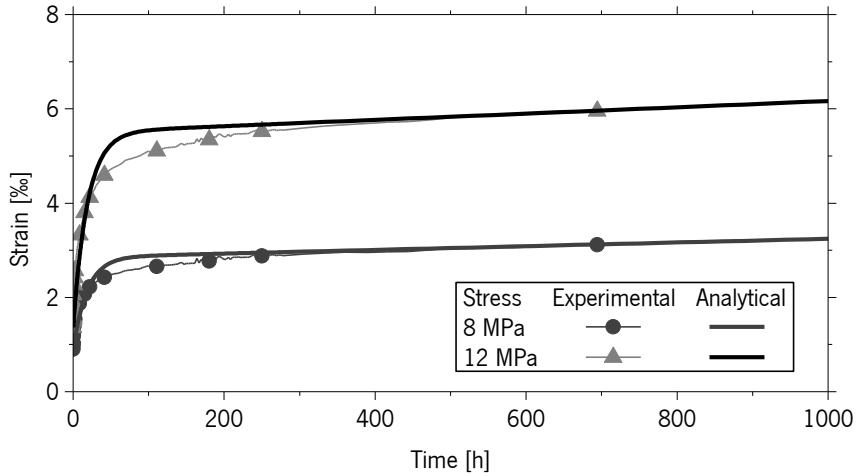

Figure 54 – Curve fitting of Series III experimental results by using Burgers model.

According to a relatively recent survey in the available research on this topic, this solution can still be further improved. Feng *et al.* (2005) showed that the prediction of the transient component of creep behaviour could be improved by introducing a new parameter, n, in the original form of Burgers model, n (Eq. 29).

$$\varepsilon(t) = \frac{\sigma}{E_M} + \frac{\sigma}{\eta_M} t + \frac{\sigma}{E_K}\left(1 - e^{\left(-\frac{E_K}{\eta_K} t\right)^{1-n}}\right) \tag{29}$$

However, unlike the parameters previously determined, it is not possible to determine n directly from the experimental results. Therefore, it was necessary to estimate n by minimizing the difference between experimental and analytical curves (see Figure 55). This was performed by forcing the slope of ε_{exp} versus ε_{ana} to be unitary, using the Generalized Reduced Gradient

(GRG2) nonlinear optimization, available in Microsoft Excel (2010). The values of n obtained by this process are reported in Table 27.

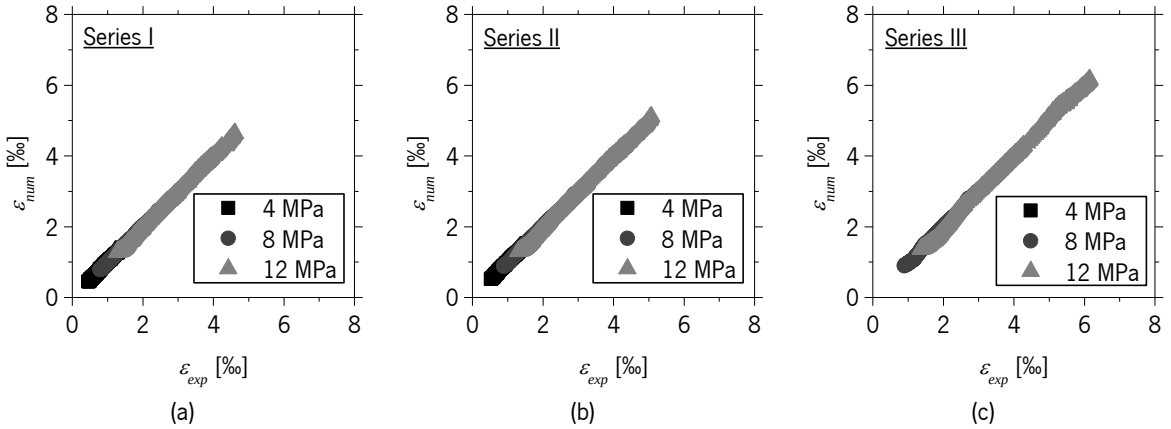

Figure 55 – Result of the optimization between experimental and analytical results: (a) Series I, (b) Series II and (c) Series III.

Table 27 – Modified Burgers equation parameters.

Series	Specimen	σ [MPa]	n	r^2	$MAPE$ [%]
I	A	4.32	0.48	0.9984	2
	B	7.81	0.48	0.9995	2
	C	11.94	0.45	0.9996	2
II	A	4.55	0.57	0.9990	1
	B	7.95	0.52	0.9995	2
	C	11.35	0.49	0.9995	2
III	A	4.47	-	-	-
	B	8.09	0.53	0.9986	2
	C	11.82	0.48	0.9992	3

Feng *et al.* (2005) concluded that for one of materials tested, a neat epoxy adhesive, the parameter n has varied between 0.5 and 0.71 for dry and saturated conditions (95% RH), respectively. Feng has also reported the results of creep tests in a commercial structural adhesive under saturated conditions and, in that case, n was determined to be 0.6. The values found in literature are in accordance with the ones obtained in this experimental program, which ranged between 0.45 and 0.57. Figures 56 to 58 show the final aspect of the fitted curves by adopting the modified Burgers model. According to the images presented, the modified Burgers model has definitely improved the analytical prediction of the creep behaviour of the adhesive especially in the first ages.

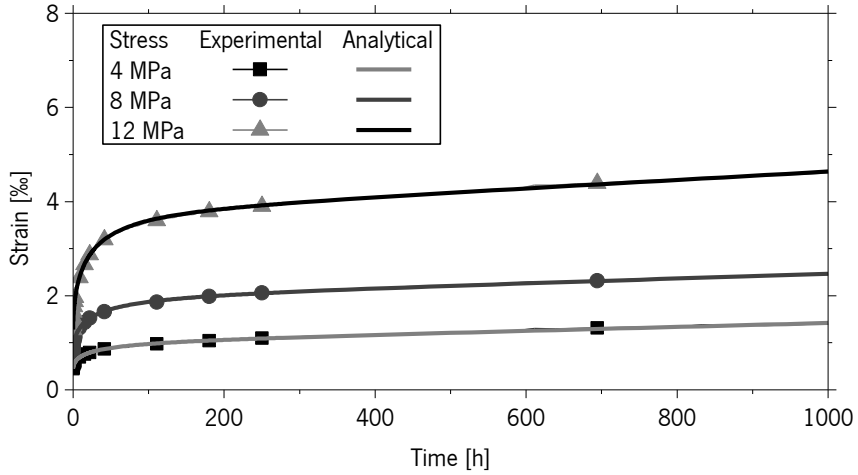

Figure 56 – Modified Burgers model – Series I.

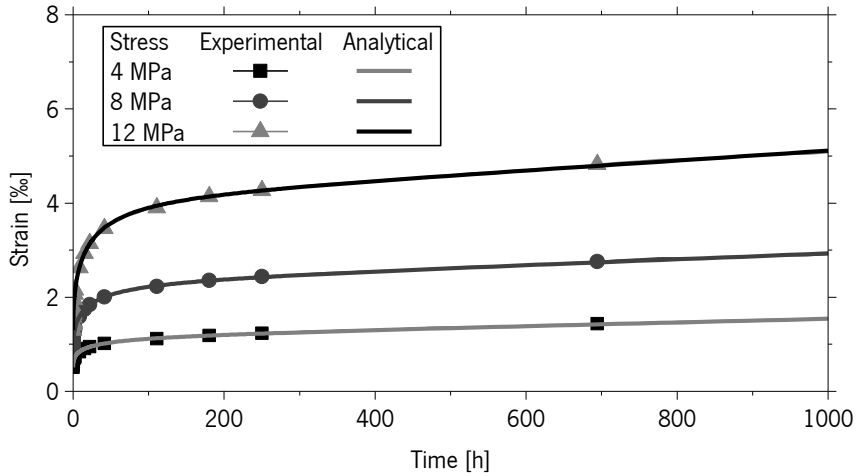

Figure 57 – Modified Burgers model – Series II.

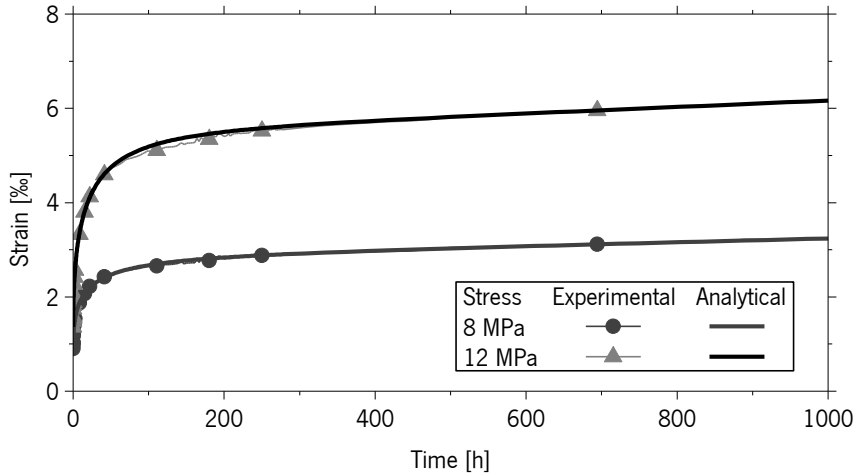

Figure 58 – Modified Burgers model – Series III.

According to the opinion of several authors collected during the literature review, it is expected to observe some type of correlation between the measured parameters and the applied stress level. Based on the assumption of the Burgers model itself, all the springs and dashpots are assumed to exhibit linear elastic or linear viscous behaviour, making possible the derivation of the creep strain equation (Eq. 22). Therefore, in theory, the behaviour of each individual rheological element should be described by a relation of proportionality between stress and strain, or stress and strain velocity. In order to verify this hypothesis, the results of the different series were plotted and analysed. The construction of the plots was performed as follows:

- To determine the behaviour of Maxwell's spring, stress was plotted against the initial strain measured, *i.e.*, $\varepsilon_M = \varepsilon(t=0)$ (Figure 59).
- For the assessment of Maxwell's coefficient of dynamic viscosity, stress was plotted against the slope of the last third of the 1000 h measuring time, which corresponds to the actual steady-state strain velocity, ε'_M (Figure 60).
- Stress was plotted over Kelvin's strain ($\varepsilon_K = \varepsilon_{eq} - \varepsilon_M$) to obtain Kelvin's elastic modulus (Figure 61).

Regarding the Kelvin's coefficient of dynamic viscosity, η_K, it is not reasonable to determine the strain velocity since the slope of the experimental results is always changing in the first ages. However, since Burgers formulation assumes that all parameters are constant, if E_K and t^* are determined to be constant, based on Eq. 27, η_K should be constant as well.

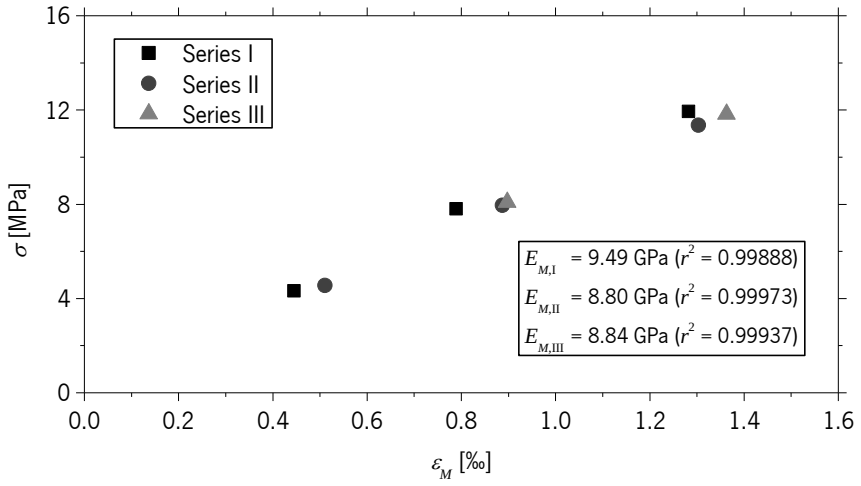

Figure 59 – Stress versus Maxwell strain.

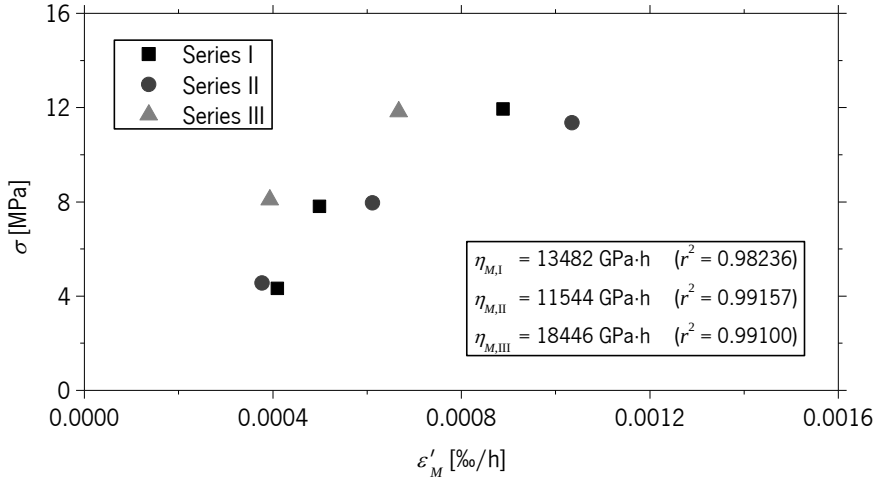

Figure 60 – Stress versus Maxwell strain velocity.

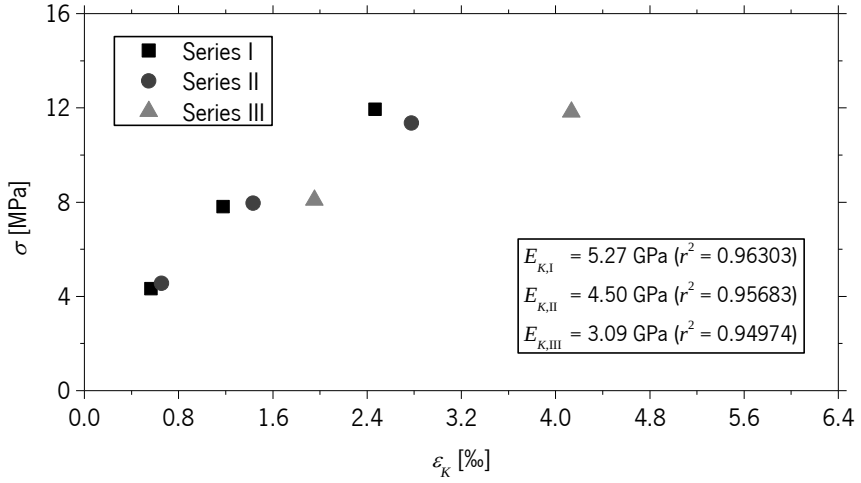

Figure 61 – Stress versus Kelvin strain.

In Figures 59 to 61 the two elastic modulus, E_M and E_K, and the steady-state coefficient of dynamic viscosity, η_M are depicted. It was observed that all Maxwell components demonstrated exceptionally linear relation with the stress as confirmed by r^2 values reported. Note that the linear regressions associated with these r^2 values were in all cases forced to intersect the plots at the origin, and therefore, the regressions performed in the results of Series III do not exhibit an unitary value of r^2.

The Kelvin elastic component, given in Figure 61 by the slope between the applied stress and Kelvin's strain (in Eq. 26), did not demonstrate the same correlation as the other components and actually appeared to decay in successive series (5.27 GPa ~ 4.50 GPa ~ 3.09 GPa). In terms of retardation time, t^*, reported in Figure 62, it was found to be approximately constant except for Series I specimens where t^* presented a slight tendency to decay with the increase of the stress

level. Regarding the n parameter plotted in Figure 63, reasonably constant values were also observed.

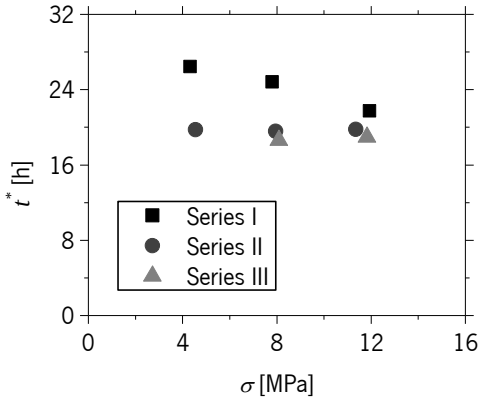

Figure 62 – Retardation time.

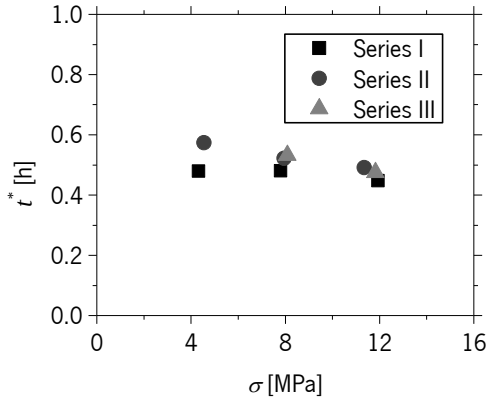

Figure 63 – Parameter n.

According to the obtained results, it is evident that most parameters present almost linear behaviour as previously assumed. Table 28 presents the summary of the linear regressions results as well as the average values of t^* and n. According to these results, E_M and n are definitely the parameters with lowest variability. On the other hand, the short term components, E_K and η_K, of the creep behaviour appear to have some tendency to decay with the age of the adhesive container, meaning that as time passes, the properties of the adhesive are expected to deteriorate since a decrease of E_K will eventually produce a larger equivalent strain, ε_{eq}, and therefore, a larger creep strain.

Table 28 – Average modified Burgers equation parameters of all series tested.

Parameter	E_M [GPa]	η_M [GPa·h]	E_K [GPa]	t^* [h]	η_K [GPa·h]	n
Series I	9.49	13482	5.27	24.3	128	0.47
Series II	8.80	11544	4.50	19.7	88.7	0.53
Series III	8.84	18446	3.09	18.8	58.1	0.50
Average	9.04 (0.39) {4%}	14491 (3560) {25%}	4.29 (1.10) {26%}	20.9 (3.0) {14%}	91.7 (35.2) {38%}	0.50 (0.03) {6%}

Average (Standard Deviation) {Coefficient of Variation}

The main objective of these tests is to obtain the creep curves of a given adhesive material. These curves virtually allow the determination of the properties of the adhesive at any age. Figure 64 presents the creep modulus curves obtained using the analytical results previously presented in Table 28 for each series of specimens, and calculated using Eq. 30.

$$E_{creep}(t) = \frac{\sigma}{\varepsilon_{creep}(t)} = E_{creep} = \frac{1}{1/E_M + t/\eta_M + 1/E_K \left(1 - e^{-\left(\frac{E_K}{\eta_K} t\right)^{1-n}}\right)} \tag{30}$$

where $E_{creep}(t)$ is the creep modulus, $\varepsilon_{creep}(t)$ is the creep strain and σ is the correspondent applied stress.

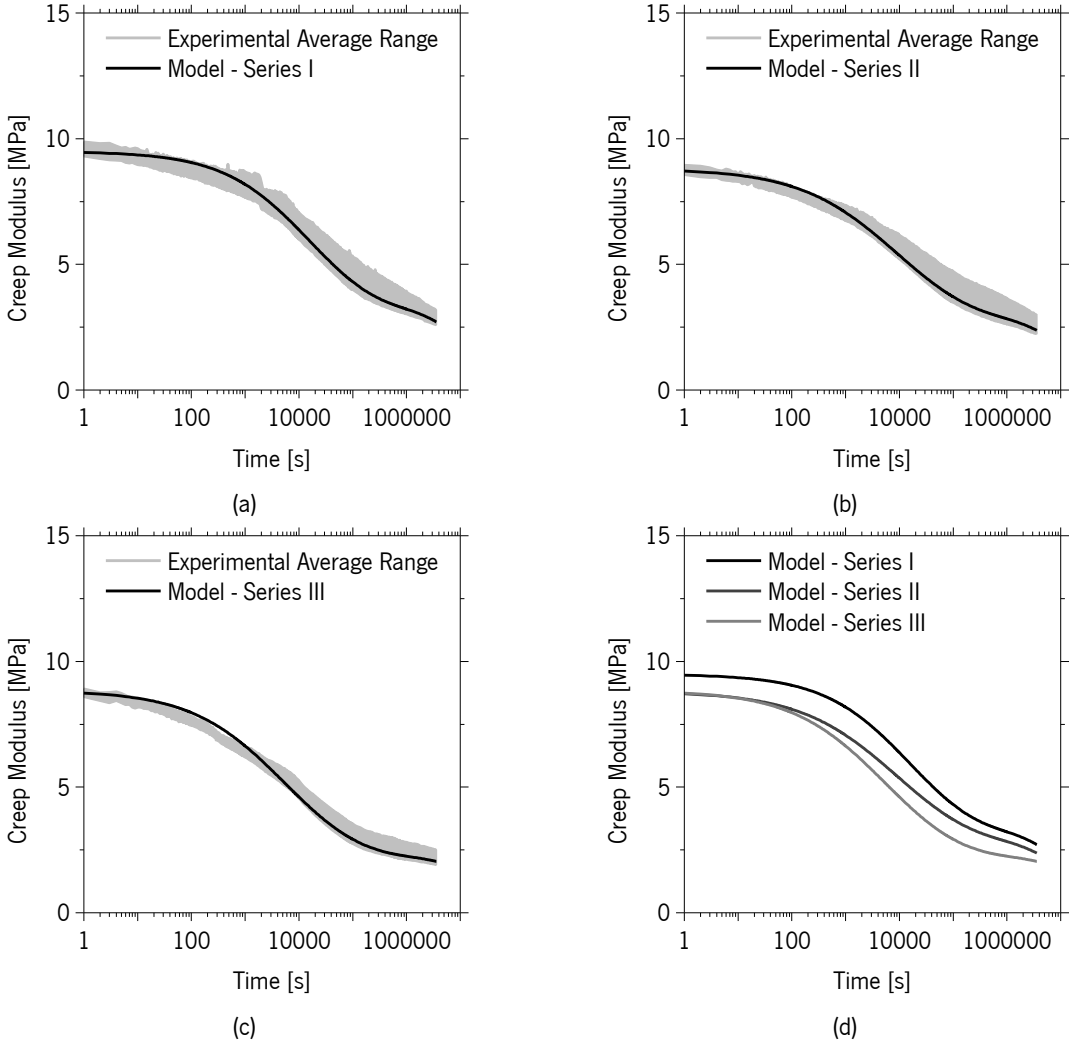

Figure 64 – Creep modulus curves based on the analytical results:
(a) Series I, (b) Series II, (c) Series III and (d) All analytical curves.

Note that, since all parameters are assumed constant, the creep modulus curves coincide within each series equal regardless the applied stress meaning that the creep modulus curve of a particular series is one unique curve, regardless the applied stress. The creep curves obtained are, as expected, localized within the boundary defined by the average creep modulus curve of each specimen and the deterioration of the parameters over time is notorious since the stiffer curve corresponds to the first series and as the adhesive container aged, the creep modulus decreased significantly. It is worth mentioning that after 1000 h loaded, the creep modulus of Series I specimens became

2.71 GPa (about 29% of the initial stiffness), while in Series II and III decreased to 2.37 GPa (27%) and 2.04 GPa (23%), respectively.

3.4 FINAL REMARKS

In this Chapter, the properties of the epoxy adhesive and the NSM-CFRP connection were assessed. According to the results obtained in these tests, it was concluded that the curing time of the adhesive can be reduced to 3 days without diminishing the characteristics of the adhesive or the bond properties of the NSM-CFRP system.

Based on the results of the tensile tests carried out, it was confirmed that after 2 days of curing the properties of the adhesive are nearly the same as obtained for the recommended curing time (7 days). The most relevant properties of the adhesive were determined and exhibited a tensile strength of 20.8±1.0 MPa, an elastic modulus of 7.47±0.24 GPa and average strain at failure of 3.062±0.297‰.

Concerning the pullout bending tests carried out, using a bond length of only 100 mm (the smallest analysed in this Chapter), it is possible to mobilize more than 50% of the nominal tensile strength of the CFRP (1157 MPa in 2000 MPa) without any clear signs of damage in the CFRP-adhesive interface or visible cracking of the adhesive. Similar to previous tests performed at University of Minho it was not possible to achieve CFRP rupture, since the governing failure mode was concrete fracture. However, even with a concrete substrate of average compressive strength of 22.4 MPa it was still possible to mobilize the CFRP up to about 1821 MPa.

Regarding the creep tests performed on samples of epoxy adhesive it was concluded that up to sustained stress levels of 60% of the adhesive's tensile strength, the adhesive behaves as a classic visco-elastic material and can easily be parameterized using the modified Burgers model. In the experimental tests performed, the results suggest that the properties of the adhesive tend to deteriorate with time and therefore, a special attention should be taken regarding the time between adhesive production and application. It is also noteworthy that after 1000 hours of loading, the adhesive samples exhibited about 4 times the deformation at time of loading (creep modulus of roughly 25% of the initial stiffness) without rupturing. According to the initial tensile tests performed, a maximum strain at rupture of about 3‰ was obtained while during the creep tests, the material was able of somehow reorganizing its internal structure to withstand almost the double of this deformation.

3.5 REFERENCES

ASTM 2990 (2001). "Standard Test Methods for Tensile, Compressive, and Flexural Creep and Creep-Rupture of Plastics." *American Society for Testing and Materials (ASTM)*, Pennsylvania, US.

Barros, J. A. O.; Dias, S. J. E. and Lima, J. L. T. (2007). "Efficacy of CFRP-based techniques for the flexural and shear strengthening of concrete beams." *Cement & Concrete Composites*, Elsevier, 29(3), 203-217.

Barros, J. A. O. ; Costa, I. G. and Ventura-Gouveia, A. (2011). "CFRP Flexural and Shear Strengthening Technique for RC Beams: Experimental and Numerical Research." *Advances in Structural Engineering*, Vol. 14, No. 3, 551-573.

Costa, I. G. and Barros, J. A. O. (2001). "Assessment of the bond behaviour of NSM FRP materials by pullout tests." *First Middle East Conference on Smart Monitoring, Assessment and Rehabilitation of Civil Structures* (SMAR2011), Dubai, UAE, 8-11 February, 9 pp.

Costa, I. G. and Barros, J. A. O. (2012). "Evaluation of the influence of adhesive properties and geometry of Carbon Fiber Laminates using pullout tests." *Report no. 12-DEC/E-08*, University of Minho, Guimarães, Portugal, March, 16 pp.

Costa, I. G. and Barros, J. A. O. (2013). "Tensile and Creep tests on Structural Adhesives." *Report no. 13-DEC/E-18*, University of Minho, Guimarães, Portugal, December, 53 pp.

De Lorenzis, L.; Rizzo A. and La Tegola, A. (2002). "A modified pull-out test for bond of near-surface mounted FRP rods in concrete." *Composites: Part B*, 33(8), 589-603.

E365 (1993). "Hardened Concrete - Determination of the modulus of elasticity of concrete in compression." *National Laboratory for Civil Engineering Specification*, 2 pp (in portuguese).

El-Refaie, S. A.; Ashour, A. F. and Garrity, S. W. (2003). "Sagging and hogging strengthening of continuous reinforced concrete beams using CFRP sheets". *ACI Structural Journal*, 100(4), 446-453.

Feng, C. W.; Keong, C. W.; Hsueh, Y. P.; Wang, Y. Y. and Sue, H. J. (2005). "Modeling of long-term creep behavior of structural epoxy adhesives." *International Journal of Adhesion & Adhesives*, 25(5), 427-436.

Gamage, K.; Al-Mahaidi, R. and Wond, B. (2009). "Investigation of CFRP-concrete bond under long-term exposure to cyclic temperature." *Proceedings of the 9th International Symposium*

on Fiber Reinforced Polymer Reinforcement for Concrete Structures (FRPRCS-8) , Sydney, Australia, 13-15 July, 4 pp.

ISO 527-1 (1993). "Plastics - Determination of tensile properties - Part 1: General principles." *International Organization for Standardization* (ISO), Geneva, SZ.

ISO 527-2 (1993). "Plastics - Determination of tensile properties - Part 2: Test conditions for moulding and extrusion plastics." *International Organization for Standardization* (ISO), Geneva, SZ.

ISO 899-1 (2003). "Plastics - Determination of creep behaviour - Part 1: Tensile creep." *International Organization for Standardization* (ISO), Geneva, SZ.

Meshgin, P.; Choi, K. K. and Taha, M. M. R. (2009). "Experimental and analytical investigations of creep of epoxy adhesive at the concrete-FRP interfaces." *International Journal of Adhesion & Adhesives*, 29(1), 56-66.

Sena-Cruz, J. M. and Barros, J. A. O. (2004). "Bond Between Near-Surface Mounted Carbon-Fiber-Reinforced Polymer Laminate Strips and Concrete." *Journal of Composites for Construction*, 8(6), 519-527.

Seracino, R.; Jones, N.; Ali, M.; Page, M. and Oehlers, D. (2007). "Bond Strength of Near-Surface Mounted FRP Strip-to-Concrete Joints." *Journal of Composites for Construction*, 11(4), 401–409.

Chapter 4

PRESTRESS APPLICATION

One of the most crucial tasks of this work is the application of NSM-CFRP prestressed laminates on reinforced concrete elements. For this purpose, a prestress line was designed and installed in the Civil Engineering Laboratory at the University of Minho. This prestress line is able of receiving reinforced concrete beams and strips of slabs up to 9 meters of length with a maximum cross section height of 300 mm and a maximum width of 750 mm, and allows the application of a total of 800 kN of prestressed laminates/bars in laboratory conditions. A representation of the prestress system is depicted in Figure 65, and given the large dimension of the apparatus some pictures of each component assembled are shown in Figure 66. The experimental program described in this Chapter is composed of three series of prestressed reinforced concrete beams.

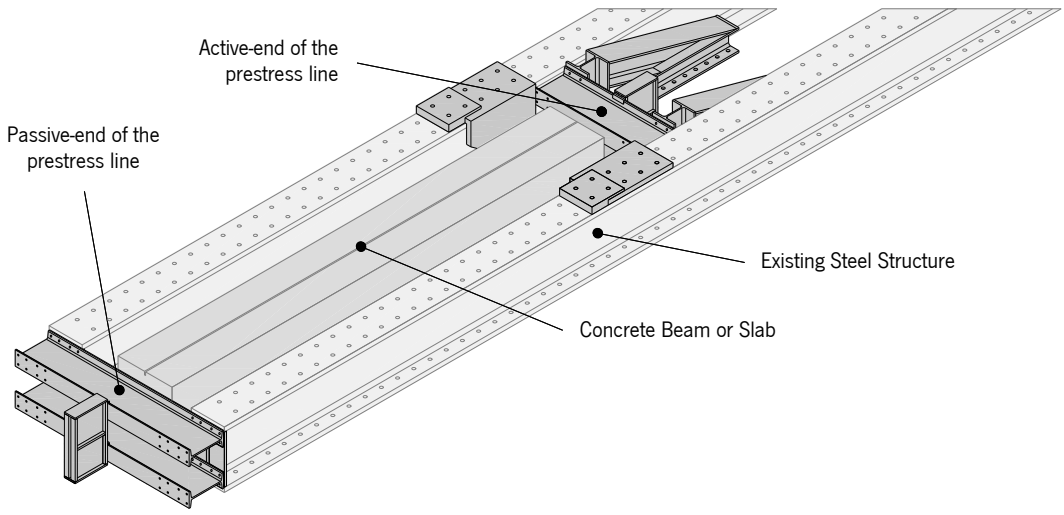

Figure 65 – Illustration of the prestress line.

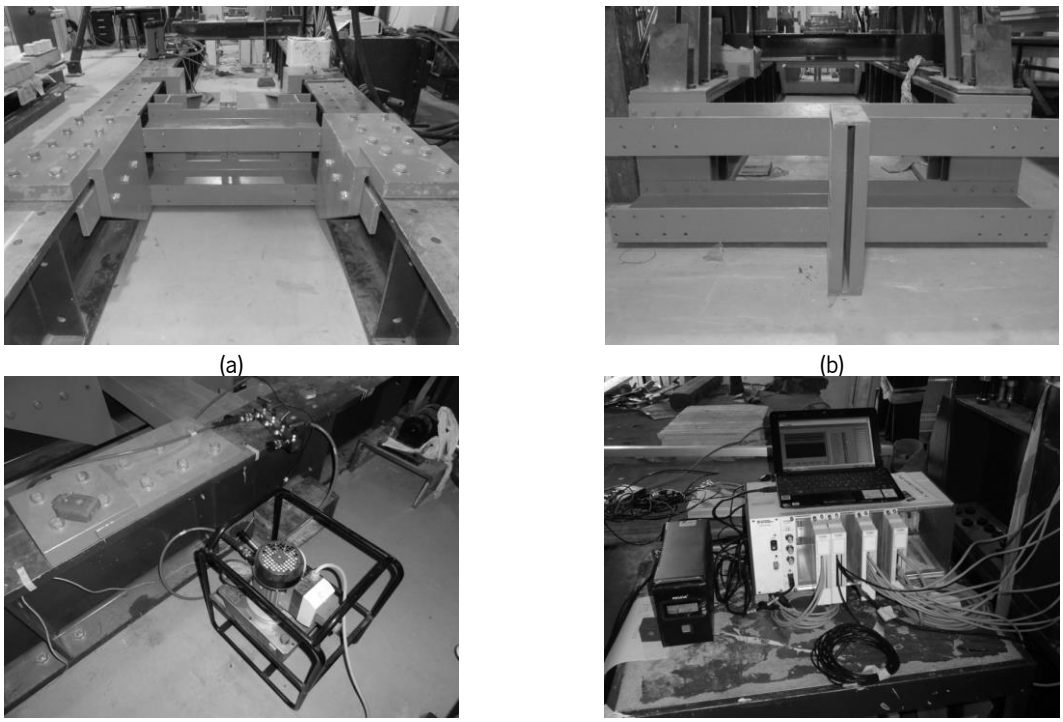

(a) (b)

(c) (d)

Figure 66 – Prestress line components: (a) Active end, (b) Passive end, (c) Hydraulic group and (d) Data acquisition system.

According to the bibliographic research carried out in the first phase of this project (summarized in Chapter 2), it was found that although several works have already been performed on this topic (Wight *et al.*, 2001, Nordin and Täljsten, 2006, Badawi and Soudki, 2008, Gaafar and El-Hacha, 2008, among others), none of them specifies a variety of practical aspects related to the strengthening process as, for example, the rate of release of the prestress. As a result, the procedure used in this experimental program was carefully defined based on previous experience and common practice.

The main steps of a prestress application are summarized in Figure 67. To prepare a prestress application, the beam is firstly introduced in the prestress line and placed on top of steel rollers to facilitate handling inside the prestress line, as well as to later guarantee that prestress release was simultaneous in both ends of the beam. The beam itself is aligned within the prestress line as much as possible and the groove is after aligned with the corresponding opening in the steel boxes positioned at each extremity of the prestress line. This alignment is essential to ensure that after stressed, the laminate will not touch the groove. The laminate, with one anchor already secured, is then inserted through the hollow plate placed on the passive end (herein referred also as free end) as demonstrated in Figure 67b. On the opposite end, also referred as active end *i.e.*, the end in which the hydraulic jack will be installed, the same hollow plate is inserted, followed by the load

cell of 200 kN capacity that will measure the applied load and, finally, the hollow hydraulic jack (Figure 67a). The anchor on this the active end is the last element to be installed and the detail of this component is shown in Figure 67c. The anchors used in this work were designed to have an almost imperceptible slit along them, in order to ensure the horizontality of the CFRP reinforcement, and the 4 bolts were fastened with a dynamometric wrench up to 100 N·m to avoid slippage of the CFRP in relation to clamping zone. It is also worth mentioning that the distance between the anchorage and the RC beam in the active end side, was at least 1000 mm for all the prestressed beams while the in the passive end side it was usually about 700 mm.

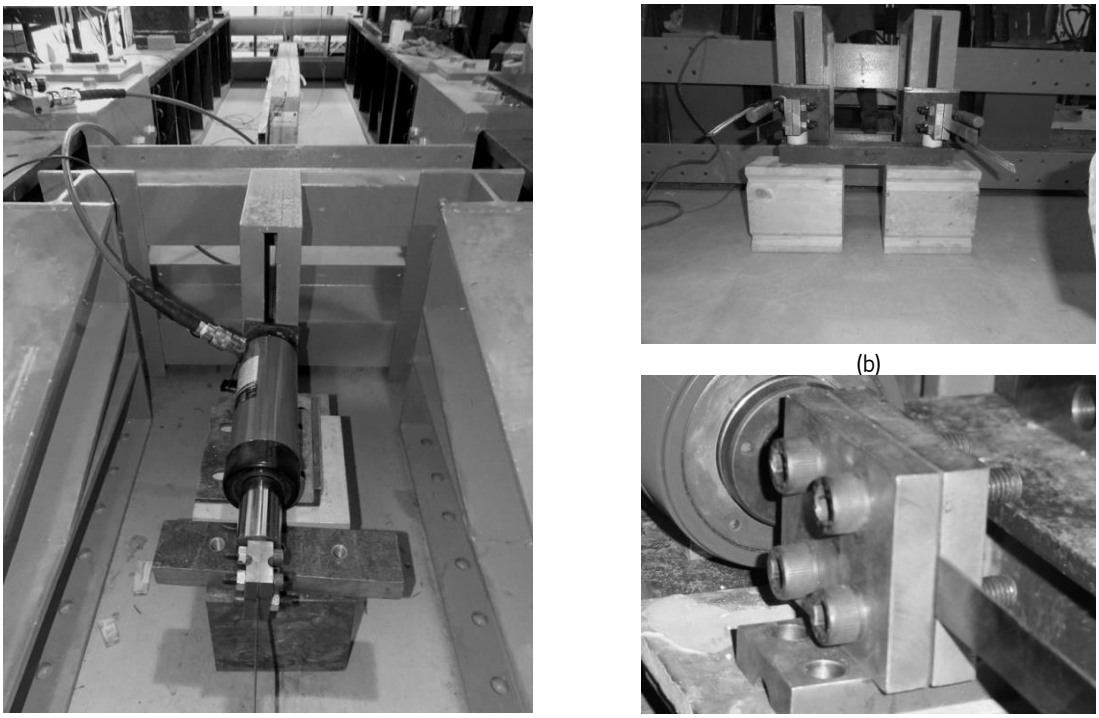

(a) (b) (c)

Figure 67 – Prestress preparation details.

Since after prestressing the length of the CFRP becomes enlarged, the initial position of the strain gauges (before prestressing) was marked on the top face of the laminate. These marks allowed repositioning the concrete beam in relation to one of the strain gauges (the strain gauge located 25 mm from the beginning of the bonded length on the active end side), before applying the epoxy adhesive (Figure 68b). The strengthening was executed by mixing small batches of adhesive (approximately 0.50 to 0.75 kg, as shown in Figure 68c) and introducing it into the groove from the most central part of the beam, towards the extremities (Figure 68d). Since the beams were not placed directly on the floor, but instead over 40 mm diameter rollers to allow free movement at time of prestress release, the application of adhesive was sometimes sufficient to promote some misalignment of the beam. When this was detected, the beam was repositioned in order to get the correct alignment.

Due to the small width of the groove (about 6 mm), and the occurrence of some occasional deviation of the groove alignment, it was extremely challenging to make sure that the CFRP was perfectly centred along the whole bond length. Because of this difficulty, it was decided to favour the centring of the CFRP in the extremities of the beam. This decision is justified by the fact that when the prestress load is released, it is mainly absorbed in the extremities of the bond length, and if the losses are minimized in these zones, the pre-strain in centre of the beam will be most likely preserved. It is also important to mention that the small width of the groove combined with the prior insertion of the CFRP laminate required an additional effort to properly introduce the adhesive into the groove.

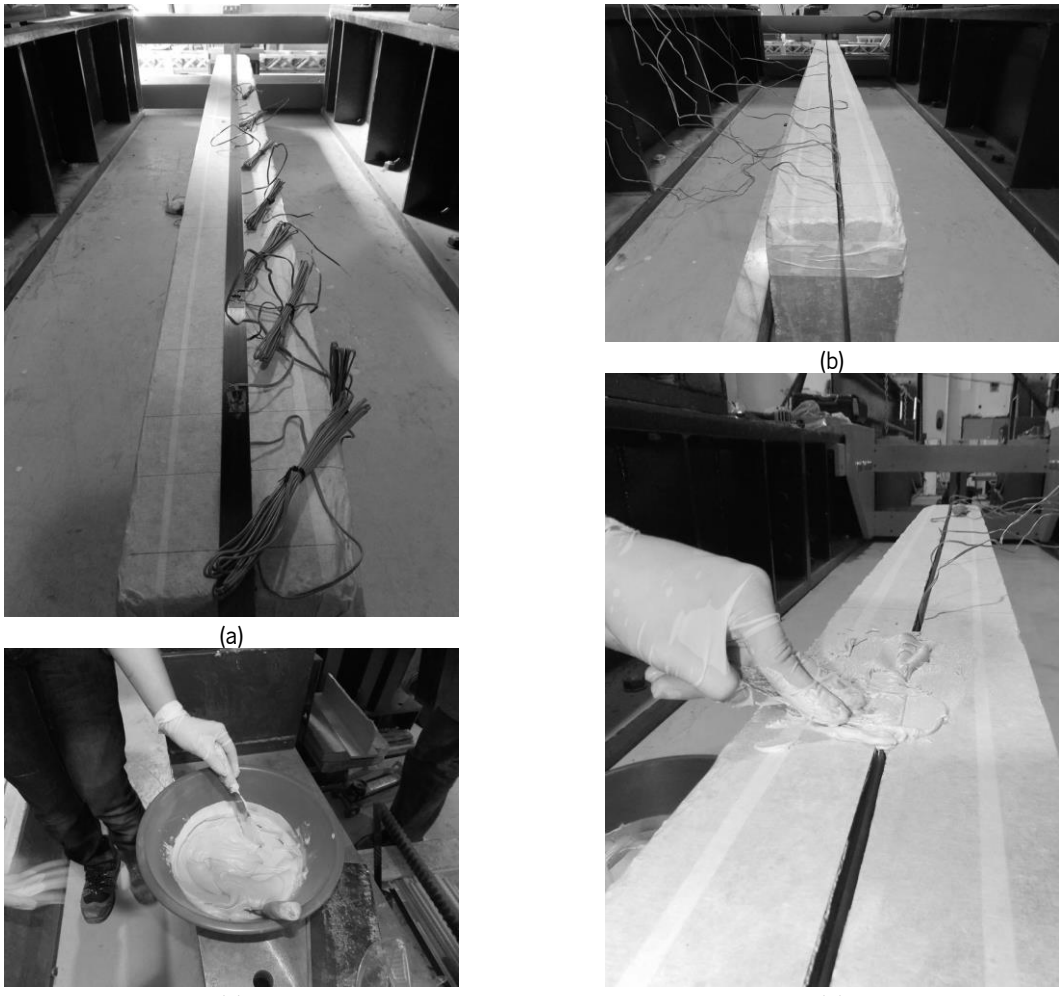

Figure 68 – Prestress application and strengthening: (a) general aspect of the CFRP after the installation of the strain gauges, (b) overall aspect of the prestressed CFRP before the application of the adhesive (c) mixture of the adhesive components and (d) application of the adhesive.

Finally, after the curing period was over, the prestress load was removed. An average rate of prestress loading of 0.5 kN/min was used, while during prestress release, to avoid damage in the

CFRP-adhesive-concrete interfaces, the release rate was decreased to 0.3 kN/min. During the period of transferring the prestress from the CFRP laminate to the surrounding substrate, all the installed strain gauges, the slip of the CFRP in the active end side (Figure 69a), and the mid-span deflection (Figure 69b) were monitored. After complete prestress transference, the loss of strain was measured in the sections of the CFRP laminate where the strain gauges were installed. These measurements provided the reading of the prestress losses for a period of approximately 1000 h, as used in the tensile creep tests performed in samples of the used adhesive, reported in Chapter 3.

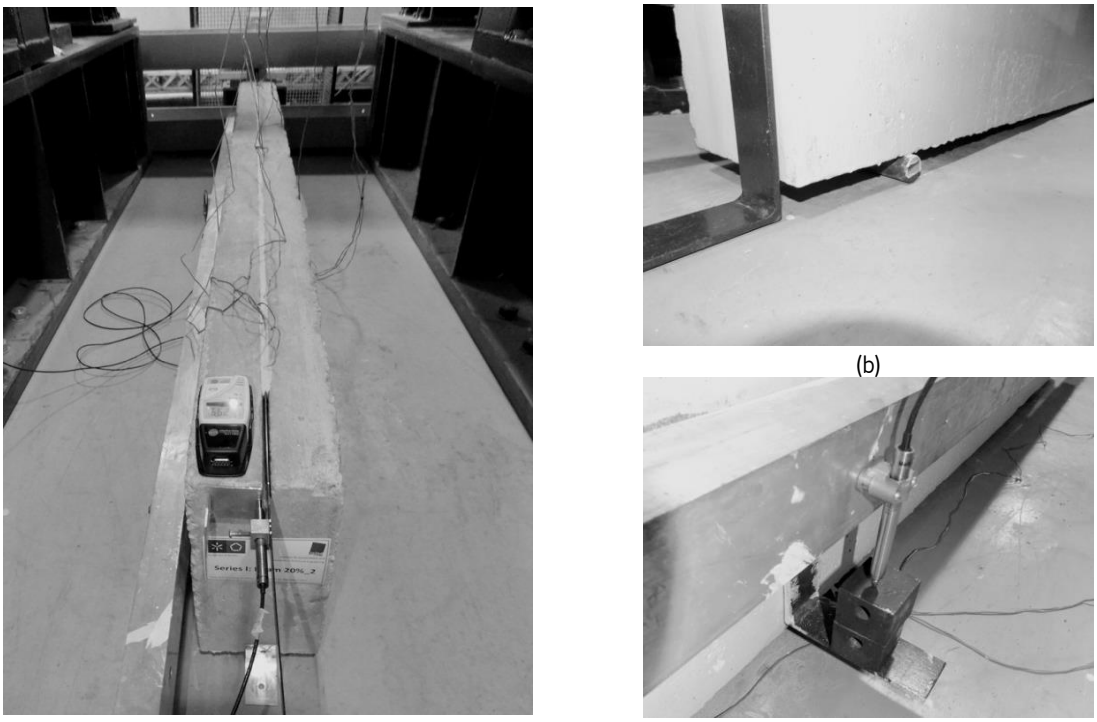

(a) (b) (c)

Figure 69 – Prestress release: (a) overall aspect of beams at time of prestress release, (b) detail of the support roller and (c) detail of the mid-span deflection monitoring.

4.1 SERIES I – PRELIMINARY TESTS ON SHORT BEAMS

One preliminary series of reinforced concrete beams was prepared not only to test the prestress line but also to monitor as many variables as possible in order to isolate the most relevant ones and rationalize the number acquisition devices in subsequent the series. Four reinforced concrete beams with 150×300×2400 mm^3, as depicted in Figure 70, were casted with a concrete with a target strength class C20/25 (target average compressive strength of 33 MPa) and two of them were selected for prestress application.

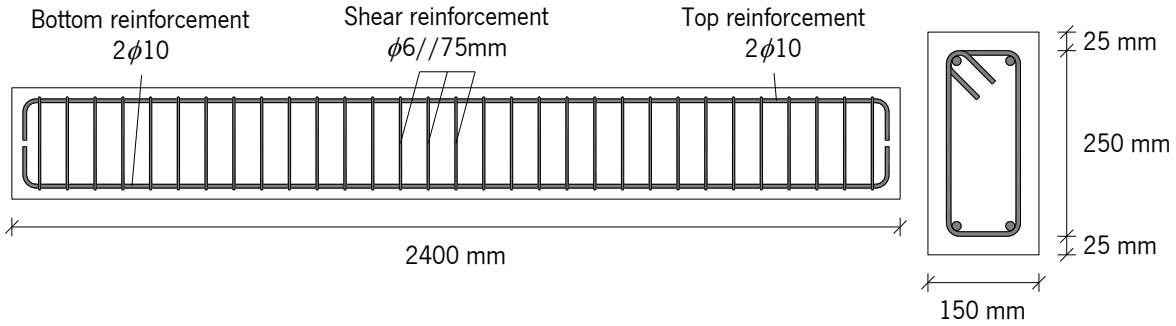

Figure 70 – Cross section and reinforcement configuration – Series I.

The steel bars used in this series were instrumented with three strain gauges to monitor the strains in the selected sections of the bottom reinforcement. Two strain gauges were positioned in the mid-span zone, one in each bar and another one was placed in one of the bars, 200 mm from the mid-span (Figure 71). All beams were casted at the same time using the same batch of concrete (Figure 72). After concrete was fully cured, a strain gauge was attached in the top surface of the concrete beam, as depicted in Figure 71, to measure the compressive strain in the concrete of this region. The beams were then turned over to manually open a groove with average cross section of 6×30 mm^2 in three beams of this series (Figure 72b).

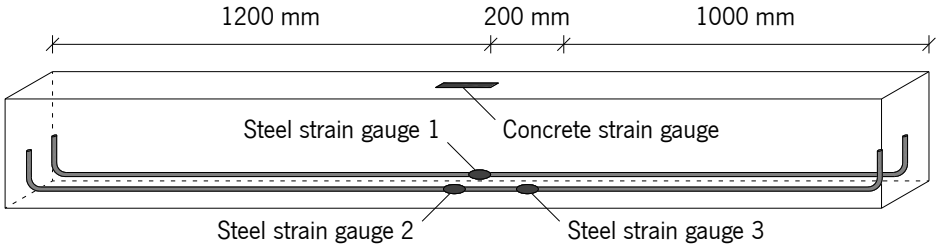

Figure 71 – Steel and concrete instrumentation details – Series I.

(a) (b)

Figure 72 – Casting and beam preparation – Series I: (a) mould preparation and (b) notched beams.

4.1.1 Application and release of prestress

After preparing the prestress system as described in the beginning of this Chapter, eight strain gauges were installed on the CFRP to prestress, as represented in Figure 73. It was decided to leave a clear distance of 150 mm between the extremities of the beam and the beginning of the bond length to not only to replicate the fact of the CFRP strengthening not being able to pass through the peripheral elements, such as columns or structural walls, but also to avoid stress concentration and unrealistic confinement in the support zone during the flexural tests. After completing the preparation of the prestress system, all strain gauges were continuously monitored.

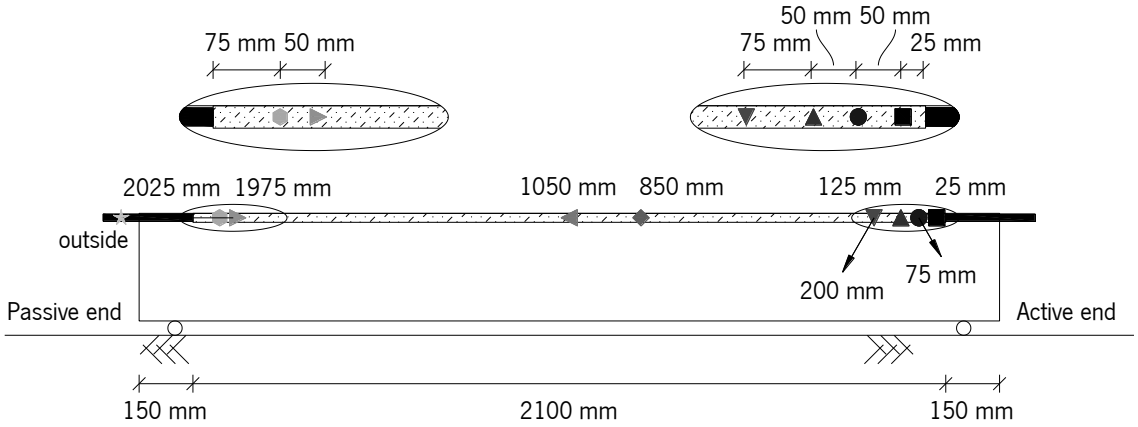

Figure 73 – Positioning of the strain gauges in the CFRP laminate – Series I.

Each beam was strengthened with a single CFRP with 1.4×20 mm^2 cross sectional area, nominal tensile strength of 2000 MPa and nominal elastic modulus of 150 GPa (values provided by the supplier). The prestress levels that were intended to apply on these elements were defined in terms of strain based on these nominal properties. This means that as the nominal ultimate strain of this material is 2000 / 150 = 13.333‰, a prestress level of 20% would indicate a target strain of 0.2 ×13.333 = 2.667‰ while a prestress of 30% requires the application of 0.3 ×13.333 = 4.000‰. These strain levels were introduced with reasonable accuracy on the material during prestress application, as reported in Table 29. The beams prestressed with 20% and 30% of the CFRP ultimate nominal strain are herein labelled as S1_20% and S1_30%, respectively.

Analysing Table 29, it is noticeable that the secant elastic modulus of the CFRP measured during the prestress is relatively close to the nominal one in the case of the S1_20%, while in the case of the S1_30% this value was much higher than expected (200 GPa according to Table 29). This variation of values was unexpected, since the same procedure and equipment was used in both prestress applications. Abnormal values of elastic modulus were already obtained in the pullout bending tests described in the previous Chapter. Those abnormal values were justified by assuming

an eventual error occurred during the acquisition or the influence of the curvature introduced by the test. However, in this case, a different acquisition system was used and nearly perfect axial tension was being introduced in the laminate. Considering the average elastic modulus obtained in quality control tests, 185 GPa, one possible explanation to this overestimation is related with the fact of the opening of the hydraulic jacks being too narrow. This opening is only 25 mm, both in the hydraulic jack and in the load cell and, despite all precautions, it is possible that at some point, inside those devices, the laminate might have contacted with an adjacent surface, requiring an unreal but necessary additional load compared to the nominal load. However, this hypothesis does not explain the smaller elastic modulus obtained in S1_20% since apparently, this laminate required less load to introduce the target strain.

Table 29 – Prestress application and prestress release results – Series I.

	Beam	S1_20%	S1_30%
Prestress Application	Applied load [kN]	11.1	22.8
	Applied stress [MPa] §	397	815
	Loading duration [s]	1199	3189
	Loading speed [kN/min]	0.56	0.43
	Average CFRP strain [‰]§§	2.610 (0.030) {1%}	4.080 (0.040) {1%}
	Secant elastic modulus [GPa]	152	200
	Temperature at strengthening (outdoor) [°C]	19.5	29.4
Curing	Curing time [days]	3.13	3.16
	Average temperature (outdoor) [°C]	21.4 (4.5) {21%}	19.8 (4.0) {20%}
Prestress release	Applied load [kN]	11.1	22.2
	Release duration [s]	2451	4633
	Release speed [kN/min]	0.27	0.29
	Average CFRP strain before prestress release [‰]§§	2.700 (0.030) {1%}	3.850 (0.070) {2%}
	Temperature (outdoor) [°C]	29.7	17.7

Average (Standard deviation) {Coefficient of Variation}

§ Applied stress = Applied load / CFRP cross sectional area.

§§ Average CFRP strain = average of the strain gauges 'outside' and at 25, 75, 125, 200, 850, 1050 mm.

The average outside temperature at the time of year at which the strengthening were applied was about 20ºC (see Table 29). Considering the results of the study on the curing time of the adhesive presented in the previous Chapter, a minimum curing time of 3 days was adopted. Loading was performed at a rate of 0.56 kN/min and 0.43 kN/min, for S1_20% and S1_30%, respectively (see Table 29).

To better understand the behaviour of the materials as well as of the monitoring system, all data collected was plotted in Figures 74 to 78. In all plots, the undulant movements of the signals recorded (load cell and strain gauges) are most likely related to the natural temperature variations during the day.

In Figure 74, the variation of sustained load over time is almost imperceptible, although it exists, and caused a very small difference of load between the application and release of the prestress load, as reported in Table 29. In the S1_20%, the amplitude of load variation was about 0.6 kN (approximately 21 MPa) while in S1_30% this variation was higher, of about 0.9 kN (or 32 MPa).

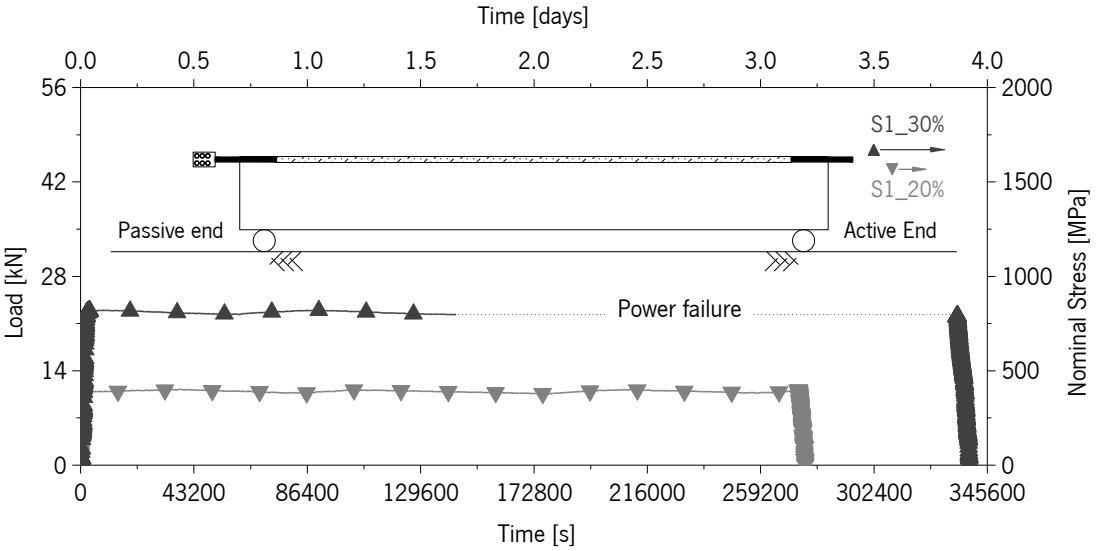

Figure 74 – Prestress load versus time during sustained load – Series I.

According to Figure 75, the variation of strain in the concrete and steel reinforcement was more visible and fairly similar among all strain gauges. Since both load cell and strain gauges recorded this fluctuation of readings it was found that this variation was in fact predominantly related to the environmental temperature. The meteorological station located outside the building indicated that at time of applying the prestress load to S1_20% the external temperature was approximately 19.5ºC, while when the prestress load was released the temperature was 29.7ºC,. The materials are therefore expected to exhibit an increment of strain at time of prestress release, mimicking the presence of an additional tensile stress. For future reference, in all the graphs presented on this Chapter, the positive signal denotes a tensile strain, while a negative signal indicates a compressive strain.

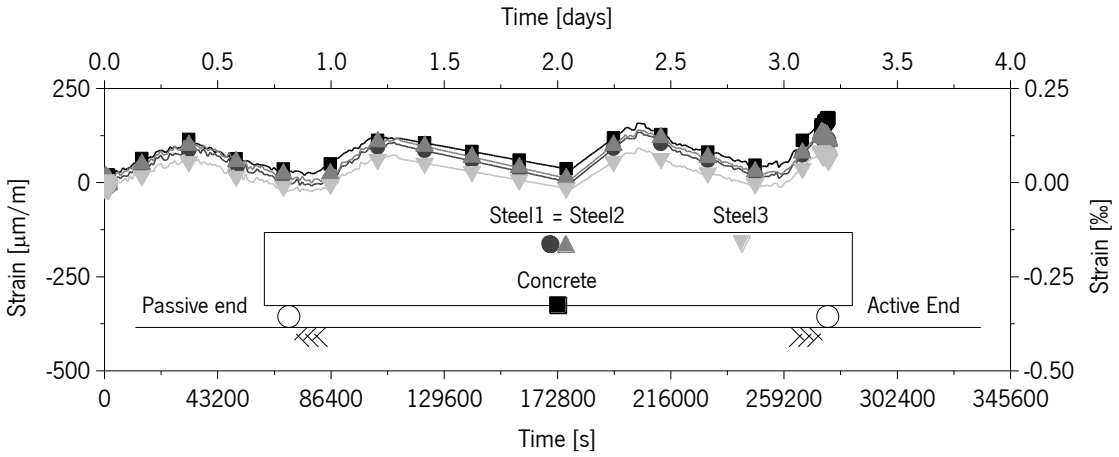

Figure 75 – Strains in steel and concrete versus time during sustained load – S1_20%.

In the case of S1_ 30% (Figure 76), a power failure avoided the continuous record of signals 1.5 days after applying the prestress load. The strains on the steel remained similar overtime while the strain in the concrete diverged a little. Considering the environmental temperature at prestress application and at prestress release, the recorded temperatures were 29.4ºC and 17.7ºC, respectively. Taking this into account, it would be expectable that the strain gauges on this beam had recorded a strain variation inverse to the one registered in S1_20% *i.e.*, a decrease of strain and load in relation to the initial values.

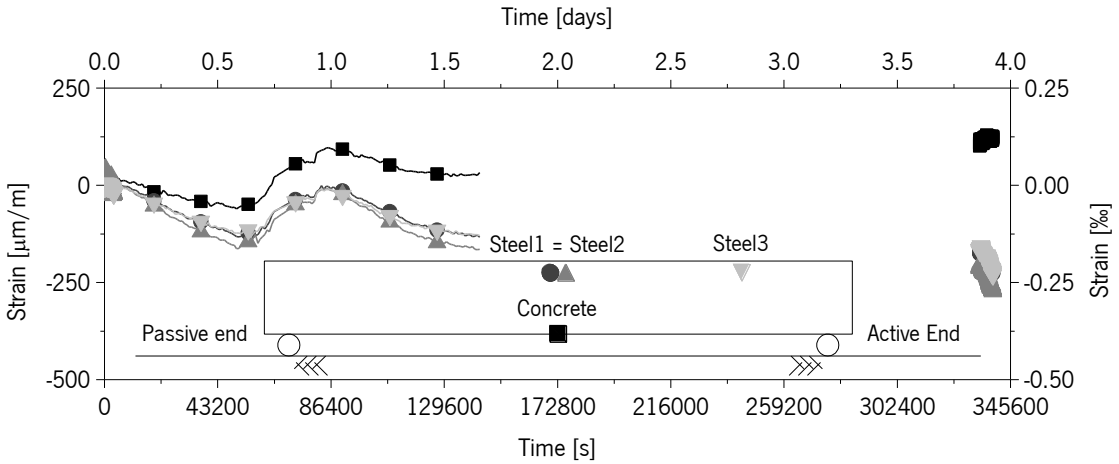

Figure 76 – Strains in steel and concrete versus time during sustained load – S1_30%.

Observing Figure 76, it is visible that the strain gauges installed on the steel bars corroborate the assumed hypothesis of a strain decrease with temperature. However, the strain gauge installed on the concrete surface, probably due to the divergence of values initially recorded, was not in agreement with this hypothesis. Anyhow, the strains recorded in Figures 75 and 76 are expected to be null during all this period since no load was effectively applied on the beam.

Figure 77 represents the strain variation in the CFRP laminate of S1_20%, where the influence of the temperature is observed, as well as the similarity of strain variation in the strain gauges. This is confirmed in Table 29, where the strain at prestress application and prestress release is indicated.

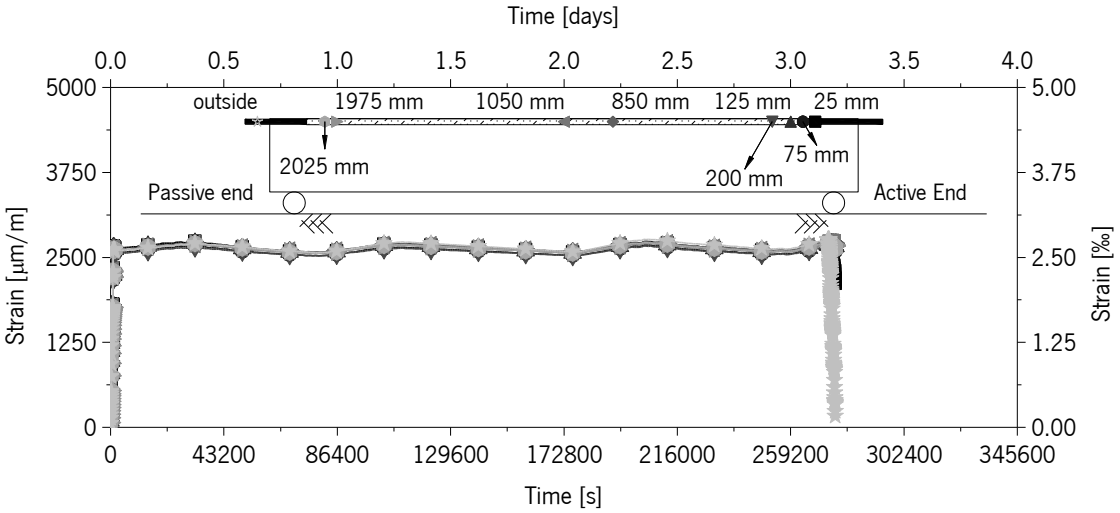

Figure 77 – Strains in the CFRP laminate versus time during sustained load – S1_20%.

The beam S1_30% has also exhibited the same identical strain variation for all the strain gauges, except for the strain gauge positioned at 75 mm which recorded a slightly smaller strain value during the application of prestress. According to Figure 78, this difference of strain persisted during the period of sustained load but this strain gauge still exhibited the same fluctuation as the other strain gauges installed in the same CFRP. However, even considering this slight difference, the coefficient of variation of strain installed in this laminate was still extremely low (2%, as reported in Table 29).

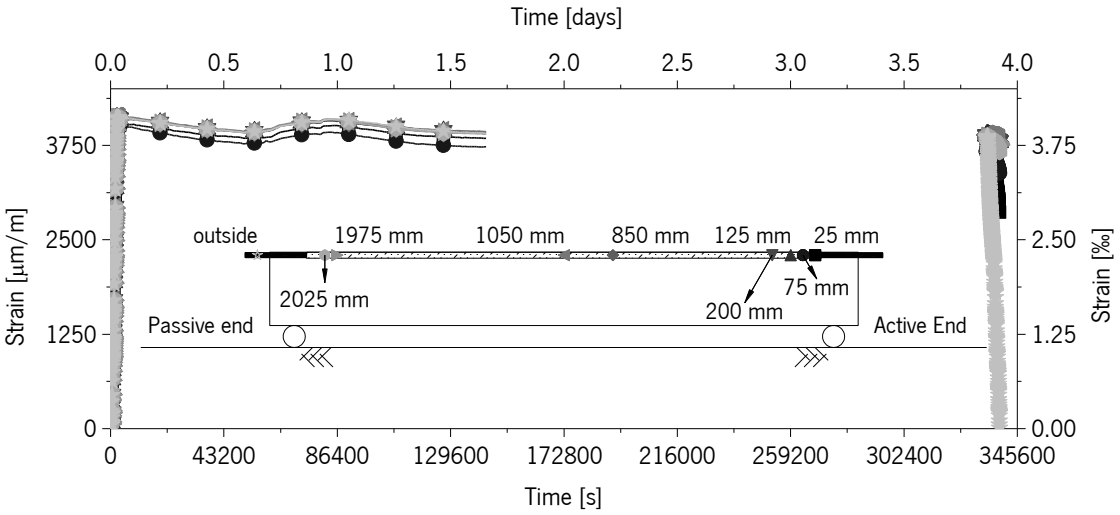

Figure 78 – Strains in the CFRP laminate versus time during sustained load – S1_30%.

Due to the variation of strain apparently caused by temperature, the instantaneous losses of prestress had to be calculated using the relative strain variation during the prestress release process, as reported in Table 30 where the following values are reported:

- ε_p is the strain registered immediately after prestress application;
- ε'_p is the strain recorded before prestress release (in this series, 3 days after epoxy curing, immediately before prestress release);
- ε_f is the strain measured immediately after the removal of the prestress load;
- $\Delta\varepsilon_p$ is the difference of strain during prestress release *i.e.*, $\varepsilon'_p - \varepsilon_f$;
- Instantaneous loss of prestress in relation to the initial strain applied, ε_p, calculated using Eq. 31.

$$Loss = \frac{\Delta\varepsilon_p}{\varepsilon_p} \times 100 \tag{31}$$

Table 30 – Instantaneous prestress losses – Series I.

Strain gauge	S1_20%					S1_30%				
	ε_p [‰]	ε'_p [‰]	ε_f [‰]	$\Delta\varepsilon_p$ [‰]	*Loss* [%]	ε_p [‰]	ε'_p [‰]	ε_f [‰]	$\Delta\varepsilon_p$ [‰]	*Loss* [%]
Concrete	0.011	0.149	0.167	-0.017	-	-0.008	0.114	0.125	-0.011	-
Steel 1	0.014	0.120	0.106	0.015	-	-0.012	-0.168	-0.227	0.059	-
Steel 2	0.000	0.135	0.109	0.026	-	-0.024	-0.203	-0.274	0.071	-
Steel 3	0.012	0.081	0.061	0.020	-	-0.014	-0.162	-0.228	0.066	-
25 mm	2.657	2.710	2.110	0.600	23	4.020	3.802	2.855	0.947	24
75 mm	2.579	2.658	2.594	0.065	3	4.005	3.672	3.378	0.294	7
125 mm	2.632	2.691	2.658	0.032	1	4.089	3.886	3.791	0.094	2
200 mm	2.573	2.655	2.640	0.015	1	4.107	3.892	3.798	0.094	2
850 mm	2.619	2.710	2.690	0.021	1	4.103	3.864	3.784	0.080	2
1050 mm	2.627	2.709	2.695	0.015	1	4.116	3.891	3.832	0.059	1
1975 mm	2.603	2.698	2.668	0.029	1	4.101	3.871	3.759	0.112	3
2025 mm	2.603	2.712	2.626	0.085	3	4.107	3.874	3.659	0.215	5
outside	2.602	2.767	0.152	2.615	100	4.100	3.858	-0.017	3.875	95

The evolution of the negative deflection during the prestress release process, depicted in Figure 79, was approximately the same in both cases, and the final values measured were 0.078 mm and 0.178 mm. The evolution of the slip with time, also depicted in Figure 79, was slightly different in the beams. S1_30% exhibited a larger level downward deflection and slip, as expectable.

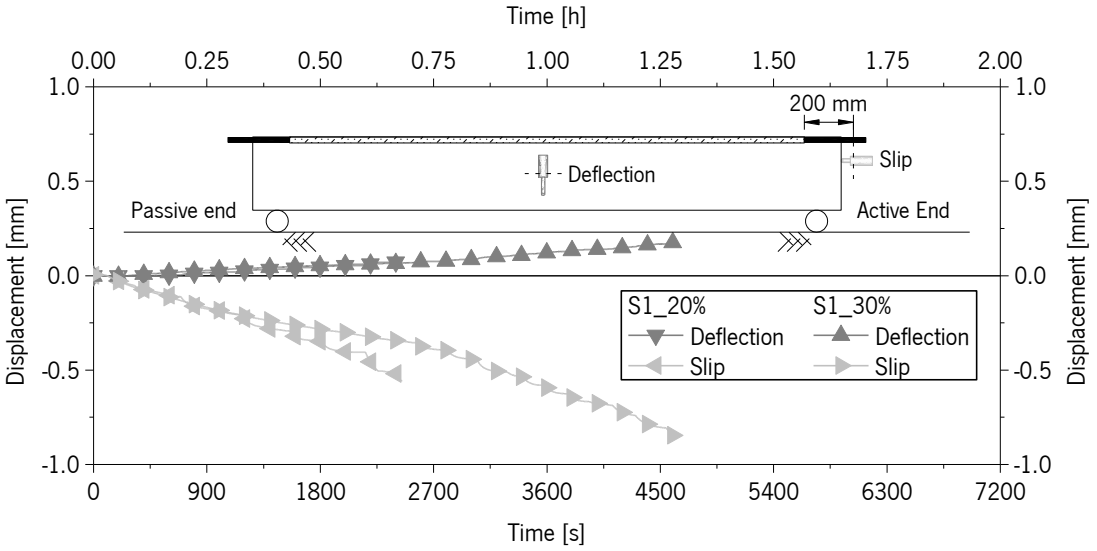

Figure 79 – Deflection and slip variation versus time during prestress release – Series I.

According to Table 30, releasing the prestress load has introduced a slight tensile strain on the concrete surface, as well as some compression in the monitored steel bars (see Figures 80 and 81). Concerning the strain on the concrete, it was observed that it decreased with the increase of prestress load (0.017‰ S1_20% and 0.011‰ in S1_30%), which is not reasonable. However, in the case of the steel bars, compression has increased with the increase of prestress, as anticipated (average strain of 0.020‰ and 0.065‰ in S1_20% and S1_30%, respectively). Nevertheless, the magnitude of strain measured in these strain gauges is extremely low, meaning that readings can be affected by the lack of precision of the equipment and, therefore, explain the abnormal readings in the concrete.

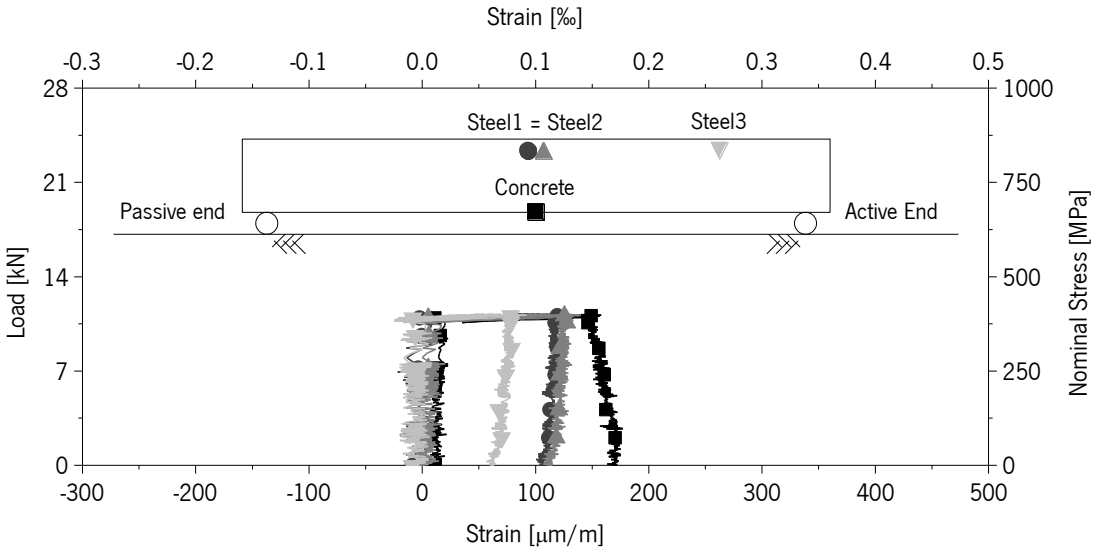

Figure 80 – Load versus strains in steel and concrete – S1_20%.

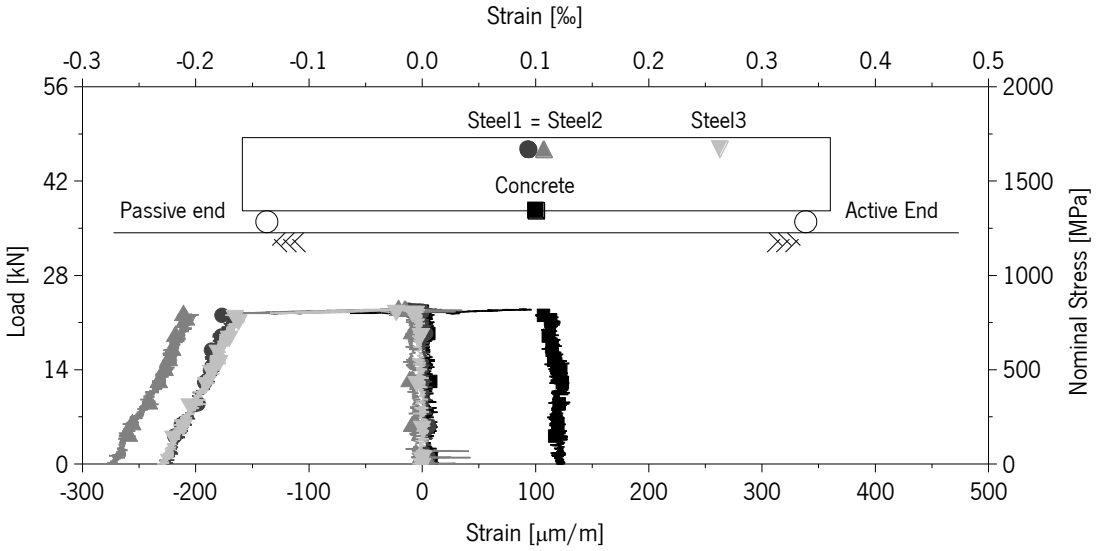

Figure 81 – Load versus strains in steel and concrete – S1_30%.

The strain in the strain gauge outside the bond length during the release of the prestress force has presented an almost linear response in both beams, as illustrated in Figures 82 and 83. Regarding the instantaneous strain loss in the CFRP after prestress release, in both cases, the highest loss was registered in the strain gauge positioned 25 mm from the beginning of the bond length, which exhibited a decrease of strain of 23%~24% (reported in Table 30). Some significant strain decrease was also registered in the nearby strain gauges and the loss at mid-span was in fact the smallest value measured in both beams, of about 1%.

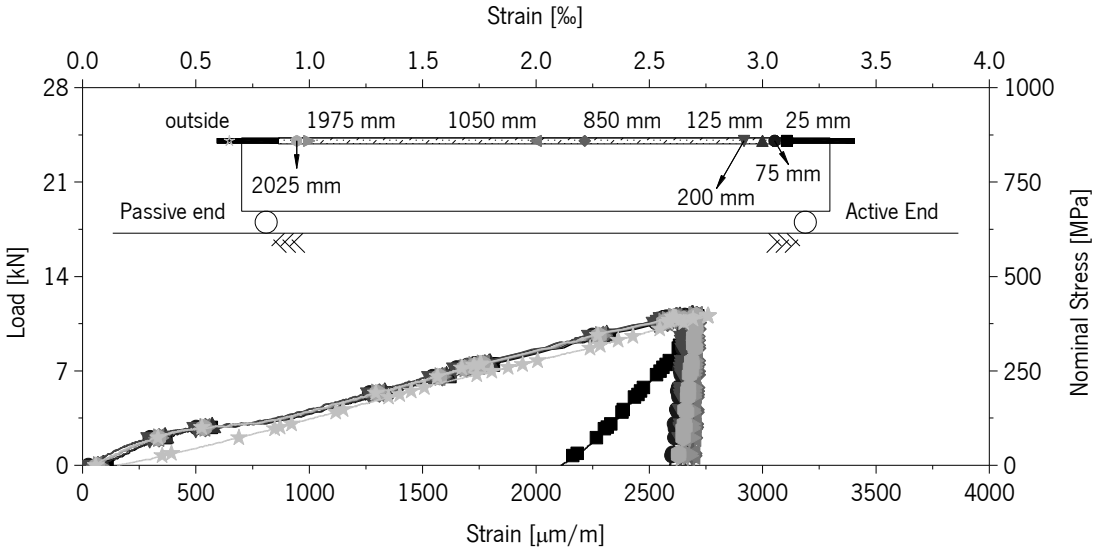

Figure 82 – Load versus strains in the CFRP – S1_20%.

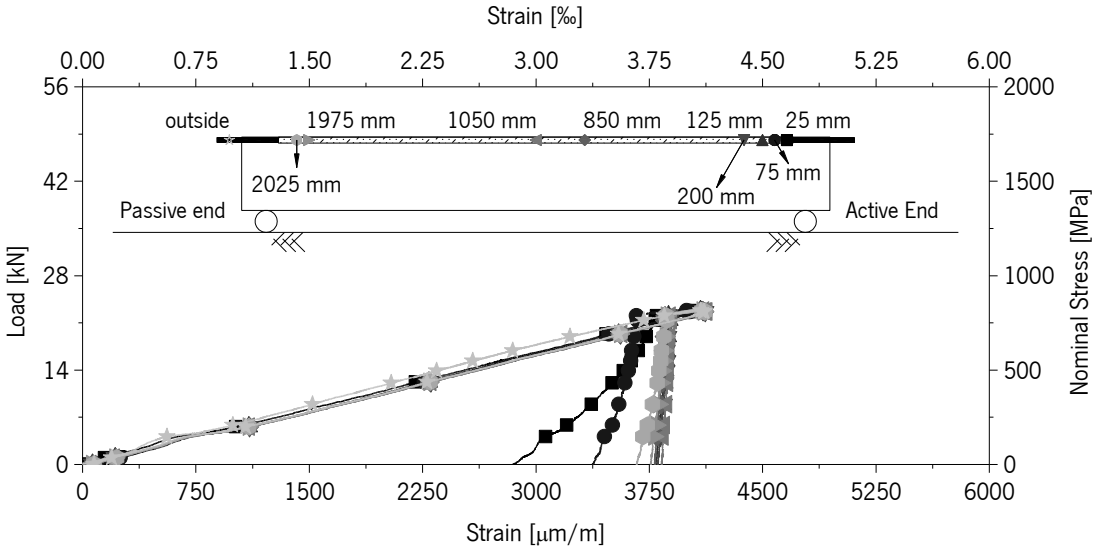

Figure 83 – Load versus strains in the CFRP – S1_30%.

Both the mid-span deflection and the slip measured during prestress release revealed a nearly linear relationship with the applied load level (see Figure 84). However, although the original slip measurement indicated a decrease proportional to the load, it was still necessary to remove the elastic deformation of the 200 mm un-bonded length (see illustration included in Figure 84).

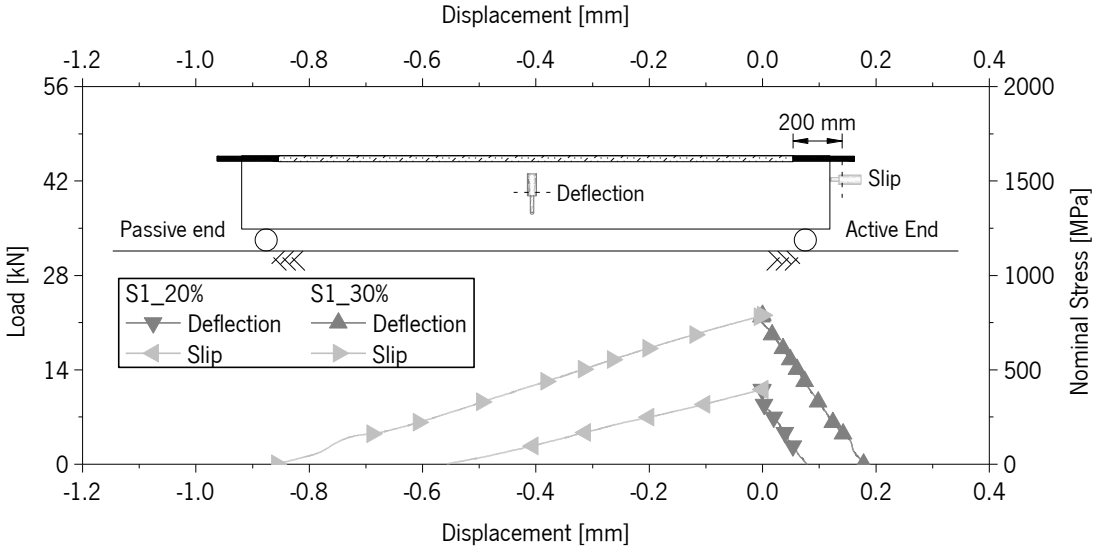

Figure 84 – Load versus mid-span deflection and slip during prestress release – Series I.

Due to the uncertainties associated to the elastic modulus of the CFRP, the calculation of the pure slip was made by multiplying the strain variation in the strain gauge outside the bond length (on the opposite end of the beam) by 200 mm and then subtracting it from the total slip presented in Figure 84. The corrected slip is depicted in Figure 85, where it is visible that in fact the CFRP contracted towards centre of the beam, almost proportionally to the applied load. After prestress

release, the recorded slip values were 0.036 mm and 0.085 mm in S1_20% and S1_30%, respectively.

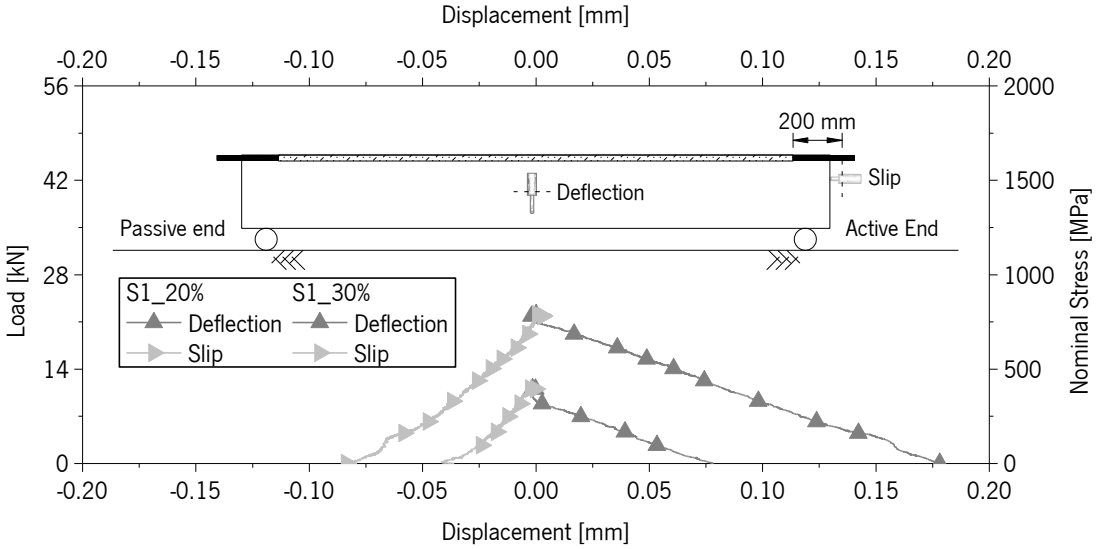

Figure 85 – Load versus mid-span deflection and corrected slip during prestress release – Series I.

Another important verification that was felt necessary to validate the procedure of prestress application was the comparison of strains in symmetrical positions. This comparison was made for both prestress levels and the strains revealed to be almost equivalent on both extremities of the beam (see Figures 86 and 87). In the case of S1_20%, release was clearly simultaneous at both ends since the ratio between CFRP strains in symmetrical positions is almost unitary.

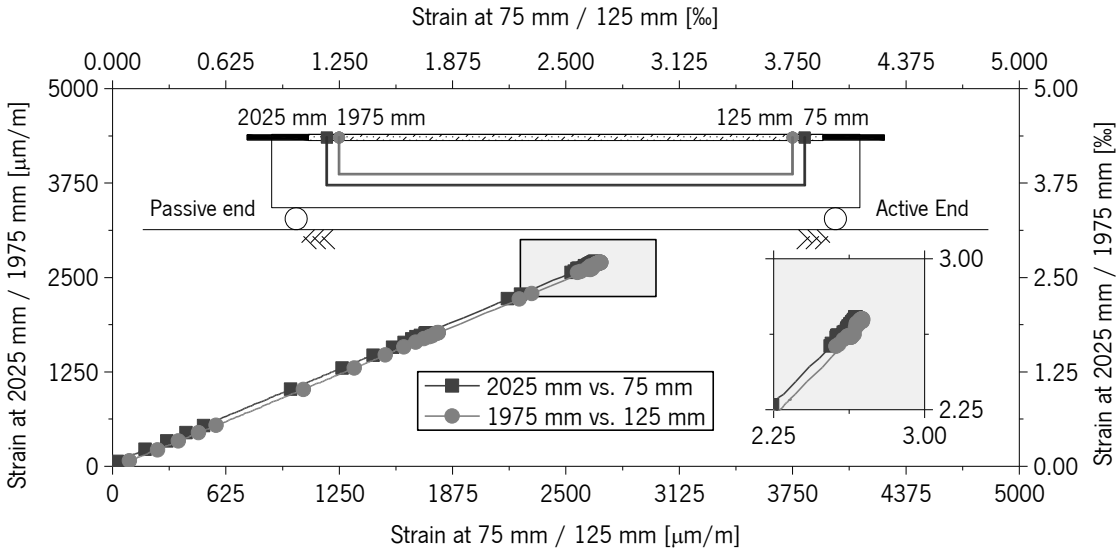

Figure 86 – Comparison of strains in symmetrical strain gauges – S1_20%.

The unique deviation was registered in S1_30% (Figure 87), in the strain gauges 75 mm from the free-ends, since the strain closer to the active end of the prestress line (right side) decreased more

than in the left side, at the same distance. However, as this strain gauge has previously demonstrated extraneous behaviour, this difference of strain loss between these two positions was considered meaningless.

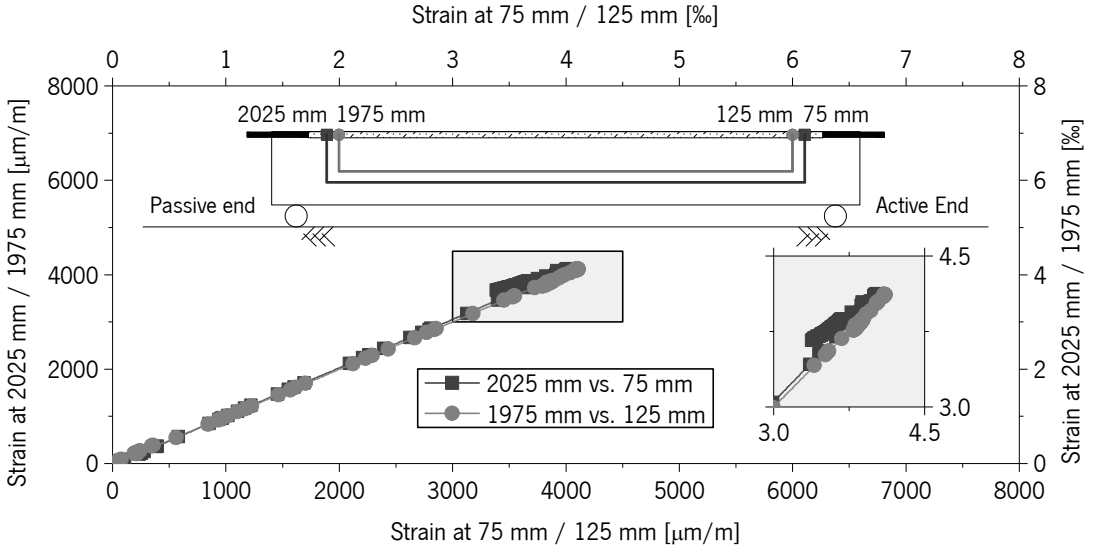

Figure 87 – Comparison of strains in symmetrical strain gauges – S1_30%.

To verify the accuracy of the values measured in the innermost strain gauges, the strains at 850 mm and at mid-span were plotted were plotted against the strain at 200 mm. Figures 88 and 89 depict the relationship between these strains and the curves resulting from this analysis are surprisingly straight.

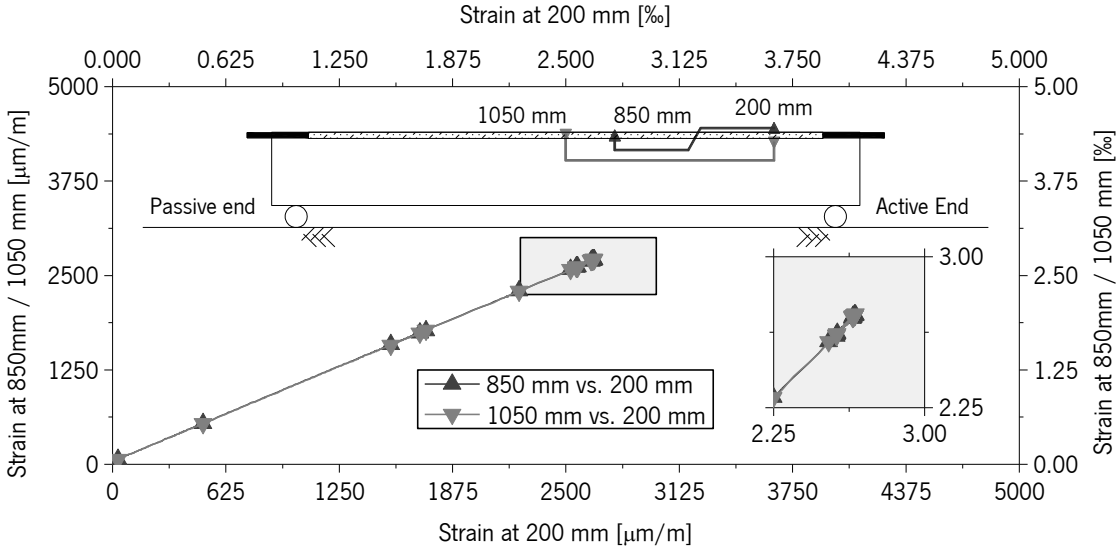

Figure 88 – Strain at mid-span versus other central strains – S1_20%.

This means that, up to 30% of applied prestress, the instantaneous loss recorded in the strain gauge 200 mm from the free-end zone is almost negligible. This observation is of major importance to

this work since it indicates that the prestressed CFRP laminates applied in the concrete beams do not require a large load transference length and therefore, prestress is applied effectively in most of the length of the beam.

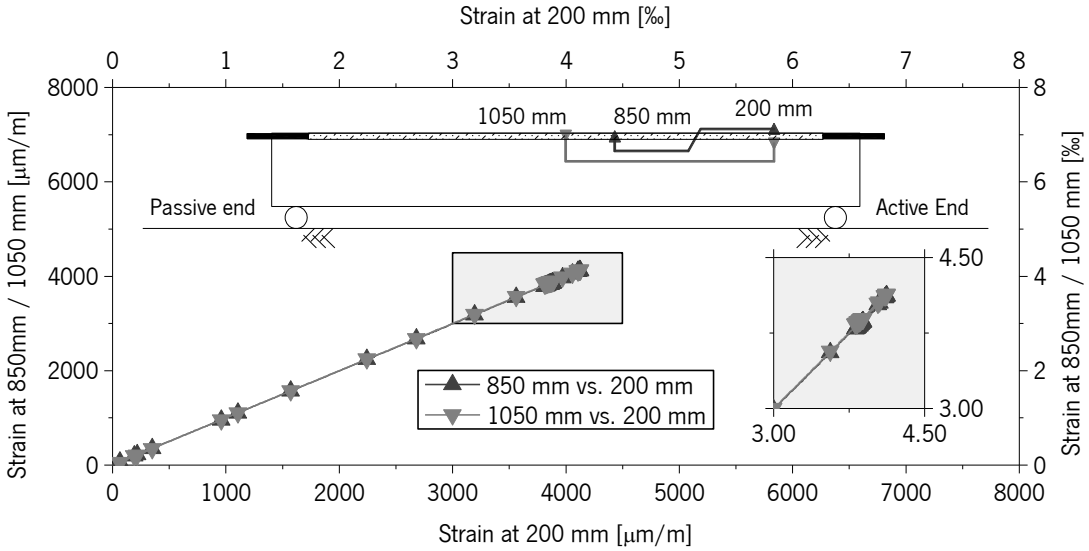

Figure 89 – Strain at mid-span versus other central strains – S1_30%.

4.1.2 Long-term losses of prestress

Since during the release of prestress the strain variations in the steel bars and concrete were extremely low, any strain variation that can occur in these materials in the subsequent phase, like relaxation, is almost impossible to be detected. Even so, the evolution of strains in concrete and steel was recorded during some days was in both beams, and the same undulant movements previously reported (in Figures 75 and 76) were again observed, as Figures 90 and 91 reveal.

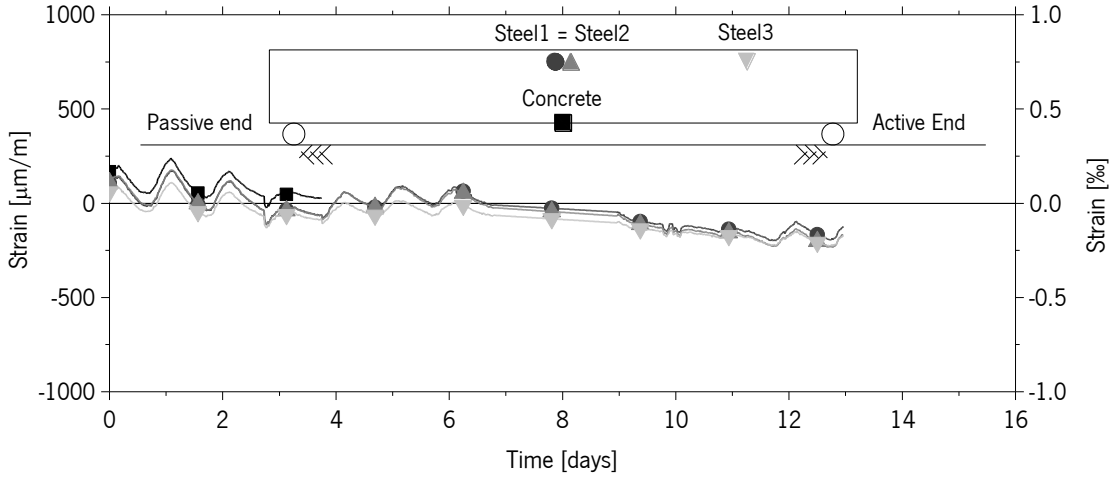

Figure 90 – Strains in concrete and steel during time after prestress release – S1_20%.

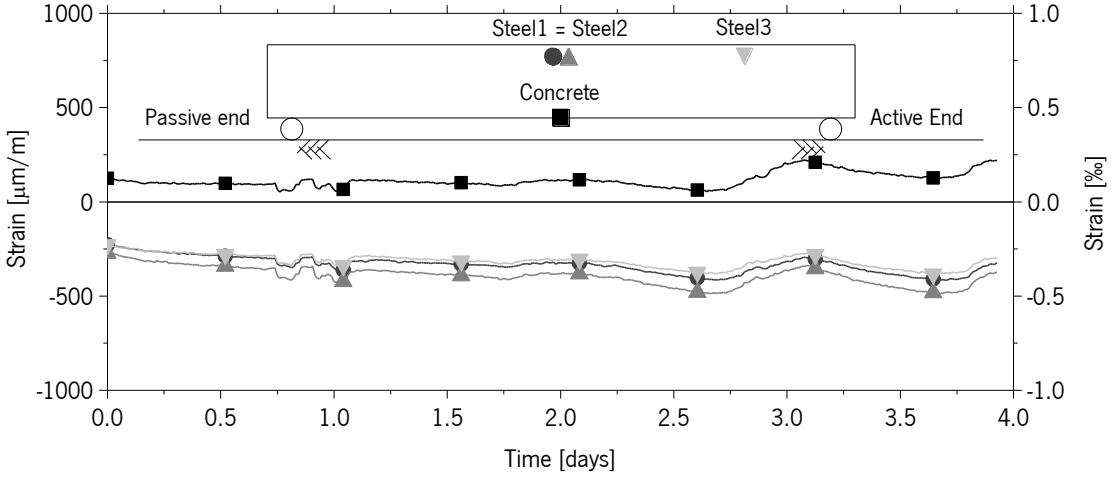

Figure 91 – Strains in concrete and steel during time after prestress release – S1_30%.

It was stipulated that CFRP monitoring would last about 40 days after prestress release but this was not possible to perform in S1_30% since the acquisition system was required for another work. According to the raw data presented in Figures 92 and 93, strains appear to have decreased in the period recorded especially the in strain-gauges located 25 mm from the free-end of the active side.

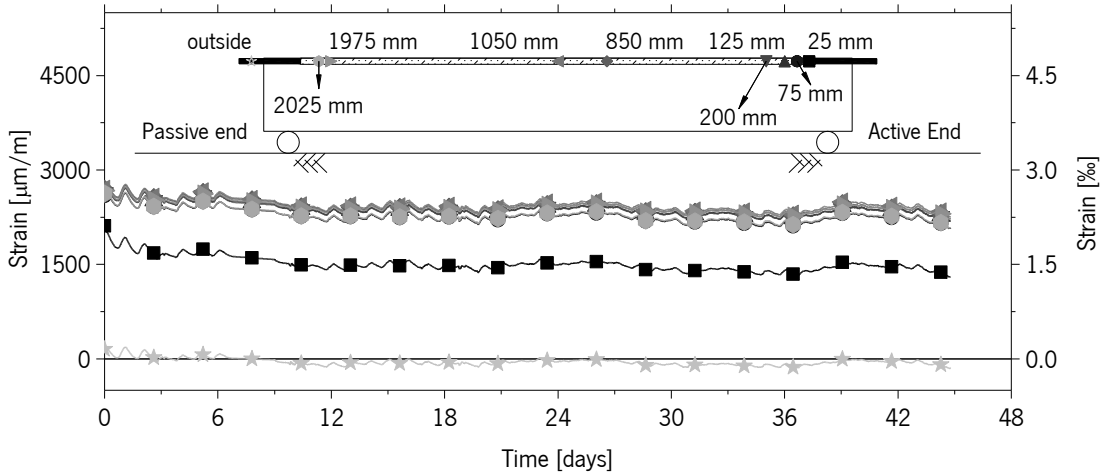

Figure 92 – Strains in the CFRP versus time after prestress release – S1_20%.

In the case of the S1_30%, plotted in Figure 93, the strains 75 mm from the free-end in the active side and its corresponding strain in the opposite end (2025 mm) also presented some tendency to diminish over time. The fluctuation of the strain during the period was again the same in the strain gauges installed in the same CFRP, as well as in the strain gauge located outside the bond length.

The analysis of this raw data clearly does not allow the assessment of the real prestress loss over time although it still provides a qualitative evaluation of the strain loss. For that reason, it is mandatory to find a strategy that allows the removal of the environmental effects.

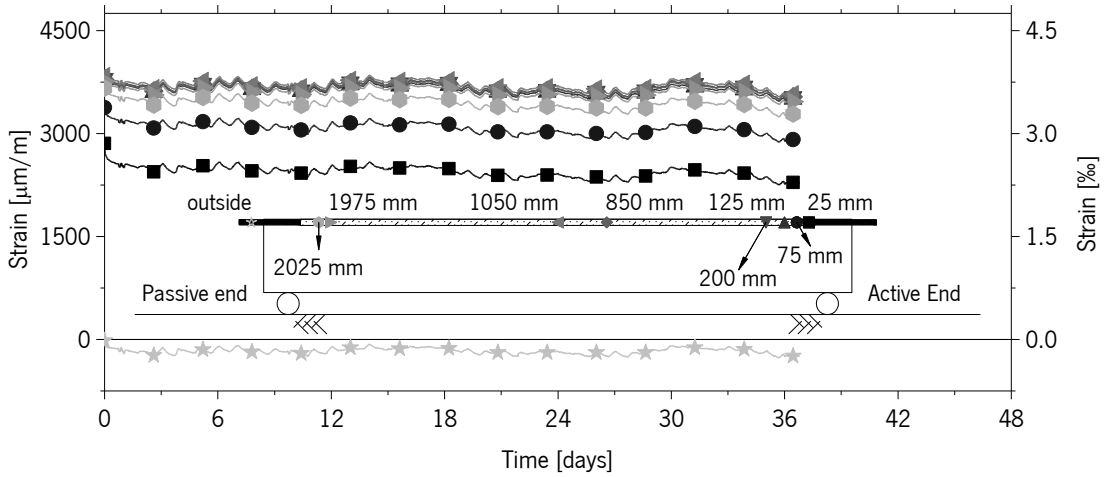

Figure 93 – Strains in the CFRP versus time after prestress release – S1_30%.

Since the beginning of prestress application that the fluctuations observed in most plots were attributed to the environmental factors, room temperature and relative humidity were monitored during the post-release period. Regarding the temperature dependency of concrete and steel strains it was found that these exhibit an almost linear relationship, as represented in Figures 94 and 95. However, due to the low magnitude of strains recorded and the short time span, some inconsistent readings are visible in the graphs, namely the strain in concrete in the S1_30%. Nevertheless, it is not possible to affirm with certainty if the inferior precision of the linear regressions is due to unintentional external actions or simply to the inherit noise of these readings.

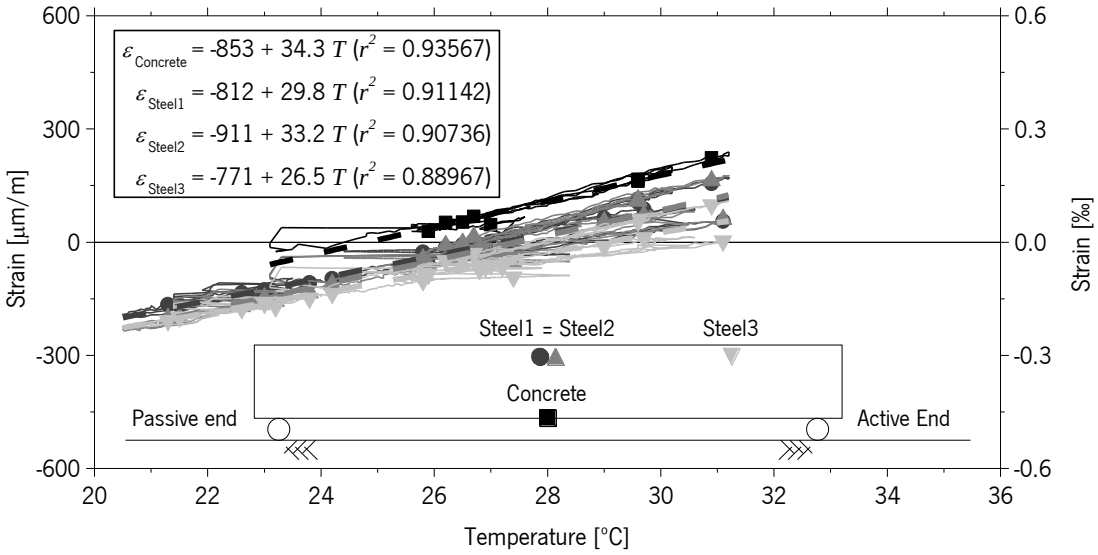

Figure 94 – Strains in concrete and steel versus room temperature – S1_20%.

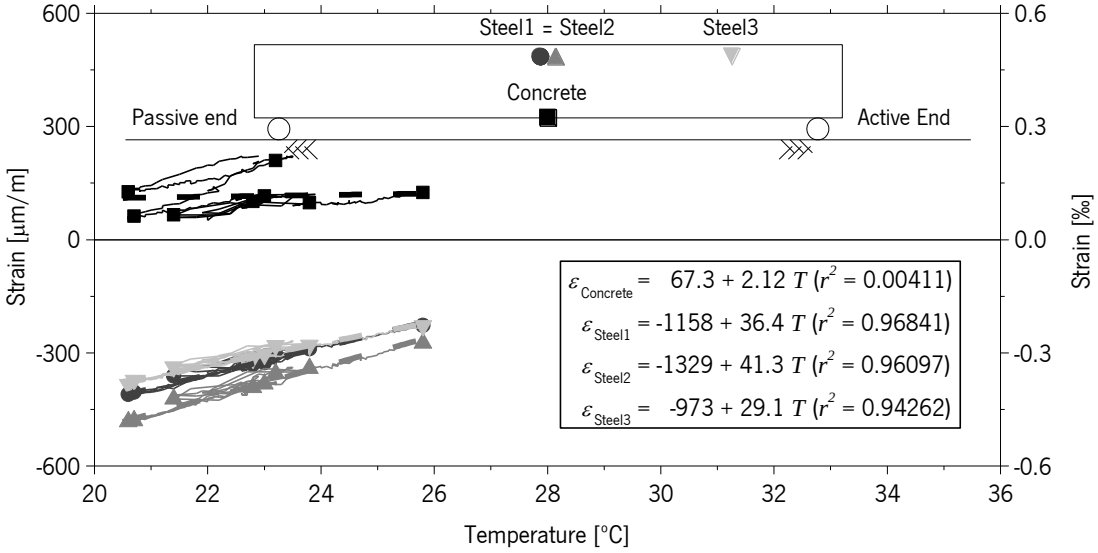

Figure 95 – Strains in concrete and steel versus room temperature – S1_30%.

Regarding the variation of strain in concrete and steel due to relative humidity, nothing could be concluded since, apparently, the strains do not relate directly with this variable. Note that in the case of S1_20%, in Figure 96, it would be admissible to consider a relationship between strains and relative humidity, as suggested by the obtained r^2 values, although not necessarily linear. However, observing the results from S1_30%, in Figure 97, the strains do not appear to depend on the relative humidity at all. In any case, as mentioned for the case of temperature dependency, the magnitude of these strains is extremely low and, therefore, the reliability of the suggested linear regressions is questionable.

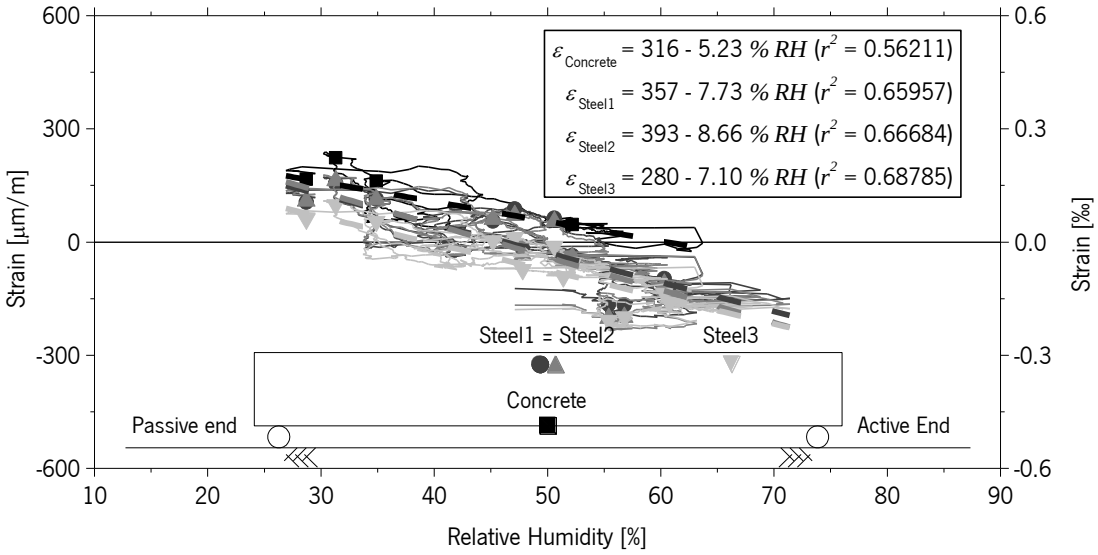

Figure 96 – Strains in concrete and steel versus relative humidity – S1_20%.

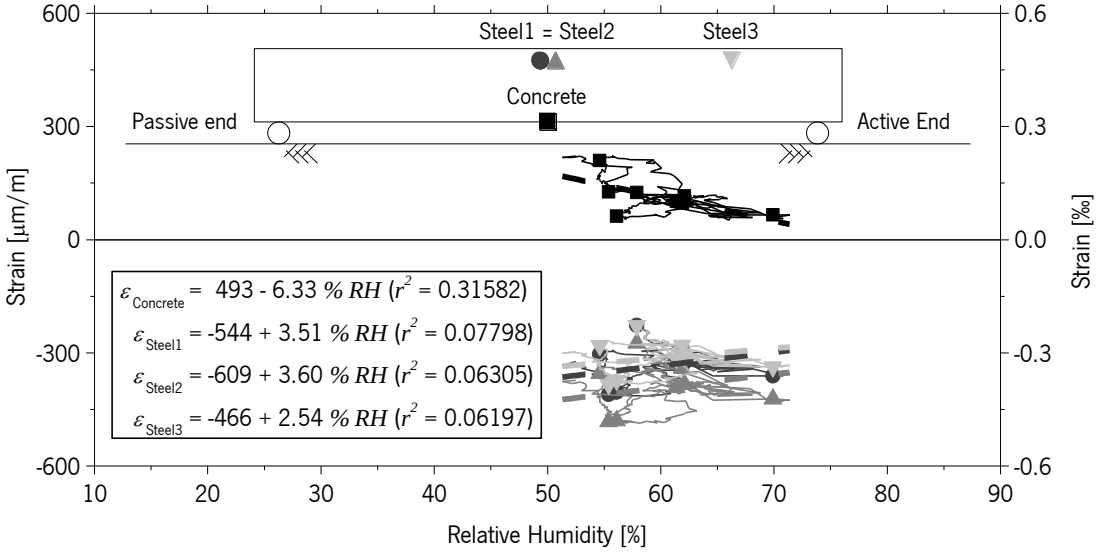

Figure 97 – Strains in concrete and steel versus relative humidity – S1_30%.

The variation of strains in the CFRP laminates with temperature was also evaluated, and the linear regressions performed strongly suggest that temperature has a direct effect in the measured strains (see Figures 98 and 99). It is interesting to observe that the linear regressions with smaller r^2 values are the ones belonging to the 25 mm position in S1_20% (Figure 98) and 25 mm, 75 mm and 2025 mm in S1_30% (Figure 99). This observation is perfectly expectable since these positions were already identified as locations where the CFRP strain loss process is more pronounced and, therefore, temperature dependency is harder to isolate in these cases.

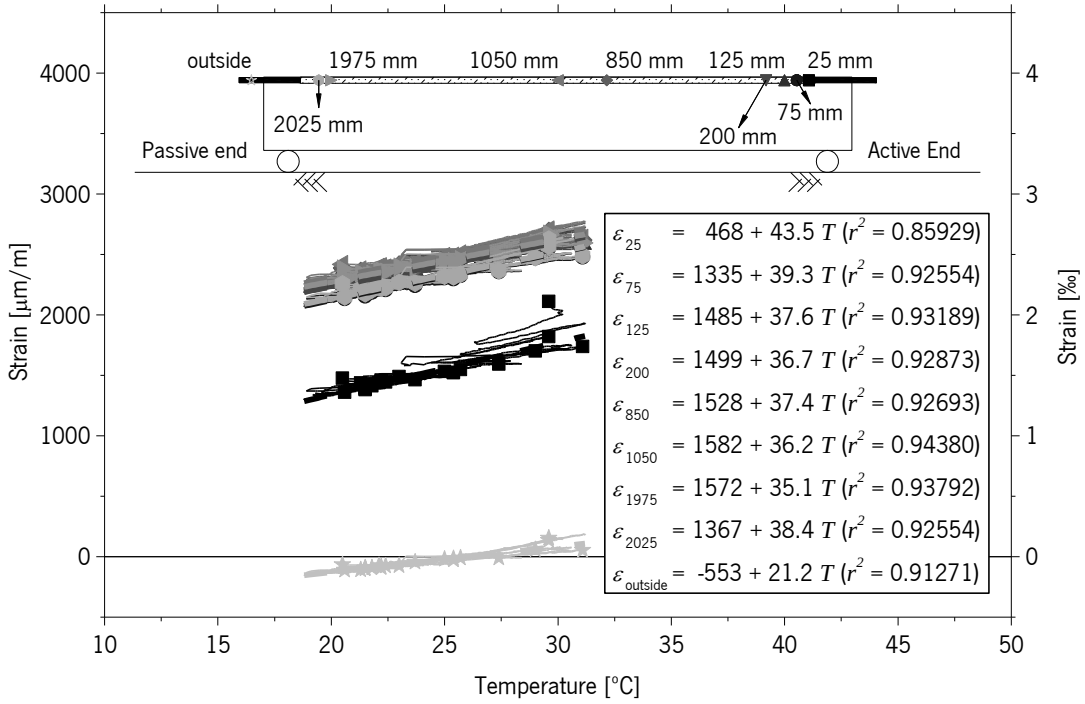

Figure 98 – CFRP strain versus environmental temperature – S1_20%.

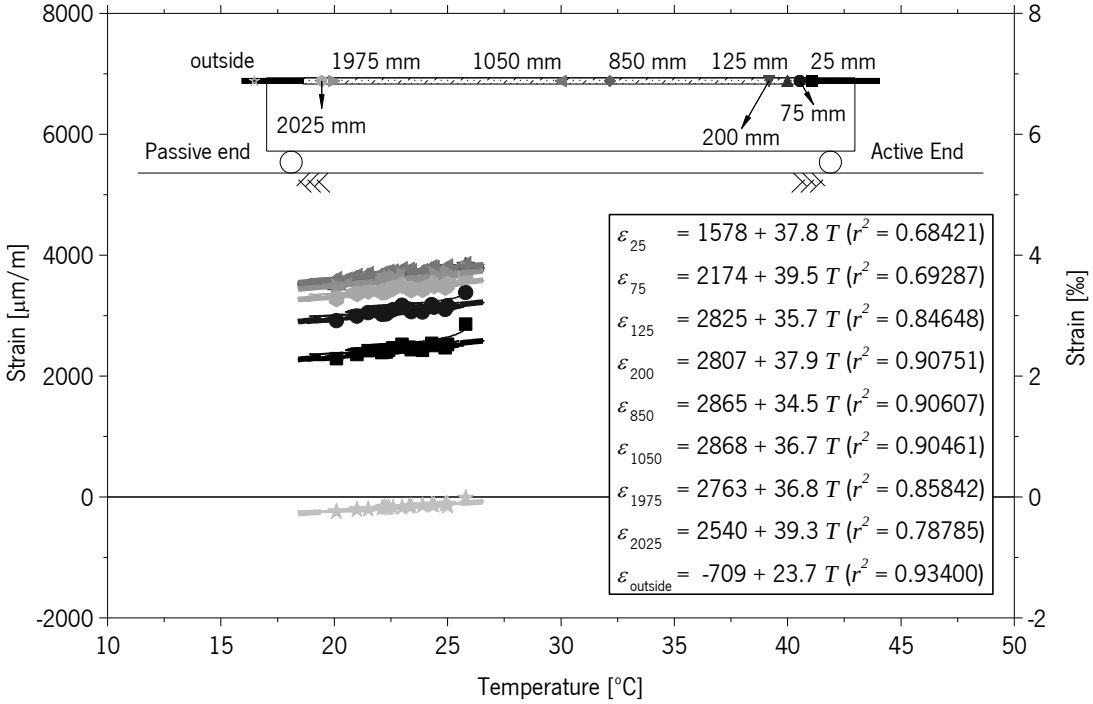

Figure 99 – CFRP strain versus environmental temperature – S1_30%.

The same analysis of strain versus relative humidity was performed with the raw CFRP strain data, and in this case, it was also concluded by analysing Figures 100 and 101 that no direct relationship can be found between these two variables. In fact, the CFRP strains of S1_20% have decreased with the increase of relative humidity while the opposite tendency is observed in S1_30%.

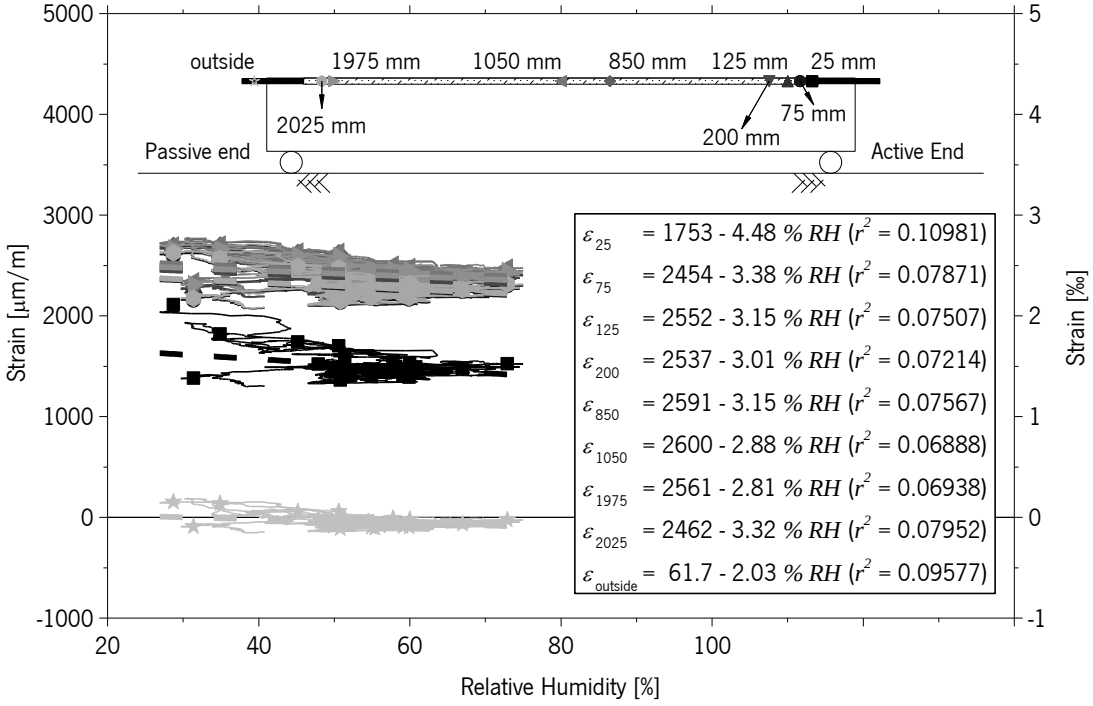

Figure 100 – CFRP strain versus relative humidity – S1_20%.

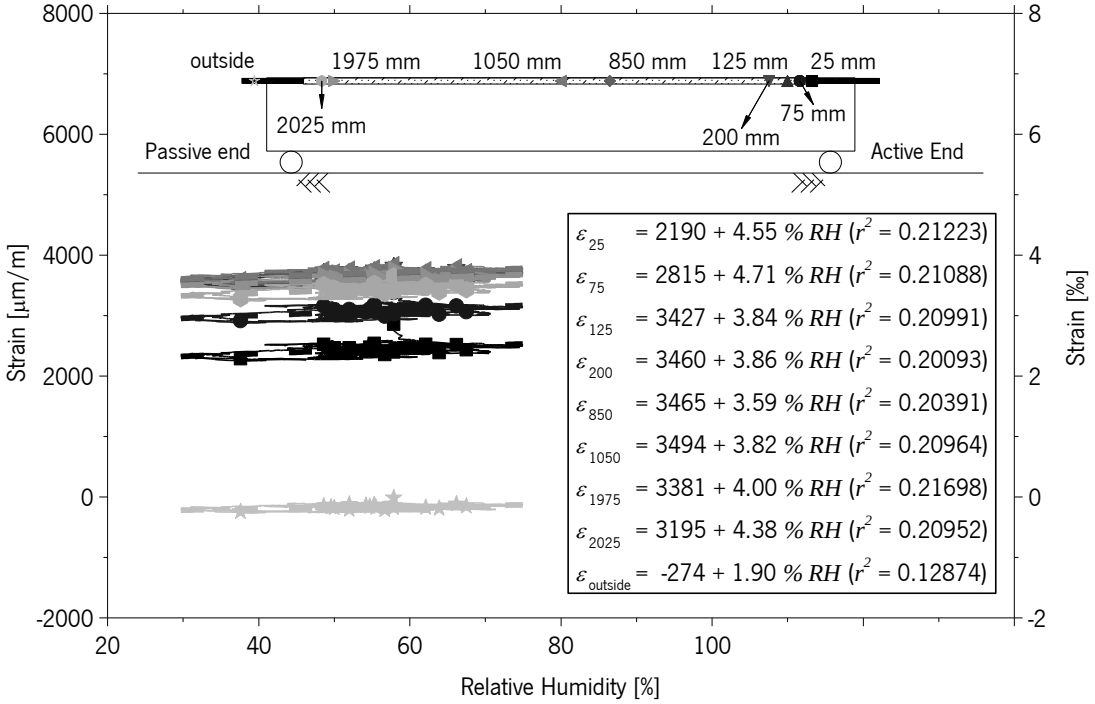

Figure 101 – CFRP strain versus relative humidity – S1_30%.

As done for the prestress release process, to confirm if there is symmetric strain distribution in the beams, some of the CFRP strains registered during the post-release phase were plotted against each other (Figures 102 and 103).

In the case of S1_20% (see Figure 102), symmetry was definitely observed since both at 75 mm and 125 mm from the free-end, the ratio between the strains recorded at these positions and those in the correspondent left side is almost the unitary value.

However, it was noted that in S1_30% (see Figure 103), the strain gauge positioned at 75 mm recorded a slightly higher deformation than its opposite, 2025 mm. In fact, it was already indicated in Table 30 that the instantaneous loss at 75 mm was about 7%, while at 2025 mm was only about 5%.This suggests that maybe a higher level of initial damage may have occurred in the active end of this beam.

In the same Figures (102 and 103), the strains in the central zone (200 mm, 850 mm and 1050 mm) exhibited not only proportionality among themselves, but also a high similarity in terms of absolute values since the linear regressions suggest an almost unitary slope.

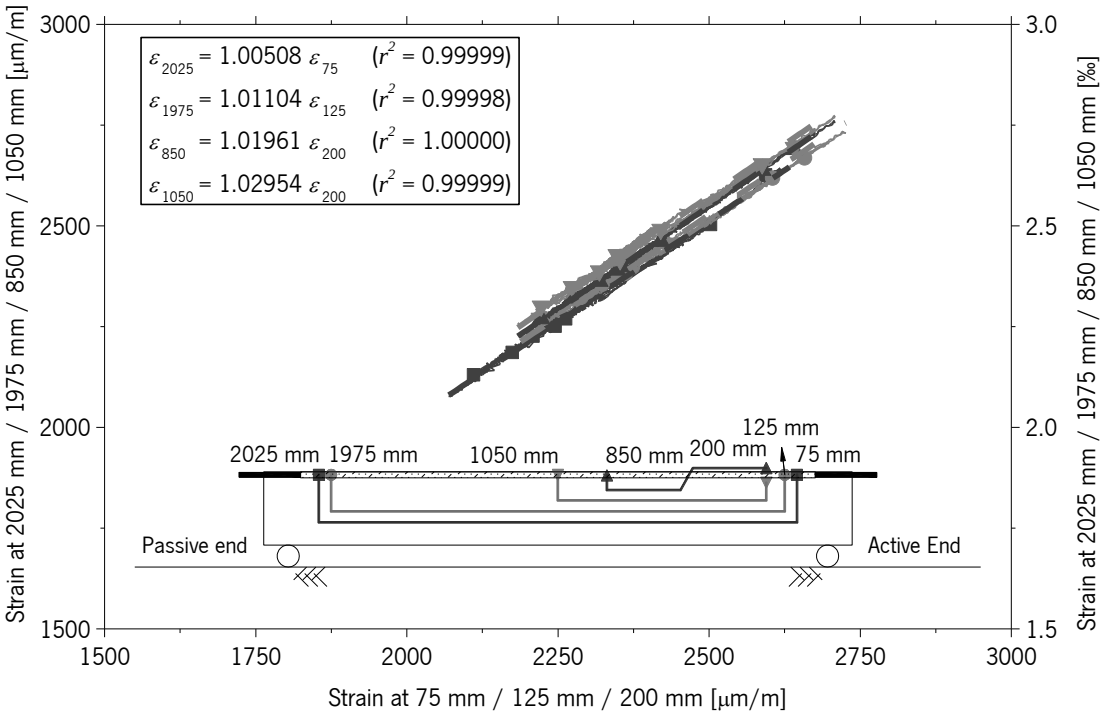

Figure 102 – Relationship between strains along the bond length – S1_20%.

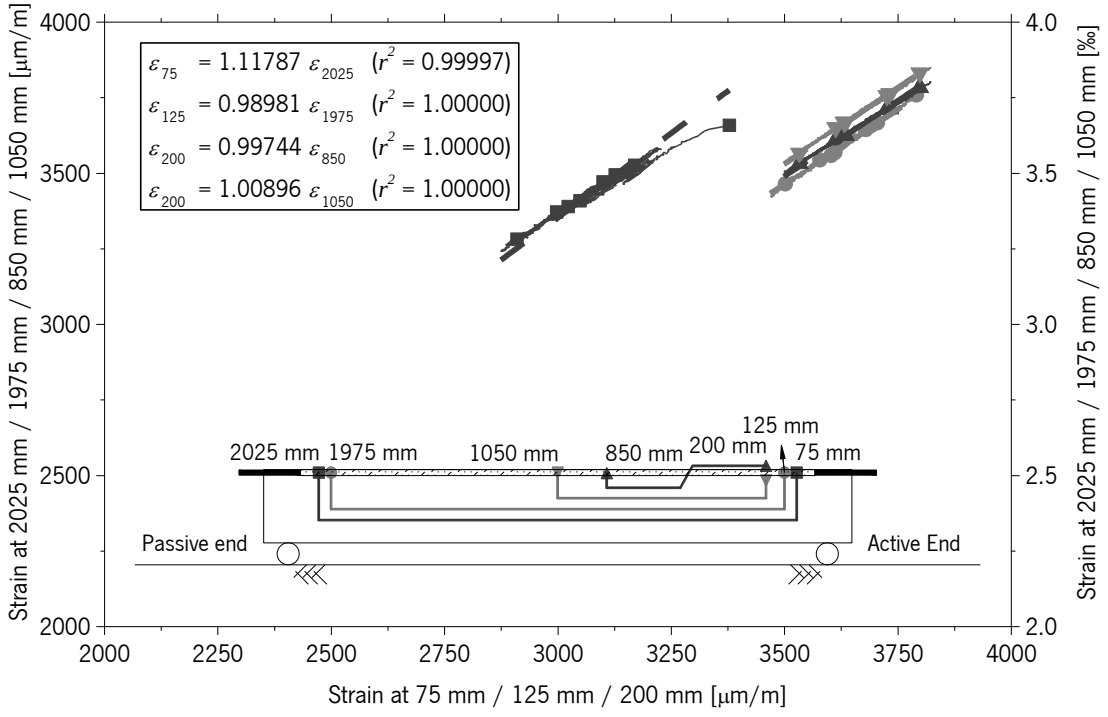

Figure 103 – Relationship between strains along the bond length – S1_30%.

The raw data obtained from these motoring periods cannot, however, be directly used for the later comparison with the results to be obtained numerically in a Chapter 6, since the environmental variables, which cause the readings to vary significantly have to be removed. In that scope, three strategies were adopted to remove the temperature effect from the readings.

The first strategy was based on the strain variation of the strain gauge installed in the CFRP outside the bonded length. According to this approach, the variation of strain in the 'outside' should be subtracted from the strain recorded in each of the strain gauges along the bond length, as defined in Eq. 32.

$$\varepsilon_{corrected}(t) = \varepsilon_{original}(t) - \Delta\varepsilon_{outside}(0,t) = \varepsilon_{original}(t) - \left(\varepsilon_{outside}(t) - \varepsilon_{outside}(0)\right) \quad (32)$$

where $\varepsilon_{corrected}(t)$ is the corrected strain at a given position at a time instant t, $\varepsilon_{original}(t)$ is the original strain recorded at a given position in the same time instant t (depicted in Figures 92 and 93), and $\varepsilon_{outside}(0)$ and $\varepsilon_{outside}(t)$ are the original strains recorded in the strain gauge placed outside the bonded length immediately after prestress release ($t = 0$) and at the time instant t, respectively.

The second strategy was based on the temperature dependency of the mid-span strain gauge, which is in fact the place where the minimum strain loss is expected. This was performed by using Eq. 33.

$$\varepsilon_{corrected}(t) = \varepsilon_{original}(t) - m_T\left(T(t) - T(0)\right) \quad (33)$$

where $\varepsilon_{corrected}(t)$ is the corrected strain at a given position at a time instant t, $\varepsilon_{original}(t)$ is the original strain recorded at a given position at the same time instant t, m_T is the slope of the linear regression performed on the mid-span strain gauge (reported in Figures 98 and 99), and $T(0)$ and $T(t)$ are the temperatures recorded immediately after prestress release ($t = 0$) and at the time instant t, respectively.

The results of these two approaches are plotted in Figures 104 and 105. As it can be observed in these plots, using the first approach, reported on the left side of the images, some undulant movements are still observable, and according to this correction, the strain gauges experienced unexplainable increases of strains from 20 to 25 days in S1_20%, and from 10 to 15 days S1_30%. This lack of accuracy of this approach is believed to be related to the difference of temperature outside and inside the bonded length. In fact, Figures 98 and 99 suggest that the slope of the linear regressions made on strain gauges within the bonded length is about 0.037‰/ºC, while the strain gauges installed outside the bonded length point to a lower value, ranging between 0.021 and 0.024‰/ºC. In the case of the second approach, depicted on the right side, the fluctuation of the strain during monitoring is definitely more accurate, although some sections still exhibit unexpected decreases/increases of strain.

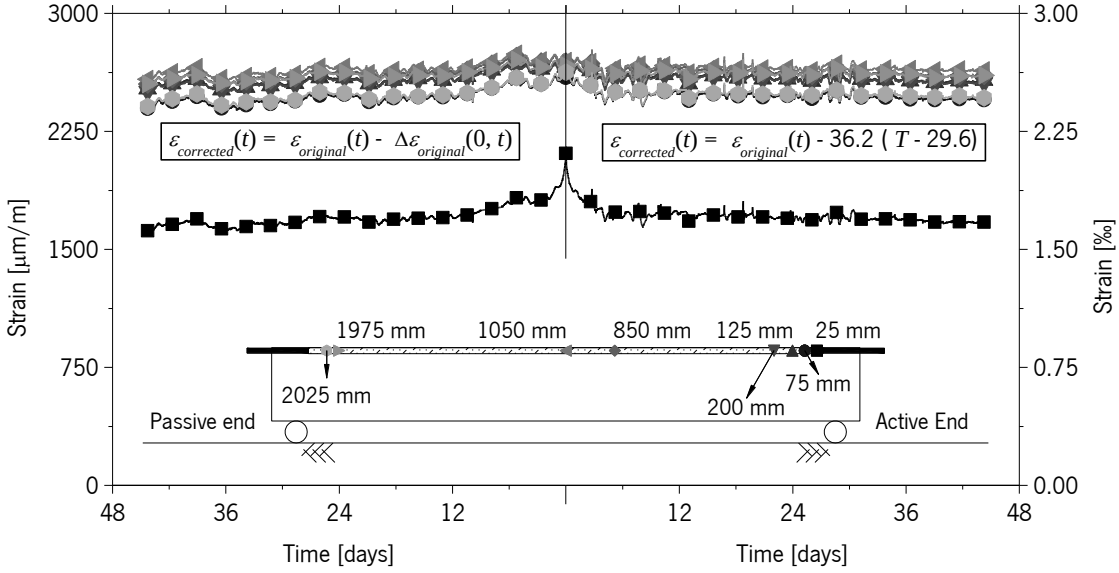

Figure 104 – Corrected strains in the CFRP – initial approaches – S1_20%.

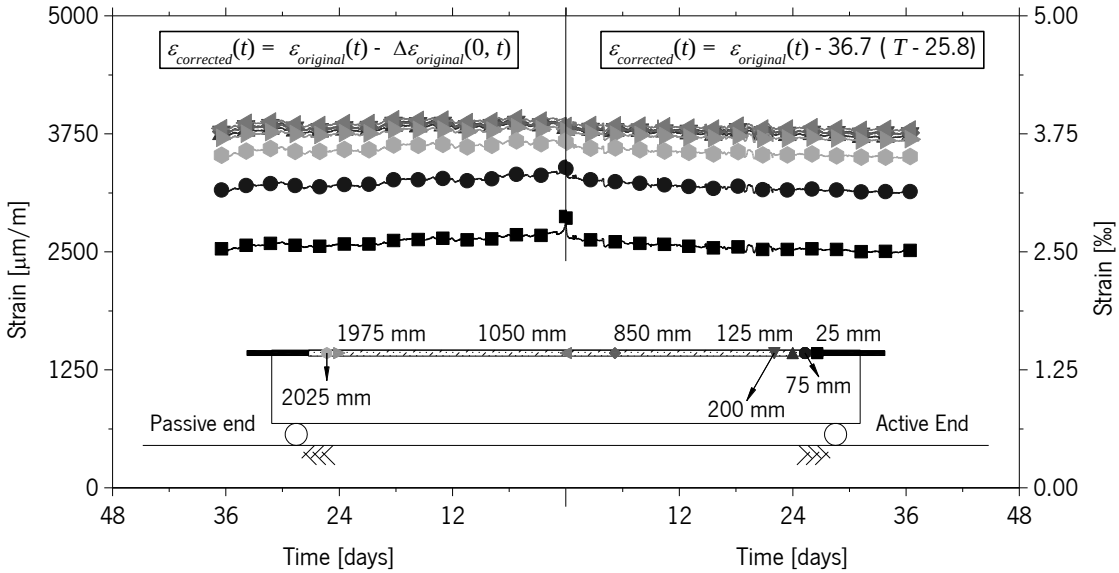

Figure 105 – Corrected strains in the CFRP – initial approaches – S1_30%.

As, in general, based on the previous approaches, the strain gauges located in the centre of the bond length (850 mm and 1050 mm), suggest that the strain remains approximately constant and, as shown previously, the central strains exhibit exceptional correlation among each other, it was decided to explore a third strategy to evaluate the effective strain loss. This third strategy consists on assuming that after removing the prestress load, no strain variation besides the instantaneous loss exists in the mid-span strain gauge, as defined in Eq. 34.

$$\varepsilon_{corrected}(t) = \varepsilon_{original}(t) - \left(\varepsilon_{1050mm}(t) - \varepsilon_{1050mm}(0)\right) \tag{34}$$

where $\varepsilon_{corrected}(t)$ is the corrected strain recorded at at a time instant t, $\varepsilon_{original}(t)$ is the original strain recorded at a given position at the same time instant t, and $\varepsilon_{1050mm}(0)$ and $\varepsilon_{1050mm}(t)$ are the

strains recorded in the strain gauge located at mid-span immediately after prestress release ($t = 0$) and at the time instant t, respectively.

The results obtained by this method, depicted in Figures 106 and 107, were definitely the smoothest of all approaches explored. As expected, according to this approach, immediately after prestress release the strain in the mid-span strain gauge remains constant. In the case S1_20%, in Figure 106, the strain gauge located at 25 mm, had already been identified as zone of considerable loss. However, using this strategy, the strain gauges located at 75 mm and 2025 mm are now recognized to display a considerable strain loss as well during approximately 5 days after the prestress release.

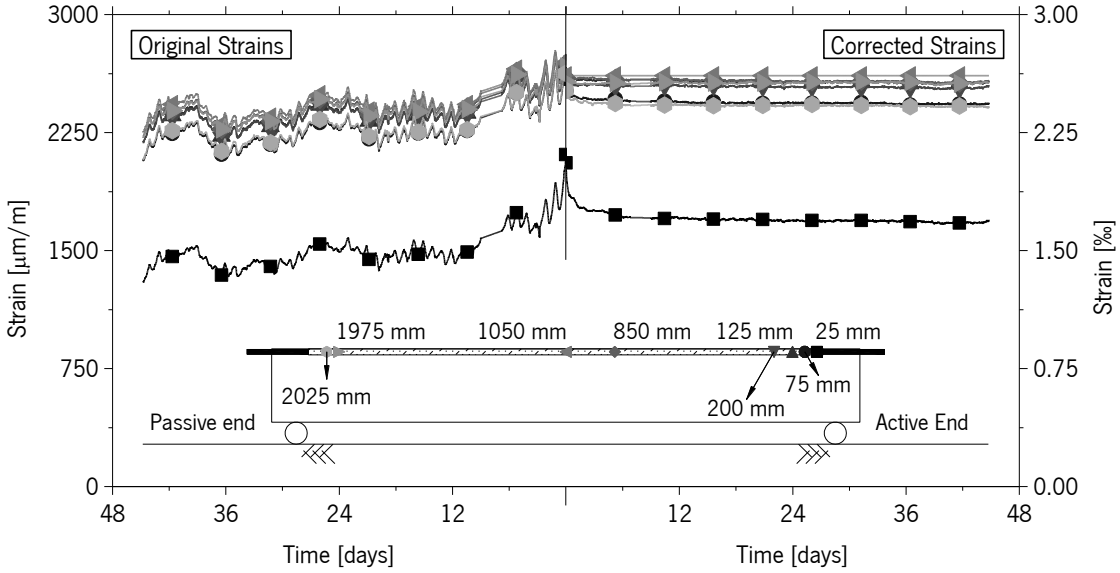

Figure 106 – Corrected strains in the CFRP – S1_20%.

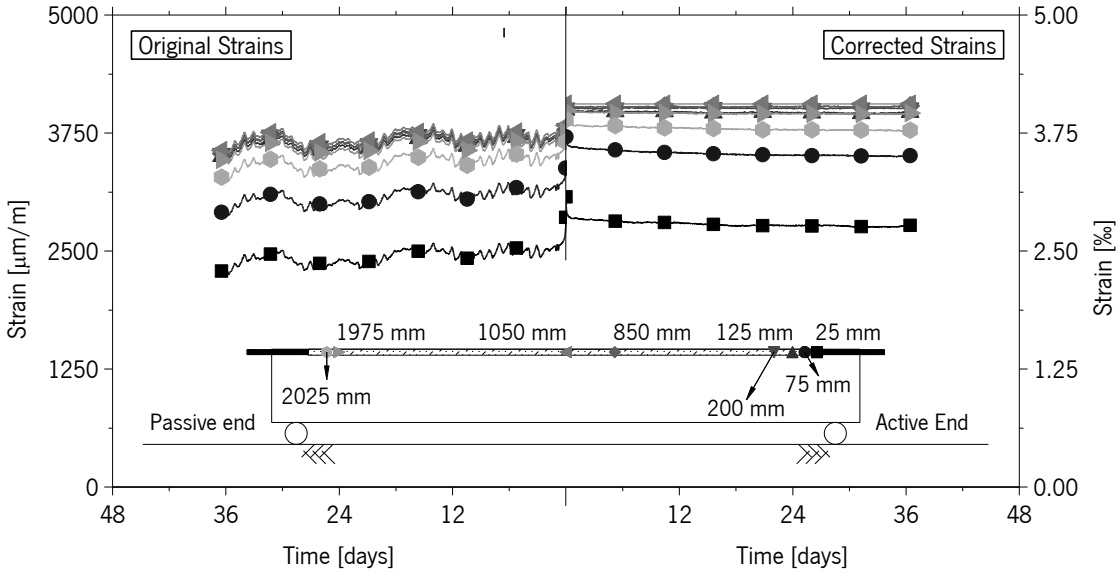

Figure 107 – Corrected strains in the CFRP – S1_30%.

In the case of the S1_30% (see Figure 107), the strain loss was confirmed to be essentially concentrated in the 25, 75 and 2025 mm strain gauges. The loss process developed apparently faster since it was basically concentrated in the first couple of days.

According to the results obtained in this preliminary series of tests, the third strategy to remove the environmental effects on the strain variation was the one to be adopted in subsequent series.

4.2 SERIES II – FULL-SCALE BEAMS

The second series of beams prepared was designed to be identical to the previous series in terms of concrete and reinforcement (both steel and CFRP reinforcement). The only adjustments made in these series were the length of the beam (4 meters), the cover of the shear reinforcement (30 mm), and the spacing of the shear reinforcement (100 mm).

This series was composed of six reinforced concrete beams, as depicted in Figure 108, casted individually with concrete target average strength of 33 MPa (C20/25). Of the six beams casted, four were prestressed, and in Figure 109 some pictures of the production process of the beams are presented.

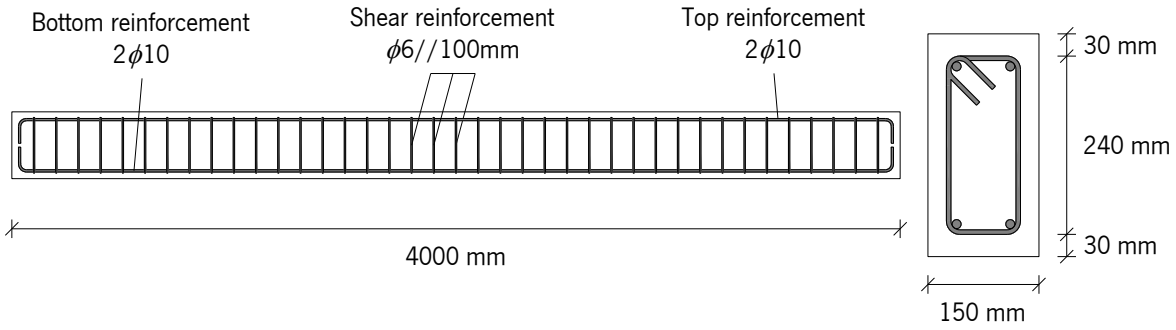

Figure 108 – Cross section and reinforcement configuration – Series II.

After concrete was cured, the beams were transported to a stone cutting company to open the grooves in five of the beams, also with a target cross section of 6×30 mm^2.

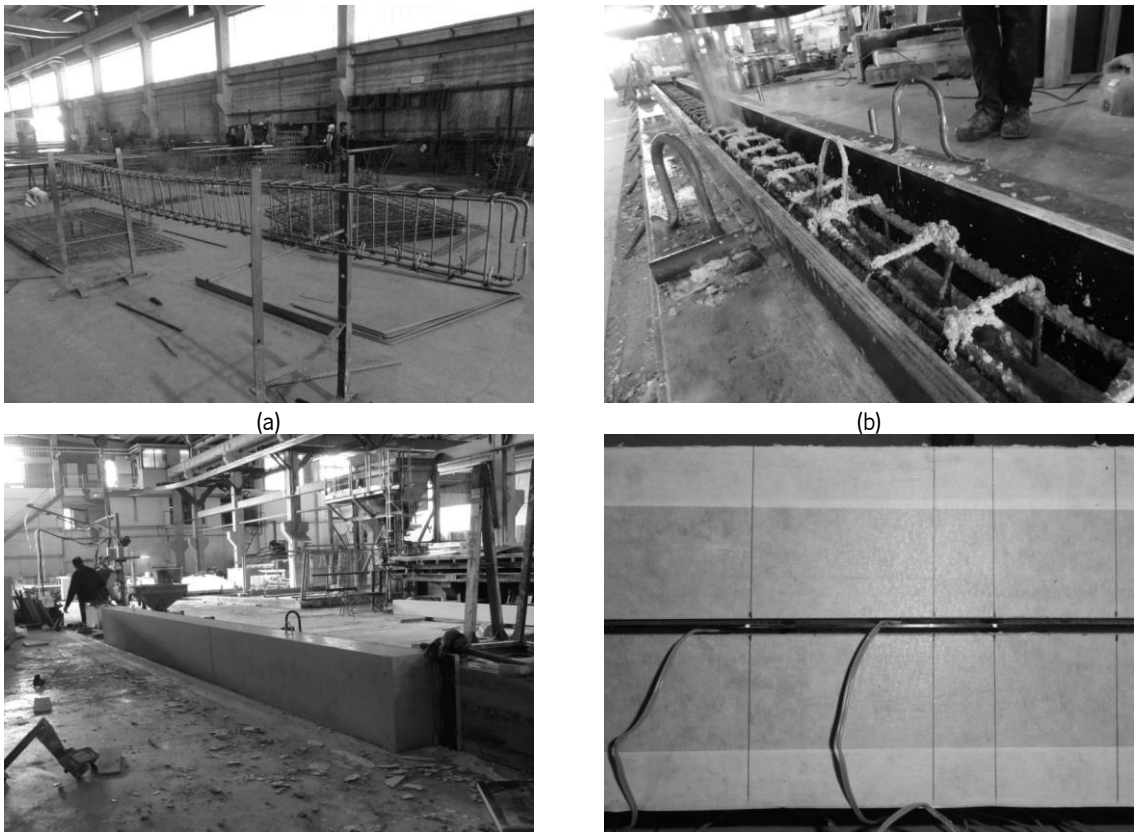

Figure 109 – Casting and preparation of the beams – Series II: (a) steel reinforcement, (b) casting (c) finished aspect of a beam and (c) prestressed CFRP before the application of the epoxy adhesive.

4.2.1 Application and release of prestress

Considering the results obtained in the previous series, it was decided to decrease the number of strain gauges installed in this series of beams. As it was realized that only the strain gauges located at 25 mm and 75 mm exhibited significant strain loss, in this series only the strain gauge located at 25 mm was maintained, as well as one strain gauge at mid-span (Figure 110).

Additionally, another strain gauge positioned 100 mm from the free-end on the active side was introduced. This decision was taken due to the fact that in this series two higher prestress levels were used (40% and 50%), and the proximity of additional strain gauges could negatively influence the bond properties, decreasing the bond capacity. Moreover, as greater prestress levels were applied, shifting the strain gauge previously placed at 75 mm by 25 mm could eventually provide a better estimation of the transfer length of the prestress load.

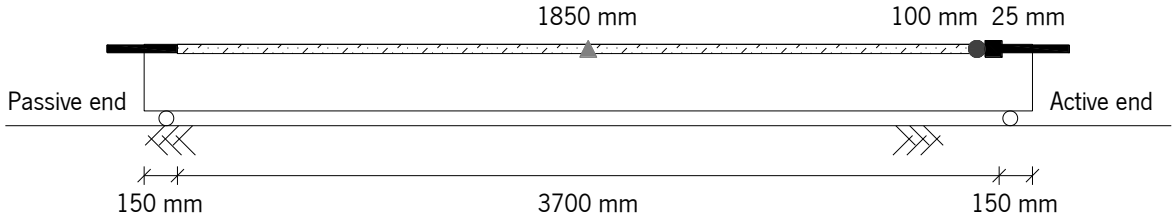

Figure 110 – CFRP instrumentation details – Series II.

In this series, the same criterion was defined to choose the prestress load level *i.e.*, percentage of ultimate nominal strain resulting in target strain values of 2.667‰, 4.000‰, 5.333‰ and 6.667‰ to apply 20%, 30%, 40% and 50% of prestress load, respectively. The beams presented in this Section were labelled similarly to the beams of Series I as S2_20%, S2_30%, S2_40% and S2_50%. Figure 111 shows that the same undulation of load was observed from the end of load application until the beginning of prestress release. Table 31 evidences that the average strain applied was extremely close to the target values. It is also verified that the secant elastic modulus obtained was again completely different from the nominal elastic modulus, E_f, indicated by the manufacturer in all the CFRP laminates, ranging between 84 GPa and 166 GPa. Since a quite low value was again obtained, the accidental contact between CFRP and surrounding equipment previously pointed out to justify the abnormal results for E_f is not anymore supported. Analysing S2_30%, the applied load was significantly lower than expected and, therefore, another cause affected this prestress application. It is believed that a deficient positioning of the load cell may be the cause of these incorrect readings. Note that the load cell is placed against one steel box, like the one showed in Figure 66b, and this steel box is flat but not completely uniform. Therefore, the load cell may be asymmetrically compressed and the recorded signal may be imprecise.

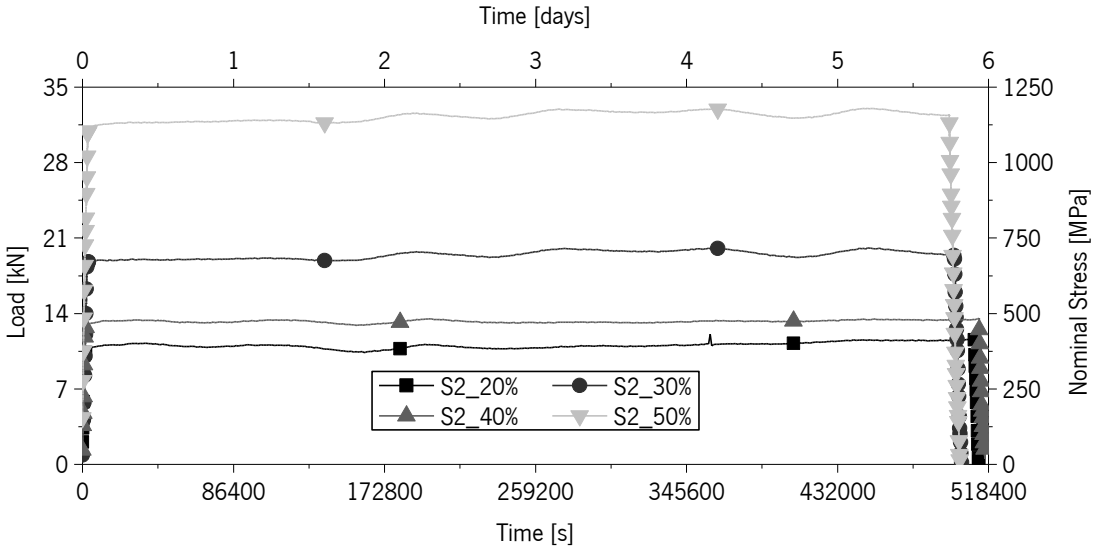

Figure 111 – Prestress load versus time during sustained load – Series II.

Table 31 – Prestress application and prestress release results – Series II.

	Beam	S2_20%	S2_30%	S2_40%	S2_50%
Prestress Application	Applied load [kN]	10.1	18.5	12.6	30.7
	Applied stress [MPa] §	360	661	449	1097
	Loading duration [s]	896	2526	1392	2995
	Loading speed [kN/min]	0.54	0.42	0.48	0.53
	Average CFRP strain [‰]§§	2.690 (0.026) {1%}	4.000 (0.027) {1%}	5.354 (0.044) {1%}	6.621 (0.107) {2%}
	Secant elastic modulus [GPa]	134	165	84	166
	Temperature at strengthening [°C]	15.7	16.9	15.7	16.9
Curing	Curing time [days]	5	5	5	5
	Average temperature [°C]	15.9 (0.6) {4%}	18.1 (1.1) {6%}	15.9 (0.6) {4%}	18.1 (1.1) {6%}
Prestress release	Applied load [kN]	11.6	19.4	13.5	32.4
	Release duration [s]	2590	4110	3380	6189
	Release speed [kN/min]	0.23	0.28	0.23	0.31
	Average CFRP strain before prestress release [‰]§§	2.634 (0.026) {1%}	3.921 (0.029) {1%}	5.262 (0.074) {1%}	6.582 (0.093) {1%}
	Temperature [°C]	16.7	17.4	16.7	17.4

Average (Standard deviation) {Coefficient of Variation}

§ Applied stress = Applied load / CFRP cross sectional area.

§§ Average CFRP strain = average of the strain gauges at 25, 100 and 1850 mm.

The applied load and corresponding strain were plotted to look for any abnormality that could indicate another reason for scattering of the secant elastic modulus. However, as shown in Figure 112, all four plots are extremely linear during loading, suggesting that maybe the load cell was either deficiently positioned and has recorded incorrect strain readings or, in fact, it had not enough precision to assess the correct load level.

Additionally, the linear regression presented in Figure 112 represents an average elastic modulus of the CFRP laminate during loading, contrasting with the secant elastic modulus presented in Table 31. It is still visible that at least the CFRP laminate of S2_30% conducted to a considerably low elastic modulus when compared with the nominal value.

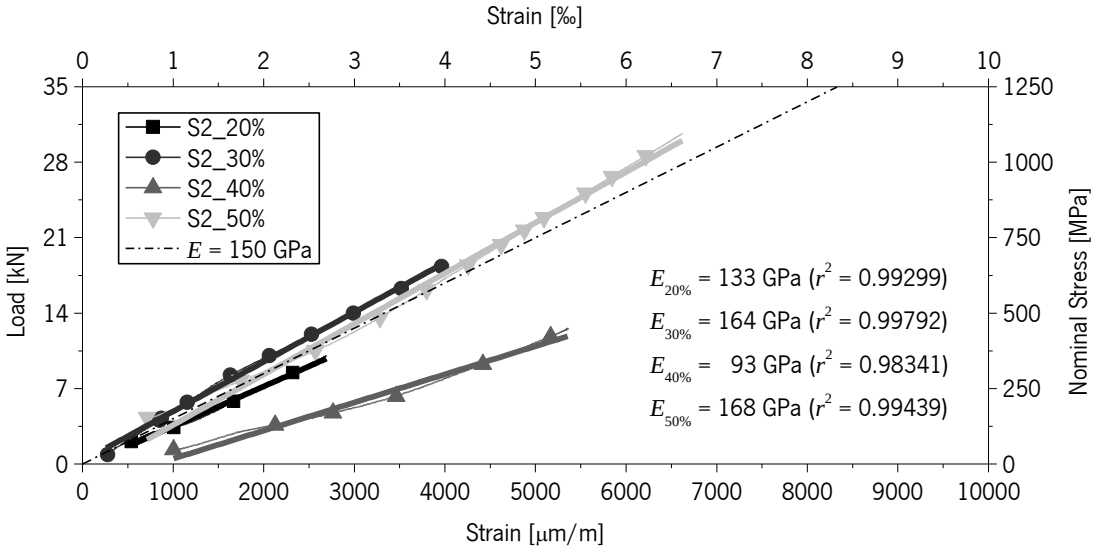

Figure 112 – Load versus strain during loading – Series II.

The instantaneous strain losses in the different prestressed beams were also analysed. According to Table 32, and similarly to what was observed in Series I, the strain gauge presenting higher loss was the one located 25 mm from free-end on the active side. The loss on this strain gauge varied between 16% and 36% while in the remaining strain gauges the loss never exceeded 2%.

Table 32 – Instantaneous prestress losses – Series II.

	S2_20%			S2_30%			S2_40%			S2_50%		
Strain gauge	25 mm	100 mm	1850 mm	25 mm	100 mm	1850 mm	25 mm	100 mm	1850 mm	25 mm	100 mm	1850 mm
ε_p [‰]	2.718	2.684	2.667	4.018	3.968	4.000	5.388	5.304	5.370	6.499	6.693	6.672
ε'_p [‰]	2.662	2.628	2.612	3.953	3.897	3.912	5.291	5.177	5.317	6.475	6.648	6.622
ε_f [‰]	2.072	2.575	2.585	3.326	3.871	3.923	3.355	5.006	5.285	5.075	6.509	6.572
$\Delta\varepsilon_p$ [‰]	0.590	0.053	0.026	0.627	0.027	-0.012	1.935	0.171	0.032	1.400	0.139	0.050
Loss [%]	22	2	1	16	1	0	36	3	1	22	2	1

Due to the impossibility of using a large number of LVDTs, and since no strain gauge was installed outside the bond length to later subtract the slip component corresponding to the elastic deformation of the CFRP laminate, in this series it was decided to only monitor the mid-span deflection. The deflection values obtained after transferring the prestress load to each specimen were 0.180 mm, 0.308 mm, 0.385 mm and 0.473 mm for the beams S2_20%, S2_30%, S2_40% and S2_50% respectively. Figure 113 shows the evolution of the mid-span deflection during the period of load transference from the CFRP to the RC beam.

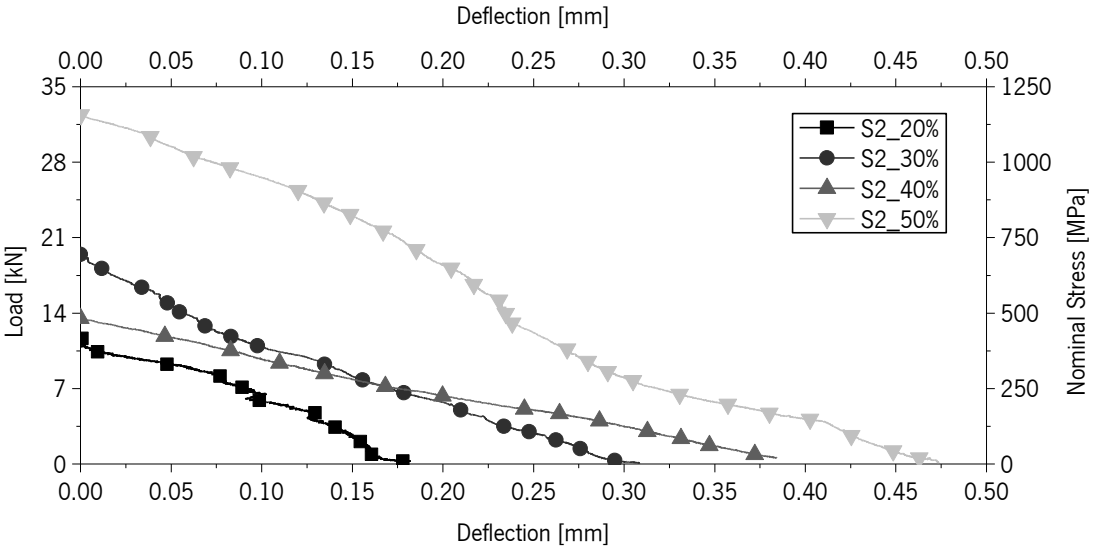

Figure 113 – Load versus mid-span deflection – Series II.

Figure 114 depicts the loss of strain in all strain gauges of Series II beams. Observing these results in combination with Table 32, it is noticeable that the strain gauges placed at 100 mm and 1850 mm experienced almost imperceptible instantaneous strain loss while the strain at 25 mm decreased significantly.

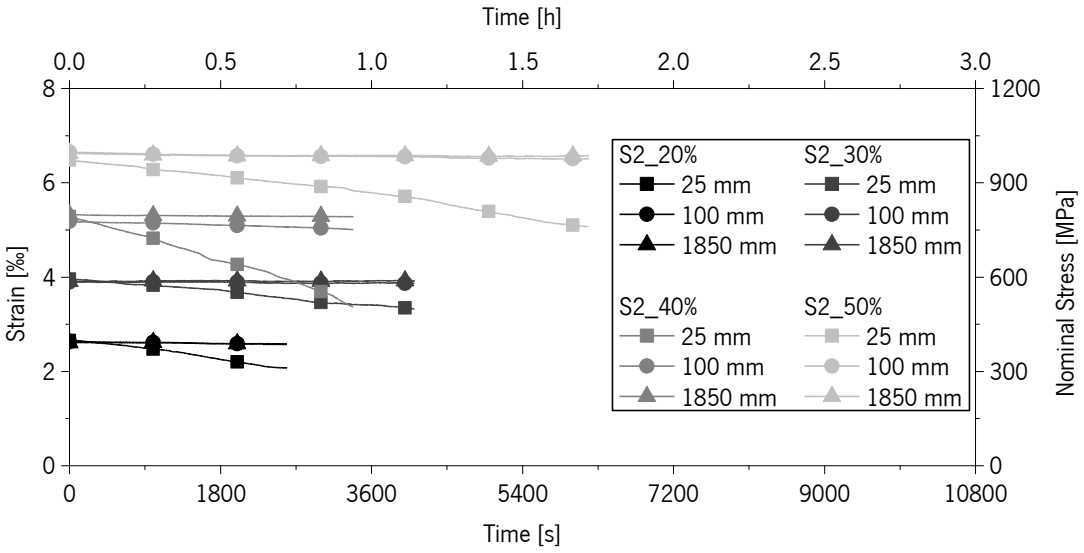

Figure 114 – Strain loss during prestress release – Series II.

4.2.2 Long-term losses of prestress

During the monitoring period of these beams, temperature and relative humidity were recorded like in Series I. However, while in Series I the equipment measuring the temperature was placed side by

side with the beam, while in this case it had to be placed in a more distant position. Due to this fact, temperature dependence was not so easy to observe, as Figure 115 demonstrates.

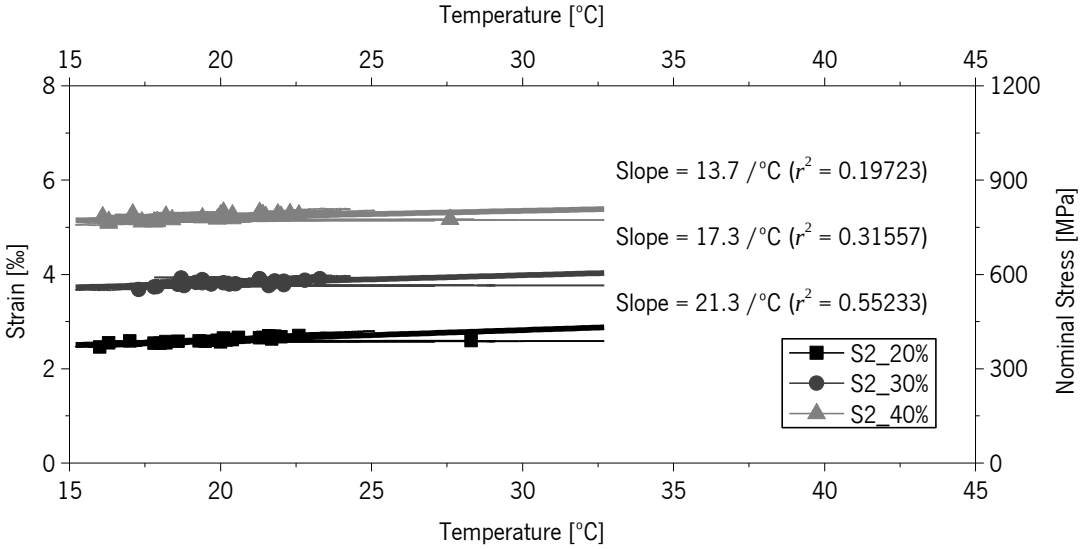

Figure 115 – Strain versus temperature – Series II.

During the monitoring of these beams, the acquisition equipment experienced some power failures, and some data had to be extrapolated during that time and therefore, the strain obtained by this process does not account for the influence of temperature. However, as concluded for Series I beams, the best method to subtract the environmental effects is the subtraction of the mid-span strain gauge variation, as defined in Eq. 34. Therefore, an accurate temperature dependency is not mandatory to assess the effective long-term loss of strain.

The long-term loss of all strain gauges is depicted in Figures 116 to 119 and, in general, a fairly smooth curve was obtained in all cases. Note that in the case of S2_50%, the strain gauge at mid-span was damaged after prestress release and therefore, the strain variation in the S2_30% was used for correction purposes, since they were unloaded at the same time/temperature.

In all cases, the strain at 25 mm was observed to decrease considerably in the 10 days following the prestress load release. Furthermore, the strain in the 100 mm strain gauge in S2_40% also decreased considerably over time, although in S2_50% no significant loss was visible at the same location.

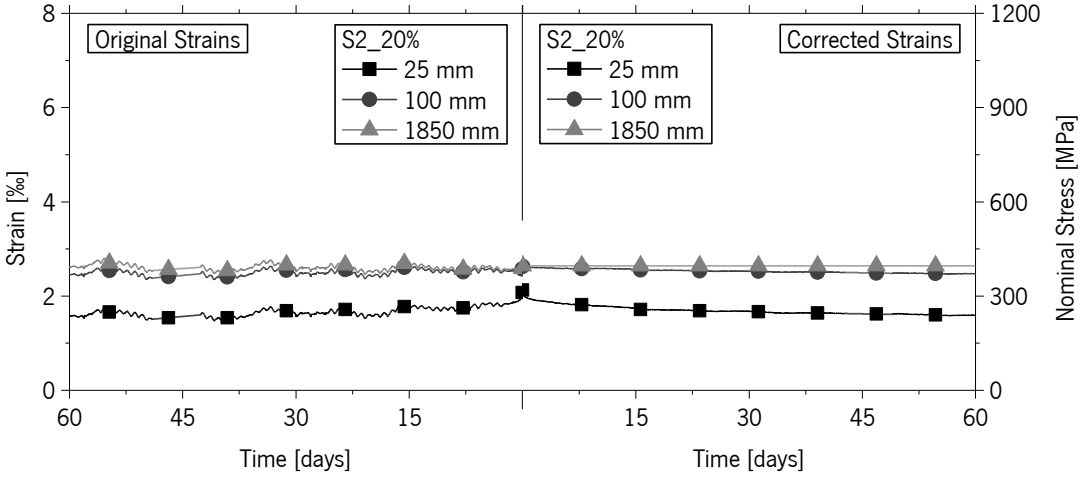

Figure 116 – Corrected strain loss – S2_20%.

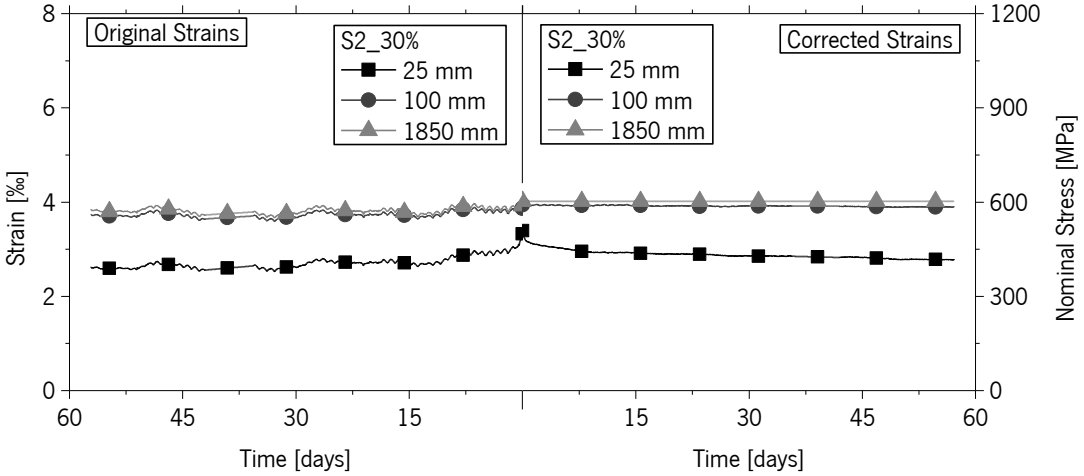

Figure 117 – Corrected strain loss – S2_30%.

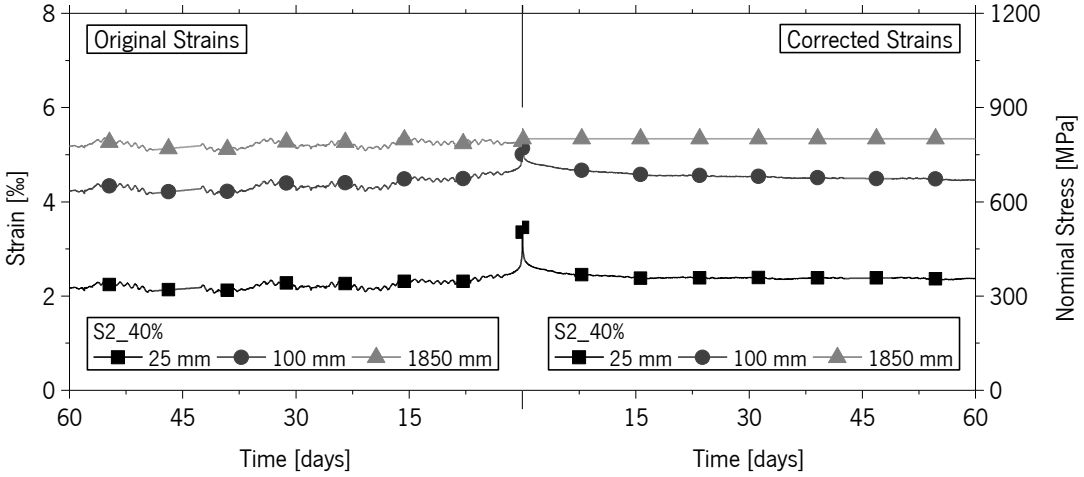

Figure 118 – Corrected strain loss – S2_40%.

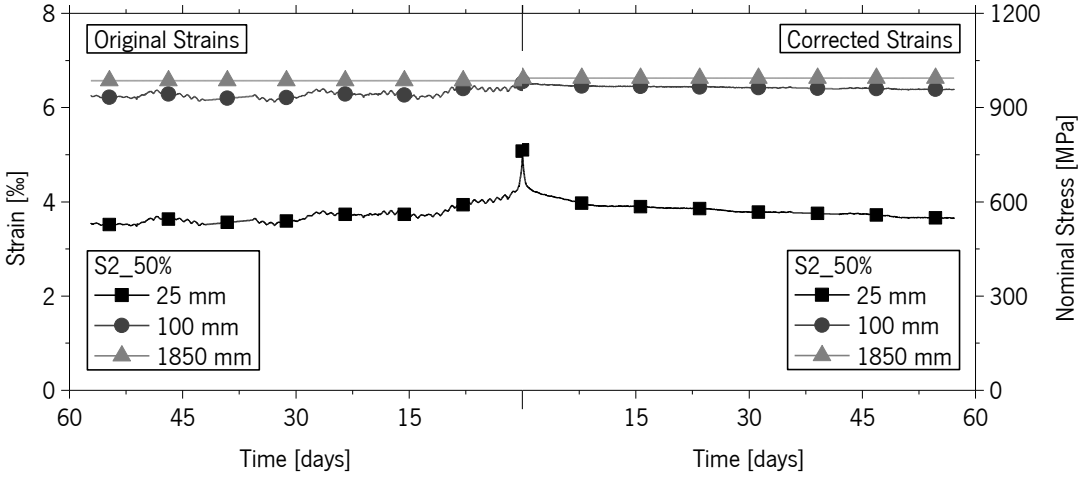

Figure 119 – Corrected strain loss – S2_50%.

As in no other plot the strain at 100 mm was so dramatically reduced over time, it is believed that, maybe, the introduction of adhesive in the groove of the this beam was less effective and the real distance between the strain gauge and the free-end was in fact reduced.

4.3 SERIES III – FULL-SCALE BEAMS

The third series of beams was ordered to a private contractor, and the six beams forming this series were provided after being completely cured. No supervision was made during the preparation of the steel reinforcement or during the casting of this series of beams. This series was requested to be practically equal to the previous series of reinforced beams but with a higher steel reinforcement ratio, as depicted in Figure 120. The grooves of these beams were also requested to have average cross section of 6×30 mm^2 in five of the beams.

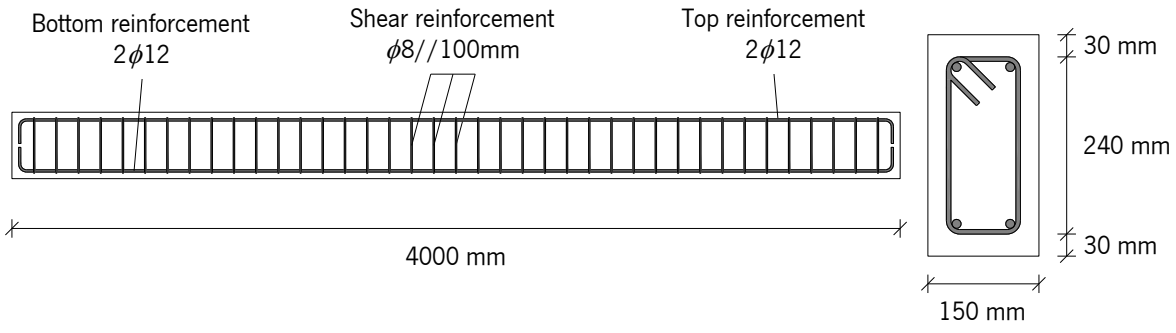

Figure 120 – Cross section and reinforcement configuration – Series III.

4.3.1 Application and release of prestress

The exact same procedure and monitoring used in Series II was repeated in the application of prestress in this Series. The prestressed beams were labelled as S3_20%, S3_30%, S3_40% and

S3_50% to denote the elements prestressed with a strain level of 2.667‰, 4.000‰, 5.333‰ and 6.667‰, respectively. In Table 33 the summary of the main parameters determined during prestress application and release are presented. The secant elastic modulus obtained in the CFRP laminates in this series was again noticeably different from the nominal modulus reported by the manufacturer. The most divergent value observed was in S3_30% since it was much higher than expected. Additionally, the CFRP laminate of S3_50% registered an abnormal variation of strain between strain gauges (Coefficient of Variation = 6%), opposed to all other prestressed beams analysed (the remaining beams of this series and all of the previous series).

Table 33 – Prestress application and prestress release results – Series III.

	Beam	S3_20%	S3_30%	S3_40%	S3_50%
Prestress Application	Applied load [kN]	12.9	24.5	21.5	33.9
	Applied stress [MPa] §	460	875	769	1209
	Loading duration [s]	1153	2300	3321	3222
	Loading speed [kN/min]	0.67	0.49	0.39	0.53
	Average CFRP strain [‰]§§	2.680 (0.037) {1%}	4.010 (0.003) {0%}	5.359 (0.026) {0%}	6.643 (0.385) {6%}
	Secant elastic modulus [GPa]	171	218	143	182
	Temperature at strengthening [°C]	20.6	23.1	20.6	23.1
Curing	Curing time [days]	5	5	5	5
	Average temperature [°C]	20.6 (1.3) {6%}	18.5 (1.6) {9%}	20.6 (1.3) {6%}	18.5 (1.6) {9%}
Prestress release	Applied load [kN]	14.2	23.3	23.6	32.9
	Release duration [s]	3014	4612	4798	6822
	Release speed [kN/min]	0.28	0.31	0.29	0.29
	Average CFRP strain before prestress release [‰]§§	2.691 (0.053) {2%}	3.721 (0.018) {0%}	5.363 (0.037) {1%}	6.173 (0.243) {4%}
	Temperature [°C]	23.3	18.4	23.3	18.4

Average (Standard deviation) {Coefficient of Variation}

§ Applied stress = Applied load / CFRP cross sectional area.

§§ Average CFRP strain = average of the strain gauges at 25, 100 and 1850 mm.

Similar to what was presented in the previous series, the load variation during the curing period of adhesive, presented fluctuations due to temperature influence (see Figure 121). Even though the load measured by the load cell was assumed less accurate (note how the application of S3_30% and S3_40% required the same level of initial load to attain two different target strains), the load decay in S3_20% and S3_40% was practically the same. These beams were prepared simultaneously and exhibited a load decrease of almost 2 kN between prestress application and beginning of release. The remaining beams, S3_30% and S3_50%, were also prepared at the same time and revealed a load decay of about 1.3 kN.

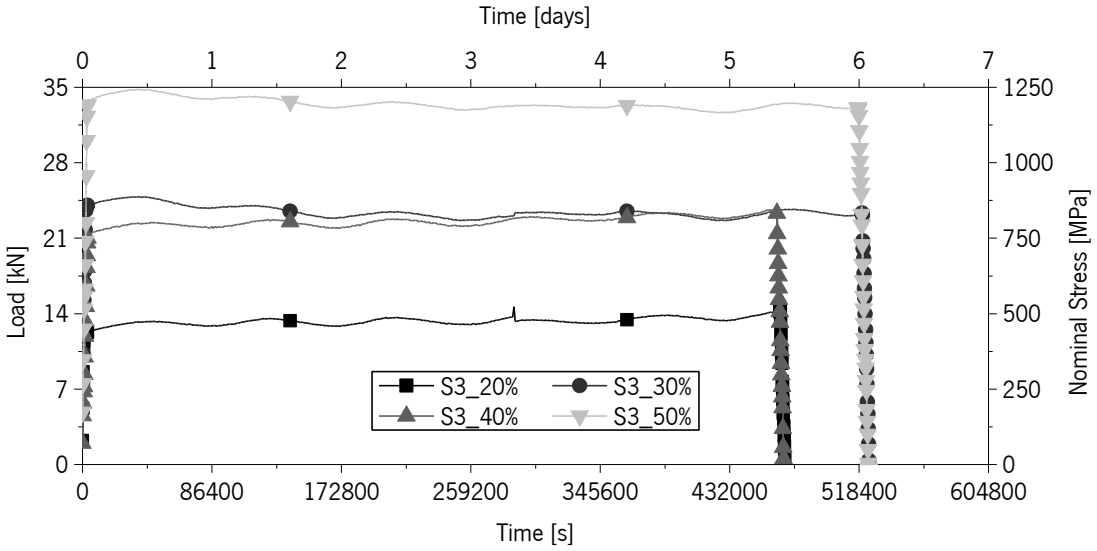

Figure 121 – Prestress load versus time during sustained load – Series III.

As executed for the previous series, the average elastic modulus of the CFRP was also obtained from the linear regression of the stress versus strain recorded during the loading process (see Figure 122). Taking as example S3_30%, while in Table 33 the reported secant elastic modulus is 218 GPa, the linear regression conducted to an even higher value, of about 224 GPa. Inversely, the secant elastic modulus of S3_20% was initially presumed to be 168 GPa, which is in agreement with the value indicated by the supplier, can apparently acceptable value, but was found to be only 132 GPa if the average slope of the stress-strain curve is considered.

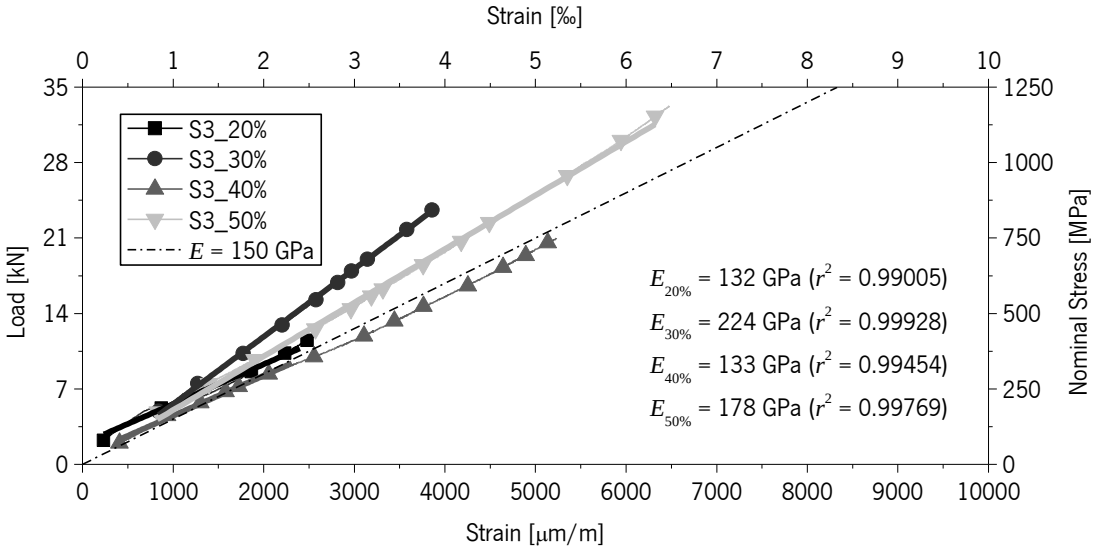

Figure 122 – Load versus strain during loading – Series III.

Table 34 summarizes the instantaneous strain loss in each of the strain gauges installed in the beams of Series III. The CFRP strain loss at mid-span was again extremely low, between 1% and 2%. Of all the beams, S3_40% experienced the largest instantaneous loss at 25 mm, around 38%.

Table 34 – Instantaneous prestress losses – Series III.

Strain gauge	S3_20%			S3_30%			S3_40%			S3_50%		
	25 mm	100 mm	1850 mm	25 mm	100 mm	1850 mm	25 mm	100 mm	1850 mm	25 mm	100 mm	1850 mm
ε_p [‰]	2.704	2.637	2.700	4.009	4.009	4.014	5.373	5.376	5.329	6.425	6.416	7.087
ε'_p [‰]	2.740	2.635	2.698	3.721	3.739	3.702	5.362	5.401	5.327	6.018	6.047	6.453
ε_f [‰]	2.281	2.585	2.656	3.224	3.677	3.666	3.313	5.206	5.265	4.25	5.908	6.391
$\Delta\varepsilon_p$ [‰]	0.459	0.050	0.041	0.497	0.062	0.035	2.049	0.195	0.062	1.768	0.139	0.062
Loss [%]	17	2	2	12	2	1	38	4	1	28	2	1

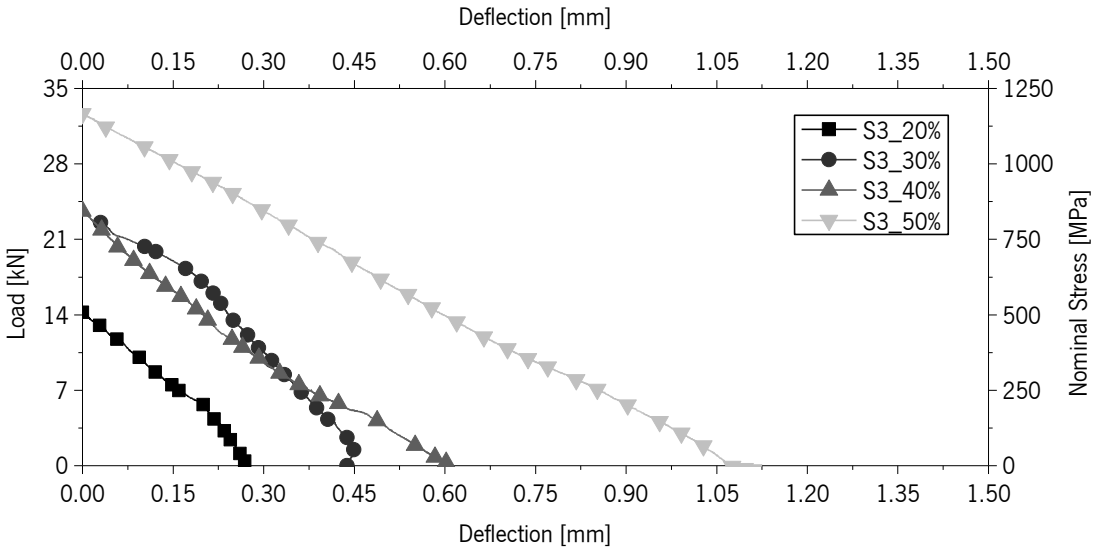

Figure 123 – Load versus mid-span deflection during prestress release – Series III.

As the prestressed elements in these series exhibited similar response in terms of strain versus temperature to the one already described for the previous series, regarding these specimens, only the load-deflection curves will be presented. Figure 123 shows some curious details regarding the mid-span deflection introduced by the prestress. One has to do with the fact that S3_50% is the one that displays the most linear behaviour of all. Another important remark can be made in in relation to the instantaneous mid-span deflections that do not increase in proportion to the increase of prestress. While the S3_20%, S3_30% and S3_40% beams exhibited a displacement of 0.270 mm, 0.433 mm and 0.606 mm, respectively, S3_50% almost doubled the maximum displacement measured and reached a final instantaneous deformation of 1.112 mm.

It is also worth mentioning that up to this series of beams, no visible cracks were detected in any specimen. However, in one of the beams of this series, one extensive crack was detected, although it was caused by the prestress transfer process, but to a deficient filling of the groove in the active end side S3_40% (see Figure 124). This beam was one of the cases where to guarantee no contact between CFRP and concrete at mid-span, the prerequisite of centring the CFRP laminate at the free-end was not possible to attend. Figure 124 shows the crack that formed, mainly caused by the high capability of the epoxy adhesive to transfer the prestress to the surrounding concrete.

Figure 124 – Crack in the free-end of the active end side – S3_40%.

4.3.2 Long-term losses of prestress

The approach used for strain correction, defined in Eq. 34, was also used in this series and all results can be seen in Figures 125 to 128. This approach removed the great majority of noise in the readings and produced fairly logical strain loss curves, avoiding the need of further data filtering.

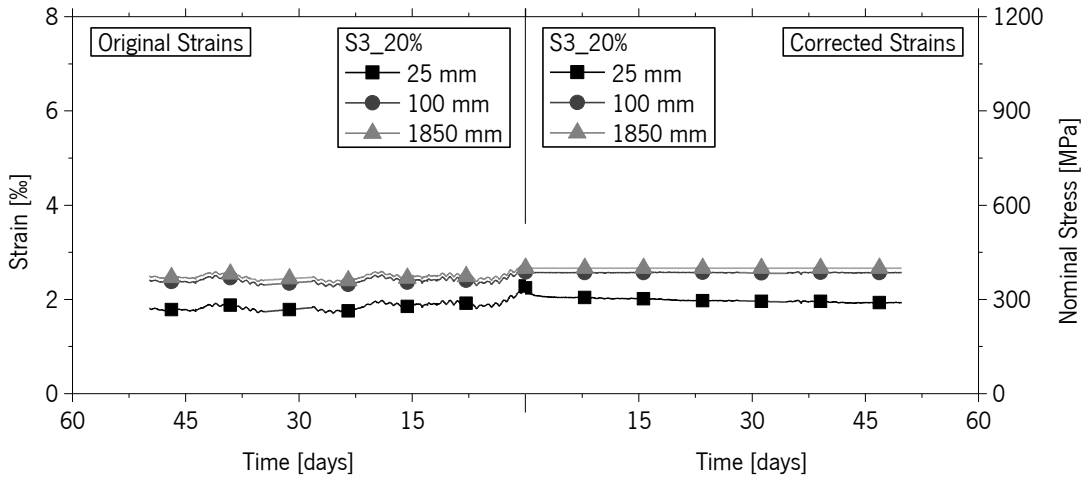

Figure 125 – Corrected strain loss – S3_20%.

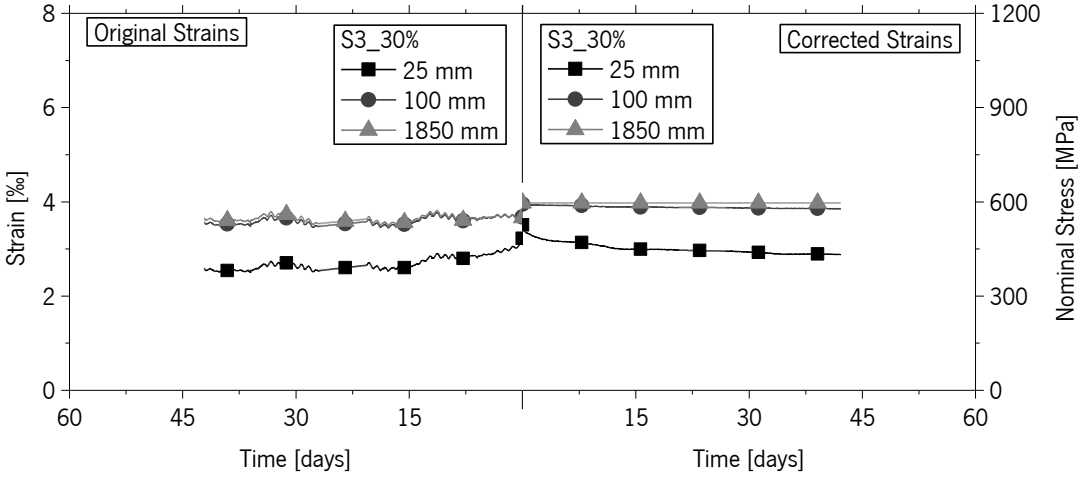

Figure 126 – Corrected strain loss – S3_30%.

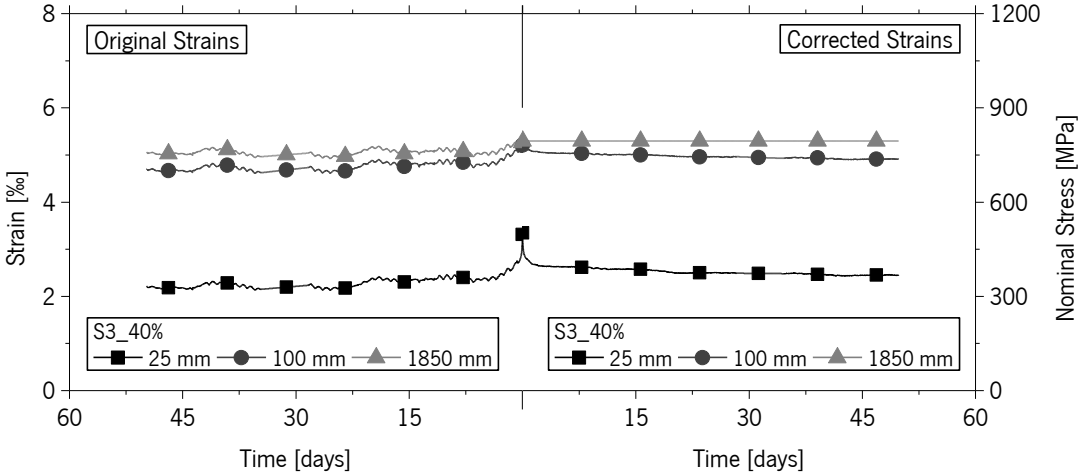

Figure 127 – Corrected strain loss – S3_40%.

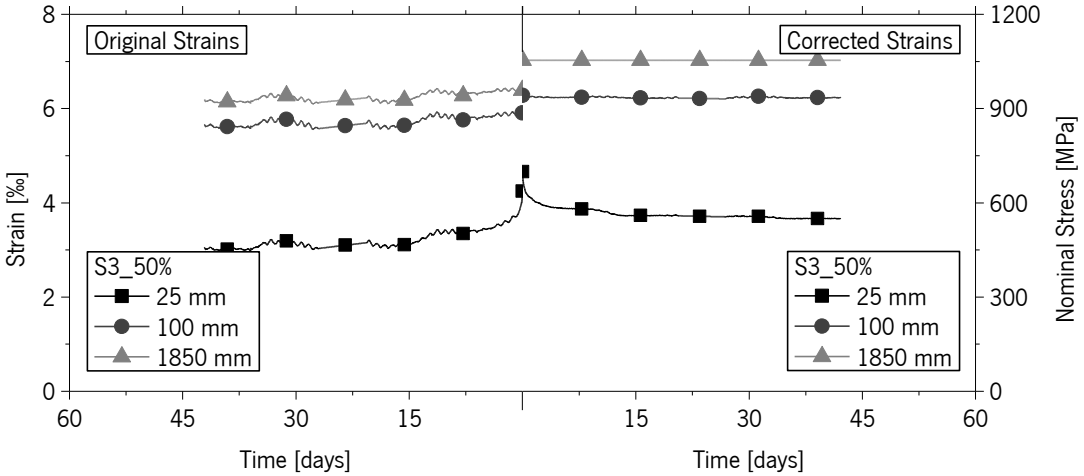

Figure 128 – Corrected strain loss – S3_50%.

Opposed to what happened in the previous series, the strain gauge located at 100 mm demonstrated a higher long-term loss of strain in S3_40% and S3_50% (see Figures 127 and 128), meaning that

the bond length was mobilized beyond the 100 mm. Another interesting observation is the fact of, in S3_50%, the stabilization of the strain gauge located at 25 mm took almost two weeks, contrasting with the few days necessary to stabilize the strain gauge placed on the same section of S3_20%.

4.4 FINAL REMARKS

In this Chapter, the procedure chosen to apply NSM-CFRP prestress to reinforced concrete beams was presented and verified to be effective. The desired prestressed load was successfully applied in all of the 10 reinforced concrete beams. In all the process, which in fact is not reproducible in real structures, the hardest task was the introduction of adhesive in the groove, since the presence of the prestressed laminate prevented the adhesive from easily circulating around the CFRP laminate, and the thinness of the groove impeded the clear observation of the deepness of insertion of the adhesive layer. Nevertheless, of most of the procedure defined, the introduction of the adhesive in the notch is a necessary task and therefore, a strategy to simplify this step of the strengthening process needs to be developed. It is suggested that in job site, the CFRP is prestressed in prior to its placement in the groove, allowing the strengthening to be performed as in the case of passive strengthening: the grove is initially filled with epoxy adhesive and the prestressed CFRP is then inserted in the groove.

Concerning the instantaneous behaviour of the prestressed beams, all beams registered low levels of strain loss along the bonded length and reasonable levels of deflection were obtained due to the prestress force. Additionally, the prestress release procedure idealized, which included the presence of rollers under the beam to allow free movement, was adequate to guarantee simultaneous release in both sides of the beam as proven by the symmetric loss of strain measured in Series I.

The environmental temperature was found to be a key parameter in order to correctly assess the load applied, as well as the strain state on the CFRP laminate, since all the monitoring devices used exhibited fluctuations of the signal due to temperature. The assessment of strain loss is therefore challenging since the recorded strains are clearly temperature dependent. Even so, the variation of signal due to external causes was successfully removed from the raw data monitored.

The long term losses of prestress were found to take between a couple of days to a couple of weeks to become stabilized. The strain gauges installed 25 mm from the free-ends were the ones registering the most relevant long-term losses, and the transfer length of the prestress force was

found to be, in most cases, around 100 mm. However, given the reduced number of strain gauges installed on the CFRP laminate, it was not possible to obtain a precise transfer length.

4.5 REFERENCES

Wight, R. G.; Green, M. F. e Erki, M-A. (2001). "Prestressed FRP Sheets for Poststrengthening Reinforced Concrete Beams." *Journal of Composites for Construction*, ASCE, 5(4), 214-220.

Nordin, H. e Täljsten, B. (2006). "Concrete Beams Strengthened with Prestressed Near Surface Mounted CFRP." *Journal of Composites for Construction*, ASCE, 10(1), 60-68.

Badawi, M. e Soudki, K. A. (2008). "Fatigue of RC beams strengthened with prestressed NSM CFRP rods." *Proceedings of the Fourth International Conference on FRP Composites in Civil Engineering* (CICE2008), Zurich, Switzerland, 22-24 July 2008, 6 pp.

Gaafar, M. A. e El-Hacha, R. (2008). "Strengthening reinforced concrete beams with prestressed FRP near surface mounted technique." *Proceedings of the Fourth International Conference on FRP Composites in Civil Engineering* (CICE2008), Zurich, Switzerland, 22-24 July 2008, 6 pp.

Chapter 5

FAILURE TESTS ON PRESTRESSED BEAMS

According to literature review, most authors reported that prestressed CFRP systems, either externally bonded (EBR) or near surface mounted (NSM), increase the crack and yield initiation loads of reinforced concrete elements and decrease deflection in relation to non-prestressed elements (Wight *et al.*, 2001, Nordin and Täljsten, 2006, Gaafar and El-Hacha, 2008, Hajihashemi *et al.*, 2011 and Wang *et al.*, 2012). Some of these same authors also claim that prestress also increases the ultimate load carrying capacity of the reinforced concrete elements (Wight *et al.*, 2001, Nordin and Täljsten, 2006, Badawi and Soudki, 2009 and Hajihashemi *et al.*, 2011), but this typically occurs when the presence of prestress modifies the original failure mode of the beam from concrete crushing, or premature debonding (normally in the case of EBR), to CFRP rupture, providing a much more effective utilization of the CFRP material.

In this Chapter, the prestressed beams described in the previous Chapter were tested up to failure in order to assess its load carrying capacity and deformational behaviour under a four-point bending configuration. All the tested series of beams included, besides the prestress beams presented previously, two additional reference beams, one made of plain reinforced concrete, labelled as 'Reference', and another one strengthened with a passive FRP laminate, herein referred as '0%' (preceded by S1, S2 or S3 in case of Series I, II or III, respectively).

For future reference, Figure 129 depicts the shows how the crack and yield points were determined from the experimental curves.

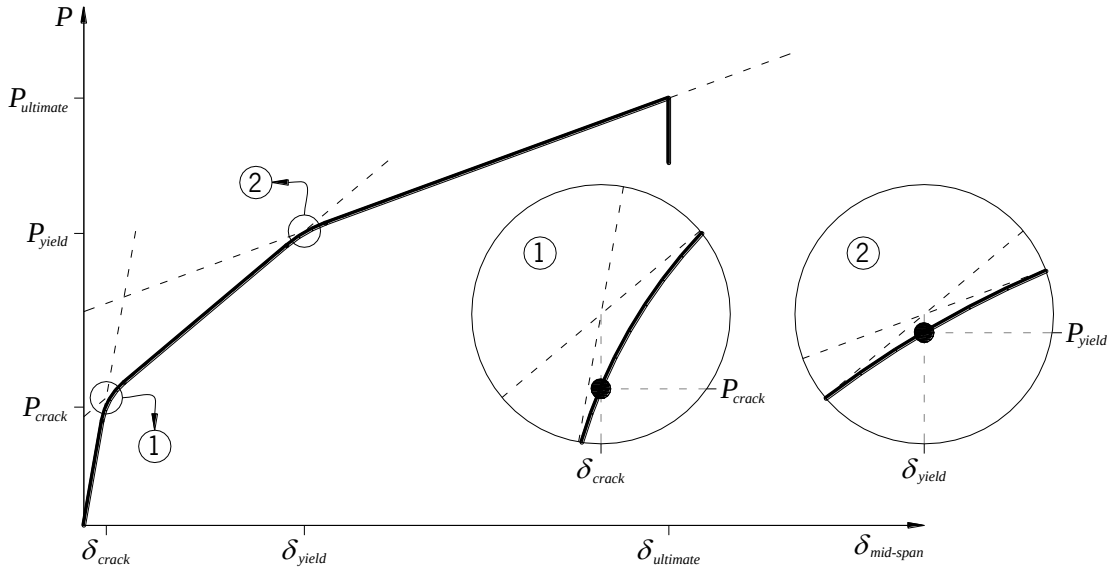

Figure 129 – Graphical depiction of the determination of the crack and yield initiation points.

5.1 SERIES I – PRELIMINARY SERIES

As referred previously, all beams were tested under four-point bending configuration, as depicted in Figure 130. In this series, the distance between loading points was selected in order to maximize the pure bending length in an attempt to avoid shear failure (shear span to height ratio of 900mm / 300mm = 3.0). All relevant geometric details and reinforcement arrangement of the beams of this series are presented in Section 4.1.

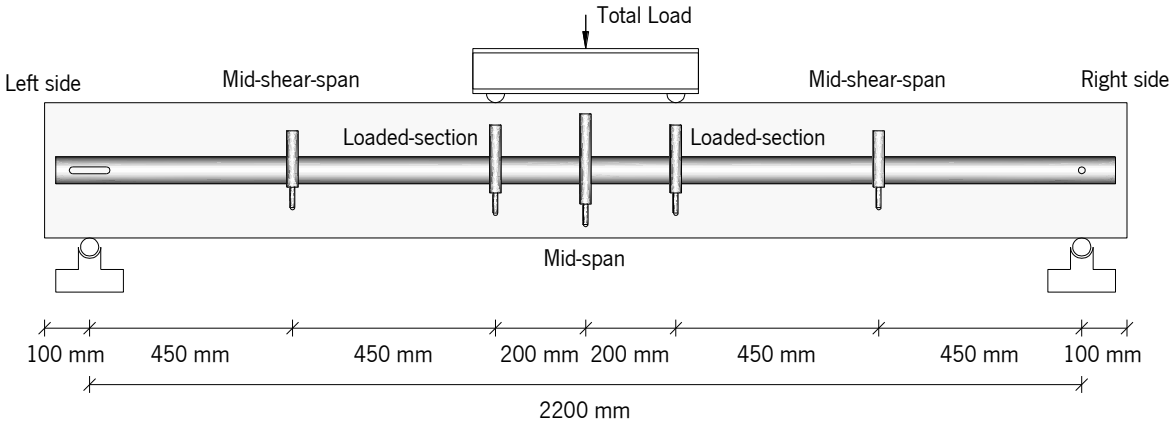

Figure 130 – Monitoring scheme of Series I beams.

The deflection of the beams was assessed using five LVDTs, one in the mid-span with ±50 mm range, one in each loaded-section (±25 mm range), and one at each mid-shear span section (±12.5 mm range). The tests were displacement controlled by a servo-hydraulic jack with a load cell of 500 kN capacity, and imposing a speed of 0.020 mm/s (see Figure 131). All strain gauges

installed on concrete and steel were monitored up to failure, while only the strain gauges installed at 75 mm, 125 mm, 200 mm, 850 mm and 1050 mm were acquired during the test (see Section 4.1).

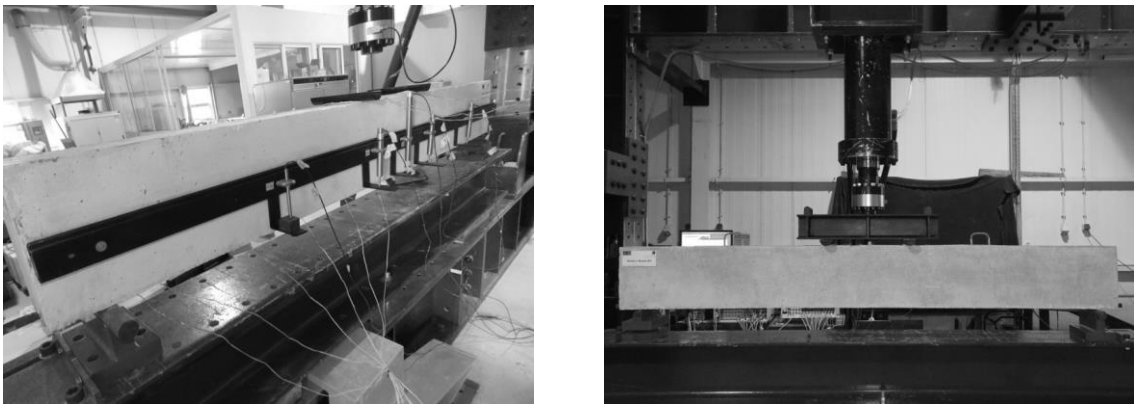

(a) (b)

Figure 131 – Photos of Series I setup: (a) frontal view of the support and loading conditions and (b) back view of the monitoring arrangement.

Analysing the main results obtained in this series, reported in Table 35, several relevant observations can be made. The first one is related to the cracking load, P_{crack}, and deflection at cracking, δ_{crack}, of the beams that increase with the prestress level reaching almost the double of the load/deflection of the Reference beam when a prestress level of 30% was applied.

The tendency is verified in terms of yielding deflection, δ_{yield}, and yielding load, P_{yield}, of the beams, but in this case the relative increase is not as high. It is worth noting that the displacement at yield of S1_0% and S1_20% prestress beams was marginally higher in relation to the Reference beam, although in terms of load capacity this increase is much more significant (22%~36%~47%).

At failure, however, the increase of the load-carrying capacity, $P_{ultimate}$, with the prestress level was marginal, since the failure mode was not changed by the increase of prestress level. Since in this series all the beams strenthened with CFRP (either passive or prestressed) failed due to CFRP rupture, the prestress did not provide any increase of the overall load carrying capacity of the beams and, therefore, no relevant increase of $P_{ultimate}$ was expected. Regarding the deflection at failure, $\delta_{ultimate}$, this value decreases proportionally to the increase of the prestress level (-21% and -31% in S1_20% and S1_30%, respectively).

Concerning the service load, $P_{l/250}$ (at a deflection of $2200 / 250 = 8.8$ mm), it consistently increased with the prestress level (32%~48%~55%), exceeding 50% for S1_30%.

Table 35 – Main results of the four-point bending tests – Series I.

Beam	δ_{crack} [mm]	P_{crack} [kN]	δ_{yield} [mm]	P_{yield} [mm]	$\delta_{ultimate}$ [mm]	$P_{ultimate}$ [kN]	$P_{l/250}$ [kN]
Reference	0.389	15.5	6.319	51.3	-	61.5	51.7
S1_0%	0.436 (12%)	18.7 (21%)	6.379 (1%)	62.5 (22%)	24.456 (-%)	93.0 (51%)	68.2 (32%)
S1_20%	0.636 (64%) {46%}	27.1 (75%) {45%}	6.414 (2%) {1%}	69.9 (36%) {12%}	19.361 (-%) {-21%}	94.0 (53%) {1%}	76.3 (48%) {12%}
S1_30%	0.744 (91%) {71%}	28.5 (84%) {53%}	7.002 (11%) {10%}	75.4 (47%) {21%}	16.925 (-%) {-31%}	95.2 (55%) {2%}	80.2 (55%) {18%}

Value (Variation in relation to the Reference beam) {Variation in relation to the S1_0% }

The load-deflection response of all the beams tested is depicted in Figure 132. Observing all the curves together, it is noticeable that all beams exhibited the same stiffness before concrete cracking (see inset in Figure 132). Comparing S1_20% and S1_30%, a higher value of P_{crack} was expected for this last one. However, a smaller concrete tensile strength may justify the relatively small increment of cracking load. In terms of ultimate load and ultimate deflection, Figure 132 clearly illustrates the insignificant variation of load-carrying capacity in the CFRP strengthened beams, as well as the proportionality of the ultimate deflection reduction (-21% and -31%, see Table 35).

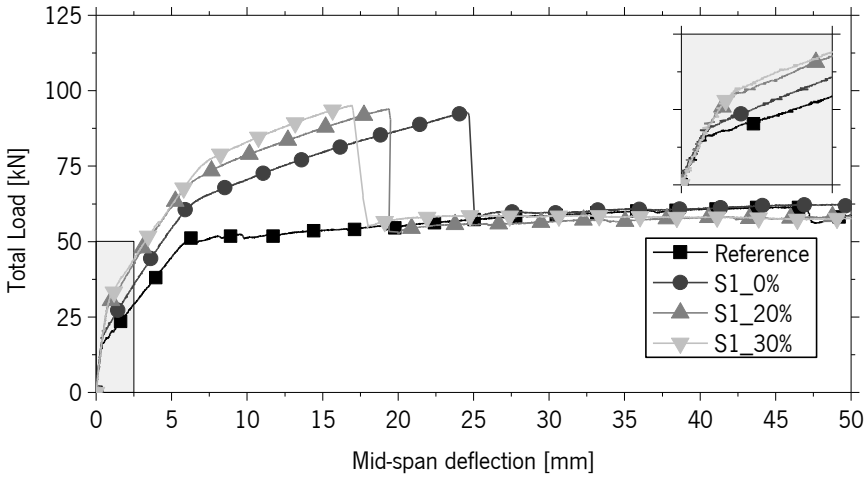

Figure 132 – Total load versus mid-span deflection in Series I beams.

Figure 133 depicts the load increment in relation to the Reference beam and to S1_0% up to a deflection level of $l/250$. According to these graphs, the prestressed beams provide a considerable load carrying capacity increment in relation to the non-strengthened and non-prestressed beams.

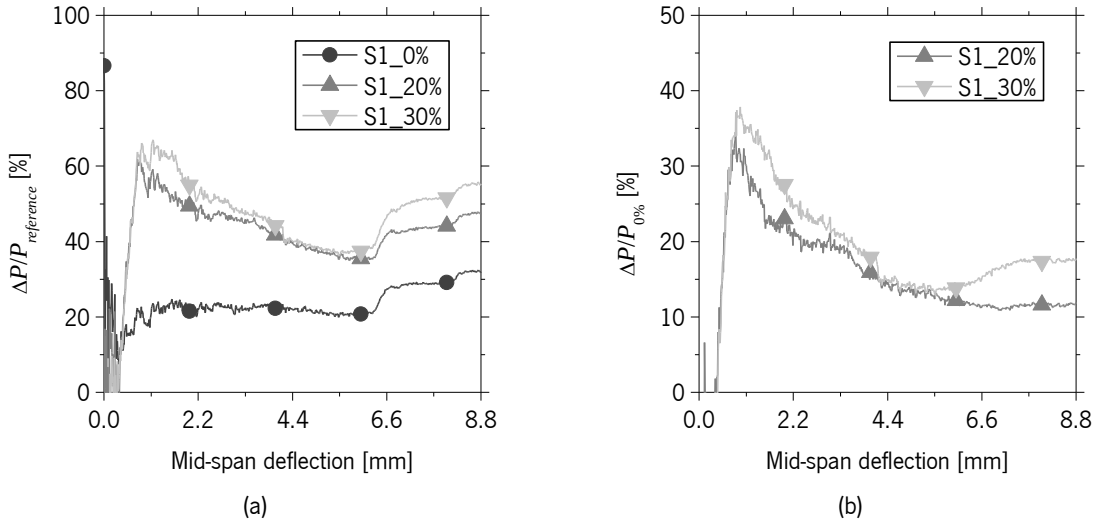

Figure 133 – Load variation versus mid-span deflection in Series I beams: (a) variation in relation to the Reference beam and (b) variation in relation to S1_0%.

In order to verify the symmetry of load application, the curves of load versus deflection at the two loaded sections (in symmetric positions, see Figure 130) are plotted in Figure 134. The same relationship is represented in Figure 135 for the mid-shear-span sections of the tested beams. According to these images, the beams experienced nearly symmetrical deformation up to failure.

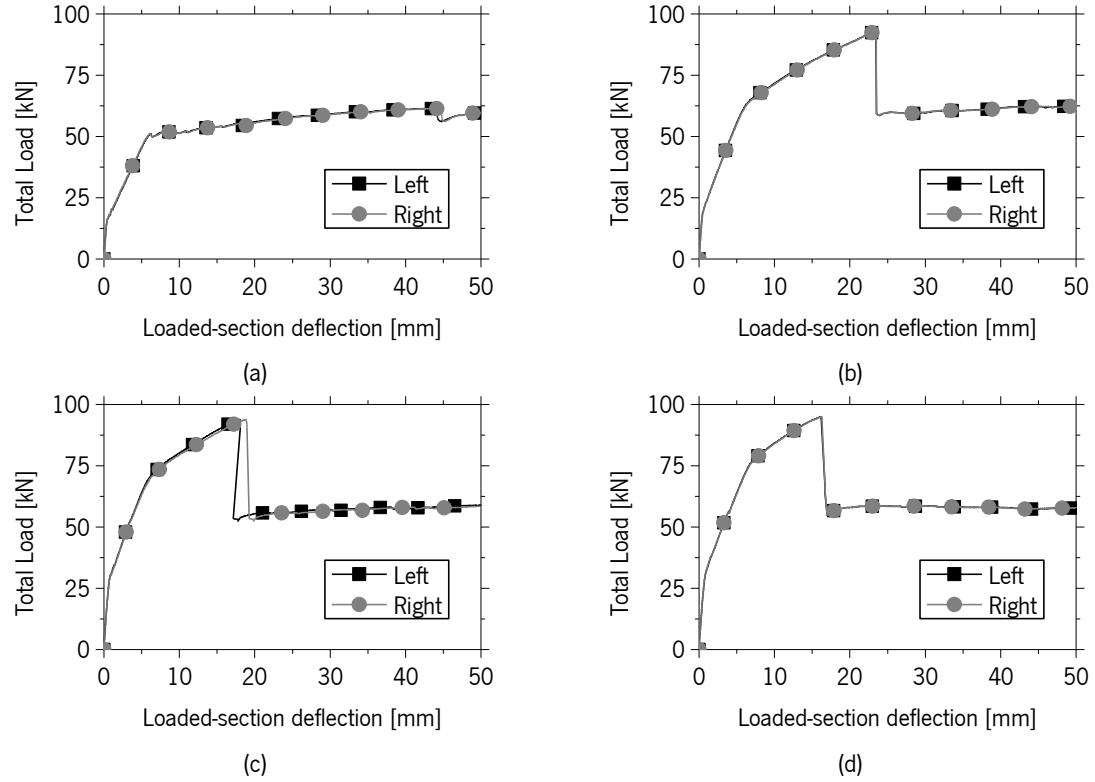

Figure 134 – Total load versus loaded-section deflection – Series I: (a) Reference, (b) S1_0%, (c) S1_20% and (d) S1_30%.

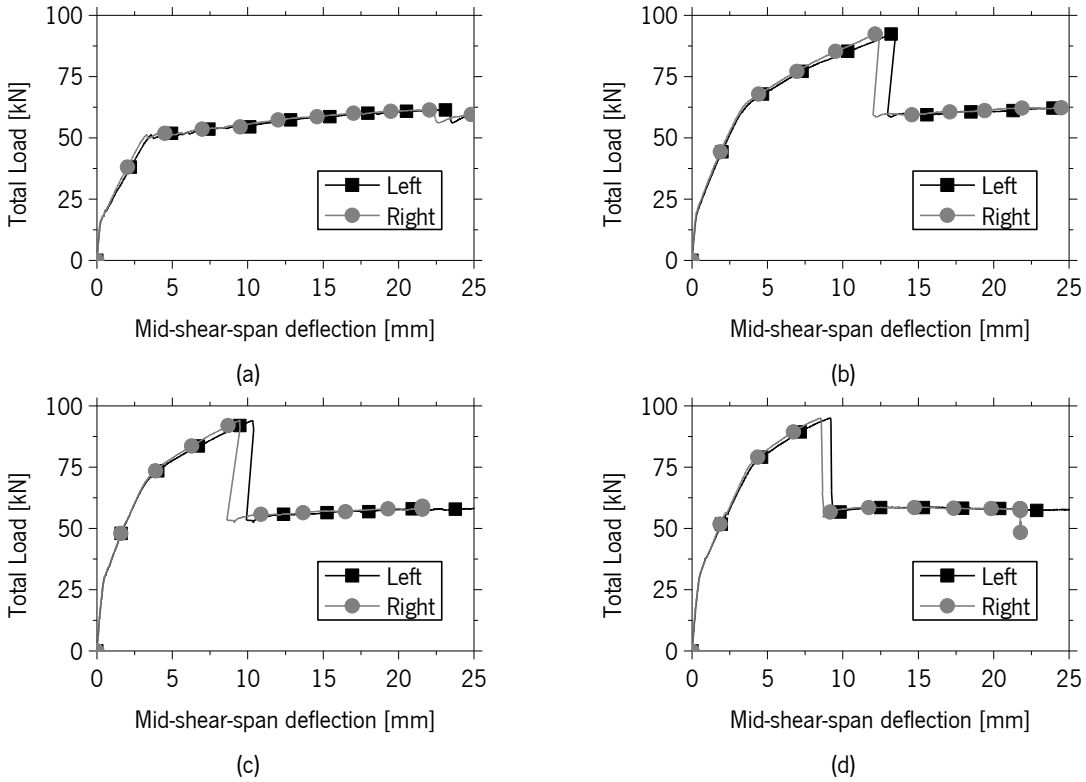

Figure 135 – Total load versus mid-shear-span deflection – Series I: (a) Reference, (b) S1_0%, (c) S1_20% and (d) S1_30%.

The strains recorded during the tests are also analysed in Figures 136 to 138 (see Figures 71 and 73 in pages 84 and 85). The strain gauges installed on the steel reinforcement frequently stopped working before yielding, and rarely functioned far beyond the yielding point (Figure 136).

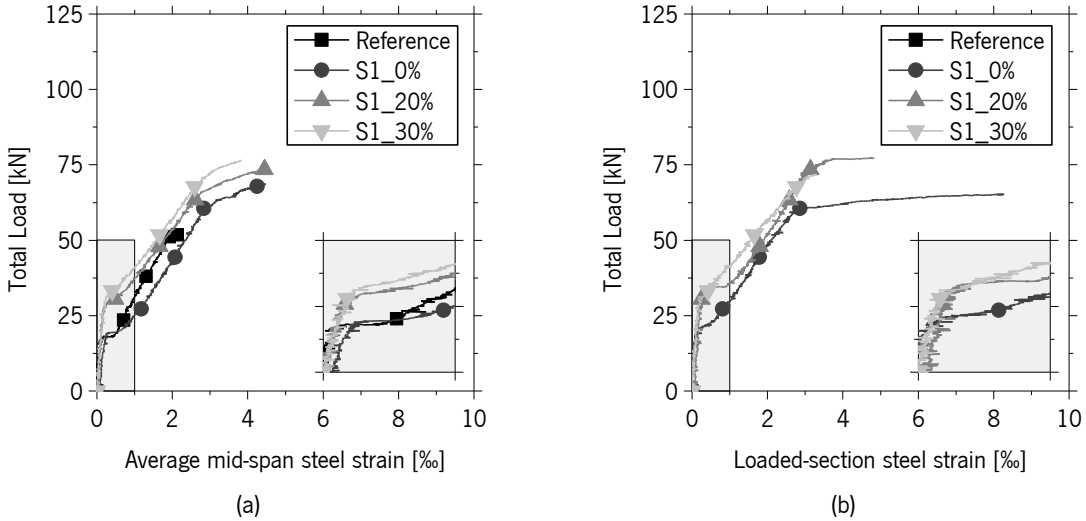

Figure 136 – Total load versus average steel strain – Series I: (a) mid-span strain and (b) loaded-section strain.

As reported in Chapter 4, the compressive strain initially introduced in the steel reinforcement was relatively small (about 0.020‰ and 0.065‰ in S1_20% and S1_30%, respectively). Therefore, this

initial compressive strain is not expected to visibly affect the strain at yield initiation, even if this strain is not added in the graphs. As expected, Figure 136 shows that the strain level in the steel bars decreases with the prestress level, which justifies the increase of the load at yield initiation. This fact is beneficial in terms of service limit states for the strengthened beams, since the stress level in the steel reinforcement and crack width are smaller at this stage.

The strains recorded in the two most central strain gauges installed in the CFRP laminate, at mid-span and loaded-section, were acquired up to the failure of the laminate (see Figure 73 in page 85). The obtained results revealed to be practically parallel in the three main branches of the curves (before concrete cracking, until steel yielding and finally, up to failure – see Figures 137a and 137b). Figure 137 also includes the total CFRP strain, including the effective prestrain measured at prestress release (in Table 30, page 90). According to Figure 137c, the strain at mid-span (at failure) is nearly the same in all the tested beams.

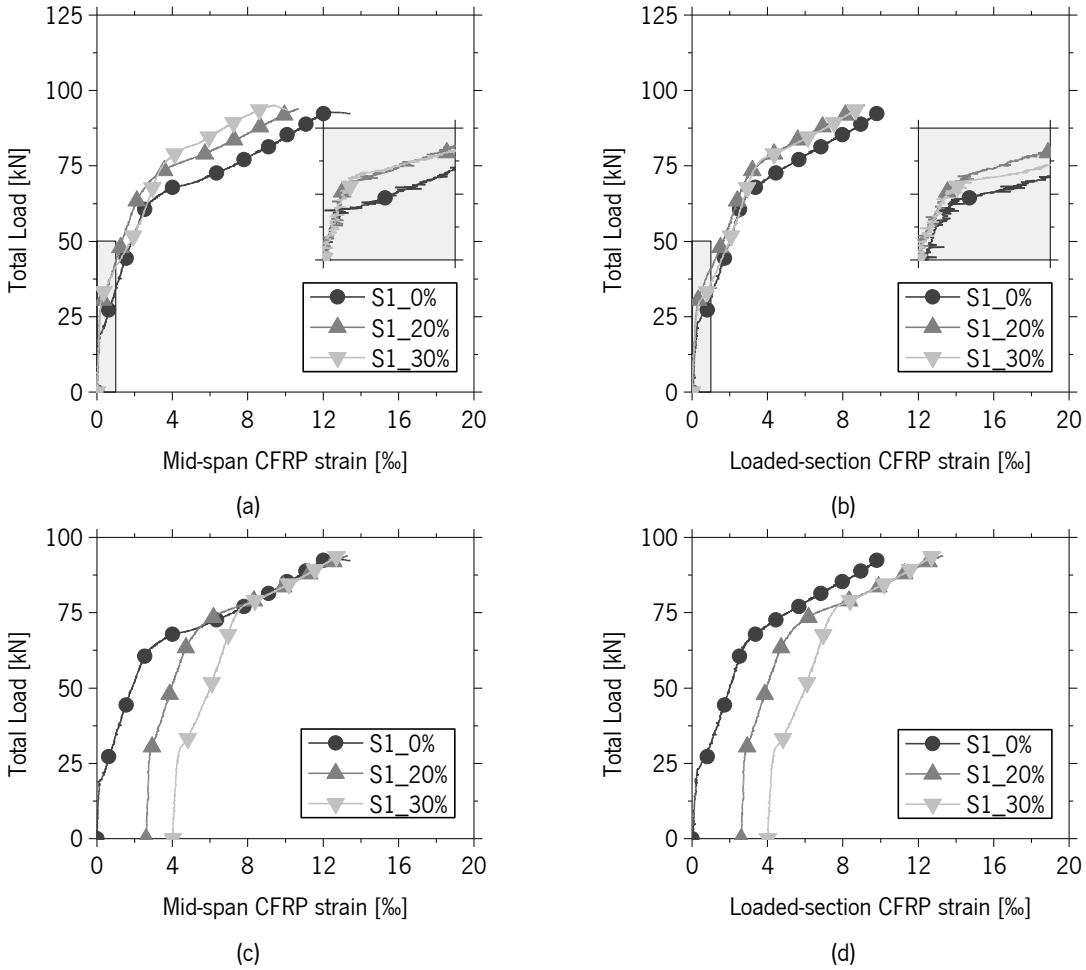

Figure 137 – Total load versus CFRP strain – Series I: (a) mid-span strain (without prestrain), (b) loaded-section strain (without prestrain), (c) mid-span strain (including prestrain) and (d) loaded-section strain (including prestrain).

In the case of concrete strain (see Figure 138), the strain recorded was not as coherent with the anticipated results since S1_30% was expected to exhibit the smallest compressive strain (Badawi and Soudki, 2009) at failure. In fact, that did not occur, since the smallest value was observed in S1_20%. This can be justified by the fact that a strain gauge only registers the strain field where it is bonded, and the localization of the concrete damage cannot be accurately estimated a priori.

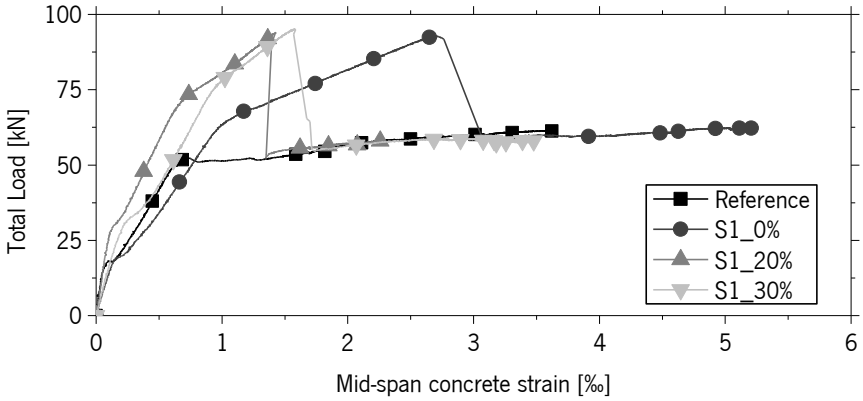

Figure 138 – Total load versus mid-span concrete strain – Series I

Another important effect analysed in the course of this investigation was the crack pattern of the beams. Hajihashemi *et al.* (2011) reported the crack pattern of the experimental program carried out in 300×350×3300 mm^3 beams strengthened with NSM-CFRP prestressed laminates, and verified that prestressing resulted in a smaller cracked length (the length between left-most and right-most visible cracks, L_{cr} (exemplified in Figure 139a), and smaller crack widths. The crack width was not directly measured during the test, but its reduction with the increase of the prestress level is already due to the lower deflection of the strengthened element. In terms of L_{cr}, Figure 139 clearly evidences its decrease with the increase of the prestress level.

In Figure 139, the crack pattern at failure is presented for each of the tested beams. The Reference beam exhibited the smallest number of cracks with smaller crack development. This beam failed in bending and concrete crushing occurred only just before the test was finished, at almost 75 mm of mid-span deflection. The L_{cr} was about 1140 mm and the average crack spacing about 76 mm, which is a value similar to the spacing of the shear reinforcement.

The beam strengthened with the passive laminate, S1_0%, exhibited a larger cracked length, as expected. Since the load applied on this element is particularly large when compared to the Reference beam, a higher bending moment is expected in a larger portion of the beam. The L_{cr} of S1_0%, depicted in Figure 139b, was about 1550 mm and the average crack spacing was approximately 86 mm, again fairly close to the spacing of the shear reinforcement. If Figures 139a

and 139b are compared, it is visible that in the Reference beam the cracks outside the pure bending moment zone did not develop above mid-height, while in S1_0% most of the cracks propagated further than mid-height. This suggests that the bond performance between CFRP laminate and surrounding medium was capable of mobilizing effectively the tensile strength capacity of the laminate with an effective stress redistribution, promoting a significant increase of the beam's flexural capacity and L_{cr} .

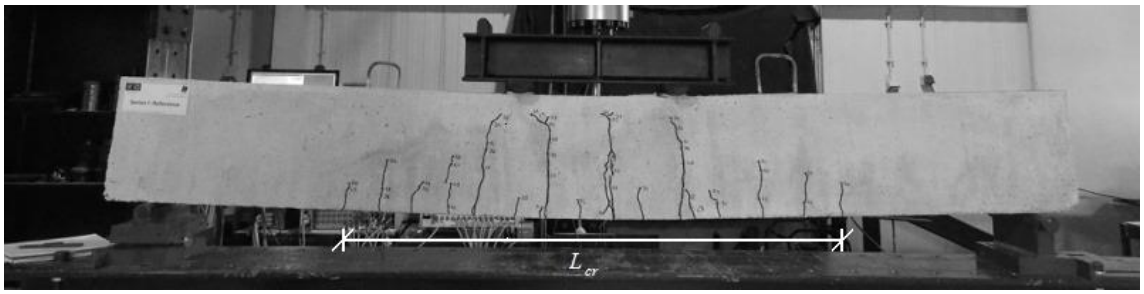

(a)

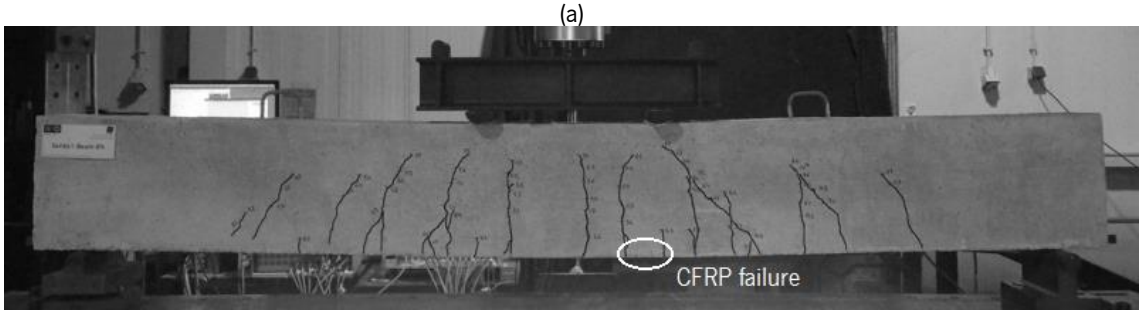

(b)

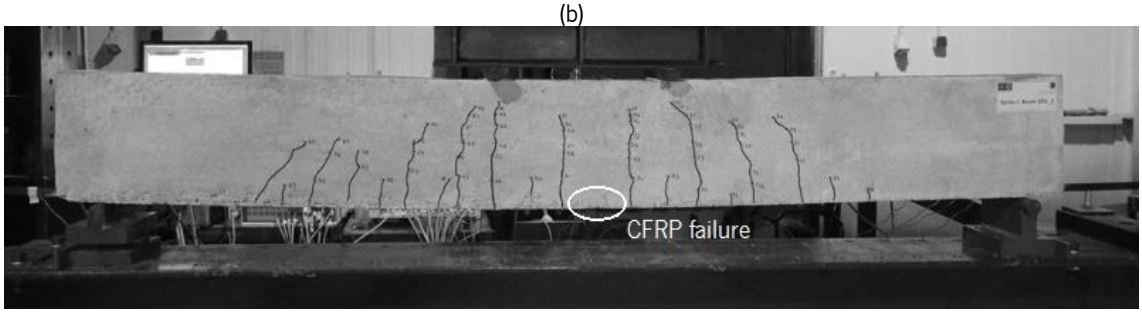

(c)

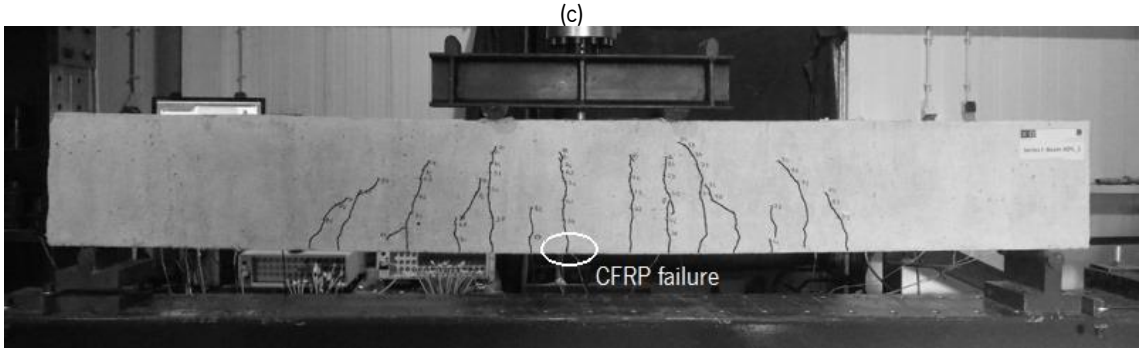

(d)

Figure 139 – Crack pattern at failure – Series I: (a) Reference, (b) S1_0%, (c) S1_20% and (d) S1_30%.

Concerning the prestressed beams, it is visible by comparing the crack patterns in Figures 139b, 139c and 139d that prestressing caused a considerable decrease of the cracked length. For the same failure load, the total cracked length of S1_20% was around 1460 mm while in S1_30% it decreased to about 1150 mm. In terms of average crack spacing, the obtained values were reasonably close to the shear reinforcement spacing (86 mm and 95 mm in S1_20% and S1_30%, respectively).

The failure aspect of the bottom of the beams strengthened with CFRP laminates is showed in Figure 140. The CFRP has ruptured in all cases in one single section of the beam, and the fracture of the individual fibres was notorious in all cases. It was also noted that S1_0% exhibited a much more extensive crack pattern in the bottom face of the beam (see Figure 140), opposed to what was observed in the prestressed beams. The compression stress field introduced by the prestressed CFRP laminate into the surrounding concrete may have contributed to restrain the concrete fracture propagation in S1_0%. In fact, V-shape fracture surfaces, whose formation was explained by Barros & Fortes (2005) in the context of the flexural strengthening of RC beams, and more recently by Bianco *et al.* (2010) in the shear strengthening of RC beams, are not so evident in the prestressed beams.

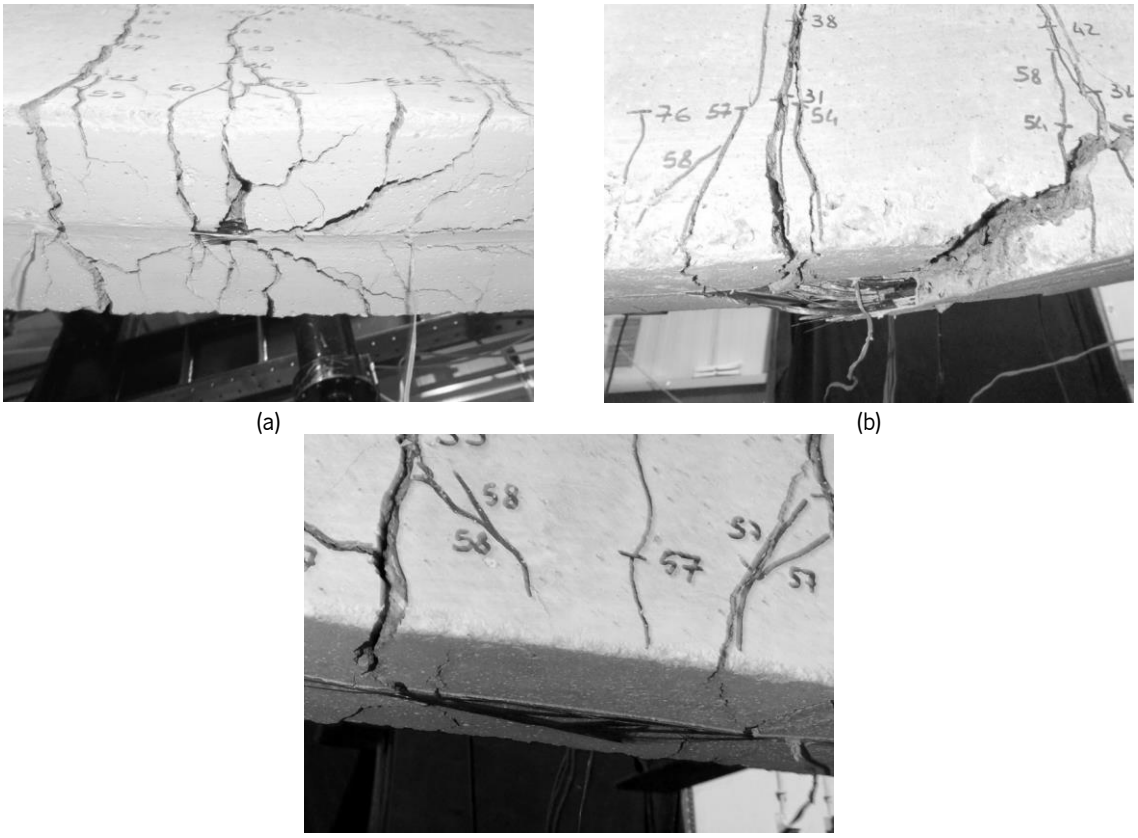

(a) (b)

(c)

Figure 140 – Failure aspect – Series I: (a) S1_0%, (b) S1_20% and (c) S1_30%.

5.2 SERIES II – FULL SCALE BEAMS

The beams of Series II were also tested under four-point bending but in this case using a "pure" bending length of 600 mm (Figure 141). The mid-span deflection was monitored using a ±50 mm LVDT, while LVDTs with a ±25 mm and a ±12.5 mm range were used to measure the loaded-section and mid-shear-span displacements, respectively.

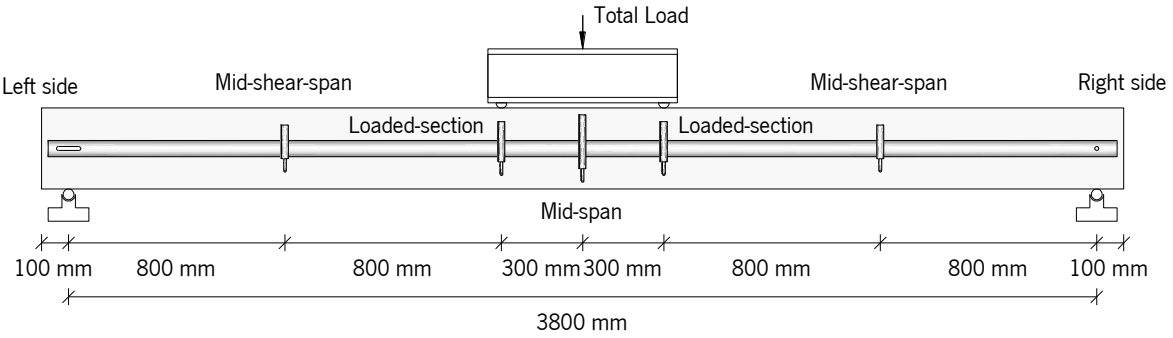

Figure 141 – Monitoring scheme of Series II beams.

The strains in all the installed strain gauges (25 mm, 100 mm and 1850 mm, see Figure 110 in page 109) were monitored during loading. The test was controlled by the displacement of the hydraulic jack piston, at a rate of 0.020 mm/s, and the applied load was measured by the 500 kN load cell attached to the piston (Figure 142).

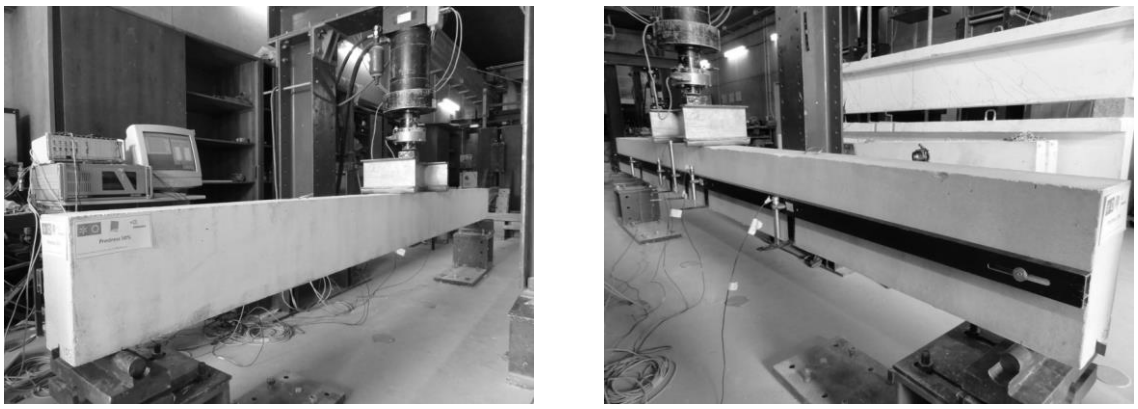

(a) (b)

Figure 142 – Photos of Series II setup: (a) frontal view of the support and loading conditions and (b) back view of the monitoring arrangement.

Concerning the results obtained for the notable points of the four-point bending loading curve (Table 36), it was noticed that S2_0% exhibited an abnormal behaviour. Analysing the displacement at cracking, δ_{crack}, of the above-mentioned beam it is evident that this parameter was extraordinarily high when compared to all the other tested beams (2.279 mm as opposed to

deflections ranging between 0.673 mm and 1.651 mm in the remaining beams). However, in terms of load at cracking, P_{crack}, some level of increase was observed with the application of the CFRP laminate. It is worth noting that although S2_20% and S2_30% conducted to roughly the same increment of P_{crack} when compared to the Reference beam (69%), S2_50% more than doubled the initial elastic load-carrying capacity of the Reference beam at this stage (126%).

In terms of yielding load, P_{yield}, the prestressed CFRP laminates have demonstrated again the capacity to retard the yield initiation stage of the longitudinal steel bars, leading to a consistent increase of P_{yield} with the prestress level. However, the deflection at yield initiation, δ_{yield}, was not significantly affected by the prestress level.

Regarding the ultimate load carrying capacity of the beams, $P_{ultimate}$, the load increment provided by the CFRP laminate was again approximately the same in all the strengthened beams (both non-prestressed and prestressed). The decrease of deflection at failure, $\delta_{ultimate}$, was again fairly proportional to the applied prestress level (take as example S2_40% that has experienced a decrease of 52% in ultimate deflection, while S2_20% endured exactly half of that amount, 26%). Finally, in terms of load carrying capacity at service deflection, $P_{l/250}$, it was successively increased with the prestress level.

Table 36 – Main results of the four-point bending tests – Series II.

Beam	δ_{crack} [mm]	P_{crack} [kN]	δ_{yield} [mm]	P_{yield} [mm]	$\delta_{ultimate}$ [mm]	$P_{ultimate}$ [kN]	$P_{l/250}$ [kN]
Reference	0.673	9.02	15.018	26.95	-	31.43	26.76
0% Prestress	2.279 (239%)	13.05 (45%)	15.642 (4%)	33.45 (24%)	60.668 (-%)	51.55 (64%)	32.1 (20%)
20% Prestress	1.150 (71%) {-50%}	15.21 (69%) {17%}	18.059 (20%) {15%}	37.99 (41%) {14%}	45.003 (-%) {-26%}	51.00 (62%) {-1%}	34.3 (28%) {7%}
30% Prestress	1.278 (90%) {-44%}	15.20 (69%) {16%}	17.314 (15%) {11%}	39.52 (47%) {18%}	37.467 (-%) {-38%}	50.30 (60%) {-2%}	36.73 (37%) {14%}
40% Prestress	1.487 (121%) {-35%}	19.32 (114%) {48%}	16.214 (8%) {4%}	41.59 (54%) {24%}	29.14 (-%) {-52%}	48.5 (54%) {-6%}	39.8 (49%) {24%}
50% Prestress	1.651 (145%) {-28%}	20.41 (126%) {56%}	17.769 (18%) {14%}	45.1 (67%) {35%}	25.214 (-%) {-58%}	49.53 (58%) {-4%}	41.71 (56%) {30%}

Value (Variation in relation to the Reference beam) {Variation in relation to the 0% Prestress beam}

To better comprehend the relative behaviour of all beams, the load versus mid-span deflection curves are plotted in Figure 143. It is visible in this plot that the application of prestress successively decreased the ultimate deflection, as already observed in the previous series of beams.

The plot inset in Figure 143 also evidences the abnormal behaviour of S2_0%, since its initial stiffness is particularly low when compared to the other beams of this series. In terms of cracking load, S2_20% and S2_30% exhibit nearly the same value. S2_40% and S2_50% have also presented almost equal cracking load. The formation of micro-cracks during transport, storage and handling is a possible explanation for the smaller stiffness in the first branch of the load-deflection response of S2_0%, since the loss of stiffness is restricted to this phase.

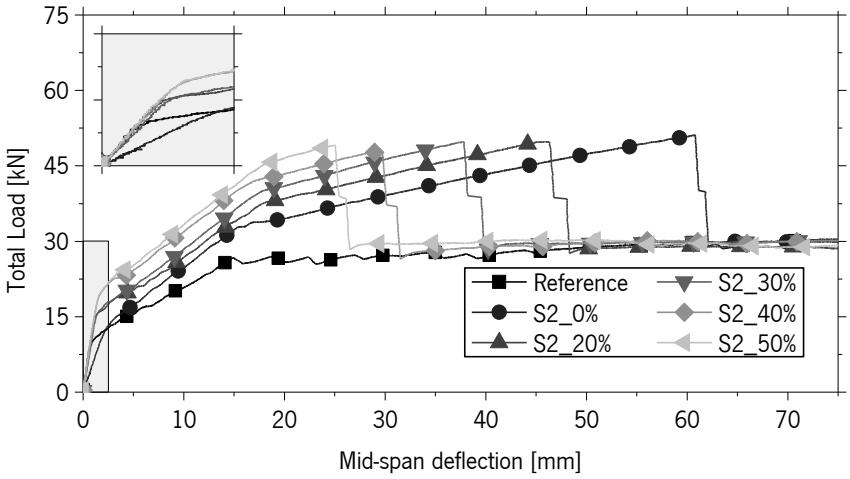

Figure 143 – Total load versus mid-span deflection in Series II beams.

Figure 143 depicts the load increment provided by the strengthened beams in relation to the Reference beam (Figure 143a), as well as in relation to the non-prestressed beam (Figure 143b). According to Figure 143a, it is visible that the prestressed CFRP laminate provides a significant increase of the load carrying capacity up to the service deflection (15.2 mm).

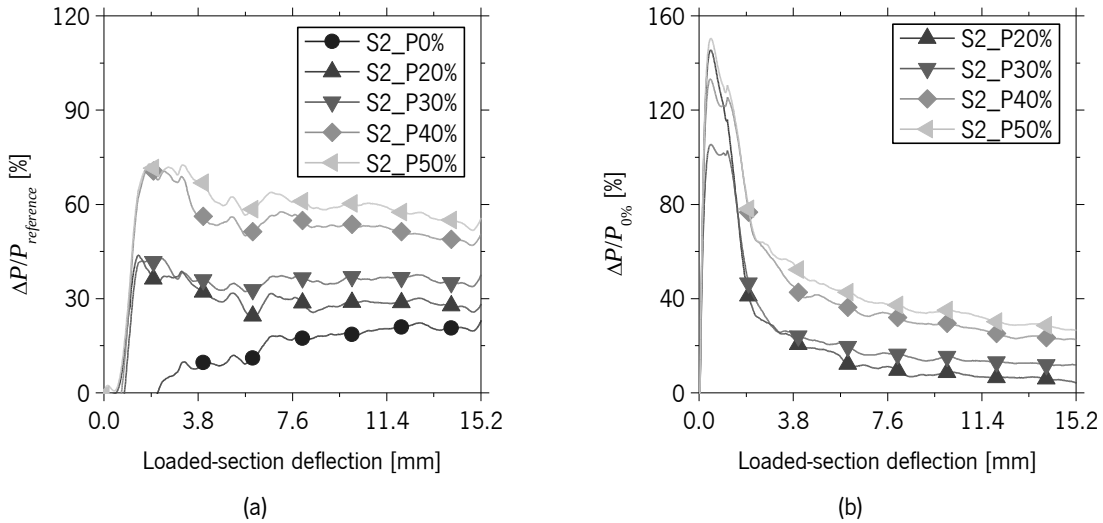

Figure 144 – Load variation versus mid-span deflection in Series II beams: (a) variation in relation to the Reference beam and (b) variation in relation to S2_0%.

In order to verify the symmetry of load application, the load versus loaded-section deflection curves and the load versus mid-shear-span deflection curves of all LVDTs are plotted in Figures 145 and 146. As it is perceptible in all the plots, the deformation of the beams was perfectly symmetrical up to its maximum load.

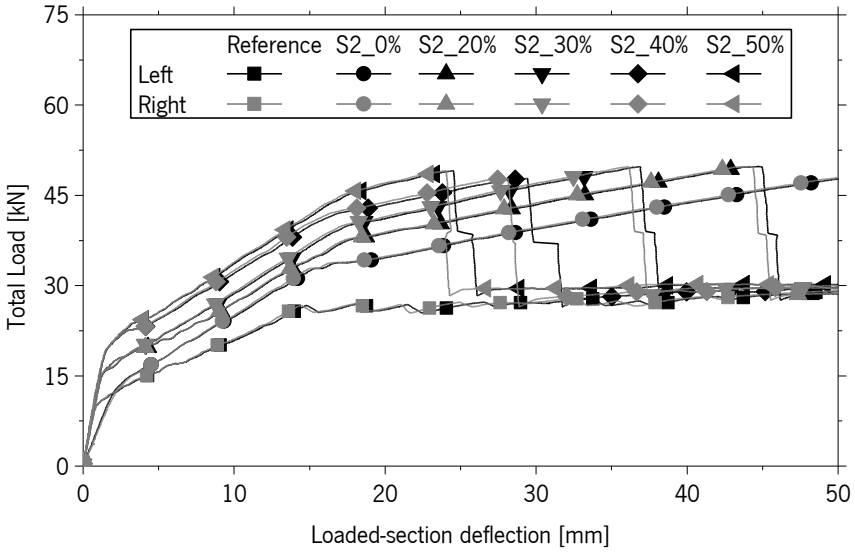

Figure 145 – Total load versus loaded-section deflection – Series II.

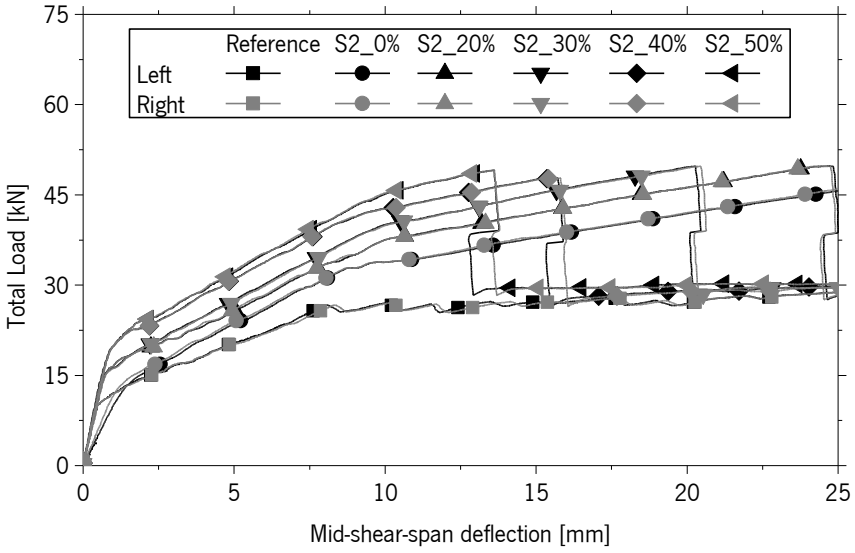

Figure 146 – Total load versus mid-shear-span deflection – Series II.

In this series of beams, the strain gauges installed at 25 mm and 100 mm from the free-end of the CFRP laminate (Figure 110 in page 109) did not reveal any strain increase during the failure test. This means that the effective anchorage length of the CFRP laminate is smaller than the distance between the outermost visible crack and the corresponding support. Therefore, only the load versus mid-span CFRP strain is presented in Figure 147. Again in this plot, the load-strain variation of

S2_0% is notoriously inferior in comparison with the remaining beams. In terms of overall aspect of the curves, it is also observable that the prestressed beams display almost equal strain evolution after steel yielding, as already predictable from Table 36, since no significant increase of yielding deflection was observed. The strain variation during the loading process in the phase between cracking and yield initiation has decreased with the increase of the prestress level due to the increase of the load at crack initiation (Figure 147a). Additionally, comparing Figures 137c and 147b, it is visible that the strain at failure of the CFRP laminate was slightly larger in the present series of beams. The average CFRP strain at failure was about 13.4‰ and 15.6‰ in Series I and II, respectively.

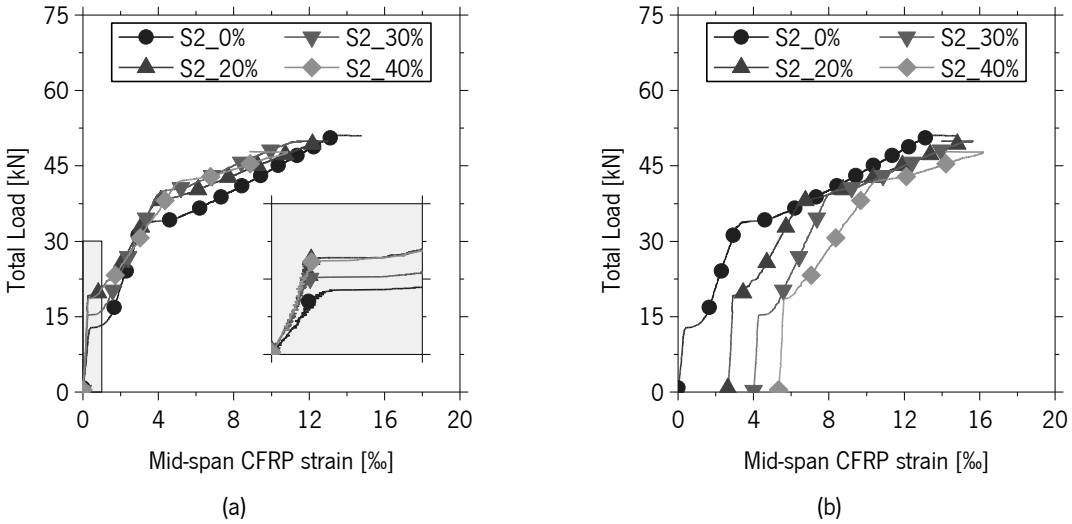

Figure 147 – Total load versus mid- span CFRP strain – Series II: (a) excluding the prestrain and (b) including the prestrain.

Figure 148 shows the crack pattern of the beams after being submitted to a mid-span deflection of 75 mm. In all pictures, the cracks observed up to $P_{ultimate}$ were darkened in order to improve their visibility at this scale. As observed in the previous Series, the total cracked length of the Reference beam (L_{cr} = 2060 mm), was smaller than the one of S2_0% (L_{cr} = 2720 mm), mostly due to the difference of applied load in these beams. The average crack spacing was approximately 108 mm and 94 mm in the Reference beam and S2_0%, respectively, which is again relatively close to the spacing of the shear reinforcement (100 mm in this series of beams).

In relation to the prestressed beams, the cracked length was again successively reduced with the increase of prestress level, as Figure 148 evidences. The cracked length was about 2440 mm, 2420 mm, 2215 mm and 2100 mm for S2_20%, S2_30%, S2_40% and S2_50%, respectively. Regarding the average crack spacing, the application of prestress did not produce any effect, and it

was again found to be about the same as the spacing of the shear reinforcement (100 mm): 94 mm, 97 mm, 96 mm and 100 mm in S2_20%, S2_30%, S2_40% and S2_50%, respectively.

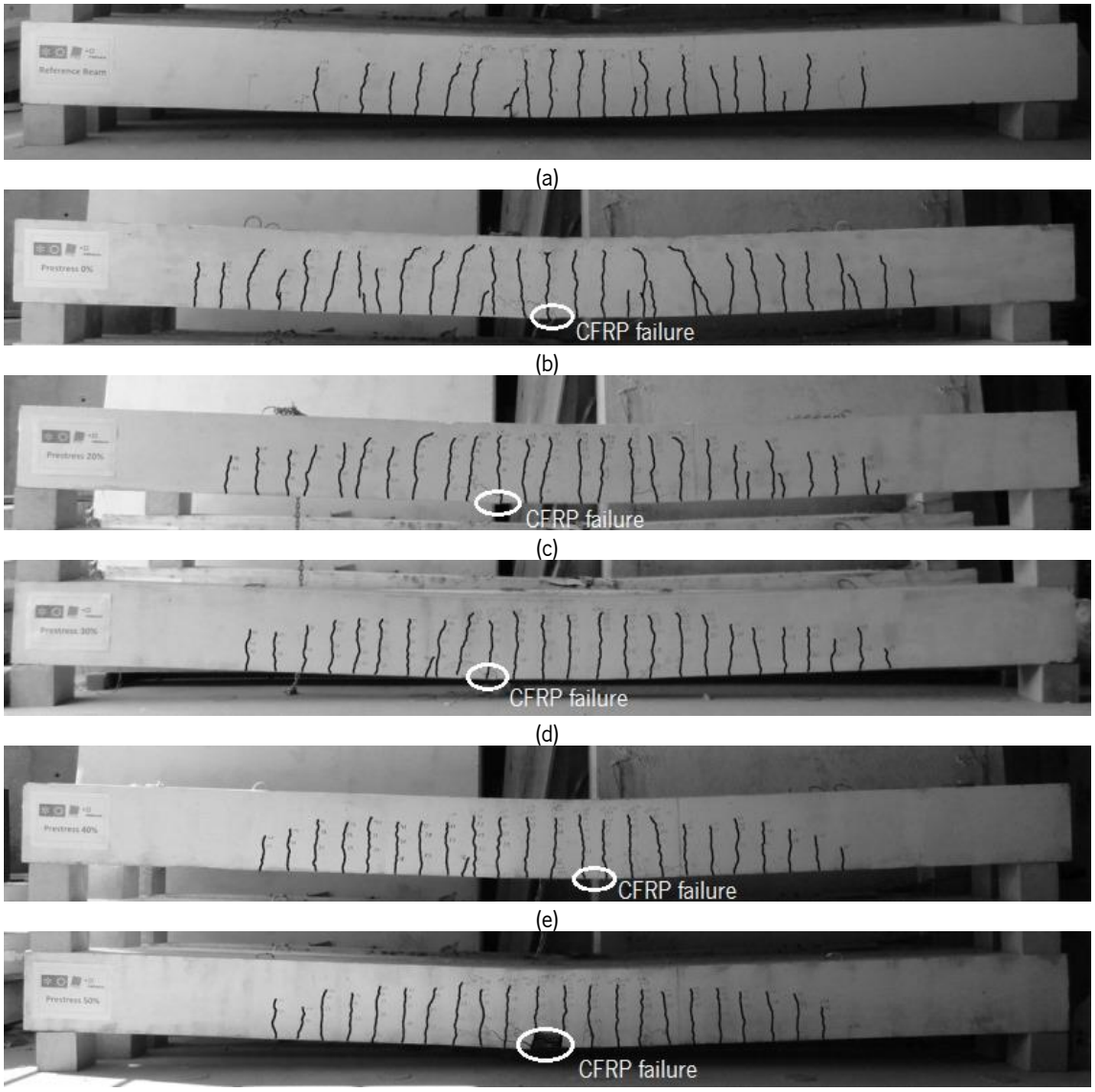

Figure 148 – Crack pattern after failure – Series II: (a) Reference, (b) S2_0%, (c) S2_20%, (d) S2_30%, (e) S2_40% and (f) S2_50%.

In relation to the aspect of the bottom face of the beams, showed in Figure 149, the amount of concrete cracking appeared to be nearly the same in all the beams, except in the case of the S2_50%, where only a few discrete cracks were observed.

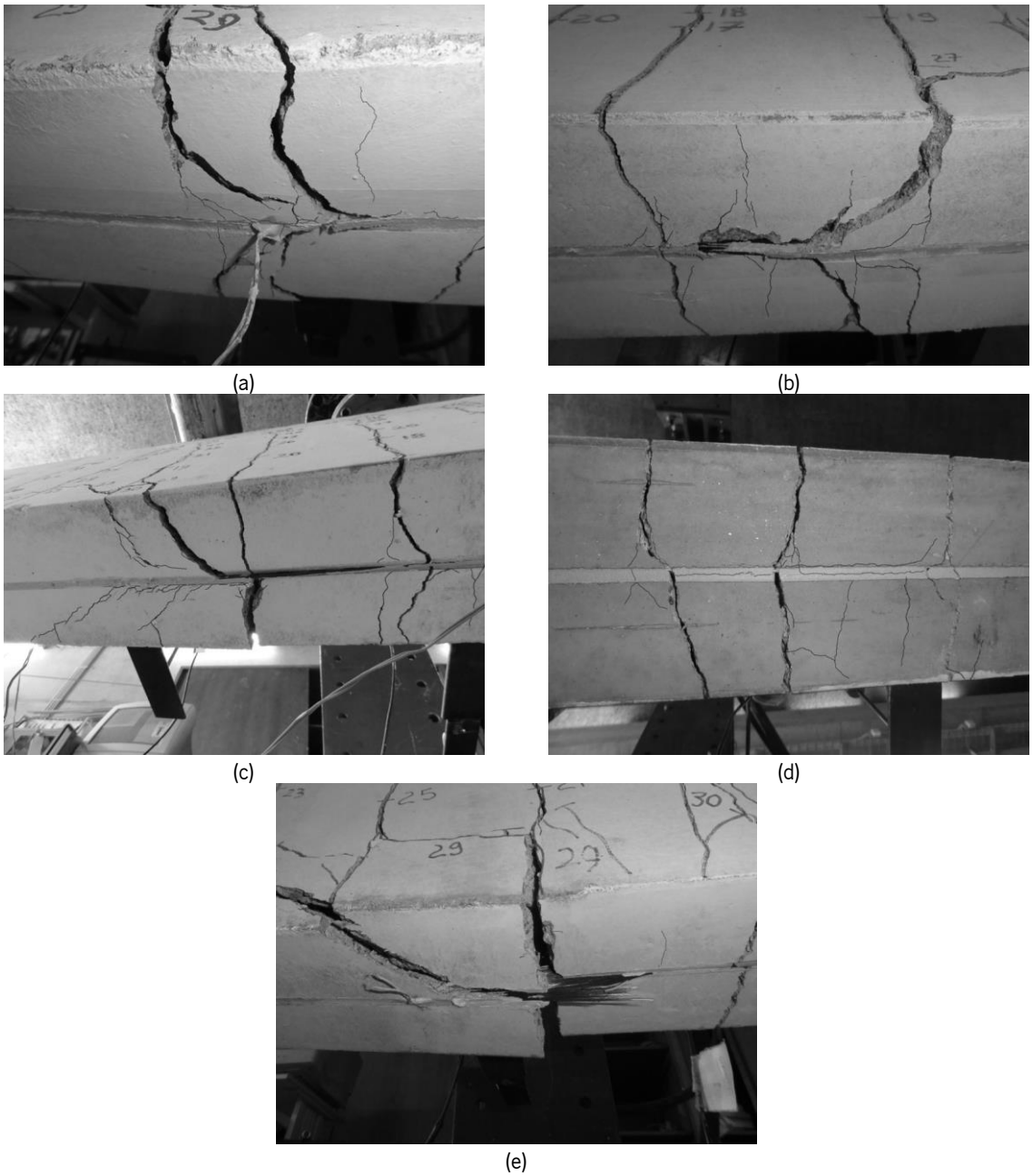

(a) (b) (c) (d) (e)

Figure 149 – Failure aspect – Series II: (a) S2_0%, (b) S2_20%, (c) S2_30%, (d) S2_40% and (e) S2_50%.

5.3 SERIES III – FULL SCALE BEAMS

The test setup used for the beams of Series III, depicted in Figure 150, was similar to the one described for Series II, both in terms of configuration as well as in terms of measuring sensors. As in this Series of beams the steel reinforcement ratio was higher than in previous Series, the increase of load carrying capacity is expected to be smaller than in the previous Series. In fact, Barros *et al.* (2007) has demonstrated that the maximum strain in the CFRP laminates that can be mobilized in flexurally strengthened beams decreases with the longitudinal steel reinforcement ratio.

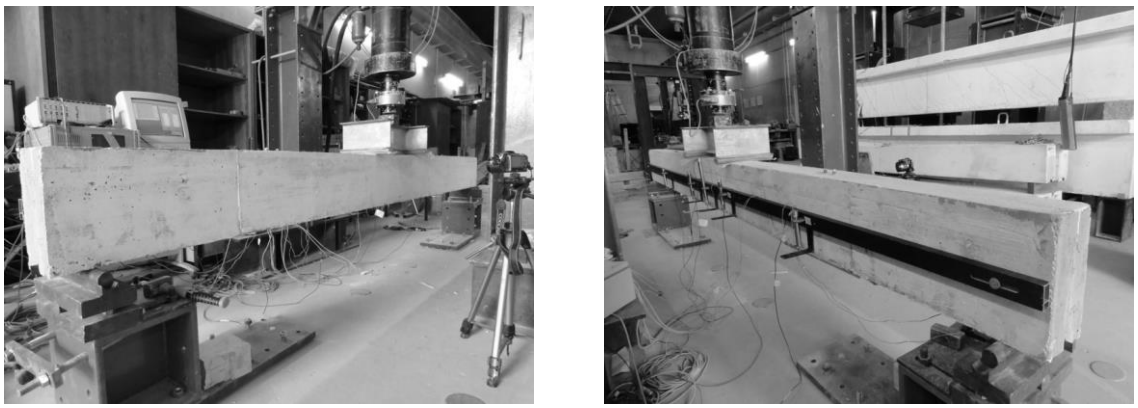

(a) (b)

Figure 150 – Photos of Series III test setup: (a) frontal view showing the support and loading conditions, and (b) back view evidencing the arrangement of the LVDTs.

Regarding the main results obtained for this series of beams, presented in Table 37, it is noticeable that S3_50% presents a cracking load smaller than the expected one, since both the displacement at cracking, δ_{crack}, and the load at cracking, P_{crack}, have decreased when compared to S3_40%. S3_40% provided an increase of cracking load of about 57%, more than the double of S3_20% (25%), while S3_30% only exhibited an increase of 17%. This is believed to be caused by differences in the concrete tensile strength of the reinforced concrete beams, and the difficulty of capturing with accuracy the cracking load for this relatively small percentage of strengthening ratio.

The variation of the displacement at yielding, δ_{yield}, was again incoherent since it increased and decreased with no apparent reason. On the other hand, the load at yielding, P_{yield}, has increased with prestress level. Analysing the results obtained in the previous series, this lack of clear variation of δ_{yield} may suggest that in reality, no significant variation is expected in relation to the S1_0%.

Once more, the displacement at failure has decreased almost proportionally with the prestress level (23%, 31%, 42% and 52%), and the ultimate load was approximately the same in all tested beams. Lastly, regarding the load-carrying capacity at the deflection corresponding to the service limit states (l / 250 = 15.2 mm), $P_{l/250}$, the increase due to prestress application was lower than in the previous series. This outcome was already expected since a unique CFRP laminate of 1.4×20 mm^2 cross section area corresponds to a relatively small strengthening ratio (ρ_l = 28/(150×290) = 0.064%), considering the steel reinforcement ratio of the beams of these series (ρ_s = 226/(150×256) = 0.589%. For the beams of these series, two prestressed CFRP laminates would

have been applied, but this was not possible due to the limitations of the prestress line mounted in the laboratory.

Table 37 – Main results of the four-point bending tests – Series III.

Beam	δ_{crack} [mm]	P_{crack} [kN]	δ_{yield} [mm]	P_{yield} [mm]	$\delta_{ultimate}$ [mm]	$P_{ultimate}$ [kN]	$P_{l/250}$ [kN]
Reference	1.117	9.76	15.052	37.90	-	48.85	38.61
0% Prestress	1.282 (15%)	10.07 (3%)	18.900 (26%)	44.78 (18%)	59.017 (-%)	63.55 (30%)	39.66 (3%)
20% Prestress	1.460 (31%) {14%}	12.19 (25%) {21%}	18.886 (25%) {0%}	47.75 (26%) {7%}	45.422 (-%) {-23%}	61.63 (26%) {-3%}	40.10 (4%) {1%}
30% Prestress	1.557 (39%) {21%}	11.43 (17%) {14%}	18.848 (25%) {0%}	50.37 (33%) {12%}	40.719 (-%) {-31%}	61.81 (27%) {-3%}	42.50 (10%) {7%}
40% Prestress	1.828 (64%) {43%}	15.31 (57%) {52%}	19.746 (31%) {4%}	54.77 (45%) {22%}	34.063 (-%) {-42%}	64.51 (32%) {2%}	46.74 (21%) {18%}
50% Prestress	1.778 (59%) {39%}	15.04 (54%) {49%}	18.332 (22%) {-3%}	55.75 (47%) {24%}	28.559 (-%) {-52%}	64.54 (32%) {2%}	48.51 (26%) {22%}

Value (Variation in relation to the Reference beam) {Variation in relation to the 0% Prestress beam}

In terms of general aspect of the load versus mid-span deflection curves, depicted in Figure 151, the behaviour of the beams was similar to the previously obtained in Series II. The proportionality of decrease of the ultimate mid-span deflection is clearly visible in the plot, and the stiffness in the uncracked and cracked phases was also approximately the same in all beams. Additionally, Figure 152 depicts the load increment resulting from strengthening application. In Figures 153 and 154 the symmetry of load application was assessed and, as in the previous series, the deformational behaviour is quite symmetrical.

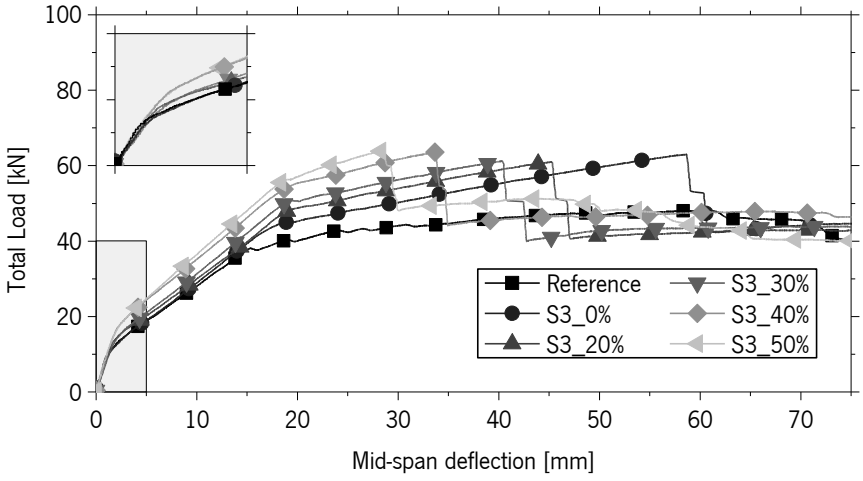

Figure 151 – Total load versus mid-span deflection in Series III beams.

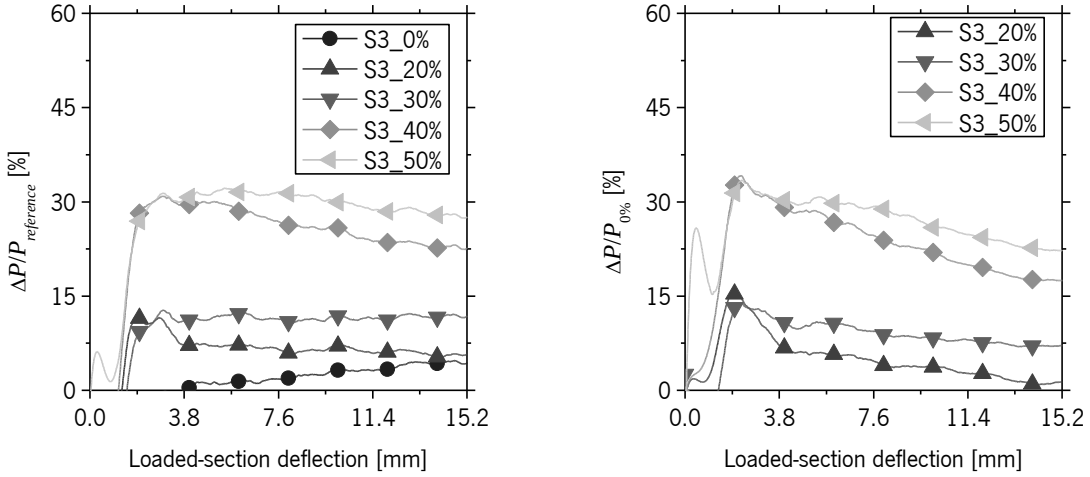

Figure 152 – Load variation versus mid-span deflection in Series II beams: (a) variation in relation to the Reference beam and (b) variation in relation to S2_0%..

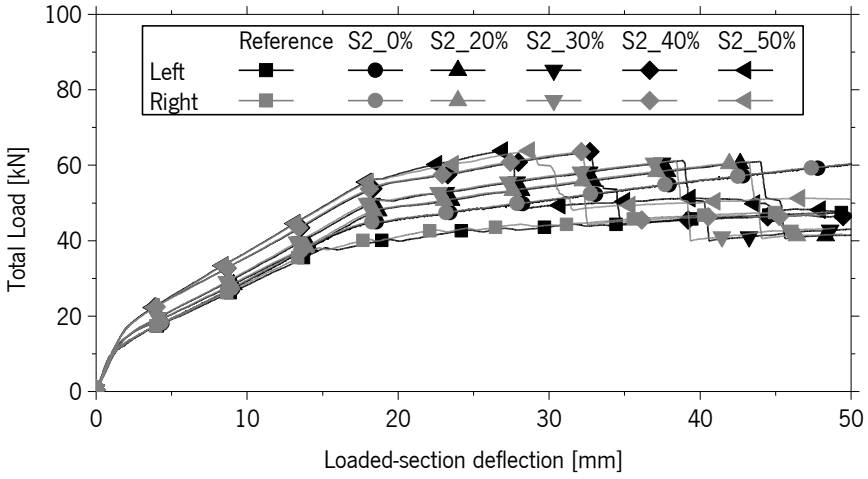

Figure 153 – Total load versus loaded-section deflection – Series III.

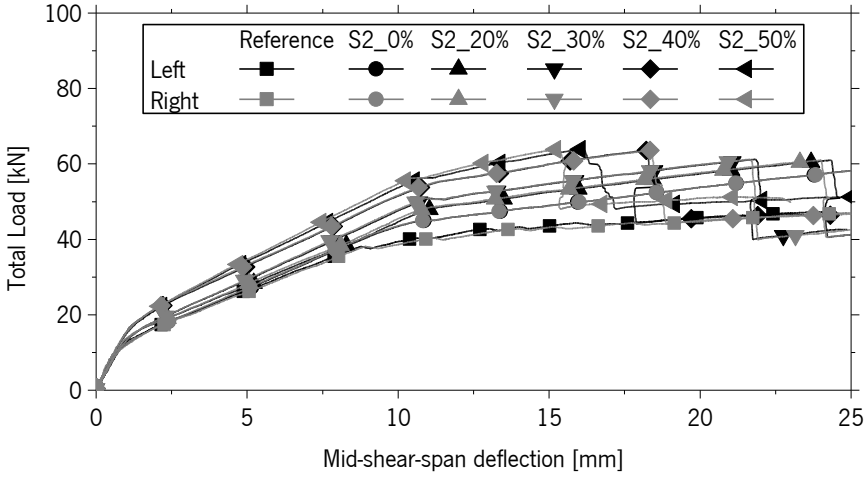

Figure 154 – Total load versus mid-shear-span deflection – Series III.

Figure 155 depicts the load versus mid-span CFRP strain and a substantial difference in the first branch of this relationship is observed in this plot. However, it remains to be proved if this difference of stiffness is caused by any difference of the material properties or by inaccuracy of the equipment measuring these low strain values. Like in the previous series of beams, the strain level for a certain load has decreased with the prestress level. According to Figure 155b, the ultimate strain of the CFRP laminate used to strengthen S3_30% was about 18.4‰, significantly higher than the values observed in the remaining beams of this series (12.7‰ to 15.3‰).

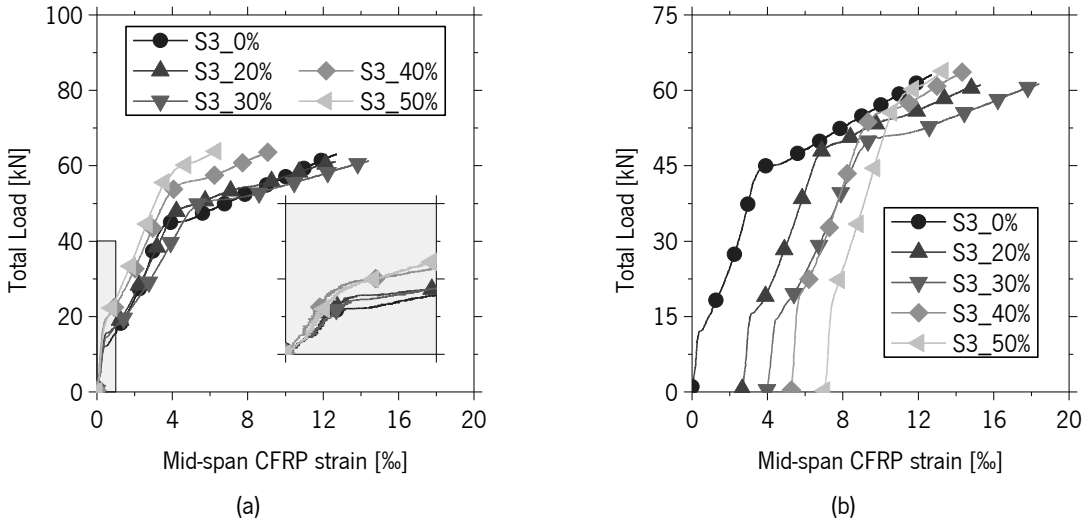

Figure 155 – Total load versus mid- span CFRP strain – Series III: (a) excluding the prestrain and (b) including the prestrain.

In Figure 156 the photos of the crack pattern of the beams after withstanding a mid-span deflection of 75 mm are presented. The interpretation of the crack patterns in the previous series analysed is in all similar to the ones obtained in this round of tests. The larger cracked length is again observed in S3_0%, and the application of increasing levels of prestress continuously decreased the length of the cracked region, L_{cr} .

As expected, the difference between the L_{cr} of the Reference beam and S3_0% beams was low (2730 mm and 2940 mm, respectively). The average crack spacing of these beams was also roughly the same as the spacing of the steel stirrups (101 mm and 98 mm). Concerning the prestressed beams, apart from S3_40%, L_{cr} was lower than in S3_0% (2720 mm, 2500 mm, 2595 mm and 2300 mm). No rational explanation was found for this exception. The average crack spacing in the prestressed beams was again about 100 mm.

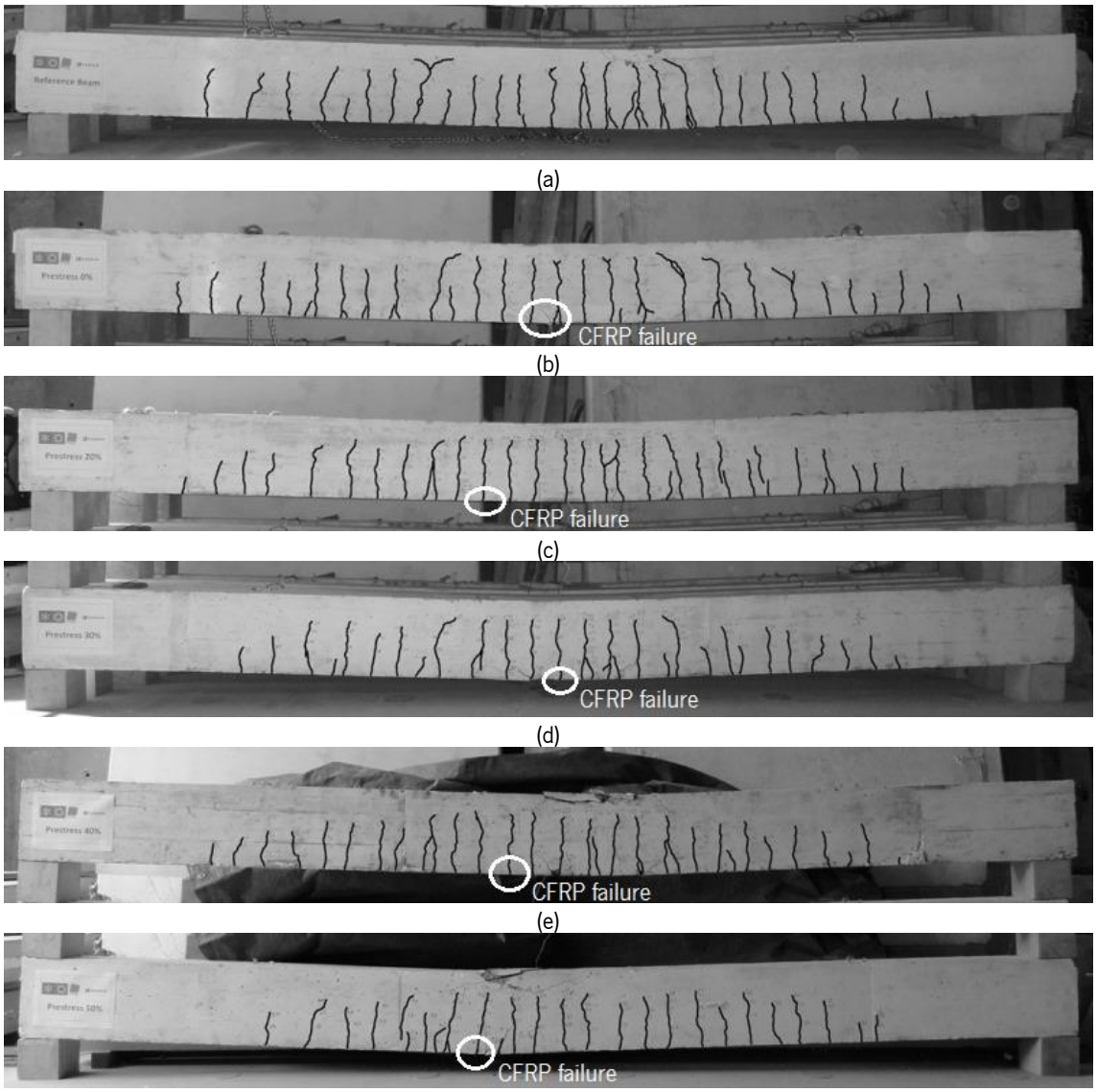

Figure 156 – Crack pattern after failure – Series III: (a) Reference, (b) S3_0%, (c) S3_20%, (d) S3_30%, (e) S3_40% and (f) S3_50%.

In Figure 157 presents the crack pattern of the bottom surface of the beams after having been subjected to a mid-span deflection of 75 mm is presented. Opposed to what happened in the first series of beams, most of the beams in this series exhibited extensive cracking around the failure zone.

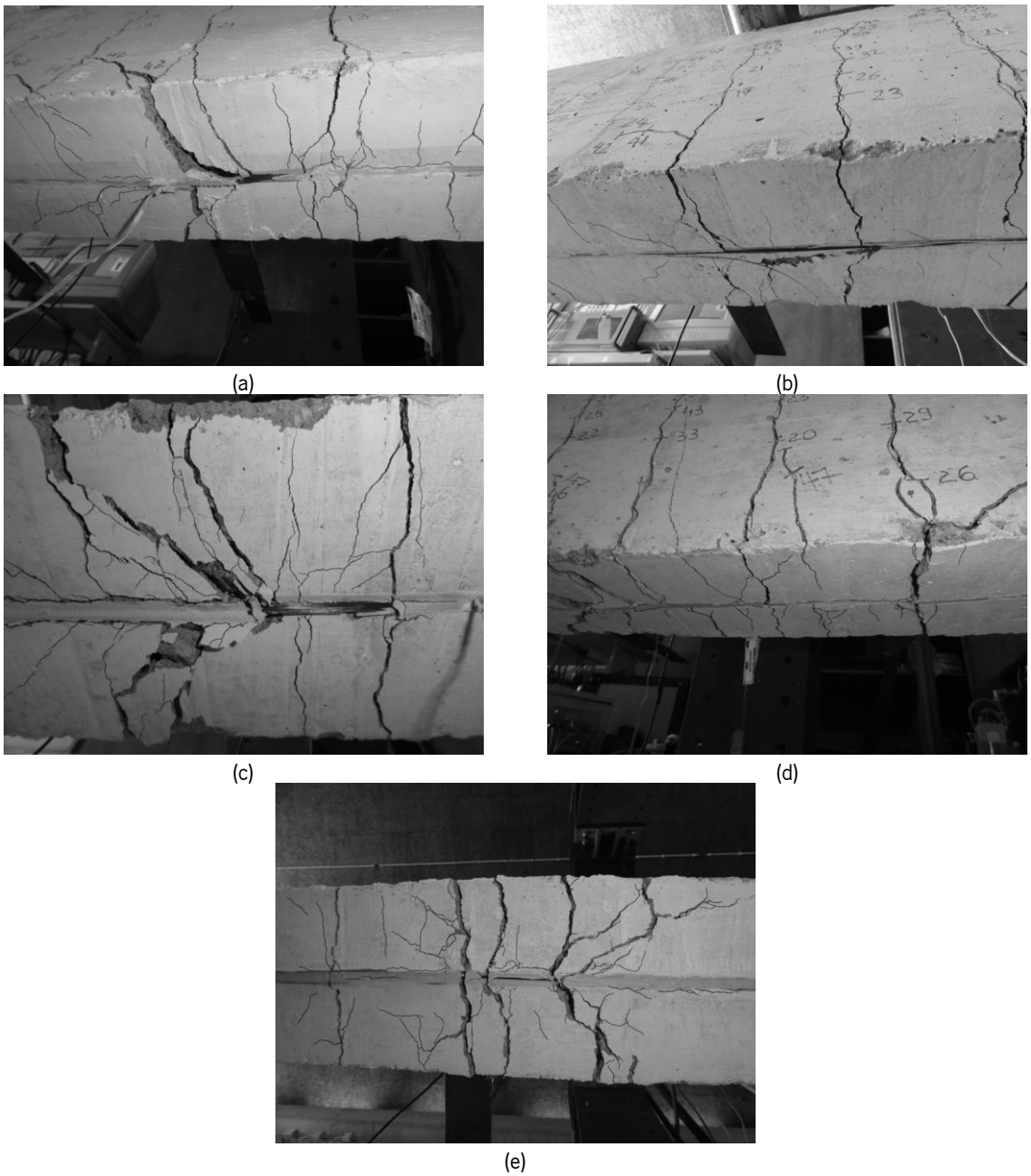

Figure 157 – Failure aspect – Series II: (a) S3_0%, (b) S3_20%, (c) S3_30%, (d) S3_40% and (e) S3_50%.

5.4 FINAL REMARKS

Three series of reinforced concrete beams strengthened with prestressed NSM CFRP laminates were tested up to failure under four-point bending to assess the effectiveness of this strengthening technique. According to the obtained results, the load at crack initiation increases significantly with the prestress level. However, the load-deflection response up to crack initiation is not affected by the CFRP reinforcement ratio or prestress level.

The load at yield initiation is increased with the prestress level, although the deflection corresponding to this load level is not considerably affected by the prestress level (is almost equal to the beam strengthened with 0% of prestress).

The prestress level applied to the CFRP laminates has no influence on the ultimate load carrying capacity of the strengthened beams, since failure was in all cases dominated by the CFRP rupture. However, the deflection at failure has significantly decreased the increase of the prestress level. The total cracked length of the beams has also decreased with the increase of the prestress level. In terms of average crack spacing, it was similar in all the tested beams and equal to the spacing of the steel stirrups.

In general, the deflections measured in the beams decreased with the increase of the applied prestress level and thus, the behaviour of these elements under service limit states was significantly improved although this evidence has as immediate consequence in the reduction of the ductility of the reinforced concrete element, as schematized in Figure 158.

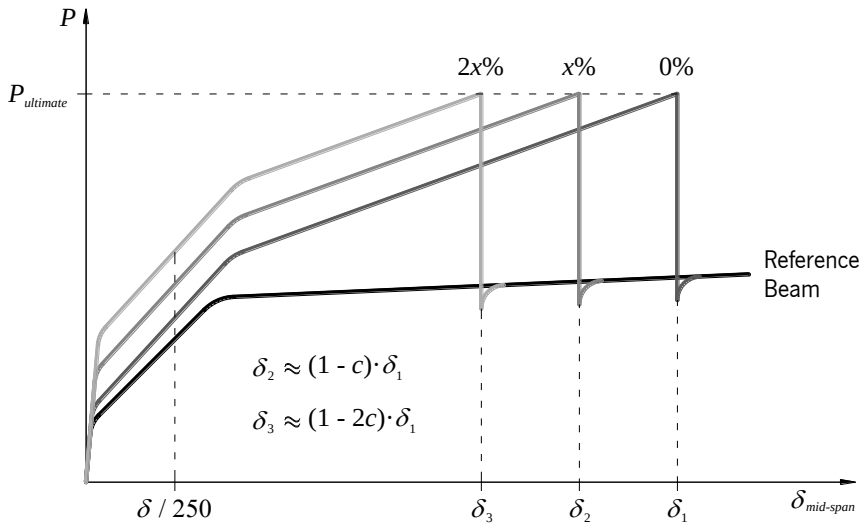

Figure 158 – Illustration of the prestress effect in reinforced concrete beams.

5.5 REFERENCES

Badawi, M. and Soudki, K. A. (2009). "Flexural strengthening of RC beams with prestressed NSM CFRP rods - Experimental and analytical investigation." *Construction and Building Materials*, Elsevier, 23(10), 3292-3300.

Barros, J. A. O. and Fortes, A. S. (2005). "Flexural strengthening of concrete beams with CFRP laminates bonded into slits." Cement and Concrete Composites, Elsevier, 27(4), 471-480.

Barros, J. A. O., Dias, S. J. E. and Lima, J. L. T. (2007). "Efficacy of CFRP-based techniques for the flexural and shear strengthening of concrete beams." *Cement and Concrete Composites*, Elsevier, 29(3), 203-217 2007.

Bianco, V., Barros, J. A. O. and Monti, G. (2010). "New approach for modeling the contribution of NSM FRP strips for shear strengthening of RC beams." *Composites for Construction*, ASCE, 14(1), 36-48.

Gaafar, M. A. and El-Hacha, R. (2008). "Strengthening reinforced concrete beams with prestressed FRP near surface mounted technique." *Proceedings of the Fourth International Conference on FRP Composites in Civil Engineering* (CICE2008), Zurich, Switzerland, 22-24 July 2008, 6 pp.

Hajihashemi. A., Mostofinejad, D and Azhari, M. (2011). "Investigation of RC Beams Strengthened with Prestressed NSM CFRP Laminates." *Journal of Composites for Construction*, ASCE, 15 (6), 887-895.

Nordin, H. and Täljsten, B. (2006). "Concrete Beams Strengthened with Prestressed Near Surface Mounted CFRP." *Journal of Composites for Construction*, ASCE, 10(1), 60-68.

Wang, W.-W., Dai, J.-G., Harries, K A. and Bao, Q.-H. (2012). "Prestress Losses and Flexural Behavior of Reinforced Concrete Beams Strengthened with Posttensioned CFRP Sheets." *Journal of Composites for Construction*, ASCE, 16 (2), 207-216.

Wight, R. G., Green, M. F. and Erki, M-A. (2001). "Prestressed FRP Sheets for Poststrengthening Reinforced Concrete Beams." *Journal of Composites for Construction*, ASCE, 5(4), 214-220.

Chapter 6

NUMERICAL MODELS

In this Chapter, the numerical modelling of the prestressed beams is executed is order to assess both their instantaneous and long term behaviour, as well as to assess the effectiveness of the proposed strengthening technique. In Tables 38 to 41 the mechanical properties of the intervening materials are summarized. The tests on the CFRPs were performed according to ISO 527-5 in samples with 250 mm of length, and clear distance between tabs of 150 mm. Five samples of the used material were stressed at a rate of 2 min/min, controlled by the internal transducer of the universal testing machine, and load was measured using a load cell of 200 kN capacity (Figure 159). Due to the abnormal load versus strain readings obtained during prestress application, the tensile properties determined by the supplier in routine quality control tests are also presented (Group 1 and 2 in Table 38).

Table 38 – Experimental properties of the FRP reinforcement.

Specimen	Series I		Supplier – Group 1		Supplier – Group 2	
	E_f [GPa]	f_f [MPa]	E_f [GPa]	f_f [MPa]	E_f [GPa]	f_f [MPa]
1	167	1925	185	2033	187	2386
2	167	1970	182	2051	184	2131
3	170	1859	181	2068	188	2148
4	170	1970	186	2091	187	2102
5	170	1941	186	1864	186	2365
Average	169	1933	184	2021	186	2226
Standard Deviation	2	46	2	91	2	137
COV	1%	2%	1%	4%	1%	6%

It is noticed that the tensile strength and elastic modulus obtained in laboratory are lower than the ones obtained by the supplier, although in all cases no significant variability is observed in terms of tensile strength and elastic modulus within the same series of samples. Regarding the aspect of the specimens at failure, all have ruptured by successive failure of the individual carbon fibres, as shown in Figure 160.

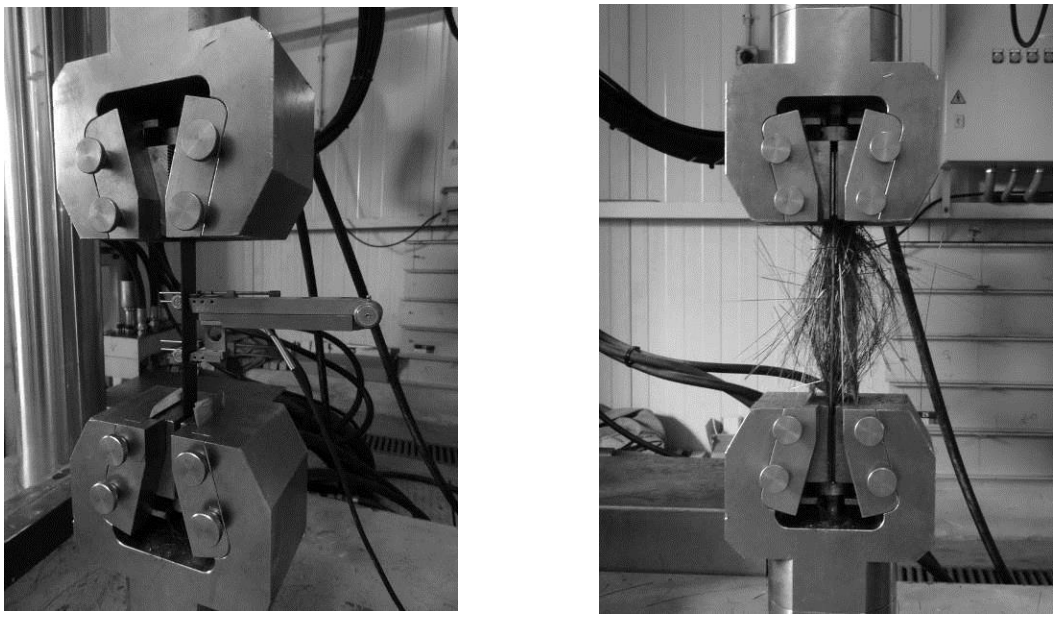

(a) (b)

Figure 159 – FRP tensile tests: (a) clip gauge positioning and (b) general failure aspect.

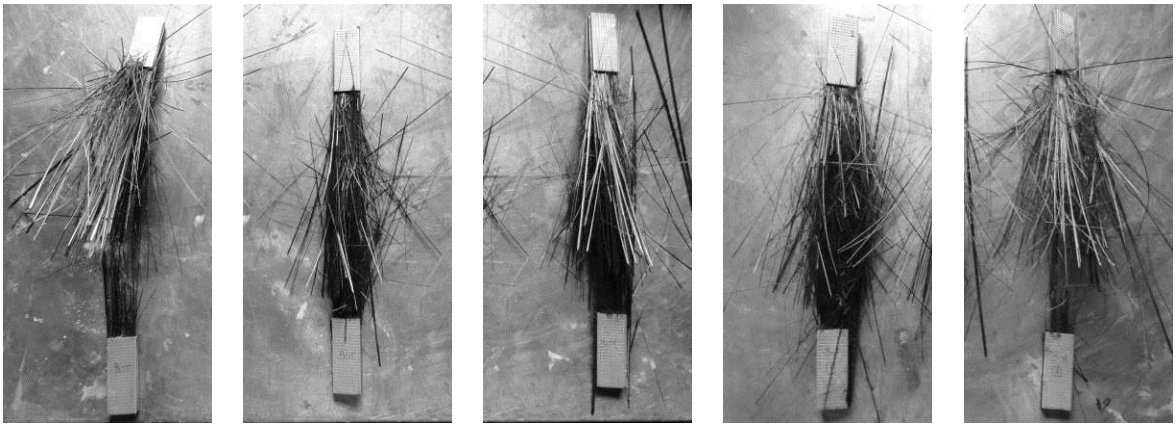

Figure 160 – Failure aspect of the FRP specimens.

Concrete samples were also collected during the casting of the beams, and the concrete compressive strength and the elastic modulus were determined immediately after testing the prestressed beams according to the Portuguese Specification E 395. Table 39 summarizes all the properties determined in these specimens. The cylinders casted for Series I and II had a diameter of 150 mm and 300 mm of height, while the samples for the characterization of the concrete of

Series III were obtained by extracting 75 mm diameter cores from a 200 mm height concrete block (see Figure 161).

Table 39 – Experimental properties of the concrete.

Specimen	Series I		Series II		Series III	
	E_c [GPa]	f_c [MPa]	E_c [GPa]	f_c [MPa]	E_c [GPa]	f_c [MPa]
1	29.10	33.0	-	33.5 §§	-	31.4
2	25.74	31.4	43.3	50.5	38.54	36.0
3	- §	-	38.1	42.8	39.27	31.2
4	- §	-	39.2	50.1	41.38	27.8
Average	27.4	32.2	40.2	47.8	39.7	31.6
Standard Deviation	2.4	1.1	2.8	4.3	1.5	3.4
COV	9%	3%	7%	9%	4%	11%

§ Some of the samples casted were mistakenly used for other purposes.

§§ Considered as an outlier and, therefore, not considered in the average calculation.

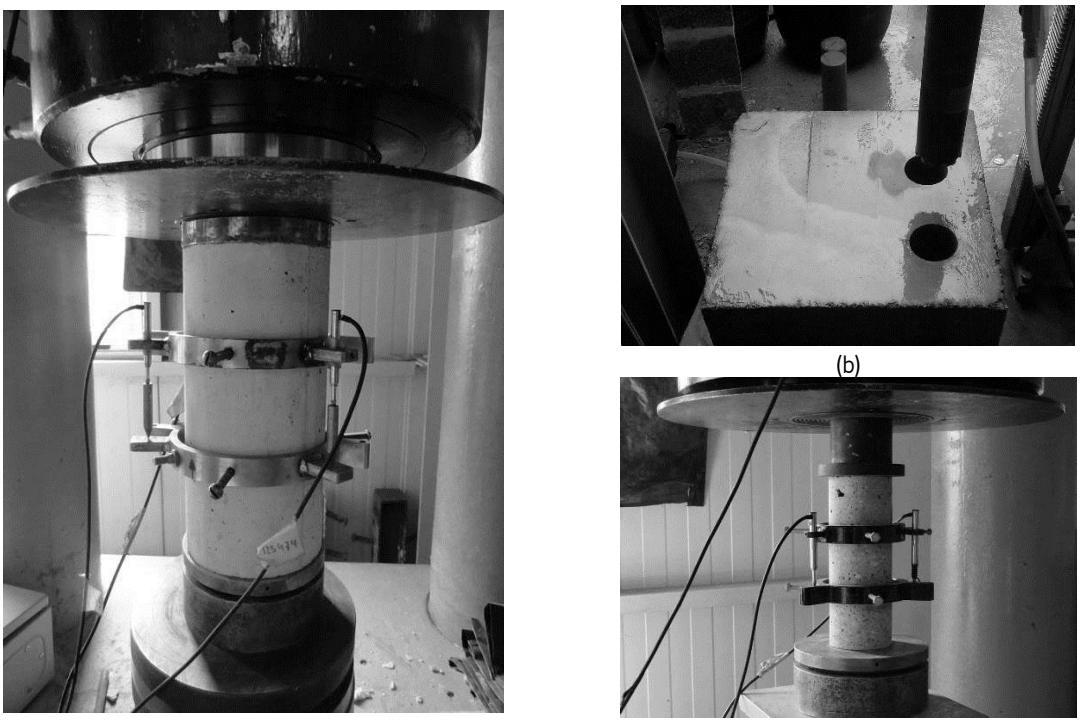

(a) (b) (c)

Figure 161 – Concrete specimens: (a) Series I and II cylinders, (b) Core extraction and (c) Series III cylinders.

The longitudinal and shear reinforcement steel bars were tested using samples of 500 mm length of the material used in each Series according to the dispositions of NP EN 10002-1. The relevant results are presented in Tables 40 and 41 and the curves in correspondence to these specimens are given in Annex B. In Figure 162, a photo of a steel bar prior to tensile testing is presented.

Table 40 – Experimental properties of the longitudinal steel bars.

Specimen	Series I – 10 mm				Series II – 10 mm				Series III – 12 mm			
	E_s	f_y	ε_u	f_u	E_s	f_y	ε_u	f_u	E_s	f_y	ε_u	f_u
	[GPa]	[MPa]	[‰]	[GPa]	[MPa]	[‰]	[GPa]	[MPa]	[‰]	[GPa]	[MPa]	[‰]
1	203	515	180	635	197	530	120	643	181	518	150	626
2	200	514	133	635	204	555	100	644	213	527	167	625
3	210	519	173	640	201	521	140	625	206	517	167	622
4	211	519	133	640	212	541	110	630	218	517	250	624
5	216	513	107	632	202	544	160	632	201	521	150	621
Average	208	516	145	636	202	538	122	634	204	520	177	624
Standard Deviation	6	3	31	4	6	12	24	8	14	4	42	2
COV	3%	1%	21%	1%	3%	2%	20%	1%	7%	1%	24%	0%

Table 41 – Experimental properties of the steel stirrups.

Specimen	Series I – 6 mm				Series II – 6 mm				Series III – 8 mm			
	E_s	f_y	ε_u	f_u	E_s	f_y	ε_u	f_u	E_s	f_y	ε_u	f_u
	[GPa]	[MPa]	[‰]	[GPa]	[MPa]	[‰]	[GPa]	[MPa]	[‰]	[GPa]	[MPa]	[‰]
1	218	629	20 §	703	216	646	33	680	194	535	100	641
2	215	605	20 §	694	213	645	33	676	196	547	125	645
3	228	618	100	703	208	642	33	673	200	541	100	646
4	209	598	100	684	216	653	50	685	-	-	-	-
5	-	-	-	-	204	653	67	688	-	-	-	-
Average	218	613	60	696	211	648	43	680	197	541	108	644
Standard Deviation	8	14	46	9	5	5	15	6	3	6	14	3
COV	4%	2%	77%	1%	3%	1%	34%	1%	1	1	13	0

§ Specimen failed outside the control length.

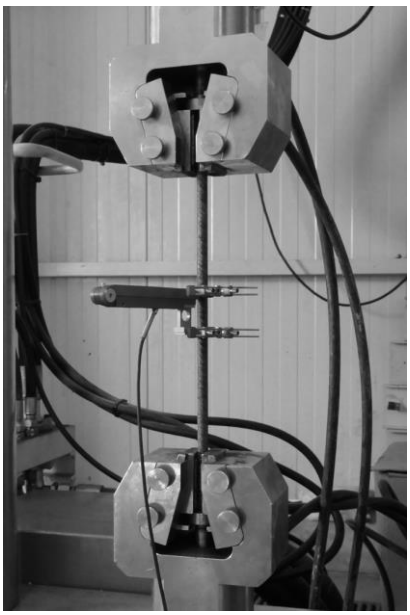

Figure 162 – Steel bars test setup.

6.1 LOSSES OF PRESTRESS

The majority of the prestress losses, as previously stated, are believed to be related with the viscoelastic behaviour of the epoxy adhesive used to bond the CFRP to the concrete. Furthermore, in Chapter 3, this material has already proven to exhibit linear viscoelastic behaviour, meaning that from the moment that the adhesive is loaded, the same decay of elastic modulus over time is expected, regardless the applied load level. Moreover, during prestress application and subsequent release, no cracks were observed due to prestress transfer on any of the specimens, meaning that after release, all materials were apparently working within their elastic limit. Given this, it was decided to predict the instantaneous and long-term losses using a conventional linear-elastic solid-element model using the computer program based on the finite element method (FEM) developed with the collaboration of members of the Structural Composites Research Group of Minho University, named FEMIX.

The mesh of the model, depicted in Figure 163, was composed of 20-nodes solid elements to simulate the concrete, adhesive and FRP, admitted as perfectly bonded to each other. A Gauss Legendre integration scheme of 2×2×2 integration points was used in all elements. Additionally, the steel reinforcement applied in each of series was also modelled by means of 3-nodes embedded cable elements, with 2 integration points per element, also admitted as perfectly bonded to the solid mesh. To decrease computational time, only one quarter of each beam was modelled, and prestress was simulated by applying a temperature variation in the elements of CFRP in correspondence with the level of strain applied in each beam.

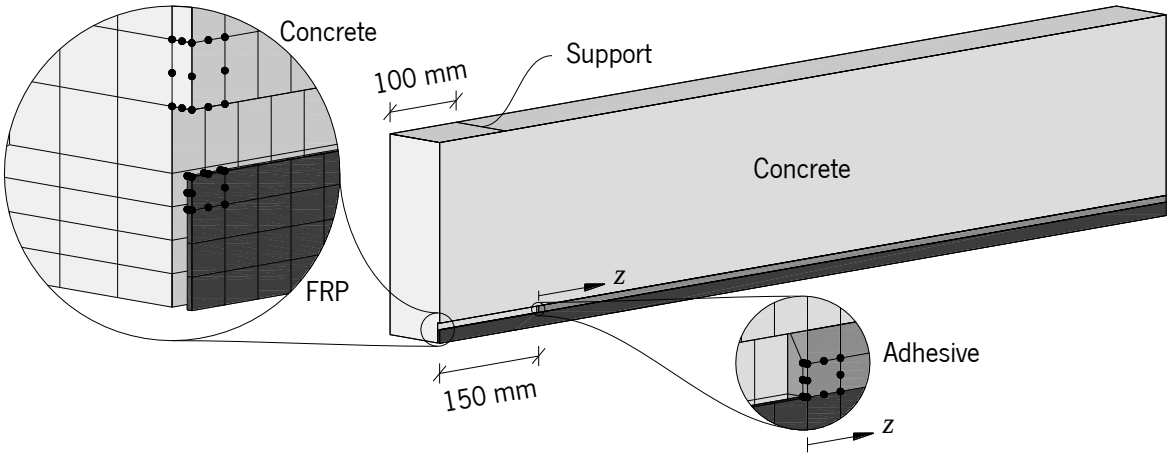

Figure 163 – Representation of the 3D mesh used to model prestressed beams.

As all materials were assumed to be in linear-elastic behaviour, the properties used to define each of the materials are summarized in Table 42 for the case of concrete (E_c and ν_c), longitudinal steel reinforcement (E_{sl} and ν_{sl}), steel shear reinforcement (E_{sv} and ν_{sv}) and CFRP laminates (E_f and $\nu_f = 0$). Taking into account the time span of prestress loss recorded (about 40 days), only a limited number of time instants were selected for purposes of experimental/numerical comparison. The average creep modulus of the epoxy adhesive corresponding to those time instants is summarized in Table 43.

Table 42 – Elastic properties of the intervening materials.

Beam	ε_p [‰]	E_c [GPa]	ν_c	E_{sl} [GPa]	ν_{sl}	E_{sv} [GPa]	ν_{sv}	E_f [GPa]
S1_20%	2.610	27.4	0.2	208	0.3	218	0.3	173
S1_30%	4.080							
S2_20%	2.690	40.2	0.2	202	0.3	211	0.3	178
S2_30%	4.000							
S2_40%	5.354							
S2_50%	6.621							
S3_20%	2.680	22.8	0.2	215	0.3	197	0.3	204
S3_30%	4.010	21.3						
S3_40%	5.360	24.6						
S3_50%	6.645	28.4						

The elastic modulus of the concrete beams of Series III is obtained by inverse analysis in Section 6.2.3 since the beams were micro-cracked when tested. Additionally, according to the results obtained in 6.2.3, the elastic modulus of the longitudinal steel bars obtained in samples of this material was not representative of the bars applied on the beams.

Table 43 – Creep modulus of the adhesive over time at 20°C.

Adhesive Series	Age of the adhesive										
	0 [GPa]	1.5 h [GPa]	3 h [GPa]	6 h [GPa]	12 h [GPa]	1 day [GPa]	2 days [GPa]	4 days [GPa]	8 days [GPa]	16 days [GPa]	32 days [GPa]
Series I	9.49	6.98	6.34	5.66	5.00	4.42	3.94	3.59	3.33	3.11	2.84
Series II	8.8	5.85	5.29	4.74	4.24	3.79	3.43	3.15	2.94	2.74	2.49
Series III	8.84	5.18	4.55	3.95	3.43	3.00	2.67	2.45	2.30	2.20	2.09
Average	9.04	6.01	5.39	4.78	4.22	3.74	3.35	3.06	2.86	2.68	2.48

The Poisson coefficient of the adhesive, ν_a, was taken as 0.3.

For future reference, the environmental temperature registered at the selected time instants in each of the beams is also summarized in Table 44.

Table 44 – Environmental temperature.

Beam	Temperature after prestress release [°C]											Min – Max {Avg} §
	0	1.5 h	3 h	6 h	12 h	1 day	2 days	4 days	8 days	16 days	32 days	[°C]
S1_20%	29.6	30.1	30.0	29.2	26.9	30.4	29.0	29.3	27.9	25.2	22.5	18.9 – 31.2 {24.4}
S1_30%	25.8	25.3	25.0	24.6	23.9	21.4	23.2	24.3	24.1	25.5	23.9	18.9 – 26.6 {22.9}
S2_20%	17.0	17.2	17.3	16.7	17.0	16.8	16.9	18.3	19.0	21.6	21.1	15.9 – 24.3 {19.4}
S2_30%	18.7	19.2	19.7	20.3	18.7	18.9	18.5	19.6	22.8	20.3	17.7	15.9 – 24.3 {19.9}
S2_40%	17.1	17.4	17.0	16.7	17.0	17.0	17.0	18.6	19.2	22.0	21.2	15.9 – 24.3 {19.4}
S2_50%	18.7	19.2	19.7	20.3	18.7	18.9	18.5	19.6	22.8	20.3	17.7	15.9 – 24.3 {19.9}
S3_20%	22.9	22.7	22.6	21.9	21.7	23.3	22.6	18.9	19.6	20.8	23.9	15.2 – 32.7 {20.0}
S3_30%	19.0	19.6	19.9	20.2	18.8	20.5	20.8	19.3	20.0	18.2	22.9	15.2 – 32.7 {20.3}
S3_40%	22.9	22.7	22.6	21.9	21.7	23.3	22.6	18.9	19.6	20.8	23.9	15.2 – 32.7 {20.0}
S3_50%	19.0	19.6	19.9	20.2	18.8	20.5	20.8	19.3	20.0	18.2	22.9	15.2 – 32.7 {20.3}

§ Min - Max is the minimum and maximum temperatures recorded during the 32 days. {Avg} is the average temperature corresponding to the 32 days period.

The three-dimensional models were initially prepared using the elastic properties reported in Table 42 and adopting the average instantaneous elastic modulus of the adhesive (age of the adhesive = 0, in Table 43). In Figure 164, the comparison between the experimental and numerical instantaneous CFRP strains is depicted and the environmental temperature at prestress release is also indicated.

According to the results obtained from the three-dimensional models, in terms of strain loss in the CFRP laminate mid-span, the instantaneous experimental loss is predicted with good accuracy as showed in Figure 164b and Table 45. Close to the extremities of the bond length, the same accuracy is not observed (see Figure 164b). When the first series (Series I) was analysed, the larger numerical strains were assumed to be related with the environmental temperature at which the prestress load was transferred to the beam. This assumption was made based on the principle that the higher the temperature the lower the elastic modulus of the adhesive. In that case, the deformability of the adhesive layer would be higher, and the strain in a given position would be lower than initially expected (see Figure 165). According to this hypothesis, the ratio between experimental and numerical strains, m, would increase with the increase of temperature, which was in fact observed for Series I (see Table 45). However, this was not observed in the remaining tested beams, which in general exhibit a m value compatible with temperatures higher than 20ºC ($m > 1$), although in most cases, the release of prestress was performed under lower temperature.

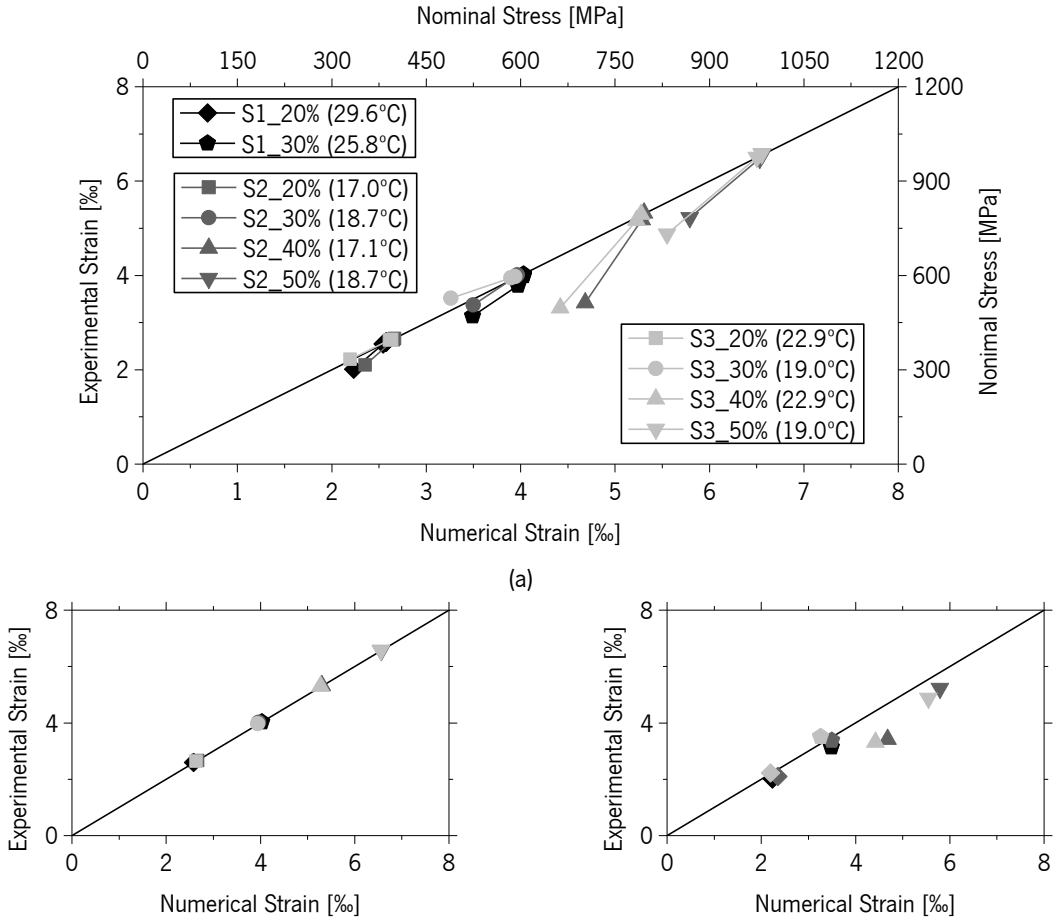

Figure 164 – Relationship between experimental and numerical instantaneous strain loss: (a) all the monitored strain gauges, (b) mid-span strain gauges and (c) strain gauges at z = 25 mm.

Table 45 – Linear regression of experimental versus numerical strains.

Beam	$\varepsilon_{num,MidSpan}$ [με]	$\varepsilon_{exp,MidSpan}$ [με]	Error § [%]	m	b [με]	r^2
S1_20%	2579	2596	-0.7	1.6923	-1767	0.99930
S1_30%	4031	4024	0.2	1.5865	-2412	0.97742
S2_20%	2666	2663	0.1	1.7878	-2106	0.99990
S2_30%	3964	4011	-1.2	1.3554	-1370	0.99952
S2_40%	5306	5322	-0.3	2.9955	-10609	0.99886
S2_50%	6562	6571	-0.1	1.7245	-4765	0.99926
S3_20%	2636	2639	-0.1	0.9625	110	0.99885
S3_30%	3940	3975	-0.9	0.6817	1291	0.99998
S3_40%	5277	5300	-0.4	2.3079	-6890	0.99989
S3_50%	6555	6580	-0.4	1.7032	-4579	0.99998

Equation of the linear regression: $\varepsilon_{exp} = m \cdot \varepsilon_{num} + b$

§ Error = $\left(\varepsilon_{num,MidSpan} - \varepsilon_{exp,MidSpan}\right) \Big/ \varepsilon_{exp,MidSpan}$.

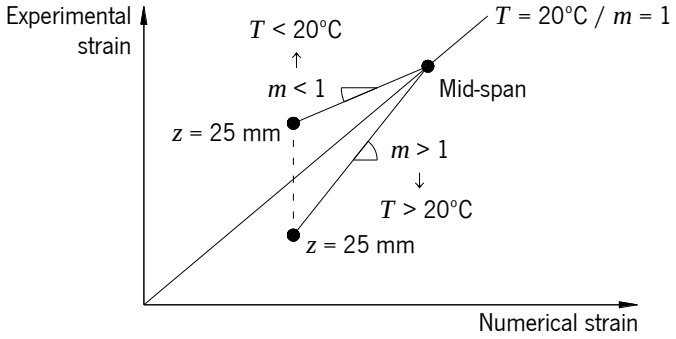

Figure 165 – Representation of the experimental versus numerical strain distribution due to temperature.

Another possibility to explain the difference between experimental and numerical CFRP strains is the existence of a region with material non-linear behaviour. It would be expectable that the existence of this zone would cause a higher m value for a higher level of applied prestress. However, according to Table 45, this did not happen. In fact, S2_40% and S3_40% are the beams exhibiting the highest difference between experimental and numerical results, and not S2_50% and S3_50%.

After analysing the instantaneous strain losses in the CFRP, it is also necessary to model the strain losses for the remaining time instants selected. Since the adhesive elastic modulus changes with time, a time dependent analysis would appear necessary. However, as this epoxy adhesive exhibits linear viscoelastic behaviour, this type of complex analysis is not necessary. Note that the elastic modulus of the adhesive is independent of the applied stress level, as demonstrated in Chapter 3. Therefore, since all portions of the adhesive layer begin absorbing the prestress load simultaneously, performing a time-dependent analysis or independent linear-elastic analysis using the appropriate elastic modulus will conduct to the same result.

In Table 46, the strains recorded in the strain gauges positioned at z = 25 mm in Series I beams, at several time instants, as well as the strains obtained numerically by updating the elastic modulus of the adhesive, are reported. As it was previously assumed that the CFRP strain could be affected by the change of deformability of the adhesive with temperature, it was also decided to estimate the elastic modulus of the adhesive to match the experimental results. Taking as example S1_20%, the effective strain after prestress release on the strain gauge located at z = 25 mm is 2.010‰ (value shaded in the third column of Table 46). However, it is concluded that to replicate the experimental strain loss, the instantaneous modulus of the adhesive should be close to the one used to model the strains at 1 and 2 days *i.e.*, between 3.35 and 3.74 GPa (see values shaded in the fourth column of Table 46). Additionally, the S1_30% beam also suggests that the elastic modulus of the adhesive should be within that range of values. Since it is not reasonable to accept an adhesive elastic

modulus of about 40% of the instantaneous elastic modulus, the initial hypothesis of temperature dependency becomes highly improbable. The graphical representation of the experimental and numerical CFRP given in Table 46 is also depicted in Figure 166a.

Table 46 – Comparison between experimental and numerical strains over time at z = 25 mm – Series I.

Time	Creep Modulus	S1_20% (T = 29.6°C)		S1_30% (T = 25.8°C)	
		$\varepsilon_{exp,25}$	$\varepsilon_{num,25}$	$\varepsilon_{exp,25}$	$\varepsilon_{num,25}$
[days]	[GPa]	[με]	[με]	[με]	[με]
0	9.04	2010	2233	3136	3491
0.0625	6.01	1907	2152	2972	3363
0.125	5.39	1873	2126	2954	3323
0.25	4.78	1823	2096	2931	3276
0.5	4.22	1791	2062	2909	3223
1	3.74	1765	2027	2906	3169
2	3.35	1720	1994	2897	3116
4	3.06	1699	1965	2887	3071
8	2.86	1662	1942	2863	3036
16	2.68	1637	1920	2846	3002
32	2.48	1639	1894	2816	2960

$\varepsilon_{exp,25}$ is the experimental strain at z = 25 mm and $\varepsilon_{num,25}$ is the numerical strain at z = 25 mm.

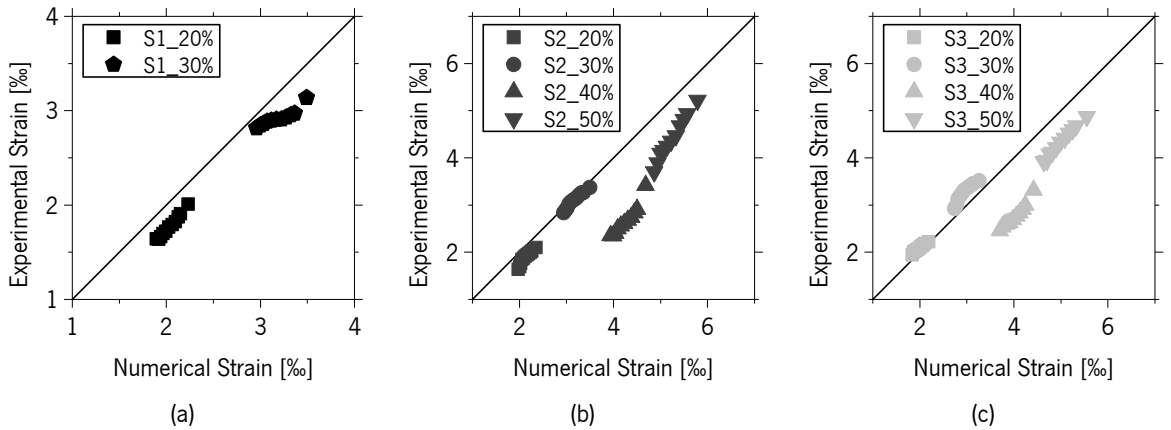

Figure 166 – Experimental versus numerical CFRP strain in the strain gauge at z = 25 mm in the selected time instants: (a) Series I, (b) Series II and (c) Series III.

As analysing one unique series of results is insufficient to draw final conclusions, the same estimation of the elastic modulus of the adhesive is performed for the beams of Series II and III (Tables 47 and 48). In the case of Series II, all the m values indicate that the elastic modulus is lower than 9.04 GPa, although the environmental temperature at prestress release was in all specimens lower than 20ºC. Table 47 reports the experimental and numerical strains at z = 25 mm of the beams of Series II. According to this table, the elastic modulus that can replicate the

deformability of S2_20% and S2_50% is in the range of 3.35 GPa to 3.74 GPa, whereas in S2_30% should be between 6.01 GPa and 9.04 GPa. Regarding S2_40%, it is concluded that the elastic modulus should be considerably lower than 2.48 GPa.

Table 47 – Comparison between experimental and numerical strains over time at 25 mm – Series II.

Time	E_{creep}	S2_20% (T = 17.0°C)		S2_30% (T = 18.7°C)		S2_40% (T = 17.0°C)		S2_50% (T = 17.0°C)	
		$\varepsilon_{exp,25}$	$\varepsilon_{num,25}$	$\varepsilon_{exp,25}$	$\varepsilon_{num,25}$	$\varepsilon_{exp,25}$	$\varepsilon_{num,25}$	$\varepsilon_{exp,25}$	$\varepsilon_{num,25}$
[days]	[GPa]	[με]	[με]	[με]	[με]	[με]	[με]	[με]	[με]
0	9.04	2100	2353	3372	3498	3419	4683	5221	5791
0.0625	6.01	2023	2263	3263	3365	2910	4503	4936	5569
0.125	5.39	1998	2234	3257	3322	2836	4447	4812	5499
0.25	4.78	1966	2200	3211	3272	2743	4380	4679	5416
0.5	4.22	1941	2163	3150	3217	2679	4305	4468	5324
1	3.74	1911	2125	3114	3159	2614	4229	4349	5229
2	3.35	1873	2087	3074	3104	2556	4155	4241	5138
4	3.06	1844	2056	3025	3057	2499	4091	4159	5060
8	2.86	1759	2031	2936	3020	2403	4043	4098	4999
16	2.68	1688	2007	2892	2984	2350	3995	3892	4940
32	2.48	1637	1978	2832	2941	2356	3936	3701	4867

$\varepsilon_{exp,25}$ is the experimental strain at z = 25 mm and $\varepsilon_{num,25}$ is the numerical strain at z = 25 mm.

Table 48 – Comparison between experimental and numerical strains over time at 25 mm – Series III.

Time	E_{creep}	S3_20% (T = 22.9°C)		S3_30% (T = 19.0°C)		S3_40% (T = 22.9°C)		S3_50% (T = 19.0°C)	
		$\varepsilon_{exp,25}$	$\varepsilon_{num,25}$	$\varepsilon_{exp,25}$	$\varepsilon_{num,25}$	$\varepsilon_{exp,25}$	$\varepsilon_{num,25}$	$\varepsilon_{exp,25}$	$\varepsilon_{num,25}$
[days]	[GPa]	[με]	[με]	[με]	[με]	[με]	[με]	[με]	[με]
0	9.04	2222	2194	3514	3261	3313	4421	4875	5551
0.0625	6.01	2182	2107	3449	3132	2995	4243	4675	5325
0.125	5.39	2161	2080	3416	3092	2912	4188	4599	5254
0.25	4.78	2139	2048	3382	3045	2833	4123	4521	5172
0.5	4.22	2113	2013	3346	2993	2770	4052	4412	5081
1	3.74	2073	1977	3305	2940	2695	3979	4335	4987
2	3.35	2054	1942	3238	2889	2625	3908	4218	4898
4	3.06	2036	1913	3173	2846	2603	3848	4117	4821
8	2.86	2017	1890	3130	2812	2592	3802	4082	4762
16	2.68	2002	1868	2993	2779	2537	3757	3944	4704
32	2.48	1938	1840	2922	2739	2455	3701	3921	4634

$\varepsilon_{exp,25}$ is the experimental strain at z = 25 mm and $\varepsilon_{num,25}$ is the numerical strain at z = 25 mm.

The results of the simulations of the beams of Series III, summarized in Table 48, reveal contradictory results as well. The strains in the CFRP laminate at z = 25 mm of S3_20% and

S3_30% are relatively well predicted with the creep modulus reported on Table 43. However, S3_40% should exhibit an elastic modulus lower than 2.48 GPa, while S3_50% could be modelled using an adhesive elastic modulus between 3.06 GPa and 3.35 GPa.

Based on the analysis of the full amount of specimens tested, a variation of the elastic/creep modulus of the adhesive due to environmental temperature is determined to be a highly unlikable reason for the inconsistencies between experimental and numerical strains. In fact, it would be more reasonable that the CFRP strain loss would be larger for higher prestress levels, most likely due to damage in the bond surface caused by excessive applied stress. However, that was not verified, and S2_20% and S2_50% are the main motives to abandon this hypothesis, since two completely prestress levels suggest the same percentage of instantaneous loss (22%, according to Chapter 4). To better understand the reason of these discrepancies, the strains measured experimentally in the CFRP laminate and the strain curves obtained numerically are depicted in Figure 167.

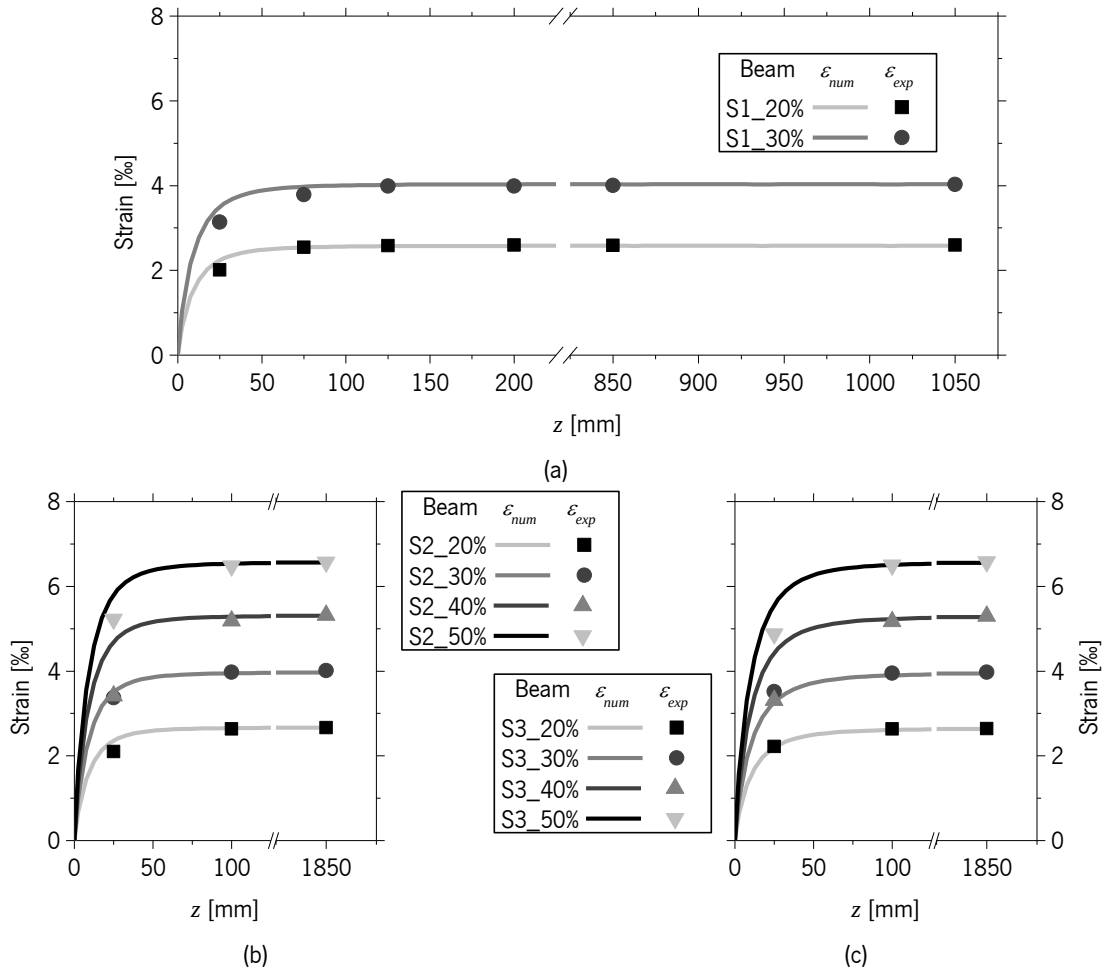

Figure 167 – Experimental and numerical distribution of strain along the bond length (t = 0 days): (a) Series I, (b) Series II and (c) Series III.

Considering the difficulty experienced while filling the groove with adhesive, as well as the recurrent need to relocate the beam during the strengthening process, already explained in Chapter 4, another possible explanation was considered. This explanation is related to the initial position of the strain gauges, which could have been slightly shifted from the desired location. In addition, the installation of the strain gauges in the CFRP laminate, which was always finalized by covering the strain gauge with a portion of 15×10 mm^2 insulating tape, could have decreased the effective bond length. As it can be observed in Figure 167, the strain in the CFRP varies abruptly in the first few millimetres of the bond length. Therefore, a minimum imprecision in the positioning of the strain gauge in the CFRP, or an insufficient penetration of the adhesive during the strengthening process, could cause a deficient reading of the CFRP strain loss.

Given this uncertainty about the correct position of the strain gages, it was decided to determine the most probable position of the first strain gauge to minimize the sum of the strain differences along the bond length as shown in Eq. 35a and b for the case of Series I or Series II/III, respectively.

$$\min\left(\begin{array}{c}\left(\varepsilon_{exp,25}-\varepsilon_{num,z_0}\right)+\left(\varepsilon_{exp,75}-\varepsilon_{num,z_0+50}\right)+\left(\varepsilon_{exp,125}-\varepsilon_{num,z_0+100}\right)+\\ +\left(\varepsilon_{exp,200}-\varepsilon_{num,z_0+175}\right)+\left(\varepsilon_{exp,850}-\varepsilon_{num,z_0+825}\right)\left(\varepsilon_{exp,1050}-\varepsilon_{num,z_0+1025}\right)\end{array}\right)\Rightarrow z \qquad (35a)$$

$$\min\left(\left(\varepsilon_{exp,25}-\varepsilon_{num,z_0}\right)+\left(\varepsilon_{exp,100}-\varepsilon_{num,z_0+75}\right)+\left(\varepsilon_{exp,1850}-\varepsilon_{num,z_0+1825}\right)\right)\Rightarrow z \qquad (35b)$$

where $\varepsilon_{exp,25}$, $\varepsilon_{exp,75}$, $\varepsilon_{exp,100}$, $\varepsilon_{exp,125}$, $\varepsilon_{exp,200}$, $\varepsilon_{exp,850}$ and $\varepsilon_{exp,1050}$ are the experimental CFRP strains determined in each strain gauge and ε_{num,z_0}, ε_{num,z_0+50}, ε_{num,z_0+50}, ε_{num,z_0+75}, $\varepsilon_{num,z_0+175}$, $\varepsilon_{num,z_0+825}$, $\varepsilon_{num,z_0+1025}$ and $\varepsilon_{num,z_0+1825}$ are the numerical CFRP strains in the probable position of the strain gauges, considering that the first installed strain gauge is not located at z = 25 mm but at a z_0 distance from the beginning of the bond length.

In Table 49, the probable effective position of the first strain gauge, z_0, is reported. According to this table, the initial position of the strain gauge, which was estimated to vary between 10.70 mm and 32.48 mm, confirms that the task of filling the groove may not have been precise as desired, as already suggested. Additionally, and as depicted in Figure 168, the ratio between experimental and numerical strains, m, after prestress release is obviously forced to be unitary. The values of r^2 in correspondence with the linear regressions executed are close to the ones previously obtained in Table 45.

Table 49 – Linear regression of experimental versus numerical strains – adjusted location.

Beam	z_0 [mm]	Error § [%]	$\varepsilon_{num,MidSpan}$ [με]	$\varepsilon_{exp,MidSpan}$ [με]	Error §§ [%]	m	b [με]	r^2
S1_20%	17.27	-31	2578	2596	-0.7	1.0260	-52	0.99979
S1_30%	17.19	-31	4030	4024	0.1	0.9519	142	0.97084
S2_20%	16.85	-33	2666	2663	0.1	0.9849	32	0.99963
S2_30%	20.78	-17	4011	4011	0.0	1.0002	37	0.99927
S2_40%	10.70	-57	5322	5322	0.0	0.9812	63	0.99758
S2_50%	17.51	-30	6562	6571	-0.1	1.0117	-95	0.99874
S3_20%	25.78	3	2636	2639	-0.1	0.9988	12	0.99803
S3_30%	32.48	30	3975	3975	0.0	1.0000	36	0.99948
S3_40%	11.75	-53	5300	5300	0.0	1.0014	-15	0.99920
S3_50%	16.61	-34	6580	6580	0.0	1.0041	-7	0.99996

Equation of the linear regression: $\varepsilon_{exp} = m \cdot \varepsilon_{num} + b$.

§ Error = $\left(z_0 - 25\right)/25$, in millimetres.

§§ Error = $\left(\varepsilon_{num,MidSpan} - \varepsilon_{exp,MidSpan}\right)/\varepsilon_{exp,MidSpan}$.

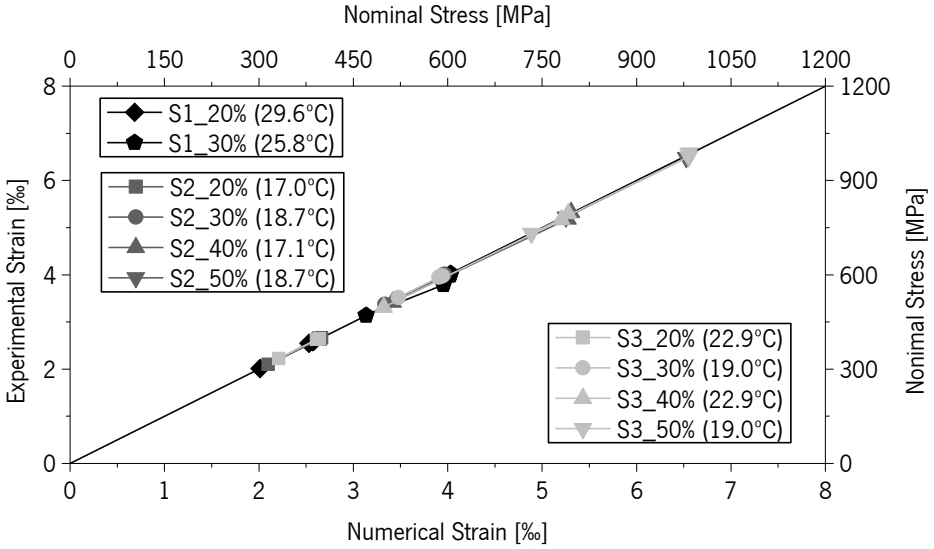

Figure 168 – Relationship between experimental and numerical instantaneous strain loss – adjusted location.

After confirming that the correction of the initial position of the strain gauge improves the correlation between experimental results and numerical models, it is still necessary to verify that this correction will also conduct to an accurate prediction of the CFRP strains over time. According to Table 50, this simple adjustment of the initial position of the strain gauge conducts, in fact, to much more accurate results 32 days after prestress transfer. The error calculated between each pair of numerical/experimental CFRP strains is in general lower than 10%.

Table 50 – Linear regression of experimental versus numerical strain – adjusted position and t = 32 days.

Beam	z [mm]	$\varepsilon_{num,25}$ [με]	$\varepsilon_{exp,25}$ [με]	Error § [%]	$\varepsilon_{num,75}$ [με]	$\varepsilon_{exp,75}$ [με]	Error § [%]	m	b [με]	r^2
S1_20%	17.27	1578	1639	-4	2472	2467	0	0.9347	163	0.99888
S1_30%	17.19	2459	2816	-13	3863	3580	8	0.7337	987	0.93624
S2_20%	16.85	2100	1637	28	2652	2524	5	1.7168	-1970	0.98946
S2_30%	20.78	2693	2832	-5	3919	3944	-1	0.9186	358	0.99961
S2_40%	10.70	2398	2356	2	5217	4587	14	0.9127	158	0.95503
S2_50%	17.51	4086	3701	10	6477	6150	5	1.0966	-785	0.98864
S3_20%	25.78	1867	1938	-4	2586	2607	-1	0.9189	222	0.99958
S3_30%	32.48	3070	2922	5	3801	3869	-2	1.2699	-974	0.99925
S3_40%	11.75	2384	2455	-3	5130	4900	5	0.9423	201	0.99265
S3_50%	16.61	3726	3921	-5	6414	6468	-1	0.9441	404	0.99996

Equation of the linear regression: $\varepsilon_{exp} = m \cdot \varepsilon_{num} + b$.

§ Error = $\left(\varepsilon_{num,i} - \varepsilon_{exp,i}\right) / \varepsilon_{exp,i}$.

In Figure 169 the simulation of the CFRP strain profile after 32 days is depicted. According to these graphs, the model forecasts with very good precision the strains at each position.

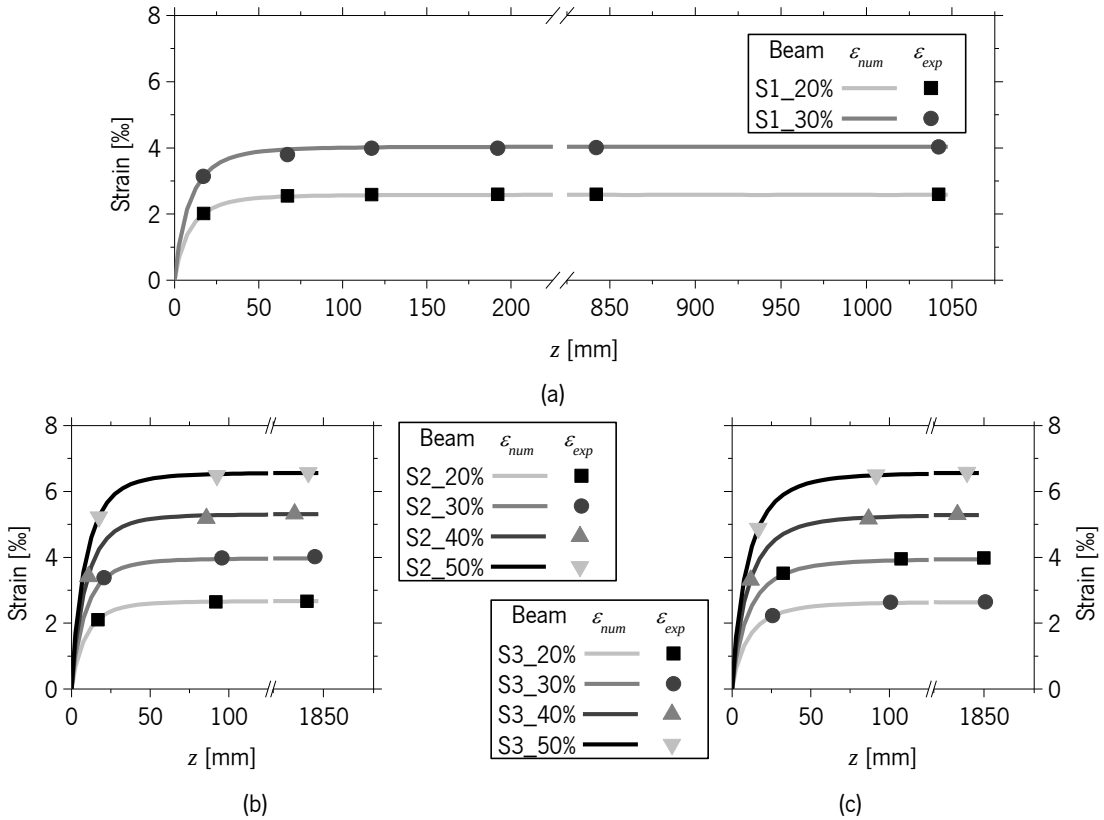

Figure 169 – Experimental and adjusted numerical strains along the bond length (t = 0 days): (a) Series I, (b) Series II and (c) Series III.

To better understand how these predictions develop over time, the experimental versus numerical strains in all the positions were plotted in Figure 170 for all the time instants modelled. The beams labelled as S1_30%, S2_20% and S2_40% are the beams that diverge more from the predicted results. The beams of Series III reveal the best relationship between experimental and numerical results for all applied prestress levels, maybe because the average temperature registered during the monitoring period was very close to 20ºC (last column of Table 44).

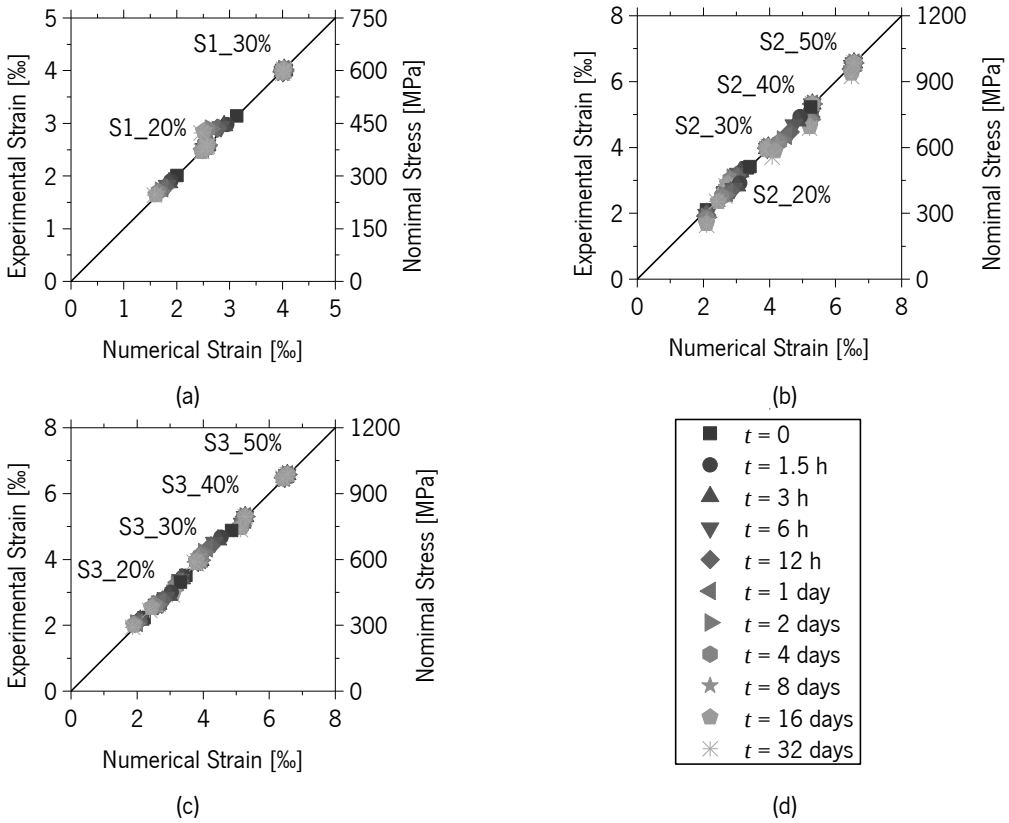

Figure 170 – Experimental versus numerical strains in the time instants selected: (a) Series I, (b) Series II, (c) Series III and (c) Legend.

The ratio between the experimental and numerical strains, m, given in Table 50, over time is depicted in Figure 171. In this graph, m at $t = 0$ is in general close to the unitary value, although in some beams diverges to higher or lower values. The beam exhibiting higher m values is S2_20%, and the beam whose m values are lower is S2_30%.

Figure 172 represents the same ratio, m, versus the environmental temperature (given in Table 44). In this plot, most m values appear to be unrelated to temperature, suggesting that the strategy adopted in Chapter 4 to subtract the environmental effects was reasonably effective. The only beam whose results appear to not be in agreement with this conclusion is S2_20%, since the m values appear to increase with the increase of temperature.

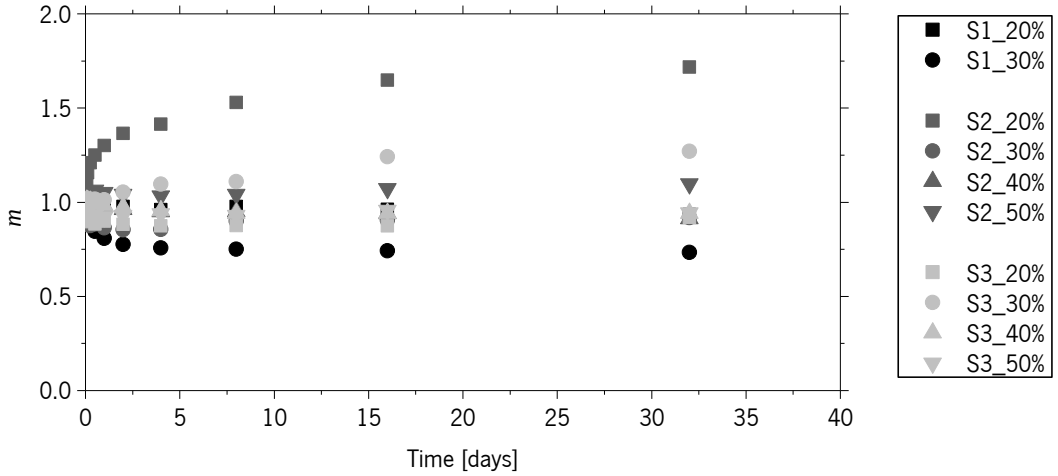

Figure 171 – Slope of the linear regression of experimental versus numerical strains versus time.

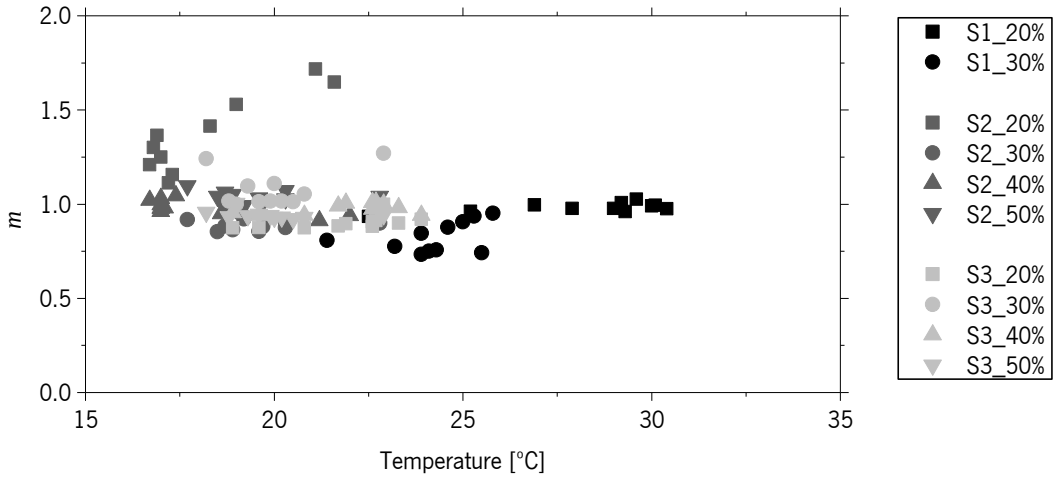

Figure 172 – m versus temperature.

Based on the obtained results, it is estimated that the viscoelastic behaviour of the adhesive is approximately constant if the reinforced concrete element is kept in an environment with temperature within the range of 15.2ºC to 32.7ºC. In that case, the creep modulus obtained in material characterization tests under 20ºC is representative of the adhesive stiffness loss over time.

From Tables 51 to 53, some of the m values depicted in the previous Figures are reported. According to these tables, the m values can either decrease or increase continuously (*e.g.* S1_30% and S2_20%), as well as fluctuate nearby the initial value (*e.g.* S2_30%).

Table 51 – Temperature and m values – Series I.

Time	E_{creep}	S1_20%		S1_30%	
		T	m	T	m
[days]	[GPa]	[°C]	(r^2)	[°C]	(r^2)
0	9.04	29.6	1.026 (0.99979)	25.8	0.9519 (0.97084)
1	3.74	30.4	0.9749 (0.99969)	21.4	0.808 (0.95534)
8	2.86	27.9	0.9764 (0.9995)	24.1	0.75 (0.94357)
16	2.68	25.2	0.9623 (0.99855)	25.5	0.741 (0.93977)
32	2.48	22.5	0.9347 (0.99888)	23.9	0.7337 (0.93624)

Table 52 – Temperature and m values – Series II.

Time	E_{creep}	S2_20%		S2_30%		S2_40%		S2_50%	
		T	m	T	m	T	m	T	m
[days]	[GPa]	[°C]	(r^2)	[°C]	(r^2)	[°C]	(r^2)	[°C]	(r^2)
0	9.04	17.0	0.9849 (0.99963)	18.7	1.0002 (0.99927)	17.1	0.9812 (0.99758)	18.7	1.0117 (0.99874)
1	3.74	16.8	1.3008 (0.99849)	18.9	0.8635 (0.99981)	17.0	0.9791 (0.98316)	18.9	1.0512 (0.9975)
8	2.86	19.0	1.5300 (0.99365)	22.8	0.9000 (0.99975)	19.2	0.9505 (0.96816)	22.8	1.0422 (0.99867)
16	2.68	21.6	1.6479 (0.99301)	20.3	0.9050 (0.99954)	22.0	0.9400 (0.96006)	20.3	1.0711 (0.99319)
32	2.48	21.1	1.7168 (0.98946)	17.7	0.9186 (0.99961)	21.2	0.9127 (0.95503)	17.7	1.0966 (0.98864)

Table 53 – Temperature and m values – Series III.

Time	E_{creep}	S3_20%		S3_30%		S3_40%		S3_50%	
		T	m	T	m	T	m	T	m
[days]	[GPa]	[°C]	(r^2)	[°C]	(r^2)	[°C]	(r^2)	[°C]	(r^2)
0	9.04	22.9	0.9988 (0.99803)	19.0	1.0000 (0.99948)	22.9	1.0014 (0.99920)	19.0	1.0041 (0.99996)
1	3.74	23.3	0.8991 (0.99943)	20.5	1.0125 (0.99722)	23.3	0.9822 (0.99763)	20.5	0.9228 (0.99999)
8	2.86	19.6	0.8758 (0.99892)	20.0	1.1088 (0.99744)	19.6	0.9419 (0.99618)	20.0	0.9293 (1.00000)
16	2.68	20.8	0.8736 (0.99842)	18.2	1.2410 (0.99823)	20.8	0.9408 (0.99508)	18.2	0.9571 (0.99999)
32	2.48	23.9	0.9189 (0.99958)	22.9	1.2699 (0.99925)	23.9	0.9423 (0.99265)	22.9	0.9441 (0.99996)

Despite all the environmental variables that are known to affect the strain profile along the CFRP, namely temperature, the observed variation of m is assumed to be natural. Note that a very simplified approach was adopted to model the obtained experimental results. The nominal target dimensions of the groove (6×30 mm^2) were assumed to model the beam and not the actual width and depth of each of the grooves opened on the beams. Therefore, it is believed that a variation in the thickness of the adhesive layer may have also contributed to the discrepancy between the experimental and numerical long-term CFRP strains.

In Chapter 4, for the elimination of the environmental effects, it was decided to admit that the CFRP strain remains constant at mid-span. At this point, it was necessary to verify if the numerical model corroborates that assumption. In Figure 173, the loss of prestress at in the mid-span in relation to the applied prestrain is presented (calculated using Eq. 36). Additionally, Figure 173 also includes the mid-span long-term CFRP strain loss in relation to the instantaneous loss (Eq. 37).

$$\Delta\varepsilon_i = \frac{\varepsilon_i - \varepsilon_t}{\varepsilon_i} \tag{36}$$

$$\Delta\varepsilon_0 = \frac{\varepsilon_0 - \varepsilon_t}{\varepsilon_0} \tag{37}$$

where ε_i is the applied prestress strain, ε_t is the strain at a given time instant t and ε_0 is the strain immediately after the release of the prestress force *i.e.*, at t = 0.

Analysing Figure 173, it is visible that the instantaneous CFRP strain loss at mid-span is by itself a significantly low value, around 1.3% in Series I, 0.9% in Series II and 1.4%~1.8% in the case of Series III. Additionally, the numerical model indicates an even lower variation of strain in the period following the release of prestress, about 0.54‰ in Series I, 0.35‰ in Series II and 0.47‰~0.60‰ in the case of Series III.

These small error values prove that for the time span analysed, it is perfectly reasonable to assume that the mid-span CFRP strain is constant. Moreover, the numerical results also allow concluding that, if the chemical connection between CFRP-adhesive-concrete does not deteriorate with time, the long term loss of strain at mid-span is negligible.

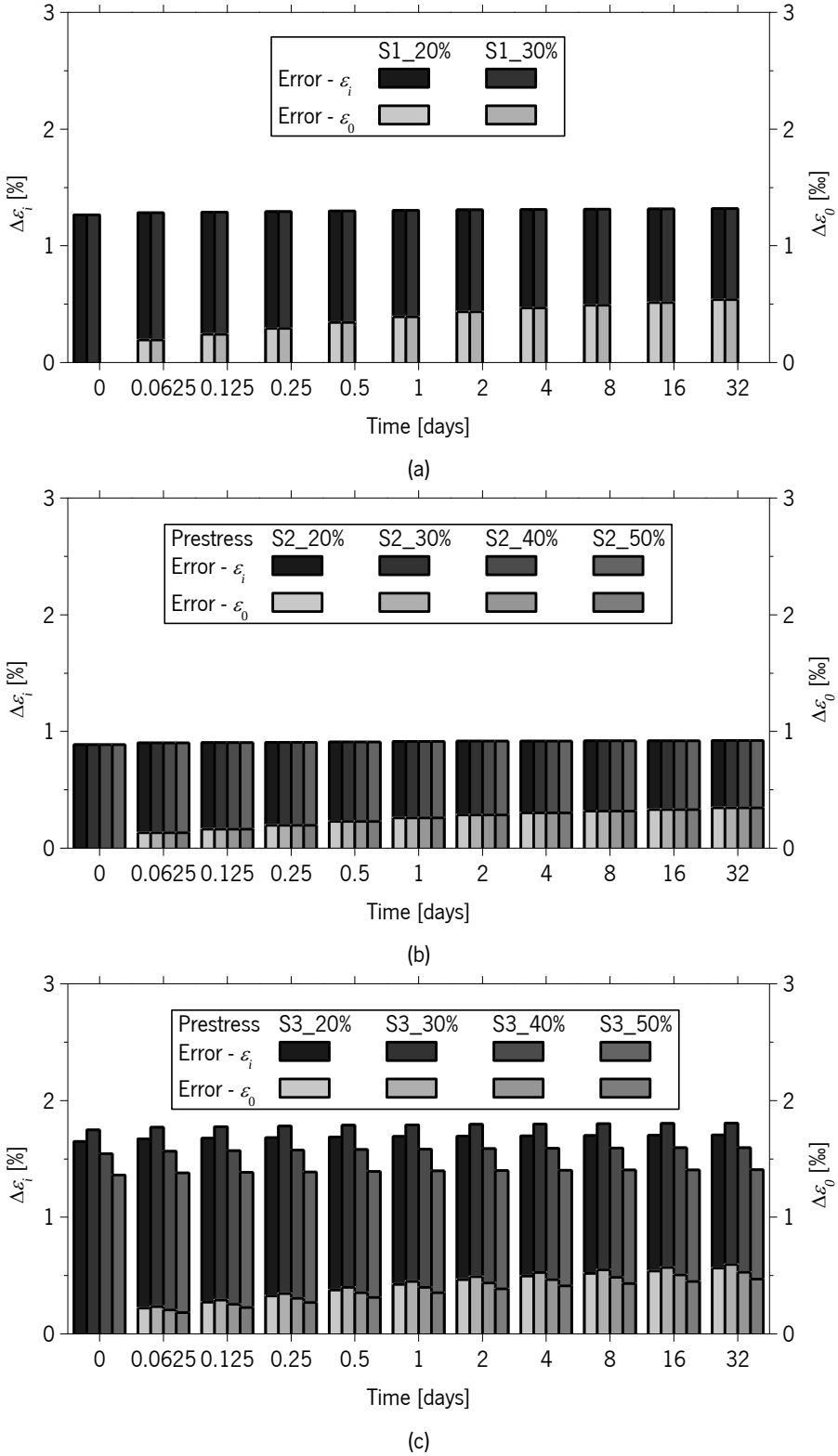

Figure 173 – Mid-span strain loss versus time: (a) Series I, (b) Series II and (c) Series III.

Finally, the mid-span deflection, one of the most relevant effects of prestress application, was also compared to the one obtained experimentally (Table 54) and the difference between these values was computed according to Eq. 38. The numerical model generally overestimates the mid-span

displacement ($\delta_{0,num} > \delta_{0,exp}$). It is believed that this difference is related to the process of prestress transfer to the surrounding concrete. Perhaps, the prestress transference process took longer than the monitoring period to deform the beam (the monitoring period was only a few minutes longer than the prestress load release).

$$\Delta\delta_0 = \frac{\delta_{0,exp} - \delta_{0,num}}{\delta_{0,exp}} \times 100 \quad (38)$$

where $\delta_{0,exp}$ and $\delta_{0,num}$ are the mid-span deflection measured experimentally and numerically, respectively.

Table 54 – Numerical mid-span deflection – 3D model.

Series	Specimen	$\delta_{0,exp}$ [mm]	$\delta_{0,num}$ [mm]	$\Delta\delta_0$ [%]
Series I	20%	0.078	0.097	-24.8
	30%	0.178	0.152	14.5
Series II	20%	0.180	0.220	-22.4
	30%	0.308	0.328	-6.4
	40%	0.385	0.439	-13.9
	50%	0.473	0.542	-14.7
Series III	20%	0.270	0.404	-49.6
	30%	0.433	0.640	-47.8
	40%	0.606	0.757	-25.0
	50%	1.112	0.829	25.4

6.2 PRESTRESS EFFECTIVENESS

The effectiveness of the prestress technique was modelled using 8-node serendipity plane stress finite elements to simulate concrete, and 3-node embedded cable elements to model the steel. Since concrete crushing was not significant at failure in most cases, all concrete elements were simulated with a multi-directional fixed smeared crack model with a total approach for the crack shear components (Barros *et al.*, 2011). In this model, the material is assumed as having a linear elastic behaviour under compression, while the normal and shear modulus of the crack, D_I^{cr} and D_{II}^{cr}, deteriorate with crack opening and sliding (Figure 174). The Mode I fracture energy, G_f^I, was calculated according to CEB-FIP Model Code (1993) recommendation, reported in Eq. 39, and the crack band width was always defined as the square root of the area of the integration point.

$$G_f^I = 0.02 \times 0.3 \times f_{cm}^{\ 0.7} \quad (39)$$

where f_{cm} is the average concrete compressive strength, in MPa.

Since it was previously determined that the long-term strain loss is practically negligible, the strains applied in the CFRPs of these models were again the same ones reported in Table 42. The level of strain was again introduced as a thermal variation in the 2-nodes perfectly bonded cable elements used to model this material, assumed with linear-elastic behaviour Figure 175b. On the other hand, the steel elements were assumed as an elasto-plastic material, as illustrated in Figure 175a.

In terms of support conditions, in all beams the vertical displacement was restrained 100 mm from the extremities of the beams and the horizontal displacement was restrained in a single node in the centre of the mesh. Load was applied symmetrically at the appropriate distance from the centre of the beam *i.e.*, 200 mm from the centre of Series I beams and 300 mm in Series II and III beams.

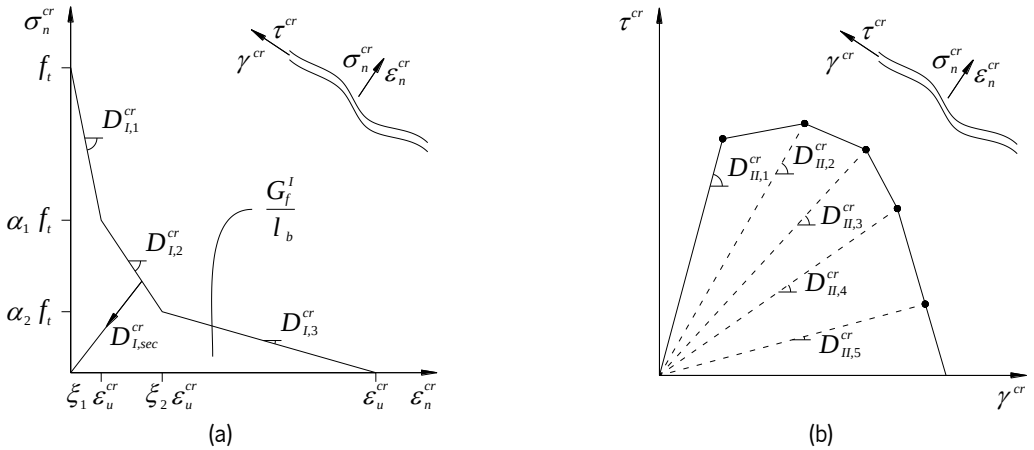

Figure 174 – Concrete behaviour: (a) Trilinear stress-strain diagram and (b) Shear stress-strain diagram.

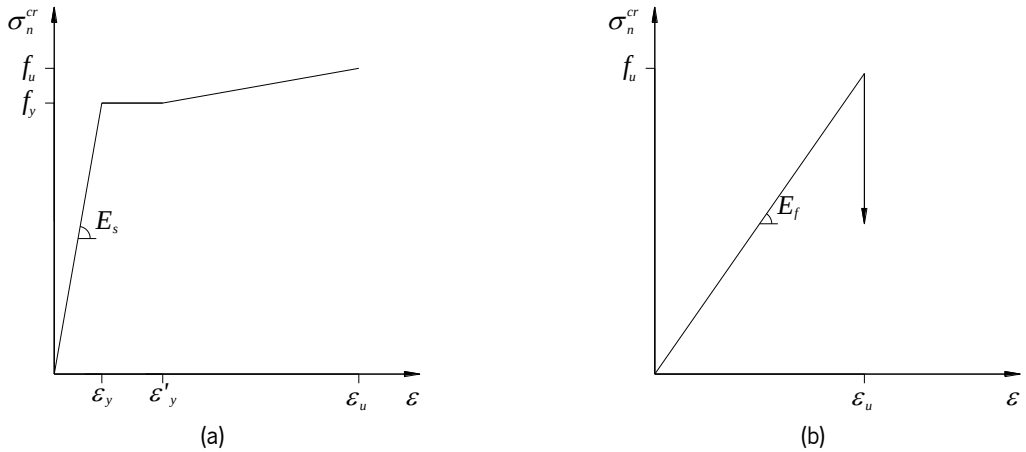

Figure 175 – Longitudinal reinforcement behaviour: (a) Steel and (b) CFRP.

The numerical models were initially prepared using the properties determined experimentally in samples of the each of the intervening materials. However, in most cases, some adjustments were necessary to improve the similarity of the experimental and numerical results.

6.2.1 Series I

Series I was the first set of beams to be tested and modelled. The mesh adopted to model these beams is depicted in Figure 176. The concrete elements had an average dimension of 25×25 mm^2 and the CFRP elements were positioned 10 mm from the bottom of the beam, and 50 mm after the supports.

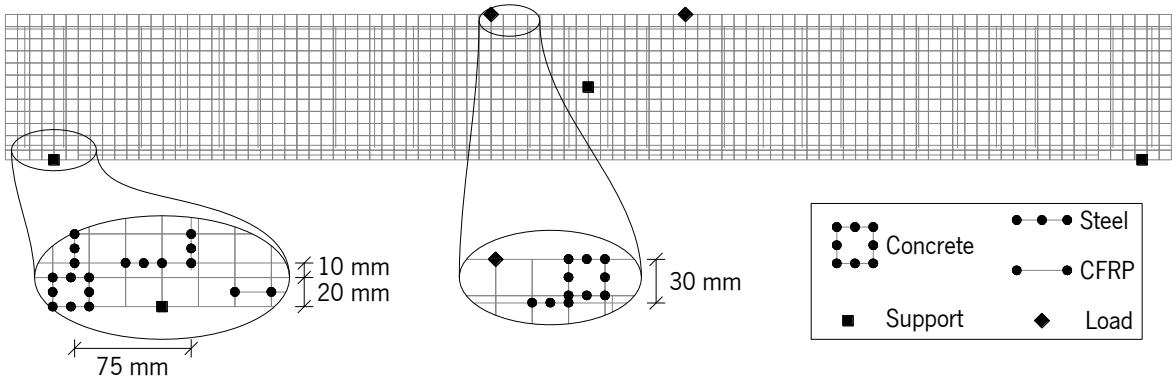

Figure 176 – Mesh and support conditions of the beams of Series I.

As previously indicated, the properties of the materials had to be slightly adjusted to fit with the desired accuracy the experimental results. From Tables 55 to 57, the properties obtained from sampling (or original properties) as well as the properties adjusted to fit experimental and numerical results are reported.

In a first approach, as the results obtained during the prestress were somewhat divergent in terms of CFRP elastic modulus (152 GPa and 200 GPa, as reported in Chapter 4), and since CFRP coupons were not tested at the time, the nominal properties of the CFRP were adopted as the original properties. Concerning the concrete tensile strength, it was assumed as the average tensile strength of concrete, defined in EN 19921-1:2004 ($f_t = 0.3 \times \left(f_{cm} - 8 \right)^{2/3}$).

Table 55 – CFRP properties used in the numerical models – Series I.

Property	Prestress Level (Original properties)			Prestress Level (Adjusted properties)		
	0%	20%	30%	0%	20%	30%
E_f [GPa]		150			173	
f_u [MPa]		2000		2291	2268	2397

Table 56 – Concrete properties used in the numerical models – Series I.

Model		ν	E_c [GPa]	f_c [MPa]	f_t [MPa]	ξ_1	α_1	ξ_2	α_2	G_f [N/mm]
Original properties	All	0.2	27.4	32.2	2.50	0.1	0.5	0.3	0.2	0.068179
Adjusted properties	Reference	0.2	27.4	32.2	1.75	0.1	0.5	0.3	0.2	0.068179
	S1_0%				2.00					
	S1_20%				2.50					
	S1_30%				2.00					

Table 57 – Steel properties used in the numerical models – Series I.

Rod	Model	ε_y [‰]	f_y [MPa]	ε'_y [‰]	ε_u [‰]	f_u [MPa]
6 mm	Original properties Adjusted properties	2.81	613	10	145	696
10 mm	Original properties	2.48	516	10	100	636
	Adjusted properties	2.76	575			

In Figure 177 the comparison between experimental and numerical mid-span deflection during loading is presented. Comparing the results obtained in the numerical models by using the original properties a couple of significant differences were observed. Firstly, the numerical model clearly underestimated the maximum capacity of the Reference beam, as depicted in Figure 177a. On the other hand, the original properties evidently overestimated the cracking load of the Reference beam, as also represented Figure 177a. On the contrary, in the remaining beams, in Figures 177b, 177c, and 177d, no excessive difference in cracking load was observed.

Additionally, in all the NSM-CFRP reinforced beams, either non-prestressed or prestressed, the yielding point was underestimated and the ultimate mid-span deflection was determined as lower as higher was the applied prestress level. Regarding the main branches of the curves, they appear to exhibit the same stiffness up to the yielding point, indicating that the elastic modulus of concrete and steel reinforcement determined by material sampling were accurate. In contrast, after yielding and up to failure, the numerical curves exhibited a lower stiffness when compared to the curves obtained experimentally, suggesting that the nominal elastic modulus considered, 150 GPa, is lower than the effective CFRP elastic modulus.

From these observations, it was decided to initially adjust the tensile strength of the concrete and the yielding strain/stress to improve the curve fitting of the Reference beam. However, the best value of tensile strength to predict the behaviour of the Reference beam revealed to be insufficient to forecast the behaviour of the NSM-CFRP reinforced beams. For that reason, in the remaining series, the tensile strength was increased from 1.75 MPa until a good match of cracking load was obtained.

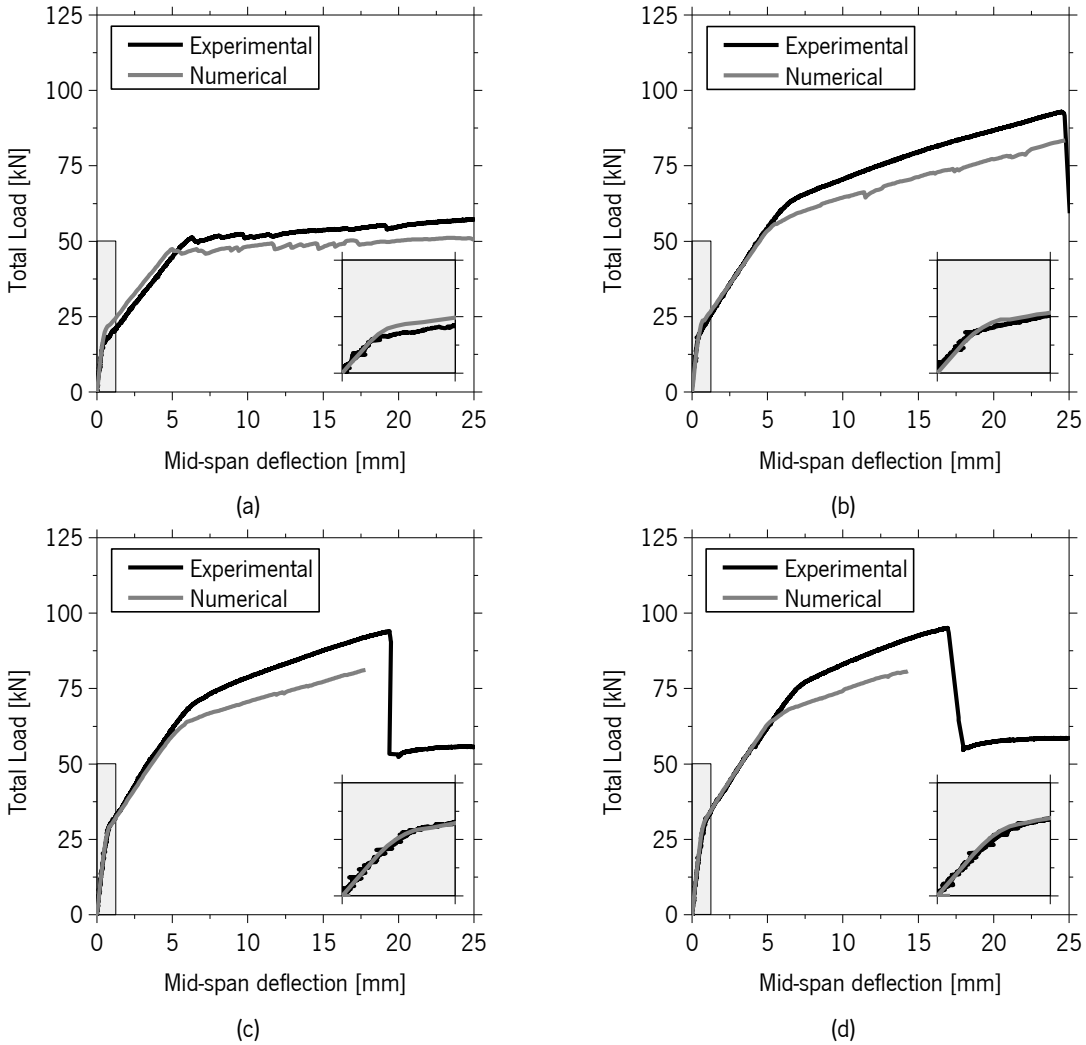

Figure 177 – Total load versus mid-span deflection – Series I (original properties):
(a) Reference, (b) S1_0%, (c) S1_20% and (d) S1_30%.

The adjustment of the yielding properties from 2.48‰ | 516 MPa to 2.76‰ | 575 MPa was sufficient to predict, in all beams, the correct location of the yielding point. However, the elastic modulus of the CFRP had to be also increased to accurately estimate the post-yielding behaviour.

Figure 178 depicts the total vertical load versus mid-span deflection obtained by using the corrected values. It is visible that the adjustments of the material properties improved the prediction

of the cracking and yielding load of the Reference beam (see Figure 178a). Regarding the NSM-CFRP reinforced beams, the numerical model was in general very accurate after increasing the elastic modulus of the CFRP from 150 GPa to 173 GPa.

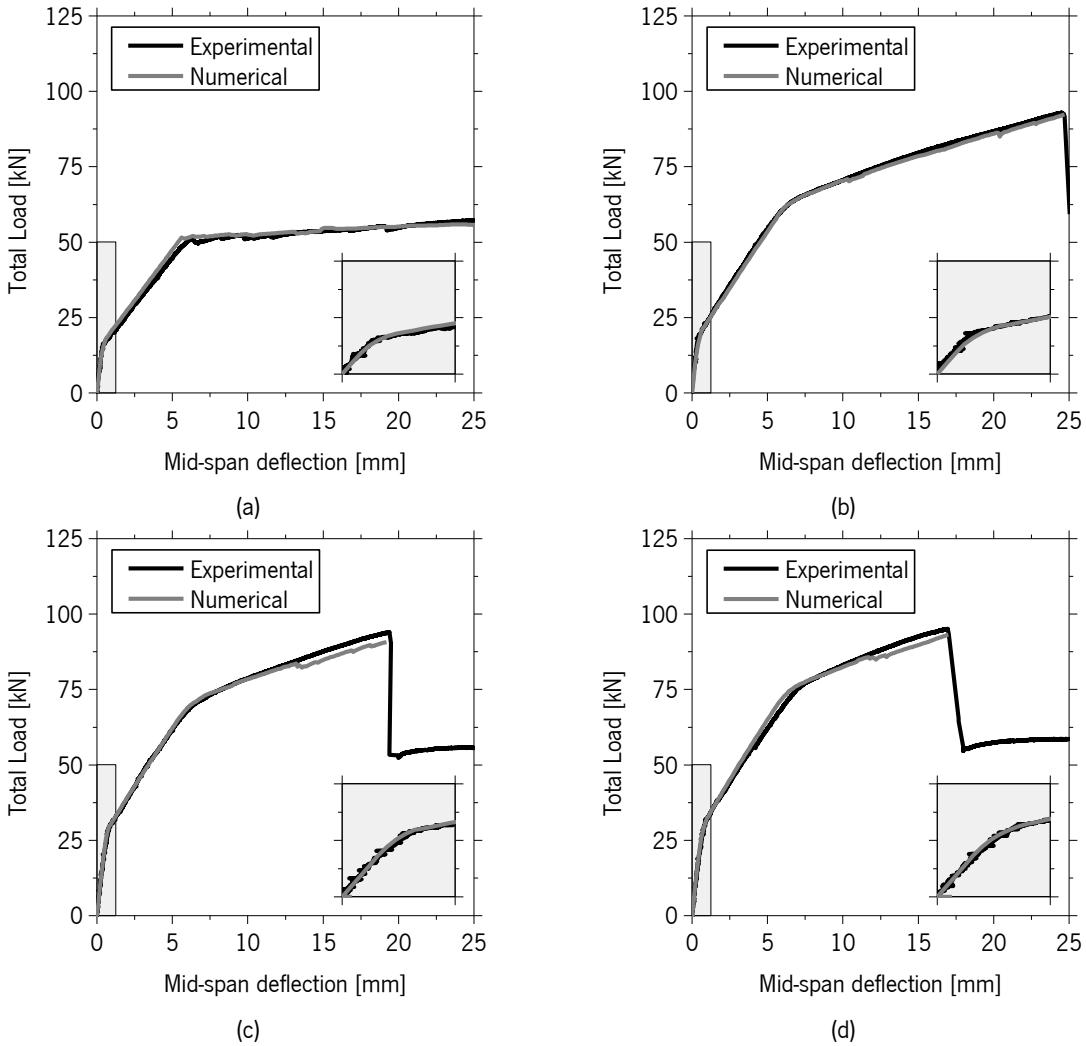

Figure 178 – Total load versus mid-span deflection – Series I (adjusted properties): (a) Reference, (b) S1_0%, (c) S1_20% and (d) S1_30%.

According to these adjusted models, the beams experienced, as expected, an upward movement due to the application of the prestress. This initial displacement, reported in Table 58, was compared to the displacements previously presented in Chapter 4. The difference between experimental and numerical results, calculated using Eq. 38 (defined in Section 6.1) was found to be relatively similar to the one obtained previously, since according to both Tables (54 and 58), the negative deflection of the beams was underestimated in S1_20%, while in S1_30% case it was somewhat overestimated.

Table 58 – Numerical mid-span deflection of Series I beams – 2D model.

Specimen	$\delta_{0,exp}$ [mm]	$\delta_{0,num}$ [mm]	$\Delta\delta_0$ [%]
20%	0.078	0.105	-34
30%	0.178	0.162	9

Note: $\Delta\delta_0 = \left(\delta_{0,exp} - \delta_{0,num}\right) \Big/ \delta_{0,exp} \times 100$

After adjusting the material properties, the average deflection of the loaded-sections and the average deflection at the mid-shear-spans were compared with the curves obtained experimentally and exhibited exceptionally good correlation, as depicted in Figures 179 and 180.

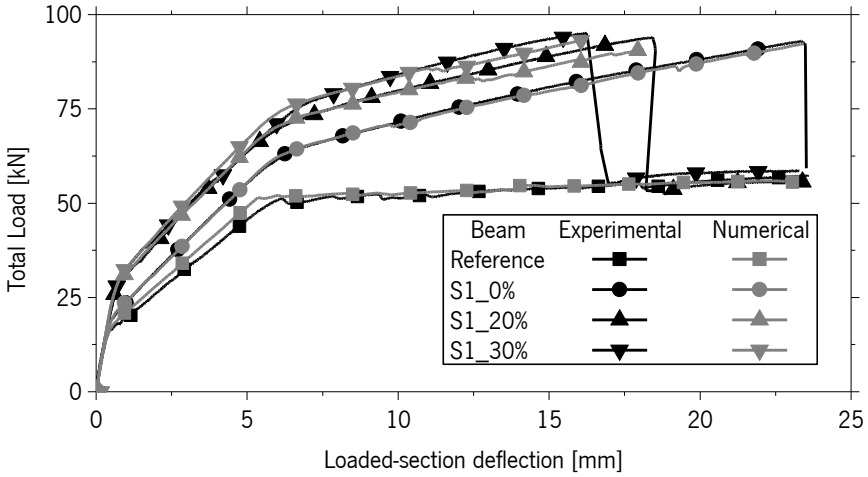

Figure 179 – Total load versus loaded-section deflection – Series I (adjusted properties).

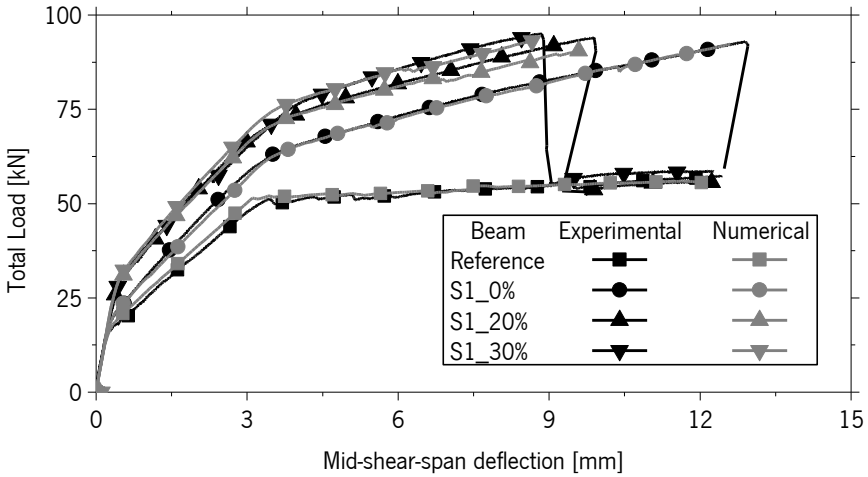

Figure 180 – Total load versus mid-shear-span deflection – Series I (adjusted properties).

Regarding the prediction of the steel strains, all were reasonably well predicted, as showed in Figures 181 and 182. This same observation can be made in terms of the strains measured in the concrete and in the CFRP (Figures 183 to 185).

In Figures 181 and 182, where the prediction of strain in the steel bars is depicted, it was noted that while the strain at mid-span was very well determined, the strain at the loaded-section was in general higher in the numerical model than in reality. This can be related to the incapacity of the strain gauge to measure strains immediately after steel yielding, as proven by the frequent malfunctioning of the strain gauges immediately after yielding.

It is also worth noting that from the analysis of the experimental results of Series I, reported in Chapter 5, the strain obtained in the concrete strain gauge of the S1_30% was found to be lower than expected. Observing the numerical results depicted in Figure 183, it was noted that, according to the numerical predictions, the concrete strain of S1:30% was apparently measured with accuracy in the experimental tests, while the remaining beams were actually overestimated during the test.

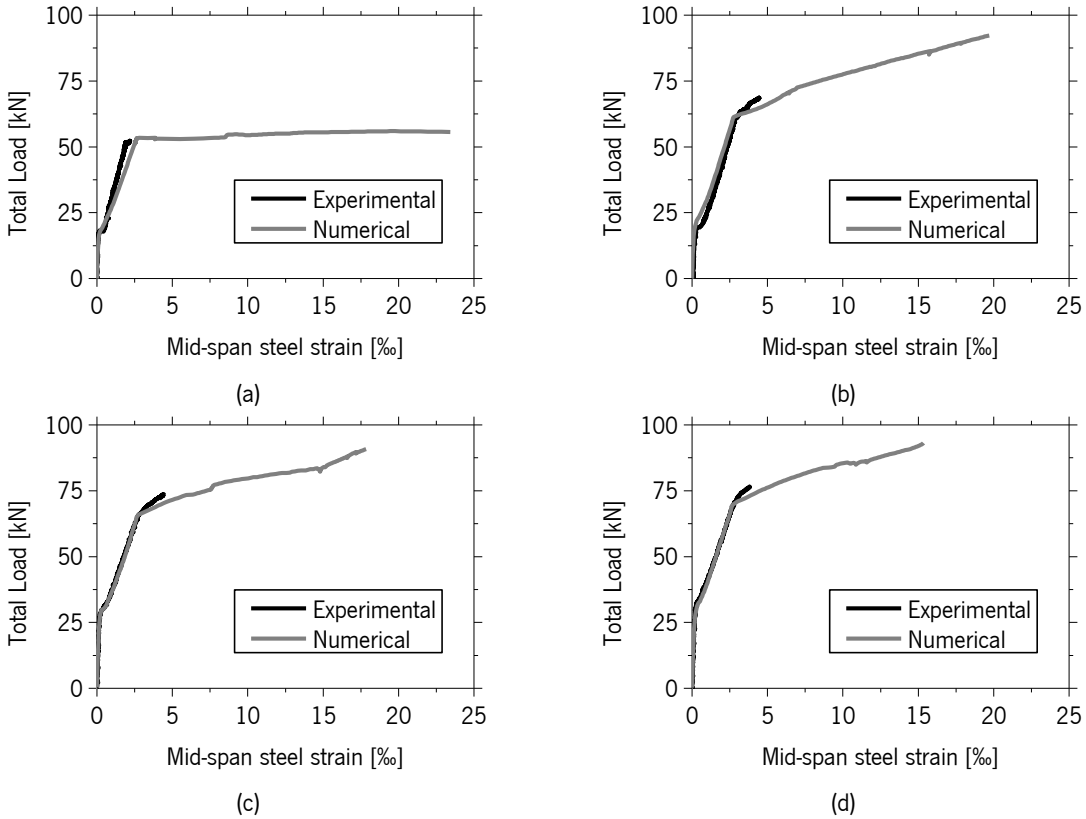

Figure 181 – Total load versus mid-span steel strain – Series I (adjusted properties):
(a) Reference, (b) S1_0%, (c) S1_20% and (d) S1_30%.

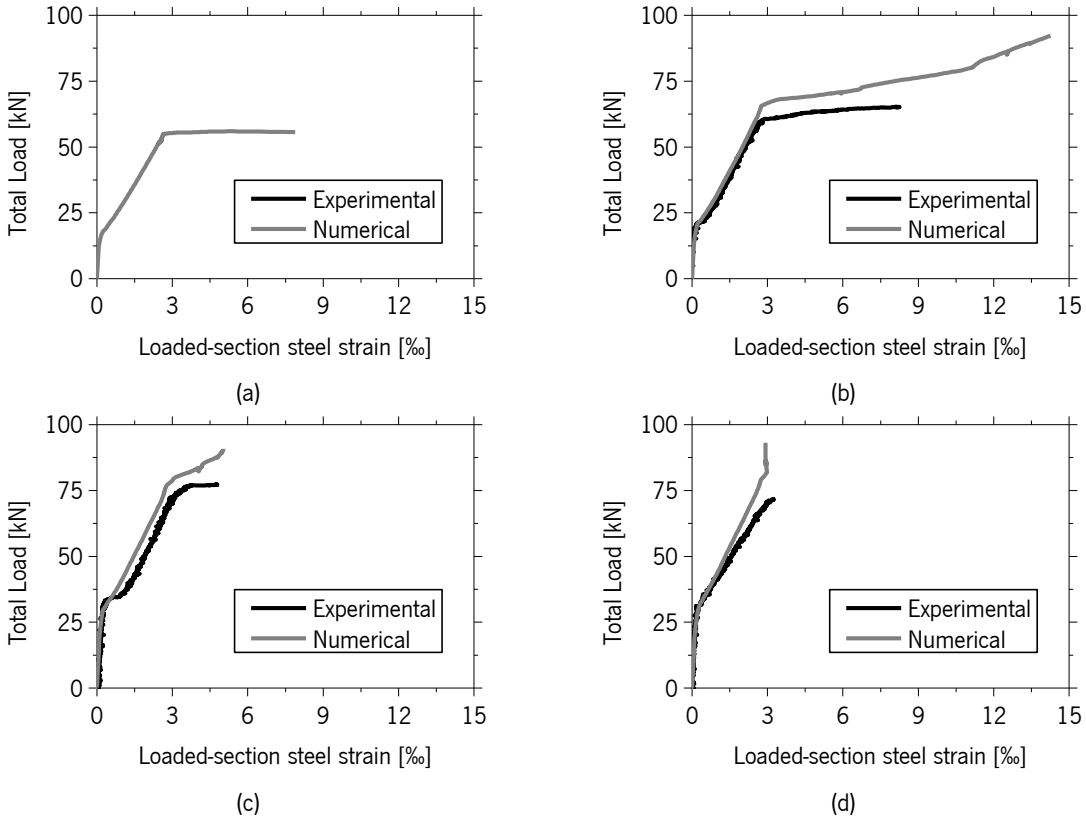

Figure 182 – Total load versus loaded-section steel strain – Series I (adjusted properties): (a) Reference, (b) S1_0%, (c) S1_20% and (d) S1_30%.

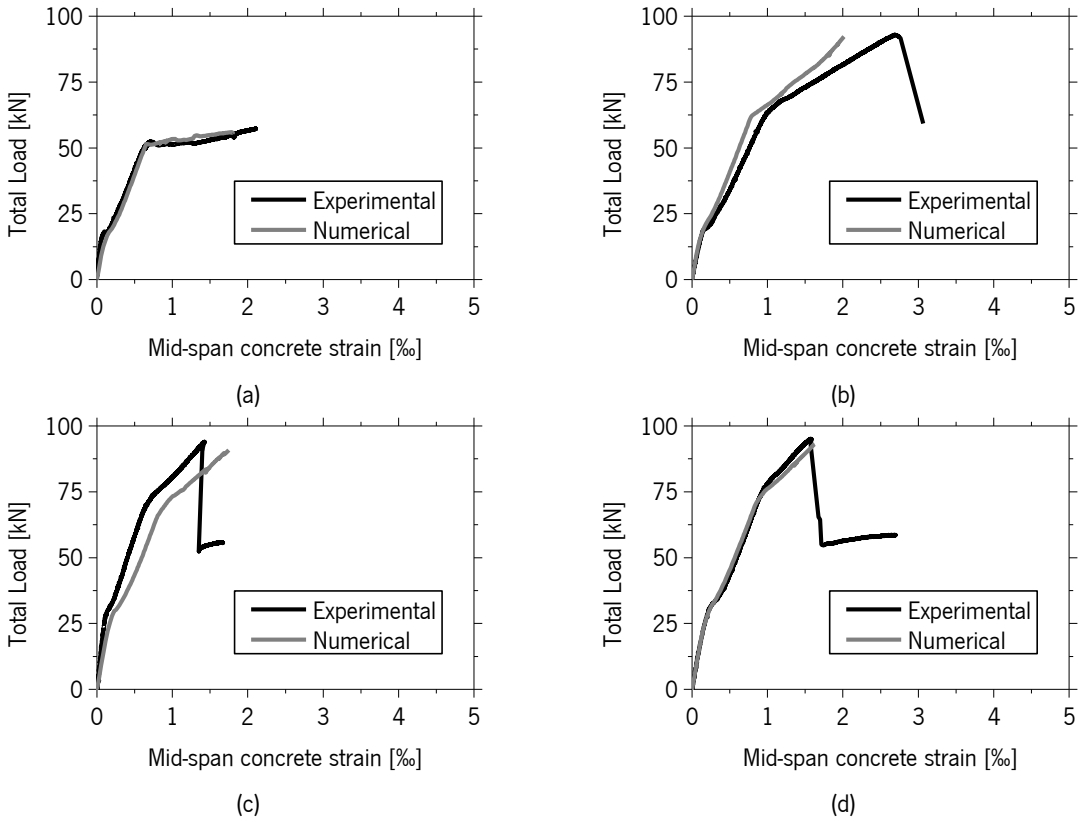

Figure 183 – Total load versus mid-span concrete strain – Series I (adjusted properties): (a) Reference, (b) S1_0%, (c) S1_20% and (d) S1_30%.

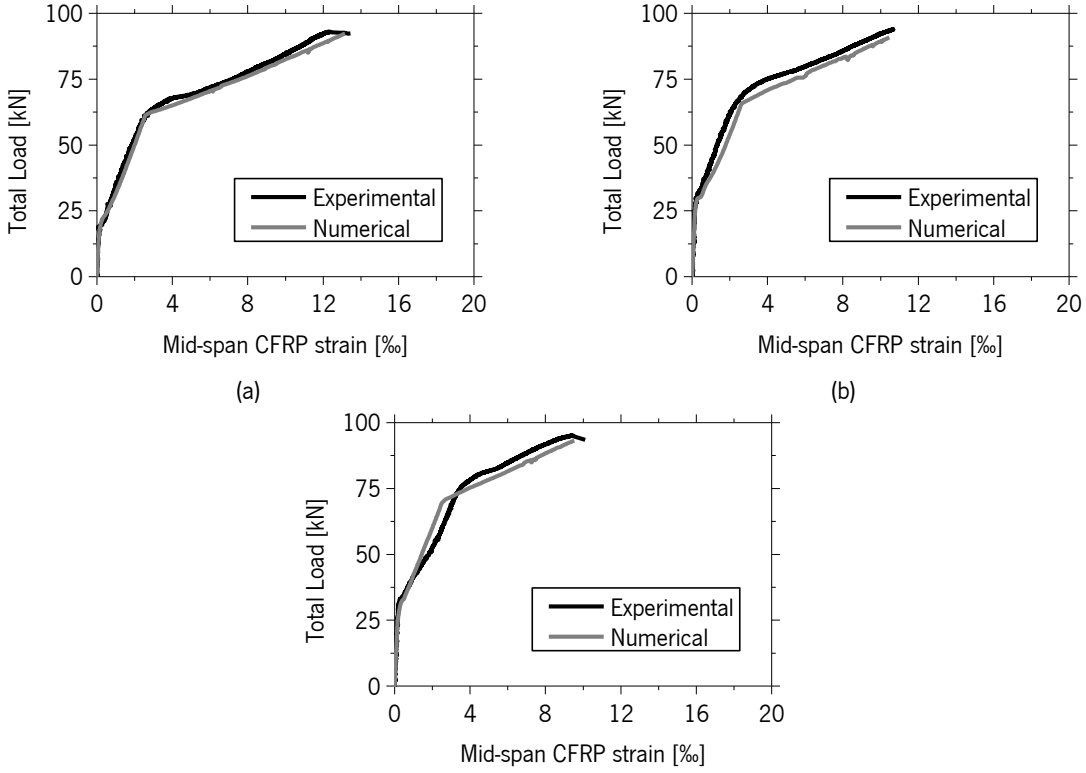

Figure 184 – Total load versus mid-span FRP strain – Series I (adjusted properties):
(a) S1_0%, (b) S1_20% and (c) S1_30%.

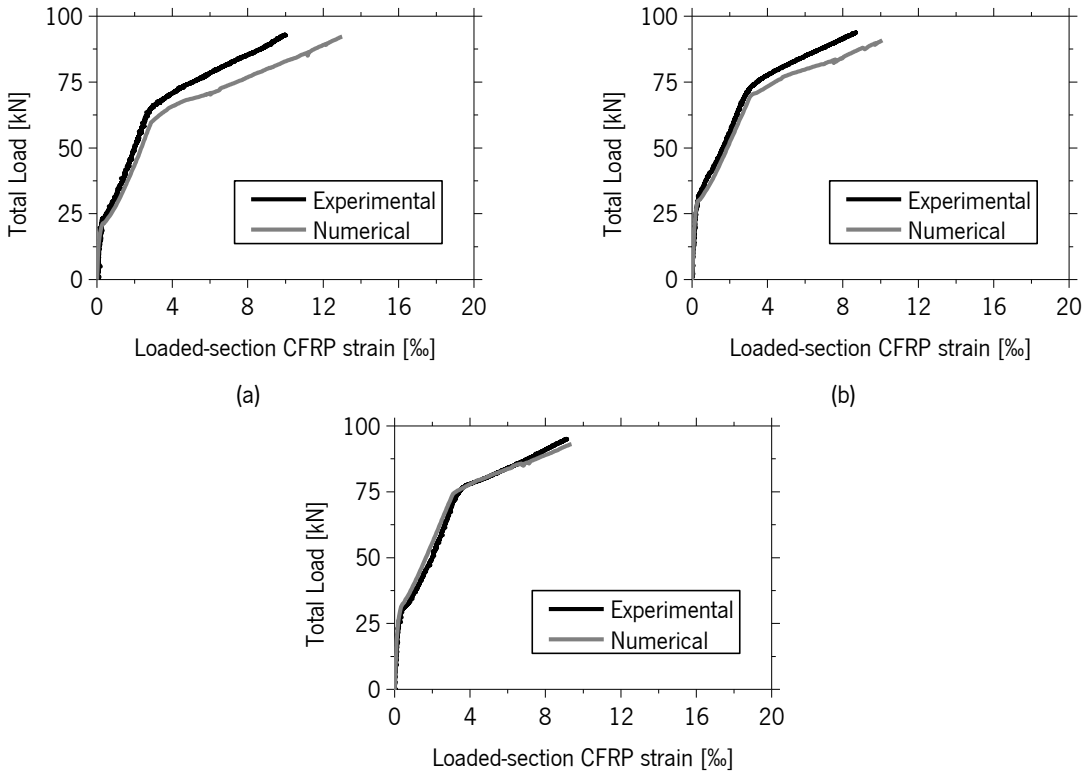

Figure 185 – Total load versus loaded-section CFRP strain – Series I (adjusted properties):
(a) S1_0%, (b) S1_20% and (c) S1_30%.

Regarding the comparison of the experimental crack pattern and the smeared crack pattern obtained numerically, it is visible from Figure 186 that they exhibit exceptional agreement, although the reduction of cracked length was not as pronounced as observed in the real beams.

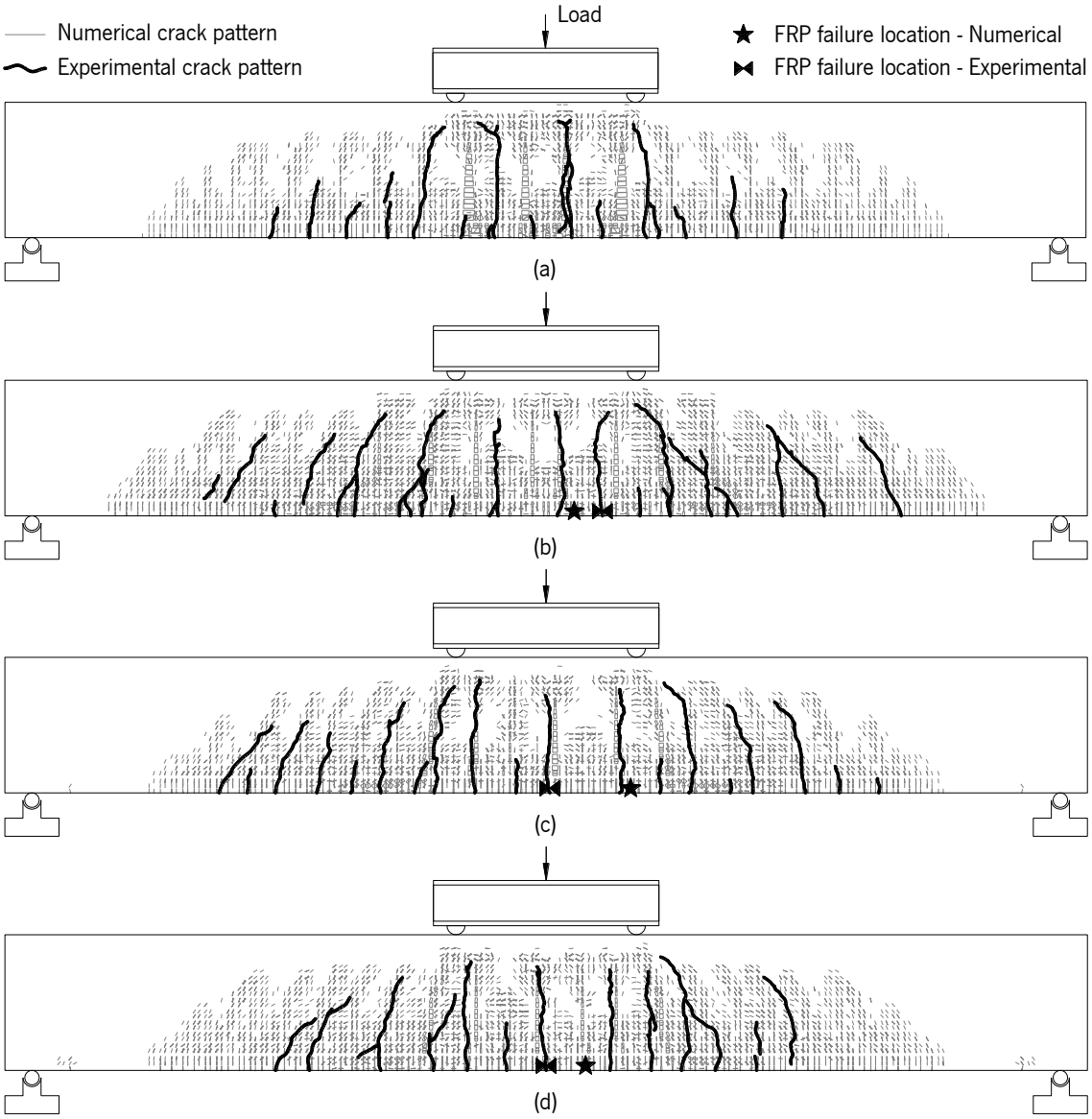

Figure 186 – Comparison between the experimental and numerical crack patterns of the beams of Series I: (a) Reference, (b) S1_0%, (c) S1_20% and (d) S1_30%.

Although Figure 186 depicts the smeared crack pattern obtained numerically, it is visible that the cracks display some tendency to group with approximately the same spacing as the discrete cracks observed. Regarding the location of the CFRP failure in the numerical model, also depicted in Figure 186, it occurred, as expected, within the pure bending zone and usually within about 100 mm of the real failure location.

6.2.2 Series II

The beams were modelled using the mesh depicted in Figure 187. Again, the properties of the materials had to be adjusted to better fit experimental and numerical results, as detailed in Tables 59 to 61. In this case, the elastic modulus of the CFRP laminate obtained during prestress application was adopted as the original elastic modulus and the tensile strength was estimated by the numerical simulations, corresponding to the deflection at maximum load capacity (Table 59).

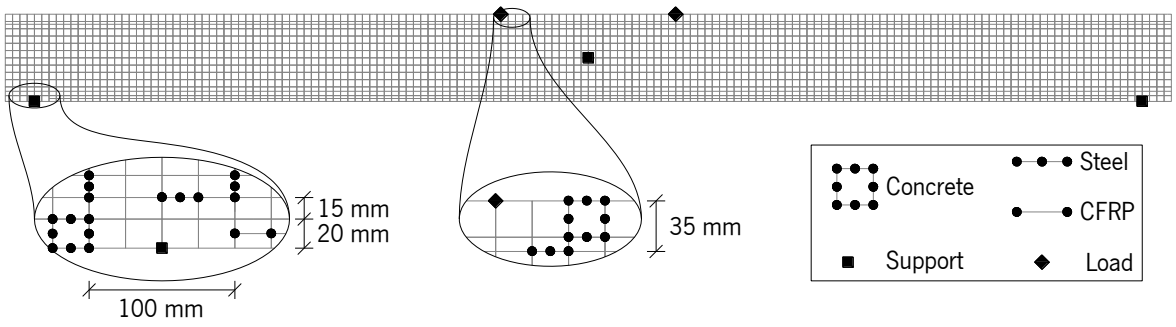

Figure 187 – Mesh and support conditions of the beams of Series II.

Table 59 – CFRP properties used in the numerical models – Series II.

Property	Prestress Level (Original Properties)					Prestress Level (Optimized Properties)				
	0%	20%	30%	40%	50%	0%	20%	30%	40%	50%
E_f [GPa]	150	146.5	150.5	112	181			178		
f_u [MPa]	2160	2039	2090	1586	2431	2510	2484	2381	2278	2395

Table 60 – Concrete properties used in the numerical models – Series II.

Model	ν	E_c [GPa]	f_c [MPa]	f_t [MPa]	ξ_1	α_1	ξ_2	α_2	G_f [N/mm]
Original properties	0.2	40.2	47.8	2.45	0.1	0.5	0.3	0.2	0.089898
Adjusted properties									

Table 61 – Steel properties used in the numerical models – Series II.

Rod	Model	ε_y [‰]	f_y [MPa]	ε'_y [‰]	ε_u [‰]	f_u [MPa]
6 mm	Original properties Adjusted properties	3.07	648	10	45	680
10 mm	Original properties Adjusted properties	2.66	538	2.66	120	634

Modelling the beams with the original properties produced, apart from S2_40%, a fairly good approachof the behaviour of the beams, as reported in Figure 188. As previously referred, the beam reinforced with the passive laminate exhibited an abnormally low initial stiffness and the numerical model confirmed that fact, since all other models revealed a good agreement. However, some

extraneous details were detected while analysing the load versus mid-span deflection curve, as will be discussed hereafter.

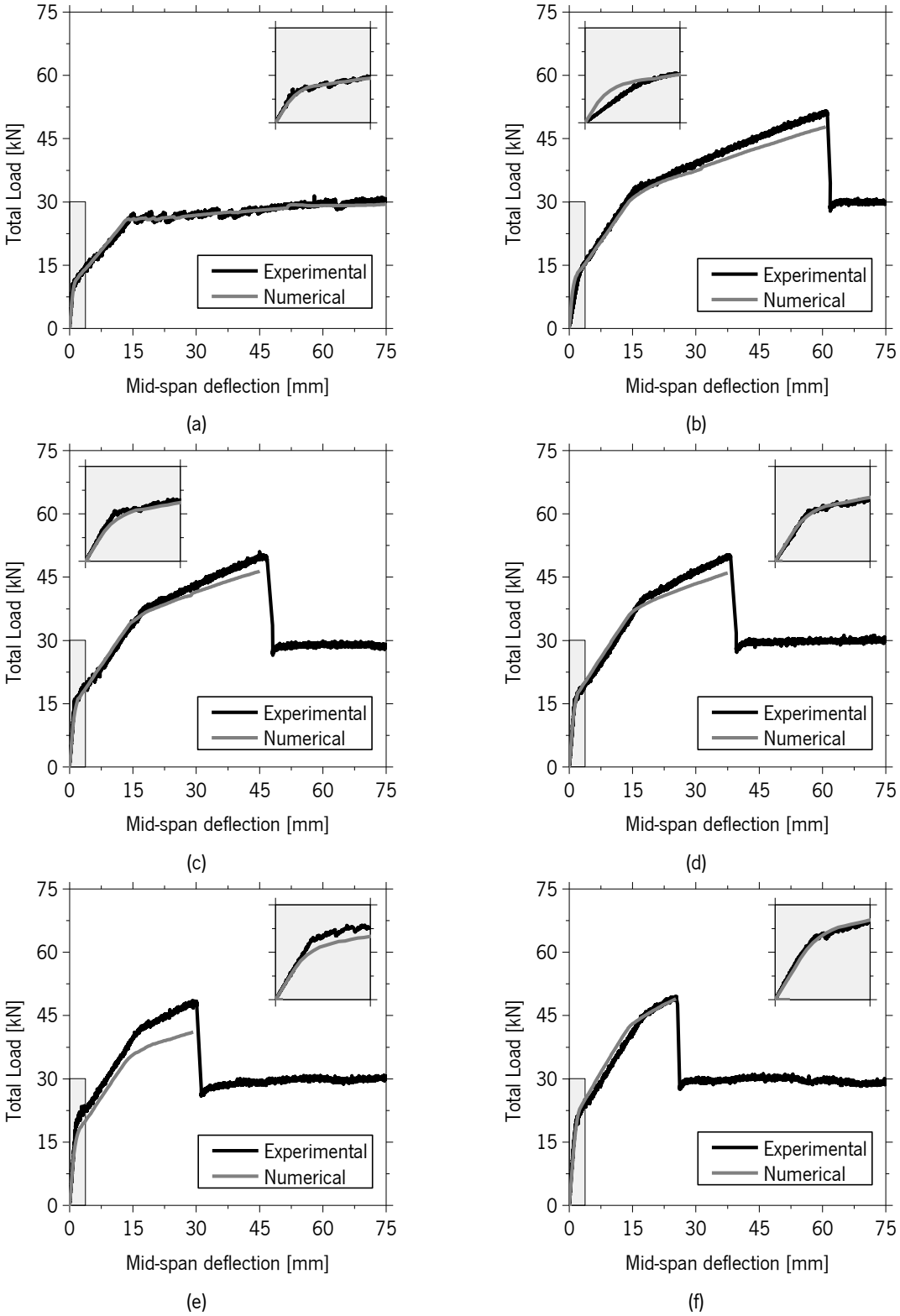

Figure 188 – Total load versus mid-span deflection – Series II (original properties): (a) Reference, (b) S2_0%, (c) S2_20%, (d) S2_30%, (e) S2_40% and (f) S2_50%.

The behaviour of the Reference beam, as depicted in Figure 188a, was very well predicted by the numerical model, indicating that the properties of both concrete and steel, determined in the individual material tests, are most likely correct. Regarding the CFRP strengthened beams, S2_50% was the one that revealed better agreement in terms of post-yielding slope, indicating that the elastic modulus used in this model is probably one that realistically represents the properties of the CFRP laminate.

Due to the consideration of different elastic modulus of the CFRP in each series, a significant difference of slope in the load-deflection curve in the post-yielding phase, as well as in the location of the yielding point, was observed in most cases.

By curve fitting process, the elastic modulus of the CFRP was estimated to be about 178 GPa, since it was the one matching with higher accuracy the response of the beams in the post-yielding phase (see Table 59). This elastic modulus value immediately improved the precision of the numerical model prediction, as depicted in Figure 189, since it shifted the location of the yielding points to a more realistic position.

As in this case the concrete properties used to model the beams were the same in all beams, a more conceptual evaluation of the prestress effectiveness can be made. For example, when observing the cracking load of the beams S2_20% and S2_40% it is visible that it was slightly underestimated by the numerical model, revealing that these beams had a higher concrete tensile strength in comparison to the other beams of this series. This confirms that a difference in tensile strength could cause the coincident load-deflection curves of S2_20% and S2_30% (and S2_40% and S2_50%), as already suggested in Chapter 5. Initially, it was suggested that these matching load-deflection curves could be caused by an insufficient prestress quality, but it is now demonstrated that it is caused by a slightly superior tensile strength.

Regarding the negative deflection produced by the prestress estimated by the numerical model, and reported in Table 62, it was verified that it was overestimated for all beams. However, in the case of the bi-dimensional model, this overestimation was more pronounced than in the three-dimensional model, since the upward deflection of the beams was in this 2D-modelling about 7% larger when compared to the corresponding values determined from the 3D approach (Table 54).

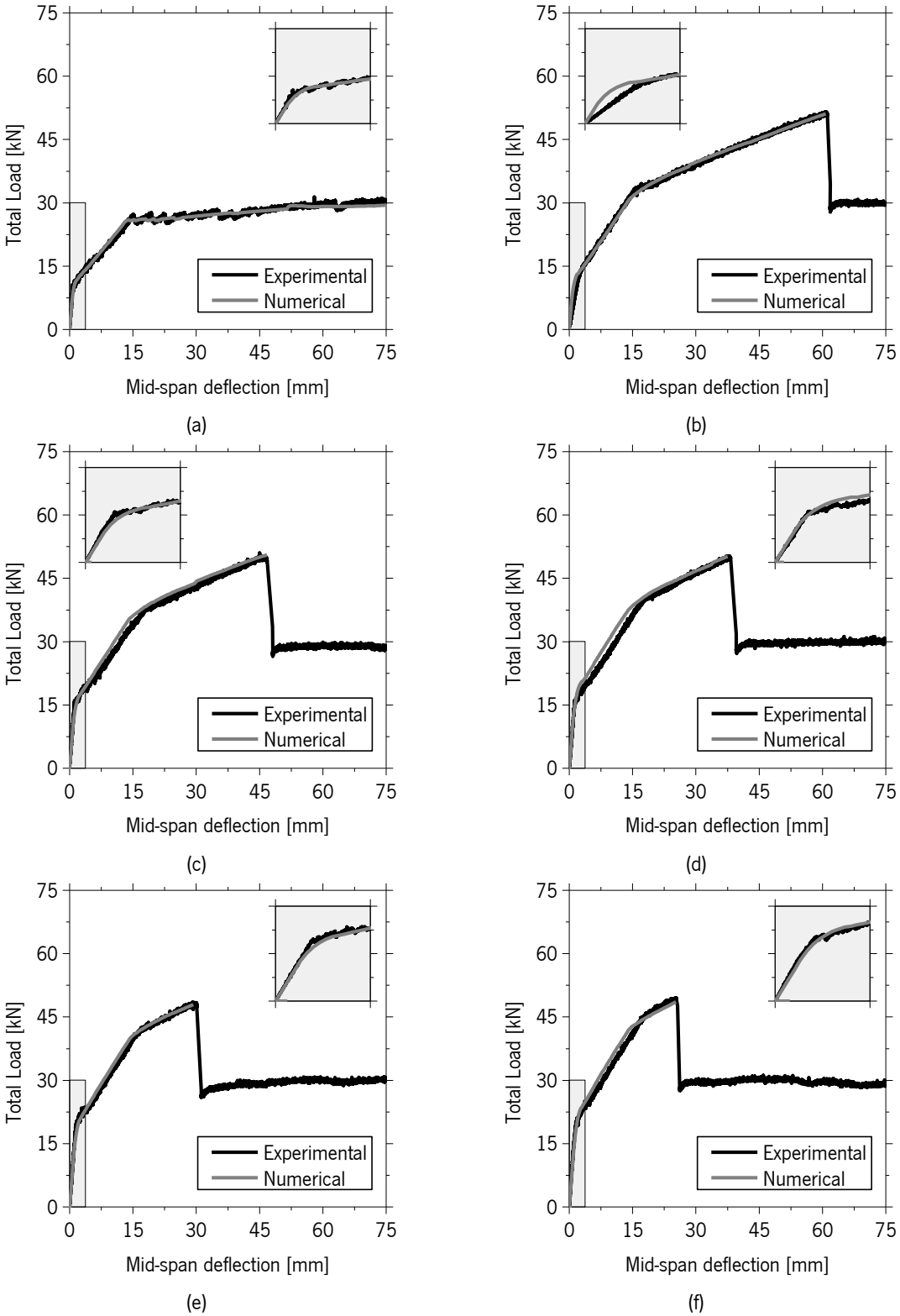

Figure 189 – Total load versus mid-span deflection – Series II (adjusted properties): (a) Reference, (b) S2_0%, (c) S2_20%, (d) S2_30%, (e) S2_40% and (f) S2_50%.

Table 62 – Numerical mid-span deflection – 2D model – Series II.

Specimen	$\delta_{0,exp}$ [mm]	$\delta_{0,num}$ [mm]	$\Delta\delta_0$ [%]
20%	0.180	0.231	-29
30%	0.308	0.347	-13
40%	0.385	0.462	-20
50%	0.473	0.578	-22

Note: $\Delta\delta_0 = \left(\delta_{0,exp} - \delta_{0,num}\right)/\delta_{0,exp} \times 100$

In terms of loaded-section deflection and mid-shear-span deflection, the behaviour of the beams was again very well predicted, as depicted in Figures 190 and 191.

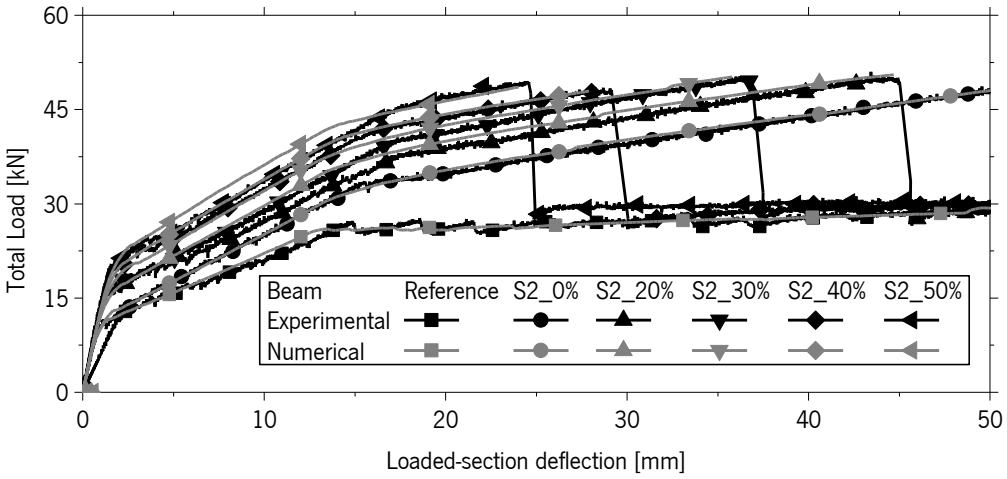

Figure 190 – Total load versus loaded-section deflection – Series II (adjusted properties).

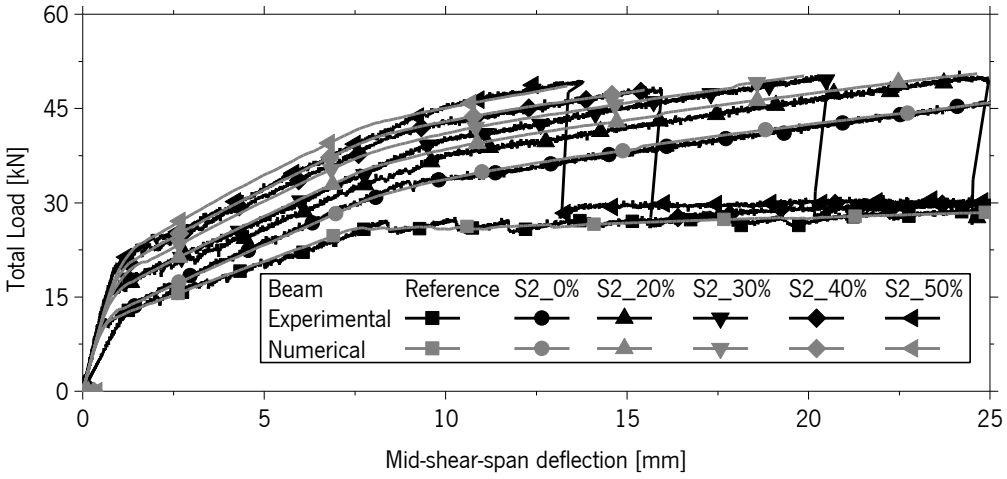

Figure 191 – Total load versus mid-shear-span deflection – Series II (adjusted properties).

The most significant difference between the experimental and numerical results is the greater difference in the location of the yielding point, since in most cases, although the load at yielding

was accurately predicted as already demonstrated in Figure 189, the deflection level was in some cases underestimated, namely in the beams strengthened with prestressed laminates.

In terms of CFRP strain prediction, depicted in Figure 192, the results were not as accurate as the deflection prediction, since the strain measured experimentally was in general abnormally large, as already referred in Chapter 4.

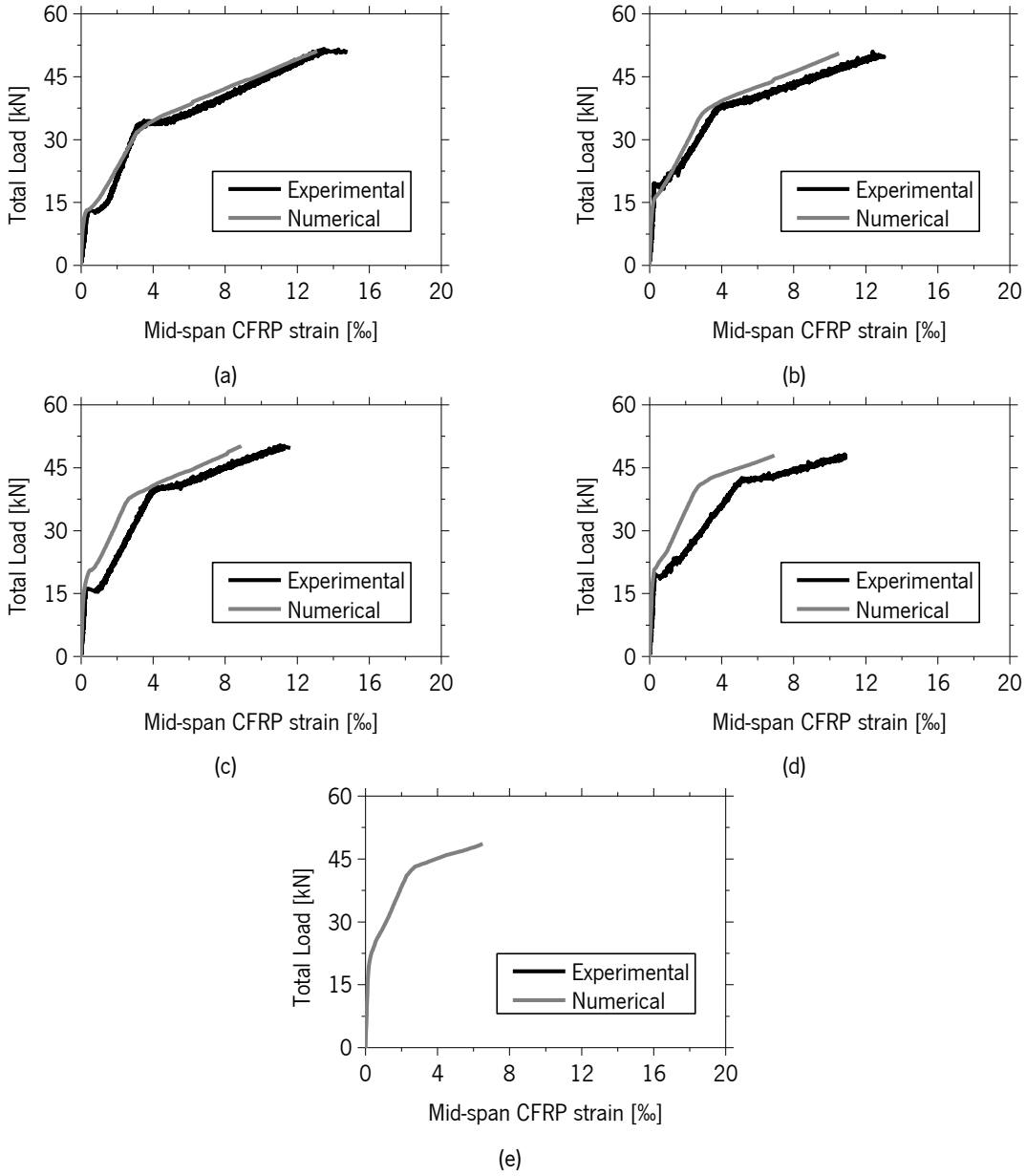

Figure 192 – Total load versus mid-span CFRP strain – Series II (adjusted properties): (a) S2_0%, (b) S2_20%, (c) S2_30%, (d) S2_40% and (e) S2_50%.

Regarding S2_50%, the strain gauge installed at mid-span was not acquired, as already reported in Chapter 4. However, it is believed that the change of acquisition system may have interfered with the strain values recorded due to the pre-existing strain on the strain gauge.

Note that, according to Figure 192, all CFRPs ruptured during the test at about 12‰ of strain, although from S2_0% to S2_40% prestress the ultimate strain was expected to be reduced by almost 50% *i.e.*, approximately 5.333‰.

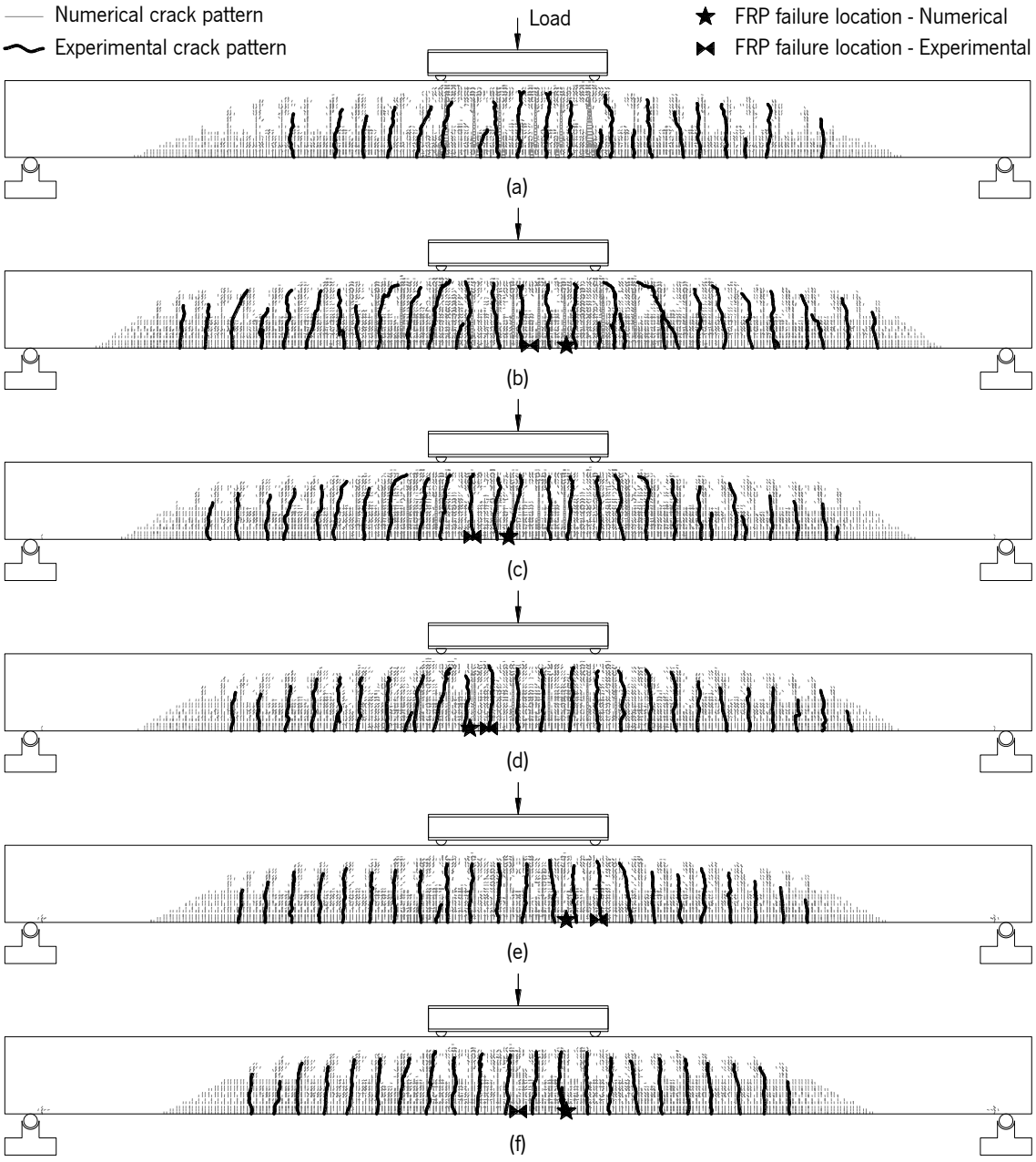

Figure 193 – Comparison between the experimental and numerical crack patterns of the beams of Series II: (a) Reference, (b) S2_0%, (c) S2_20%, (d) S2_30%, (e) S2_40% and (f) S2_50%.

Finally, the comparison between experimental and numerical crack pattern revealed good agreement in terms of distribution and also spacing of the main cracks, as depicted in Figure 193. Concerning the location of the FRP failure, also reported in Figure 193, it was observed to occur within the pure bending zone, quite close to the zones where CFRP rupture was observed experimentally.

6.2.3 Series III

The mesh used to model Series III beams is depicted in Figure 194. This mesh is essentially equal to the mesh used in the previous Series but in this case, the position of the longitudinal steel bars was corrected to match right depth of installation. In Tables 63 to 65 the original and adjusted properties of the materials are presented.

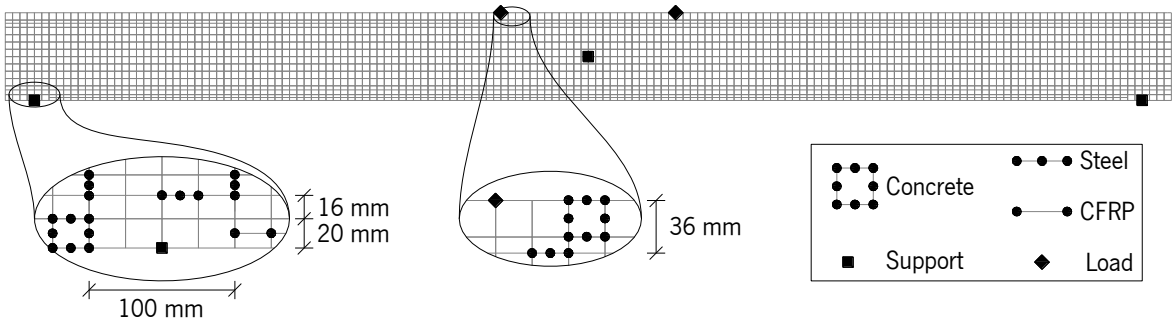

Figure 194 – Mesh and support conditions of the beams of Series III.

Table 63 – Steel properties used in the numerical models – Series III.

Rod	Model		ε_y [‰]	f_y [MPa]	ε'_y [‰]	ε_u [‰]	f_u [MPa]
8 mm	Original properties Adjusted properties		2.75	541	10	110	644
12 mm	Original properties		2.56	520	10	175	624
	Adjusted properties	Reference S3_0% S3_20% S3_30%	2.56	550	2.56		
		S3_40% S3_50%	2.75	590	2.75		

Table 64 – Concrete properties used in the numerical models – Series III.

Model		ν	E_c [GPa]	f_c [MPa]	f_t [MPa]	ξ_1	α_1	ξ_2	α_2	G_f [N/mm]
Original properties	All	0.2	39.7	31.6	2.45	0.1	0.5	0.3	0.2	0.06727
Adjusted properties	Reference	0.2	37.6	31.6	2.45	0.1	0.5	0.3	0.2	0.06727
	S3_0%		30.3		2.20					
	S3_20%		22.8		2.40					
	S3_30%		21.3		1.70					
	S3_40%		24.6		2.00					
	S3_50%		28.4		1.10					

Table 65 – CFRP properties used in the numerical models – Series III.

Property	Prestress Level (Original Properties)					Prestress Level (Adjusted Properties)				
	0%	20%	30%	40%	50%	0%	20%	30%	40%	50%
E_f [GPa]	150	139	219	135.5	176			204		
f_t [MPa]	2107	1987	2985	1964	2425	2662	2590	2661	2611	2634

From the analysis of Figure 195, it is visible that the original properties lead to a relatively high level of inaccuracy in the predictive performance of the simulations. While a constant elastic modulus of the concrete was adequate to model the previous two series of beams, in this case, a larger range of concrete elastic modulus has to be used to match experimental and numerical load-deflection relationship, especially in the linear-elastic stage. As the beams of these series were delivered ready and cured, it is believed that the company casted each of these beams using different batches of concrete, causing this unexpected variation of stiffness.

Figure 195a also suggests that the average steel reinforcement properties indicated in Table 40 do not correspond to the properties of the steel applied in this beam, since in the post-cracking phase of the Reference beam, the slope of numerical and experimental curves was relatively different. Given these observations a more realistic value for the elastic modulus of the longitudinal steel reinforcement was determined, as well as a new yielding strain.

By using the new yielding point determined by inverse analysis, the optimum elastic modulus of the CFRP was assessed by using this same methodology. Observing the curves of Figure 195, it is visible that the best simulation, mainly in the branch governed by the properties of the CFRP laminate (the last branch before CFRP rupture), was S3_30%. This indicates that for this series of beams, the elastic modulus of the FRP used is larger than in the previous series. It was found that to match the load-deflection relationship of the branch after yield initiation, the consideration of an elastic modulus of the CFRP of about 204 GPa was required. Although this value is unexpectedly high, it is within the range of values obtained in the pullout bending tests described in Chapter 3 (between 179 GPa and 236 GPa). Nonetheless, to be able to match the yielding point in S3_40% and S3_50%, the steel yield stress had to be further increased.

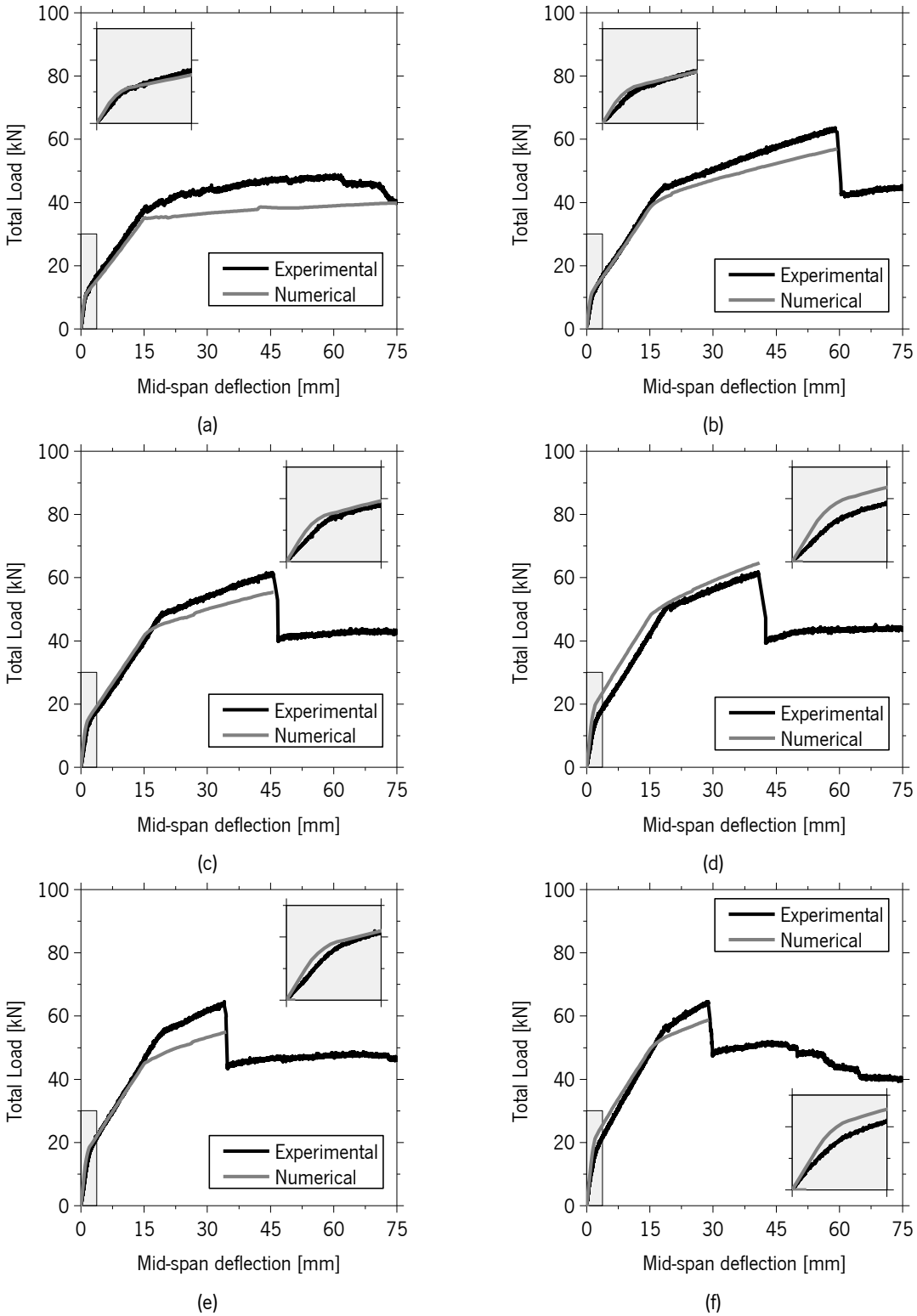

Figure 195 – Total load versus mid-span deflection – Series III (original properties): (a) Reference, (b) S3_0%, (c) S3_20%, (d) S3_30%, (e) S3_40% and (f) S3_50%.

The new values of the properties determined exhibit much more potential to predict the behaviour of the beams of this series, as depicted in Figure 196.

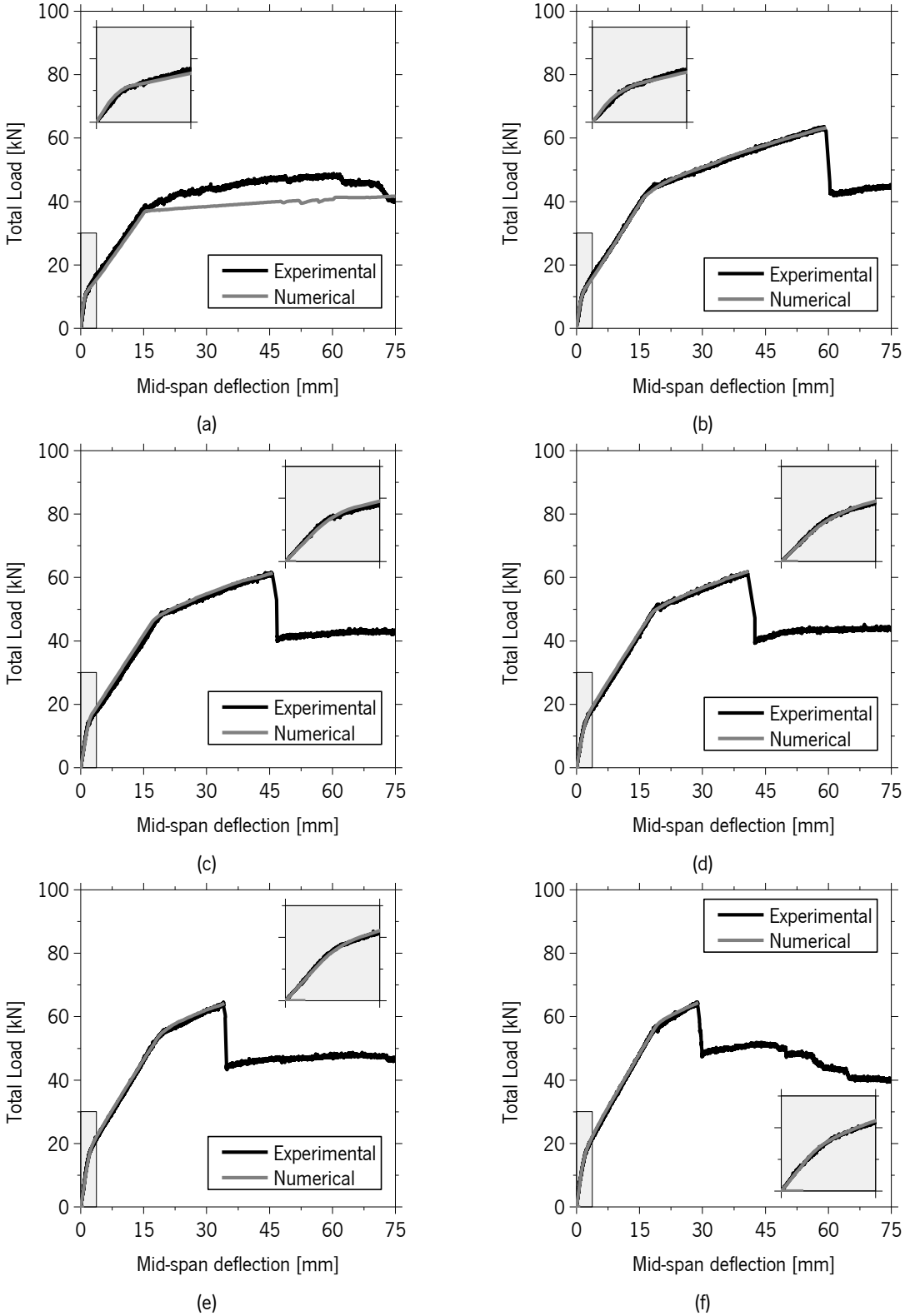

Figure 196 – Total load versus mid-span deflection – Series III (adjusted properties): (a) Reference, (b) S3_0%, (c) S3_20%, (d) S3_30%, (e) S3_40% and (f) S3_50%.

The predictive performance was increased significantly in all cases, except in the case of the post-yielding branch of the Reference beam, which exhibited a relatively high hardening response. This

hardening was not captured by the numerical simulation since an almost rigid plastic behaviour was assumed the steel bars after yield initiation. It is believed that, given the irregularities of the beam's surface, some abnormally high sliding resistance was introduced by the supports on this beam, contributing to the increase of its load carrying capacity at this stage.

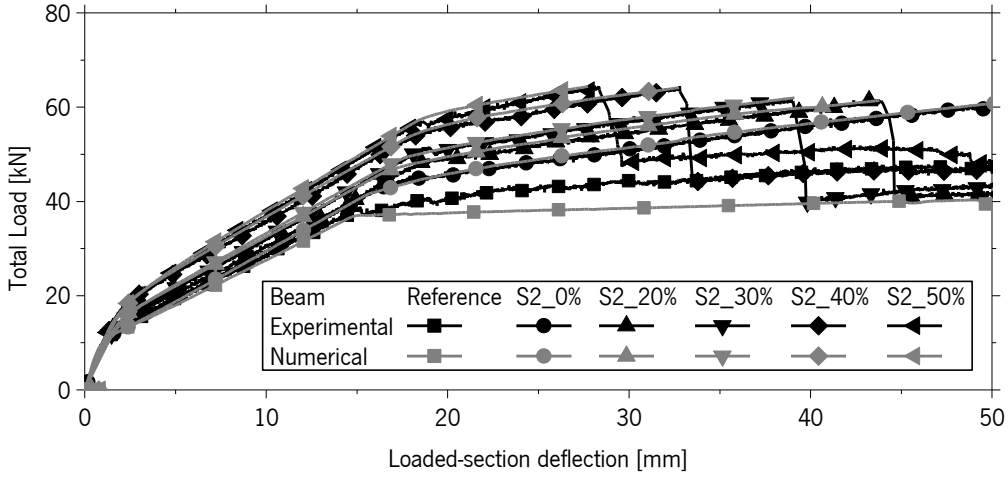

Figure 197 – Total load versus loaded-section deflection – Series III (adjusted properties).

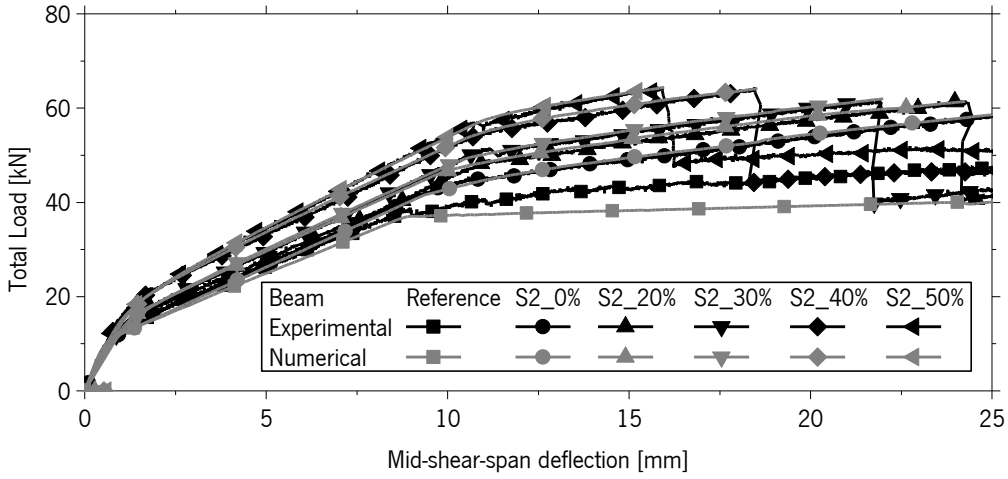

Figure 198 – Total load versus mid-shear-span deflection – Series III (adjusted properties)-

In terms of load versus CFRP strain response, only S3_0% and S3_50% demonstrated a good agreement with the experimental results. However, as suggested in Section 6.2.2, some of the strains obtained experimentally are illogical. According to the experimental results, the failure strain of the S3_0% and S3_50% would be 12.690‰ and (6.645 (due to prestress) + 6.348(during the test)) = 12.993‰, respectively. However, S3_30%, for example, according to the experimental results, would have presented a strain in the CFRP of about (4.010 (due to prestress) + 14.421(during the test)) = 18.431‰, which is not acceptable.

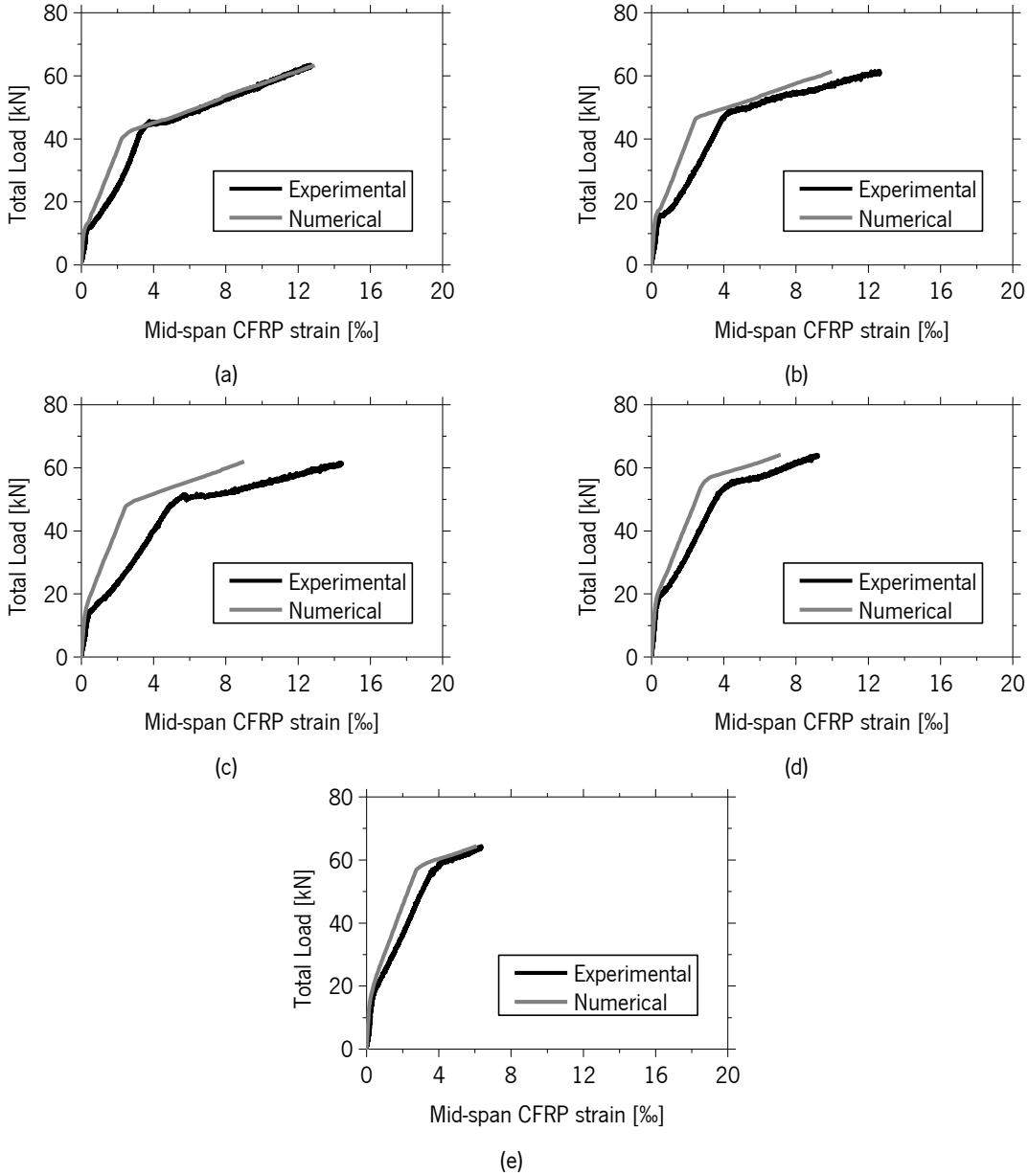

Figure 199 – Total load versus mid-span FRP strain – Series III (adjusted properties): (a) S3_0%, (b) S3_20%, (c) S3_30%, (d) S3_40% and (e) S3_50%.

The crack distribution numerically predicted was again, in general, similar to the one obtained experimentally, except for S3_50% that apparently exhibited less cracks in reality than in the numerical model. Moreover, the failure of the CFRP was again reasonably predicted since it was always located within the pure bending moment zone.

As presented for the previous series, after determining the optimum properties to describe the behaviour of the beams up to failure, the initial deflection of the beams obtained numerically is compared to the one registered experimentally (Table 66). Like in the previous series, the bi-dimensional model predicts a larger upward deflection than the three dimensional model

(Table 54), and both numerical approaches overestimate the values measured experimentally (Table 66). As already presented for the previous series, the load versus loaded-section deflection and the load versus mid-shear-span deflection are also presented in Figures 197 and 198 in order to confirm the accuracy of the predictions.

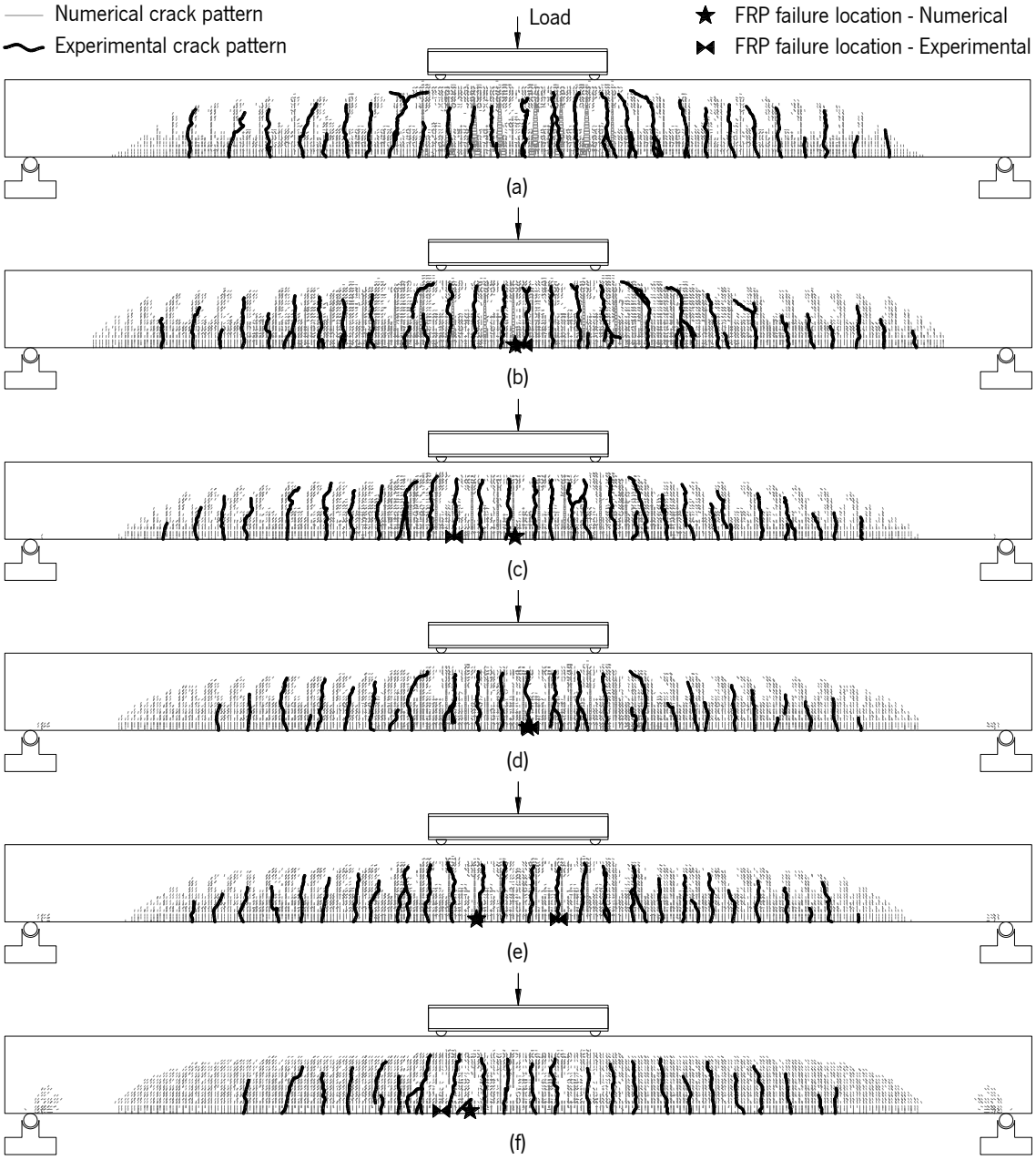

Figure 200 – Comparison between the experimental and numerical crack patterns of the beams of Series III: (a) Reference, (b) S3_0%, (c) S3_20%, (d) S3_30%, (e) S3_40% and (f) S3_50%.

Table 66 – Numerical mid-span deflection – 2D model – Series III.

Specimen	$\delta_{0,exp}$ [mm]	$\delta_{0,num}$ [mm]	$\Delta\delta_0$ [%]
20%	0.27	0.423	-57
30%	0.433	0.671	-55
40%	0.606	0.792	-31
50%	1.112	0.874	21

Note: $\Delta\delta_0 = \left(\delta_{0,exp} - \delta_{0,num}\right) \big/ \delta_{0,exp} \times 100$

6.2.4 One-dimensional model

Since the previous two-dimensional analysis of the reinforced beams were capable of simulating the experimental results with high accuracy, it was decided to explore the possibility of modelling the beams using the moment-curvature section analysis combined with the matrix displacement method (Barros & Fortes 2005, Varma 2012). For this purpose, the cross section of each of the tested beams was discretized in 6 macro-layers, as depicted in Figure 201. Each of these layers was then divided in smaller slices, making a total of 60 layers per beam, as reported in Table 67.

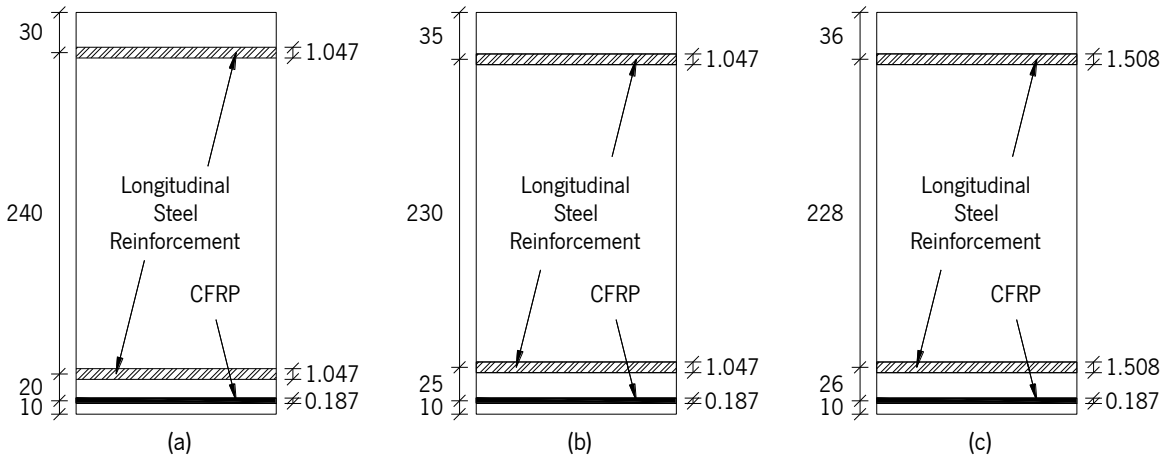

Figure 201 – Concrete section macro-layers (dimensions in millimetres): (a) Series I, (b) Series II and (c) Series III.

The CFRP and steel layers were considered using the exact same properties and behaviour previously presented in the plane stress model while the concrete properties were adjusted to improve curve fitting preserving the proportionality of the tri-linear post-cracking behaviour resulting in the tensile stress-strain relationship illustrated in Figure 202. The area of the plot after cracking, G_f', was kept constant within the same series but as the cracking strain, ε_1, varied in some specimens, the remaining strains of the tri-linear law were changed accordingly in beams of the same series.

Table 67 – Size and number of layers.

Layer	Series I		Series II		Series III	
	No. of layers	Thickness [mm]	No. of layers	Thickness [mm]	No. of layers	Thickness [mm]
Top layer of concrete	5	5.89528024	6	5.74606687	6	5.87433629
Top steel layer	1	1.04719755	1	1.04719755	1	1.50796447
Intermediate layer of concrete	47	5.08410218	45	5.08784005	45	5.03315635
Bottom layer of steel	1	1.04719755	1	1.04719755	1	1.50796447
Central layer of concrete	3	6.46102263	4	6.09576697	4	6.28817111
CFRP layer	1	0.18666667	1	0.18666667	1	0.18666667
Bottom layer of concrete	2	4.95333333	2	4.95333333	2	4.95333333

The compressive resistance of the concrete of each series was enlarged by 8 MPa to account for the confinement provided by the steel stirrups to the concrete, and the peak strain in compression was computed according to EN 1992-1-1:2004. In Tables 68 to 70, each of the notable points of the curves characterizing the concrete behaviour is presented.

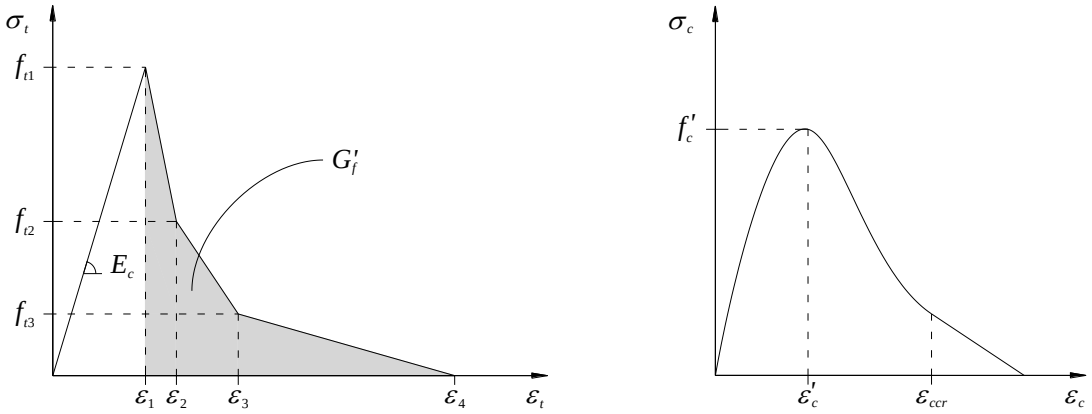

Figure 202 – Concrete behaviour: (a) tensile and (b) compressive.

Table 68 – Concrete properties used for section analysis – Series I.

Model	E_c [GPa]	ε_c' [‰]	f_c' [MPa]	ε_1 [‰]	f_{t1} [MPa]	ε_2 [‰]	f_{t2} [MPa]	ε_3 [‰]	f_{t3} [MPa]	ε_4 [‰]	G_f'
Reference	27.4	2.05	40.2	0.0639	1.75	0.4263	0.875	1.1511	0.350	3.6880	0.00136
S1_0%				0.0730	2.00	0.3901	1.000	1.0243	0.400	3.2441	
S1_20%				0.0912	2.50	0.3449	1.250	0.8523	0.500	2.6281	
S1_30%				0.0730	2.00	0.3901	1.000	1.0243	0.400	3.2441	

Table 69 – Concrete properties used for section analysis – Series II.

Model	E_c [GPa]	ε_c' [‰]	f_c' [MPa]	ε_1 [‰]	f_{t1} [MPa]	ε_2 [‰]	f_{t2} [MPa]	ε_3 [‰]	f_{t3} [MPa]	ε_4 [‰]	G_f'
All	40.2	2.32	55.8	0.0609	2.45	0.2560	1.225	0.6461	0.4900	2.0114	0.00103

Table 70 – Concrete properties used for section analysis – Series III.

Model	E_c [GPa]	ε_c' [‰]	f_c' [MPa]	ε_1 [‰]	f_{t1} [MPa]	ε_2 [‰]	f_{t2} [MPa]	ε_3 [‰]	f_{t3} [MPa]	ε_4 [‰]	G_f'
Reference	37.6	2.04	39.6	0.0652	2.45	0.2111	1.225	0.5030	0.490	0.0652	0.00077
S3_0%	30.3			0.0726	2.20	0.2351	1.100	0.5602	0.440	0.0726	
S3_20%	22.8			0.1053	2.40	0.2543	1.200	0.5522	0.480	0.1053	
S3_30%	21.3			0.0798	1.70	0.2902	0.850	0.7108	0.340	0.0798	
S3_40%	24.6			0.0813	2.00	0.2601	1.000	0.6177	0.400	0.0813	
S3_50%	28.4			0.0387	1.10	0.3638	0.550	1.0140	0.220	0.0387	

The moment-curvature relationships obtained by section-analysis for Series I is shown in Figure 203. According to this plot, it is clearly demonstrated that the moment at cracking initiation is approximately the same in the 20% and 30% prestress beams.

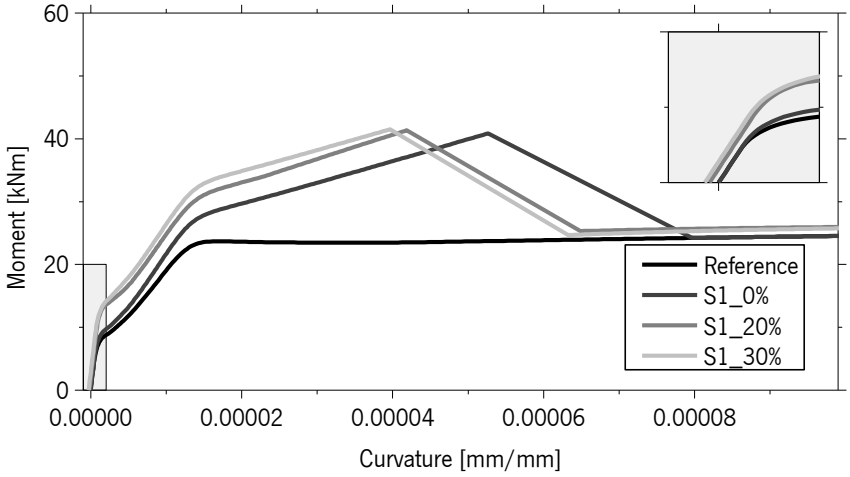

Figure 203 – Moment-curvature relationship – Series I.

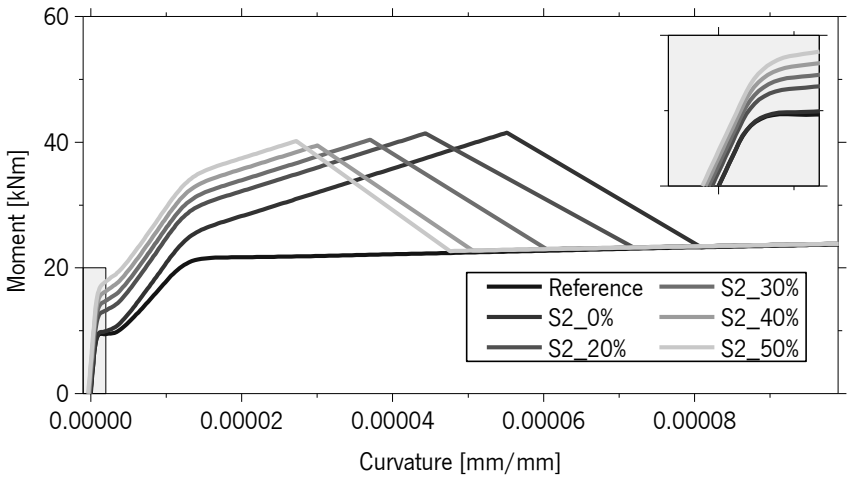

Figure 204 – Moment-curvature relationship – Series II.

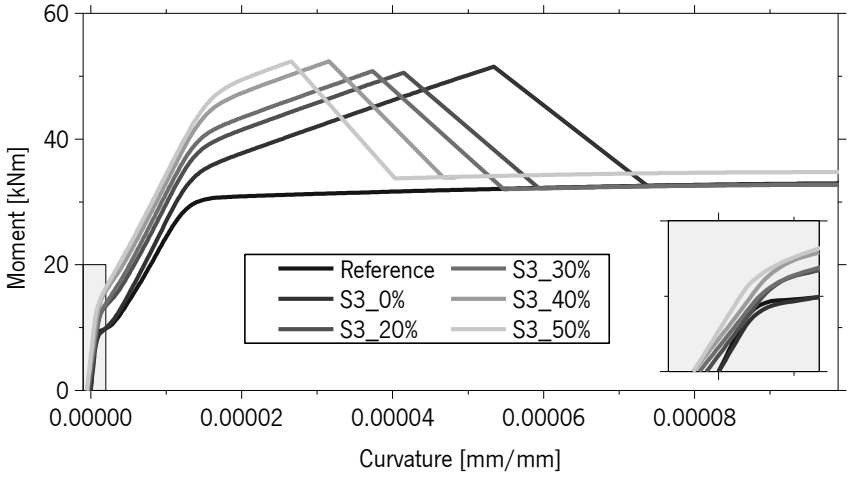

Figure 205 – Moment-curvature relationship – Series III.

In Figures 204 and 205, the moment-curvature relationship of Series II and III is also depicted, and the characteristics of these curves are practically the same observed for the corresponding load versus mid-span deflection predicted numerically with the FEM approach.

Using the initial curvature, χ_0, from the moment-curvature relationship, it is possible to estimate the initial mid-span deflection, δ_0, introduced in a simply supported beam by the prestress, using Eq. 40 (see deduction in Annex C). Table 71 summarizes the mid-deflection obtained from the initial curvature and the high variation of results is in agreement with the values previously obtained both in the 3D and 2D simulations.

$$\delta_0 = \chi_0 \left(\frac{L^2}{8} - \frac{a^2}{2} \right) \tag{40}$$

where L is the total length of the beam, between supports and a is the distance between the support and the free end of the prestressed CFRP.

Table 71 – Numerical mid-span deflection – 1D model.

Series	Specimen	χ_0 [$\times 10^{-6}$/m]	$\delta_{0,exp}$ [mm]	$\delta_{0,num}$ [mm]	$\Delta\delta_0$ [%]
Series I	S1_20%	0.18161	0.078	0.110	-41
	S1_30%	0.27548	0.178	0.167	6
Series II	S2_20%	0.13064	0.180	0.236	-31
	S2_30%	0.19609	0.308	0.354	-15
	S2_40%	0.26165	0.385	0.473	-23
	S2_50%	0.32752	0.473	0.592	-25
Series III	S3_20%	0.24143	0.270	0.436	-62
	S3_30%	0.38267	0.433	0.691	-60
	S3_40%	0.45214	0.606	0.817	-35
	S3_50%	0.51122	1.112	0.923	17

Comparing the results obtained by the one-dimensional model with the ones previously obtained in with the 3D model (in Table 54) and with the 2D model (in Tables 58, 62 and 66) it is visible that as the simplification of the model increased, the discrepancy between experimental and numerical mid-span deflection also increased.

However, in terms of load-deflection prediction obtained using this simplified approach, shown in Figures 206 to 208, the accuracy of the prediction is fairly good.

The short beams were the ones exhibiting the lowest ultimate mid-span displacement, and this fact is possibly due to the larger contribution of the shear components than in the other series of beams. In the full-scale beams, where the behaviour up to failure is dominated by the flexural components, the prediction of the ultimate deflection was remarkably good.

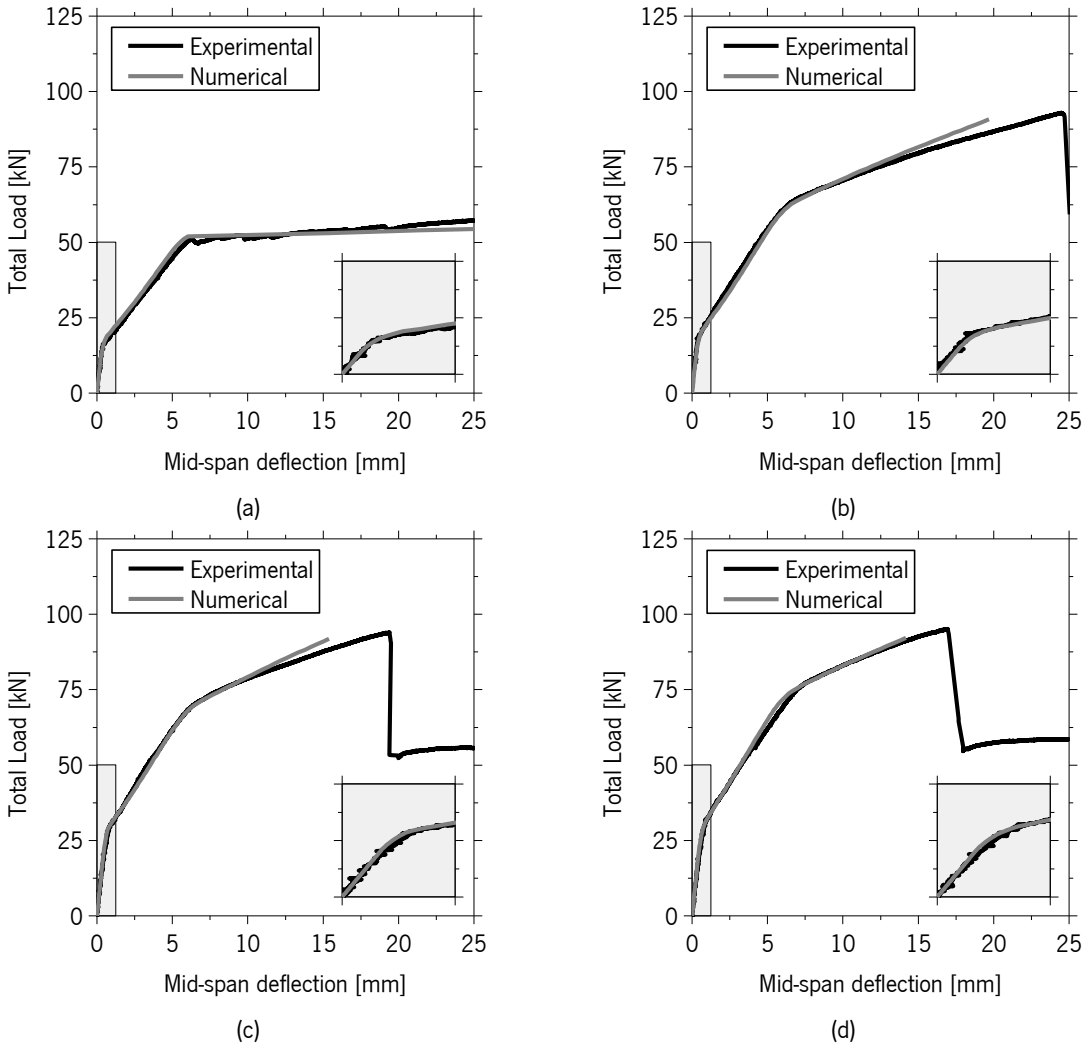

Figure 206 – Total load versus mid-span deflection – Series I (original properties):
(a) Reference, (b) S1_0%, (c) S1_20% and (d) S1_30%.

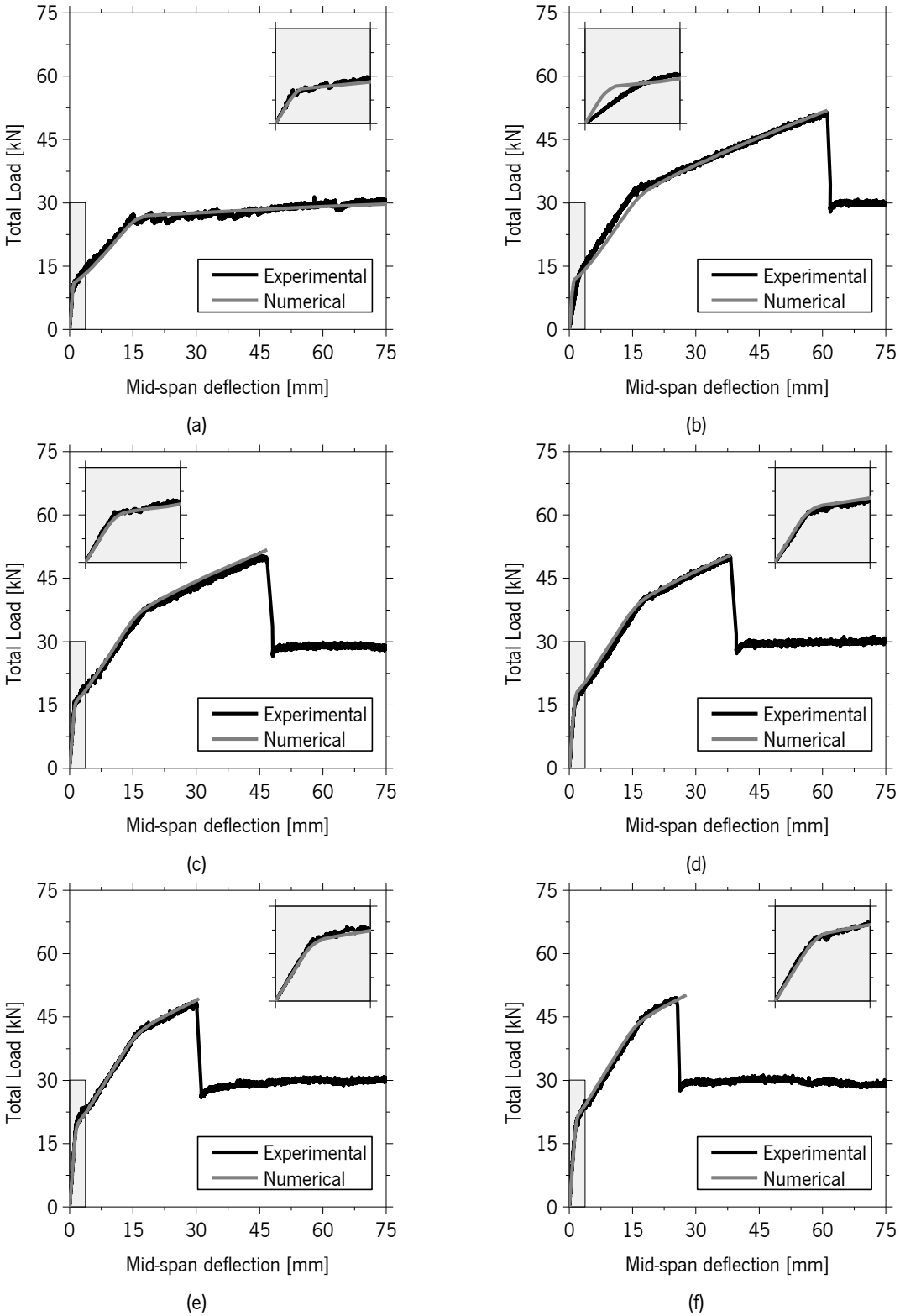

Figure 207 – Total load versus mid-span deflection – Series II (original properties):
(a) Reference, (b) S2_0%, (c) S2_20%, (d) S2_30%, (e) S2_40% and (f) S2_50%.

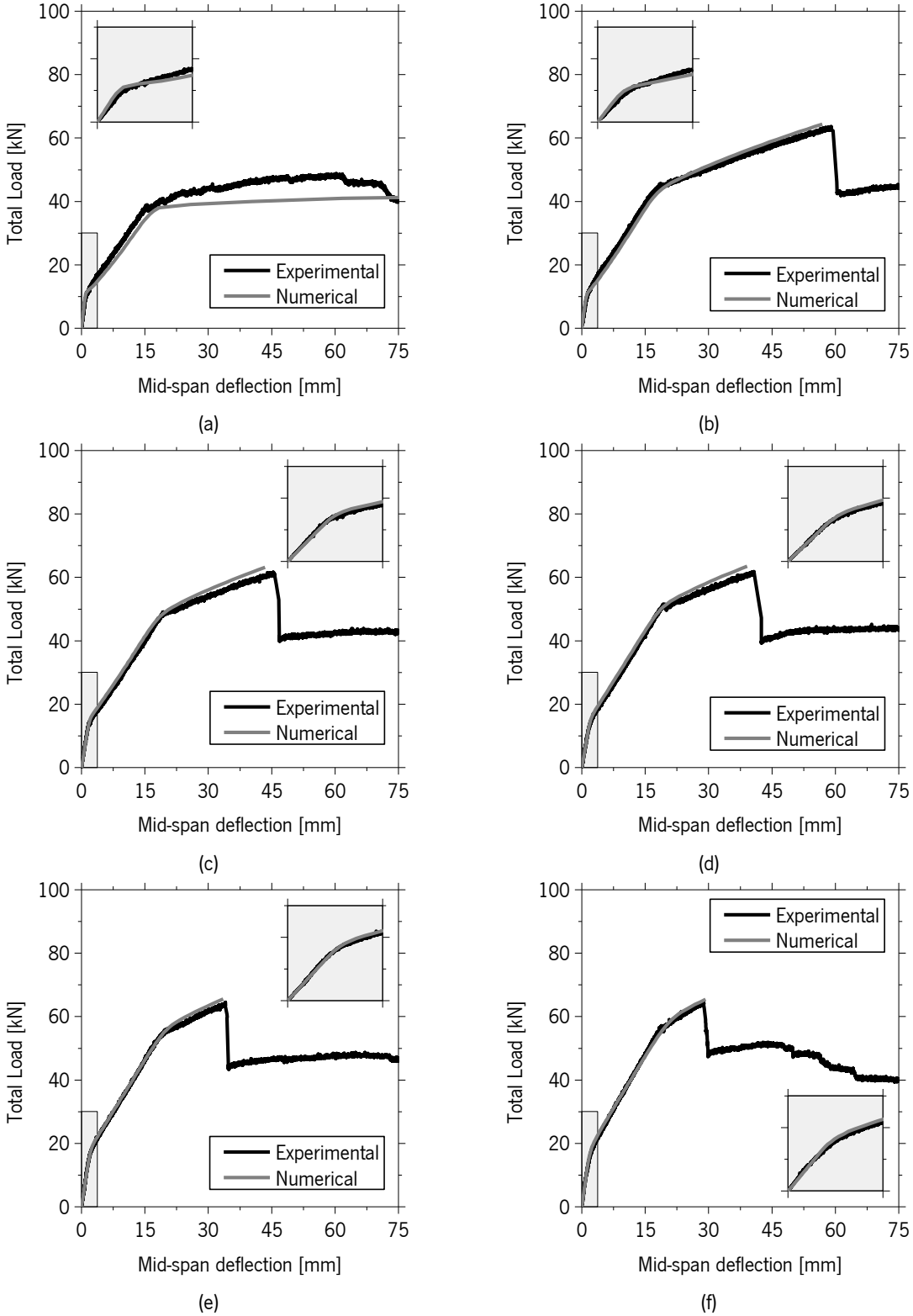

Figure 208 – Total load versus mid-span deflection – Series III (original properties): (a) Reference, (b) S3_0%, (c) S3_20%, (d) S3_30%, (e) S3_40% and (f) S3_50%.

6.3 FINAL CONSIDERATIONS

The losses of strain along the CFRP laminates were determined in this Chapter by a relatively simple numerical approach, considering that only the adhesive displays linear viscoelastic behaviour and neglecting the relaxation of the CFRP and the creep behaviour of the concrete. The agreement between the results obtained by this process and the ones registered experimentally was surprisingly excellent considering the simplicity of the adopted model. This demonstrates that the epoxy adhesive used is one of the most relevant constituents of the strengthening system influencing the long-term behaviour of the reinforced concrete beams prestressed with CFRP laminates. Concerning the environmental temperature variation, it was concluded that it probably does not produce significant effects in the long term CFRP strain profile if the average temperature is about 20.0ºC and within the range of 15.2ºC to 32.7ºC.

Regarding the prediction of the initial deflection of the beams it was concluded that it was probably deficiently assessed during prestress release since the deflections observed experimentally were generally lower than the ones obtained numerically. However, given the smallness of the deflection induced by the prestress, the inaccurate determination of this parameter is not significant for the determination of the deformation of the beams up to failure.

Regarding the prediction of the behaviour of the reinforced concrete beams up to failure using the 2D plane stress model, the load-deflection curves exhibited exceptional good correlation between experimental and numerical results in all the monitored locations. However, in some cases, the accurate prediction of the location of the yielding deflection was not possible to attain, but apart from that, the all notable points of the curves, as well as their rate of growth were correctly predicted.

In the specific case of the beams of Series I, the strains in all the intervening materials (concrete, steel and CFRP) were in general well predicted by the numerical model. However, in the remaining Series, the estimation of the CFRP strain was not so good, but in these cases, the strains registered experimentally in the CFRP may have been affected by uncontrolled effects, as described in Section 6.2.2.

The smeared crack pattern obtained numerically also revealed good agreement with the crack pattern obtained experimentally, and the location of the failure section was also found to be within the expected zone.

Using the moment-curvature section analysis combined with the matrix displacement method it was possible to predict with exceptional accuracy the load-deflection curves of the last two series of beams (Series II and III). However, in relation to Series I, although the load was correctly assessed at cracking, yielding and ultimate stages, the deflection in correspondence with those points was slightly underestimated after the yielding of the longitudinal reinforcement, most likely due to the non-consideration of the shear components.

6.4 REFERENCES

Barros, J. A. O. and Fortes, A. S. (2005). "Flexural strengthening of concrete beams with CFRP laminates bonded into slits." *Cement & Concrete Composites*, Elsevier, 27(4), 471-480.

Barros, J. A. O. , Costa, I. G. and Ventura-Gouveia, A. (2011). "CFRP Flexural and Shear Strengthening Technique for RC Beams: Experimental and Numerical Research." *Advances in Structural Engineering*, Vol. 14, No. 3, 551-573.

CEB-FIP (1993). CEB-FIP Model Code 1990: Design Code, *Thomas Telford*, Lausanne, Switzerland.

E365 (1993). "Hardened Concrete - Determination of the modulus of elasticity of concrete in compression." *National Laboratory for Civil Engineering Specification*, 2 pp (in Portuguese).

EN 1992-1-1 (2004). "Eurocode 2: Design of concrete structures - Part 1-1: General rules and rules for buildings." *European Committee for Standardization*, 225 pp.

ISO 527-5 (1997). "Plastics - Determination of tensile properties – Part 5: Test conditions for unidirectional fibre-reinforced plastic composites." *International Organization for Standardization*, 12 pp.

NPEN10002-1 (1990). "Metallic materials - Tensile testing. Part 1: Method of test (at ambient temperature)." *European Committee for Standardization* (CEN), 34 pp. (in Portuguese)

Varma, R. K. (2012). "Numerical models for the simulation of the cyclic behaviour of RC structures incorporating new advanced materials." *PhD thesis*, University of Minho, Guimarães, Portugal.

Chapter 7

ANALYTICAL MODELS

The experimental investigation carried out in the scope of this work was essentially focused on the losses of prestress in the anchorage zone and the effectiveness of the prestress technique for the flexural strengthening of RC beams. According to the presented results, it was verified that the available numerical tools combined with an accurate description of the material properties are able of predicting with good accuracy the losses of prestress, as well as the and the load-carrying capacity and deflection behaviour of the RC beams. As a result, in this Chapter, an analytical approach is proposed to predict the distribution and evolution of the strain along the CFRP, as well as the force-deflection of RC beams strengthened with the developed technique.

7.1 PRESTRESS LOSSES

The losses of prestress due to adhesive creep are believed to be in general restricted to a small zone near the anchorage, and therefore, if a sufficient anchorage length is provided, there is no reason to believe that creep threatens the ultimate load-carrying capacity of the beams strengthened with FRPs. In fact, if the bond between FRP-adhesive-concrete is not weakened over time, these prestress losses at the anchorage may be observed as a constructive disposition, similar to the anchorage length of steel rods or FRP reinforcement.

For the determination of the evolution of the anchorage length several three-dimensional numerical models similar to the ones presented in Section 6.1 were prepared considering that all materials are working within the linear elastic/viscoelastic range. A schematic strain profile obtained from some

of these models is depicted in Figure 209. Observing the obtained curves, it is visible that alterations in the elastic modulus of the FRP, E_f, and in the elastic modulus of the adhesive, E_a, produce a significant variation of the FRP strain profile. Therefore, a parametric study was conducted to assess and quantify the influence of several parameters in the long term behaviour of beams strengthened with prestressed NSM-CFRP laminates.

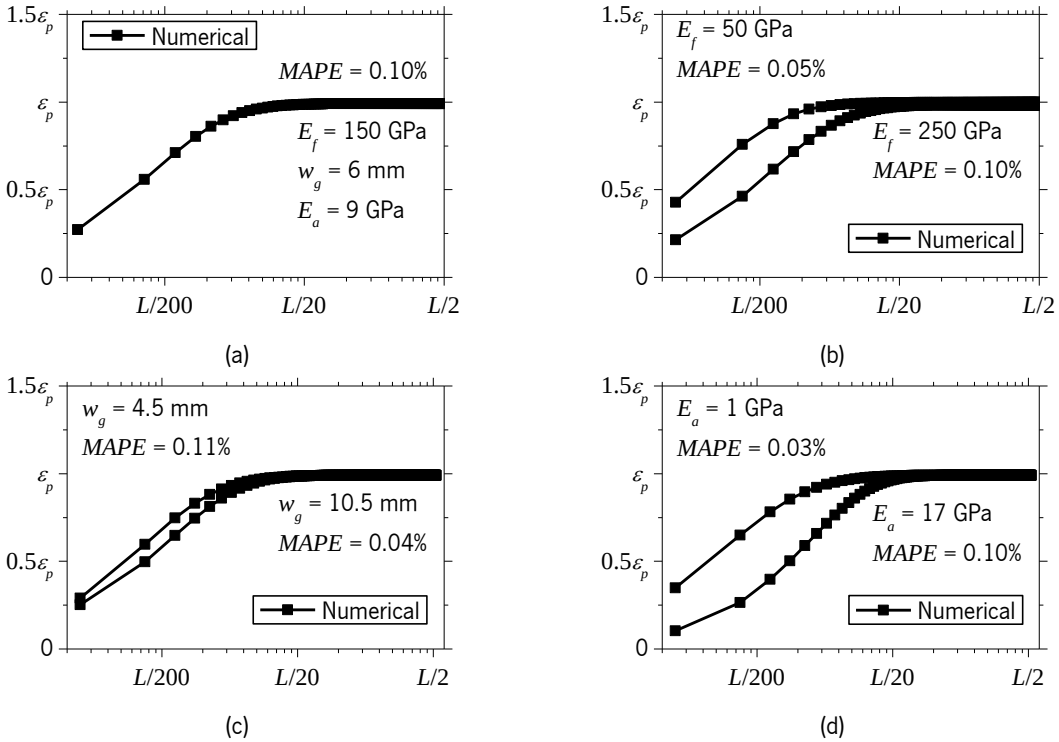

Figure 209 – Strain distribution along the beam: (a) Reference beam; (b) FRP modulus influence; (c) Groove thickness influence and (d) Adhesive modulus influence.

In the present parametric study, it was adopted as Reference a RC beam of 150×300×2400 mm^3, reinforced with $2\phi10$ in the top and bottom surface, and strengthened with a CFRP laminate of 1.4×20 mm^2 cross section (see Figure 210). The influence of most of the parameters involved was analysed considering the variation range reported in Table 72. To assess the influence of a certain parameter, the values of the remaining parameters of the Reference beam (shaded in Table 72) were adopted. As an example, to assess the influence of the concrete elastic modulus, five numerical models were prepared, all considering E_f = 150 GPa, E_a = 9 GPa, ε_p = 2.667‰, A_s = 157.08 mm^2, w_g = 6 mm, b = 150 mm, h = 300 mm, L = 2400 mm, and a = 50 mm. The only difference between those five models, was the elastic modulus of the concrete, E_c, which was taken as 27 GPa, 30 GPa, 33 GPa, 36 GPa, and 39 GPa in 'Model 1', 'Model 2', 'Model 3', 'Model 4', and 'Model 5', respectively (see Annex E).

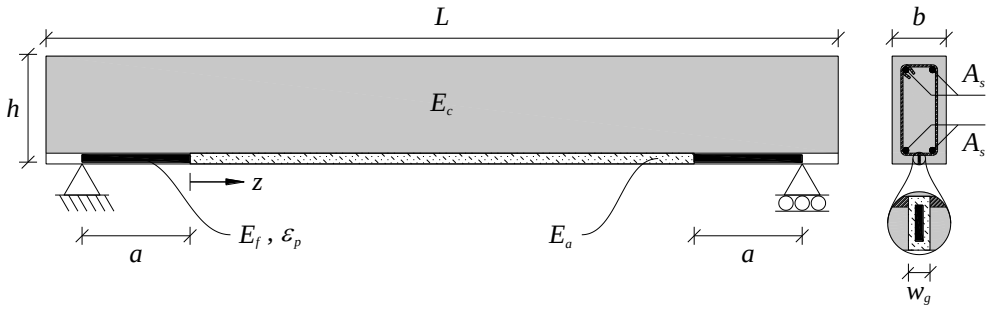

Figure 210 – Geometrical and material characteristics of the reinforced concrete beam.

Table 72 – Variation range used in the parametric study.

Variable			Model 1	Model 2	Model 3	Model 4	Model 5
Concrete elastic modulus	E_c	[GPa]	27	30	33	36	39
FRP elastic modulus	E_f	[GPa]	50	100	150	200	250
Adhesive elastic modulus	E_a	[GPa]	1	5	9	13	17
Initial prestrain	ε_p	[‰]	200	400	600	800	1000
Longitudinal steel reinforcement	A_s	[mm²] §	157.08	226.19	402.12	628.32	981.75
Width of the groove	w_g	[mm]	4.50	6.00	7.50	9.00	10.5
Width of the beam	b	[mm]	100	150	200	250	300
Height of the beam	h	[mm]	100	200	300	400	500
Width and height of the beam	$b \times h$	[mm²] §§	100×340	125×317	150×300	175×286	200×274
Length of the beam	L	[mm]	2400	3200	4000	4800	5600
Distance between support and prestress	a	[mm]	50	100	150	200	250

The shaded values correspond to the Reference beam.

§ Reinforcement ratio $\rho_s = A_s / (b \cdot d_s)$: 0.35%, 0.50%, 0.89%, 1.40% and 2.18%.

§§ The combination of these dimensions produces the same flexural stiffness in all cases.

Taking as advantage the knowledge assimilated during literature review, it was noticed that an expression similar to Eq. 41 could be adopted to define the strain evolution along the bond length. Each of the relevant parameters, $\Delta\varepsilon_p$, η and n, were determined for each of the numerical models according to the Generalized Reduced Gradient (GRG2) nonlinear optimization, available in Microsoft Excel, by minimizing as much as possible the Mean Absolute Percentage Error ($MAPE$).

$$\varepsilon(z) = (\varepsilon_p - \Delta\varepsilon_p)\left(1 - \exp\left(-\left(\frac{E_f \cdot z}{\eta}\right)^{(1-n)}\right)\right) \tag{41}$$

where $\varepsilon(z)$ is the strain along the bonded length, ε_p is the applied prestrain on the FRP, $\Delta\varepsilon_p$ is the prestress loss, E_f is the elastic modulus of the FRP, η and n are coefficients defining the shape of the strain profile and z is the distance from the left free-end up to mid-span (see Figure 210).

It is worth noting that the first term of Eq. 41, $\left(\varepsilon_p - \Delta\varepsilon_p\right)$, corresponds to the effective strain installed in FRP, *i.e.*, the plateau of the strain curve after the anchorage zone, visible in Figure 209.

Based on the results obtained from the numerical models, the following procedure was adopted to obtain an empirical expression:

- Numerical strain profiles: 45 three-dimensional models in correspondence with the parametric variation indicated in Table 72 were prepared. The strain distribution along the FRP corresponding to each of those 45 models was collected;
- Assessment of the numerical strain curves: for each of the 45 models, the values of $\Delta\varepsilon_p$, η and n were obtained using GRG2 nonlinear optimization;
- Dependency between parameters: based on the obtained values of $\Delta\varepsilon_p$, η and n the level variation of each of those values with the varied parameters was assessed by means of a linear regression.
- Multiple regression: based on the linear regressions obtained in the previous step, a multiple regression, was adjusted to quantify the values of $\Delta\varepsilon_p$, η and n.

7.1.1 Numerical strain profiles

This step consisted of preparing the numerical models and exporting the strains in each of the FRP elements. The obtained strain profiles are detailed in Annex E.

7.1.2 Numerical strain profiles

As previously explained, all the strain profiles corresponding to the three-dimensional models prepared were adjusted to Eq. 41. The obtained values of $\Delta\varepsilon_f$, η and n corresponding to each of those models can be consulted in Annex E. Figures 211, 212 and 213 represent the influence of each of the analysed parameters on the values of $\Delta\varepsilon_p$, η and n, respectively.

Observing Figure 211, it is immediately visible that the FRP elastic modulus, E_f, as well as the prestress strain, ε_p, are directly proportional to the prestress loss ($\Delta\varepsilon_p$). On the other hand, as already mentioned, the properties of the adhesive (thickness and elastic modulus) and the elastic modulus of the FRP are parameters that significantly affect the strain distribution. However, if the plots are closely analysed, it is visible that other parameters, such as the concrete elastic modulus or the reinforcement ratio also produce some variation on $\Delta\varepsilon_p$.

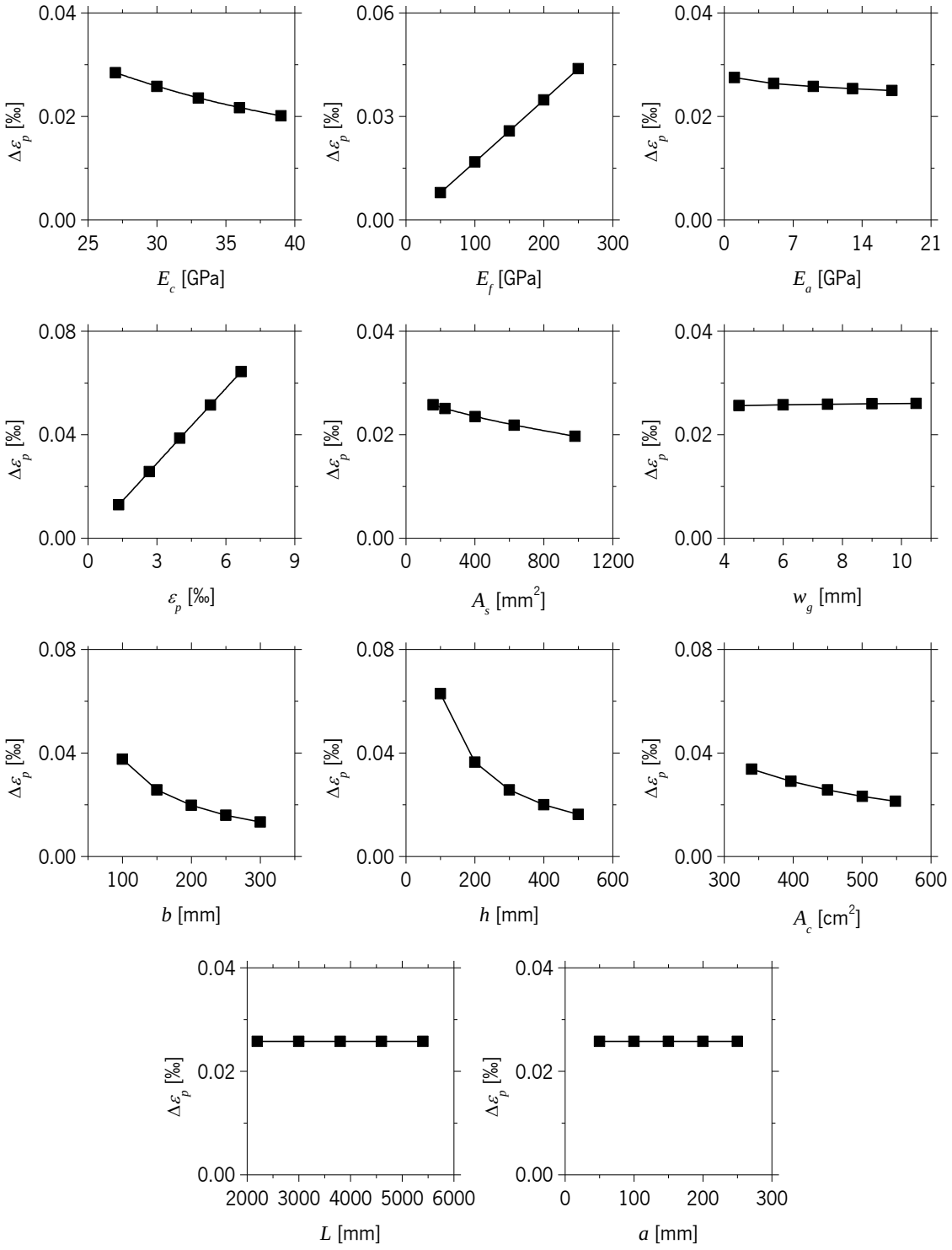

Figure 211 – Influence of the investigated parameters on the variation of $\Delta\varepsilon_p$.

During this analysis, it was concluded that both the beam length, L, and the distance from the support to the beginning of the bonded length, a, (see Figure 210) have absolutely no effect on the strain profile.

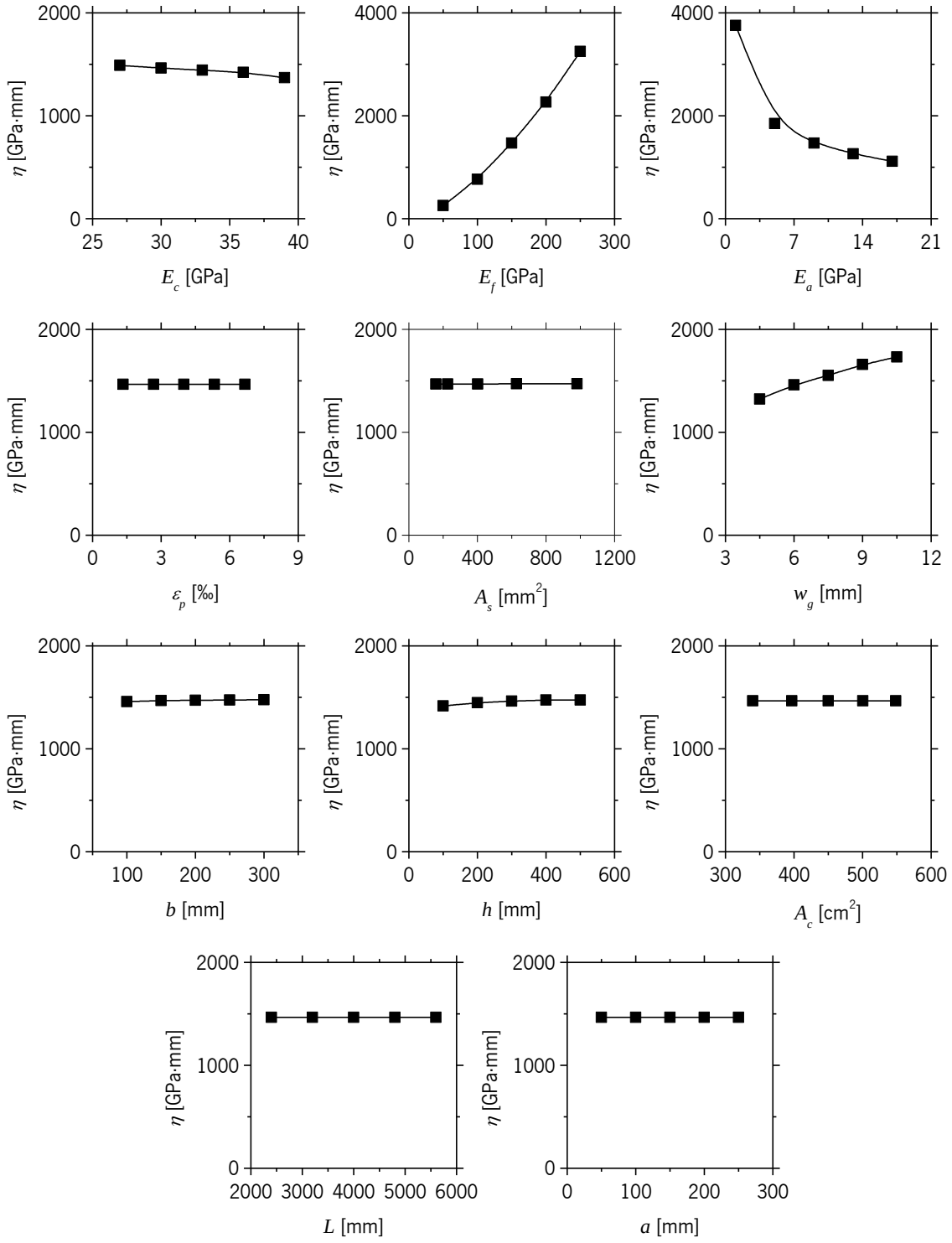

Figure 212 – Influence of the investigated parameters on the variation of η.

In the specific case of n (depicted in Figure 213), only the variables directly related to the adhesive layer have major effect on this parameter, especially the elastic modulus (E_a).

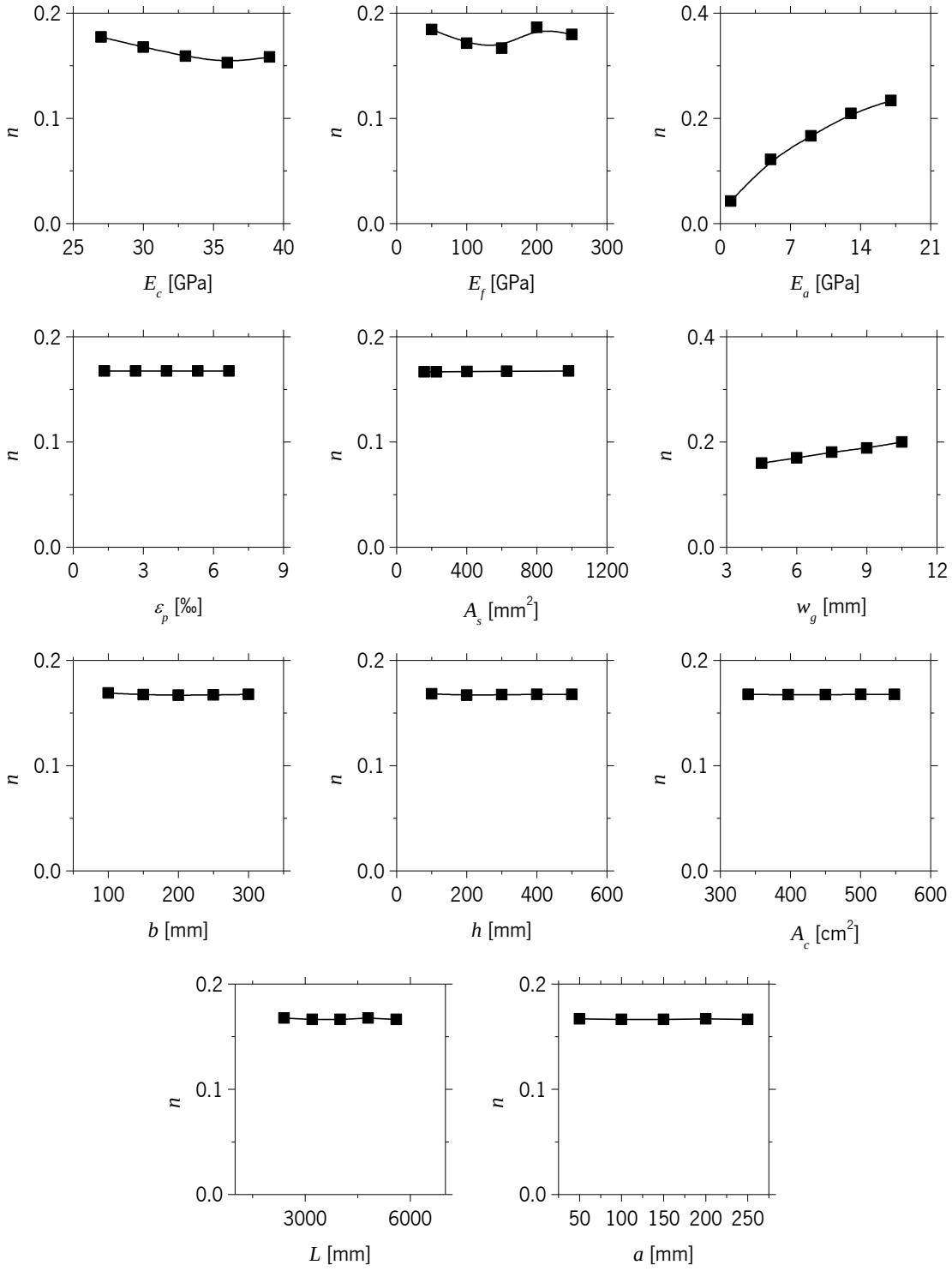

Figure 213 – Influence of the investigated parameters on the variation of n.

7.1.3 Dependency between parameters

At this stage, it was attempted to relate each of the parameters with the variables determined ($\Delta\varepsilon_p$, η and n) as depicted in Figures 214 to 216. For that purpose, each of the parameters were

powered to an adequate constant, α_i, in order to observe which value α_i of would produce a linear relationship. For example, in Figure 214, it is visible that $\Delta\varepsilon_p$ increases almost linearly with the inverse of E_c.

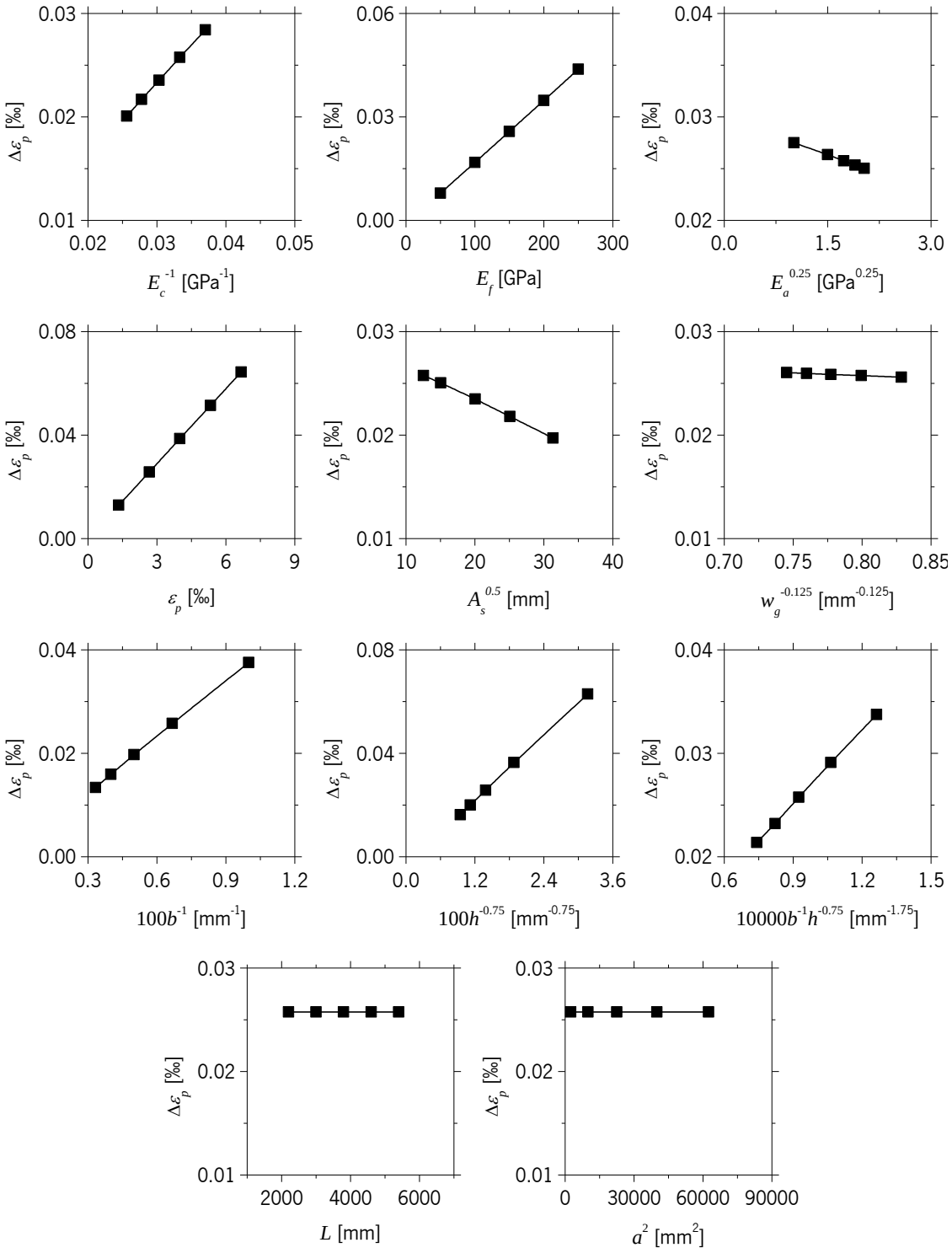

Figure 214 – Parameterization of $\Delta\varepsilon_p$.

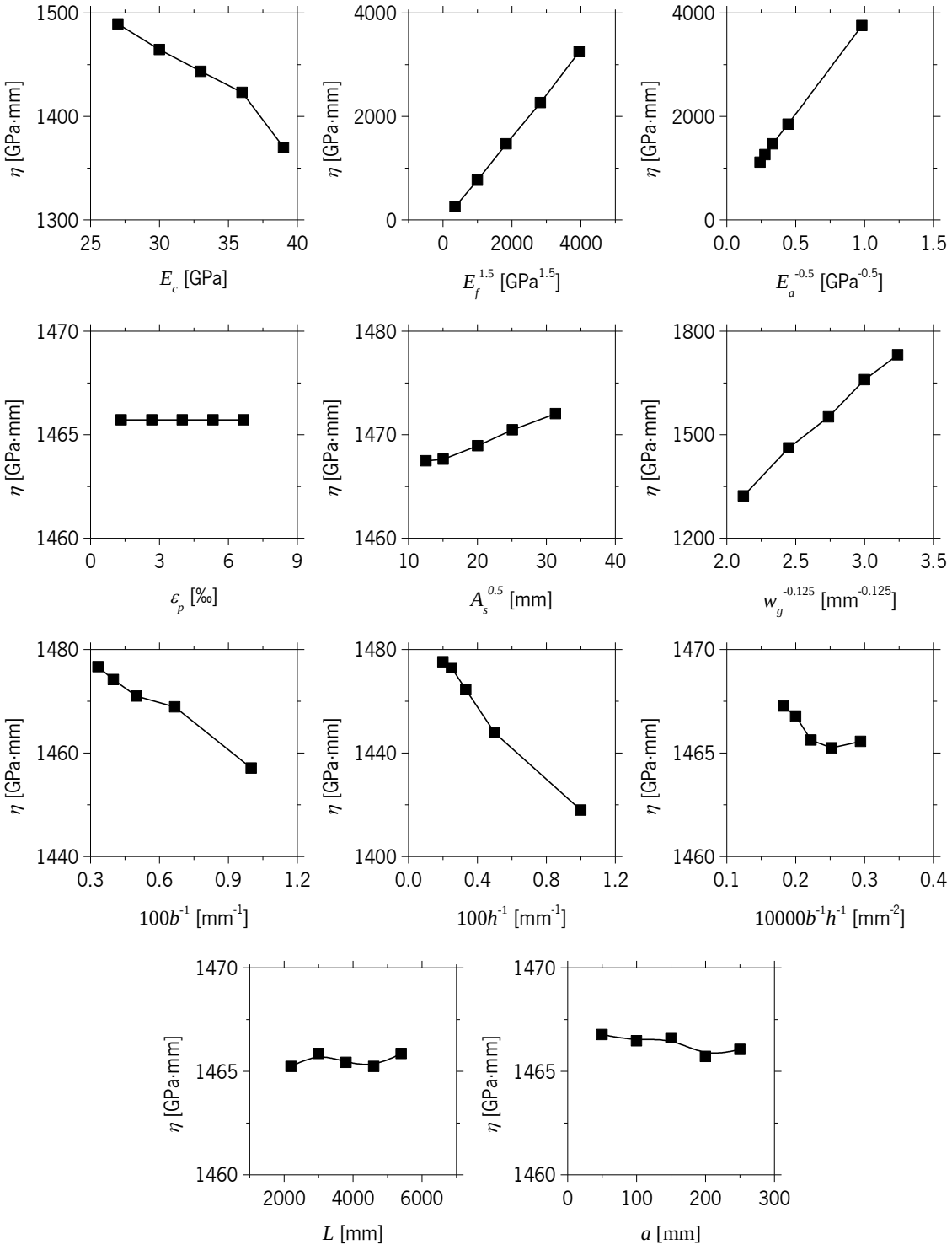

Figure 215 – Parameterization of η.

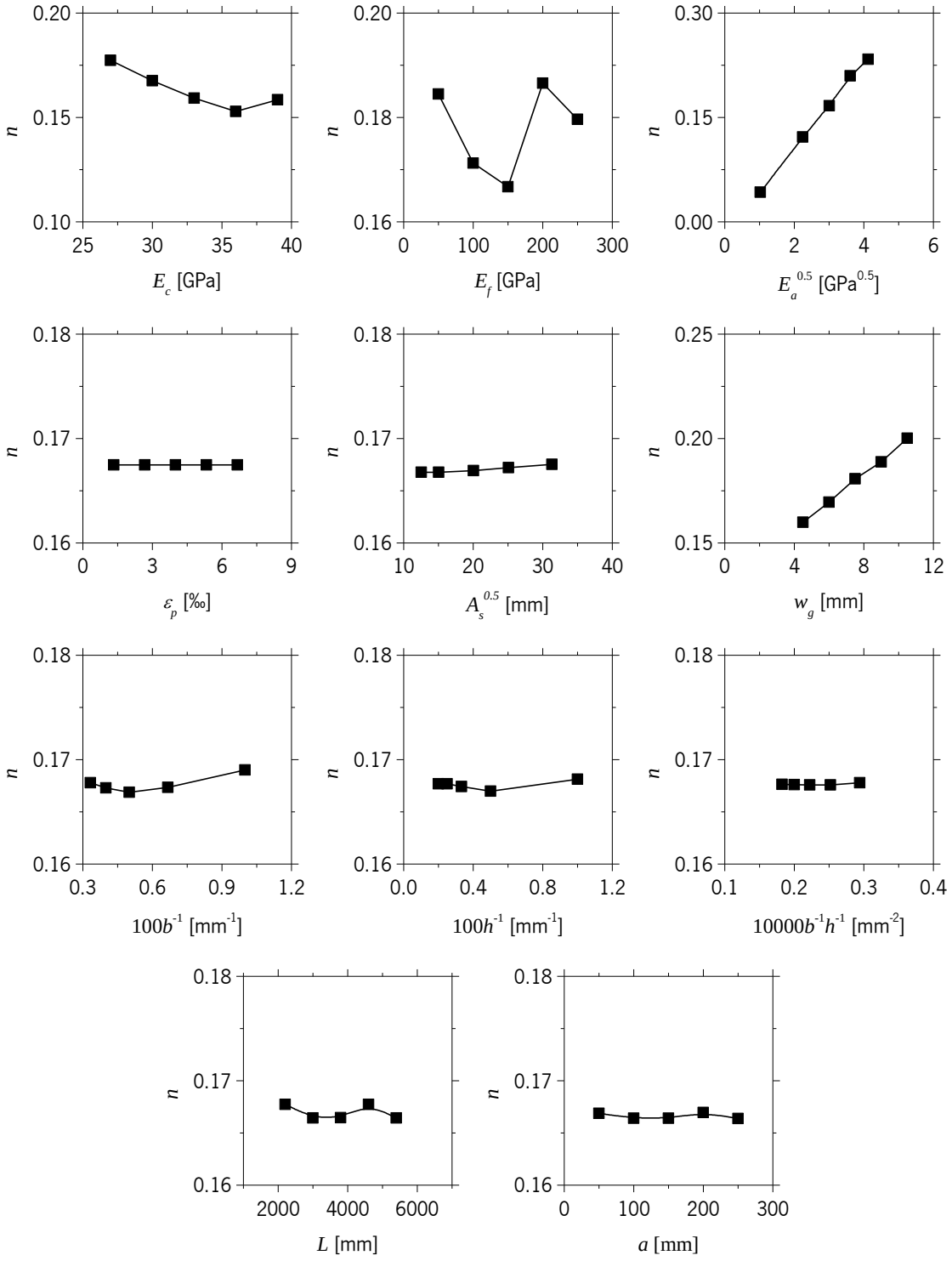

Figure 216 – Parameterization of n.

Note that the power associated with each of the dependent variables was assumed to be a multiple of 0.125, even if other values could produce a better coefficient of determination (r^2). Each of the linear regressions was determined in accordance with the formulation given in Eq. 42.

$$\Delta\varepsilon_p(\psi) = m_{\Delta\varepsilon} \cdot \psi^{\alpha,\Delta\varepsilon} + b_{\Delta\varepsilon} \quad (42a)$$

$$\eta(\psi) = m_{\eta} \cdot \psi^{\alpha,\eta} + b_{\eta} \quad (42b)$$

$$n(\psi) = m_{n} \cdot \psi^{\alpha,n} + b_{n} \quad (42c)$$

In Tables 73 to 75 the results of each of the linear regressions are presented, and the parameters considered relevant are indicated. The consideration of a parameter was made based on the accuracy of the associated coefficient of determination, r^2, although in some cases, the parameter was left out due to its small influence in the final result. Taking as example w_g, in Table 73, although the value of r^2 was practically unitary, due to the insignificant change produced in $\Delta\varepsilon_p$, its contribution was ignored.

Table 73 – Coefficients of the linear regressions for the parameterization of $\Delta\varepsilon_p$.

ψ	$\alpha_{\Delta\varepsilon}$	$m_{\Delta\varepsilon}$	$b_{\Delta\varepsilon}$	r^2	Consider?
E_c	-1.00	7.3095E-01	1.3723E-03	0.99995	✓
E_f	1.00	1.7962E-04	-1.1354E-03	0.99998	✓
E_a	0.25	-2.4370E-03	2.9979E-02	0.99985	✓
ε_p	1.00	9.6576E-03	-1.3477E-08	1.00000	✓
A_s	0.50	-3.2329E-04	2.9889E-02	0.99932	✓
w_g	0.125	-5.2991E-03	2.9996E-02	0.99917	×
b	-1.00	3.6195E+00	1.4865E-03	0.99975	✓
h	-0.75	2.1572E+00	-4.1453E-03	0.99987	✓
bh	-1.00 and -0.75	2.3838E+02	3.6766E-03	0.99988	✓
L	1.00	0.0000E+00	2.5757E-02	-	×
a §	2.00	2.4866E-12	2.5757E-02	0.99680	×

Table 74 – Coefficients of the linear regressions for the parameterization of η.

ψ	α_{η}	m_{η}	b_{η}	r^2	Consider?
E_c	1.00	-9.3502E+00	1.7467E+03	0.95514	✓
E_f	1.50	8.3125E-01	-5.6600E+01	0.99972	✓
E_a	-0.50	3.5587E+03	2.6918E+02	0.99989	✓
ε_p	1.00	8.3803E-08	1.4657E+03	0.00000	×
A_s	0.50	2.5478E-01	1.4640E+03	0.98931	✓
w_g	0.50	3.6476E+02	5.5676E+02	0.99661	✓
b	-1.00	-2.8227E+03	1.4859E+03	0.98075	×
h	-1.00	-9.4100E+03	1.4953E+03	0.98625	×
bh	-1.00	-1.6042E+05	1.4698E+03	0.65579	×
L	1.00	7.8223E-05	1.4652E+03	0.09732	×
a	1.00	-4.3325E-03	1.4670E+03	0.63939	×

Table 75 – Coefficients of the linear regressions for the parameterization of n.

ψ	α_n	m_n	b_n	r^2	Consider?
E_c	1.00	-1.7494E-03	2.2082E-01	0.75913	✓
E_f	1.00	1.1330E-05	1.7602E-01	0.01103	×
E_a	0.50	6.2214E-02	-1.9497E-02	0.99833	✓
ε_p	1.00	8.3195E-13	1.6747E-01	0.37502	×
A_s	0.50	4.1766E-05	1.6618E-01	0.95777	✓
w_g	1.00	6.6540E-03	1.2991E-01	0.99788	✓
b	-1.00	2.2543E-01	1.6636E-01	0.53515	×
h	-1.00	-2.4747E-01	1.6823E-01	0.20266	×
bh	-1.00	1.3475E+01	1.6732E-01	0.40558	×
L	1.00	-1.6194E-07	1.6757E-01	0.08484	×
a	1.00	-9.2378E-07	1.6674E-01	0.06445	×

This deeper analysis showed that while for the quantification of $\Delta\varepsilon_p$ most of the parameters analysed are indispensable, η and n are less dependent on the geometrical properties of the beams.

Concerning the η, although E_f, E_a and w_g are the variables that expressively affect the shape of the strain profile as already demonstrated in Figure 209, the reinforcement ratio (in the form of A_s) and the concrete elastic modulus (E_c) also produce a moderate interference in the strain distribution. Additionally, although the dimensions of the cross section, b and h, initially indicated a minor level of correlation with η, the product of these properties produced a r^2 value of about 0.66 and therefore, the consideration of these geometrical characteristics in the quantification of η was abandoned.

7.1.4 Multiple regressions

The main objective of this procedure is the determination of an expression or set of expressions to properly assess the strain distribution along the anchorage. For that purpose, the empirical quantification of $\Delta\varepsilon_p$, η and n was performed using a multiple regression (Eq. 43).

$$y(x_1,...,x_i,...,x_n) = \beta_0 + \beta_1 \cdot x_1 + ... + \beta_i \cdot x_i + ... + \beta_n \cdot x_n \quad (43)$$

where y is a dependent variable, x_i denotes each of the independent variables of y, β_0 is a constant coefficient, β_i denotes the coefficient in correspondence to x_i, and n is the number of independent variables.

Although Microsoft Excel also allows the determination of the coefficients of multiple regressions, it was decided to determine them manually. Therefore, for the determination of $\Delta\varepsilon_p$, η and n, each of the relevant linear regressions (Tables 73 to 75) were summed. Additionally, a correction of the resultant slope (μ_ε, μ_η and μ_n) and y-intercept value ($\Delta\varepsilon_0$, η_0 and n_0), was also performed, as indicated in Eq. 44. Additional information about this calculation can be found in Annex E.

$$\Delta\varepsilon_{p,emp}\left(E_c, E_f, E_a, \varepsilon_p, A_s, b, h\right) = \mu_\varepsilon \sum_i \Delta\varepsilon_{p,i}\left(\psi\right) - \Delta\varepsilon_0 \tag{44a}$$

$$\eta_{emp}\left(E_c, E_f, E_a, A_s, w_g\right) = \mu_\eta \sum_i \eta_i\left(\psi\right) - \eta_0 \tag{44b}$$

$$n_{emp}\left(E_c, E_a, A_s, w_g\right) = \mu_n \sum_i n_i\left(\psi\right) - n_0 \tag{44c}$$

The relationship between the empirical values (produced by Eq. 44) and numerical values (obtained by GDR2 nonlinear optimization) is shown in Figures 217 to 219 where the accuracy of the prediction is evident. In all Figures, the result of the simple summation of the linear regressions is also plotted to demonstrate the accuracy of the relationship prior to the slope and y-intercept correction. In fact, during this process, it was noticed that the correction of the slope was not essential since μ_ε, μ_η and μ_n are already quite close to the unitary value.

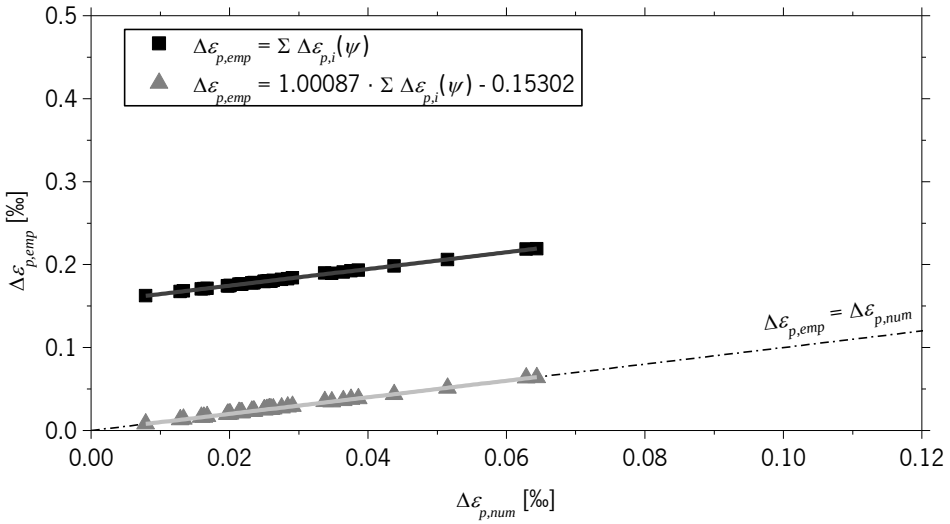

Figure 217 – Multi-linear regression of the parameter $\Delta\varepsilon_p$.

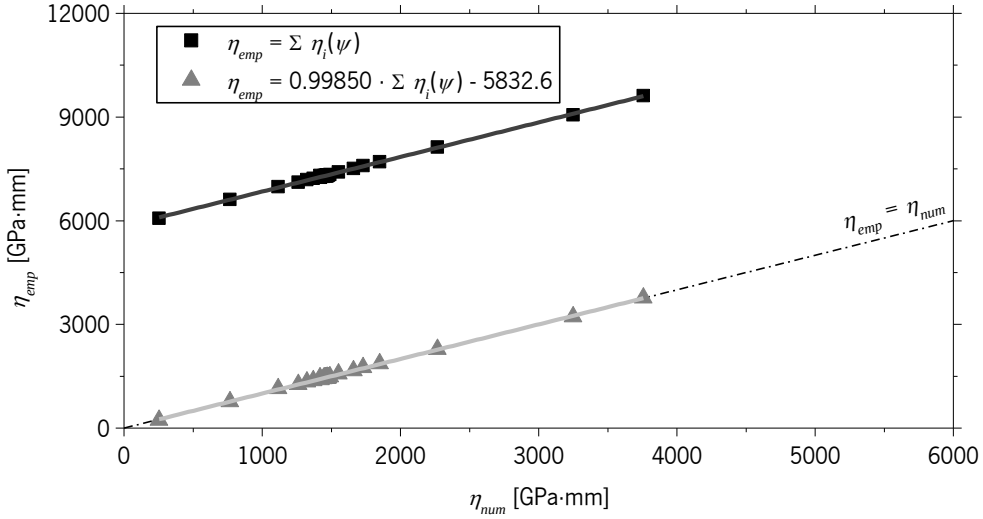

Figure 218 – Multi-linear regression of the parameter η.

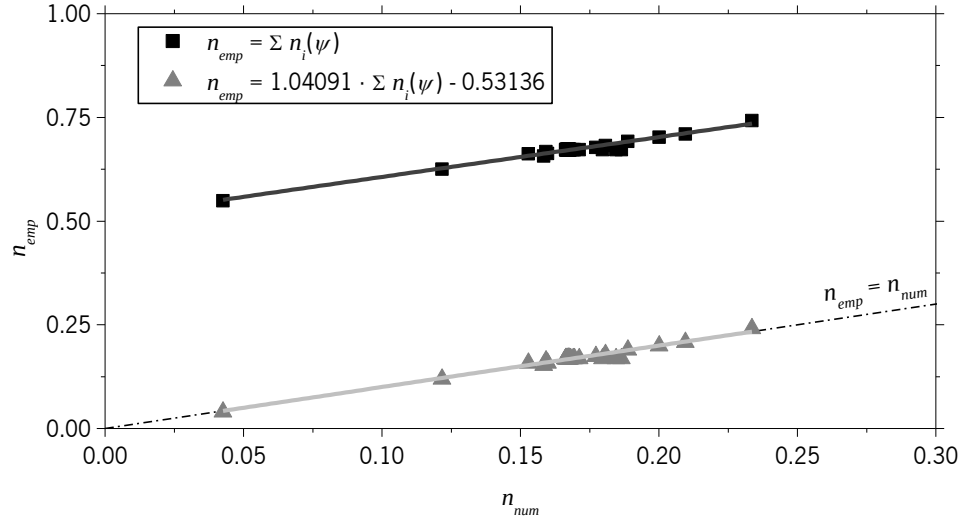

Figure 219 – Multi-linear regression of the parameter n.

Moreover, in order to better understand the accuracy of the obtained values, the error between empirical and numerical values of $\Delta\varepsilon_p$, η and n is shown in Figures 220 to 222. The variation of values was found to be about 6%, 3% and 11% in the case of $\Delta\varepsilon_p$, η and n, respectively. It is worth noting that these variations are perfectly acceptable since the influence of several other parameters was neglected in the course of this analysis.

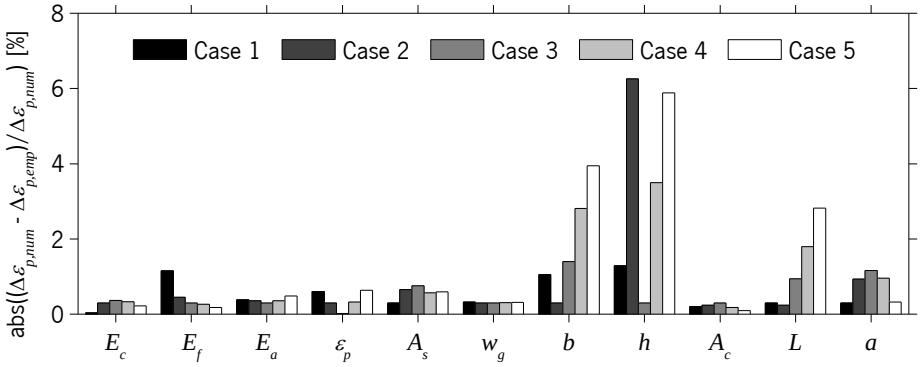

Figure 220 – Error between empirical and numerical determination of $\Delta\varepsilon_p$.

Analysing Figure 220, it is verified that the largest error occurs when the dimensions of the beam are changed. It is possible that the ratio between b and h also influences the strain variation at mid-span. The same effect is observed in Figure 221, although the associated error exhibits smaller magnitude.

Nevertheless, it is worth noting that the relative weight of the parameters captured by the empirical model is not the most accurate.

Furthermore, it is also noticeable that the variation of elastic modulus of the materials produces a greater difference between the empirical and numerical coefficients that define the shape of the strain profile (η and n). This fact suggests that the linear relationship considered may lose its accuracy if the materials exhibit characteristics significantly outside the considered range.

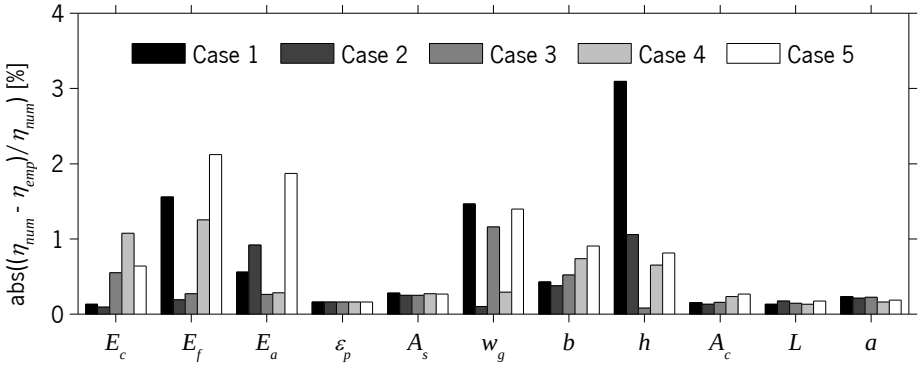

Figure 221 – Error between empirical and numerical determination of η.

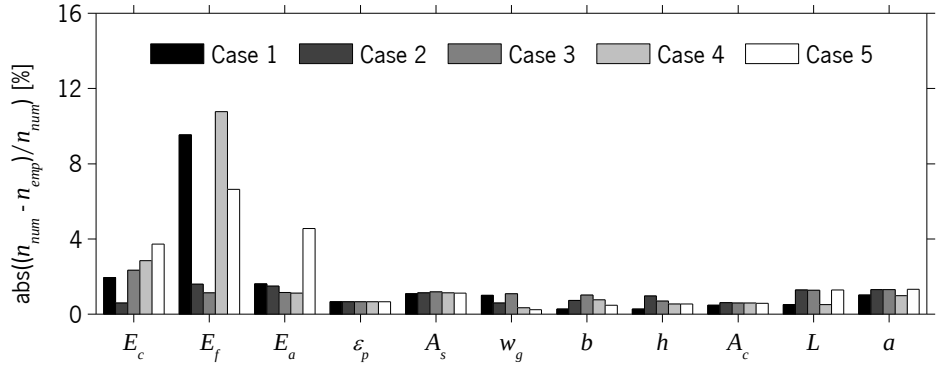

Figure 222 – Error between empirical and numerical determination of n.

In conclusion, the expressions enabling the quantification of the parameters necessary to describe the strain profile along a prestressed laminate are given in Eq. 45 as a function of all relevant parameters.

$$\Delta\varepsilon_{p,emp} = (7246.3E_c^{-1} + 1.7807E_f - 24.159E_a^{0.25} + 95.741\varepsilon_p - 3.2049A_s^{0.5} + \\ + 35882b^{-1} + 21385h^{-0.75} - 960.71)\times 10^{-4} \quad (45a)$$

$$\eta_{emp} = -9.3362E_c + 0.83000E_f^{1.5} + 3553.4E_a^{-0.5} + 0.25440A_s^{0.5} + 364.21w_g^{0.5} - 1858.6 \quad (45b)$$

$$n_{emp} = \left(-182.10E_c + 6475.9E_a^{0.5} + 4.3474A_s^{0.5} + 692.61w_g - 1361.0\right)\times 10^{-5} \quad (45c)$$

As an example, the strain profiles obtained by using the coefficients determined empirically in some of the analysed cases are depicted in Figure 223 for two of the cases previously showed in Figure 209. The Mean Average Percentage Error ($MAPE$) between the numerical and empirical curves was again computed and revealed to be approximately the same as obtained numerically.

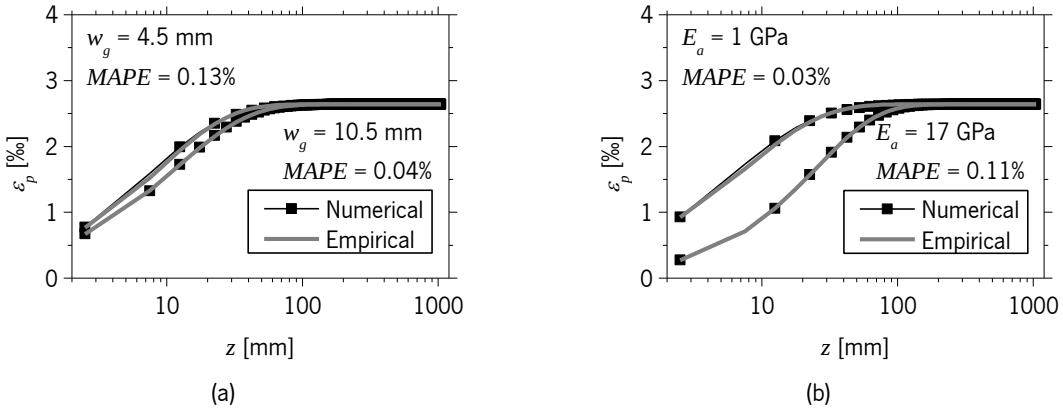

Figure 223 – Strain distribution along the beam using the empirical coefficients: (a) Groove thickness influence and (b) Adhesive modulus influence.

Using Eqs. 41 and 45 as well as the properties previously detailed in Chapter 6, the strain distribution along all of the beams prestressed experimentally was computed and plotted in

Figure 224. From the results obtained it is evident that the obtained results are perfectly realistic even if it is taken into account that some of the parameters involved are outside the range considered in the parametric analysis.

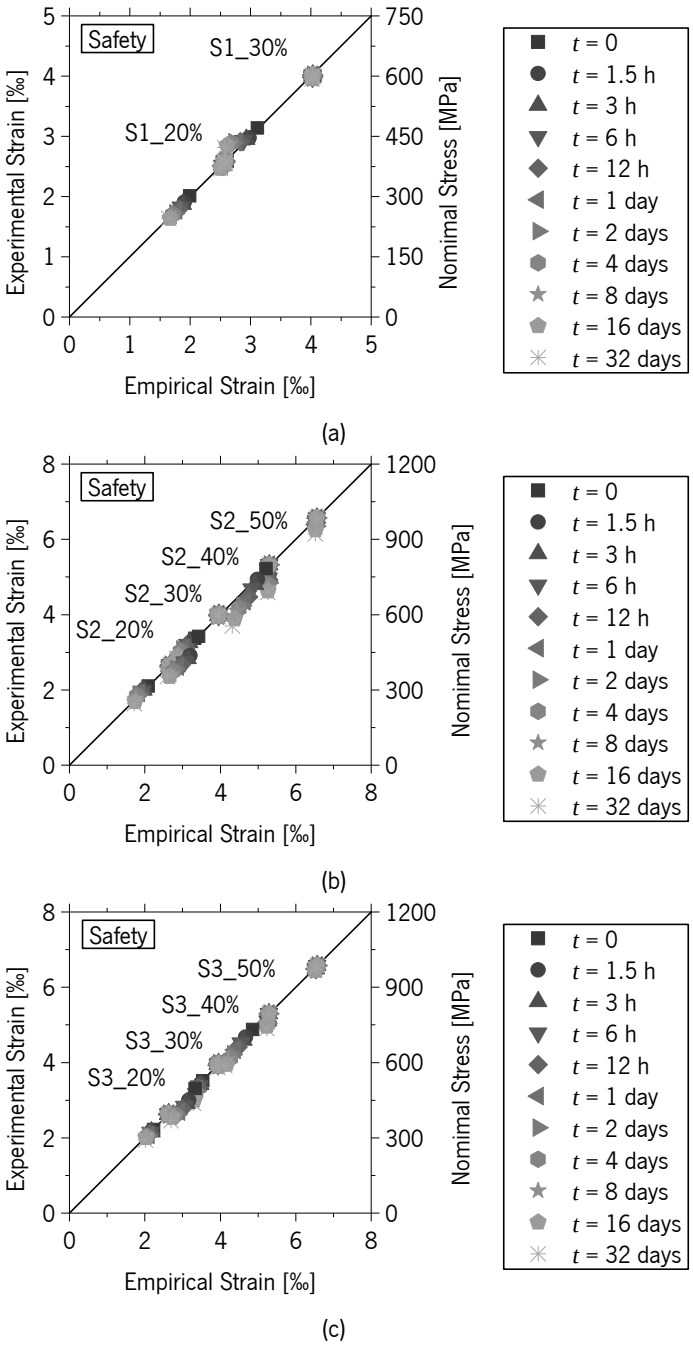

Figure 224 – Experimental versus empirical strain: (a) Series I (b) Series II and (c) Series III.

7.2 PRESTRESS EFFECTIVENESS

A spreadsheet was developed for the determination of the most significant points of the moment-curvature of reinforced concrete beams using the formulation described in this section (Figure 225). This spreadsheet allows the calculation of the cracking, yielding and ultimate curvature as well as the corresponding bending moment of rectangular reinforced concrete sections with one layer of conventional tensile reinforcement, one layer of conventional compressive reinforcement and one layer of composite strengthening to which a certain amount of prestress can be applied.

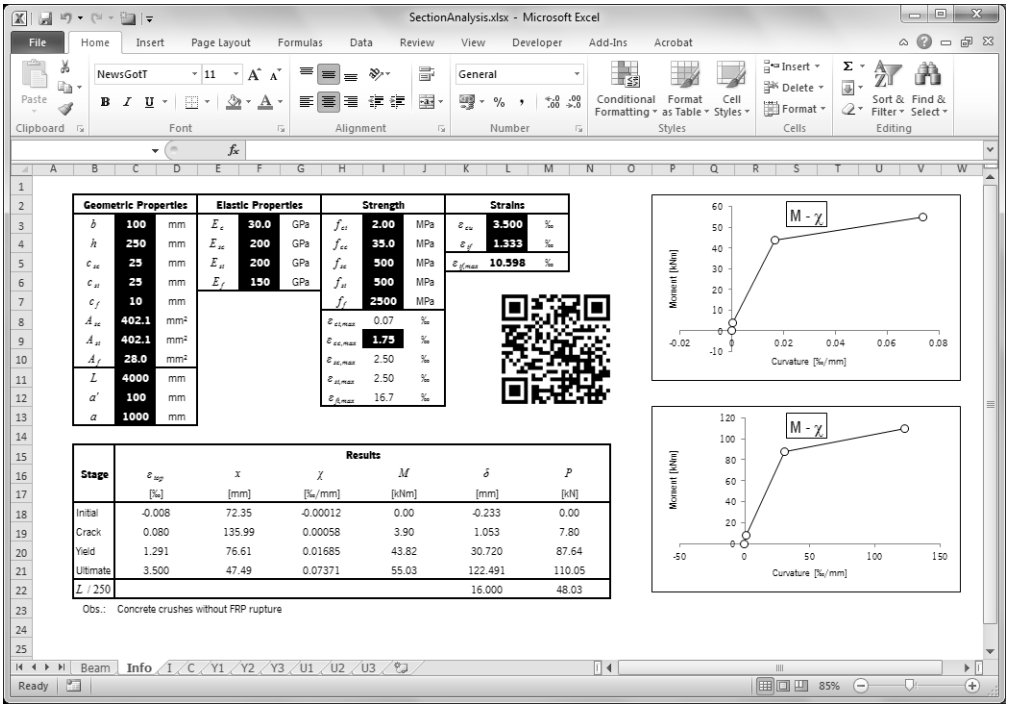

Figure 225 – Screenshot of the spreadsheet developed.
Available for download at https://www.dropbox.com/sh/b97wzurovz51kjf/Y5dSXRTyHe

The formulation used in this spreadsheet is based on conventional sectional analysis, theory in which the distribution of strain is assumed to be linear along the height of the beam. In this spreadsheet, the behaviour of concrete and steel are assumed to be in accordance with EC2 (see Figures 226 and 227) while the FRP was assumed as having linear elastic behaviour up to failure.

As discussed in the previous Chapters, both the moment-curvature and load-deflection curves of FRP strengthened beams consist of three main branches, bounded by the following notable states:

- Curvature/displacement induced by prestress application;
- Curvature/displacement and bending moment/applied load at crack initiation;
- Curvature/displacement and bending moment/applied load at yield initiation;
- Curvature/displacement and bending moment/applied load at failure.

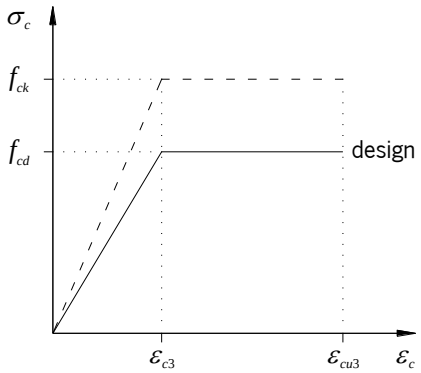

Figure 226 – Concrete compressive behaviour for design purposes: bi-linear stress-strain relation (EC2).

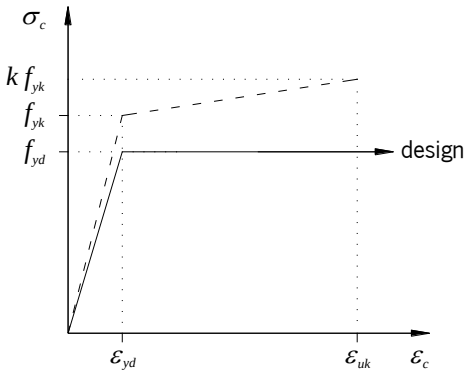

Figure 227 – Reinforcing steel behaviour for design purposes: bi-linear stress-strain relation (EC2).

7.2.1 Curvature induced by prestress application

For the calculation of the curvature induced by prestress application, the strain and stress distribution adopted are depicted in Figure 228. It is assumed that both the concrete and steel reinforcement are working within their elastic range.

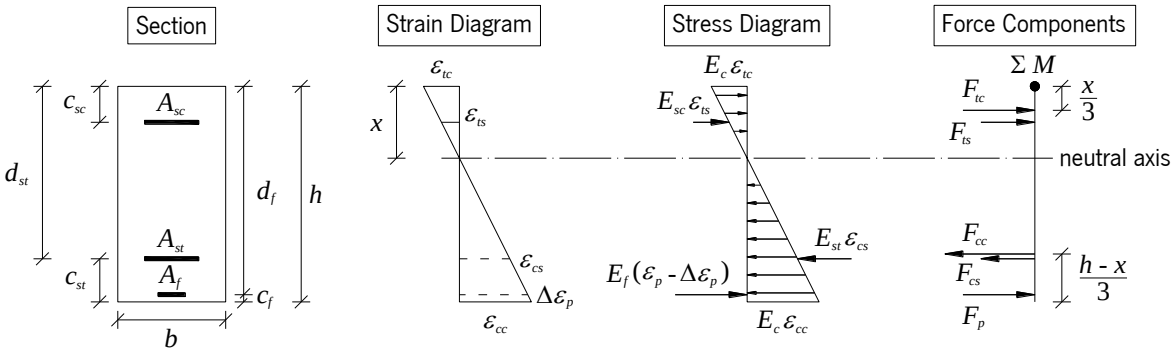

Figure 228 – Strain and stress diagram of the cross section due to prestress application, and force components.

The full process for the determination of the neutral axis depth can be found in Annex F. According to the performed calculations, the depth of the neutral axis is given by (Eq. 46).

$$x = \frac{E_c b h^2 \left(3d_f - 2h\right) + 6\left(E_{sc}A_{sc}c_{sc}\left(d_f - c_{sc}\right) + E_{st}A_{st}d_{st}\left(d_f - d_{st}\right)\right)}{3\left(E_c b h\left(2d_f - h\right) + 2\left(E_{sc}A_{sc}\left(d_f - c_{sc}\right) + E_{st}A_{st}\left(d_f - d_{st}\right)\right)\right)} \tag{46}$$

It is interesting to notice that that the position of the neutral axis does not depend on the prestress level, but only on elastic and geometrical characteristics. The strain in the most compressed fibre, ε_{cc}, can be determined using the expression given in Eq. 47.

$$\varepsilon_{cc} = \frac{2E_f \varepsilon_p A_f \left(h - x\right)}{E_c bh\left(h - 2x\right) + 2\left(E_{st} A_{st} \left(d_{st} - x\right) - E_{sc} A_{sc} \left(x - c_{sc}\right) + E_f A_f \left(d_f - x\right)\right)} \quad (47)$$

Knowing one of the strains along the height, it is also possible to determine all other strains along the cross section using geometrical equivalences. Of all the strains, the most relevant ones are the tensile strain at the top fibre of the concrete, ε_{tc}, given in Eq. 48, and the FRP strain relief, $\Delta\varepsilon_p$, resulting from the compression of the bottom layer of concrete, quantified in Eq. 49. Note that, in fact, Eq. 49 represents a closed-form solution for effective strain applied on the CFRP, in alternative to the expression previously presented in Eq. 45a.

$$\varepsilon_{tc} = \frac{2E_f \varepsilon_p A_f x}{E_c bh\left(h - 2x\right) + 2\left(E_{st} A_{st} \left(d_{st} - x\right) - E_{sc} A_{sc} \left(x - c_{sc}\right) + E_f A_f \left(d_f - x\right)\right)} \quad (48)$$

$$\Delta\varepsilon_p = \frac{2E_f \varepsilon_p A_f \left(d_f - x\right)}{E_c bh\left(h - 2x\right) + 2\left(E_{st} A_{st} \left(d_{st} - x\right) - E_{sc} A_{sc} \left(x - c_{sc}\right) + E_f A_f \left(d_f - x\right)\right)} \quad (49)$$

The curvature, $\chi_{initial}$, produced by the prestress can be defined as the strain at the top fibre, ε_{tc}, divided by the neutral axis depth, x, as indicated in Eq. 50.

$$\chi_{initial} = \frac{2E_f \varepsilon_p A_f}{E_c bh\left(h - 2x\right) + 2\left(E_{st} A_{st} \left(d_{st} - x\right) - E_{sc} A_{sc} \left(x - c_{sc}\right) + E_f A_f \left(d_f - x\right)\right)} \quad (50)$$

Moreover, although all the relevant variables are already well defined, it is important to determine one additional boundary condition that can be later useful for design purposes. This boundary condition consists on the limitation of the prestress level that avoids concrete cracking on the top surface (obtained from Eq. 48). This limitation can be defined based on the geometry of the cross section, the elastic properties of the materials and the tensile strength of the concrete, f_{ct}, as defined in Eq. 51.

$$\varepsilon_p \leq \frac{f_{ct}\left(E_c bh\left(h - 2x\right) + 2\left(E_{st} A_{st} \left(d_{st} - x\right) - E_{sc} A_{sc} \left(x - c_{sc}\right) + E_f A_f \left(d_f - x\right)\right)\right)}{2E_c E_f A_f x} \quad (51)$$

7.2.2 Curvature and bending moment at crack initiation

The curvature and bending moment at crack initiation can be determined using the procedure previously described. The strain distribution along the height is again assumed to be linear and the stress and load diagrams corresponding to the crack initiation state are depicted in Figure 229. The geometric relationships between strains along the cross section are given in Eq. 52 as a function of the cracking tensile strain of concrete, ε_{ct}.

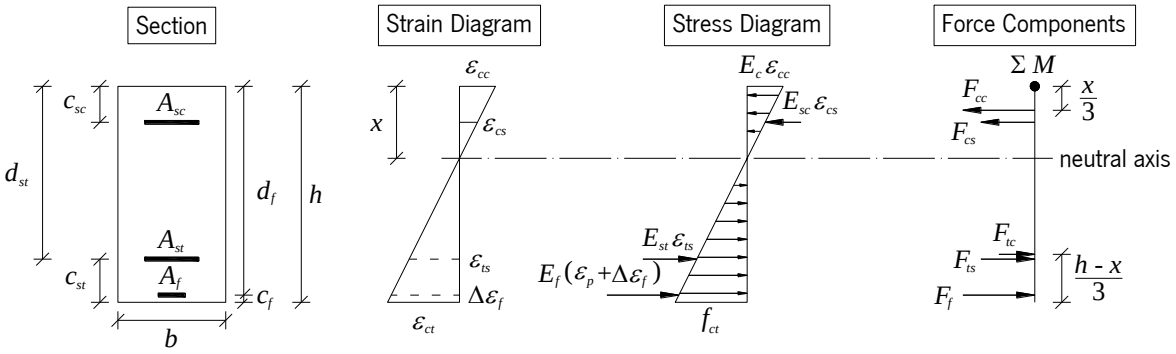

Figure 229 – Strain and stress diagram of the cross section at crack initiation, and force components.

$$\frac{\varepsilon_{cc}}{x}=\frac{\varepsilon_{ct}}{h-x}\Leftrightarrow\varepsilon_{cc}=\frac{x}{h-x}\varepsilon_{ct}\Leftrightarrow\varepsilon_{cc}=\frac{f_{ct}x}{E_c\left(h-x\right)} \tag{52a}$$

$$\frac{\varepsilon_{cs}}{x-c_{sc}}=\frac{\varepsilon_{ct}}{h-x}\Leftrightarrow\varepsilon_{cs}=\frac{x-c_{sc}}{h-x}\varepsilon_{ct}\Leftrightarrow\varepsilon_{cs}=\frac{f_{ct}\left(x-c_{sc}\right)}{E_c\left(h-x\right)} \tag{52b}$$

$$\frac{\varepsilon_{ts}}{h-x-c_{st}}=\frac{\varepsilon_{ct}}{h-x}\Leftrightarrow\varepsilon_{ts}=\frac{d_{st}-x}{h-x}\varepsilon_{ct}\Leftrightarrow\varepsilon_{ts}=\frac{f_{ct}\left(d_{st}-x\right)}{E_c\left(h-x\right)} \tag{52c}$$

$$\frac{\Delta\varepsilon_f}{h-x-c_f}=\frac{\varepsilon_{ct}}{h-x}\Leftrightarrow\Delta\varepsilon_f=\frac{d_f-x}{h-x}\varepsilon_{ct}\Leftrightarrow\Delta\varepsilon_f=\frac{f_{ct}\left(d_f-x\right)}{E_c\left(h-x\right)} \tag{52d}$$

Calculating the equilibrium of internal forces in the cross section (detailed in Annex F), the depth of the neutral axis can be determined (Eq. 53).

$$x=\frac{E_c b h^2 f_{ct}+2\left(E_f A_f\left(E_c\varepsilon_p h+f_{ct}d_f\right)+\left(E_{sc}A_{sc}c_{sc}+E_{st}A_{st}d_{st}\right)f_{ct}\right)}{2\left(E_c b h f_{ct}+E_f A_f\left(E_c\varepsilon_{tf}+f_{ct}\right)+\left(E_{sc}A_{sc}+E_{st}A_{st}\right)f_{ct}\right)} \tag{53}$$

The curvature at this loading stage, χ_{crack}, is defined again by the ratio between the strain at top fibre (ε_{cc}, given in Eq. 54) and the depth of the neutral axis, as given in Eq. 55.

$$\varepsilon_{cc} = \frac{x}{(h-x)} = \frac{f_{ct} x}{E_c (h-x)} \tag{54}$$

$$\chi_{crack} = \frac{\varepsilon_{cc}}{x} = \frac{\varepsilon_{tc}}{h-x} = \frac{f_{ct}}{E_c (h-x)} \tag{55}$$

Additionally, the bending moment corresponding to this curvature level can be determined by the sum of the internal moments produced by the forces at any point of the cross section (Eq. 56).

$$M_{crack} = \frac{E_c b}{6}\left(\frac{f_{ct}}{E_c}\left(2h^2 - hx - x^2\right) - \varepsilon_{cc} x^2 \right) + E_{st}\varepsilon_{ts} A_{st} d_{st} + E_f \left(\varepsilon_p + \Delta\varepsilon_f\right) A_f d_f - E_{sc}\varepsilon_{cs} A_{sc} c_{sc} \tag{56}$$

7.2.3 Curvature and bending moment at yield initiation

For the determination of the yield initiation curvature and corresponding bending moment, some simplifications were assumed in relation to the method previously adopted. In this case, the section is assumed to be made of plain concrete, the contribution of the concrete in tension was neglected at this stage. Additionally, as the neutral axis depth is, in the majority of the cases, smaller than half of the height of the section, the compressive strain in the top of the concrete section will be in general lower than the conventional reinforcement yielding strain. However, if the cross section is highly reinforced in tension, the strain on the most compressed fibre may exceed the strain of the first branch of the bi-linear stress-strain relation, ε_{c3}, defined in Figure 226. However, the occurrence of concrete crushing prior to steel yielding is strongly improbable. As a result, three possible solutions will be considered for design purposes, and accepted or rejected in the order in which they are presented:

- Design assumption 1: the tensile steel reinforcement yields and the concrete in compression are working well below the linear range which in this methodology was defined to be $\varepsilon_{cc} \le 0.3\, f_{cd} / E_c$;
- Design assumption 2: the tensile steel reinforcement yields and the concrete in compression already exhibits a stiffness smaller than the one corresponding to the linear phase ($0.3 f_{cd} / E_c \le \varepsilon_{cc} \le \varepsilon_{c3}$);
- Design assumption 3: the tensile steel reinforcement yields and the concrete in compression has already exceeded ε_{c3} ($\varepsilon_{c3} \le \varepsilon_{cc} \le \varepsilon_{cu3}$).

7.2.3.1 Design assumption 1: $\varepsilon_{cc} \le 0.3\, f_{cd}/E_c$

The strain and stress distribution in correspondence with this design assumption is depicted in Figure 230 and the geometric relationships of the strains along the height sre given in Eq. 57. The balance of internal forces is detailed in Annex F, and the depth of the neutral axis obtained by this process is given in Eq. 58. After determining the depth of the neutral axis, x, the curvature can also be obtained by Eq. 59.

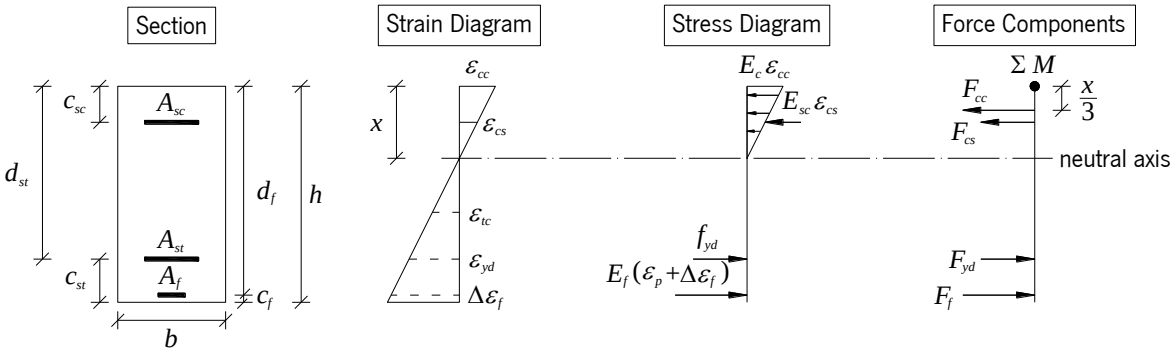

Figure 230 – Strain and stress diagram of the cross section at yield initiation – Design assumption 1.

$$\frac{\varepsilon_{cc}}{x} = \frac{\varepsilon_{yd}}{h-x-c_{st}} \Leftrightarrow \varepsilon_{cc} = \frac{x}{d_{st}-x}\varepsilon_{yd} \Leftrightarrow \varepsilon_{cc} = \frac{f_{yd}\,x}{E_{st}\left(d_{st}-x\right)} \tag{57a}$$

$$\frac{\varepsilon_{cs}}{x-c_{sc}} = \frac{\varepsilon_{yd}}{h-x-c_{st}} \Leftrightarrow \varepsilon_{cs} = \frac{x-c_{sc}}{d_{st}-x}\varepsilon_{yd} \Leftrightarrow \varepsilon_{cs} = \frac{f_{yd}\left(x-c_{sc}\right)}{E_{st}\left(d_{st}-x\right)}\varepsilon_{yd} \tag{57b}$$

$$\frac{\Delta\varepsilon_f}{h-x-c_f} = \frac{\varepsilon_{yd}}{h-x-c_{st}} \Leftrightarrow \Delta\varepsilon_f = \frac{d_f-x}{d_{st}-x}\varepsilon_{yd} \Leftrightarrow \Delta\varepsilon_f = \frac{f_{yd}\left(d_f-x\right)}{E_{st}\left(d_{st}-x\right)}\varepsilon_{yd} \tag{57c}$$

$$x = \frac{-B+\sqrt{B^2-4AC}}{2A} \tag{58a}$$

with

$$A = \frac{1}{2}E_c b \tag{58b}$$

$$B = E_{sc}A_{sc} + E_{st}A_{st} + E_f A_f\left(1+\frac{\varepsilon_p}{\varepsilon_{yd}}\right) \tag{58c}$$

$$C = -\left(E_{sc}A_{sc}c_{sc} + E_{st}A_{st}d_{st} + E_f A_f\left(d_f + d_{st}\frac{\varepsilon_p}{\varepsilon_{yd}}\right)\right) \tag{58d}$$

$$\chi_{yield} = \frac{\varepsilon_{cc}}{x} = \frac{f_{yd}}{E_{st}\left(d_{st}-x\right)} \tag{59}$$

The resisting bending moment in correspondence to this loading configuration can be computed by Eq. 60.

$$M_{yield} = -\frac{1}{6} E_c \varepsilon_{cc} b x^2 - E_{sc} \varepsilon_{cs} A_{sc} c_{sc} + f_{yd} A_{st} d_{st} + E_f \left(\varepsilon_p + \Delta\varepsilon_f \right) A_f d_f \tag{60}$$

7.2.3.2 Design assumption 2: $0.3 f_{cd} / E_c \le \varepsilon_{cc} \le \varepsilon_{c3}$

In the case of this design assumption, the depth of the neutral axis, x, strain at the top fibre, ε_{cc}, curvature, χ_{yield}, and bending moment can be obtained by the exact same procedure used in 7.2.3.1. It is only necessary to consider a diminished concrete elastic modulus, E_c', inspired on Figure 226, as given in Eq. 61.

$$E_c' = \frac{f_{cd}}{\varepsilon_{c3}} \tag{61}$$

7.2.3.3 Design assumption 3: $\varepsilon_{c3} \le \varepsilon_{cc} \le \varepsilon_{cu}$

The internal force distribution corresponding to this design assumption is depicted in Figure 231 and the relationship between the strains is the same as defined in Eq. 57. However, a supplementary expression needs to be defined, to quantify x' (Eq. 62). Computing the equilibrium of internal forces (see Annex F) the depth of the neutral axis is found to be given by Eq. 63. The curvature of the section, χ_{yield}, and the bending moment in correspondence to this stress state can be computed using Eqs. 64. The Eq. 65.

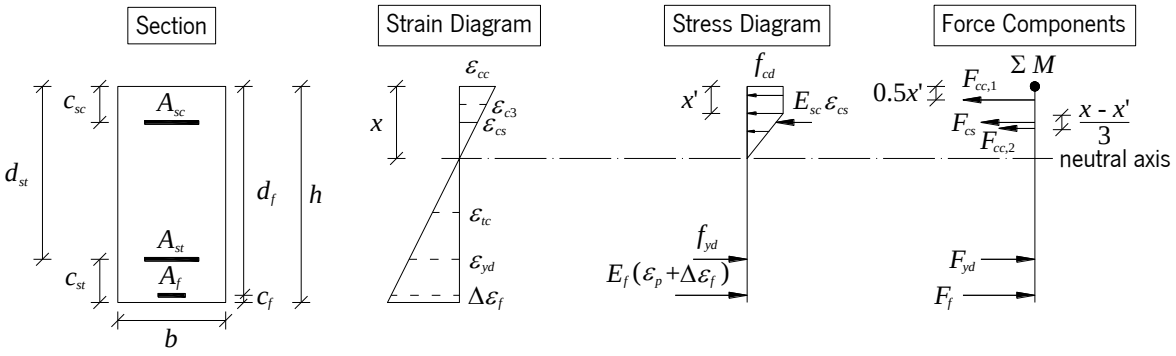

Figure 231 – Strain and stress diagram of the cross section at yield initiation – Design assumption 3.

$$\frac{\varepsilon_{yd}}{h - x - c_{st}} = \frac{\varepsilon_{c3}}{x - x'} \Leftrightarrow x' = \frac{\left(\varepsilon_{c3} + \varepsilon_{yd} \right) x - d_{st} \varepsilon_{c3}}{\varepsilon_{yd}} \tag{62}$$

$$x = \frac{-B - \sqrt{B^2 - 4AC}}{2A} \tag{63a}$$

with

$$A = \frac{f_{cd} b\left(\varepsilon_{c3} + 2\varepsilon_{yd}\right)}{2\varepsilon_{yd}^{\ 2}} \tag{63b}$$

$$B = -\left(\frac{f_{cd} b d_{st} \left(\varepsilon_{c3} + \varepsilon_{yd}\right)}{\varepsilon_{yd}^{\ 2}} + E_{sc} A_{sc} + \frac{f_{yd} A_{st}}{\varepsilon_{yd}} + E_f A_f \left(1 + \frac{\varepsilon_p}{\varepsilon_{yd}}\right)\right) \tag{63c}$$

$$C = \frac{f_{cd} b d_{st}^{\ 2} \varepsilon_{c3}}{2\varepsilon_{yd}^{\ 2}} + E_{sc} A_{sc} c_{sc} + \frac{f_{yd} A_{st}}{\varepsilon_{yd}} d_{st} + E_f A_f \left(d_f + d_{st} \frac{\varepsilon_p}{\varepsilon_{yd}}\right) \tag{63d}$$

$$\chi_{yield} = \frac{\varepsilon_{cc}}{x} = \frac{f_{yd}}{E_{st}\left(d_{st} - x\right)} \tag{64}$$

$$M_{yield} = -\frac{f_{cc} b}{6}\left(x^2 + xx' + x'^2\right) + f_{yd} A_{st} d_{st} + E_f \left(\varepsilon_p + \Delta\varepsilon_f\right) A_f d_f - E_{sc} \varepsilon_{cs} A_{sc} c_{sc} \tag{65}$$

7.2.4 Curvature and bending moment at failure

Identical to the case of yield initiation, failure is expected to be caused by one of three possible conditions, all of which will be analysed in the following Sections and accepted/rejected based on the associated boundary conditions:

- Design assumption 1: the FRP strengthening ruptures, $\varepsilon_p + \Delta\varepsilon_f = \varepsilon_f$, while the concrete can no longer be assumed to be in the initial linear elastic phase ($0.3 f_{cd}/E_c \le \varepsilon_{cc} \le \varepsilon_{c3}$);
- Design assumption 2: the FRP strengthening ruptures, $\varepsilon_p + \Delta\varepsilon_f = \varepsilon_f$, while the concrete in compression has already exceeded ε_{c3} ($\varepsilon_{c3} \le \varepsilon_{cc} \le \varepsilon_{cu}$);
- Design assumption 3: the concrete in compression reaches the maximum design limit, ε_{cu3}, and the section fails due to concrete crushing ($\varepsilon_p + \Delta\varepsilon_f < \varepsilon_f$).

Note that in all cases, the strain in tensile steel reinforcement is assumed to be higher than ε_{yd}.

7.2.4.1 Design assumption 1: $\varepsilon_p + \Delta\varepsilon_f = \varepsilon_f$ and $0.3 f_{cd}/E_c \le \varepsilon_{cc} \le \varepsilon_{c3}$

The strain distribution along the cross section is assumed to be similar to the one represented previously in Figure 231 and the relationship between strains is given in Eq. 66 as a function of $\Delta\varepsilon_p$. Although the applicable boundary conditions are in this case slightly different (see Annex F). Forcing the internal load equilibrium, the neutral axis depth is found to be given by Eq. 67. Knowing the depth of the neutral axis enables the determination of the curvature, $\chi_{ultimate}$, and bending moment, $M_{ultimate}$, with Eqs. 68 and 69, respectively.

$$\frac{\varepsilon_{cc}}{x}=\frac{\Delta\varepsilon_f}{h-x-c_f}\Leftrightarrow\varepsilon_{cc}=\frac{x}{d_f-x}\Delta\varepsilon_f\Leftrightarrow\varepsilon_{cc}=\frac{\left(\varepsilon_f-\varepsilon_p\right)x}{\left(d_f-x\right)} \tag{66a}$$

$$\frac{\varepsilon_{cs}}{x-c_{sc}}=\frac{\Delta\varepsilon_f}{h-x-c_f}\Leftrightarrow\varepsilon_{cs}=\frac{x-c_{sc}}{d_f-x}\Delta\varepsilon_f\Leftrightarrow\varepsilon_{cs}=\frac{\left(\varepsilon_f-\varepsilon_p\right)\left(x-c_{sc}\right)}{\left(d_f-x\right)} \tag{66b}$$

$$x=\frac{-B+\sqrt{B^2-4AC}}{2A} \tag{67a}$$

with

$$A=\frac{1}{2}E_c'b \tag{67b}$$

$$B=E_{sc}A_{sc}+\frac{f_{yd}A_{st}}{\varepsilon_f-\varepsilon_p}+E_fA_f\left(1+\frac{\varepsilon_p}{\varepsilon_f-\varepsilon_p}\right) \tag{67c}$$

$$C=-\left(E_{sc}A_{sc}c_{sc}+\left(\frac{f_{yd}A_{st}}{\varepsilon_f-\varepsilon_p}+E_fA_f\left(1+\frac{\varepsilon_p}{\varepsilon_f-\varepsilon_p}\right)\right)d_f\right) \tag{67d}$$

$$\chi_{ultimate}=\frac{\varepsilon_{cc}}{x}=\frac{\varepsilon_f-\varepsilon_p}{d_f-x} \tag{68}$$

$$M_{ultimate}=-\frac{1}{6}E_c'\varepsilon_{cc}bx^2-E_{sc}\varepsilon_{cs}A_{sc}c_{sc}+f_{yd}A_{st}d_{st}+f_fA_fd_f \tag{69}$$

7.2.4.2 Design assumption 2: $\varepsilon_p+\Delta\varepsilon_f=\varepsilon_f$ and $\varepsilon_{c3}\le\varepsilon_{cc}\le\varepsilon_{cu3}$

The resolution of this design assumption is basically equal to the one previously presented in Section 7.2.3.3 for the determination of yield initiation (see Figure 231). The strains should be expressed as a function of $\Delta\varepsilon_f$ as in Eq. 66 and the value of x' is given in Eq. 70. The internal balance of loads yields that the depth of the neutral axis is the one given in Eq. 71. The curvature and bending moment of the cross section are a function of x and are given by Eqs. 72 and 73.

$$\frac{\Delta\varepsilon_{tf}}{h-x-c_f}=\frac{\varepsilon_{c3}}{x-x'}\Leftrightarrow x'=\frac{\left(\varepsilon_{c3}+\Delta\varepsilon_f\right)x-d_f\varepsilon_{c3}}{\Delta\varepsilon_f}\Leftrightarrow x'=\frac{\left(\varepsilon_{c3}+\varepsilon_f-\varepsilon_p\right)x-d_f\varepsilon_{c3}}{\varepsilon_f-\varepsilon_p} \tag{70}$$

$$x=\frac{-B-\sqrt{B^2-4AC}}{2A} \tag{71a}$$

with

$$A = \frac{f_{cd} b\left(\varepsilon_{c3} + 2\left(\varepsilon_f - \varepsilon_p\right)\right)}{2\left(\varepsilon_f - \varepsilon_p\right)^2} \tag{71b}$$

$$B = -\left(\frac{f_{cd} b d_f \left(\varepsilon_{c3} + \varepsilon_f - \varepsilon_p\right)}{\left(\varepsilon_f - \varepsilon_p\right)^2} + E_{sc} A_{sc} + \frac{f_{yd} A_{st}}{\varepsilon_f - \varepsilon_p} + E_f A_f \left(1 + \frac{\varepsilon_p}{\varepsilon_f - \varepsilon_p}\right)\right) \tag{71c}$$

$$C = \frac{f_{cd} b d_f{}^2 \varepsilon_{c3}}{2\left(\varepsilon_f - \varepsilon_p\right)^2} + E_{sc} A_{sc} c_{sc} + \left(\frac{f_{yd} A_{st}}{\varepsilon_f - \varepsilon_p} + E_f A_f \left(1 + \frac{\varepsilon_p}{\varepsilon_f - \varepsilon_p}\right)\right) d_f \tag{71d}$$

$$\chi_{ultimate} = \frac{\varepsilon_{cc}}{x} = \frac{\varepsilon_f - \varepsilon_p}{d_f - x} \tag{72}$$

$$M_{ultimate} = -\frac{f_{cc} b}{6}\left(x^2 + x x' + x'^2\right) + f_{yd} A_{st} d_{st} + f_f A_f d_f - E_{sc} \varepsilon_{cs} A_{sc} c_{sc} \tag{73}$$

7.2.4.3 Design assumption 3: $\varepsilon_p + \Delta\varepsilon_f < \varepsilon_f$ and $\varepsilon_{cc} = \varepsilon_{cu3}$

For this specific design assumption, the EC2 suggests a simplified approach for the determination of ultimate bending moment capacity which consists on the approximation of the bi-linear stress-strain relationship of concrete to a rectangular block of $0.8x$ height. Therefore, in this design assumption, the distribution of internal strain/stress is assumed to be given by Figure 232. The geometrical relationship between the unknown strains is given in Eq. 74

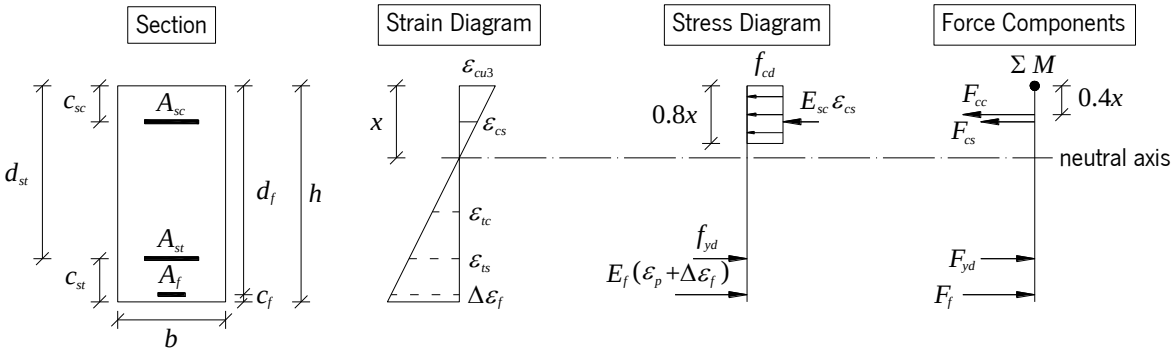

Figure 232 – Strain and stress diagram of the cross section at failure – Design assumption 3.

$$\frac{\varepsilon_{cs}}{x - c_{sc}} = \frac{\varepsilon_{cu3}}{x} \Leftrightarrow \varepsilon_{cs} = \frac{x - c_{sc}}{x}\varepsilon_{cu3} \tag{74a}$$

$$\frac{\Delta\varepsilon_f}{h - x - c_f} = \frac{\varepsilon_{cu3}}{x} \Leftrightarrow \Delta\varepsilon_f = \frac{d_f - x}{x}\varepsilon_{cu3} \tag{74b}$$

The depth of the neutral axis, the corresponding curvature and bending moment can be computed by Eqs. 75, 76 and 77.

$$x = \frac{-B + \sqrt{B^2 - 4AC}}{2A} \tag{75a}$$

with

$$A = 0.8 f_{cd} b \tag{75b}$$

$$B = E_{sc} A_{sc} \varepsilon_{cc} - f_{yd} A_{st} - E_f A_f \left(\varepsilon_p - \varepsilon_{cu3} \right) \tag{75c}$$

$$C = -\left(E_{sc} A_{sc} c_{sc} + E_f A_f d_f \right) \varepsilon_{cu3} \tag{75d}$$

$$\chi_{ultimate} = \frac{\varepsilon_{cu3}}{x} \tag{76}$$

$$M_{ultimate} = -0.32 f_{cd} b x^2 - E_{sc} \varepsilon_{cs} A_{sc} c_{sc} + f_{yd} A_{st} d_{st} + E_f \left(\varepsilon_p + \Delta\varepsilon_f \right) A_f d_f \tag{77}$$

7.2.5 Load-displacement relationship

In the course of this work, it was decided to include in the spreadsheet the calculation of the load-deflection notable points. This spreadsheet was designed to allow the determination of the mid-span deflection of a simply supported beam subjected to four-point bending exhibiting a single type moment-curvature relationship. As previously mentioned, the load-deflection curve can be characterized by four main notable stages:

- The initial displacement distribution along the beam induced by prestress application;
- The crack initiation displacement and load;
- The yielding initiation point, relevant to validate service limit states requirements;
- The ultimate deflection and corresponding load.

In the first two stress states the algebraic solution exhibits a relatively compact format and therefore, the closed-form solution is presented. In the remaining cases, a numerical approximation of the double integral of the curvature was adopted. Moreover, as the deformational behaviour is expected to be symmetrical in all cases, only half of the displacement curve is presented in relation to each loading stage.

7.2.5.1 The initial state

The response of a beam immediately after prestress application can be easily determined based on the classical beam theory. Assuming that a certain amount of curvature, $\chi_{initial}$, is introduced along a limited length of beam (see Figure 233), and since this curvature is constant, the double integration can be performed effortlessly (see Annex C).

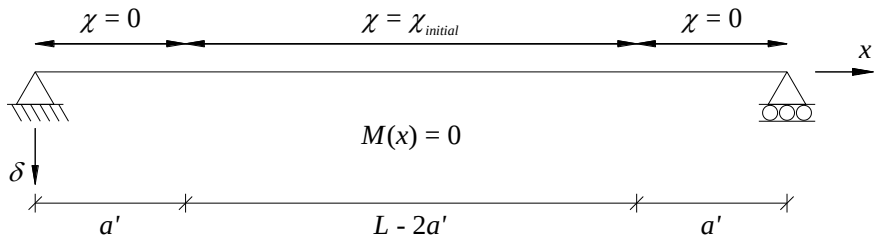

Figure 233 – Curvature distribution due to prestress application.

Since there is a change in initial curvature along the beam, the displacement equation is composed of two branches, as shown in Eq. 78. The maximum displacement is located at mid-span, where the rotation is null and is given by Eq. 79.

$$\delta(x) = \begin{cases} \dfrac{\chi_{initial}}{2}(L - 2a')x & 0 \le x \le a' \\ \dfrac{\chi_{initial}}{2}\left(Lx - x^2 - (a')^2\right) & a' \le x \le L/2 \end{cases} \tag{78}$$

$$\delta_{max} = \chi_{initial}\frac{L^2 - 4(a')^2}{8} \tag{79}$$

7.2.5.2 The cracking point

When cracking commences, the totality of the beam is still under linear elastic behaviour and the stiffness is constant along the totality of the length. For this reason, to obtain the deflection along the element, the evolution of displacement can be determined using the expressions available in academic literature. In Figure 234 the representation of the bending moment resultant of the four-point bending configuration is presented.

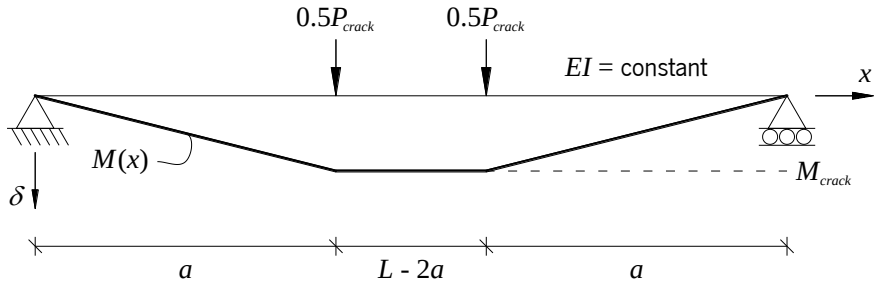

Figure 234 – Moment distribution at crack initiation.

The stiffness of the section is in this case assumed to be the slope of the moment-curvature curve between the initial point and the crack initiation point, as given in Eq. 80.

$$EI_{crack} = \frac{M_{crack}}{\chi_{crack} - \chi_{initial}} \tag{80}$$

The displacements along the beam are given by Eq. 81 and its maximum value by Eq. 82. The detailed deduction of these expressions can be found in Annex D.

$$\delta(x) = \begin{cases} \dfrac{P_{crack}\left(3a(L-a)-x^2\right)\cdot x}{12EI_{crack}} & 0 \le x \le a \\ \dfrac{P_{crack}a}{12EI_{crack}}\left(a(3L-4a)+3(L-a-x)\cdot(x-a)\right) & a \le x \le L/2 \end{cases} \tag{81}$$

$$\delta_{max} = \frac{P_{crack}a\left(3L^2-4a^2\right)}{24EI_{crack}} \tag{82}$$

7.2.5.3 The yielding point

There are a variety of processes that can enable the determination of the mid-span deflection at this stage. Additionally, due to the nonlinear character of the flexural stiffness variation along the beam, it was decided to use the classical beam theory to calculate the deflection of the beam. This method consists of discretizing the beam in relatively small elements in order to be able to approximate the double integral to a cumulative sum of trapezoidal areas. This process, schematized in Figure 235, can be mathematically described as follows.

The bending moment installed in each portion i of the beam loaded under four-point bending increases linearly up to the distance a from the support (Eq. 83). After this distance, the bending moment, M_i, becomes constant and equal to the yielding bending moment, M_{yield}. Since immediately after the cracking bending moment is exceeded the stiffness of the cross section changes, it was also recognised that it was important to determine the distance at which M_{crack} is exceeded, herein labelled as x_{yy} and evaluated by Eq. 84.

$$M_i = \begin{cases} \frac{x_i}{a} \cdot M_{yield} & 0 \le x_i \le a \\ M_{yield} & a \le x_i \le L/2 \end{cases} \tag{83}$$

$$x_{yy} = \frac{M_{crack}}{M_{yield}} \cdot a \tag{84}$$

To assess the correct stiffness of each element, the curvature of the cross section, in correspondence with the applied bending moment was calculated for each portion i of the beam. This curvature, χ_i, was determined based on Eq. 85. Regardless the load level applied to the beam, the flexural stiffness is always maximum in the support, according to Eq. 86.

$$\chi_i = \begin{cases} \frac{x_i}{x_{yy}}\left(\chi_{crack} - \chi_{initial}\right) & 0 \le x_i \le x_{yy} \\ \left(\chi_{crack} - \chi_{initial}\right) + \frac{\left(M_i - M_{crack}\right)}{\left(M_{yield} - M_{crack}\right)}\left(\chi_{yield} - \chi_{crack}\right) & x_{yy} \le x_i \le a \\ \chi_{yield} - \chi_{initial} & a \le x_i \le L/2 \end{cases} \tag{85}$$

$$EI_i = \begin{cases} \frac{M_{crack}}{\chi_{crack} - \chi_{initial}} & x_i = 0 \\ \frac{M_i}{\chi_i} & x_i > 0 \end{cases} \tag{86}$$

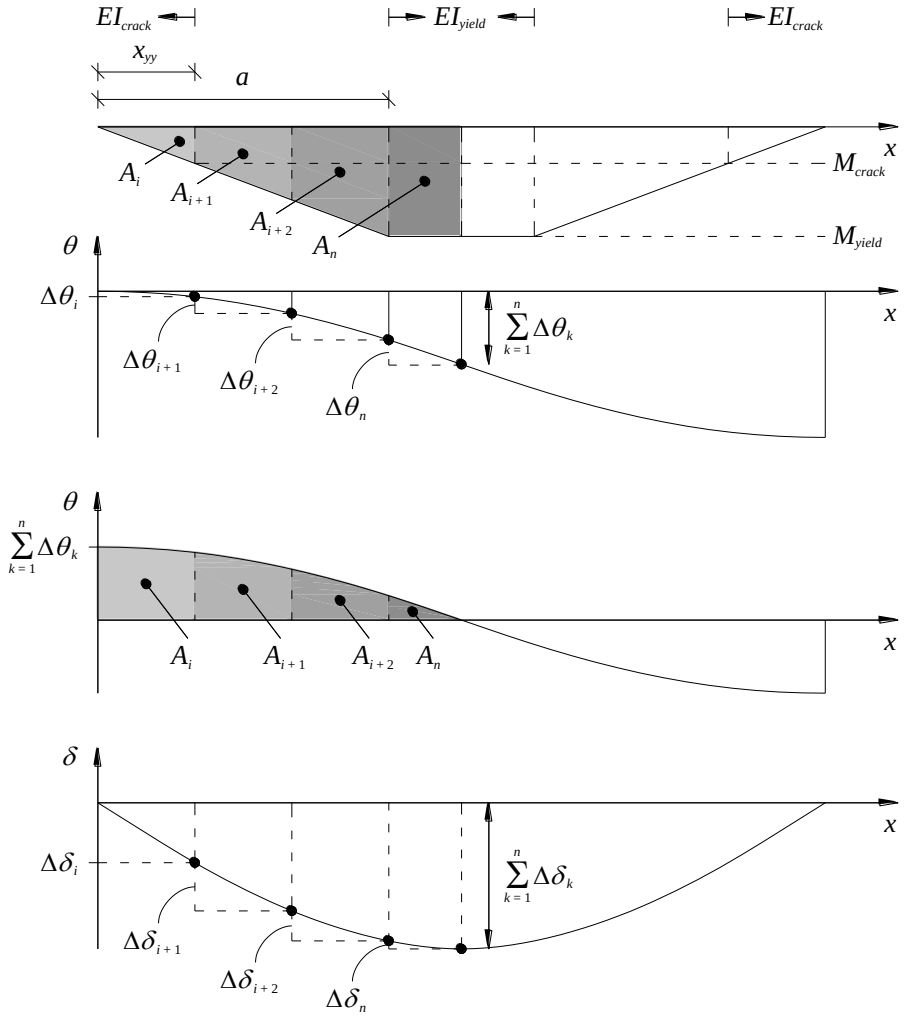

Figure 235 – Schematization of the double integral at yield initiation.

Regarding the first integration of the curvature, firstly the area of each of the trapezoids is calculated. Assuming that the moment-curvature relationship is linear between M_{i-1} and M_i the area of each trapezoid is then divided by the average stiffness of its boundaries, resulting in an increment of rotation, $\Delta\theta_i$, as quantified in Eq. 87. In order to respect the boundary condition according to which the rotation at mid-span is null, the rotation function needs to start from a positive value. In this case, this value corresponds to the absolute value of the sum of all the rotation increments up to mid-span ($-\sum_{k=1}^{n}\Delta\theta_k$). After determining this cumulative sum of rotation increments, the effective rotation can be defined as indicated in Eq. 88.

$$\Delta\theta_i = -\frac{\left(M_i + M_{i-1}\right)\left(x_i - x_{i-1}\right)}{\left(EI_i + EI_{i-1}\right)} \tag{87}$$

$$\theta_i = -\sum_{k=1}^{n} \Delta\theta_k + \sum_{k=1}^{i} \Delta\theta_k \tag{88}$$

For the determination of the displacement curve, a second integration should be performed, using the same approach described above, resulting in Eqs. 89 and 90. Note that in the case of the displacement, the boundary condition is respected by default since the cumulative sum of displacement increments, already starts from zero.

$$\Delta\delta_i = -\frac{(\theta_i + \theta_{i-1})(x_i - x_{i-1})}{2} \tag{89}$$

$$\delta_{max} = \sum_{k=1}^{n} \Delta\delta_k \tag{90}$$

7.2.5.4 The ultimate point

The ultimate deflection can be approximated using the same process previously described. The schematic representation of the double integration is shown in Figure 236.

The moment at the pure bending zone is assumed to be $M_{ultimate}$ and the growth of this moment along the beam is given by Eq. 91. In this approach, it is necessary to determine two special coordinates, x_{uy}, which corresponds to the distance at which the cracking moment is reached and x_{uu}, the distance at which the yielding moment is achieved (Eqs. 92 and 93, respectively).

$$M_i = \begin{cases} \frac{x_i}{a} \cdot M_{ultimate} & 0 \le x_i \le a \\ M_{ultimate} & a \le x_i \le L/2 \end{cases} \tag{91}$$

$$x_{uy} = \frac{M_{crack}}{M_{ultimate}} \cdot a \tag{92}$$

$$x_{uu} = \frac{M_{yield}}{M_{ultimate}} \cdot a \tag{93}$$

Concerning the curvature in correspondence to each bending moment, M_i, it can be determined based on Eq. 94. The remaining procedure is in all equal to the one previously described in section 7.2.5.3 from Eqs. 86 to 90.

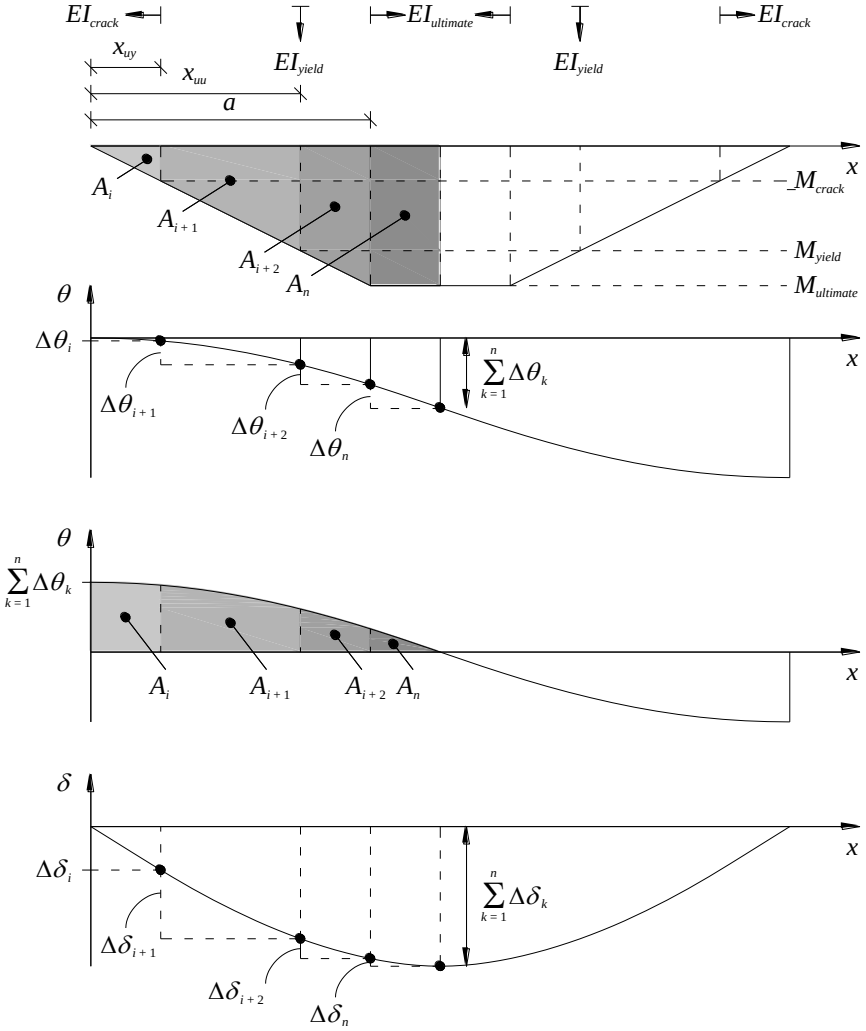

Figure 236 – Schematization of the double integral at ultimate stage.

$$\chi_i = \begin{cases} \dfrac{x_i}{x_{uy}}\left(\chi_{crack} - \chi_{initial}\right) & 0 \le x_i \le x_{uy} \\ \left(\chi_{crack} - \chi_{initial}\right) + \dfrac{\left(M_i - M_{crack}\right)}{\left(M_{yield} - M_{crack}\right)}\left(\chi_{yield} - \chi_{crack}\right) & x_{uy} \le x_i \le x_{uu} \\ \left(\chi_{yield} - \chi_{initial}\right) + \dfrac{\left(M_i - M_{yield}\right)}{\left(M_{ultimate} - M_{yield}\right)}\left(\chi_{ultimate} - \chi_{yield}\right) & x_{uu} \le x_i \le a \\ \chi_{ultimate} - \chi_{initial} & a \le x_i \le L/2 \end{cases} \quad (94)$$

7.2.6 Application of the numerical model to the experimental results

The predictive performance of the formulation implemented in the spreadsheet already introduced presented was assessed using the results obtained in the experimental program described in Chapter 5. A summary of the obtained notable points is presented in Tables 1 to 78and in Figures 237 to 239 these points are compared with the force-deflection response registered experimentally.

Table 76 – Summary of the analytical results – Series I.

Beam	δ_{crack} [mm]	P_{crack} [kN]	δ_{yield} [mm]	P_{yield} [kN]	$\delta_{ultimate}$ [mm]	$P_{ultimate}$ [kN]	$P_{l/250}$ [kN]
Reference	0.200	9.64	5.934	47.89	33.824	52.61	48.37
S1_0%	0.230	11.16	6.075	55.92	20.747	89.54	62.17
S1_20%	0.399	19.35	6.014	62.77	16.279	88.91	70.13
S1_30%	0.405	19.60	6.152	66.60	15.228	90.91	74.13

Table 77 – Summary of the analytical results – Series II.

Beam	δ_{crack} [mm]	P_{crack} [kN]	δ_{yield} [mm]	P_{yield} [kN]	$\delta_{ultimate}$ [mm]	$P_{ultimate}$ [kN]	$P_{l/250}$ [kN]
Reference	0.560	7.32	15.624	25.09	108.239	28.65	24.59
S2_0%	0.561	7.38	16.277	29.76	62.992	50.96	28.22
S2_20%	0.807	10.59	16.244	33.93	49.120	50.45	32.71
S2_30%	0.926	12.15	16.250	35.95	39.990	48.00	34.86
S2_40%	1.050	13.76	16.269	38.03	31.933	46.60	37.07
S2_50%	1.165	15.27	16.297	39.97	29.485	47.44	39.12

Table 78 – Summary of the analytical results – Series III.

Beam	δ_{crack} [mm]	P_{crack} [kN]	δ_{yield} [mm]	P_{yield} [kN]	$\delta_{ultimate}$ [mm]	$P_{ultimate}$ [kN]	$P_{l/250}$ [kN]
Reference	0.599	7.58	17.187	33.55	80.233	39.09	30.44
S3_0%	0.670	7.05	17.966	39.67	60.186	62.69	34.45
S3_20	1.427	11.69	18.246	45.89	45.152	61.88	40.58
S3_30%	1.459	11.26	18.789	48.59	41.044	62.43	42.33
S3_40%	1.601	13.97	20.044	53.05	35.480	64.37	44.49
S3_50%	1.286	12.69	20.400	54.10	31.870	64.32	44.75

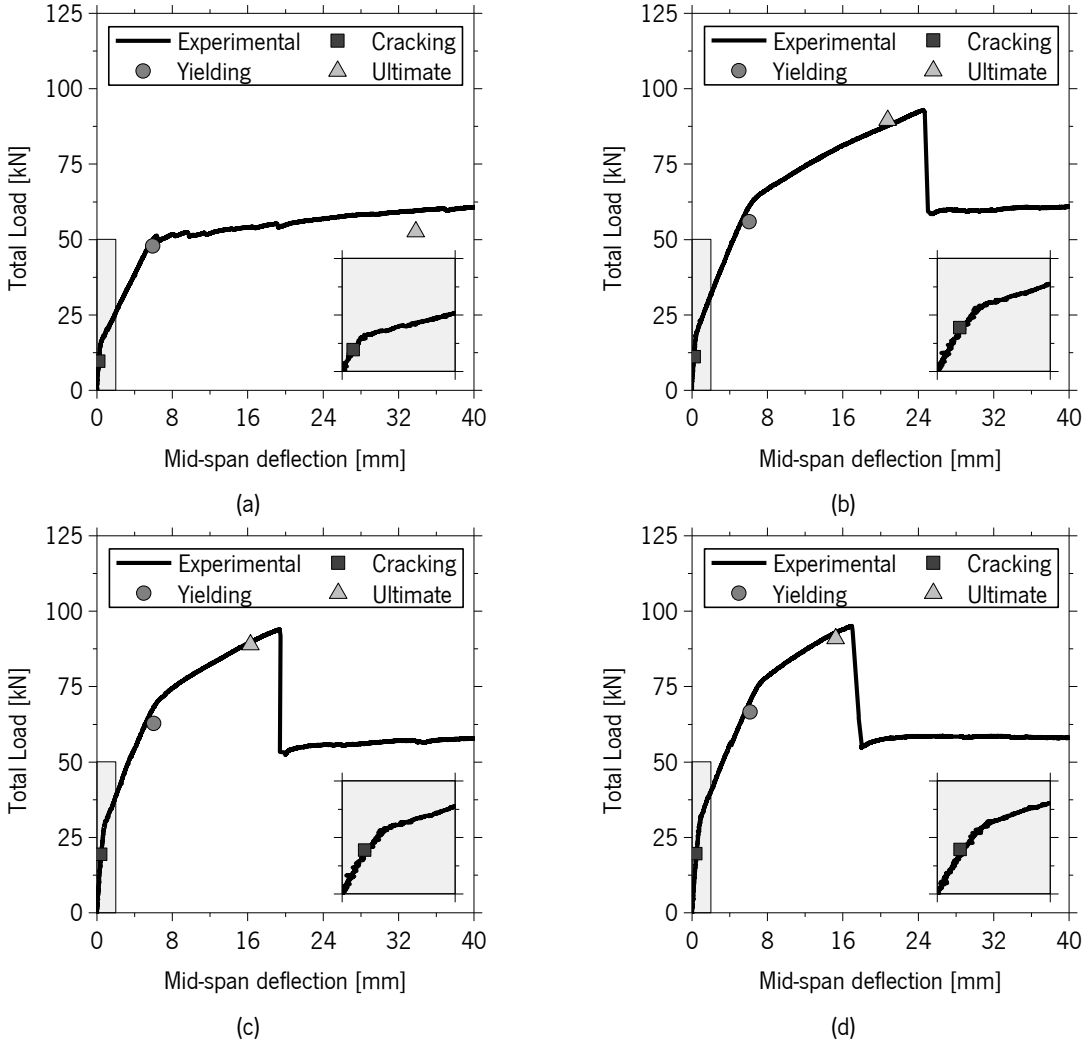

Figure 237 – Comparison between experimental and analytical load-deflection – Series I: (a) Reference, (b) S1_0%. (c) S1_20% and (d) S1_30%.

Concerning the results obtained for Series I, it was noticed that the analytical model predicts the moment of crack initiation since in all cases, P_{crack} was underestimated in relation to the experimental results. Moreover, in resemblance to the results obtained in Chapter 6 using the one-dimensional model, the ultimate deflection was in most cases underestimated, most likely due to the disregard of the shear contribution.

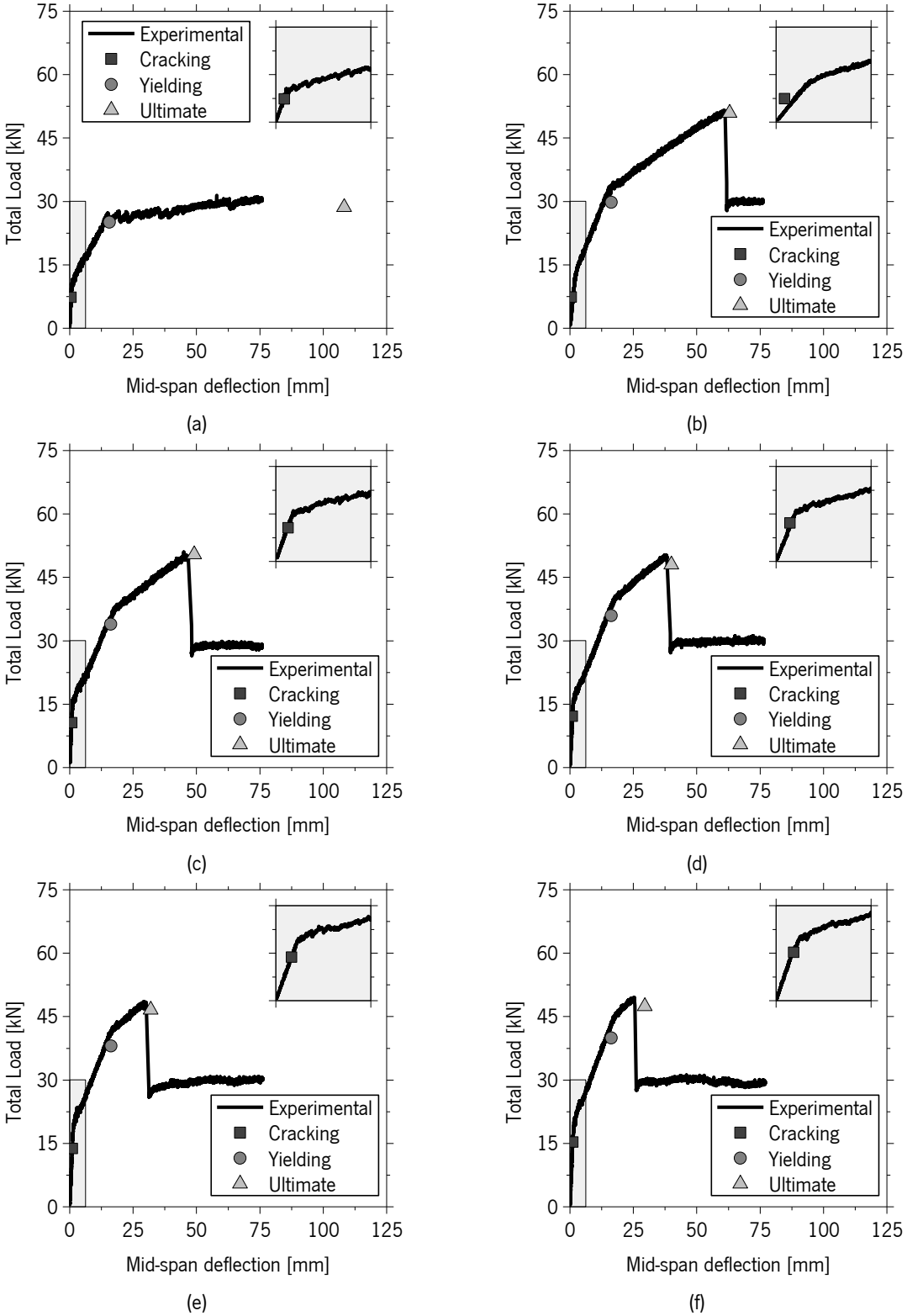

Figure 238 – Comparison between experimental and analytical load-deflection – Series II: (a) Reference, (b) S2_0%, (c) S2_20%, (d) S2_30%, (e) S2_40% and (f) S2_50%.

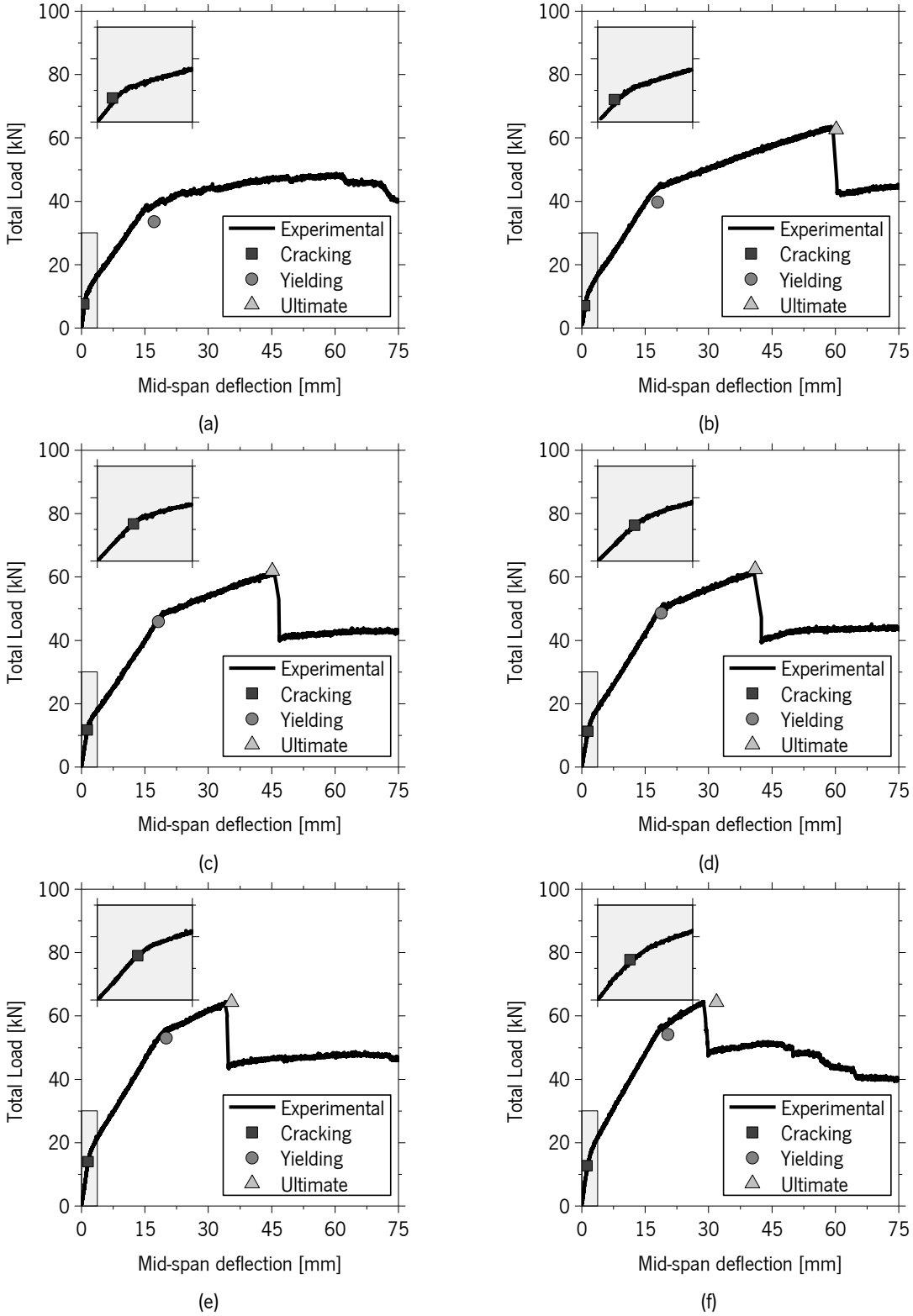

Figure 239 – Comparison between experimental and analytical load-deflection – Series III: (a) Reference, (b) S2_0%, (c) S2_20%, (d) S2_30%, (e) S2_40% and (f) S2_50%.

Contrasting with the previous Series, the prediction of the ultimate deflection of the beams of Series II and III is exceptionally accurate while the crack initiation moment was again

underestimated in comparison to the experimental results. Nevertheless, observing Figures 238 and 239, the notable points are better predicted than in the previous Series.

7.3 FINAL REMARKS

In this Chapter, an analytical approach was established to predict the strain distribution along the bond length, as well as the load-carrying capacity of the beam at different load stages. The developed models demonstrated good ability to predict the effects of prestressed NSM-CFRP on reinforced concrete beams at different loading stages.

Regarding the multiple regression model developed, it is worth remembering that it is only valid if no damage is produced in the FRP-adhesive-concrete-interface and if all materials are working within the linear elastic range. The use of prestress levels that introduce shear sliding higher than the sliding at peak bond strength of the above interfaces is not recommended, and the limit of prestress level should be determined case by case depending on the FRP strengthening system used. The multiple regression approach has revealed to be suitable for the determination of the long term strain along the bond length of the all the tested beams since the CFRP strains over time were accurately determined.

The section analysis model used for the assessment of the load carrying capacity of reinforced concrete elements strengthened with prestressed CFRP has predicted with good accuracy the results obtained experimentally. However, it is worth mentioning that this is only valid if a sufficient anchorage length is provided to the CFRP.

An analytical formulation was developed for the determination of the notable points of the load-displacement relationship of the type of tested beams. This model was capable of predicting with accuracy these notable points in the series of beams tested experimentally. However, the level of NSM-FRP strengthening utilized in the experimental program was not sufficient to promote more complex failure modes such as the case of concrete cover rip-off. Therefore, additional research should be carried out to define reasonable limits to the analytical methodology developed.

In conclusion, considering that adequate shear reinforcement is provided, it is suggested that for the design of reinforced concrete sections prestressed with FRP materials, the constructive dispositions illustrated in Figure 240 are followed in order to not only guarantee an adequate anchorage in maximum bending moment zone, as well as a suitable amount of anchorage length for the prestress load. The main objective of this disposition would be to guarantee that enough length is provided to

absorb the maximum CFRP strain increment at failure ($l_{b,static}$) and simultaneously, that the prestress initially applied is available in the majority of the CFRP laminate ($l_{b,creep}$).

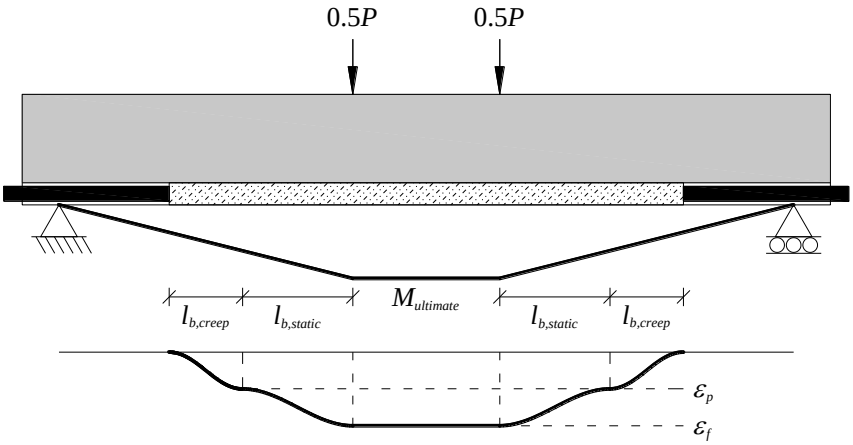

Figure 240 – Suggestion of constructive disposition for prestressed NSM-FRP strengthned beams.

7.4 REFERENCES

EN 1992-1-1 (2004). "Eurocode 2: Design of concrete structures - Part 1-1: General rules and rules for buildings." *European Committee for Standardization*, 225 pp.

Chapter 8

CONCLUSIONS

8.1 MAIN CONCLUSIONS

In this chapter, a comprehensive analysis of the main benefits and limitations of the application of prestressed NSM-CFRP laminates for the flexural strengthening of reinforced concrete (RC) beams is done.

In a first phase (Chapter 3), tests conducted on the adhesive and NSM-CFRP system allowed to conclude that a curing time of 3 days, at a temperature of 20ºC, is sufficient to guarantee an adequate adhesive elastic modulus, as well as a suitable bond performance of the NSM-CFRP strengthening system.
Regarding the creep tests performed on samples of epoxy adhesive cured for 3 days, it was concluded that up to sustained stress levels of 60% of the adhesive's tensile strength, the adhesive behaves as a linear viscoelastic material and can be easily parameterized using the modified Burgers model.

In a subsequent phase of this work (Chapter 4), prestressed NSM-CFRP laminates were successfully applied on ten RC beams. All beams registered low levels of strain loss along the majority of the bonded length (maximum losses of about 3%), and reasonable initial deflection levels (0.078 mm to 1.112 mm) of were obtained due to the prestress application.

The long term losses of prestress in the strain gauges placed 25 mm from the free-ends of the CFRP were found to be stabilize in 2 days to 15 days. The long term transfer length of the prestress force was found to be, in the case of Series I beams, lower than 200 mm.

In Chapter 5, all the beams flexurally strengthened with prestressed NSM CFRP laminates were tested up to failure under four-point bending loading configuration in order to assess the effectiveness of this strengthening technique. According to the obtained results, the load at crack and yield initiation increases significantly with the prestress level.

The prestress level applied to the CFRP laminates revealed to have no influence on the ultimate load carrying capacity of the strengthened beams, since failure was in all cases dominated by the CFRP rupture. Other important effects registered at failure were the considerable decrease of ultimate deflection and total cracked length of the beam with the increase of the prestress level. It should be noted that the decrease of deflection at failure, $\delta_{ultimate}$, has advantages, but also disadvantages. In fact, a lower $\delta_{ultimate}$ produces an immediate reduction of the ductility of the prestressed member, in relation to the passively strengthened member. However, the load carrying capacity at the deflection corresponding to service limit states (SLS, $\delta/250$) increases with the prestress level, favouring the occurrence of crack patterns in prestressed NSM-CFRP strengthened members with a smaller crack width than in passively NSM-CFRP strengthened elements (Figure 241).

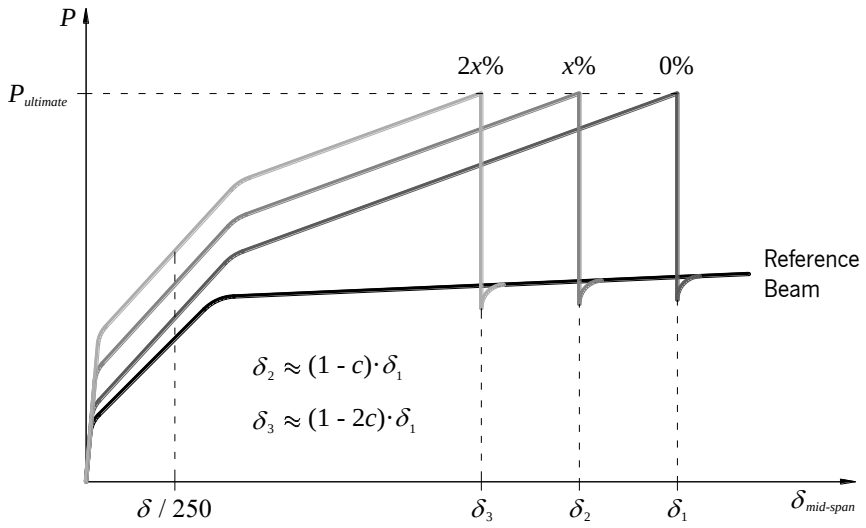

Figure 241 – Illustration of NSM-CFRP the prestress effect on the force-deflection response of reinforced concrete beams.

Once the experimental program was finished, the losses of strain experienced by the CFRP laminate were modelled using a relatively simple numerical approach (Chapter 6). The agreement between the results obtained by this process and the ones registered experimentally was

surprisingly excellent considering the simplicity of the adopted model. This demonstrates that the used epoxy adhesive is one of the most relevant constituents of the strengthening system influencing the long-term behaviour of the reinforced concrete beams prestressed with CFRP laminates.

Regarding the prediction of the behaviour of the reinforced concrete beams up to failure using a plane stress model, the load-deflection and load-strain curves, obtained by numerical simulations have fitted with good accuracy the corresponding curves registered experimentally. Additionally, the crack patterns obtained numerically also revealed good agreement with the crack patterns observed experimentally. The location of the failure section of the tested beams was also predicted with good accuracy. Moreover, modelling the strengthened beams using moment-curvature section analysis combined with the matrix displacement method also predicted with exceptional accuracy the load-deflection curves of the majority of the strengthened beams.

Finally, an analytical strategy was proposed to predict long term strain distribution along CFRP, as well as the load-carrying capacity at different load stages of a NSM flexurally strengthened RC beam (Chapter 7). The developed models demonstrated good ability to predict the effects of prestressed NSM-CFRP on reinforced concrete beams at different loading stages.

The multiple regression approach developed revealed to be suitable for the determination of the long term strain along the bond length of all the tested beams, since the CFRP strains over time were accurately predicted. Additionally, a section analysis model was developed for the assessment of the load carrying capacity and deflection of reinforced concrete elements strengthened with prestressed. This model was implemented in a spreadsheet and has predicted with good accuracy the results obtained experimentally.

Regarding this last chapter, a constructive disposition is proposed (see Figure 242) to guarantee that enough length is provided to absorb the maximum CFRP strain increment at failure ($l_{b,static}$) and, simultaneously, that the prestress initially applied is available in the majority of the CFRP laminate. The value of $l_{b,static}$ can be determined by means of pull out bending tests, with the adopted NSM-CFRP strengthening system, following the strategy presented in Chapter 3. On the other hand, the value of $l_{b,creep}$ can be quantified for this NSM-CFRP strengthening system using the empirical approach presented in Chapter 7.

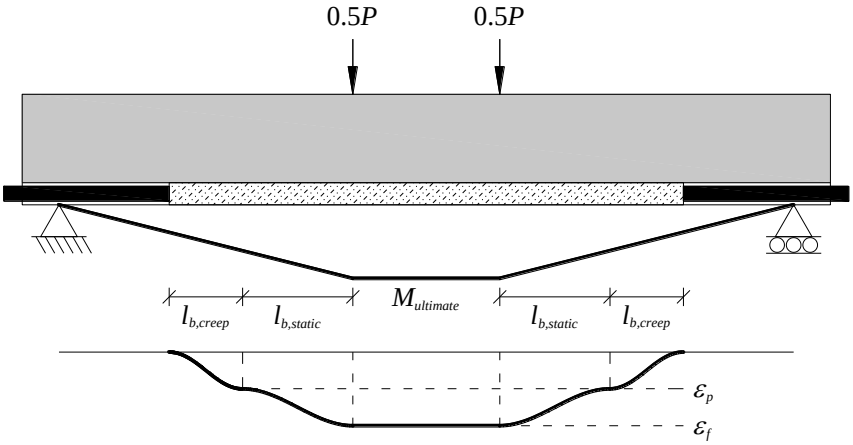

Figure 242 – Suggestion of constructive disposition for prestressed NSM-FRP reinforced beams.

8.2 RECOMMENDATIONS FOR FUTURE RESEARCH

Applying prestressed NSM-CFRP laminates to RC members is still a relatively recent strengthening approach and a lot of investigation still needs to be developed on this topic. However, there are some topics of major importance to transform this strengthening system in a real practice of the strengthening activity.

Nowadays, externally bonded prestressed CFRP laminates are already being applied in reinforced concrete structures. However, for the case of prestressed NSM-CFRP laminates, an appropriate device allowing their application in job site conditions needs to be developed.

The creep properties assessed in the scope of this work revealed to be sufficient for the quantification of the prestress losses during the monitored time span. Additionally, as the application of prestress was always performed indoors, the average environmental temperature was always close to the one used in the tensile creep tests. However, as the properties of the adhesive are usually identified as being dependent of the environmental medium, the creep tests should also be performed under other temperature and relative humidity conditions. Moreover, although in this work only the tensile creep properties were evaluated, the creep under compression should also be characterized for a more holistic and reliable modelling approach.

Finally, creep tests on loaded RC elements strengthened with prestressed NSM-CFRP laminates should also be performed in order to validate the accuracy of the proposed approaches or, to eventually propose/include additional adjustments to improve its predictive performance.

Annex A

DEDUCTION OF THE CLASSICAL RHEOLOGICAL MODELS

Rheology is by definition the part of mechanics that studies the response of materials to the actions that provoke flow. This discipline of continuum mechanics enables the characterization of the two most relevant time-dependent phenomena:

- Creep: increase of the deformation under constant stress;
- Relaxation: decrease of stress under constant deformation.

Rheological models can be composed by a series of simple elements connected in a variety of ways. Those simple elements can reflect elastic or viscous components of the material's behaviour by means of springs or dashpots, respectively (see Figure A.1). In the scope of this work, only the components with linear properties will be addressed. However, for certain applications, the use of non-linear stress-strain laws can be of interest.

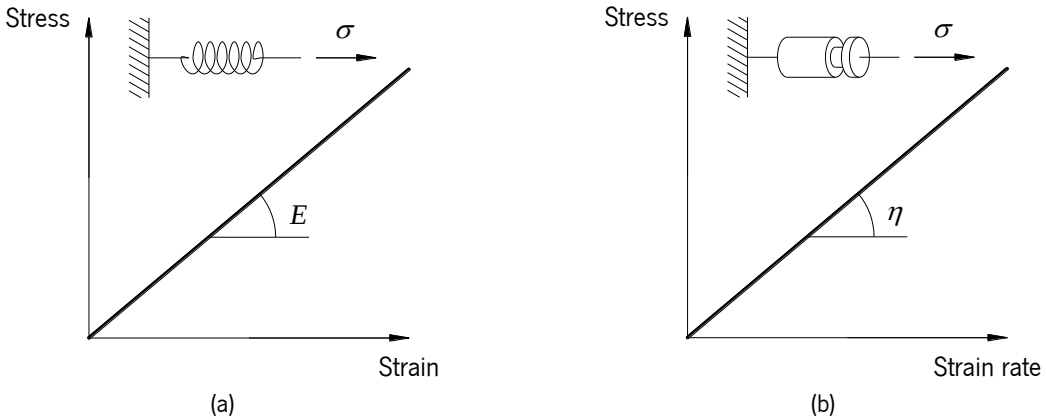

Figure A.1 – Rheological elements with linear behaviour: (a) Hookean spring; (b) Newtonian dashpot.

Observing Figures A.1a and A.1b, the following relationships can be established:

$$\sigma = E \cdot \varepsilon \tag{A.1}$$

$$\sigma = \eta \cdot \dot{\varepsilon} \tag{A.2}$$

where σ is the level of applied stress, usually expressed in MPa, ε is the strain induced by σ, $\dot{\varepsilon}$ is the strain velocity, i.e., the derivative of the strain with respect to time, E is the stiffness of the spring, also known as the elastic modulus and η is the dashpot's coefficient of dynamic viscosity.

Now that the individual elements are characterized, it is also necessary to define the laws ruling the behaviour of an arbitrary combination of these elements. There are fundamentally two ways to connect the rheological elements: in series or in parallel. If n rheological elements are connected in series, the stress transmitted through them is constant and the strains induced are additive (Eq. A.3). If, on the other hand, n rheological elements are assembled in parallel, the total deformation is equal in all the elements and, as a result, the installed stresses will be additive (Eq. A.4).

$$\varepsilon = \sum_{i=1}^{n} \varepsilon_i \tag{A.3}$$

$$\sigma = \sum_{i=1}^{n} \sigma_i \tag{A.4}$$

In the following topics, the differential equations that describe the most noteworthy rheological models are deduced. Keep in mind that all the derivatives presented in the subsequent topics are always derivatives with respect to time.

A.1 MAXWELL'S MODEL

The model proposed by Maxwell is a 2-parameter model composed by a Hookean spring and a Newtonian dashpot connected in series. Considering now that this model is subjected to an arbitrary stress function, $\sigma(t)$ or simply σ, as depicted in Figure A.2, the final deformation can be easily deduced:

- the applied stress function, $\sigma(t)$, is equally transmitted by all the elements of the model and produces at the support a reaction of equal value;
- the spring deforms instantly as a result of $\sigma(t)$ and this deformation is in Figure A.2 designated as ε_1;
- σ provokes in the dashpot a delayed deformation, described by Newton's law, and herein labelled as ε_2.

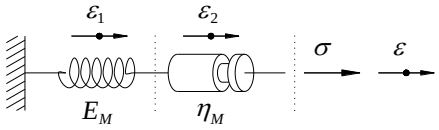

Figure A.2 – Schematization of Maxwell's model.

As stated previously the total strain ($\varepsilon(t)$ or simply ε) in this type of systems is given by the sum of the individual strains measured in the different rheological elements (Eq. A.5a). It can be useful to rewrite this equation in its differential form, as presented in Eq. A.5b.

$$\varepsilon = \varepsilon_1 + \varepsilon_2 \tag{A.5a}$$

$$\dot{\varepsilon} = \dot{\varepsilon}_1 + \dot{\varepsilon}_2 \tag{A.5b}$$

The first term of Eq. A.5b, $\dot{\varepsilon}_1$, can be easily obtained by deriving Hooke's Law with respect to the time.

$$\varepsilon_1 = \frac{\sigma}{E_M} \tag{A.6a}$$

$$\dot{\varepsilon}_1 = \frac{\dot{\sigma}}{E_M} \tag{A.6b}$$

As for the second term of Eq. A.5b, $\dot{\varepsilon}_2$, the derivative of the strain can be obtained by directly applying Newton's Law

$$\dot{\varepsilon}_2 = \frac{\sigma}{\eta_M} \tag{A.7}$$

Now, substituting Eq. A.6 and A.7 in Eq. A.5b the following equation is obtained.

$$\dot{\varepsilon} = \frac{\dot{\sigma}}{E_M} + \frac{\sigma}{\eta_M} \tag{A.8}$$

Multiplying all terms by $E_M \eta_M$, the differential equation that rules creep and/or relaxation of a given material is:

$$E_M \eta_M \dot{\varepsilon} = \eta_M \dot{\sigma} + E_M \sigma \tag{A.9}$$

In the special case of creep under a constant stress (where $\dot{\sigma} = 0$), the solution of Eq. A.9, will be[1]

$$\varepsilon(t) = \frac{\sigma}{E_M} + \frac{\sigma}{\eta_M} t \tag{A.10}$$

A.2 KELVIN'S MODEL

Kelvin's model is also a 2-parameter rheological model but, in this case, the elements are disposed in parallel. The approach to be used is slightly different, i.e., in case of elements connected in parallel, the total strain is the same in all the individual elements (Eq. A.11) while the total stress is the addition of the stresses installed in all the components (Figure A.3).

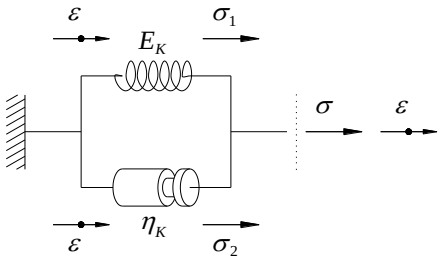

Figure A.3 – Schematization of Kelvin's model.

$$\varepsilon = \varepsilon_1 = \varepsilon_2 \tag{A.11}$$

Therefore, in case of parallel elements the equilibrium is defined by equalling the total applied stress (σ) to the sum of the individual stresses.

$$\sigma = \sigma_1 + \sigma_2 \tag{A.12}$$

The total strain induces in the spring a stress given by Eq. A.13 while the dashpot develops a different stress given in Eq. A.14.

$$\sigma_1 = E_K \varepsilon \tag{A.13}$$

$$\sigma_2 = \eta_K \dot{\varepsilon} \tag{A.14}$$

[1] Verification: $\dot{\varepsilon}(t) = \frac{\sigma}{\eta_M}$; $E_M \eta_M \frac{\sigma}{\eta_M} = \eta_M \cdot 0 + E_M \sigma \Leftrightarrow \sigma = \sigma$

Replacing Eq. A.13 and A.14 in Eq. A.12, the differential equation that describes Kelvin's model is obtained.

$$\eta_K \dot{\varepsilon} + E_K \varepsilon = \sigma \tag{A.15}$$

Considering creep under a constant stress (where $\dot{\sigma} = 0$), the solution of Eq. A.15 is[2]

$$\varepsilon(t) = \frac{\sigma}{E_K}\left(1 - e^{-\frac{E_K}{\eta_K}t}\right) \tag{A.16}$$

A.3 BURGER'S MODEL

The concepts previously described can be combined in order to obtain the differential equation Burger's model. This 4-parameter model, depicted in Figure A.4, can be divided in three independent branches, subjected to the same applied stress, σ. The sum of the strains produced in each branch provides the total strain response (Eq. A.17).

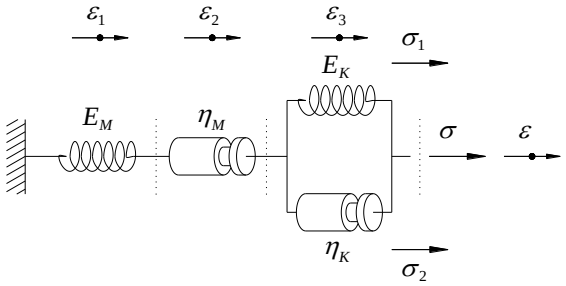

Figure A.4 – Schematization of Burger's model.

$$\varepsilon = \varepsilon_1 + \varepsilon_2 + \varepsilon_3 \tag{A.17a}$$

$$\dot{\varepsilon} = \dot{\varepsilon}_1 + \dot{\varepsilon}_2 + \dot{\varepsilon}_3 \tag{A.17b}$$

The first and second terms of Eq. A.17b can be obtained with the same process used in Section A.1.

[2] Verification: $\dot{\varepsilon}(t) = \frac{\sigma}{\eta_K} e^{-\frac{E_K}{\eta_K}t}$; $\eta_K \frac{\sigma}{\eta_K} e^{-\frac{E_K}{\eta_K}t} + E_K \frac{\sigma}{E_K}\left(1 - e^{-\frac{E_K}{\eta_K}t}\right) = \sigma \Leftrightarrow \sigma = \sigma$

$$\varepsilon_1 = \frac{\sigma}{E_M} \tag{A.18a}$$

$$\dot{\varepsilon}_1 = \frac{\dot{\sigma}}{E_M} \tag{A.18b}$$

$$\dot{\varepsilon}_2 = \frac{\sigma}{\eta_M} \tag{A.19}$$

Regarding the third term of Eq. A.17b, Kelvin's differential equation (Eq. A.15) can be taken as reference.

$$\sigma = \eta_K \dot{\varepsilon}_3 + E_K \varepsilon_3 \tag{A.20}$$

Rearranging Eq. A.20, the required term becomes

$$\dot{\varepsilon}_3 = \frac{\sigma}{\eta_K} - \frac{E_K \varepsilon_3}{\eta_K} \tag{A.21}$$

Substituting Eq. A.18, A.19 and A.21 in Eq. A.17b, the derivative of the total strain becomes

$$\dot{\varepsilon} = \frac{\dot{\sigma}}{E_M} + \frac{\sigma}{\eta_M} + \frac{\sigma}{\eta_K} - \frac{E_K \varepsilon_3}{\eta_K} \tag{A.22}$$

Deriving Eq. A.22,

$$\ddot{\varepsilon} = \frac{\ddot{\sigma}}{E_M} + \frac{\dot{\sigma}}{\eta_M} + \frac{\dot{\sigma}}{\eta_K} - \frac{E_K \dot{\varepsilon}_3}{\eta_K} \tag{A.23}$$

Isolating $\dot{\varepsilon}_3$ from Eq. A.17b,

$$\dot{\varepsilon}_3 = \dot{\varepsilon} - \dot{\varepsilon}_1 - \dot{\varepsilon}_2 \tag{A.24}$$

Substituting the terms known so far,

$$\dot{\varepsilon}_3 = \dot{\varepsilon} - \frac{\dot{\sigma}}{E_M} - \frac{\sigma}{\eta_M} \tag{A.25}$$

Substituting Eq. A.25 in Eq. A.23,

$$\ddot{\varepsilon} = \frac{\ddot{\sigma}}{E_M} + \frac{\dot{\sigma}}{\eta_M} + \frac{\dot{\sigma}}{\eta_K} - \frac{E_K}{\eta_K}\left(\dot{\varepsilon} - \frac{\dot{\sigma}}{E_M} - \frac{\sigma}{\eta_M}\right) \tag{A.26a}$$

$$\ddot{\varepsilon} + \frac{E_K}{\eta_K}\dot{\varepsilon} = \frac{\ddot{\sigma}}{E_M} + \frac{\dot{\sigma}}{\eta_M} + \frac{\dot{\sigma}}{\eta_K} + \frac{E_K}{\eta_K}\frac{\dot{\sigma}}{E_M} + \frac{E_K}{\eta_K}\frac{\sigma}{\eta_M} \tag{A.26b}$$

And multiplying Eq. A.26 by $E_M \eta_K \eta_M$, the differential equation of Burger's model yields.

$$E_M \eta_K \eta_M \ddot{\varepsilon} + E_K E_M \eta_M \dot{\varepsilon} = \eta_K \eta_M \ddot{\sigma} + \left(E_M \eta_K + E_M \eta_M + E_K \eta_M\right)\dot{\sigma} + E_M E_K \sigma \tag{A.27}$$

Considering creep under a constant stress (where $\dot{\sigma} = \ddot{\sigma} = 0$), the solution of Eq. A.27 is[3]

$$\varepsilon(t) = \frac{\sigma}{E_M} + \frac{\sigma}{\eta_M} t + \frac{\sigma}{E_K}\left(1 - e^{-\frac{E_K}{\eta_K}t}\right) \tag{A.28}$$

Note that this model reveals the possibility of applying the so-called superposition principle, *i.e.*, if Maxwell and Kelvin's model are associated in chain, the solution of the resultant model can be instantly obtained by adding the individual solutions (Eq. A.10 and A.16).

[3] Verification: $\dot{\varepsilon}(t) = \frac{\sigma}{\eta_M} + \frac{\sigma}{\eta_K} e^{-\frac{E_K}{\eta_K}t}$; $\ddot{\varepsilon}(t) = -E_K \frac{\sigma}{\eta_K^{\,2}} e^{-\frac{E_K}{\eta_K}t}$;

$$-E_K E_M \eta_K \eta_M \frac{\sigma}{\eta_K^{\,2}} e^{-\frac{E_K}{\eta_K}t} + E_K E_M \eta_M \left(\frac{\sigma}{\eta_M} + \frac{\sigma}{\eta_K} e^{-\frac{E_K}{\eta_K}t}\right) = E_M E_K \sigma \Leftrightarrow \sigma = \sigma$$

Annex B

REINFORCING STEEL STRESS-STRAIN CURVES

B.1 SERIES I

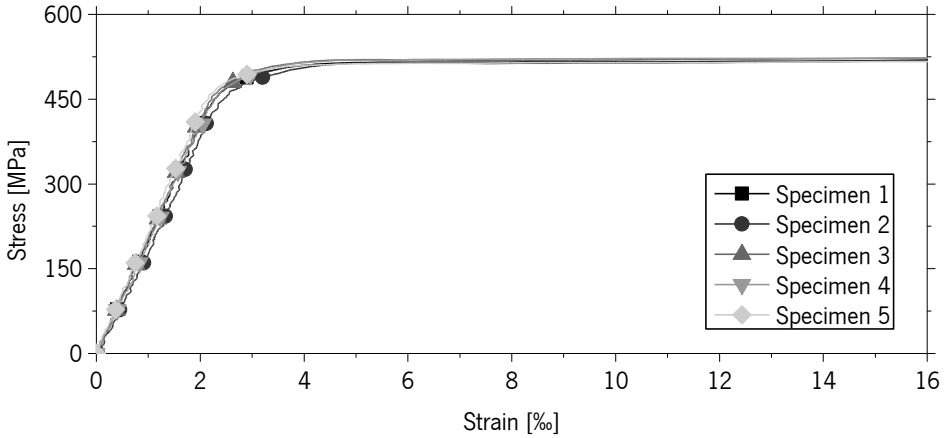

Figure B.1 – Stress versus strain in samples of the longitudinal bars (ϕ = 10 mm).

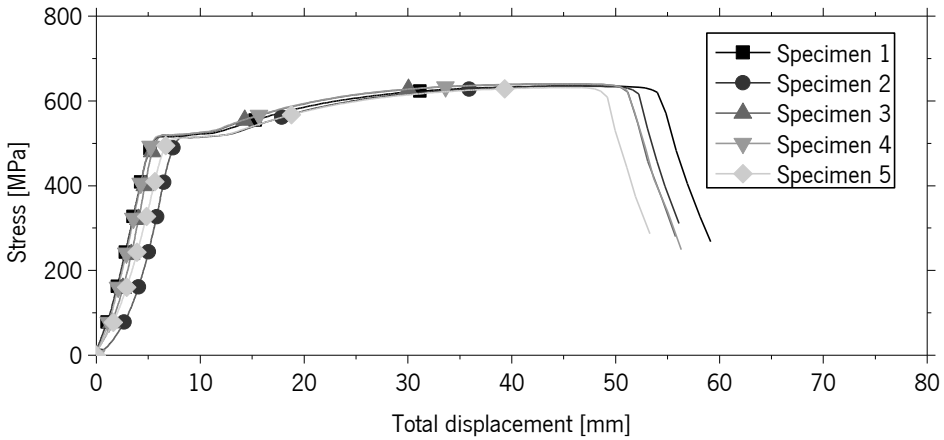

Figure B.2 – Stress versus total displacement in samples of the longitudinal bars (ϕ = 10 mm).

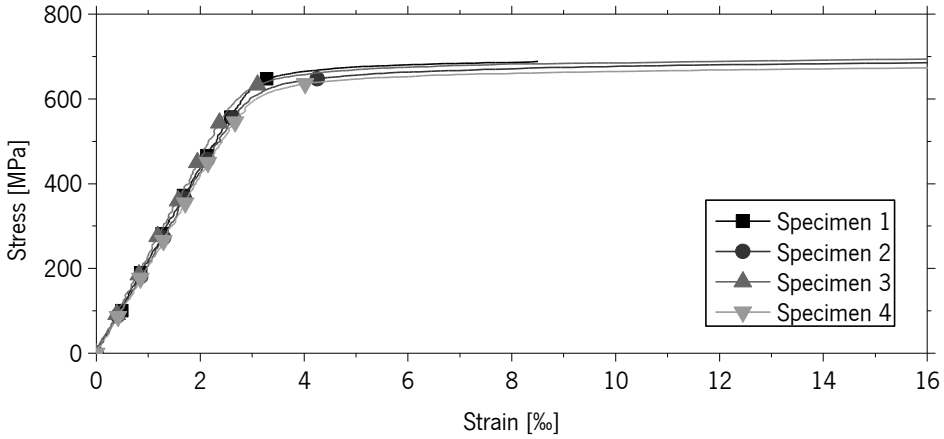

Figure B.3 – Stress versus strain in samples of the shear reinforcement bars(ϕ = 6 mm).

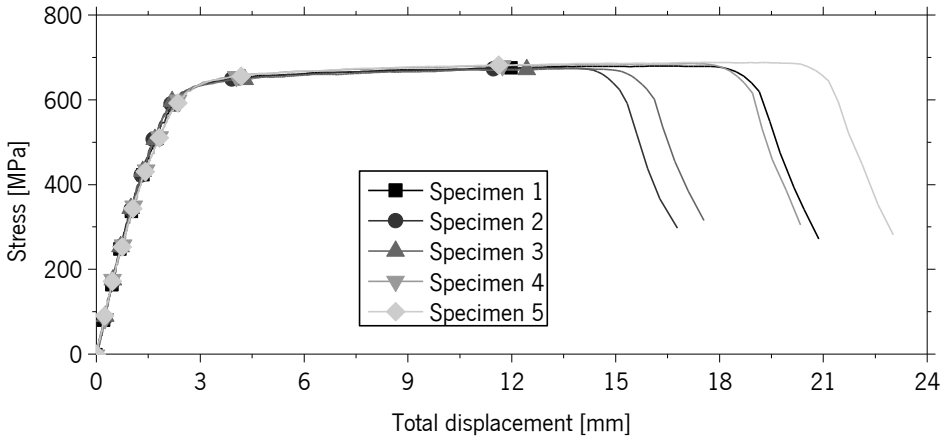

Figure B.4 – Stress versus total displacement in samples of the shear reinforcement bars (ϕ = 6 mm).

B.2 SERIES II

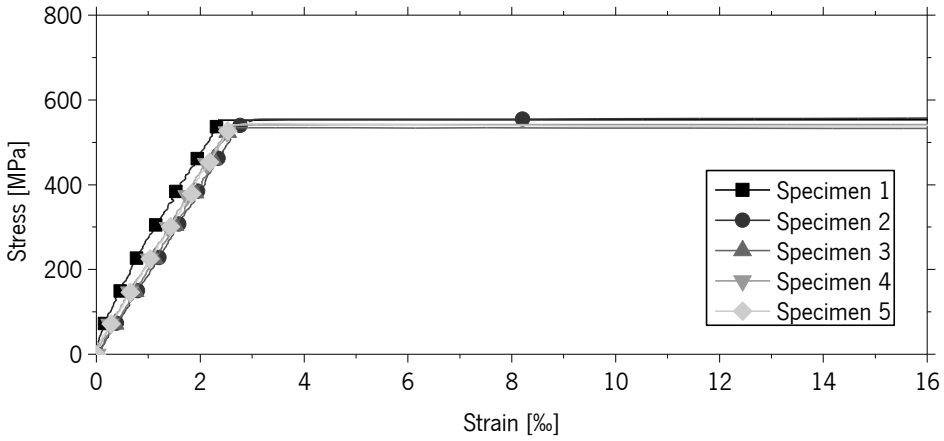

Figure B.5 – Stress versus strain in samples of the longitudinal bars (ϕ = 10 mm).

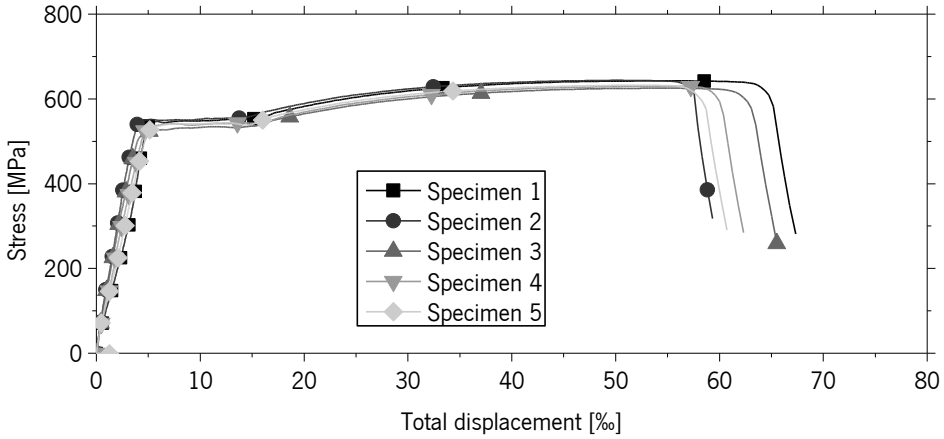

Figure B.6 – Stress versus total displacement in samples of the longitudinal bars (ϕ = 10 mm).

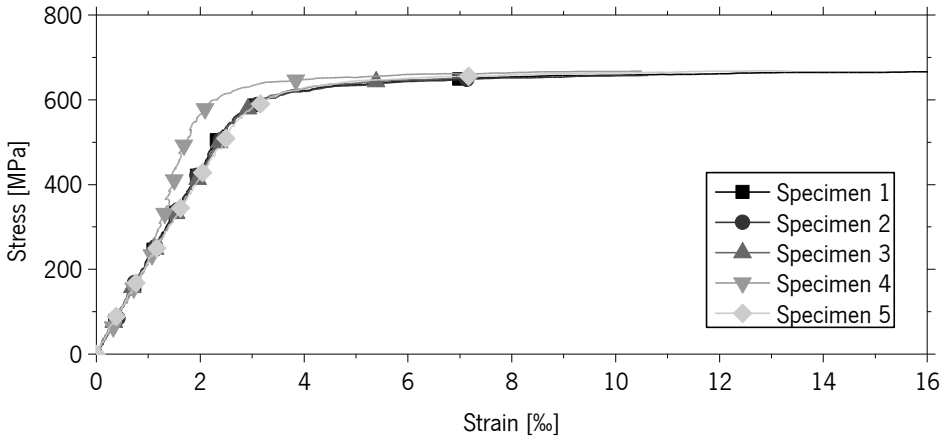

Figure B.7 – Stress versus strain in samples of the shear reinforcement bars (ϕ = 6 mm).

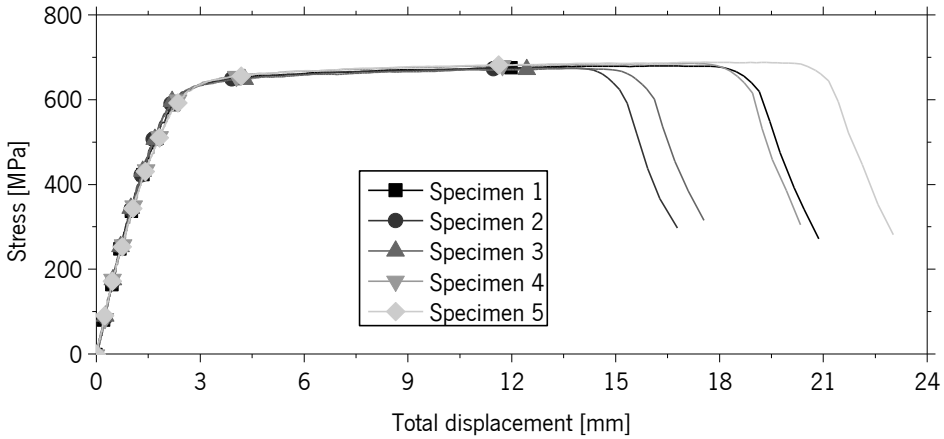

Figure B.8 – Stress versus total displacement in samples of the shear reinforcement bars (ϕ = 6 mm).

B.3 SERIES III

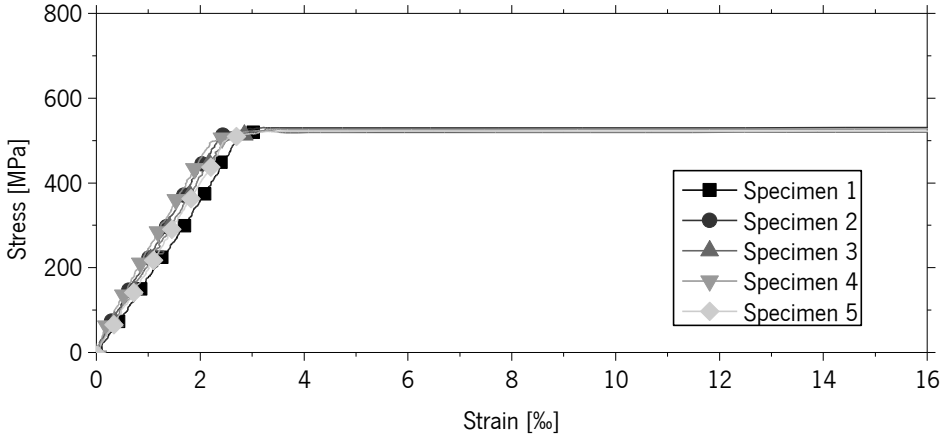

Figure B.9 – Stress versus strain in samples of the longitudinal bars (ϕ = 12 mm).

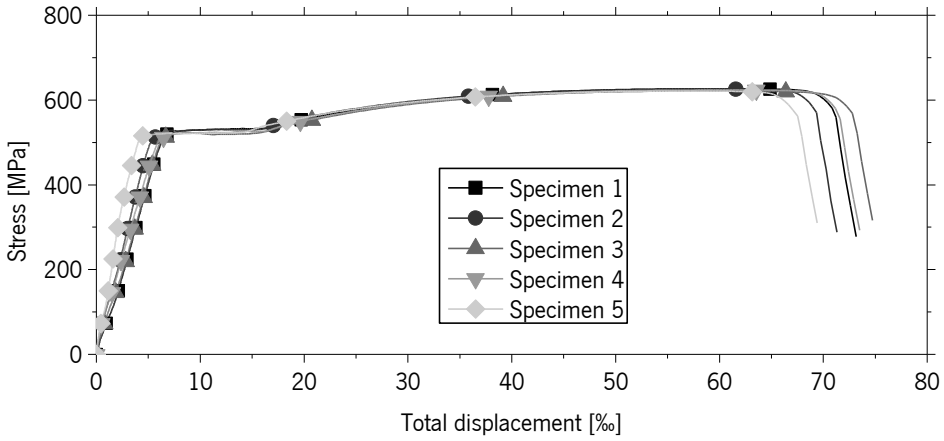

Figure B.10 – Stress versus total displacement in samples of the longitudinal bars (ϕ = 12 mm).

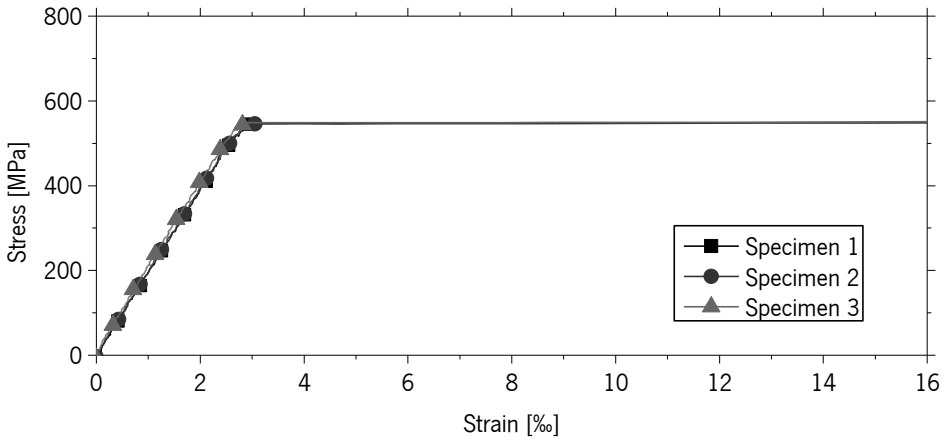

Figure B.11 – Stress versus strain in samples of the shear reinforcement bars (ϕ = 8 mm).

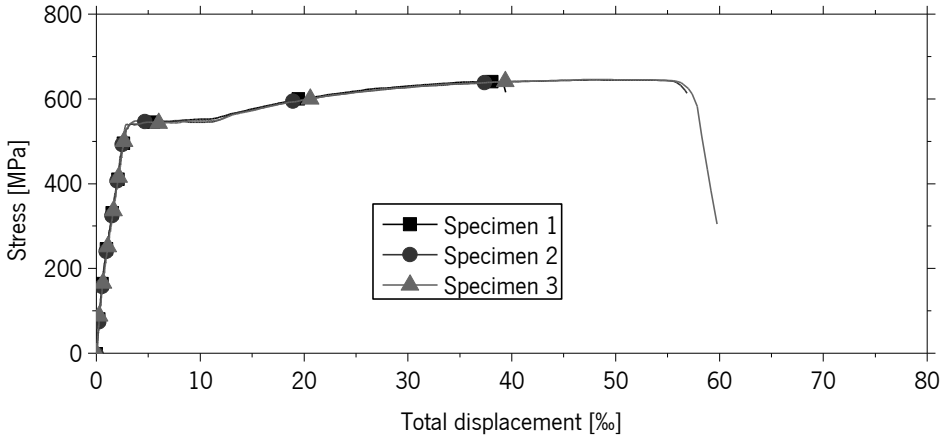

Figure B.12 – Stress versus total displacement in samples of the shear reinforcement bars (ϕ = 8 mm).

Annex C

DEFLECTION INDUCED BY PRESTRESS APPLICATION

Considering a beam subjected to an initial curvature of constant value χ_1 up to a distance of a, and a curvature of constant value χ_2 in the central portion, $L-2a$, as depicted in Figure C.1.

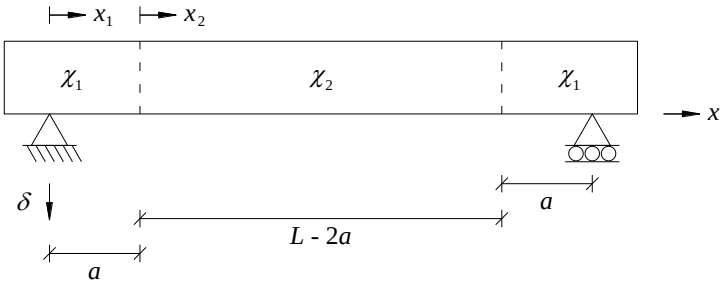

Figure C.1 – Curvature distribution in a simply supported beam.

As no external loads are applied on the beam, the curvature is considered equal to the value of curvature (Eq. C.1)

$$\chi(x)=\begin{cases}\chi_1 & 0\le x\le a\\ \chi_2 & a\le x\le L/2\end{cases} \tag{C.1}$$

The rotation and displacement corresponding to this applied curvature is, in general terms, given by Eq. C.2

$$\theta(x)=\int \chi(x)\,dx \tag{C.2a}$$

$$\delta(x)=\int \theta(x)\,dx \tag{C.2b}$$

Integrating Eq. C.1 in the first branch, where $x_1\le a$, keeping in mind that χ_1 is constant,

$$\theta_1(x_1)=\int -\chi_1\,dx_1=-\chi_1 x_1+C_{1,1} \tag{C.3a}$$

$$\delta_1(x_1)=\int\left(-\chi_1 x_1+C_{1,1}\right)dx_1=-\chi_1\frac{x_1^{\,2}}{2}+C_{1,1}\cdot x_1+C_{1,2} \tag{C.3b}$$

Integrating Eq. C.1 in the second branch, where $0 \le x_2 \le L/2 - a$, keeping in mind that χ_2 is constant,

$$\theta_2(x_2) = \int -\chi_2 \, dx_2 = -\chi_2 x_2 + C_{2,1} \tag{C.4a}$$

$$\delta_2(x_2) = \int \left(-\chi_2 x_2 + C_{2,1}\right) dx_2 = -\chi_2 \frac{x_2^{\,2}}{2} + C_{2,1} \cdot x_2 + C_{2,2} \tag{C.4b}$$

To determine the integration constants, the following boundary conditions have to be verified:

$$\delta_1(x_1 = 0) = 0 \tag{C.5a}$$

$$\theta_2\left(x_2 = L/2 - a\right) = 0 \tag{C.5b}$$

As well as the following compatibility conditions:

$$\theta_1(x_1 = a) = \theta_2(x_2 = 0) \tag{C.6a}$$

$$\delta_1(x_1 = a) = \delta_2(x_2 = 0) \tag{C.6b}$$

From these equations, the constants are determined to be[4]

$$C_{1,1} = \chi_1 \cdot a + \chi_2\left(L/2 - a\right) \tag{C.7a}$$

$$C_{1,2} = 0 \tag{C.7b}$$

$$C_{2,1} = \chi_2\left(L/2 - a\right) \tag{C.7c}$$

$$C_{2,2} = \chi_1 \frac{a^2}{2} + \chi_2 a\left(L/2 - a\right) \tag{C.7d}$$

Eqs. C.3a and C.4a can now be re-written as a function of x_1 and x_2,

[4] Verification:
$$\begin{cases} 0 = -\chi_1 \dfrac{0^2}{2} + C_{1,1} \cdot 0 + C_{1,2} \\ 0 = -\chi_2\left(L/2 - a\right) + C_{2,1} \\ -\chi_2 \cdot 0 + C_{2,1} = -\chi_1 \cdot a + C_{1,1} \\ -\chi_2 \dfrac{0^2}{2} + C_{2,1} \cdot 0 + C_{2,2} = -\chi_1 \dfrac{a^2}{2} + C_{1,1} \cdot a + C_{1,2} \end{cases} \Rightarrow \begin{cases} C_{1,2} = 0 \\ C_{2,1} = \chi_2\left(L/2 - a\right) \\ C_{1,1} = \chi_2\left(L/2 - a\right) + \chi_1 \cdot a \\ C_{2,2} = -\chi_1 \dfrac{a^2}{2} + \left(\chi_2\left(L/2 - a\right) + \chi_1 \cdot a\right) \cdot a \end{cases}$$

$$\theta(x_1,x_2)=\begin{cases}-\chi_1 x_1+\chi_1\cdot a+\chi_2\left(L/2-a\right) & 0\le x_1\le a\\ -\chi_2 x_2+\chi_2\left(L/2-a\right) & 0\le x_2\le L/2-a\end{cases} \tag{C.8}$$

Or as a function of x

$$\theta(x)=\begin{cases}\chi_1(a-x)+\chi_2\left(L/2-a\right) & 0\le x\le a\\ \chi_2\left(L/2-x\right) & a\le x\le L/2\end{cases} \tag{C.9}$$

Eqs. C.3b and C.4b can also be re-written as a function of x_1 and x_2,

$$\delta(x_1,x_2)=\begin{cases}-\chi_1\frac{x_1^{\,2}}{2}+\left(\chi_1\cdot a+\chi_2\left(L/2-a\right)\right)\cdot x_1 & 0\le x_1\le a\\ -\chi_2\frac{x_2^{\,2}}{2}+\chi_2\left(L/2-a\right)\cdot x_2+\chi_1\frac{a^2}{2}+\chi_2 a\left(L/2-a\right) & 0\le x_2\le L/2-a\end{cases} \tag{C.10}$$

And as a function of x

$$\delta(x)=\begin{cases}\chi_1(2a-x)\cdot\frac{x}{2}+\chi_2\left(L/2-a\right)\cdot x & 0\le x\le a\\ \chi_1\frac{a^2}{2}+\frac{\chi_2}{2}\left((L-x)\cdot x-a^2\right) & a\le x\le L/2\end{cases} \tag{C.11}$$

Using Eq. C.11, the mid-span deflection can be obtained

$$\delta\left(L/2\right)=\chi_1\frac{a^2}{2}+\chi_2\left(\frac{L^2-4a^2}{8}\right) \tag{C.12}$$

Annex D

DISPLACEMENT CURVE UNDER FOUR-POINT BENDING

The deduction of the displacement distribution in a beam subjected to four-point bending can be performed considering the geometrical characteristics depicted in Figure D.1.

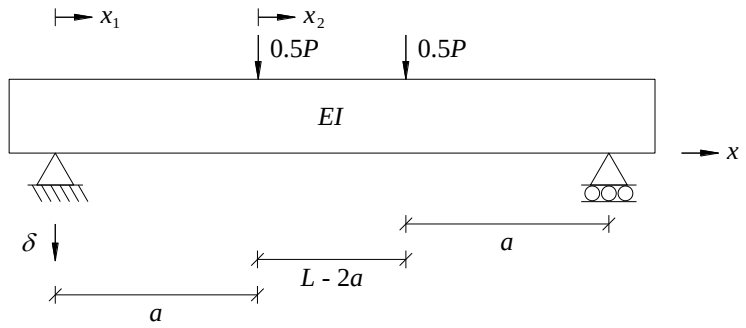

Figure D.1 – Geometric characteristics of a beam loaded under four-point bending.

The vertical reactions in each of the supports are equal as defined in Eq. D.1

$$R_{left} = 0.5P \tag{D.1a}$$

$$R_{right} = 0.5P \tag{D.1b}$$

The bending moment resulting from this load configuration is given by Eq. D.2

$$M(x) = \begin{cases} 0.5P \cdot x & 0 \le x \le a \\ 0.5Pa & a \le x \le L/2 \end{cases} \tag{D.2}$$

The curvature, rotation and displacement corresponding to this applied loading is, in general terms, given by Eq. D.3

$$\chi(x) = -\frac{M(x)}{EI} \tag{D.3a}$$

$$\theta(x) = \int \chi(x)\, dx \tag{D.3b}$$

$$\delta(x) = \int \theta(x)\, dx \tag{D.3c}$$

Integrating the first branch of the moment equation, where $0 \le x_1 \le a$,

$$\chi_1(x_1) = -\frac{P}{2EI} \cdot x_1 \tag{D.4a}$$

$$\theta_1(x_1) = \int -\frac{P}{2EI} \cdot x_1 \, dx_1 = -\frac{P}{2EI} \cdot \frac{x_1^2}{2} + C_{1,1} \tag{D.4b}$$

$$\delta_1(x_1) = \int \left(-\frac{P}{2EI} \cdot \frac{x_1^2}{2} + C_{1,1} \right) dx_1 = -\frac{P}{2EI} \cdot \frac{x_1^3}{6} + C_{1,1} \cdot x_1 + C_{1,2} \tag{D.4c}$$

As for the second branch, where $0 \le x_2 \le L/2 - a$,

$$\chi_2(x_2) = -\frac{Pa}{2EI} \tag{D.5a}$$

$$\theta_2(x_2) = \int -\frac{Pa}{2EI} \, dx_2 = -\frac{Pa}{2EI} \cdot x_2 + C_{2,1} \tag{D.5b}$$

$$\delta_2(x_2) = \int \left(-\frac{Pa}{2EI} \cdot x_2 + C_{2,1} \right) dx_2 = -\frac{Pa}{2EI} \cdot \frac{x_2^2}{2} + C_{2,1} \cdot x_2 + C_{2,2} \tag{D.5c}$$

To determine the integration constants, the following boundary conditions have to be verified:

$$\delta_1(x_1 = 0) = 0 \tag{D.6a}$$

$$\theta_2\left(x_2 = L/2 - a\right) = 0 \tag{D.6b}$$

As well as the following compatibility conditions:

$$\theta_1(x_1 = a) = \theta_2(x_2 = 0) \tag{D.7a}$$

$$\delta_1(x_1 = a) = \delta_2(x_2 = 0) \tag{D.7b}$$

Substituting Eq. D.4c in Eq. D.6a,

$$0 = -\frac{P}{2EI}\frac{0^3}{6} + C_{1,1} \cdot 0 + C_{1,2} \Rightarrow C_{1,2} = 0 \tag{D.8}$$

Substituting Eq. D.5b in Eq. D.6b,

$$0 = -\frac{Pa}{2EI} \cdot \left(L/2 - a\right) + C_{2,1} \Rightarrow C_{2,1} = \frac{Pa(L - 2a)}{4EI} \tag{D.9}$$

Substituting Eqs. D.4b, D.5b and D.9 in Eq. D.7a,

$$-\frac{Pa}{2EI}\cdot 0+\frac{Pa\left(L-2a\right)}{4EI}=-\frac{P}{2EI}\cdot\frac{a^2}{2}+C_{1,1}\Rightarrow$$
$$\Rightarrow C_{1,1}=\frac{Pa}{4EI}\left(\left(L-2a\right)+a\right)\Rightarrow C_{1,1}=\frac{Pa\left(L-a\right)}{4EI} \tag{D.10}$$

Substituting Eqs. D.4c, D.5c, D.8 and D.10 in Eq. D.7a

$$-\frac{Pa}{2EI}\frac{0^2}{2}+C_{2,1}\cdot 0+C_{2,2}=-\frac{P}{2EI}\frac{a^3}{6}+\frac{Pa\left(L-a\right)}{4EI}a+0\Rightarrow$$
$$\Rightarrow C_{2,2}=\frac{Pa^2}{4EI}\left(\left(L-a\right)-\frac{a}{3}\right)\Rightarrow C_{2,2}=\frac{Pa^2}{12EI}\left(\left(3L-3a\right)-a\right)\Rightarrow C_{2,2}=\frac{Pa^2\left(3L-4a\right)}{12EI} \tag{D.11}$$

The rotation can now be expressed in terms of x_1 and x_2,

$$\theta\left(x_1,x_2\right)=\begin{cases}\dfrac{P\left(a\left(L-a\right)-x_1^{\,2}\right)}{4EI} & 0\le x_1\le a\\ \dfrac{Pa\left(L-2\left(a+x_2\right)\right)}{4EI} & 0\le x_2\le L/2-a\end{cases} \tag{D.12}$$

Or in terms of x

$$\theta\left(x_1,x_2\right)=\begin{cases}\dfrac{P\left(a\left(L-a\right)-x^2\right)}{4EI} & 0\le x\le a\\ \dfrac{Pa\left(L-2x\right)}{4EI} & a\le x\le L/2\end{cases} \tag{D.13}$$

The displacement can also be re-written as a function of x_1 and x_2,

$$\delta\left(x_1,x_2\right)=\begin{cases}\dfrac{P\left(3a\left(L-a\right)-x_1^{\,2}\right)\cdot x_1}{12EI} & 0\le x_1\le a\\ \dfrac{Pa}{12EI}\left(a\left(3L-4a\right)+3\left(L-2a-x_2\right)\cdot x_2\right) & 0\le x_2\le L/2-a\end{cases} \tag{D.14}$$

And as a function of x

$$\delta(x)=\begin{cases}\dfrac{P\left(3a\left(L-a\right)-x^2\right)\cdot x}{12EI} & 0\le x\le a\\ \dfrac{Pa}{12EI}\left(a\left(3L-4a\right)+3\left(L-a-x\right)\cdot\left(x-a\right)\right) & a\le x\le L/2\end{cases} \tag{D.15}$$

The maximum deflection corresponds to the deflection at mid-span and is given by Eq. D.16 [5]

$$\delta\left(L/2\right)=\frac{Pa\left(3L^2-4a^2\right)}{48EI} \tag{D.16}$$

[5] Verification: $\frac{Pa}{12EI}\left(a\left(3L-4a\right)+3\left(L-a-\frac{L}{2}\right)\cdot\left(\frac{L}{2}-a\right)\right)=\frac{Pa}{12EI}\left(a\left(3L-4a\right)+3\left(\frac{L}{2}-a\right)\cdot\left(\frac{L}{2}-a\right)\right)=$

$=\frac{Pa}{12EI}\left(a\left(3L-4a\right)+3\left(\frac{L^2}{4}-aL+a^2\right)\right)=\frac{Pa}{12EI}\left(\left(3aL-4a^2\right)+\left(\frac{3L^2}{4}-3aL+3a^2\right)\right)=$

$=\frac{Pa}{12EI}\left(3aL-4a^2+\frac{3L^2}{4}-3aL+3a^2\right)=\frac{Pa}{12EI}\left(\frac{3L^2}{4}-a^2\right)=\frac{Pa}{48EI}\left(3L^2-4a^2\right)$

Annex E

NUMERICAL STRAIN PROFILES IN THE CFRP LAMINATE

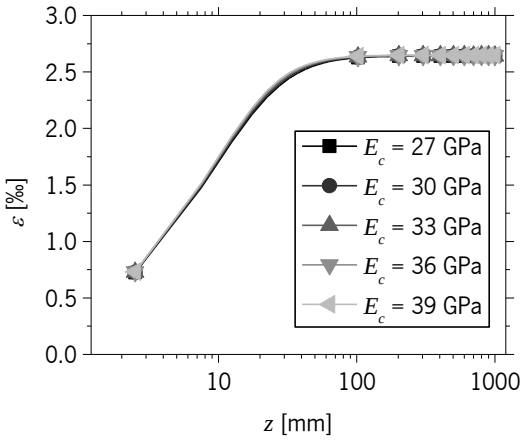

Figure E.1 – Strain profile variation with E_c .

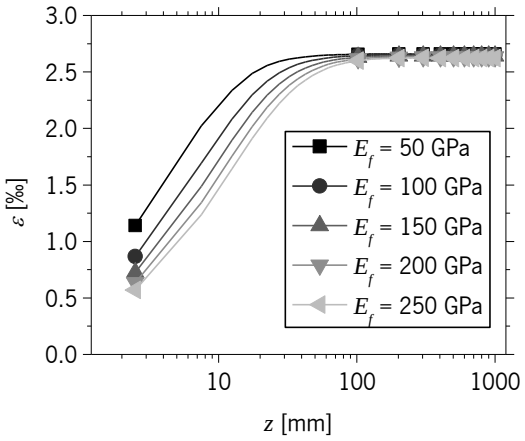

Figure E.2 – Strain profile variation with E_f .

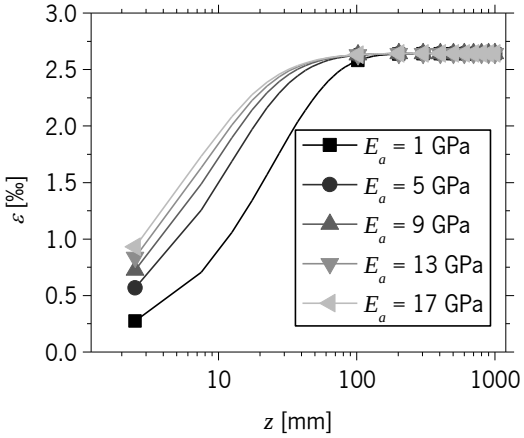

Figure E.3 – Strain profile variation with E_a .

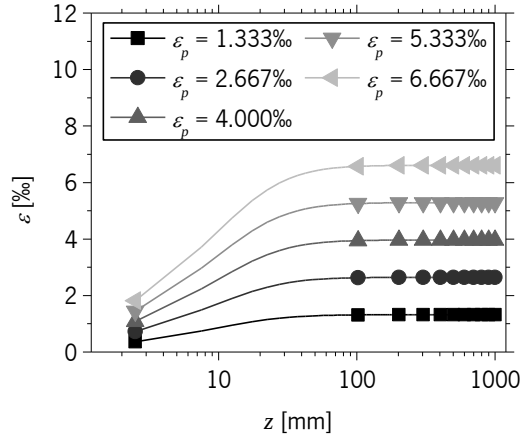

Figure E.4 – Strain profile variation with ε_p .

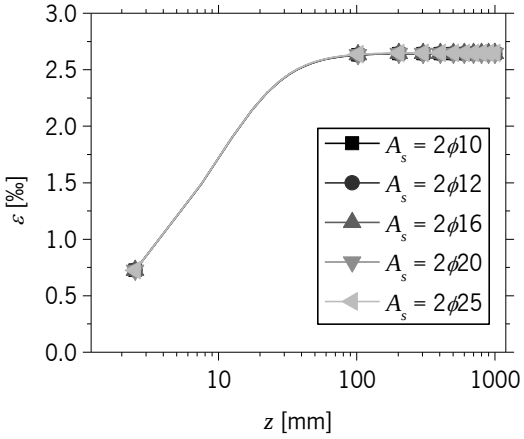

Figure E.5 – Strain profile variation with A_s .

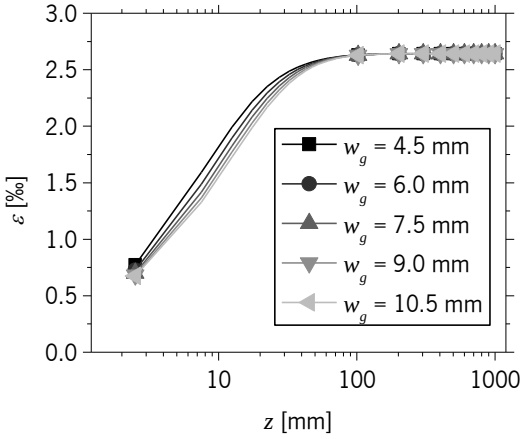

Figure E.6 – Strain profile variation with w_g .

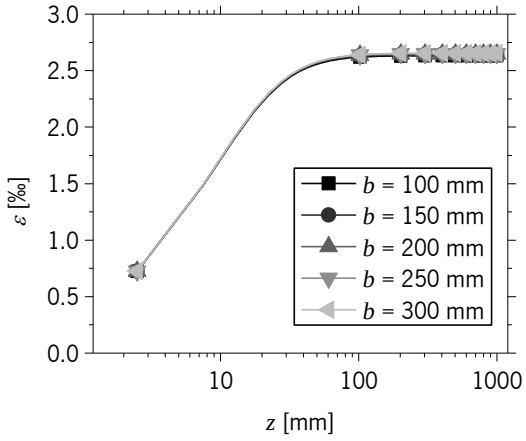

Figure E.7 – Strain profile variation with b .

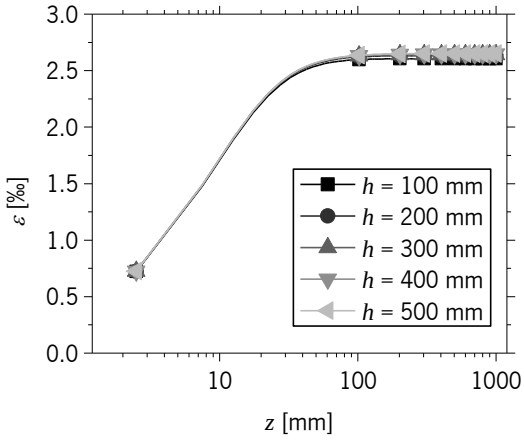

Figure E.8 – Strain profile variation with h .

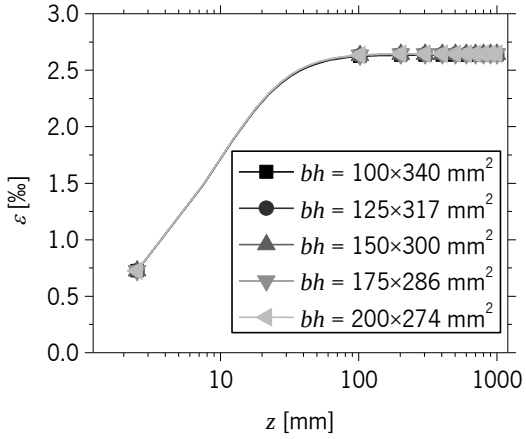

Figure E.9 – Strain profile variation with bh .

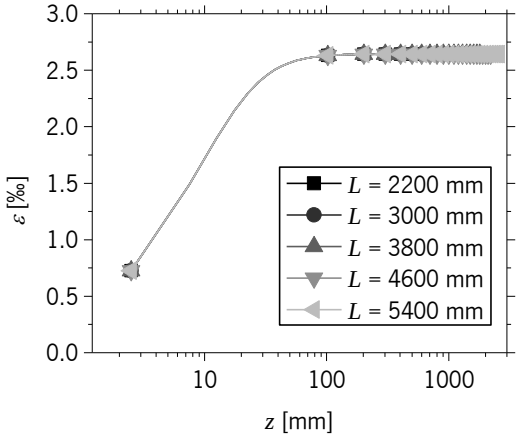

Figure E.10 – Strain profile variation with L .

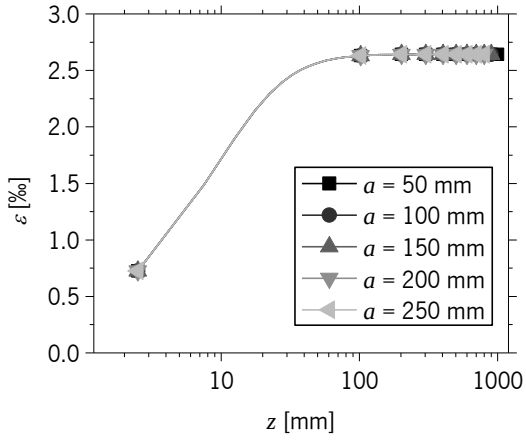

Figure E.11 – Strain profile variation with a .

Table E.1 – GDR2 nonlinear optimization results.

E_c [GPa]	E_f [GPa]	E_a [GPa]	ε_p [‰]	A_s [mm^2]	w_g [mm]	b [mm]	h [mm]	L [mm]	a [mm]	$\Delta\varepsilon_p$ [‰]	η [GPa·mm]	n
27	150	9	2.667	157.08	6	150	300	2200	50	0.0284	1489	0.177
30	150	9	2.667	157.08	6	150	300	2200	50	0.0258	1465	0.168
33	150	9	2.667	157.08	6	150	300	2200	50	0.0235	1443	0.159
36	150	9	2.667	157.08	6	150	300	2200	50	0.0217	1423	0.153
39	150	9	2.667	157.08	6	150	300	2200	50	0.0201	1370	0.158
30	50	9	2.667	157.08	6	150	300	2200	50	0.0079	255	0.184
30	100	9	2.667	157.08	6	150	300	2200	50	0.0168	766	0.171
30	150	9	2.667	157.08	6	150	300	2200	50	0.0258	1467	0.167
30	200	9	2.667	157.08	6	150	300	2200	50	0.0348	2268	0.187
30	250	9	2.667	157.08	6	150	300	2200	50	0.0438	3251	0.180
30	150	1	2.667	157.08	6	150	300	2200	50	0.0275	3758	0.043
30	150	5	2.667	157.08	6	150	300	2200	50	0.0263	1851	0.122
30	150	9	2.667	157.08	6	150	300	2200	50	0.0258	1467	0.167
30	150	13	2.667	157.08	6	150	300	2200	50	0.0253	1261	0.210
30	150	17	2.667	157.08	6	150	300	2200	50	0.0250	1115	0.234
30	150	9	1.333	157.08	6	150	300	2200	50	0.0129	1466	0.167
30	150	9	2.667	157.08	6	150	300	2200	50	0.0258	1466	0.167
30	150	9	4.000	157.08	6	150	300	2200	50	0.0386	1466	0.167
30	150	9	5.333	157.08	6	150	300	2200	50	0.0515	1466	0.167
30	150	9	6.667	157.08	6	150	300	2200	50	0.0644	1466	0.167
30	150	9	2.667	157.08	6	150	300	2200	50	0.0258	1467	0.167
30	150	9	2.667	226.19	6	150	300	2200	50	0.0251	1468	0.167
30	150	9	2.667	402.12	6	150	300	2200	50	0.0235	1469	0.167
30	150	9	2.667	628.32	6	150	300	2200	50	0.0218	1470	0.167
30	150	9	2.667	981.75	6	150	300	2200	50	0.0197	1472	0.168
30	150	9	2.667	157.08	4.5	150	300	2200	50	0.0256	1322	0.160
30	150	9	2.667	157.08	6	150	300	2200	50	0.0258	1462	0.170
30	150	9	2.667	157.08	7.5	150	300	2200	50	0.0259	1552	0.181
30	150	9	2.667	157.08	9	150	300	2200	50	0.0260	1660	0.189
30	150	9	2.667	157.08	10.5	150	300	2200	50	0.0261	1731	0.200
30	150	9	2.667	157.08	6	100	300	2200	50	0.0376	1457	0.169
30	150	9	2.667	157.08	6	150	300	2200	50	0.0258	1469	0.167
30	150	9	2.667	157.08	6	200	300	2200	50	0.0198	1471	0.167
30	150	9	2.667	157.08	6	250	300	2200	50	0.0159	1474	0.167
30	150	9	2.667	157.08	6	300	300	2200	50	0.0134	1477	0.168
30	150	9	2.667	157.08	6	150	100	2200	50	0.0629	1418	0.168
30	150	9	2.667	157.08	6	150	200	2200	50	0.0364	1448	0.167
30	150	9	2.667	157.08	6	150	300	2200	50	0.0258	1465	0.167
30	150	9	2.667	157.08	6	150	400	2200	50	0.0200	1473	0.168
30	150	9	2.667	157.08	6	150	500	2200	50	0.0163	1475	0.168

E_c [GPa]	E_f [GPa]	E_a [GPa]	ε_p [‰]	A_s [mm^2]	w_g [mm]	b [mm]	h [mm]	L [mm]	a [mm]	$\Delta\varepsilon_p$ [‰]	η [GPa·mm]	n
30	150	9	2.667	157.08	6	100	340	2200	50	0.0337	1466	0.168
30	150	9	2.667	157.08	6	125	317	2200	50	0.0291	1465	0.168
30	150	9	2.667	157.08	6	150	300	2200	50	0.0258	1466	0.168
30	150	9	2.667	157.08	6	175	286	2200	50	0.0232	1467	0.168
30	150	9	2.667	157.08	6	200	274	2200	50	0.0214	1467	0.168
30	150	9	2.667	157.08	6	150	300	2200	50	0.0258	1465	0.168
30	150	9	2.667	157.08	6	150	300	3000	50	0.0258	1466	0.166
30	150	9	2.667	157.08	6	150	300	3800	50	0.0258	1465	0.166
30	150	9	2.667	157.08	6	150	300	4600	50	0.0258	1465	0.168
30	150	9	2.667	157.08	6	150	300	5400	50	0.0258	1466	0.166
30	150	9	2.667	157.08	6	150	300	2200	50	0.0258	1467	0.167
30	150	9	2.667	157.08	6	150	300	2200	100	0.0258	1466	0.166
30	150	9	2.667	157.08	6	150	300	2200	150	0.0258	1467	0.166
30	150	9	2.667	157.08	6	150	300	2200	200	0.0258	1466	0.167
30	150	9	2.667	157.08	6	150	300	2200	250	0.0258	1466	0.166

The coefficents for the correction of the slope (μ_ε, μ_η and μ_n) and y-intercept value ($\Delta\varepsilon_0$, η_0 and n_0) are determined in the following order:

Step 1: Correction of the slope

Based on Figures 217, 218 and 219, the slope is adjusted as:

$$\mu_\varepsilon = 1/1.00087 = 0.99913 \quad \text{(E.1a)}$$

$$\mu_\eta = 1/0.99850 = 1.00150 \quad \text{(E.1b)}$$

$$\mu_n = 1/1.04091 = 0.96070 \quad \text{(E.1c)}$$

Step 2: Correction of the y-intercept value

Multiplication of the corrected slope by the respective y-intercept value (in Figures 217, 218 and 219)

$$\Delta\varepsilon_0 = 0.99913 \times 0.15302 = 0.15289 \quad \text{(E.2a)}$$

$$\eta_0 = 1.00150 \times 5832.6 = 5841.3 \quad \text{(E.2b)}$$

$$n_0 = 0.96070 \times 0.53136 = 0.51048 \quad \text{(E.2c)}$$

Step 3: Final expressions

The final expressions of the parameters defining the strain profile (Eq. 45), are obtained using the coefficients given in Tables 73 to 75, the correction parameters in Eqs. E.1 and E.2, according to Eq. 44.

Annex F

SECTION ANALYSIS

In this Annex, the step by step calculation of moment-curvature relationship given in Chapter 7 is presented. A list containing all the variables used in the formulation is given hereafter:

Latin upper case letters

- A_f Cross sectional area of the FRP
- A_{sc} Cross sectional area of the compressive steel reinforcement
- A_{st} Cross sectional area of the tensile steel reinforcement
- E_c Elastic modulus of the concrete
- E_c' Reduced elastic modulus of the concrete
- E_f Elastic modulus of the FRP
- E_{sc} Elastic modulus of the compressive steel reinforcement
- E_{st} Elastic modulus of the tensile steel reinforcement
- F_{cc} Concentrated load due to concrete in compression
- $F_{cc,1}$ Concentrated load due to a constant applied stress
- $F_{cc,2}$ Concentrated load due to a constant applied stress
- F_{cs} Concentrated load due to steel in compression
- F_{tc} Concentrated load due to concrete in tension
- F_{tf} Concentrated load due to FRP in tension
- F_{ts} Concentrated load due to steel in tension
- M Bending moment

Latin lower case letters

- b Width of the beam
- b_{cc} Internal lever arm in correspondence to F_{cc}
- b_{cs} Internal lever arm in correspondence to F_{cs}
- b_{tc} Internal lever arm in correspondence to F_{tc}
- b_{tf} Internal lever arm in correspondence to F_{tf}
- b_{ts} Internal lever arm in correspondence to F_{ts}
- c_f Distance between the bottom surface of the beam and the geometric centre of A_f
- c_{sc} Distance between the top surface of the beam and the geometric centre of A_{sc}

c_{st} Distance between the bottom surface of the beam and the geometric centre of A_{st}

d_f Depth of the FRP ($d_f = h - c_f$)

d_{st} Depth of the tensile steel reinforcement ($d_{st} = h - c_{st}$)

f_{cc} Concrete compressive strength

f_{ct} Concrete tensile strength

f_f FRP tensile strength

f_{st} Yield stress of the compressive steel reinforcement

f_{sc} Yield stress of the tensile steel reinforcement

h Height of the beam

x Depth of the neutral axis

x' Portion of x subjected to constant compressive stress

Greek letters

ε_{cc} Strain in the most compressed fibre of concrete

ε_{cs} Compressive strain in the steel reinforcement

ε_{tc} Strain in the most tensioned fibre of concrete

ε_{tf} FRP prestrain

ε_{ts} Tensile strain in the steel reinforcement

ε_{sc} Yield strain of the compressive steel reinforcement

ε_{st} Yield strain of the tensile steel reinforcement

χ Curvature of the cross section

$\Delta\varepsilon_{tf}$ Strain variation in the FRP due to curvature

F.1 CURVATURE INDUCED BY PRESTRESS APPLICATION

For the calculation of the curvature induced by prestress application, the strain and stress distribution adopted are depicted in Figure F.1. The distribution of strain along the height is assumed linear.

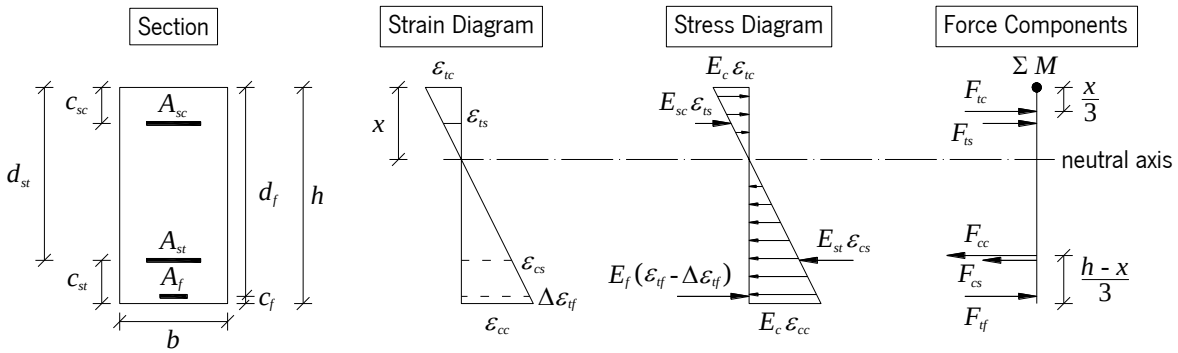

Figure F.1 – Strain and stress diagram of the cross section due to prestress application.

Step 1 – Definition of the boundary conditions

$$\varepsilon_{tc} \le \frac{f_{ct}}{E_c} \tag{F.1a}$$

$$\varepsilon_{ts} \le \frac{f_{sc}}{E_{sc}} \tag{F.1b}$$

$$\varepsilon_{cs} \le \frac{f_{st}}{E_{st}} \tag{F.1c}$$

$$\varepsilon_{cc} \le \frac{f_{cc}}{E_c} \tag{F.1d}$$

$$\varepsilon_{tf} - \Delta\varepsilon_{tf} \le \frac{f_f}{E_f} \tag{F.1e}$$

Step 2 – Geometrical relationships between strains

$$\frac{\varepsilon_{tc}}{x} = \frac{\varepsilon_{cc}}{h-x} \Leftrightarrow \varepsilon_{tc} = \frac{x}{h-x}\varepsilon_{cc} \tag{F.2a}$$

$$\frac{\varepsilon_{ts}}{x-c_{sc}} = \frac{\varepsilon_{cc}}{h-x} \Leftrightarrow \varepsilon_{ts} = \frac{x-c_{sc}}{h-x}\varepsilon_{cc} \tag{F.2b}$$

$$\frac{\varepsilon_{cs}}{h-x-c_{st}} = \frac{\varepsilon_{cc}}{h-x} \Leftrightarrow \varepsilon_{cs} = \frac{d_{st}-x}{h-x}\varepsilon_{cc} \tag{F.2c}$$

$$\frac{\Delta\varepsilon_{tf}}{h-x-c_f} = \frac{\varepsilon_{cc}}{h-x} \Leftrightarrow \Delta\varepsilon_{tf} = \frac{d_f-x}{h-x}\varepsilon_{cc} \tag{F.2d}$$

Step 3 – Quantification of the internal loads

$$F_{tc} = \frac{1}{2}E_c\varepsilon_{tc}\cdot bx \tag{F.3a}$$

$$F_{ts} = E_{sc}\varepsilon_{ts}\cdot A_{sc} \tag{F.3b}$$

$$F_{cc} = \frac{1}{2}E_c\varepsilon_{cc}\cdot b\left(h-x\right) \tag{F.3c}$$

$$F_{cs} = E_{st}\varepsilon_{cs}\cdot A_{st} \tag{F.3d}$$

$$F_{tf} = E_f\left(\varepsilon_{tf} - \Delta\varepsilon_{tf}\right)\cdot A_f \tag{F.3e}$$

Step 4 – Equilibrium of internal forces

$$\sum_i^n F_{t,i} - \sum_j^m F_{c,j} = 0 \tag{F.4a}$$

$$F_{tc} + F_{ts} + F_{tf} - F_{cc} - F_{cs} = 0 \tag{F.4b}$$

$$\frac{1}{2}E_c\varepsilon_{tc}bx+E_{sc}\varepsilon_{ts}A_{sc}+E_f\left(\varepsilon_{tf}-\Delta\varepsilon_{tf}\right)A_f-\frac{1}{2}E_c\varepsilon_{cc}b\left(h-x\right)-E_{st}\varepsilon_{cs}A_{st}=0 \quad \text{(F.4c)}$$

Step 5 – Rewriting Eq. F.4c in order to $E_f\left(\varepsilon_{tf}-\Delta\varepsilon_{tf}\right)A_f\left(h-x\right)/\varepsilon_{cc}$ and substituting Eq. F.2

$$\Leftrightarrow E_f\left(\varepsilon_{tf}-\Delta\varepsilon_{tf}\right)A_f=\frac{1}{2}E_c\varepsilon_{cc}b\left(h-x\right)-\frac{1}{2}E_c\varepsilon_{tc}bx+E_{st}\varepsilon_{cs}A_{st}-E_{sc}\varepsilon_{ts}A_{sc}\Leftrightarrow \quad \text{(F.5a)}$$

$$\Leftrightarrow E_f\left(\varepsilon_{tf}-\Delta\varepsilon_{tf}\right)A_f= =\frac{1}{2}E_cb\left(\varepsilon_{cc}\left(h-x\right)-\left(\frac{x}{h-x}\varepsilon_{cc}\right)x\right)+E_{st}\left(\frac{d_{st}-x}{h-x}\varepsilon_{cc}\right)A_{st}-E_{sc}\left(\frac{x-c_{sc}}{h-x}\varepsilon_{cc}\right)A_{sc}\Leftrightarrow \quad \text{(F.5b)}$$

$$\Leftrightarrow \frac{E_f\left(\varepsilon_{tf}-\Delta\varepsilon_{tf}\right)A_f}{\varepsilon_{cc}}=\frac{1}{2}E_cb\left(\frac{\left(h-x\right)^2}{h-x}-\frac{x^2}{h-x}\right)+E_{st}A_{st}\frac{d_{st}-x}{h-x}-E_{sc}A_{sc}\frac{x-c_{sc}}{h-x}\Leftrightarrow \quad \text{(F.5c)}$$

$$\Leftrightarrow \frac{E_f\left(\varepsilon_{tf}-\Delta\varepsilon_{tf}\right)A_f}{\varepsilon_{cc}}\left(h-x\right)=\frac{1}{2}E_cb\left(\left(h-x\right)^2-x^2\right)+E_{st}A_{st}\left(d_{st}-x\right)-E_{sc}A_{sc}\left(x-c_{sc}\right)\Leftrightarrow \quad \text{(F.5d)}$$

$$\Leftrightarrow \frac{E_f\left(\varepsilon_{tf}-\Delta\varepsilon_{tf}\right)A_f}{\varepsilon_{cc}}\left(h-x\right)=\frac{1}{2}E_cbh\left(h-2x\right)+E_{st}A_{st}\left(d_{st}-x\right)-E_{sc}A_{sc}\left(x-c_{sc}\right) \quad \text{(F.5e)}$$

Step 6 – Determining the lever arms of the internal forces in relation to the top fibre

$$b_{tc}=\frac{x}{3} \quad \text{(F.6a)}$$

$$b_{ts}=c_{sc} \quad \text{(F.6b)}$$

$$b_{cc}=h-\frac{1}{3}\left(h-x\right)=\frac{2h+x}{3} \quad \text{(F.6c)}$$

$$b_{cs}=h-c_{st}=d_{st} \quad \text{(F.6d)}$$

$$b_{tf}=h-c_f=d_f \quad \text{(F.6e)}$$

Step 7 – Summing the internal moments

$$\sum_i^n F_{ti}\cdot b_{ti}-\sum_j^m F_{cj}\cdot b_{cj}=0 \quad \text{(F.7a)}$$

$$F_{tc}\cdot b_{tc}+F_{ts}\cdot b_{ts}+F_{tf}\cdot b_{tf}-F_{cc}\cdot b_{cc}-F_{cs}\cdot b_{cs}=0 \quad \text{(F.7b)}$$

Step 8 – Rewriting Eq. F.7b in order to $E_f\left(\varepsilon_{tf}-\Delta\varepsilon_{tf}\right)A_f d_f\left(h-x\right)/\varepsilon_{cc}$ and substituting Eq. F.2

$$\frac{1}{2}E_c\varepsilon_{tc}\frac{bx^2}{3}+E_{sc}\varepsilon_{ts}A_{sc}c_{sc}+E_f\left(\varepsilon_{tf}-\Delta\varepsilon_{tf}\right)A_f d_f-\frac{1}{2}E_c\varepsilon_{cc}b\left(h-x\right)\frac{2h+x}{3}-E_{st}\varepsilon_{cs}A_{st}d_{st}=0\Leftrightarrow \quad \text{(F.8a)}$$

$$\Leftrightarrow E_f\left(\varepsilon_{tf}-\Delta\varepsilon_{tf}\right)A_f d_f = \\ =\frac{1}{2}E_c\varepsilon_{cc}b\left(h-x\right)\frac{2h+x}{3}-\frac{1}{2}E_c\varepsilon_{tc}\frac{bx^2}{3}+E_{st}\varepsilon_{cs}A_{st}d_{st}-E_{sc}\varepsilon_{ts}A_{sc}c_{sc}\Leftrightarrow \quad \text{(F.8b)}$$

$$\Leftrightarrow E_f\left(\varepsilon_{tf}-\Delta\varepsilon_{tf}\right)A_f d_f=\frac{1}{2}E_c b\left(\varepsilon_{cc}\left(h-x\right)\frac{2h+x}{3}-\left(\frac{x}{h-x}\varepsilon_{cc}\right)\frac{x^2}{3}\right)+ \\ +E_{st}\left(\frac{d_{st}-x}{h-x}\varepsilon_{cc}\right)A_{st}d_{st}-E_{sc}\left(\frac{x-c_{sc}}{h-x}\varepsilon_{cc}\right)A_{sc}c_{sc}\Leftrightarrow \quad \text{(F.8c)}$$

$$\Leftrightarrow \frac{E_f\left(\varepsilon_{tf}-\Delta\varepsilon_{tf}\right)A_f d_f}{\varepsilon_{cc}}=\frac{1}{2}E_c b\left(\frac{\left(h-x\right)^2}{h-x}\frac{2h+x}{3}-\frac{x^3}{3\left(h-x\right)}\right)+E_{st}A_{st}d_{st}\frac{d_{st}-x}{h-x}+ \\ -E_{sc}A_{sc}c_{sc}\frac{x-c_{sc}}{h-x}\Leftrightarrow \quad \text{(F.8d)}$$

$$\Leftrightarrow \frac{E_f\left(\varepsilon_{tf}-\Delta\varepsilon_{tf}\right)A_f d_f}{\varepsilon_{cc}}\left(h-x\right)=\frac{1}{2}E_c b\left(\left(h-x\right)^2\frac{2h+x}{3}-\frac{x^3}{3}\right)+E_{st}A_{st}d_{st}\left(d_{st}-x\right)+ \\ -E_{sc}A_{sc}c_{sc}\left(x-c_{sc}\right)\Leftrightarrow \quad \text{(F.8e)}$$

$$\Leftrightarrow \frac{E_f\left(\varepsilon_{tf}-\Delta\varepsilon_{tf}\right)A_f d_f}{\varepsilon_{cc}}\left(h-x\right)=\frac{1}{6}E_c bh^2\left(2h-3x\right)+E_{st}A_{st}d_{st}\left(d_{st}-x\right)-E_{sc}A_{sc}c_{sc}\left(x-c_{sc}\right) \quad \text{(F.8f)}$$

Step 9 – It is concluded that Eq. F.8f is equal to Eq. F.5e multiplied by d_f

$$\frac{1}{6}E_c bh^2\left(2h-3x\right)+E_{st}A_{st}d_{st}\left(d_{st}-x\right)-E_{sc}A_{sc}c_{sc}\left(x-c_{sc}\right)= \\ =\frac{1}{2}E_c bh\left(h-2x\right)d_f+E_{st}A_{st}\left(d_{st}-x\right)d_f-E_{sc}A_{sc}\left(x-c_{sc}\right)d_f \quad \text{(F.9a)}$$

The obtained expression is turn out to be a first degree polynomial equation in which x is the only unknown.

$$2E_c bh^3-3E_c bh^2x+6E_{st}A_{st}{d_{st}}^2-6E_{st}A_{st}d_{st}x-6E_{sc}A_{sc}c_{sc}x+6E_{sc}A_{sc}{c_{sc}}^2= \\ =3E_c bh^2d_f-6E_c bhd_f x+6E_{st}A_{st}d_{st}d_f-6E_{st}A_{st}d_f x-6E_{sc}A_{sc}d_f x+6E_{sc}A_{sc}c_{sc}d_f\Leftrightarrow \quad \text{(F.9b)}$$

$$\Leftrightarrow 6E_c bhd_f x+6E_{st}A_{st}d_f x+6E_{sc}A_{sc}d_f x-3E_c bh^2x-6E_{st}A_{st}d_{st}x-6E_{sc}A_{sc}c_{sc}x= \\ =3E_c bh^2d_f+6E_{st}A_{st}d_{st}d_f+6E_{sc}A_{sc}c_{sc}d_f-2E_c bh^3-6E_{st}A_{st}{d_{st}}^2-6E_{sc}A_{sc}{c_{sc}}^2 \quad \text{(F.9c)}$$

$$\Leftrightarrow \left(6E_c bhd_f - 3E_c bh^2 + 6E_{sc}A_{sc}d_f - 6E_{sc}A_{sc}c_{sc} + 6E_{st}A_{st}d_f - 6E_{st}A_{st}d_{st}\right)x = \\ = 3E_c bh^2 d_f - 2E_c bh^3 + 6E_{sc}A_{sc}c_{sc}d_f - 6E_{sc}A_{sc}{c_{sc}}^2 + 6E_{st}A_{st}d_{st}d_f - 6E_{st}A_{st}{d_{st}}^2 \quad \text{(F.9d)}$$

$$\Leftrightarrow \left(3E_c bh\left(2d_f - h\right) + 6E_{sc}A_{sc}\left(d_f - c_{sc}\right) + 6E_{st}A_{st}\left(d_f - d_{st}\right)\right)x = \\ = E_c bh^2\left(3d_f - 2h\right) + 6E_{sc}A_{sc}c_{sc}\left(d_f - c_{sc}\right) + 6E_{st}A_{st}d_{st}\left(d_f - d_{st}\right) \Leftrightarrow \quad \text{(F.9e)}$$

$$\Leftrightarrow 3\left(E_c bh\left(2d_f - h\right) + 2E_{sc}A_{sc}\left(d_f - c_{sc}\right) + 2E_{st}A_{st}\left(d_f - d_{st}\right)\right)x = \\ = E_c bh^2\left(3d_f - 2h\right) + 6E_{sc}A_{sc}c_{sc}\left(d_f - c_{sc}\right) + 6E_{st}A_{st}d_{st}\left(d_f - d_{st}\right) \quad \text{(F.9f)}$$

$$x = \frac{E_c bh^2\left(3d_f - 2h\right) + 6\left(E_{sc}A_{sc}c_{sc}\left(d_f - c_{sc}\right) + E_{st}A_{st}d_{st}\left(d_f - d_{st}\right)\right)}{3\left(E_c bh\left(2d_f - h\right) + 2\left(E_{sc}A_{sc}\left(d_f - c_{sc}\right) + E_{st}A_{st}\left(d_f - d_{st}\right)\right)\right)} \quad \text{(F.9g)}$$

Step 10 – Simplifying Eq. F.5e in order to x to obtain ε_{cc}

$$\Leftrightarrow \frac{2E_f\varepsilon_{tf}A_f}{\varepsilon_{cc}}\left(h-x\right) - \frac{2E_f\Delta\varepsilon_{tf}A_f}{\varepsilon_{cc}}\left(h-x\right) = E_c bh\left(h-2x\right) + 2E_{st}A_{st}\left(d_{st}-x\right) + \\ - 2E_{sc}A_{sc}\left(x-c_{sc}\right) \Leftrightarrow \quad \text{(F.10a)}$$

$$\Leftrightarrow \frac{2E_f\varepsilon_{tf}A_f}{\varepsilon_{cc}}\left(h-x\right) - \frac{2E_fA_f}{\varepsilon_{cc}}\frac{d_f-x}{h-x}\varepsilon_{cc}\left(h-x\right) = E_c bh\left(h-2x\right) + 2E_{st}A_{st}\left(d_{st}-x\right) + \\ - 2E_{sc}A_{sc}\left(x-c_{sc}\right) \Leftrightarrow \quad \text{(F.10b)}$$

$$\Leftrightarrow \frac{2E_f\varepsilon_{tf}A_f}{\varepsilon_{cc}}\left(h-x\right) = E_c bh\left(h-2x\right) - 2E_{sc}A_{sc}\left(x-c_{sc}\right) + 2E_{st}A_{st}\left(d_{st}-x\right) + \\ + 2E_fA_f\left(d_f-x\right) \Leftrightarrow \quad \text{(F.10c)}$$

$$\Leftrightarrow \varepsilon_{cc} = \frac{2E_f\varepsilon_{tf}A_f\left(h-x\right)}{E_c bh\left(h-2x\right) - 2\left(E_{sc}A_{sc}\left(x-c_{sc}\right) - E_{st}A_{st}\left(d_{st}-x\right) - E_fA_f\left(d_f-x\right)\right)} \quad \text{(F.10d)}$$

The curvature will be given by the ratio between ε_{cc} and $\left(h-x\right)$.

F.2 CURVATURE AND BENDING MOMENT AT CRACK INITIATION

The curvature and bending moment at crack initiation can be determined using the procedure previously described. The strain distribution along the height is again assumed to be linear and the stress and load diagrams corresponding to the crack initiation state are depicted in Figure F.2.

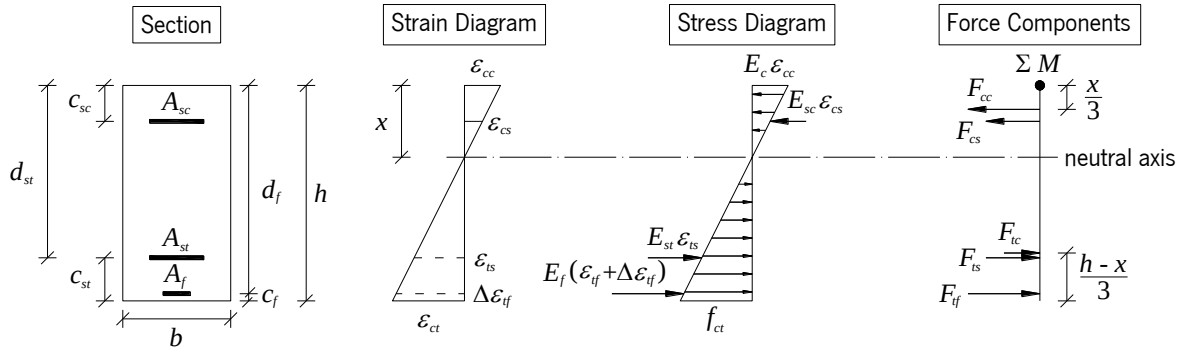

Figure F.2 – Strain and stress diagram of the cross section at crack initiation.

Step 1 – Definition of the boundary conditionsx\

$$\varepsilon_{cc} \le \frac{f_{cc}}{E_c} \tag{F.11a}$$

$$\varepsilon_{cs} \le \frac{f_{yc}}{E_{sc}} \tag{F.11b}$$

$$\varepsilon_{ts} \le \frac{f_{yt}}{E_{st}} \tag{F.11c}$$

$$\varepsilon_{tc} = \frac{f_{ct}}{E_c} \tag{F.11d}$$

$$\varepsilon_{tf} + \Delta\varepsilon_{tf} \le \frac{f_f}{E_f} \tag{F.11e}$$

Step 2 – Geometrical relationships between strains

$$\frac{\varepsilon_{cc}}{x} = \frac{\varepsilon_{tc}}{h-x} \Leftrightarrow \varepsilon_{cc} = \frac{x}{h-x}\varepsilon_{tc} \tag{F.12a}$$

$$\frac{\varepsilon_{cs}}{x-c_{sc}} = \frac{\varepsilon_{tc}}{h-x} \Leftrightarrow \varepsilon_{cs} = \frac{x-c_{sc}}{h-x}\varepsilon_{tc} \tag{F.12b}$$

$$\frac{\varepsilon_{ts}}{h-x-c_{st}} = \frac{\varepsilon_{tc}}{h-x} \Leftrightarrow \varepsilon_{ts} = \frac{d_{st}-x}{h-x}\varepsilon_{tc} \tag{F.12c}$$

$$\frac{\Delta\varepsilon_{tf}}{h-x-c_f} = \frac{\varepsilon_{tc}}{h-x} \Leftrightarrow \Delta\varepsilon_{tf} = \frac{d_f-x}{h-x}\varepsilon_{tc} \tag{F.12d}$$

Step 3 - Quantification of the internal loads

$$F_{cc} = \frac{1}{2}E_c\varepsilon_{cc}\cdot bx \tag{F.13a}$$

$$F_{cs} = E_{sc}\varepsilon_{cs}\cdot A_{sc} \tag{F.13b}$$

$$F_{tc} = \frac{1}{2}E_c\varepsilon_{tc}\cdot b(h-x) \tag{F.13c}$$

$$F_{ts} = E_{st}\varepsilon_{ts} \cdot A_{st} \tag{F.13d}$$

$$F_{tf} = E_f\left(\varepsilon_{tf} + \Delta\varepsilon_{tf}\right) \cdot A_f \tag{F.13e}$$

Step 4 – Equilibrium of internal forces

$$\sum_i^n F_{t,i} - \sum_j^m F_{c,j} = 0 \tag{F.14a}$$

$$F_{tc} + F_{ts} + F_{tf} - F_{cc} - F_{cs} = 0 \tag{F.14b}$$

$$\frac{1}{2}E_c\varepsilon_{tc}b(h-x) + E_{st}\varepsilon_{ts}A_{st} + E_f\left(\varepsilon_{tf} + \Delta\varepsilon_{tf}\right)A_f - \frac{1}{2}E_c\varepsilon_{cc}bx - E_{sc}\varepsilon_{cs}A_{sc} = 0 \Leftrightarrow \tag{F.14c}$$

Step 5 – Substituting Eq. F.12 in Eq. F.14c to determine x.

$$\Leftrightarrow E_f\varepsilon_{tf}A_f = \frac{1}{2}E_c\varepsilon_{cc}bx - \frac{1}{2}E_c\varepsilon_{tc}b(h-x) + E_{sc}\varepsilon_{cs}A_{sc} - E_{st}\varepsilon_{ts}A_{st} - E_f\Delta\varepsilon_{tf}A_f \Leftrightarrow \tag{F.15a}$$

$$\begin{aligned}\Leftrightarrow E_f\varepsilon_{tf}A_f = {} & \frac{1}{2}E_cb\left(\left(\frac{x}{h-x}\varepsilon_{tc}\right)x - \varepsilon_{tc}(h-x)\right) + E_{sc}\left(\frac{x-c_{sc}}{h-x}\varepsilon_{tc}\right)A_{sc} + \\ & - E_{st}\left(\frac{d_{st}-x}{h-x}\varepsilon_{tc}\right)A_{st} - E_f\left(\frac{d_f-x}{h-x}\varepsilon_{ct}\right)A_f \Leftrightarrow\end{aligned} \tag{F.15b}$$

$$\begin{aligned}\Leftrightarrow \frac{E_f\varepsilon_{tf}A_f}{\varepsilon_{tc}} = {} & \frac{1}{2}E_cb\left(\frac{x^2}{h-x} - \frac{(h-x)^2}{h-x}\right) + E_{sc}A_{sc}\frac{x-c_{sc}}{h-x} - E_{st}A_{st}\frac{d_{st}-x}{h-x} + \\ & - E_fA_f\frac{d_f-x}{h-x} \Leftrightarrow\end{aligned} \tag{F.15c}$$

$$\begin{aligned}\Leftrightarrow \frac{E_f\varepsilon_{tf}A_f}{\varepsilon_{tc}}(h-x) = {} & \frac{1}{2}E_cb\left(x^2 - (h-x)^2\right) + E_{sc}A_{sc}(x-c_{sc}) - E_{st}A_{st}(d_{st}-x) + \\ & - E_fA_f(d_f-x) \Leftrightarrow\end{aligned} \tag{F.15d}$$

$$\begin{aligned}\Leftrightarrow \frac{E_f\varepsilon_{tf}A_f}{\varepsilon_{tc}}(h-x) = {} & \frac{1}{2}E_cbh(2x-h) + E_{sc}A_{sc}(x-c_{sc}) - E_{st}A_{st}(d_{st}-x) + \\ & - E_fA_f(d_f-x) \Leftrightarrow\end{aligned} \tag{F.15e}$$

$$\begin{aligned}\Leftrightarrow \frac{E_f\varepsilon_{tf}A_f}{\varepsilon_{tc}}h - \frac{E_f\varepsilon_{tf}A_f}{\varepsilon_{tc}}x = {} & E_cbhx - \frac{1}{2}E_cbh^2 + E_{sc}A_{sc}x - E_{sc}A_{sc}c_{sc} - E_{st}A_{st}d_{st} + \\ & + E_{st}A_{st}x - E_fA_fd_f + E_fA_fx \Leftrightarrow\end{aligned} \tag{F.15f}$$

$$\Leftrightarrow 2\left(E_c bh + E_{sc}A_{sc} + E_{st}A_{st} + E_f A_f + \frac{E_f \varepsilon_{tf} A_f}{\varepsilon_{tc}} \right) x = E_c bh^2 + 2E_{sc}A_{sc}c_{sc} + \\ + 2E_{st}A_{st}d_{st} + 2E_f A_f d_f + \frac{2E_f \varepsilon_{tf} A_f}{\varepsilon_{tc}} h \Leftrightarrow \quad \text{(F.15g)}$$

$$\Leftrightarrow 2\left(E_c bh + E_{sc}A_{sc} + E_{st}A_{st} + E_f A_f \left(1 + \frac{\varepsilon_{tf}}{\varepsilon_{tc}} \right) \right) x = E_c bh^2 + \\ + 2\left(E_{sc}A_{sc}c_{sc} + E_{st}A_{st}d_{st} + E_f A_f \left(d_f + h\frac{\varepsilon_{tf}}{\varepsilon_{tc}} \right) \right) \Leftrightarrow \quad \text{(F.15h)}$$

$$\Leftrightarrow 2\left(f_{ct} bh + \varepsilon_{tc}\left(E_{sc}A_{sc} + E_{st}A_{st} \right) + E_f A_f \left(\varepsilon_{tc} + \varepsilon_{tf} \right) \right) x = E_c \varepsilon_{tc} bh^2 + \\ + 2\varepsilon_{tc}\left(E_{sc}A_{sc}c_{sc} + E_{st}A_{st}d_{st} \right) + E_f A_f \left(d_f \varepsilon_{tc} + h\varepsilon_{tf} \right) \Leftrightarrow \quad \text{(F.15i)}$$

$$\Leftrightarrow x = \frac{bh^2 f_{ct} + 2\varepsilon_{tc}\left(E_{sc}A_{sc}c_{sc} + E_{st}A_{st}d_{st} \right) + 2E_f A_f \left(d_f \varepsilon_{tc} + h\varepsilon_{tf} \right)}{2\left(f_{ct} bh + \varepsilon_{tc}\left(E_{sc}A_{sc} + E_{st}A_{st} \right) + E_f A_f \left(\varepsilon_{tc} + \varepsilon_{tf} \right) \right)} \quad \text{(F.15j)}$$

Step 6 – Determining the lever arms of the internal forces in relation to the top fibre

$$b_{cc} = \frac{x}{3} \quad \text{(F.16a)}$$

$$b_{cs} = c_{sc} \quad \text{(F.16b)}$$

$$b_{ts} = h - c_{st} = d_{st} \quad \text{(F.16c)}$$

$$b_{tc} = x + \frac{2}{3}\left(h - x \right) = \frac{2h + x}{3} \quad \text{(F.16d)}$$

$$b_{tf} = h + c_f = d_f \quad \text{(F.16e)}$$

Step 7 – Summing the internal moments

$$M_{crack} = \sum_i^n F_{ti} \cdot b_{ti} - \sum_j^m F_{cj} \cdot b_{cj} \quad \text{(F.17a)}$$

$$M_{crack} = F_{tc} \cdot b_{tc} + F_{ts} \cdot b_{ts} + F_{tf} \cdot b_{tf} - F_{cc} \cdot b_{cc} - F_{cs} \cdot b_{cs} \quad \text{(F.17b)}$$

Step 8 – Simplification of the bending moment by substituting Eqs. F.13 and F.16 in Eq. F.17b

$$M_{crack} = \frac{1}{2} E_c \varepsilon_{tc} \cdot b\left(h - x \right) \cdot \frac{2h + x}{3} + E_{st}\varepsilon_{ts}A_{st} \cdot d_{st} + E_f \left(\varepsilon_{tf} + \Delta\varepsilon_{tf} \right) A_f \cdot d_f \\ - \frac{1}{2} E_c \varepsilon_{cc} \cdot bx \cdot \frac{x}{3} - E_{sc}\varepsilon_{cs}A_{sc} \cdot c_{sc} \Leftrightarrow \quad \text{(F.18a)}$$

$$\Leftrightarrow M_{crack} = \frac{1}{6} E_c \varepsilon_{tc} b\left(h-x\right)\left(2h+x\right) + E_{st}\varepsilon_{ts}A_{st}d_{st} + E_f\left(\varepsilon_{tf}+\Delta\varepsilon_{tf}\right)A_f d_f + \\ -\frac{1}{6}E_c\varepsilon_{cc}bx^2 - E_{sc}\varepsilon_{cs}A_{sc}c_{sc} \Leftrightarrow \quad \text{(F.18b)}$$

$$\Leftrightarrow M_{crack} = \frac{1}{6} E_c \varepsilon_{tc} b\left(h-x\right)\left(2h+x\right) - \frac{1}{6}E_c\varepsilon_{cc}bx^2 + E_{st}\varepsilon_{ts}A_{st}d_{st} + \\ + E_f\left(\varepsilon_{tf}+\Delta\varepsilon_{tf}\right)A_f d_f - E_{sc}\varepsilon_{cs}A_{sc}c_{sc} \Leftrightarrow \quad \text{(F.18c)}$$

$$\Leftrightarrow M_{crack} = \frac{1}{6} E_c b\left(\varepsilon_{tc}\left(h-x\right)\left(2h+x\right) - \varepsilon_{cc}x^2\right) + E_{st}\varepsilon_{ts}A_{st}d_{st} + \\ + E_f\left(\varepsilon_{tf}+\Delta\varepsilon_{tf}\right)A_f d_f - E_{sc}\varepsilon_{cs}A_{sc}c_{sc} \quad \text{(F.18d)}$$

F.3 CURVATURE AND BENDING MOMENT AT YIELD INITIATION

F.3.1 Design Assumption 1

The strain and stress distribution in correspondence with this design assumption is depicted in Figure F.3 and all strains along the cross section height can be defined as a function of the strain in the bottom layer of reinforcement, $\varepsilon_{ts} = \varepsilon_{st}$.

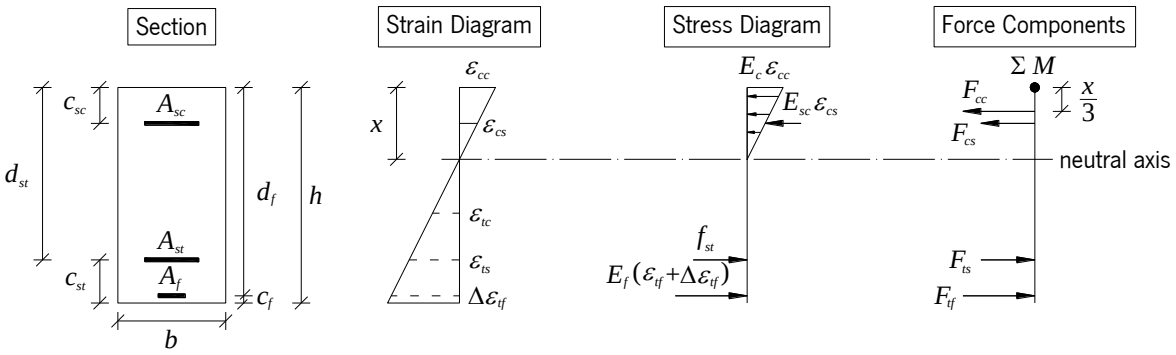

Figure F.3 – Strain and stress diagram of the cross section at yield initiation – Design assumption 1.

Step 1 – Boundary conditions

$$0.3 f_{cc}/E_c \le \varepsilon_{cc} \le \varepsilon_{c3} \quad \text{(F.19a)}$$

$$\varepsilon_{cs} \le \frac{f_{sc}}{E_{sc}} \quad \text{(F.19b)}$$

$$\varepsilon_{ts} = \frac{f_{st}}{E_{st}} \quad \text{(F.19c)}$$

$$\varepsilon_{tf} + \Delta\varepsilon_{tf} \le \frac{f_f}{E_f} \quad \text{(F.19d)}$$

Step 2 – Geometrical relationships between strains

$$\frac{\varepsilon_{cc}}{x} = \frac{\varepsilon_{ts}}{h - x - c_{st}} \Leftrightarrow \varepsilon_{cc} = \frac{x}{d_{st} - x}\varepsilon_{ts} \tag{F.20a}$$

$$\frac{\varepsilon_{cs}}{x - c_{sc}} = \frac{\varepsilon_{ts}}{h - x - c_{st}} \Leftrightarrow \varepsilon_{cs} = \frac{x - c_{sc}}{d_{st} - x}\varepsilon_{ts} \tag{F.20b}$$

$$\frac{\Delta\varepsilon_{tf}}{h - x - c_f} = \frac{\varepsilon_{ts}}{h - x - c_{st}} \Leftrightarrow \Delta\varepsilon_{tf} = \frac{d_f - x}{d_{st} - x}\varepsilon_{ts} \tag{F.20c}$$

Step 3 - Quantification of the internal loads

$$F_{cc} = \frac{1}{2}E_c\varepsilon_{cc} \cdot bx \tag{F.21a}$$

$$F_{cs} = E_{sc}\varepsilon_{cs} \cdot A_{sc} \tag{F.21b}$$

$$F_{ts} = E_{st}\varepsilon_{ts} \cdot A_{st} = f_{st} \cdot A_{st} \tag{F.21c}$$

$$F_{tf} = E_f\left(\varepsilon_{tf} + \Delta\varepsilon_{tf}\right) \cdot A_f \tag{F.21d}$$

Step 4 – Equilibrium of internal forces

$$\sum_i^n F_{ti} - \sum_i^n F_{ci} = 0 \tag{F.22a}$$

$$F_{ts} + F_{tf} - F_{cc} - F_{cs} = 0 \tag{F.22b}$$

$$f_{st}A_{st} + E_f\left(\varepsilon_{tf} + \Delta\varepsilon_{tf}\right)A_f - \frac{1}{2}E_c\varepsilon_{cc}bx - E_{sc}\varepsilon_{cs}A_{sc} = 0 \tag{F.22c}$$

Step 5 – Substituting Eq. F.20 in Eq. F.22c

$$f_{st}A_{st} + E_f\left(\varepsilon_{tf} + \Delta\varepsilon_{tf}\right)A_f - \frac{1}{2}E_c\varepsilon_{cc}bx - E_{sc}\varepsilon_{cs}A_{sc} = 0 \Leftrightarrow \tag{F.23a}$$

$$\Leftrightarrow E_{st}\varepsilon_{ts}A_{st} + E_f\left(\varepsilon_{tf} + \frac{d_f - x}{d_{st} - x}\varepsilon_{ts}\right)A_f - \frac{1}{2}E_c\left(\frac{x}{d_{st} - x}\varepsilon_{ts}\right)bx - E_{sc}\left(\frac{x - c_{sc}}{d_{st} - x}\varepsilon_{ts}\right)A_{sc} = 0 \Leftrightarrow \tag{F.23b}$$

$$\begin{aligned}\Leftrightarrow \frac{1}{2}E_c\left(\frac{x}{d_{st} - x}\varepsilon_{ts}\right)bx + E_{sc}\left(\frac{x - c_{sc}}{d_{st} - x}\varepsilon_{ts}\right)A_{sc} - E_{st}\varepsilon_{ts}A_{st}\frac{d_{st} - x}{d_{st} - x} - E_f\frac{d_f - x}{d_{st} - x}\varepsilon_{ts}A_f + \\ - E_f\varepsilon_{tf}A_f\frac{\left(d_{st} - x\right)\varepsilon_{ts}}{\left(d_{st} - x\right)\varepsilon_{ts}} = 0 \Leftrightarrow\end{aligned} \tag{F.23c}$$

$$\Leftrightarrow \frac{1}{2}E_cbx^2 + E_{sc}A_{sc}\left(x - c_{sc}\right) - E_{st}A_{st}\left(d_{st} - x\right) - E_fA_f\left(d_f - x\right) - E_f\varepsilon_{tf}A_f\frac{\left(d_{st} - x\right)}{\varepsilon_{ts}} = 0 \Leftrightarrow \tag{F.23d}$$

$$\Leftrightarrow \frac{1}{2}E_c b x^2 + E_{sc}A_{sc}x - E_{sc}A_{sc}c_{sc} - E_{st}A_{st}d_{st} + E_{st}A_{st}x - E_f A_f d_f + E_f A_f x + \\ - \frac{E_f \varepsilon_{tf} A_f d_{st}}{\varepsilon_{ts}} + \frac{E_f \varepsilon_{tf} A_f x}{\varepsilon_{ts}} = 0 \Leftrightarrow \tag{F.23e}$$

$$\Leftrightarrow \frac{1}{2}E_c b x^2 + \left(E_{sc}A_{sc} + E_{st}A_{st} + E_f A_f \left(1 + \frac{\varepsilon_{tf}}{\varepsilon_{ts}} \right) \right) x + \\ - \left(E_{sc}A_{sc}c_{sc} + E_{st}A_{st}d_{st} + E_f A_f \left(d_f + d_{st}\frac{\varepsilon_{tf}}{\varepsilon_{ts}} \right) \right) = 0 \tag{F.23f}$$

Step 6 – Solution of the quadratic equation

By definition, the quadratic equation has two solutions,

$$Ax^2 + Bx + C = 0 \Rightarrow x = \begin{cases} \dfrac{-B + \sqrt{B^2 - 4AC}}{2A} & if\ \ 2Ax + B \geq 0 \\ \dfrac{-B - \sqrt{B^2 - 4AC}}{2A} & if\ \ 2Ax + B \leq 0 \end{cases} \tag{F.24}$$

Since in this case only C is negative, the first solution applies.

$$x = \frac{-B + \sqrt{B^2 - 4AC}}{2A} \tag{F.25a}$$

$$A = \frac{1}{2}E_c b \tag{F.25b}$$

$$B = E_{sc}A_{sc} + E_{st}A_{st} + E_f A_f \left(1 + \frac{\varepsilon_{tf}}{\varepsilon_{ts}} \right) \tag{F.25c}$$

$$C = -\left(E_{sc}A_{sc}c_{sc} + E_{st}A_{st}d_{st} + E_f A_f \left(d_f + d_{st}\frac{\varepsilon_{tf}}{\varepsilon_{ts}} \right) \right) \tag{F.25d}$$

Step 7 – Determining the lever arms of the internal forces in relation to the top fibre

$$b_{cc} = \frac{x}{3} \tag{F.26a}$$

$$b_{cs} = c_{sc} \tag{F.26b}$$

$$b_{ts} = h - c_{st} = d_{st} \tag{F.26c}$$

$$b_{tf} = h - c_f = d_f \tag{F.26d}$$

Step 8 – Bending moment

$$M_{yield} = \sum_i^n F_{ti} \cdot b_{ti} - \sum_j^m F_{cj} \cdot b_{cj} \tag{F.27a}$$

$$M_{yield} = F_{ts}b_{ts} + F_{tf}b_{tf} - F_{cc}b_{cc} - F_{cs}b_{cs} \tag{F.27b}$$

Step 9 – Simplification of the bending moment by substituting Eqs. F.21 and F.26 in Eq. F.27b

$$M_{yield} = -\frac{1}{6} E_c \varepsilon_{cc} b x^2 - E_{sc} \varepsilon_{cs} A_{sc} c_{sc} + f_{st} A_{st} d_{st} + E_f \left(\varepsilon_{tf} + \Delta\varepsilon_{tf} \right) A_f d_f \tag{F.28}$$

F.3.2 Design Assumption 3

The strain and stress distribution in correspondence with this design assumption is depicted in Figure F.4, and all strains along the cross section height can be defined as a function of the yielding strain, ε_{ts} .

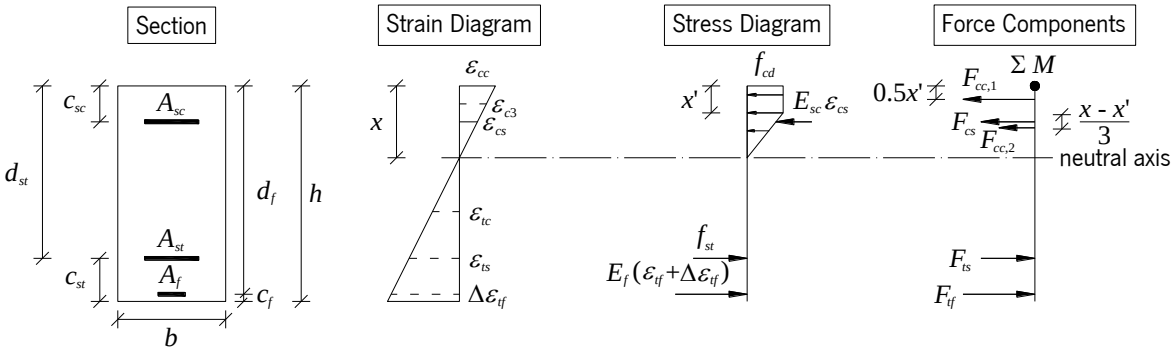

Figure F.4 – Strain and stress diagram of the cross section at yield initiation – Design assumption 3.

Step 1 – Boundary conditions

$$\varepsilon_{cc} \geq \varepsilon_{c3} \tag{F.29a}$$

$$\varepsilon_{cs} \leq \frac{f_{sc}}{E_{sc}} \tag{F.29b}$$

$$\varepsilon_{ts} = \frac{f_{sc}}{E_{st}} \tag{F.29c}$$

$$\varepsilon_{tf} + \Delta\varepsilon_{tf} \leq \frac{f_f}{E_f} \tag{F.29d}$$

Step 2 – Geometrical relationships between strains

$$\frac{\varepsilon_{cc}}{x} = \frac{\varepsilon_{ts}}{h - x - c_{st}} \Leftrightarrow \varepsilon_{cc} = \frac{x}{d_{st} - x} \varepsilon_{ts} \tag{F.30a}$$

$$\frac{\varepsilon_{cs}}{x - c_{sc}} = \frac{\varepsilon_{ts}}{h - x - c_{st}} \Leftrightarrow \varepsilon_{cs} = \frac{x - c_{sc}}{d_{st} - x} \varepsilon_{ts} \tag{F.30b}$$

$$\frac{\Delta\varepsilon_{tf}}{h - x - c_f} = \frac{\varepsilon_{ts}}{h - x - c_{st}} \Leftrightarrow \Delta\varepsilon_{tf} = \frac{d_f - x}{d_{st} - x} \varepsilon_{ts} \tag{F.30c}$$

$$\frac{\varepsilon_{ts}}{h-x-c_{st}}=\frac{\varepsilon_{c3}}{x-x'}\Leftrightarrow x'=\frac{\left(\varepsilon_{c3}+\varepsilon_{ts}\right)x-d_{st}\varepsilon_{c3}}{\varepsilon_{ts}} \tag{F.30d}$$

Step 3 - Quantification of the internal loads

$$F_{cc,1}=f_{cc}\cdot bx' \tag{F.31a}$$

$$F_{cc,1}=\frac{1}{2}f_{cc}\cdot b\left(x-x'\right) \tag{F.31b}$$

$$F_{cs}=E_{sc}\varepsilon_{cs}\cdot A_{sc} \tag{F.31c}$$

$$F_{ts}=E_{st}\varepsilon_{ts}\cdot A_{st}=f_{st}\cdot A_{st} \tag{F.31d}$$

$$F_{tf}=E_f\left(\varepsilon_{tf}+\Delta\varepsilon_{tf}\right)\cdot A_f \tag{F.31e}$$

Step 4 – Equilibrium of internal forces

$$\sum_i^n F_{ti}-\sum_i^n F_{ci}=0 \tag{F.32a}$$

$$F_{ts}+F_{tf}-F_{cc,1}-F_{cc,2}-F_{cs}=0 \tag{F.32b}$$

$$f_{st}A_{st}+E_f\left(\varepsilon_{tf}+\Delta\varepsilon_{tf}\right)A_f-f_{cc}bx'-\frac{1}{2}f_{cc}b\left(x-x'\right)-E_{sc}\varepsilon_{cs}A_{sc}=0 \tag{F.32c}$$

Step 5 – Substituting Eq. F.30 in Eq. F.32c.

$$f_{st}A_{st}+E_f\left(\varepsilon_{tf}+\Delta\varepsilon_{tf}\right)A_f-f_{cc}bx'-\frac{1}{2}f_{cc}b\left(x-x'\right)-E_{sc}\varepsilon_{cs}A_{sc}=0\Leftrightarrow \tag{F.33a}$$

$$\Leftrightarrow f_{st}A_{st}+E_f\left(\varepsilon_{tf}+\left(\frac{d_f-x}{d_{st}-x}\varepsilon_{ts}\right)\right)A_f-\frac{f_{cc}b}{2}\left(2x'+\left(x-x'\right)\right)-E_{sc}\left(\frac{x-c_{sc}}{d_{st}-x}\varepsilon_{ts}\right)A_{sc}=0\Leftrightarrow \tag{F.33b}$$

$$\Leftrightarrow f_{st}A_{st}+E_f\left(\varepsilon_{tf}+\left(\frac{d_f-x}{d_{st}-x}\varepsilon_{ts}\right)\right)A_f-\frac{f_{cc}b}{2}\left(x+x'\right)-E_{sc}A_{sc}\left(\frac{x-c_{sc}}{d_{st}-x}\varepsilon_{ts}\right)=0\Leftrightarrow \tag{F.33c}$$

$$\begin{aligned}\Leftrightarrow\ &\frac{f_{cc}b}{2}\left(x+x'\right)\frac{\left(d_{st}-x\right)\varepsilon_{ts}}{\left(d_{st}-x\right)\varepsilon_{ts}}+E_{sc}A_{sc}\left(\frac{x-c_{sc}}{d_{st}-x}\varepsilon_{ts}\right)-f_{st}A_{st}\frac{\left(d_{st}-x\right)\varepsilon_{ts}}{\left(d_{st}-x\right)\varepsilon_{ts}}+\\&-E_fA_f\left(\varepsilon_{tf}+\left(\frac{d_f-x}{d_{st}-x}\varepsilon_{ts}\right)\right)\frac{\left(d_{st}-x\right)\varepsilon_{ts}}{\left(d_{st}-x\right)\varepsilon_{ts}}=0\Leftrightarrow\end{aligned} \tag{F.33d}$$

$$\begin{aligned}\Leftrightarrow\ &\frac{f_{cc}b}{2}\left(x+x'\right)\frac{\left(d_{st}-x\right)}{\varepsilon_{ts}}+E_{sc}A_{sc}\left(x-c_{sc}\right)-f_{st}A_{st}\frac{\left(d_{st}-x\right)}{\varepsilon_{ts}}+\\&-E_fA_f\left(\varepsilon_{tf}+\left(\frac{d_f-x}{d_{st}-x}\varepsilon_{ts}\right)\right)\frac{\left(d_{st}-x\right)}{\varepsilon_{ts}}=0\Leftrightarrow\end{aligned} \tag{F.33e}$$

$$\Leftrightarrow \frac{f_{cc}b}{2\varepsilon_{ts}}\left(-x^2 - x\cdot x' + d_{st}x + d_{st}x'\right) + E_{sc}A_{sc}\left(x - c_{sc}\right) - \frac{f_{st}A_{st}}{\varepsilon_{ts}}\left(d_{st} - x\right) + \\ - \frac{E_f A_f}{\varepsilon_{ts}}\left(\frac{d_{st} - x}{d_{st} - x}\varepsilon_{tf} + \frac{d_f - x}{d_{st} - x}\varepsilon_{ts}\right)\left(d_{st} - x\right) = 0 \Leftrightarrow \quad \text{(F.33f)}$$

$$\Leftrightarrow \frac{f_{cc}b}{2\varepsilon_{ts}}\left(-x^2 - \frac{\left(\varepsilon_{c3} + \varepsilon_{ts}\right)x - d_{st}\varepsilon_{c3}}{\varepsilon_{ts}}x + d_{st}x + d_{st}\frac{\left(\varepsilon_{c3} + \varepsilon_{ts}\right)x - d_{st}\varepsilon_{c3}}{\varepsilon_{ts}}\right) + \\ + E_{sc}A_{sc}\left(x - c_{sc}\right) - \frac{f_{st}A_{st}}{\varepsilon_{ts}}\left(d_{st} - x\right) - \frac{E_f A_f}{\varepsilon_{ts}}\left(d_{st} - x\right)\varepsilon_{tf} - E_f A_f\left(d_f - x\right) = 0 \Leftrightarrow \quad \text{(F.33g)}$$

$$\Leftrightarrow \frac{f_{cc}b}{2\varepsilon_{ts}}\left(-\frac{\varepsilon_{ts}}{\varepsilon_{ts}}x^2 - \frac{\left(\varepsilon_{c3} + \varepsilon_{ts}\right)x - d_{st}\varepsilon_{c3}}{\varepsilon_{ts}}x + d_{st}\frac{\varepsilon_{ts}}{\varepsilon_{ts}}x + \frac{\left(\varepsilon_{c3} + \varepsilon_{ts}\right)x - d_{st}\varepsilon_{c3}}{\varepsilon_{ts}}d_{st}\right) + \\ - + E_{sc}A_{sc}\left(x - c_{sc}\right) - \frac{f_{st}A_{st}}{\varepsilon_{ts}}\left(d_{st} - x\right)\frac{E_f A_f}{\varepsilon_{ts}}\left(d_{st} - x\right)\varepsilon_{tf} - E_f A_f\left(d_f - x\right) = 0 \Leftrightarrow \quad \text{(F.33h)}$$

$$\Leftrightarrow \frac{f_{cc}b}{2\varepsilon_{ts}^{\,2}}\left(-\varepsilon_{ts}x^2 - \left(\varepsilon_{c3} + \varepsilon_{ts}\right)x^2 + d_{st}\varepsilon_{c3}x + d_{st}\varepsilon_{ts}x + \left(\varepsilon_{c3} + \varepsilon_{ts}\right)d_{st}x - d_{st}^{\,2}\varepsilon_{c3}\right) + \\ + E_{sc}A_{sc}\left(x - c_{sc}\right) - \frac{f_{st}A_{st}}{\varepsilon_{ts}}\left(d_{st} - x\right) - \frac{E_f A_f}{\varepsilon_{ts}}\left(d_{st} - x\right)\varepsilon_{tf} - E_f A_f\left(d_f - x\right) = 0 \Leftrightarrow \quad \text{(F.33i)}$$

$$\Leftrightarrow \frac{f_{cc}b}{2\varepsilon_{ts}^{\,2}}\left(-\left(\varepsilon_{c3} + 2\varepsilon_{ts}\right)x^2 + 2\left(d_{st}\varepsilon_{c3} + d_{st}\varepsilon_{ts}\right)x - d_{st}^{\,2}\varepsilon_{c3}\right) + E_{sc}A_{sc}x - E_{sc}A_{sc}c_{sc} + \\ - \frac{f_{st}A_{st}}{\varepsilon_{ts}}d_{st} + \frac{f_{st}A_{st}}{\varepsilon_{ts}}x - \frac{E_f A_f \varepsilon_{tf}}{\varepsilon_{ts}}d_{st} + \frac{E_f A_f \varepsilon_{tf}}{\varepsilon_{ts}}x - E_f A_f d_f + E_f A_f x = 0 \Leftrightarrow \quad \text{(F.33j)}$$

$$\Leftrightarrow \frac{f_{cc}b}{2\varepsilon_{ts}^{\,2}}\left(\varepsilon_{c3} + 2\varepsilon_{ts}\right)x^2 - \frac{f_{cc}bd_{st}}{\varepsilon_{ts}^{\,2}}\left(\varepsilon_{c3} + \varepsilon_{ts}\right)x + \frac{f_{cc}b}{2\varepsilon_{ts}^{\,2}}d_{st}^{\,2}\varepsilon_{c3} - E_{sc}A_{sc}x + E_{sc}A_{sc}c_{sc} + \\ + \frac{f_{st}A_{st}}{\varepsilon_{ts}}d_{st} - \frac{f_{st}A_{st}}{\varepsilon_{ts}}x + \frac{E_f A_f \varepsilon_{tf}}{\varepsilon_{ts}}d_{st} - \frac{E_f A_f \varepsilon_{tf}}{\varepsilon_{ts}}x + E_f A_f d_f - E_f A_f x = 0 \Leftrightarrow \quad \text{(F.33k)}$$

$$\Leftrightarrow \frac{f_{cc}b\left(\varepsilon_{c3} + 2\varepsilon_{ts}\right)}{2\varepsilon_{ts}^{\,2}}x^2 - \left(\frac{f_{cc}bd_{st}}{\varepsilon_{ts}^{\,2}}\left(\varepsilon_{c3} + \varepsilon_{ts}\right)x + E_{sc}A_{sc}x + \frac{f_{st}A_{st}}{\varepsilon_{ts}}x + \frac{E_f A_f \varepsilon_{tf}}{\varepsilon_{ts}}x + E_f A_f x\right) + \\ + \left(\frac{f_{cc}b}{2\varepsilon_{ts}^{\,2}}d_{st}^{\,2}\varepsilon_{c3} + E_{sc}A_{sc}c_{sc} + \frac{f_{st}A_{st}}{\varepsilon_{ts}}d_{st} + \frac{E_f A_f \varepsilon_{tf}}{\varepsilon_{ts}}d_{st} + E_f A_f d_f\right) = 0 \Leftrightarrow \quad \text{(F.33l)}$$

$$\Leftrightarrow \frac{f_{cc}b\left(\varepsilon_{c3} + 2\varepsilon_{ts}\right)}{2\varepsilon_{ts}^{\,2}}x^2 - \left(\frac{f_{cc}bd_{st}\left(\varepsilon_{c3} + \varepsilon_{ts}\right)}{\varepsilon_{ts}^{\,2}} + E_{sc}A_{sc} + \frac{f_{st}A_{st}}{\varepsilon_{ts}} + E_f A_f\left(1 + \frac{\varepsilon_{tf}}{\varepsilon_{ts}}\right)\right)x + \\ + \left(\frac{f_{cc}bd_{st}^{\,2}\varepsilon_{c3}}{2\varepsilon_{ts}^{\,2}} + E_{sc}A_{sc}c_{sc} + \frac{f_{st}A_{st}}{\varepsilon_{ts}}d_{st} + E_f A_f\left(d_f + d_{st}\frac{\varepsilon_{tf}}{\varepsilon_{ts}}\right)\right) = 0 \quad \text{(F.33m)}$$

Step 6 – Solution of the quadratic equation

Since by definition $d_{st} > x$, and all the constants involved in the determination of A and B are positive,

$$2Ax + B = \frac{2 f_{cc} b\left(\varepsilon_{c3} + 2\varepsilon_{ts}\right)}{2{\varepsilon_{ts}}^2} x - \left(\frac{f_{cc} b d_{st} \left(\varepsilon_{c3} + \varepsilon_{ts}\right)}{{\varepsilon_{ts}}^2} + E_{sc} A_{sc} + \frac{f_{st} A_{st}}{\varepsilon_{ts}} + E_f A_f \left(1 + \frac{\varepsilon_{tf}}{\varepsilon_{ts}}\right)\right) \Leftrightarrow \quad \text{(F.34a)}$$

$$\Leftrightarrow 2Ax + B = -\left(\frac{f_{cc} b\left(\varepsilon_{c3} + 2\varepsilon_{ts}\right)}{{\varepsilon_{ts}}^2} \left(d_{st} - x\right) + E_{sc} A_{sc} + \frac{f_{st} A_{st}}{\varepsilon_{ts}} + E_f A_f \left(1 + \frac{\varepsilon_{tf}}{\varepsilon_{ts}}\right)\right) \Rightarrow \quad \text{(F.34b)}$$

$$\Rightarrow 2Ax + B \leq 0 \quad \text{(F.34c)}$$

According to Eq. F.24, the solution of the quadratic equation is,

$$x = \frac{-B - \sqrt{B^2 - 4AC}}{2A} \quad \text{(F.35a)}$$

$$A = \frac{f_{cc} b\left(\varepsilon_{c3} + 2\varepsilon_{ts}\right)}{2{\varepsilon_{ts}}^2} \quad \text{(F.35b)}$$

$$B = -\left(\frac{f_{cc} b d_{st} \left(\varepsilon_{c3} + \varepsilon_{ts}\right)}{{\varepsilon_{ts}}^2} + E_{sc} A_{sc} + \frac{f_{st} A_{st}}{\varepsilon_{ts}} + E_f A_f \left(1 + \frac{\varepsilon_{tf}}{\varepsilon_{ts}}\right)\right) \quad \text{(F.35c)}$$

$$C = \frac{f_{cc} b {d_{st}}^2 \varepsilon_{c3}}{2{\varepsilon_{ts}}^2} + E_{sc} A_{sc} c_{sc} + \frac{f_{st} A_{st}}{\varepsilon_{ts}} d_{st} + E_f A_f \left(d_f + d_{st} \frac{\varepsilon_{tf}}{\varepsilon_{ts}}\right) \quad \text{(F.35d)}$$

Step 7 – Determining the lever arms of the internal forces in relation to the top fibre

$$b_{cc,1} = \frac{x'}{2} \quad \text{(F.36a)}$$

$$b_{cc,2} = x' + \frac{\left(x - x'\right)}{3} = \frac{x + 2x'}{3} \quad \text{(F.36b)}$$

$$b_{cs} = c_{sc} \quad \text{(F.36c)}$$

$$b_{ts} = h - c_{st} = d_{st} \quad \text{(F.36d)}$$

$$b_{tf} = h - c_f = d_f \quad \text{(F.36e)}$$

Step 8 – Bending moment

$$M_{yield} = \sum_i^n F_{ti} \cdot b_{ti} - \sum_j^m F_{cj} \cdot b_{cj} \quad \text{(F.37a)}$$

$$M_{yield} = F_{ts} b_{ts} + F_{tf} b_{tf} - F_{cc,1} b_{cc,1} - F_{cc,2} b_{cc,2} - F_{cs} b_{cs} \quad \text{(F.37b)}$$

Step 9 – Simplification of the bending moment by substituting Eqs. F.31 and F.36 in Eq. F.37b

$$M_{yield} = f_{st} A_{st} d_{st} + E_f \left(\varepsilon_{tf} + \Delta\varepsilon_{tf}\right) A_f d_f - f_{cc} b x' \frac{x'}{2} - \frac{1}{2} f_{cc} b\left(x - x'\right) \frac{x + 2x'}{3} - E_{sc} \varepsilon_{cs} A_{sc} c_{sc} \Leftrightarrow \quad \text{(F.38b)}$$

$$\Leftrightarrow M_{yield} = -f_{cc} b \left(\frac{x'^2}{2} + \frac{x^2 + xx' - 2x'^2}{6} \right) + f_{st} A_{st} d_{st} + E_f \left(\varepsilon_{tf} + \Delta\varepsilon_{tf} \right) A_f d_f - E_{sc} \varepsilon_{cs} A_{sc} c_{sc} \Leftrightarrow \quad \text{(F.38b)}$$

$$\Leftrightarrow M_{yield} = -\frac{f_{cc} b}{6} \left(3x'^2 + x^2 + xx' - 2x'^2 \right) + f_{st} A_{st} d_{st} + E_f \left(\varepsilon_{tf} + \Delta\varepsilon_{tf} \right) A_f d_f - E_{sc} \varepsilon_{cs} A_{sc} c_{sc} \Leftrightarrow \quad \text{(F.38b)}$$

$$\Leftrightarrow M_{yield} = -\frac{f_{cc} b}{6} \left(x^2 + xx' + x'^2 \right) + f_{st} A_{st} d_{st} + E_f \left(\varepsilon_{tf} + \Delta\varepsilon_{tf} \right) A_f d_f - E_{sc} \varepsilon_{cs} A_{sc} c_{sc} \quad \text{(F.38b)}$$

F.4 CURVATURE AND BENDING MOMENT AT FAILURE

F.4.1 Design Assumption 1

The strain and stress diagram depicted in Figure F.3 is applicable, but in this case, ε_{ts} is unknown and the elastic modulus of concrete is E'_c.

Step 1 – Boundary conditions

$$0.3 f_{cc} / E_c \le \varepsilon_{cc} \le \varepsilon_{c3} \quad \text{(F.39a)}$$

$$\varepsilon_{cs} \le \frac{f_{sc}}{E_{sc}} \quad \text{(F.39b)}$$

$$\varepsilon_{ts} \ge \frac{f_{st}}{E_{st}} \quad \text{(F.39c)}$$

$$\varepsilon_{tf} + \Delta\varepsilon_{tf} = \frac{f_f}{E_f} \quad \text{(F.39d)}$$

Step 2 – Geometrical relationships between strains

$$\frac{\varepsilon_{cc}}{x} = \frac{\Delta\varepsilon_{tf}}{h - x - c_f} \Leftrightarrow \varepsilon_{cc} = \frac{x}{d_f - x} \Delta\varepsilon_{tf} \quad \text{(F.40a)}$$

$$\frac{\varepsilon_{cs}}{x - c_{sc}} = \frac{\Delta\varepsilon_{tf}}{h - x - c_f} \Leftrightarrow \varepsilon_{cs} = \frac{x - c_{sc}}{d_f - x} \Delta\varepsilon_{tf} \quad \text{(F.40b)}$$

Step 3 - Quantification of the internal loads

$$F_{cc} = \frac{1}{2} E'_c \varepsilon_{cc} \cdot bx \quad \text{(F.41a)}$$

$$F_{cs} = E_{sc} \varepsilon_{cs} \cdot A_{sc} \quad \text{(F.41b)}$$

$$F_{ts} = f_{st} \cdot A_{st} \quad \text{(F.41c)}$$

$$F_{tf} = E_f \left(\varepsilon_{tf} + \Delta\varepsilon_{tf} \right) \cdot A_f \quad \text{(F.41d)}$$

Step 4 – Equilibrium of internal forces

$$\sum_{i}^{n} F_{ti} - \sum_{j}^{m} F_{cj} = 0 \tag{F.42a}$$

$$F_{ts} + F_{tf} - F_{cc} - F_{cs} = 0 \tag{F.42b}$$

$$f_{st} A_{st} + E_f \left(\varepsilon_{tf} + \Delta\varepsilon_{tf} \right) A_f - \frac{1}{2} E_c' \varepsilon_{cc} bx - E_{sc} \varepsilon_{cs} A_{sc} = 0 \tag{F.42c}$$

Step 5 – Substituting Eq. F.40 in Eq. F.42c

$$f_{st} A_{st} + E_f \left(\varepsilon_{tf} + \Delta\varepsilon_{tf} \right) A_f - \frac{1}{2} E_c' \left(\frac{x}{d_f - x} \Delta\varepsilon_{tf} \right) bx - E_{sc} \left(\frac{x - c_{sc}}{d_f - x} \Delta\varepsilon_{tf} \right) A_{sc} = 0 \Leftrightarrow \tag{F.43a}$$

$$\Leftrightarrow f_{st} A_{st} \frac{\left(d_f - x \right) \Delta\varepsilon_{tf}}{\left(d_f - x \right) \Delta\varepsilon_{tf}} + E_f \left(\varepsilon_{tf} + \Delta\varepsilon_{tf} \right) A_f \frac{\left(d_f - x \right) \Delta\varepsilon_{tf}}{\left(d_f - x \right) \Delta\varepsilon_{tf}} - \frac{1}{2} E_c' \left(\frac{x}{d_f - x} \Delta\varepsilon_{tf} \right) bx + \\ - E_{sc} \left(\frac{x - c_{sc}}{d_f - x} \Delta\varepsilon_{tf} \right) A_{sc} = 0 \Leftrightarrow \tag{F.43b}$$

$$\Leftrightarrow f_{st} A_{st} \frac{\left(d_f - x \right)}{\Delta\varepsilon_{tf}} + E_f \left(\varepsilon_{tf} + \Delta\varepsilon_{tf} \right) A_f \frac{\left(d_f - x \right)}{\Delta\varepsilon_{tf}} - \frac{1}{2} E_c' bx^2 - E_{sc} A_{sc} \left(x - c_{sc} \right) = 0 \Leftrightarrow \tag{F.43c}$$

$$\Leftrightarrow \frac{1}{2} E_c' bx^2 + E_{sc} A_{sc} \left(x - c_{sc} \right) - \frac{f_{st} A_{st}}{\Delta\varepsilon_{tf}} \left(d_f - x \right) - E_f \varepsilon_{tf} A_f \frac{\left(d_f - x \right)}{\Delta\varepsilon_{tf}} - E_f A_f \left(d_f - x \right) = 0 \Leftrightarrow \tag{F.43d}$$

$$\Leftrightarrow \frac{1}{2} E_c' bx^2 + E_{sc} A_{sc} x - E_{sc} A_{sc} c_{sc} - \frac{f_{st} A_{st}}{\Delta\varepsilon_{tf}} d_f + \frac{f_{st} A_{st}}{\Delta\varepsilon_{tf}} x - \frac{E_f \varepsilon_{tf} A_f d_f}{\Delta\varepsilon_{tf}} + \frac{E_f \varepsilon_{tf} A_f}{\Delta\varepsilon_{tf}} x + \\ - E_f A_f d_f + E_f A_f x = 0 \Leftrightarrow \tag{F.43e}$$

$$\Leftrightarrow \frac{1}{2} E_c' bx^2 + \left(E_{sc} A_{sc} + \frac{f_{st} A_{st}}{\Delta\varepsilon_{tf}} + E_f A_f \left(1 + \frac{\varepsilon_{tf}}{\Delta\varepsilon_{tf}} \right) \right) x + \\ - \left(E_{sc} A_{sc} c_{sc} + \left(\frac{f_{st} A_{st}}{\Delta\varepsilon_{tf}} + E_f A_f \left(1 + \frac{\varepsilon_{tf}}{\Delta\varepsilon_{tf}} \right) \right) d_f \right) = 0 \tag{F.43f}$$

Step 6 – Solution of the quadratic equation

As in this case $2Ax + B \geq 0$,

$$x = \frac{-B + \sqrt{B^2 - 4AC}}{2A} \tag{F.44a}$$

$$A = \frac{1}{2} E_c' b \tag{F.44b}$$

$$B = E_{sc} A_{sc} + \frac{f_{st} A_{st}}{\Delta\varepsilon_{tf}} + E_f A_f \left(1 + \frac{\varepsilon_{tf}}{\Delta\varepsilon_{tf}}\right) \tag{F.44c}$$

$$C = -\left(E_{sc} A_{sc} c_{sc} + \left(\frac{f_{st} A_{st}}{\Delta\varepsilon_{tf}} + E_f A_f \left(1 + \frac{\varepsilon_{tf}}{\Delta\varepsilon_{tf}}\right)\right) d_f\right) \tag{F.44d}$$

Step 7 – Determining the lever arms of the internal forces in relation to the top fibre

$$b_{cc} = \frac{x}{3} \tag{F.45a}$$

$$b_{cs} = c_{sc} \tag{F.45b}$$

$$b_{ts} = h - c_{st} = d_{st} \tag{F.45c}$$

$$b_{tf} = h - c_f = d_f \tag{F.45d}$$

Step 8 – Bending moment

$$M_{ultimate} = \sum_i^n F_{ti} \cdot b_{ti} - \sum_j^m F_{cj} \cdot b_{cj} \tag{F.46a}$$

$$M_{ultimate} = F_{ts} b_{ts} + F_{tf} b_{tf} - F_{cc} b_{cc} - F_{cs} b_{cs} \tag{F.46b}$$

Step 9 – Simplification of the bending moment by substituting Eqs. F.21 and F.26 in Eq. F.46b

$$M_{ultimate} = -\frac{1}{6} E_c' \varepsilon_{cc} b x^2 - E_{sc} \varepsilon_{cs} A_{sc} c_{sc} + f_{st} A_{st} d_{st} + E_f \left(\varepsilon_{tf} + \Delta\varepsilon_{tf}\right) A_f d_f \tag{F.47}$$

F.4.2 Design assumption 2

The strain and stress diagram depicted in Figure F.4 is applicable, but in this case, ε_{ts} is unknown.

Step 1 – Boundary conditions

$$f_{cc} / E_c \le \varepsilon_{cc} \le \varepsilon_{c3} \tag{F.48a}$$

$$\varepsilon_{cs} \le \frac{f_y}{E_{sc}} \tag{F.48b}$$

$$\varepsilon_{ts} \geq \frac{f_y}{E_{st}} \tag{F.48c}$$

$$\varepsilon_{tf} + \Delta\varepsilon_{tf} = \frac{f_f}{E_f} \tag{F.48d}$$

Step 2 – Geometrical relationships between strains

$$\frac{\varepsilon_{cc}}{x} = \frac{\Delta\varepsilon_{tf}}{h - x - c_f} \Leftrightarrow \varepsilon_{cc} = \frac{x}{d_f - x}\Delta\varepsilon_{tf} \tag{F.49a}$$

$$\frac{\varepsilon_{cs}}{x - c_{sc}} = \frac{\Delta\varepsilon_{tf}}{h - x - c_f} \Leftrightarrow \varepsilon_{cs} = \frac{x - c_{sc}}{d_f - x}\Delta\varepsilon_{tf} \tag{F.49b}$$

$$\frac{\Delta\varepsilon_{tf}}{h - x - c_f} = \frac{\varepsilon_{c3}}{x - x'} \Leftrightarrow x' = \frac{\left(\varepsilon_{c3} + \Delta\varepsilon_{tf}\right)x - d_f\varepsilon_{c3}}{\Delta\varepsilon_{tf}} \tag{F.49c}$$

Step 3 - Quantification of the internal loads

$$F_{cc,1} = f_{cc} \cdot bx' \tag{F.50a}$$

$$F_{cc,1} = \frac{1}{2} f_{cc} \cdot b\left(x - x'\right) \tag{F.50b}$$

$$F_{cs} = E_{sc}\varepsilon_{cs} \cdot A_{sc} \tag{F.50c}$$

$$F_{ts} = E_{st}\varepsilon_{ts} \cdot A_{st} = f_{st} \cdot A_{st} \tag{F.50d}$$

$$F_{tf} = E_f\left(\varepsilon_{tf} + \Delta\varepsilon_{tf}\right) \cdot A_f \tag{F.50e}$$

Step 4 – Equilibrium of internal forces

$$\sum_i^n F_{ti} - \sum_j^m F_{cj} = 0 \tag{F.51a}$$

$$F_{ts} + F_{tf} - F_{cc,1} - F_{cc,2} - F_{cs} = 0 \tag{F.51b}$$

$$f_{st}A_{st} + E_f\left(\varepsilon_{tf} + \Delta\varepsilon_{tf}\right)A_f - f_{cc}bx' - \frac{1}{2} f_{cc}b\left(x - x'\right) - E_{sc}\varepsilon_{cs}A_{sc} = 0 \tag{F.51c}$$

Step 5 – Substituting Eq. F.49 in Eq. F.51c.

$$f_{st}A_{st} + E_f\left(\varepsilon_{tf} + \Delta\varepsilon_{tf}\right)A_f - f_{cc}bx' - \frac{1}{2} f_{cc}b\left(x - x'\right) - E_{sc}\varepsilon_{cs}A_{sc} = 0 \Leftrightarrow \tag{F.52a}$$

$$\Leftrightarrow -\frac{f_{cc}b}{2}\left(2x' + \left(x - x'\right)\right) - E_{sc}\varepsilon_{cs}A_{sc} + f_{st}A_{st} + E_f\left(\varepsilon_{tf} + \Delta\varepsilon_{tf}\right)A_f = 0 \Leftrightarrow \tag{F.52b}$$

$$\Leftrightarrow \frac{f_{cc}b}{2}\left(x + x'\right) + E_{sc}\varepsilon_{cs}A_{sc} - f_{st}A_{st} - E_f\left(\varepsilon_{tf} + \Delta\varepsilon_{tf}\right)A_f = 0 \Leftrightarrow \tag{F.52c}$$

$$\Leftrightarrow \frac{f_{cc}b}{2}\left(x+\left(\frac{\left(\varepsilon_{c3}+\Delta\varepsilon_{tf} \right)x-d_f\varepsilon_{c3}}{\Delta\varepsilon_{tf}} \right) \right)+E_{sc}\left(\frac{x-c_{sc}}{d_f-x}\Delta\varepsilon_{tf} \right)A_{sc}+ \\ -f_{st}A_{st}-E_f\varepsilon_{tf}A_f-E_f\Delta\varepsilon_{tf}A_f=0\Leftrightarrow \tag{F.52d}$$

$$\Leftrightarrow \frac{f_{cc}b}{2}\left(\frac{\Delta\varepsilon_{tf}x}{\Delta\varepsilon_{tf}}+\left(\frac{\left(\varepsilon_{c3}+\Delta\varepsilon_{tf} \right)x-d_f\varepsilon_{c3}}{\Delta\varepsilon_{tf}} \right)\frac{\left(d_f-x \right)\Delta\varepsilon_{tf}}{\left(d_f-x \right)\Delta\varepsilon_{tf}} \right)+E_{sc}\left(\frac{x-c_{sc}}{d_f-x}\Delta\varepsilon_{tf} \right)A_{sc}+ \\ -f_{st}A_{st}\frac{\left(d_f-x \right)\Delta\varepsilon_{tf}}{\left(d_f-x \right)\Delta\varepsilon_{tf}}-E_f\varepsilon_{tf}A_f\frac{\left(d_f-x \right)\Delta\varepsilon_{tf}}{\left(d_f-x \right)\Delta\varepsilon_{tf}}-E_f\Delta\varepsilon_{tf}A_f\frac{\left(d_f-x \right)}{\left(d_f-x \right)}=0\Leftrightarrow \tag{F.52e}$$

$$\Leftrightarrow \frac{f_{cc}b}{2\Delta\varepsilon_{tf}^{\,2}}\left(\Delta\varepsilon_{tf}x+\left(\varepsilon_{c3}+\Delta\varepsilon_{tf} \right)x-d_f\varepsilon_{c3} \right)\left(d_f-x \right)+E_{sc}A_{sc}\left(x-c_{sc} \right)+ \\ -\frac{f_{st}A_{st}}{\Delta\varepsilon_{tf}}\left(d_f-x \right)-\frac{E_f\varepsilon_{tf}A_f}{\Delta\varepsilon_{tf}}\left(d_f-x \right)-E_fA_f\left(d_f-x \right)=0\Leftrightarrow \tag{F.52f}$$

$$\Leftrightarrow \frac{f_{cc}b}{2\Delta\varepsilon_{tf}^{\,2}}\left(\Delta\varepsilon_{tf}x+\varepsilon_{c3}x+\Delta\varepsilon_{tf}x-d_f\varepsilon_{c3} \right)\left(d_f-x \right)+E_{sc}A_{sc}\left(x-c_{sc} \right)+ \\ -\frac{f_{st}A_{st}}{\Delta\varepsilon_{tf}}\left(d_f-x \right)-\frac{E_f\varepsilon_{tf}A_f}{\Delta\varepsilon_{tf}}\left(d_f-x \right)-E_fA_f\left(d_f-x \right)=0\Leftrightarrow \tag{F.52g}$$

$$\Leftrightarrow \frac{f_{cc}b}{2\Delta\varepsilon_{tf}^{\,2}}\left(\left(\varepsilon_{c3}+2\Delta\varepsilon_{tf} \right)x-d_f\varepsilon_{c3} \right)\left(d_f-x \right)+E_{sc}A_{sc}\left(x-c_{sc} \right)+ \\ -\frac{f_{st}A_{st}}{\Delta\varepsilon_{tf}}\left(d_f-x \right)-\frac{E_f\varepsilon_{tf}A_f}{\Delta\varepsilon_{tf}}\left(d_f-x \right)-E_fA_f\left(d_f-x \right)=0\Leftrightarrow \tag{F.52h}$$

$$\Leftrightarrow \frac{f_{cc}b}{2\Delta\varepsilon_{tf}^{\,2}}\left(-\left(\varepsilon_{c3}+2\Delta\varepsilon_{tf} \right)x^2+2d_f\left(\varepsilon_{c3}+\Delta\varepsilon_{tf} \right)x-d_f^{\,2}\varepsilon_{c3} \right)+E_{sc}A_{sc}x-E_{sc}A_{sc}c_{sc}+ \\ -\frac{f_{st}A_{st}d_f}{\Delta\varepsilon_{tf}}+\frac{f_{st}A_{st}}{\Delta\varepsilon_{tf}}x-\frac{E_f\varepsilon_{tf}A_fd_f}{\Delta\varepsilon_{tf}}+\frac{E_f\varepsilon_{tf}A_f}{\Delta\varepsilon_{tf}}x-E_fA_fd_f+E_fA_fx=0\Leftrightarrow \tag{F.52i}$$

$$\Leftrightarrow -\frac{f_{cc}b\left(\varepsilon_{c3}+2\Delta\varepsilon_{tf} \right)}{2\Delta\varepsilon_{tf}^{\,2}}x^2+\frac{f_{cc}bd_f\left(\varepsilon_{c3}+\Delta\varepsilon_{tf} \right)}{\Delta\varepsilon_{tf}^{\,2}}x+E_{sc}A_{sc}x+\frac{f_{st}A_{st}}{\Delta\varepsilon_{tf}}x+\frac{E_f\varepsilon_{tf}A_f}{\Delta\varepsilon_{tf}}x+ \\ +E_fA_fx-\frac{f_{cc}bd_f^{\,2}\varepsilon_{c3}}{2\Delta\varepsilon_{tf}^{\,2}}-E_{sc}A_{sc}c_{sc}-\frac{f_{st}A_{st}d_f}{\Delta\varepsilon_{tf}}-\frac{E_f\varepsilon_{tf}A_fd_f}{\Delta\varepsilon_{tf}}-E_fA_fd_f=0\Leftrightarrow \tag{F.52j}$$

$$\Leftrightarrow \frac{f_{cc}b\left(\varepsilon_{c3}+2\Delta\varepsilon_{tf} \right)}{2\Delta\varepsilon_{tf}^{\,2}}x^2-\left(\frac{f_{cc}bd_f\left(\varepsilon_{c3}+\Delta\varepsilon_{tf} \right)}{\Delta\varepsilon_{tf}^{\,2}}+E_{sc}A_{sc}+\frac{f_{st}A_{st}}{\Delta\varepsilon_{tf}}+E_fA_f\left(1+\frac{\varepsilon_{tf}}{\Delta\varepsilon_{tf}} \right) \right)x+ \\ +\left(\frac{f_{cc}bd_f^{\,2}\varepsilon_{c3}}{2\Delta\varepsilon_{tf}^{\,2}}+E_{sc}A_{sc}c_{sc}+\left(\frac{f_{st}A_{st}}{\Delta\varepsilon_{tf}}+E_fA_f\left(1+\frac{\varepsilon_{tf}}{\Delta\varepsilon_{tf}} \right) \right)d_f \right)=0 \tag{F.52k}$$

Step 6 – Solution of the quadratic equation

As all the constants used for the determination of A and B are positive and $d_f > x$

$$2Ax + B = \frac{2 f_{cc} b\left(\varepsilon_{c3} + 2\Delta\varepsilon_{tf}\right)}{2\Delta\varepsilon_{tf}^{\ 2}} x + \\ -\left(\frac{f_{cc} b d_f \left(\varepsilon_{c3} + \Delta\varepsilon_{tf}\right)}{\Delta\varepsilon_{tf}^{\ 2}} + E_{sc} A_{sc} + \frac{f_{st} A_{st}}{\Delta\varepsilon_{tf}} + E_f A_f \left(1 + \frac{\varepsilon_{tf}}{\Delta\varepsilon_{tf}}\right)\right) \Leftrightarrow \tag{F.53a}$$

$$\Leftrightarrow 2Ax + B = \frac{f_{cc} b\left(\varepsilon_{c3} + 2\Delta\varepsilon_{tf}\right)}{\Delta\varepsilon_{tf}^{\ 2}} x + \\ -\left(\frac{f_{cc} b d_f \left(\varepsilon_{c3} + \Delta\varepsilon_{tf}\right)}{\Delta\varepsilon_{tf}^{\ 2}} + E_{sc} A_{sc} + \frac{f_{st} A_{st}}{\Delta\varepsilon_{tf}} + E_f A_f \left(1 + \frac{\varepsilon_{tf}}{\Delta\varepsilon_{tf}}\right)\right) \Leftrightarrow \tag{F.53b}$$

$$\Leftrightarrow 2Ax + B = \frac{f_{cc} b \Delta\varepsilon_{tf}}{\Delta\varepsilon_{tf}^{\ 2}} x + \\ -\left(\frac{f_{cc} b\left(\varepsilon_{c3} + \Delta\varepsilon_{tf}\right)}{\Delta\varepsilon_{tf}^{\ 2}} \left(d_f - x\right) + E_{sc} A_{sc} + \frac{f_{st} A_{st}}{\Delta\varepsilon_{tf}} + E_f A_f \left(1 + \frac{\varepsilon_{tf}}{\Delta\varepsilon_{tf}}\right)\right) \tag{F.53c}$$

Since $\left(\varepsilon_{c3} + \Delta\varepsilon_{tf}\right)\left(d_f - x\right) > \Delta\varepsilon_{tf} x$, the only positive term is absorbed by the remaining expression and therefore, the condition is found to be lower than zero.

$$x = \frac{-B - \sqrt{B^2 - 4AC}}{2A} \tag{F.54a}$$

$$A = \frac{f_{cc} b\left(\varepsilon_{c3} + 2\Delta\varepsilon_{tf}\right)}{2\Delta\varepsilon_{tf}^{\ 2}} \tag{F.54b}$$

$$B = -\left(\frac{f_{cc} b d_f \left(\varepsilon_{c3} + \Delta\varepsilon_{tf}\right)}{\Delta\varepsilon_{tf}^{\ 2}} + E_{sc} A_{sc} + \frac{f_{st} A_{st}}{\Delta\varepsilon_{tf}} + E_f A_f \left(1 + \frac{\varepsilon_{tf}}{\Delta\varepsilon_{tf}}\right)\right) \tag{F.54c}$$

$$C = \frac{f_{cc} b d_f^{\ 2} \varepsilon_{c3}}{2\Delta\varepsilon_{tf}^{\ 2}} + E_{sc} A_{sc} c_{sc} + \left(\frac{f_{st} A_{st}}{\Delta\varepsilon_{tf}} + E_f A_f \left(1 + \frac{\varepsilon_{tf}}{\Delta\varepsilon_{tf}}\right)\right) d_f \tag{F.54d}$$

Step 7 – Internal arms of the forces

$$b_{cc,1} = \frac{x'}{2} \tag{F.55a}$$

$$b_{cc,2} = x' + \frac{\left(x - x'\right)}{3} = \frac{x + 2x'}{3} \tag{F.55b}$$

$$b_{cs} = c_{sc} \tag{F.55c}$$

$$b_{ts} = h - c_{st} = d_{st} \tag{F.55d}$$

$$b_{tf} = h - c_f = d_f \tag{F.55e}$$

Step 8 – Bending moment

$$M_{ultimate} = \sum_{i}^{n} F_{ti} \cdot b_{ti} - \sum_{j}^{m} F_{cj} \cdot b_{cj} \tag{F.56a}$$

$$M_{ultimate} = F_{ts} b_{ts} + F_{tf} b_{tf} - F_{cc,1} b_{cc,1} - F_{cc,2} b_{cc,2} - F_{cs} b_{cs} \tag{F.56b}$$

Step 9 – Simplification of the bending moment by substituting Eqs. F.50 and F.55 in Eq. F.56b

$$M_{ultimate} = -\frac{f_{cc} b}{6}\left(x^2 + xx' + x'^2\right) + f_{st} A_{st} d_{st} + E_f \left(\varepsilon_{tf} + \Delta\varepsilon_{tf}\right) A_f d_f - E_{sc} \varepsilon_{cs} A_{sc} c_{sc} \tag{F.57}$$

F.4.3 Design assumption 3

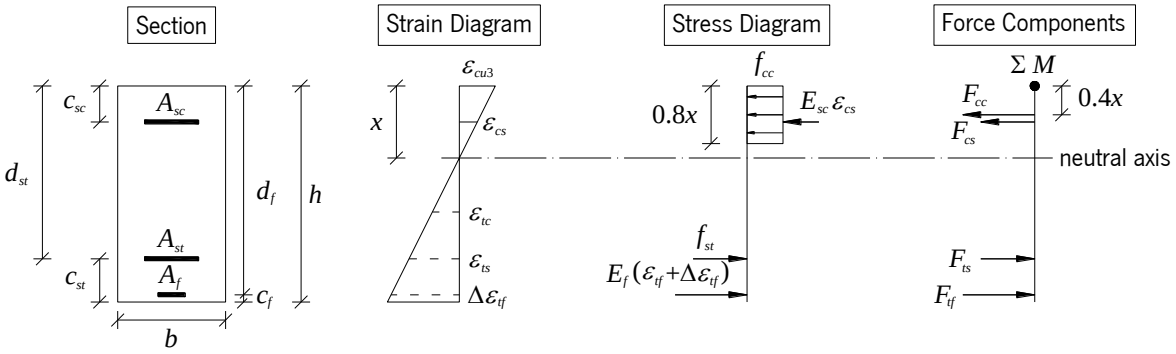

Figure F.5 – Strain and stress diagram of the cross section at failure – Design assumption 3.

Step 1 – Boundary conditions

$$\varepsilon_{cc} = \varepsilon_{cu3} \tag{F.58a}$$

$$\varepsilon_{cs} \le \frac{f_y}{E_{sc}} \tag{F.58b}$$

$$\varepsilon_{ts} \ge \frac{f_y}{E_{st}} \tag{F.58c}$$

$$\varepsilon_{tf} + \Delta\varepsilon_{tf} \le \frac{f_f}{E_f} \tag{F.58d}$$

Step 2 – Geometrical relationships between strains

$$\frac{\varepsilon_{cs}}{x - c_{sc}} = \frac{\varepsilon_{cc}}{x} \Leftrightarrow \varepsilon_{cs} = \frac{x - c_{sc}}{x} \varepsilon_{cc} \tag{F.59a}$$

$$\frac{\Delta\varepsilon_{tf}}{h - x - c_f} = \frac{\varepsilon_{cc}}{x} \Leftrightarrow \Delta\varepsilon_{tf} = \frac{d_f - x}{x} \varepsilon_{cc} \tag{F.59b}$$

Step 3 – Quantification of the internal loads

$$F_{cc} = f_{cc} \cdot b \cdot 0.8x \tag{F.60a}$$

$$F_{cs} = E_{sc}\varepsilon_{cs} \cdot A_{sc} \tag{F.60b}$$

$$F_{ts} = f_{st} \cdot A_{st} \tag{F.60c}$$

$$F_{tf} = E_f \left(\varepsilon_{tf} + \Delta\varepsilon_{tf}\right) \cdot A_f \tag{F.60d}$$

Step 4 – Equilibrium of internal forces

$$\sum_i^n F_{ti} - \sum_j^m F_{cj} = 0 \tag{F.61a}$$

$$F_{ts} + F_{tf} - F_{cc} - F_{cs} = 0 \tag{F.61b}$$

$$f_{st}A_{st} + E_f \left(\varepsilon_{tf} + \Delta\varepsilon_{tf}\right)A_f - 0.8 f_{cc} bx - E_{sc}\varepsilon_{cs}A_{sc} = 0 \tag{F.61c}$$

Step 5 – Substituting Eq. F.59 in Eq. F.61c.

$$f_{st}A_{st} + E_f \left(\varepsilon_{tf} + \Delta\varepsilon_{tf}\right)A_f - 0.8 f_{cc} bx - E_{sc}\varepsilon_{cs}A_{sc} = 0 \Leftrightarrow \tag{F.62a}$$

$$\Leftrightarrow f_{st}A_{st} + E_f \left(\varepsilon_{tf} + \left(\frac{d_f - x}{x}\varepsilon_{cc}\right)\right)A_f - 0.8 f_{cc} bx - E_{sc}\left(\frac{x - c_{sc}}{x}\varepsilon_{cc}\right)A_{sc} = 0 \Leftrightarrow \tag{F.62b}$$

$$\Leftrightarrow f_{st}A_{st}\frac{x\varepsilon_{cc}}{x\varepsilon_{cc}} + E_f \left(\frac{x\varepsilon_{tf}}{x} + \left(\frac{d_f - x}{x}\varepsilon_{cc}\right)\right)A_f \frac{x\varepsilon_{cc}}{x\varepsilon_{cc}} - 0.8 f_{cc} bx \frac{x\varepsilon_{cc}}{x\varepsilon_{cc}} - E_{sc}\left(\frac{x - c_{sc}}{x}\varepsilon_{cc}\right)A_{sc} = 0 \Leftrightarrow \tag{F.62c}$$

$$\Leftrightarrow \frac{f_{st}A_{st}}{\varepsilon_{cc}}x + \left(x\varepsilon_{tf} + \left(d_f - x\right)\varepsilon_{cc}\right)\frac{E_f A_f}{\varepsilon_{cc}} - \frac{0.8 f_{cc} b}{\varepsilon_{cc}}x^2 - E_{sc}A_{sc}\left(x - c_{sc}\right) = 0 \Leftrightarrow \tag{F.62d}$$

$$\Leftrightarrow \frac{0.8 f_{cc} b}{\varepsilon_{cc}}x^2 + E_{sc}A_{sc}\left(x - c_{sc}\right) - \frac{f_{st}A_{st}}{\varepsilon_{cc}}x - \left(x\varepsilon_{tf} + \left(d_f - x\right)\varepsilon_{cc}\right)\frac{E_f A_f}{\varepsilon_{cc}} = 0 \Leftrightarrow \tag{F.62e}$$

$$\Leftrightarrow \frac{0.8 f_{cc} b}{\varepsilon_{cc}}x^2 + E_{sc}A_{sc}x - E_{sc}A_{sc}c_{sc} - \frac{f_{st}A_{st}}{\varepsilon_{cc}}x - \left(\left(\varepsilon_{tf} - \varepsilon_{cc}\right)x + d_f\varepsilon_{cc}\right)\frac{E_f A_f}{\varepsilon_{cc}} = 0 \Leftrightarrow \tag{F.62f}$$

$$\Leftrightarrow \frac{0.8 f_{cc} b}{\varepsilon_{cc}}x^2 + E_{sc}A_{sc}x - E_{sc}A_{sc}c_{sc} - \frac{f_{st}A_{st}}{\varepsilon_{cc}}x - \frac{E_f A_f \left(\varepsilon_{tf} - \varepsilon_{cc}\right)}{\varepsilon_{cc}}x - E_f A_f d_f = 0 \Leftrightarrow \tag{F.62g}$$

$$\Leftrightarrow \frac{0.8 f_{cc} b}{\varepsilon_{cc}}x^2 + E_{sc}A_{sc}x - \frac{f_{st}A_{st}}{\varepsilon_{cc}}x - \frac{E_f A_f \left(\varepsilon_{tf} - \varepsilon_{cc}\right)}{\varepsilon_{cc}}x - E_{sc}A_{sc}c_{sc} - E_f A_f d_f = 0 \Leftrightarrow \tag{F.62h}$$

$$\Leftrightarrow 0.8 f_{cc} bx^2 + \left(E_{sc}A_{sc}\varepsilon_{cc} - f_{st}A_{st} - E_f A_f \left(\varepsilon_{tf} - \varepsilon_{cc}\right)\right)x - \left(E_{sc}A_{sc}c_{sc} + E_f A_f d_f\right)\varepsilon_{cc} = 0 \tag{F.62i}$$

Step 6 – Solution of the quadratic equation

Since A and C have opposite signals, the discriminant of the quadratic formula is positive in all cases, this equation always yields two real solutions. However, it is not possible to guarantee in this case, using algebraic notation, that $2Ax + B \geq 0$. For these reasons, and considering that $\sqrt{B^2 - 4AC} = |B| + |D|$,

$$x = \frac{-B \pm \left(|B| + |D|\right)}{2A} \tag{F.63a}$$

$$x = \begin{cases} B < 0 \Rightarrow x = \dfrac{|B| + \left(|B| + |D|\right)}{2A} \Leftrightarrow x = \dfrac{|B| + |B| + |D|}{2A} \Leftrightarrow x = \dfrac{2|B| + |D|}{2A} > 0 & \checkmark \\ B < 0 \Rightarrow x = \dfrac{|B| - \left(|B| + |D|\right)}{2A} \Leftrightarrow x = \dfrac{|B| - |B| - |D|}{2A} \Leftrightarrow x = -\dfrac{|D|}{2A} < 0 & \times \\ B > 0 \Rightarrow x = \dfrac{-|B| + \left(|B| + |D|\right)}{2A} \Leftrightarrow x = \dfrac{-|B| + |B| + |D|}{2A} \Leftrightarrow x = \dfrac{|D|}{2A} > 0 & \checkmark \\ B > 0 \Rightarrow x = \dfrac{-|B| - \left(|B| + |D|\right)}{2A} \Leftrightarrow x = \dfrac{-|B| - |B| - |D|}{2A} \Leftrightarrow x = -\dfrac{2|B| + |D|}{2A} < 0 & \times \end{cases} \tag{F.63b}$$

Consequently, regardless the signal of B, the neutral axis is always given by the positive signal.

$$x = \frac{-B + \sqrt{B^2 - 4AC}}{2A} \tag{F.64a}$$

$$A = 0.8 f_{cc} b \varepsilon_{cc} \tag{F.64b}$$

$$B = E_{sc} A_{sc} \varepsilon_{cc} - f_{st} A_{st} - E_f A_f \left(\varepsilon_{tf} - \varepsilon_{cc}\right) \tag{F.64c}$$

$$C = -\left(E_{sc} A_{sc} c_{sc} + E_f A_f d_f\right) \varepsilon_{cc} \tag{F.64d}$$

Step 7 – Determining the lever arms of the internal forces in relation to the top fibre

$$b_{cc} = 0.4x \tag{F.65a}$$

$$b_{cs} = c_{sc} \tag{F.65b}$$

$$b_{ts} = h - c_{st} = d_{st} \tag{F.65c}$$

$$b_{tf} = h - c_f = d_f \tag{F.65d}$$

Step 8 – Bending moment

$$M_{yield} = \sum_i^n F_{ti} \cdot b_{ti} - \sum_j^m F_{cj} \cdot b_{cj} \tag{F.66a}$$

$$M_{yield} = F_{ts} b_{ts} + F_{tf} b_{tf} - F_{cc} b_{cc} - F_{cs} b_{cs} \tag{F.66b}$$

Step 9 – Simplification of the bending moment by substituting Eqs. F.60 and F.65 in Eq. F.66b

$$M_{ultimate} = -0.32 f_{cc} b x^2 - E_{sc} \varepsilon_{cs} A_{sc} c_{sc} + f_{st} A_{st} d_{st} + E_f \left(\varepsilon_{tf} + \Delta\varepsilon_{tf}\right) A_f d_f \tag{F.67}$$